SANDIA REPORT

SAND2009-4164
Unlimited Release
Printed July 2009

Handbook on Dynamics of Jointed Structures

Daniel J. Segalman, Danny L. Gregory, Michael J. Starr,
Brian R. Resor, Michael D. Jew, James P. Lauffer, & Nicoli M. Ames

Prepared by
Sandia National Laboratories
Albuquerque, New Mexico 87185 and Livermore, California 94550

Sandia is a multiprogram laboratory operated by Sandia Corporation,
a Lockheed Martin Company, for the United States Department of Energy's
National Nuclear Security Administration under Contract DE-AC04-94-AL85000.

Issued by Sandia National Laboratories, operated for the United States Department of Energy by Sandia Corporation.

Available to DOE and DOE contractors from
U.S. Department of Energy
Office of Scientific and Technical Information
P.O. Box 62
Oak Ridge, TN 37831

Telephone: (865) 576-8401
Facsimile: (865) 576-5728
E-Mail: reports@adonis.osti.gov
Online ordering: http://www.osti.gov/bridge

Available to the public from
U.S. Department of Commerce
National Technical Information Service
5285 Port Royal Rd
Springfield, VA 22161

Telephone: (800) 553-6847
Facsimile: (703) 605-6900
E-Mail: orders@ntis.fedworld.gov
Online ordering: http://www.ntis.gov/help/ordermethods.asp?loc=7-4-0#online

SAND2009-4164
Unlimited Release
Printed July 2009

Handbook on Dynamics of Jointed Structures

Daniel J. Segalman, Danny L. Gregory, Michael J. Starr,
Brian R. Resor, Michael D. Jew, James P. Lauffer, & Nicoli M. Ames

Abstract

The problem of understanding and modeling the complicated physics underlying the action and response of the interfaces in typical structures under dynamic loading conditions has occupied researchers for many decades. This handbook presents an integrated approach to the goal of dynamic modeling of typical jointed structures, beginning with a mathematical assessment of experimental or simulation data, development of constitutive models to account for load histories to deformation, establishment of kinematic models coupling to the continuum models, and application of finite element analysis leading to dynamic structural simulation. In addition, formulations are discussed to mitigate the very short simulation time steps that appear to be required in numerical simulation for problems such as this.

This handbook satisfies the commitment to DOE that *Sandia will develop the technical content and write a Joints Handbook. The content will include: (1) Methods for characterizing the nonlinear stiffness and energy dissipation for typical joints used in mechanical systems and components. (2) The methodology will include practical guidance on experiments, and reduced order models that can be used to characterize joint behavior. (3) Examples for typical bolted and screw joints will be provided.*

Acknowledgment

The authors thank the many managers and members of technical staff who have worked on this challenging problem at various times since its inception. For all of them, this involved a tremendous amount of hard work and for our management team it involved taking a substantial risk. To put significant resources year-after-year into a problem that had so successfully resisted the best efforts of the scientific community can be a gutsy decision on the part of manager. The authors believe that we have justified our managers' faith in us.

Among the managers who should be recognized are David Martinez, James Redmond, Thomas Baca, David Clauss, Jamie Moya, and Peter Wilson. Besides the authors, the following members of the Sandia technical community have played significant roles sometimes repeatedly in the joints research program: Jeff Dohner, Ronald Hopkins, Donald Lobitz, David Epp, David Smallwood, Matt Sagartz, Fernando Bitsie,Todd Simmermacher, Randy Mayes, Brendan Rogillio, John Laing, Tom Paez, John Holland, and Anton Sumali. As the authors approached an important Level II Milepost, Mike Christian shared his expertise in technical writing to help maintain some coherence in this large document and Matt Brake helped with the translation of a crucial chapter from MS Word to LaTeX.

The support of two people not officially in our management chain should be recognized as well. T.Y. Chu has been a patient, insightful, and consistent supporter of this effort. He has been helpful in providing funding and advocacy and he has been especially effective in reminding us to stay focused. Dr. Kevin Greenaugh of NNSA showed early interest in the importance and depth of technical difficulty in these issues.

Finally we must acknowledge the valuable interactions that we have had with our colleagues in academia. In some cases our relationships were formal collaborations and in some cases we benefited from just helpful comments here and there. Among those whose collaborations have been especially valuable to us are Professor Lawrence Bergman of the University of Illinois Champaign-Urbana, Professor Alexander Vakakis of National Technical University of Athens, Professor David Ewins FRS of Imperial College London, Professor Dane Quinn of the University of Akron, Professor Kambiz Farhang of Southern Illinois University, Professor Daniel Kammer of the University of Wisconsin, Professor Edward Berger of the University of Virginia, and Professor Lothar Gaul of the University of Stuttgart.

Contents

List of Figures

List of Tables

Preface

The material presented in this monograph represents the efforts of many Sandians and our partners in their institutions over approximately a decade. Many people have cycled in and out of this effort over the years. The technical team has included experimentalists, computational modelers, and theoreticians. These have been Sandians, university researchers with whom we have had contractual relations, and many other friends in the research community who have contributed informally. Among the academics who have worked directly with Sandia on this effort are Professor Lawrence Bergman at the University of Illinois, Professor Dane Quinn of the University of Akron, and Professor Edward Berger of the University of Virginia. Additionally, there have been a series of very capable and supportive managers who managed to keep us focused and funded.

Beyond Sandia and its academic partners, there has been significant work done in the last decade in a number of other institutions and research communities. Two communities deserving special mention are David Ewins, FRS, his colleagues, and students at Imperial College London, and Lothar Gaul, and his colleagues and academic progeny at the University of Stuttgart. Each of these centers has collaborative relations with prominent researchers in other institutions around Europe. There are a number of scattered researchers around the US who have contributed to important recent publications on this topic, and interest in the US is gradually growing.

It is not the purpose of this monograph to provide an encyclopedic presentation of the literature on joints. Instead, the content is chosen to provide the reader the minimum guidance necessary to measure joint properties and to incorporate those properties into structural dynamics models. Additionally, some guidance is provided with respect to the use of evolving computational tools to estimate joint properties on an *ab initio* basis.

There is no intention to suggest that any of this technology is fully mature. In fact, it is only recently that models have been developed that can reproduce the properties of joints from which they are derived and calibrated. A similar statement can be made about joint measurement technology. Micro-modeling of joint mechanics is even more primitive. The significance of this monograph is that these technologies are now sufficiently mature that the engineering community can begin to use them in some engineering applications.

A serious effort has been made to make all elements appear well motivated, but this misrepresents how the work was actually done. The institutional motivation of pursuing this issue was clear at the beginning of this effort, but the proper forms in which to pose technical questions evolved over time. As in any other research effort, it was only by digging in and exploring that the key features of these problems and the appropriate research directions began to become clear. A discussion of appropriate future research directions is placed near the end of this work.

Finally, the authors take the opportunity to note that the presence of mixed units in this hand-

book is a reflection of the end of the cold war. Old specifications were written in inch-pound-second units, and much of our laboratory instrumentation remains calibrated in those units. Occasionally, measurements have been taken in newer research laboratories that are calibrated in the meter-Newton-second system and experimental results are reported in those units. We hope that the reader will bear with us.

Summary

Underground testing of nuclear weapons was discontinued by the United States in 1992. Even conventional testing is highly limited because of expense, environmental considerations, and logistic difficulty. These circumstances have motivated various technical and science-based campaigns aimed at stockpile stewardship, wherein the balance between computational simulation and test would be weighted increasingly on the side of simulation. This has occasioned investments both in computational resources and in the science that underlies core processes.

One of the key barriers to predictive structural dynamics of mechanical systems is an inability to incorporate the impact of mechanical joints on the structural response into structural dynamics predictions. Mechanical joints are ubiquitous in such built-up systems, including such diverse sorts of interfaces as threaded connections, tape joints [1, 2], and many configurations of bolted/lap joints.

As illustrated by the growing literature on structural dynamics of built-up systems, these issues extend to many areas beyond nuclear weapons. Examples of the economic impact of an inability to predict dynamics of such systems can be found in the certification/recertification of nuclear power plants and the design costs of jet engine components.

The problem of understanding and modeling the complicated physics underlying the action and response of the interfaces in typical structures under dynamic loading conditions has occupied researchers for many decades. This handbook reports on a ten year effort to address the problem, presenting an integrated approach to the goal of dynamic modeling of typical jointed structures, beginning with a mathematical assessment of experimental or simulation data, development of constitutive models to account for load histories to deformation, establishment of kinematic models coupling to the continuum models, and application of finite element analysis leading to dynamic structural simulation. In addition, formulations are discussed to mitigate the very short simulation time steps that appear to be required in numerical simulation for problems such as this.

This handbook satisfies the commitment to DOE that *Sandia will develop the technical content and write a Joints Handbook. The content will include: (1) Methods for characterizing the nonlinear stiffness and energy dissipation for typical joints used in weapon systems and components. (2) The methodology will include practical guidance on experiments, and reduced order models that can be used to characterize joint behavior. (3) Examples for typical bolted and screw joints will be provided.* These criteria are met specifically as follows

1. *Methods for characterizing the nonlinear stiffness and energy dissipation for typical joints used in mechanical systems and components.*

   The experimental characterization of lap type joints is presented in Chapters 3 through 5.1. Specific equations to express joint energy dissipation and joint stiffness in terms of mea-

sured properties are presented in Chapters 3, 5, and 11. Measurement of macroslip force is explained and illustrated in Chapter 7.

Corresponding measurements are presented and discussed on a mock AOS in Chapter 8.

2. *The methodology will include practical guidance on experiments, and reduced order models that can be used to characterize joint behavior.*

   Practical guidance to experiments is presented in experimental chapters, with special attention to shaker control in Chapter 6.

   The *whole-joint* strategy for capturing the key behavior of lap joints in low order models is presented in Chapter 12. A specific low order joint model is found in Chapter 12. Methods for deducing parameters for that model are presented in Appendix B.

   A strategy for representing a threaded connection with coarse meshes where the region of the threads is approximated by an anisotropic elastic material is presented in Chapter 13.

   Additional methods of structural level model reduction are presented in Chapter 17.

3. *Examples for typical bolted and screw joints will be provided.*

   Example calculations are presented in Chapter 18.

   The methods discussed above are illustrated in the calculation of structural response to blast type axial loads for a mock System A, AOS. The load path passes through the manufacturing joint and the nonlinearities of that joint are manifest in the predicted response.

   Linear structural response of a unclassified structure including the threaded connection that connects exterior aeroshell of System A mechanical system is calculated using the equivalent material method.

Nomenclature

AFM	Atomic Force Microscopy, page 467
AOS	Axially Oriented Subsystem, page 49
ASC	Advanced Scientific Computing, page 41
BMD	Big Mass Device, page 39
CMS	Component Mode Synthesis, page 439
DNS	Direct Numerical Simulation, page 37
EDM	Electric Discharge Machining, page 71
EMF	Electromagnetic Force, page 229
ESPI	Electronic Speckle Pattern Interferometry, page 291
FMFE	Fine Mesh Finite Element, page 473
GP	Genetic Programming, page 61
HWT	Harmonic Wavelet Transform, page 293
IFT	Inverse Fourier Transform, page 230
IIR	Inverse Impulse Response, page 230
LDV	Laser Doppler Vibrometer, page 62
LOS	Laterally Oriented Subsystem, page 158
LVDT	Linear Voltage Displacement Transducer, page 240
MDBF	Method of Discontinuous Basis Functions, page 441
MEMS	Micro-Electro Mechanical Systems, page 290
MPC	Multi-Point Constraint, page 296
RMS	Root Mean Squared, page 410
SDOF	Single Degree of Freedom, page 39
SNL	Sandia National Laboratories, page 27
SRS	Shock Response Spectrum, page 227
UQ	Uncertainty Quantification, page 33

Chapter 1

Introduction

Daniel J. Segalman

1.1 The Purpose of this Monograph

The research presented here was driven by the programmatic necessity of relying more on computer prediction and less on the massive testing program of the past. That predictive capability requires far better understanding and models for joint behavior than existed at the inception of this program. At the beginning of this effort there was a sense in some parts of the scientific community that computing alone could answer most of the outstanding questions. As investigation of the important joint phenomena progressed, it became clear the first and most important explorations would have to be experimental and that experimental results would guide the modeling and simulation efforts. Research presented here is the result of a very productive, synergistic collaboration of experiment, modeling, and computing. Despite this progress, the reader will see that there is still much to be done.

A number of contributing factors have motivated the writing of this document. Among those factors is the desire to preserve the products of a decade of research at Sandia National Laboratories (SNL). Another is to provide some guidance to those who must employ some sort of tool for incorporation of joint physics in structural modeling within our institution. Finally, and of probably greater importance, is the desire to provide a reasonable starting point to those people who might be interested in beginning research in joints and jointed structures.

The authors realize that they are presenting only a small part of what is known about experimental, theoretical, and computational aspects of joint mechanics and the modeling of built-up structures. For instance, we discuss only minimally the important work over the years of the team lead by David Ewins at Imperial College London or that by the team lead by Lothar Gaul of the University of Stuttgart. Nor do we discuss work by many other colleagues at the University of Michigan, Carnegie-Mellon University, or Oxford. On the other hand, by focusing on work that was performed for a single integrated purpose and using a single integrated strategy, we hope to provide a more coherent - though limited - discussion of the topic.

1.2 Qualities of Jointed Structures

There are many types of joints, but the mechanics of interfaces of built-up structures often most closely resemble those of lap joints. (Figure 1.1). These configurations involve normal compressive loads holding components together combined with dynamic lateral (and/or normal) loads inducing some amount of shear slip in the interface.

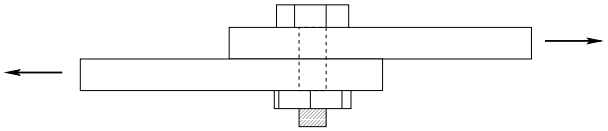

Figure 1.1. The Interface Mechanics of Built-up Structures Most Closely Resembles That of a Simple Lap Joint.

Exploring the physics of joints directly is not readily done because key interactions takes place at the interface of surfaces, where instrumentation cannot be placed without changing the problem. Indirect studies are obscured by the elastic compliances of specimens outside of the interface, of the test apparatus, and of the fixturing attachments [3]. From a combination of experiments, computer simulations, and reference to the few known analytic elastic contact solutions, the following qualitative joint behaviors have been identified:

As small extensional loads are applied to the specimen, along with all of the elastic response, a further compliance arises from the development of small slip zones within the contact patch. At higher loads, the extent of the slip region increases monotonically with load until the initiation of macroslip.[1] When the direction of loading is reversed, the contact patch instantaneously goes entirely into the "stuck" mode. As the magnitude of that reverse load increases, the slip zone again initiates and grows across the contact patch. The frictional energy dissipation that takes place in the slip zone is responsible for the vibration damping attributed to the joints.

The complexities of the slip process are responsible for the nonlinear nature of the interfaces, both in terms of stiffness and dissipation. The many attempts over the years to address and understand the detailed physics of this process are outlined in review articles by Berger [4], Gaul and Nitsche [5], and Ferri [6]. For the purposes of this introduction, it will be sufficient to summarize the key phenomenological properties of such interfaces.

Because of the issues of extraneous compliance discussed above, much experimental effort has turned to dynamic resonance experiments. From such experiments it is possible to deduce the energy dissipation per cycle and the effective stiffness of the joint [7, 8]. Goodman [9] examined several analytic solutions to elastic-frictional contact problems under oscillating shear loads and

[1]The nomenclature in the literature is inconsistent with respect to the terms "microslip", "partial slip", and "macroslip". Here, we use the term "partial slip" for cases where part of the interface is slipping and part is not; we use the term "macroslip" when all of the interface slips; and we employ "microslip" when the slipping region is a small fraction of the interface.)

noted that they all manifested a power-law dependence of dissipation on the amplitude of the shear force. In each of Goodman's cases, the power-law slope was approximately 3.0. Postulating that this was common to contacting bodies in shear, he examined the Mindlin-Cattaneo [10, 11] solution for spheres in contact and showed that the dependence of frictional energy dissipation on lateral load was cubic in the limit of small load amplitudes.

Ungar [12, 13] performed a number of historic resonant experiments in the early 1960s demonstrating how examination of the dependence of dissipation per cycle on load amplitude can facilitate identification of the source of energy dissipation. Ungar showed that situations causing riveted plates to dissipate energy as the square of the applied load were due to air pumping. Other geometries (ones that looked more like lap joints) also yielded power-law type dependence of dissipation on applied force, but at power-law slopes greater than 2.0.

Out of the work of Ungar grew the practice of employing log-log plots of energy dissipation vs load amplitude as a useful characterization of joint dissipative properties. Generally, experimental data tends to support a power-law characterization until loads approach those necessary to initiate macroslip. Linearity would require a power-law slope of exactly 2.0[2] and Goodman's analysis generates a slope of 3.0, but experiments on real joints tend to yield values between 2.2 and 2.8. Heinstein and Segalman [14] suggests that the power-law slope is less than three in lap joints because the general non-symmetric nature of joint deformation during loading violates the Goodman hypothesis, namely, that the contact patch does not evolve. In reality, bending in the joint causes the contact patch to shrink during the tension portion of each cycle, releasing shear stress in the slip zones at the edges of the contact patch. Conversely, during the compression portion of each cycle, bending induces growth of the contact patch and localized pinning at lap boundaries.

The key qualitative properties of joints discussed above are notionally presented in Figures 1.2, 1.3, and 1.4. In Figure 1.2 the dissipation attributed to the joint increases as a power-law having a log-log slope substantially greater than 2, while linear systems necessarily have dissipation slopes of exactly 2.0. The apparent "softening" properties of joints are illustrated in Figure 1.3 for a notional force-displacement curve under monotonic loading. (See also Figure 7.2 on page 242 for actual experimental data.) At very low loads, the tangent stiffness is roughly that of a welded interface and the response *appears* linear. Even at this point there is some microslip and dissipation. As the load is increased, the force-displacement curve begins to bend down as increasing portions of the interface move from a "stuck" to a "slip" state. Finally, the full interface is in slip, and the macroslip state is manifest as zero-slope on the force-displacement curve. One of the other outstanding features of mechanical joints is illustrated in Figure 1.4, where the discrete Fourier spectra (absolute value) of acceleration of two, nominally identical, structures are shown. The fact that a structural response has so much part-to-part variability identifies joints as a major source of uncertainty in design or certification of mechanical systems.

[2]The most general linear model is that of linear viscoelasticity and dissipation for such models can be shown to be exactly quadratic in amplitude.

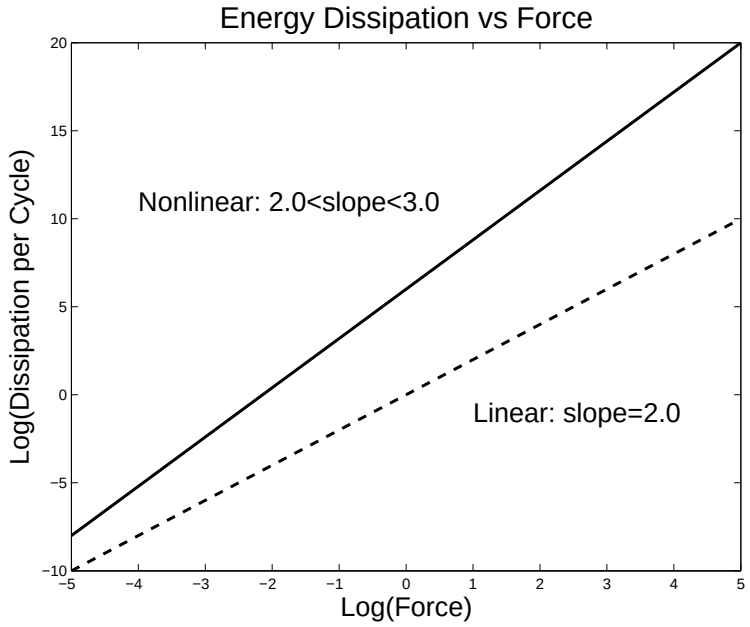

Figure 1.2. Dissipation From Base Excitation or Free Vibration.

For a lap-type joint subjected to oscillatory longitudinal loads, the dissipation per cycle is observed to conform to a power-law relationship with force amplitude over large ranges of load. For linear systems, the dissipation is quadratic in force amplitude so a power-law slope other than 2.0 is an indication of nonlinearity.

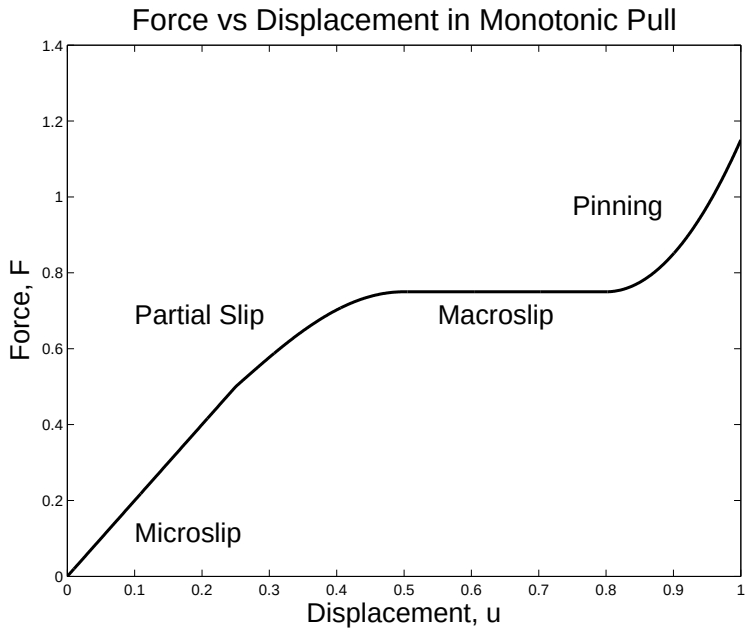

Figure 1.3. Monotonic Pull of a Lap Joint.

For a lap-type joint subjected to monotonic loading, the first portion of the force displacement curve appears linear. At larger loads the joint appears to "soften", and at sufficiently high loads macroslip initiates.

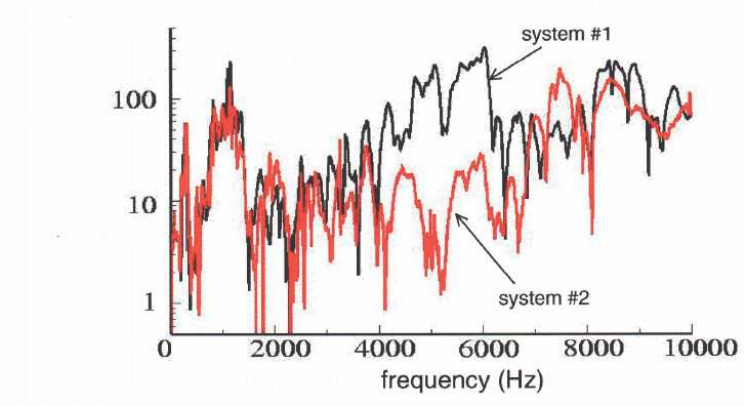

Figure 1.4. Shock Response Spectra of Nominally Identical Structures.

The shock response spectra of identical shell structures each connected to a base by nominally identical joints. The vast difference in spectra illustrates the variability in properties among even nominally identical joints.

1.3 Current Emphasis on Joint Properties and Incorporation into Structural Dynamics

Historically the analysis community has acknowledged the role of joints in structural dynamics ambivalently. Structural nonlinearities are ascribed to the presence of joints, but nonetheless, analysts persist in using linear models. Within linear models, analysts acknowledge the nonlinearity by calibrating those models against experiments performed at load amplitudes in the ranges for which predictions are sought.[3] It is argued that a lack of proper tools to model joint nonlinearities or the solution to the resulting nonlinear systems of equations forces the use of calibrated linear models. However, linear structural dynamics analyses have several, exploitable, advantages:

- Frequency response functions can be used to predict the response of a system to *arbitrary* excitation.
- Modal truncation can be employed for model reduction.
- Comparison to experiments can be made in terms of modes and resonance frequencies.

It is reasonable to believe that the true reason for the reluctance to move away from linear models is an expectation that the answers obtained from brute force, numerical solution of the relevant nonlinear equations would not be as easy to interpret or as rich in intuitive meaning as the current linear tools.

Numerous efforts to extend tools of linear structural dynamics to acknowledge the role of joints have been made in the past. One of the more interesting of these efforts has been that of employing *describing functions* [20] for joints and inserting these into the frequency domain form of the equations of motion [21, 22, 23]. In this context, describing functions are the coefficients of Fourier series expansions of the force response of a joint to prescribed harmonic displacements, normalized so as to appear as nonlinear stiffness or damping coefficients. These coefficients all carry the amplitude of the driving displacement as a parameter. When the resulting frequency domain system model is evaluated at different load amplitudes, some sense of the effect of joint nonlinearities can be obtained. The above definitions are all based on harmonic (monochromatic) excitation and harmonic response and should be interpreted in the sense of harmonic balance [24]. Additional work has been done along these lines to deduce joint locations and their describing functions from experimental data [25, 26, 27].

There is a major development driving analysis away from tuned modal analysis and toward direct, transient, finite element analysis. That new factor is the growing prominence of massively parallel computers and structural dynamics computer codes that can exploit that hardware. The analyst is now asked to perform *predictive* simulation on the basis of finely gridded finite element meshes and deterministic models for joints, interfaces, and boundary conditions. Extreme care must be exercised at this stage especially with the increasing focus on uncertainty quantification

[3] A tremendous amount of work has been done to deduce equivalent linear joint properties from measured vibratory response. Several references that indicate the general approaches are [15], [16], [17], [18],& [19].

(UQ) and probabilistic modeling. The most efficient means of exploiting these new resources is yet to be determined.

There are several outstanding topics where the economics (or prohibition) of testing complemented by the development of enhanced computing machinery have lead major research initiatives in understanding mechanical joints and integrating them into structural dynamics. These topics are described below.

1.3.1 Jet Engines

A very good overview on the role of joints in jet engine dynamics and how the jet engine community addresses these issues can be found in a discussion by Ewins [28]. Some of his observations are repeated here.

There are hundreds of mechanical joints in a jet engine. Some of these, primarily casing joints, must be characterized just to have reasonable resolution on natural frequencies and vibration damping. Other joints, particularly high stress joints on rotating components, manifest strongly nonlinear properties which are critical to the survival and lifetime of the engine.

Currently, the contributions of casing joints to structural response are accommodated by:

1. Employing conventional methods of approximating structure response by linear models and modal damping.

2. Employing nonlinear spring/damper/slider mechanisms at the joints.

Deducing parameters for these linear or nonlinear structural models is an advanced art supported by a large literature.

The issues of joints in rotating components are substantially more difficult and substantially more crucial. For instance, traditional compressors consist of a notched hub into which blades are individually placed. Frictional rubbing between the blade roots and the hub is expected to provide sufficient damping to prevent large vibration and consequent metal fatigue. More modern compressors employ bladed disks (blisks) machined from a single piece of metal to achieve much better balance than has been possible with traditional designs. This new technology, even with greatly improved balance, requires the introduction of frictional damping elements to suppress vibration and prevent metal fatigue. The design of a damping mechanism is so critical and testing *in situ* is so expensive that a quantitative understanding that can guide reliable design adds substantial value to the enterprise.

1.3.2 Nuclear Weapons

Underground testing of nuclear weapons was discontinued by the United States in 1992. Even conventional testing is highly limited because of expense, environmental considerations, and logistic difficulty. These circumstances have motivated various technical and science-based campaigns aimed at stockpile stewardship, wherein the balance between computational simulation and test would be weighted increasingly on the side of simulation. This has occasioned investments both in computational resources and in the science that underlies core processes.

The key barriers to a science-based stewardship with respect to structural dynamics of weapons systems are uncertainty in load and boundary conditions, and the complexity of structural response. The issues with respect to structural response have to do with such things as variability in the as-built structure (such as whether one batch of foam has been as adhesive as the previous, where in the structure the foam actually adheres and where it does not, as well as in-place foam density and mean void size) and with intrinsic ignorance in modeling the material physics that underlie structural mechanics. All the above issues must be addressed for the mission of stockpile stewardship and one of those that has particularly motivated research efforts in the nuclear weapons laboratories is that of mechanical joints. These include such diverse sorts of interfaces as threaded connections, tape joints [1, 2], and many flavors of bolted/lap joints.

The properties of the joints enter into structural dynamics calculations through the flexibilities that they introduce at their locations and through the nonlinear damping that is produced. All of these properties - which generally are not known in the absence of structure-level experiments - will have to be accommodated into structural dynamics calculations in order to meet the demands of science-based stockpile stewardship.

1.3.3 Other Areas of Importance

The development of the technologies for understanding joints and incorporating that understanding into structural dynamics calculations typically resides in high-stakes industries. Though individual joints are not generally a subject of scrutiny in aircraft dynamics, they are accounted for through ground vibration tests. As the technology of simulation of fluid-structure interactions matures, the same focus is expected on the nonlinear structural response in aeroelasticity that currently exists in the jet engine and nuclear weapons world.

1.4 The Numerical Challenge

Given the current explosion of capability in raw computing power, it is natural to ask why a concerted research effort in measuring, understanding, modeling, and predicting joint properties is necessary. Given that there is a need for making predictions that account for nonlinear structural response, why not just model structures with very fine meshes - especially fine near interfaces -

and solve the resulting numerical problem to obtain structural response? The answer comes in two flavors. The first has to do with the intrinsic multi-scale nature of mechanical interfaces, and the second has to do with the current state of understanding of interface physics.

1.4.1 Multiple Scales and Time-Step Limitations

The outstanding computational problem derives from the multiple length and time scales of engineering problems. For instance, the structures of interest to us may have characteristic length of meters - such is the case in nuclear weapons and in jet engines. We generally want to calculate through the duration of significant events or even out to steady state. For the sake of discussion, assume predictions must be made over a response period on the order of seconds. The components of these systems have dimensions on the order of centimeters. These components play a significant role in the internal dynamics of structures and often have their own vibration modes within the frequency range of interest. Were it not for the complexities of the joints, the characteristic finite element size would be just sufficiently small to capture the kinematics of the deformations of the components. That length scale would be on the order of fractions of a centimeter. Some sense of the dimensions of components may be deduced by examination of Figure 1.5.

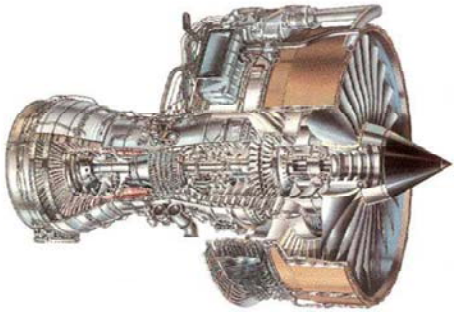

Figure 1.5. Complex Built-Up Engineering Structures

The characteristic lengths of the structures of interest are expressed in meters. The characteristic lengths of components are measured in centimeters.

However, there are two, smaller length scales that must also be considered. For bolted joints, the contact patch of the interface will generally have dimension on the order of a fraction of a centimeter. At accelerations substantially lower than those necessary to cause macroslip, the frictional slip will occur only in the outer portions of the contact patch. (See Figure 1.6). During each cycle, the width of the slip annulus will grow from zero to fractions of a millimeter and then shrink back to zero. The physics in each of these length scales are coupled. An effort to perform direct numerical simulation (DNS) of the full system requires such small elements to capture the contact mechanics correctly that the calculations become intractable.

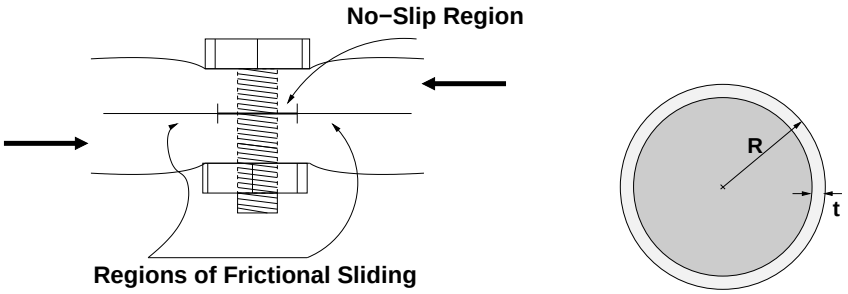

Figure 1.6. Contact Regions in a Lap Joint.

The characteristic lengths of the contact patch, R, will be on the order of a centimeter, but the width, t, of the slip annulus may be measured in nanometers, depending on load.

This situation is illustrated by the problem of the lap joint in Figure 1.7. The laps are each chosen to be one centimeter thick, the normal tractions are distributed so that the contact patch is two centimeters in diameter, and the magnitude of the normal force N is set at 4 kN (about the working load in a quarter inch bolt).

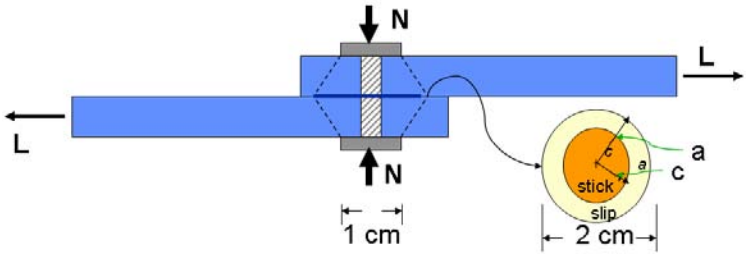

Figure 1.7. Representative Lap Joint Geometry Illustrating Solution Difficulties.

The range of longitudinal load of interest is assumed to be on the order of $L \in (0.05\mu N, 0.8\mu N)$ where μ is the coefficient of friction. This places the load range comfortably in "normal environments" - stretching from enough to cause just a little slipping at the edges of the contact patch to just short of enough to cause macroslip. We also assume that the dynamic range of interest lies in $f \in (100Hz, 3500Hz)$ - also representative of structures of interest. For the sake of estimation, we further assume that the contact patch is invariant over that load cycle(Goodman assumption), and that the stick slip boundary abides by the Mindlin solution for the two-sphere problem, so that

$$\frac{c}{a} = \left[1 - \frac{L}{N\mu}\right]^{1/3} \Rightarrow \frac{c}{a} \in (0.58, 0.98) \Rightarrow \frac{a-c}{a} \in (0.02, 0.42)$$

Resolution on the dissipation process requires approximately ten elements through the thickness of the slip annulus. In the case of lower loads this means that elements must be on the order of $20\mu m$. For structural materials, a representative speed of sound would be 6000 meters/second, and the Courant time would be less than 4 ns. To model just one cycle of structural response at 100 Hz, would require 2,500,000 explicit time steps. Simulation of at least ten cycles would be necessary for any kind of frequency resolution and the problem is very quickly seen to be intractable. If a quasistatic contact analysis of the same fine mesh for the interface was slaved to a dynamic model of the full structure, the problem would again be intractable because of the number of iterations necessary to follow the nonlinear contact process.

1.4.2 Limitations of Current Interface Models

Beyond the intractable nature of DNS of the contact domain as part of the dynamic problem, there are other reservations with a direct finite element treatment of the interface. Those reservations have much to do with the idealizations of Coulomb friction on real surfaces. Refining the mesh in the contact patch pushes the credible use of the Coulomb friction assumption.

There are actually a plethora of credible interface models. (There is a very good review article by Berger [4].) These models range from plasticity models to heuristically motivated models with asperity interaction in mind. Most involve several parameters, which may explain the continued popularity of Coulomb friction as a function of its simple model form and that it employs only one parameter.

There is no reason to expect that any particular interface model - particularly the simplest such model - would provide quantitatively correct numerical predictions for joint behavior. Indeed various studies, including work reported in one of these chapters within, have demonstrated some of those limitations.

Coulomb friction does not yield numerical results that are quantitatively consistent with experimental data, and is unsuitable as a prime source of knowledge of joint mechanics. Additionally, because of the computational time issues discussed above, it is impractical for structural dynamics calculations. Still, as will be shown in later chapters of this document, this simple friction model can be used with fine resolution finite element code to provide some insight into interface mechanics.

1.5 Integrated Strategy for Defining, Measuring, and Modeling Lap-Type Joint Properties

This handbook presents an approach to dynamic modeling of jointed structures, going from measured (or estimated) properties of individual joints to structural level, computational simulation. Specifically, this approach was taken at Sandia National Laboratories in order to satisfy a set of

programmatic requirements. Given the time, material, and financial constraints, the approach was one avenue that could achieve the promised deliverables. In this process, we introduced a number of conceptual ingredients:

- The use of corresponding monolithic specimens to assess the results of experiments on jointed specimens. This simple notion is crucial in the definition of joint properties.
- Mathematical constructs to interpret experimental (or simulation) data on individual joints
- Constitutive models to integrate that data into a mapping from deformation histories to load (or load histories to deformation)
- Kinematic models to couple low dimensional models of joints to continuum models for solid mechanics.
- Tools within finite element analysis to perform structural level dynamic simulation

The above constructs, along with finite element investigations into joints themselves, are elements of an integrated conceptual model for dynamics of structures built up through frictional, lap-type joints, and they are milestones along the critical path of simulating and predicting such structures.

This handbook is organized in a manner reflecting that critical path to basic modeling of built up structures. Additionally, there are several sections pertaining to additional aspects of modeling of real structures. These include a notional, distributed dissipation approach for accommodating structures with many frictional joints, a very basic approach to modeling threaded connections, and a section on future research opportunities. In summarizing components of the integrated strategy discussed above, high level overviews of elements that are discussed in much greater detail in following chapters are described here.

1.5.1 Experimental Program

The fundamental difficulties of measuring joint properties directly are suggested above, and are discussed in much greater detail in the sections on experimental methods. They may be summarized by the facts that point measurements in the interfaces during exercise of the joint are not practical, and that measurements on experimental specimens containing joints can yield at most indirect information about joint properties. The problem is even more difficult because the contribution of joints to the force-displacement measurements of jointed specimens is extremely small at loads less than those necessary to cause macroslip.

Accommodating these limitations required a means to map indirect measurements into properties ascribable to the joints in question. This was done by performing experiments where there was a re-enforcement of data associated with the joints. Monolithic, unjointed, reference specimens were compared directly to the jointed configuration; the differences are attributable to the properties of the interface.

The quintessential experiment is that of the "Big Mass Device" (BMD) explained in the experimental section. A specimen is placed between a large reaction mass and a high force shaker. Attachment between the specimen and the rest of the experimental set up is made using types of connections that add their own compliances, but dissipate very little energy and are highly reproducible.

The shaker is driven at the resonant frequency of the system at several different levels of excitation. Simple single degree of freedom (SDOF) analysis quantifies the net energy dissipation per cycle of the mechanical system, as well as the net compliance of the specimen and its attachments. The experiment is repeated with the joint-free specimen and similar analysis is performed. Each experiment is performed over many cycles, both bringing the system to steady state and magnifying the signal to noise ratio. Analysis of this data provides two properties that can be ascribed to the joint: joint energy dissipation per cycle and effective joint stiffness averaged over a cycle, each as a function of load amplitude.

Another class of experiment performed on jointed specimens is quasistatic tension and compression. For reasons discussed earlier, meaningful force-displacement relationships for the joint are not expected from these experiments. By noting the force at which the force-displacement curves of the specimen become noticeable nonlinear, the force necessary to initiate macroslip is directly observed.

The scalar parameters deduced from these experiments embody an experimental characterization of the joint. They are only a coarse representation of the joint; relating time-averaged, scalar inputs (amplitude of applied harmonic forces) to time-averaged scalar outputs (energy dissipation per 'cycle and effective stiffness). Further, these are measurements taken from experiments in which all the loads were imposed in the same axis.

The experimental chapters (approximately 1/2 of this handbook) will discuss these and more general classes of experiments. Obtaining meaningful data in joint related problems is notoriously difficult and much of the experimental sections focuses on techniques that have been developed over a decade. Employing the above described scalar data from harmonic experiments for dynamic predictions of a full structure requires several more developments.

1.5.2 Discrete Joint Models

The joint characterization that has been discussed so far provides just a few quantities associated with harmonic loading and the quasistatic force which initiates macroslip. How can the response of the joint be expressed when exposed to general load or deformation histories? Accommodating these features requires a constitutive equation that maps arbitrary inputs (histories, forces or displacements) into the energetically conjugate quantities (displacements or forces).

There are at least a countably infinite number of constitutive model forms that could reproduce the available experimental data to within the inherent uncertainty. However, there are a few measures of merit which bias a choice of one constitutive equation over another:

1. How well is it able to reproduce simultaneously the most important qualitative nonlinear properties of joints?

2. Is the numerical evaluation of the constitutive equation efficient and stable?

3. How many parameters must be deduced from experiments? Fewer is better; it is highly desirable that those parameters should be deduced from a small number of experiments so that there remains other data with which to compare model predictions.

4. Is there a well-conditioned process for deducing the model parameters from limited experimental data? This last feature requires that a unique parameter set be deduced from a set of data.

Only one class of constitutive model (the Bauschinger[29], Prandtl [30], Ishlinskii [31], Iwan [32, 33] model) is explored to any depth in this this handbook. This constitutive model, discussed primarily in Chapter 12, satisfies all the above conditions reasonably well and additionally lends itself to mathematical analysis. Certainly other researchers will find other models just as good as the one presented in this handbook, but the value of those models can be demonstrated only after thorough testing against experiment. The editor, having experience in constitutive modeling of several flavors, asserts that the community does not need more constitutive equations; it needs *better* constitutive equations.

1.5.3 Kinematic Simplifications

After performing a sufficient number of experiments to characterize the joints of interest, selecting a constitutive form, and deducing parameters that reproduce the data, the constitutive model must still be integrated into a structural dynamics model.

The challenge is the connection of a one-dimensional equation with the finite element kinematics - an essentially three-dimensional world. This is the same problem that is encountered regularly in connecting spring elements to plates, shells, and solids. Analogously, this problem is regularly addressed by analysts connecting plates and shells to three-dimensional element blocks.

The mathematics of this problem are still challenging after over twenty years of concerted effort in the mathematics and applied mechanics worlds. The issues of non-physical stress singularities and retarded mesh convergence appear important to those communities more for philosophical than practical reasons. Typically, because the singularities are integrable, and the uncertainty in loads and boundary conditions and the intrinsic variability in joint response dwarf discretization error, engineering analysts do not mind living with a few mathematical anomalies, if they notice them at all.

The approach employed in this handbook for coupling one-dimensional joint models with three dimensional finite element component models is comfortably within the class of tools used by the general analysis community, though care must be taken to use the approach consistently. These issues are discussed in detail in Chapter 11 of this handbook.

1.5.4 Application in Finite Elements

Finally, all of the preceding numerical constructions must be incorporated into finite element modeling of structures. At a minimum, this includes: coding the constitutive equations into the structures code, conveying to the code the surfaces to be treated as being in contact, and instantiating the model parameters.

This process has been demonstrated with the Salinas [34] structural dynamics code. Salinas is one of the *Codes for the Complex* developed under the ASC Program of the US National Nuclear Security Agency. It is generally quite robust and is structured so that adding new features is not prohibitively difficult.

Salinas is a parallelized code and can take advantage of massively parallel computers. Additionally, Salinas reads from and writes to the publicly defined Exodus database format, and can leverage the preprocessing and post processing tools built for Exodus.

The process of posing a joints-related problem for Salinas is presented in Chapter 15. This chapter also presents some numerical results for a real structure. Numerical artifacts are unavoidably introduced into the dynamics calculations. The chapter provides a discussion of the origin of these artifacts and their mitigation.

1.6 Other Important Joints Issues Covered in this Handbook

There are other research elements that are important to the dynamics of jointed structures that do not conveniently fit into the above critical path. Some of these elements have been addressed recently and have a place in this handbook.

1.6.1 Analysis of Finely Meshed Joint Models

The nature of the contact problem causes DNS of the joint mechanics as part of the dynamics analysis to be impractical. Additionally, the friction model commonly available in finite element code does not quantitatively reproduce experimental data. It is expected, however, that quasistatic DNS of mechanical joints can provide some insight into the relevant mechanics. For instance, can the huge variability in joint response be explained by incorporating relevant factors into finite element analysis?

If there is a mechanical joint for which there is *no* experimental data, it may be necessary to use quasistatic DNS of the joint to numerically perform the experiments that ordinarily are run in a laboratory to deduce joint constitutive parameters. These joint parameters will undoubtedly differ from those obtained from physical experiment, but they will be a starting point for structural dynamics calculations.

This problem is still very much a research issue, but some valuable lessons have been learned and some insights achieved already. Among the lessons learned are: many well known finite element codes will not converge on some physically reasonable elastic-frictional-contact problems, and some codes will regularly converge on incorrect answers. The Sandia team has adopted a policy that before a finite element code is used to model any joint, it must first be tested against a suite of verification problems developed for the purpose.

The verification suite and some of the results of testing a few nonlinear quasistatic finite element codes on those problems are presented in Chapter 14. Strategies for DNS of joints, some representative Adagio results, and a few resulting insights are presented in Chapters 15 and 16.

1.6.2 Spatially Distributed Joints

The majority of this handbook addresses models for joints that resemble a class of lap joints (this includes actual lap joints, flange joints, and some threaded joints). There are frequently instances where there are far too many joints distributed about the structure to incorporate them all individually into a structural model. Is there a way to model that structure so as to reproduce the "joint-like" dissipation and the softening effects found experimentally?

An approach to modeling such structures involves employing the gross modal kinematics of a reference elastic structure and nonlinear evolution equations for the modal coordinates is presented in a chapter of its own. This is a very new research effort and preliminary results are presented both to demonstrate that there are modeling approaches suitable to fully built-up, complex structures, and to encourage further research.

1.6.3 Threaded Connections

A class of joint that does not fit into the theoretical framework developed for lap-type joints is that of threaded connections. The focus of the work presented in Chapter 13 is that of predicting the effective stiffness of a threaded connection. Such results are required by analysts attempting to capture the effects of threaded connections on structural response without having to employ a micro-model in the dynamics calculations.

The technique presented here is very much in the theme of traditional multi-scale modeling. Very fine mesh analysis is performed on a unit cell and an equivalent material is defined for use in a coarse mesh model for the full dynamic structure. The relevant development is discussed in Appendix C.

There is much about threaded connections that is not presented in this handbook. One particularly relevant piece of work is that of Doebling et al. [35] where transient DNS was performed on a significantly detailed model to predict the response of the structure to an explosive shock. It is worth noting that the application of DNS was particularly appropriate since the calculations were designed to predict structural response over a short time period.

1.7 A Call To Action

Considerable effort has been made to achieve coherence in this handbook and to make the document readable. Several compromises were made: the literature review is extensive but incomplete. Only that work that fits into the thread of the presentation was included, and many important topics have been touched on only lightly.

On the other hand, the reader has numerous clues throughout this document of significant work yet to be done. Not only is there a chapter specifically suggesting topics fertile for investigation, but, hopefully, the informed reader will be stimulated by much of the work presented here to explore other - more practical and more elegant - methods to address these problems.

Part I

Experiment

Chapter 2

Introduction to Experimental Program

Danny L. Gregory and Brian R. Resor

2.1 Motivation

A fundamental challenge in a research program aimed at understanding and modeling the behavior of bolted joints is the sheer magnitude of the parameter space associated with the simple bolted joint. An example illustrating a simple shear, lap joint with a single bolt is featured in Figure 2.1 .

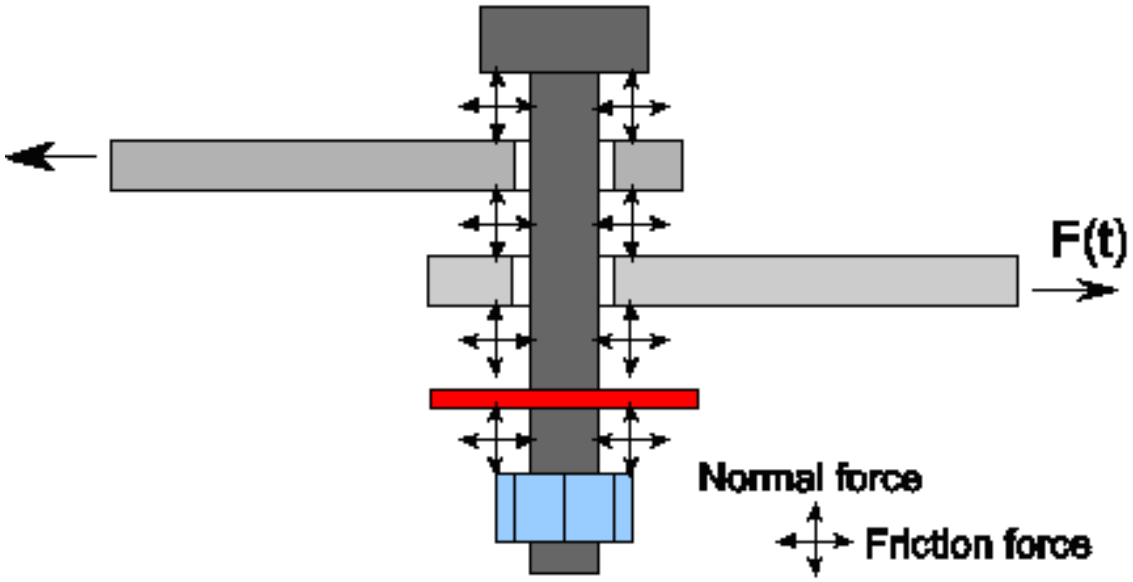

Figure 2.1. Simple Bolted Shear Connection.

There are four slip interfaces associated with a single bolt, nut and washer. Each interface potentially involves different surface tractions, material types, surface properties, and contact areas. The parameters associated with the joint include: preload, interface geometry, interface material(s),

surface finish(s), lubrication, bolt material, bolt type, washer material, washer geometry, loading configuration, loading type (static, dynamic, vibratory...), load direction, etc.

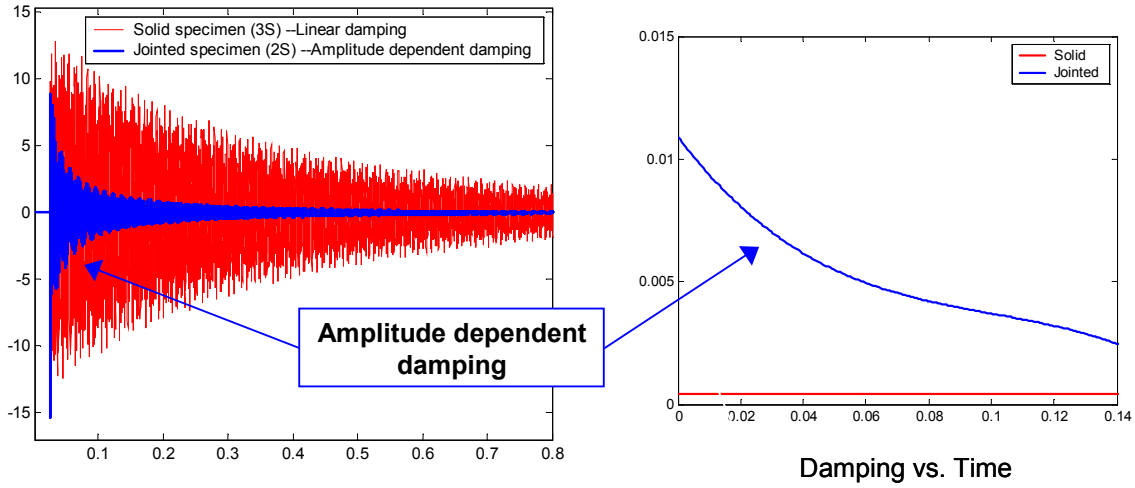

Figure 2.2. Jointed Interface Damping Effects on Decay Rate of a Structure.

Response waveforms and instantaneous damping are shown for both a monolithic and a jointed specimen with transient loading input. Acceleration amplitude is shown on the left and instantaneous fraction of critical damping is shown on the right. All curves originate in experimental data.

Figure 2.2 illustrates the large effect that joint damping can have on the response of a structure. Shown are response waveforms and instantaneous damping values for a structure that was excited by the same transient impact. The red curves illustrate the response of a linear system containing only material damping. The blue curves illustrate the response of a system with the same exact geometry, but also with a jointed interface. Not only does the overall level of damping increase, but the damping is dependent on amplitude. A goal of this experimental effort is to understand the contributing factors to the unique behavior of this problem.

2.2 Review of Experimental Literature

Understanding that jointed interfaces produce large amounts of energy dissipation in structures is not new. The effort to understand the specific mechanisms of interface damping dates back to the 1960s. Additionally, efforts to quantify and then model the interface behavior have been attempted ever since there have been experimental observations of the behavior.

This chapter in the Handbook is dedicated to discussion of experimental techniques and prac-

tices that can be used to understand behavior of nonlinear, jointed interfaces. Following is a review of some of the literature addressing experimental efforts.

In the 1960s, Ungar [12] set out to understand several different types of aerospace joints. He studied point connections as well as certain distributed connections. Examples include rivets, bolts or screws, spot welds, and continuous welds, in addition to riveted and bolted panels. The experiment consisted of a suspended plate with various attached small beams, with the apparatus being driven by a single exciter. Damping was determined by measuring the decay rate of the structural response after turning off the input. He studied variation of bolt torque, bolt spacing, hardware geometry, materials, surface finish, atmospheric pressure and lubricants. He concluded that the dominant damping mechanism for motions normal to the interface was gas pumping, while the damping mechanism for motions parallel to the interface was likely interface slip. Ungar developed the power dissipation plot that was first used to illustrate and distinguish the behavior of different joints.

For the most part, experiments have focused on shear loads in the joints, with the exception of early work by Ungar [12], which focused on gas-pumping. Also, Maidanik [36] performed experiments to demonstrate effects of gas-pumping on joint damping. His experiments at low atmospheric pressure showed that gas-pumping helps to account for energy dissipation of structures consisting of beams riveted to plates.

Most experimentalists have used the concept of the load-vs-relative-deformation hysteresis curve to calculate energy dissipation of their experimental structures. The concept was shown by Metherell [37], who in the same work introduced the concept of effective joint stiffness, which is dependent on the amplitude of load in the interface.

Ungar [13] summarized the current state of jointed interface damping at the time. Applicable efforts had focused primarily on damping of built-up beams and skin-stringer structures, or in other words, aircraft construction. Relevant published work appearing later began to explore how an experimentalist can measure the more intricate details of the jointed interface so that better descriptions, or models, of their behavior could be created.

A special experimental setup described by Rogers [38] was capable of measuring the necessary parameters for construction of accurate load hysteresis curves during shear loading of metal interfaces. He used the experiment to study frictional interaction of various metals at cyclical speeds up to 200 Hz. Rogers was perhaps the first to mention the presence of a time-history, or breaking-in effect characterizing the energy dissipation occurring within the first several loading cycles. Crawley [39] introduced the concept of experimental determination of the force-state mapping of joints behavior. Other published works mentioning interesting and useful experimental apparatus include Gaul [40], Padmanabhan [41] and Ren [42, 43].

Perhaps one of the most important ideas that has been implemented in all Sandia joints experiments is the concept of the monolithic joint specimen. It truly serves as a deceptively simple control specimen because its response is directly related to that of the jointed hardware. This idea was utilized by Moloney [44] in his work that compared the structural dynamic response behavior of simple, jointed-beam specimens to monolithic specimens of identical geometry. Moloney also

approached the calculation of amplitude-dependent damping in a similar manner to experimental techniques adopted by Sandia in that he analyzed the envelope of the transient decay of certain dynamic resonances of the specimens. A similar approach to decay-rate analysis was also used by Feeny [45].

The authors believe that one of the best ways to make accurate, indirect measurements of the motions occurring within an interface during microslip is to find a way to utilize a structural dynamic resonance of the system. The work of Moloney [44] was an early example of the concept. Gaul [7] proposed an experiment that truly has all the flavor of the experiments that are utilized currently by Sandia experimentalists. His experiment consists of a "longitudinal resonator" that is driven harmonically by an exciter. The frequency of excitation can be tuned so that the motion in the resonator, or dumbbell, exerts cyclic shear force in the joint specimen. Measured parameters include force input, specimen acceleration, and mass acceleration. The hysteresis curves are plotted using the measured data, and energy dissipation values can be calculated by finding the area under the curves. The forcing levels in the experiment can be high enough for observation of macroslip effects in the joint. Similarly, a novel experimental structure developed by Sandia has demonstrated an ability to excite the torsional response of the joint specimens in a way that lends itself to reliable measurement.

2.3 Sandia National Laboratories Experimental Efforts

Sandia initiated and supported a lengthy experimental program to develop understanding and insight into the underlying physics associated with energy dissipation of bolted joints. As discussed previously, the inherent limitation of predictive structural dynamic models is the inability to model the nonlinear energy dissipation (damping) of bolted interfaces in assembled structures.

Early experimental work in bolted joints was done largely to gain basic understanding to aid the development of a suitable modeling approach. The early work resulted in implementation of sound experimental techniques and then focused on comprehension of the basic parameters of interest in the nonlinear interface. Experiments first utilized differencing of acceleration signals and measurement of input forces to calculate hysteresis curves from which information describing the interface nonlinearity could be gathered [8], [46]. Soon after, better techniques to measure response were developed utilizing the measurements made with the system at resonance [47].

Early investigations at Sandia focused on microslip in the interface and one-dimensional loading directly along the axis of the joint element, or shear loading. The two major measurement characteristics that were the focus of these studies were the energy dissipation and the nonlinear stiffness. An example of the first finely-meshed finite element modeling of an interface was published by Lobitz [48]. Early work at Sandia also revealed the large amount of inherent response variability that occurs due to randomness associated with the interfaces.

With sound experimental techniques as a basis, Sandia experimenters next undertook accurate measurements for calibration and validation activities concerning new joint models. At first, ana-

lytical models were simulations of very basic, jointed interfaces. Soon after began the application of the techniques to very specific hardware configurations, such as System A-0 and System A-1 Axially Oriented Subsystem (AOS) bolted joints [49]. The need for more experimental data to support various levels of model validation efforts also led to the development of additional experimental configurations. After completion of a major calibration and validation effort, the basic experimental techniques outlined in this section became robust and reliable, involving several levels of hardware and model complexity. (See [50] and Section 8 of this document).

The most recent investigations of jointed interfaces have revealed that the character and distribution of interface contact pressure is much more complex than would be predicted by simple theory. The primary source of the discrepancy stems from imperfections present in interfaces due to the manufacturing processes [51]. Laboratory investigation into this issue will help to explain much of the unexpected behavior of joint interfaces. In a later chapter, computational investigations also shed light on this phenomenon.

Sandia experimentalists feel that there are now some very useful, reliable and well understood techniques available for basic characterization of nonlinear joint interfaces. Current research thrusts are aiming to understand more concepts, such as effects of macroslip and combined loading in interfaces. Not all of the newest work is published in this handbook because the experiments are still being perfected and techniques for meaningful data analysis have yet to be explored. These questions, and others, are still under investigation and are among the topics in need of more detailed study in the future.

2.4 Introduction to the Sandia Experimental Apparatuses

Experimentalists realized early on that the key to a robust and accurate experimental setup for jointed interfaces was to maintain simplicity in the setup. Boundary conditions of the experiment are extremely important and need to be both controlled and understood. Also important, as with any study of the basic behavior of nonlinear phenomena, was the design of experiments with behavior that could be understood by engineering analysis.

For this reason, the first and perhaps most successfully utilized experiment was designed to behave very much like a simple, fixed-base, SDOF system, including a large, rigid mass. Nonlinear elements would represent the stiffness and damping of the joint specimens that are incorporated into the experiment. Relatively simple equations of motion could be used to describe the behavior of this system.

The system is exposed to controlled, sinusoidal excitation, and all input loads and responses measured. Useful information can be gathered by taking various measurements at the resonance of the system. Energy dissipation can be determined at various input levels. Also, time histories can be recorded and analyzed to arrive at useful hysteresis curves that illustrate details of the interface nonlinearities as well as offer additional means to measure the desired parameters.

An extension of the SDOF base-excited experiment is a perhaps even simpler and cleaner

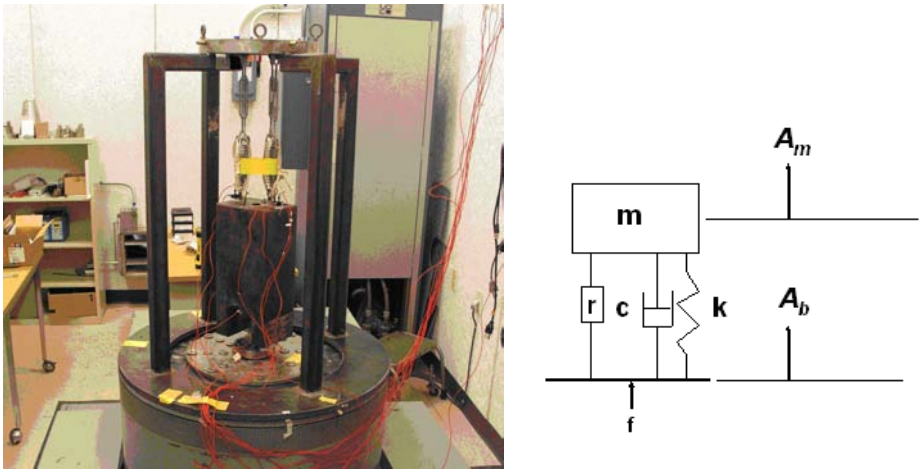

Figure 2.3. Photo of SDOF Device and Schematic of Relevant Dynamics.

setup utilizing a simple dumbbell configuration. The jointed specimens are installed between the two dumbbell masses. The whole assembly is suspended by soft bungees. Excitation is provided via a single sided input pulse to the end of one of the masses. The excitation is designed in such a manner to excite primarily the first axial mode of the system. The transient ring-down of the system is analyzed to quantify the parameters of interest.

Tests have also been performed in quasistatic load frames on jointed specimens (Figure 2.5). These tests are used to make load vs force measurements, usually best for having another means to quantify stiffness of the joint element. The quasistatic experiments were also useful in gaining initial understanding of the macroslip phenomenon.

2.5 Foreword to Experimental Chapters

As will be discussed throughout the experimental portion of this handbook the design of experiments to isolate and measure the energy dissipation of bolted interfaces requires an integrated approach of experiment design and measurement techniques tailored to the type of experiment being conducted. Quantification of all mechanisms of energy dissipation, such as might be found in the boundary condition of the experiment, must always be addressed.

One of the main challenges in bolted joint experiment design is to measure the response of the simple bolted connection without the ability to directly observe the microslip which is occurring in the interface. The experimental techniques discussed in this handbook can be described as indirect techniques where the total energy dissipation of the joint is calculated by measuring some characteristic of the response of the system to an applied force to infer the energy dissipation.

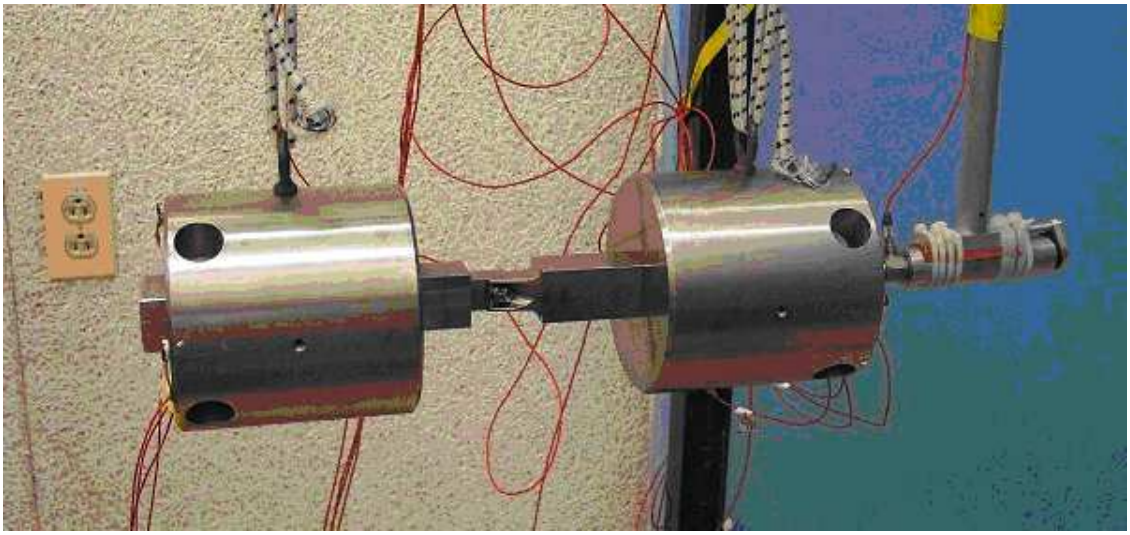

Figure 2.4. Photo of Basic Dumbbell Experimental Setup.

A number of experimental approaches will be described in the following sections along with measurement and data analysis techniques for isolating and computing the energy dissipation of bolted interfaces.

The parameter space must be reduced to pose a tractable research program using information about the intended applications of the bolted joints under study. Without some amount of specific focus it becomes prohibitive to try to study every combination of parameters associated with a generic bolted joint.

Following are some of the aspects of joint interface behavior that have been studied in the Sandia experimental program and are included in this handbook:

- Calculation of energy dissipation
  - Hysteresis curve area
  - Power supplied to an experimental apparatus
  - Utilizing Q at resonance
- Designing experiments with emphasis on simplicity, particularly the ability to be modeled by simple and well-known equations of motion.
  - Harmonic excitation
  - Transient excitation
- Signal processing techniques that enable the experimentalist to determine final response measures from a variety of data.

Figure 2.5. Quasistatic Experimental Setup

- Designing appropriate inputs to apply to the experimental structures.
- Experiments on hardware that contain more than one joint element.
- Understanding the effects that various joint interface parameters (preload, distribution, materials, surface finishes, etc) can have on the overall response of the structures.
- Suggested methods to obtain a rough idea of the real distribution of contact pressure in actual interface hardware.

It should be noted that these experimental approaches are by no means the only way to approach this problem but should only serve as a starting point for future researchers in this challenging, but important research effort.

Chapter 3

Dynamic Sinusoidal Excitation Experiments

Danny L. Gregory and Brian R. Resor

Bolted joint experiments may utilize a variety of load techniques including sinusoidal, random, transient, and quasistatic loading. Each excitation type has advantages and disadvantages depending upon the type of bolted joint and the objective of the experiment. Sinusoidal excitation has proven to be a very useful excitation source and provides several measures of joint response and quantification of the joint nonlinearities.

Throughout this chapter, the behavior of a structure at resonance can yield valuable information about the energy dissipation and stiffness of the structure. A useful configuration is to design an experiment with a bolted joint (or multiple bolted joints) that can be approximated as an SDOF system. A simplified representation of an SDOF system with a bolted joint is shown in Figure 3.1. The inertial mass is the mass, m, and the base is driven by the force, f. A linear spring, k, and a linear damping element, c, represent the linear part of the system. The nonlinear restoring force of the joint is lumped into R, and will include any stiffness or damping mechanisms. The energy dissipation due to microslip is a nonlinear mechanism, and the effective stiffness of the joint is also nonlinear. The response of the mass to base excitation is very sensitive to changes in the bolted interface such as preload, geometry, contact, lubrication, etc.

At the mechanical resonance of the SDOF system the inertia and stiffness forces are balanced. During this condition, the energy dissipation is equal to the energy supplied to the system to maintain steady response of the system.

Measurements of the input and response of the simple system allow calculation of the energy dissipation per cycle. The energy dissipation can be computed in a number of ways, several of which are discussed in the sections that follow. Examples of experiments configured to realize the SDOF approximation are discussed in Sections 4.1 and 4.4 along with experimentally measured data.

3.0.1 Measuring Energy Dissipation Per Cycle

3.0.1.1 Measuring the energy dissipation per cycle by finding the area within the force/relative-displacement hysteresis loop

In the literature on frictional joints, the traditional way to measure energy loss for harmonic motion is to measure the area within the closed plot (hysteresis plot) of force vs relative displacement. An example is shown in Figure 3.2.

The relative displacement between the mass and the base is very small and are difficult to resolve in the presence of instrumentation noise and numerical round-off errors. This is particularly true if measurements are taken at frequencies different from the resonant frequency of the system. At resonance, the maximum relative motions are realized and more accurate hysteresis curves can be generated for calculation of the traditional, relative hysteresis curves.

3.0.1.2 Measuring the energy loss by looking at the power supplied at the base

The energy dissipated during steady-state response in a single-input, passive system must be equal to the energy supplied at the input to the system to sustain the steady-state response. For a simple harmonic input the input energy is

$$D = FX\sin\phi \tag{3.1}$$

where F is the magnitude of the force input,
X is the magnitude of the base displacement,
and ϕ is phase angle between the force and displacement.

The relationship between the magnitude of the acceleration and the magnitude of the displacement is simply

$$A = -\omega^2 X. \tag{3.2}$$

Only the component of displacement out of phase with the force will dissipate energy. At resonance, $\sin\phi = 1$. The orthogonality of sine and cosine functions shown in Equation (3.3) assure that if either the force or acceleration is a pure sinusoid, $\sin\theta$, then harmonic distortion, $\sin n\theta$, in the other measure will not dissipate energy.

$$\begin{aligned} \int_0^{2\pi} \sin n\theta \sin m\theta \,\mathrm{d}\theta &= 0 \text{ for } n \neq m \\ \int_0^{2\pi} \cos n\theta \cos m\theta \,\mathrm{d}\theta &= 0 \text{ for } n \neq m \end{aligned} \tag{3.3}$$

Only the fundamental component will dissipate energy. If both the force and displacement of the base are distorted, then the harmonics can dissipate energy. At resonance, almost all the harmonic distortion observed in our experiments was in the base acceleration waveform. The inertial mass acceleration waveform is nearly a scaled version of the base input force, $A_m = F/M$.

At resonance, the inertia and stiffness forces are balanced. The motion required at the base to maintain a steady state response with a prescribed force is very small for a lightly damped system. To estimate the small base motion in the presence of background shaker and instrumentation noise, additional knowledge about the response of the system to sinusoidal excitation was leveraged. If a linear system is excited by a sinusoidal force at frequency ω, the response will occur at exactly that same frequency. If the excited system is nonlinear, higher harmonics may be evoked, but the orthogonality discussed above assures that all of the energy will reside in the first harmonic. If the excitation is at a fundamental frequency and several of its harmonics, the dissipation consists of components associated with motions at the fundamental and all harmonics common to both the force and the motion.

This knowledge can be applied by fitting a best least-squares fit to the measured base and inertial mass motions (typically accelerations) with a sum of phase-shifted sinusoids at the fundamental frequency and higher harmonics. In other words, the Fourier coefficients of the base and mass motions are calculated. This signal processing technique selectively filters the response at only the fundamental frequency and its harmonics, eliminating all other portions of the measured signals due to noise (assuming that power line frequency and harmonics do not coincide with the resonant frequency and harmonics). The number of harmonics required to reconstruct the base and mass motion will be determined by the type of nonlinearity in the bolted connection. Many of the experiments discussed later utilize the fundamental frequency and the first seven harmonics, though only the first harmonic is necessary to calculate energy dissipation. Users of this technique should experiment with the number of harmonics required to provide a good reconstruction by adding harmonics until additional harmonics no longer change the character of the reconstruction.

3.0.1.3 Measuring the Energy Loss per cycle, D, by Measuring Q

The energy dissipation of an SDOF system can also be computed by measuring the transmissibility function at the resonant frequency. From Thomson [52] the transmissibility of a viscous, damped, base-excited, SDOF system is given by the well known equation

$$T = \sqrt{\frac{1 + (2\zeta\omega/\omega_n)^2}{(1 - \omega^2/\omega_n^2)^2 + (2\zeta\omega/\omega_n)^2}} \tag{3.4}$$

where ω is the driving frequency,
ω_n is the resonant frequency of the system,
and ζ is the damping factor (fraction of critical damping).

At the undamped resonant frequency, ω_n, $\omega/\omega_n = 1$ and for $\zeta << 1$ the transmissibility is approximately

$$T \approx 1/2\zeta \tag{3.5}$$

The motion measures of interest are the accelerations of the base and the mass. For this system the force at the base is simply the product of mass and acceleration. Therefore, the driving point accelerance (ratio of base acceleration to base force) is the reciprocal of the transmissibility scaled by the mass.

The transmissibility at resonance is called the amplification factor or quality factor Q of the system, where

$$Q = T(\omega_n) = 1/2\zeta \tag{3.6}$$

The viscous damping coefficient of the corresponding m, c, k second-order equation is related to the damping factor by

$$c = 2m\zeta\omega_n \tag{3.7}$$

For forced harmonic motion, Thomson [52] defines an equivalent viscous damping for systems with other types of damping on the basis of an equivalent energy dissipated per cycle, as

$$D = \pi c_{eq}\omega X^2 \tag{3.8}$$

which gives

$$D = \frac{\pi m A_m^2}{Q\omega_n^2} = \frac{\pi m Q A_b^2}{\omega_n^2} \tag{3.9}$$

where A_m is the acceleration of the mass,
A_b is the acceleration of the base,
$Q = A_m/A_b$ is the Quality Factor,
$A_m >> A_b$,
and $A_m = \omega_n^2 Y$ where Y is the displacement amplitude.

The logarithm of this equation gives

$$\log Q + \log D = \log\left(\pi m/\omega_n^2\right) + 2\log A_m \tag{3.10}$$

Therefore, for the linear case where Q is a constant independent of input amplitude, the slope on a log-log plot of Q vs A (either A_b or A_m) is zero, and for D vs A is two.

$$\frac{\mathrm{d}(\log D)}{\mathrm{d}(\log A)} = 2 \tag{3.11}$$

Now consider the nonlinear case where a log-log plot of Q vs A is still a straight line, but with a slope, $-n$, in which case

$$Q = KA^{-n} \tag{3.12}$$

Note that for a positive n, Q decreases with amplitude and the corresponding damping factor ($\zeta = 1/Q$) increases accordingly.

Taking the log of both sides of Equation (3.12) gives

$$\log Q = \log K - n \log A \tag{3.13}$$

or

$$\frac{\mathrm{d}(\log Q)}{\mathrm{d}(\log A)} = -n \tag{3.14}$$

If the equivalent viscous damping is used instead of Q, the results are

$$\frac{\mathrm{d}(\log \zeta)}{\mathrm{d}(\log A)} = n \tag{3.15}$$

Combining Equations (3.10) and (3.14), and differentiating gives

$$\frac{\mathrm{d}(\log D)}{\mathrm{d}(\log A)} = 2 + n \tag{3.16}$$

For example, if the slope of ζ vs A on a log-log plot is +1.0, the slope of the energy dissipated per cycle will have a slope of +3.0.

3.0.1.4 Summary of Energy Dissipation Measurements

Experimentalists at Sandia National Laboratories have used all three methods previously discussed to measure energy dissipation. When properly applied, all three give essentially the same result.

For ease of use, and versatility, almost all of the experimental data reported in this document are determined by measuring Q in some manner.

3.0.2 The Damping Force

Thomson [*ibid* Sec 3.7] shows that for a linear SDOF system, a plot of force vs relative displacement, z, will plot as an ellipse. The major axis will fall along the line of linear stiffness. The input force, f, is the same force that drives the mass, m. If the force is a sinusoid, the force and the acceleration of the mass will be in phase. The force and displacement of the mass, m, will be 180° out of phase. The relative displacement will consist of three components: a coincident component (either 0° or 180°), a quadrature component (90° or 270°), and the harmonic distortion. The quadrature component will be represented by the quadrature component of the fundamental part of the base motion. Generally, for linear and lightly damped systems the linear stiffness term, k, dominates, and the hysteresis curve of force vs relative displacement is shaped like a narrow ellipse with the major axis on the linear stiffness line as shown in Figure 3.2 above.

The hysteresis curve is distorted from an ellipse for a nonlinear system. Integration of this curve to derive the energy loss is difficult because small errors in phase between the force and relative displacement result in large errors in the energy loss. If the system is driven at the fixed-base resonant frequency, the phase between the fundamental component of the base displacement and the force or mass displacement is 90°, the linear elastic term vanishes. The base displacement then represents the dissipative fraction of the motion. If only the fundamental component of the base motion is plotted, the hysteresis curve represents the equivalent viscous damping. For a sinusoidal force the harmonic terms of the base displacement do not dissipate energy.

The system can also be viewed as a passive system being driven from the base. The energy dissipated in the joint (the only significant energy loss in the experiment) must be supplied through the base motion. When the input force is plotted as a function of base displacement, the area within the curve represents the input energy. The area within the curves (force vs relative displacement, force vs base motion, force vs fundamental) are all the same.

Examples of base motion vs force hysteresis curves at resonance are shown and discussed below. For a linear system, the hysteresis curve is an ellipse. At a given amplitude, nonlinear systems are often described by a linear system defined by an elliptical hysteresis curve having the same area and secant (stiffness) as does the actual hysteresis curve. The nature of the nonlinearity is often explored through examinations of the higher harmonics of the hysteresis.

3.1 Computation of the Nonlinear Restoring Force

Proper processing of the experimental data for a sinusoidal excitation of a bolted joint configured into an SDOF experiment can yield a technique for isolating the nonlinear restoring force for the microslip in a bolted joint.

The equation that describes the motion of a base-excited SDOF system shown in Figure 3.1 subjected to a known oscillatory input force is

$$m\ddot{x} = -kz - c\dot{z} - R(z,\dot{z}) \tag{3.17}$$

where m is the mass of the SDOF system,
x is the absolute displacement of the mass,
and z is the relative displacement between the base and the mass.

The coefficients k and c are the linear spring and damping constants of the system, respectively, and $R(z,\dot{z})$ is the unknown nonlinear restoring force generated by the microslip phenomenon that we seek to isolate and quantify in our experiments.

Using the least-squares technique described earlier to obtain the Fourier coefficients for the periodic motions of the mass and the base (typically accelerometer measurements) will allow the broadband shaker/instrumentation and line frequency noise to be eliminated. The relative displacement, z, and the relative velocity, $\dot{z}$, are computed by integrating the fitted acceleration data.

The "linear" portion of the restoring force, $(-kz - c\dot{z})$, is estimated by performing a least squares analysis of the fitted data to solve for the linear stiffness and damping constants k and c. The nonlinear component of the restoring force, $R(z,\dot{z})$, is then obtained by subtracting the linear portion of the restoring force from the response of the mass

$$R(z,\dot{z}) = -m\ddot{x} - kz - c\dot{z} \tag{3.18}$$

This derived, nonlinear, restoring force can be a powerful tool for subsequent analyses to gain insight and understanding of the nonlinear behavior of the bolted joint.

Gregory [53] utilized the derived, nonlinear, restoring force in a simple lap joint for the identification of a functional form for microslip damping using directed genetic programming (GP). Both a three-term and a four-term expression for the nonlinear restoring force provided an adequate fit to the restoring force. An example of the experimentally determined restoring force, R, and the GP–resultant, four-term expression are shown in Figure 3.5.

Four-Term GP fit:

$$R(z,\dot{z})_{GP4} = 5.0|z|^4 \operatorname{sign}(\dot{z})\,|\dot{z}|^{1.1} + 3.7|z|^{4.1} - 3.8|\dot{z}|^{4.3} - 1.2\operatorname{sign}(\dot{z})\,|\dot{z}|^{7.8}$$
$$err_{GP4} = 0.1336$$

where

$$\mathrm{err}_{GPi} = \mathrm{std}\left(R(z,\dot{z})_{ex} - R(z,\dot{z})_{GPi}\right) / \mathrm{std}\left(R(z,\dot{z})_{ex}\right) \qquad i = 3,4$$

and std is the standard deviation.

3.2 Sine Wave Excitation and Control Utilizing Shakers

The sine wave excitation is typically provided with the use of electrodynamic shaker systems. These shaker systems can range from a few pounds of force up to thousands of pounds. The electrodynamic shakers are typically linear systems that can provide very clean, sinusoidal, force and acceleration inputs to the experimental system. For the purposes of bolted joint research the shaker system must be sized to provide the required amount of force for the type of bolted joint that is being investigated. Most shakers are single-axis devices designed to provide minimum motions in the cross-axis directions, but do have their own dynamics that occur at certain frequencies. At low frequencies ($<$ 10 Hz), there are typically modes that are related to the suspension system for the moving element. At higher frequencies ($>$2000 Hz), modes of the moving element become active, including the axial armature resonance. Care should be taken to understand the modes of the shakers and to design the bolted joint experiments to avoid these troublesome frequencies. An excellent discussion of vibration shakers is provided by Smallwood in Chapter 25 of [54].

The best technique for control of the sine wave excitation is with a digital, vibration control system with real-time, closed-loop control. The control system can be configured to perform various types of sinusoidal inputs. It can perform sinusoidal sweeps at selectable sweep rates (linear or logarithmic) between defined beginning and ending frequencies. The use of slow sine sweeps proved to be very useful in our experiments. Each realization of a bolted joint will have an effective stiffness, and the resonant frequency can vary from joint to joint (and even after a reassembly of the same joint). A sweep over a selected range will allow the transmissibility function to be fully defined without trial and error to locate the peak. The researcher should adjust the sweep rate to allow the system to reach it full amplification factor, Q. The systems can also be programmed to perform sinusoidal dwells at selected frequencies and set up to perform phase-lock control to adjust the drive frequency to maintain the input at the resonant frequency. An excellent discussion of digital vibration control techniques is provided by Underwood in Chapter 27 of [54].

3.3 Instrumentation for Sine Vibration Experiments

A variety of transducers is available for making measurements of the input and response of an SDOF system subjected to sinusoidal excitations. A piezoelectric force transducer inserted in the load path between the shaker and the bolted joint can be used to directly measure the input force level. Piezoelectric accelerometers provide a means of accurately measuring the absolute accelerations of the base and the mass. Other motion transducers, such as a Laser Doppler Vibrometer (LDV), can also be employed, but some experiments are difficult to configure so that line of sight for the laser beam is available in the direction of the input.

At the fixed-base resonance of the system, the base acceleration becomes very small to maintain a given force level in the joint (motion of the mass is greatly amplified at resonance). Very small contributions of modes far removed from the driving frequency can have large effects on the measurements of the base acceleration, causing errors in the calculation of the transmissibility

functions. It is recommended that the base accelerometer be collocated with the force gage on the centerline of the excitation to minimize contributions of other modes. The accelerometer on the mass should also be located near the centerline of the experiment to reduce the contribution of unwanted bending and rocking modes.

The relative motion between the base and the mass is desired, but the direct differencing of raw accelerometer signals can prove very difficult due to instrumentation and shaker noise. As discussed in previous sections, fitting the individual signals utilizing the Fourier coefficients prior to differencing appears to yield much improved results.

3.4 Boundary Condition Quantification for Sine Wave Experiments

In any experimental configuration for investigating bolted joints, including sine wave testing with vibration shakers, the boundary conditions need to be identified and quantified. The contributions to the energy dissipation due to loss mechanisms other than the joint in the experiment must be quantified. Similarly, it is required to measure compliances in the experiment other than the joint to allow the effective compliance of the joint to be determined.

A very useful technique to accomplish this result is to fabricate a geometrically identical, monolithic test specimen without the interface. This method permits the loss mechanisms in the experiment to be quantified and allows the energy dissipation due only to the joint to be identified utilizing techniques described in previous sections. The effective compliance of the joint can be calculated by measuring the frequency difference between the monolithic and jointed test specimen. The effective joint compliance can be solved by knowing the mass and using the frequency equation for an SDOF system $\omega = \sqrt{\frac{k}{m}}$.

The use of the solid equivalent structure to quantify the boundary conditions and isolate the physics of the joint will be discussed in several other sections, as this proved to be an invaluable tool in our research efforts.

3.5 Introduction to Load History Effects

During initial sine wave experiments it was noted that the amplification factor would change (increase) if additional sine sweeps (load cycles) were made on a given joint configuration. The most discouraging aspect of this effect was that after a higher level force test was performed, the results at a lower level could never be repeated; the Q was always higher (less damping) than for the initial sweep at the lower level. The decrease in damping was also accompanied by a slight increase in the resonant frequency, indicating an increase in the stiffness joint. For a given input force level the behavior would asymptotically reach a steady state where additional sweeps did not change the

results. This feature is illustrated in Figure 3.6 from data taken in one of the experiments that will be discussed in the next section. We found that if we disassembled the joint and repeated the sine sweeps, then we could achieve repeatable results for the initial sweep and the subsequent sweeps would demonstrate the same trend of decreasing damping and increasing joint stiffness.

This load history (time-dependence) effect has been observed in all the bolted joint experiments we have performed, including the transient dumbbell testing discussed in later sections. Upon further examination of the literature, this same phenomenon was reported by other authors [38, 41] for their experiments. The authors also noted just as well as we did that even after many cycles of vibration the surfaces could be reestablished and similar results achieved.

This phenomenon has the appearance of a hardening effect where the joint becomes stiffer and dissipates less energy after a number of loading cycles. The effect can be significant with values of energy dissipation changing by a factor of four between the first load cycle and the asymptotic state.

It is postulated that the phenomenon is due to surface asperities locking up after the interface is loaded with an oscillatory input. When the joint is reassembled the process begins again.

Models to explain this effect have been developed by Gorbatikh and Popova [55] by postulating that the locking mechanism is due to the tendency of the interface to adapt its contact micro-structure to the loading conditions.

Regardless of the physics of this load-history phenomenon, it presents a challenge to the researcher to decide how the effect will be dealt with. There are at least two possible approaches available. The first is to use the first sine sweep at each input force level as the data set for comparison. The second is to use a data set at each level after the joint has reached its asymptotic state. Possibly the actual use environment for the structure with the joint of interest will suggest the answer. If the joint will see substantial vibration before the event to be modeled occurs, then the asymptotic state may be desired. An example of this case might be a staging shock in a missile after launch vibration. On the other hand, if the structure is assembled and then sees a substantial environment without any vibration preconditioning of the joint, then the initial results may be desired. An example of this case might be the launch environment of a missile.

3.6 Summary of Sine Wave Excitation

Experiments utilizing sine wave excitation can provide several important measures of response of the bolted joint. The careful processing of the input and response of an experiment configured to approximate an SDOF system can estimate the nonlinear restoring force of a particular bolted joint configuration. Results from the sine wave testing can assist in bolted joint constitutive modeling development, calibration, and validation. Care must be taken to quantify the boundary conditions to isolate the physics of the bolted joint. The use of a solid-equivalent bolted joint provides a valuable tool for accomplishing this requirement.

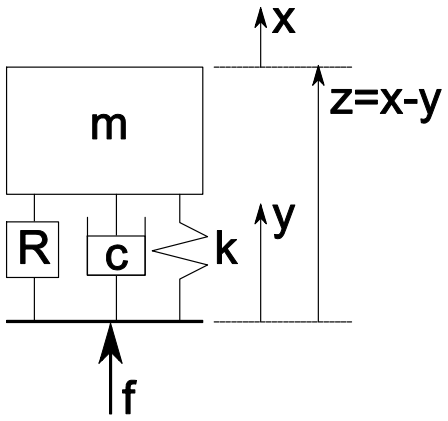

Figure 3.1. Base-Excited SDOF System.

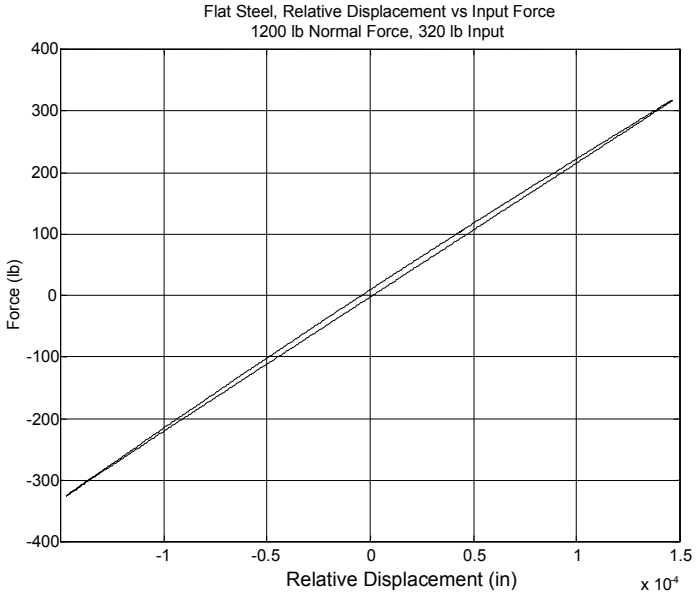

Figure 3.2. Relative Displacement Hysteresis Curve at Resonance.

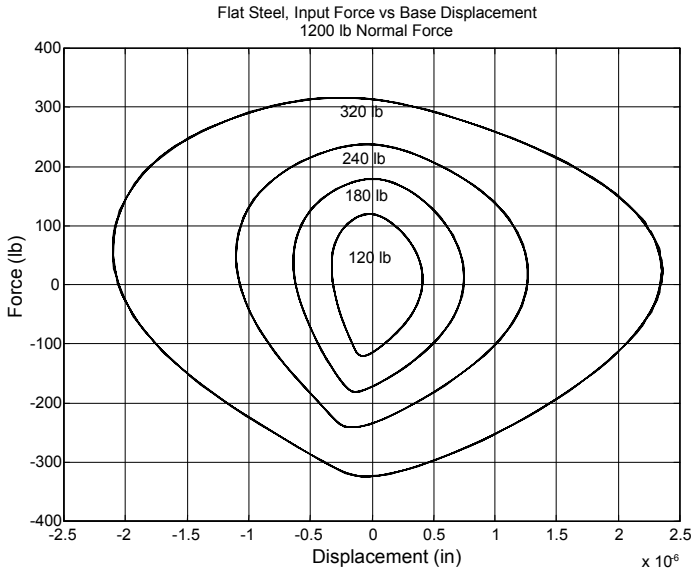

Figure 3.3. Base Motion Hysteresis Curves at Resonance.

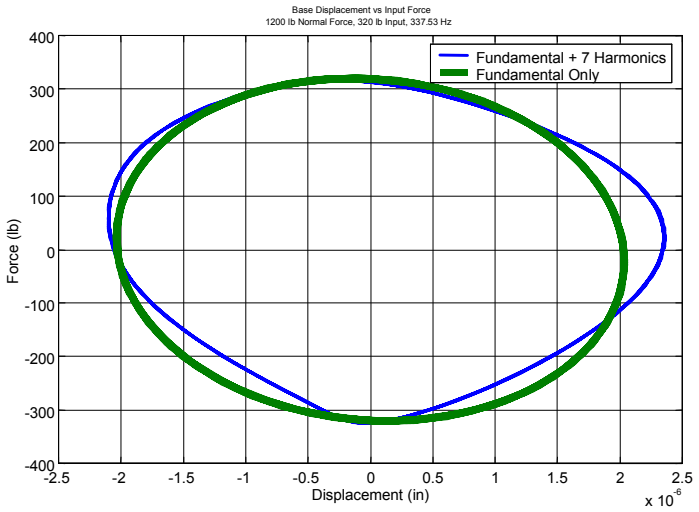

Figure 3.4. Comparison of Hysteresis Computed with Fundamental Only and with Harmonics.

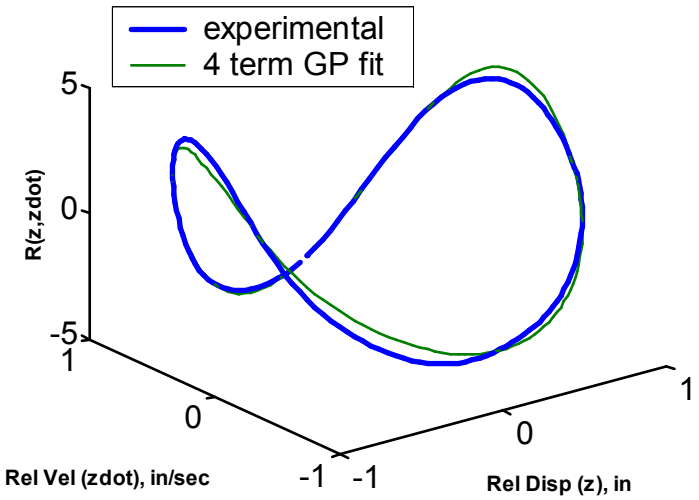

Figure 3.5. Fit of the Four-Term GP Model to the Experimental Data.

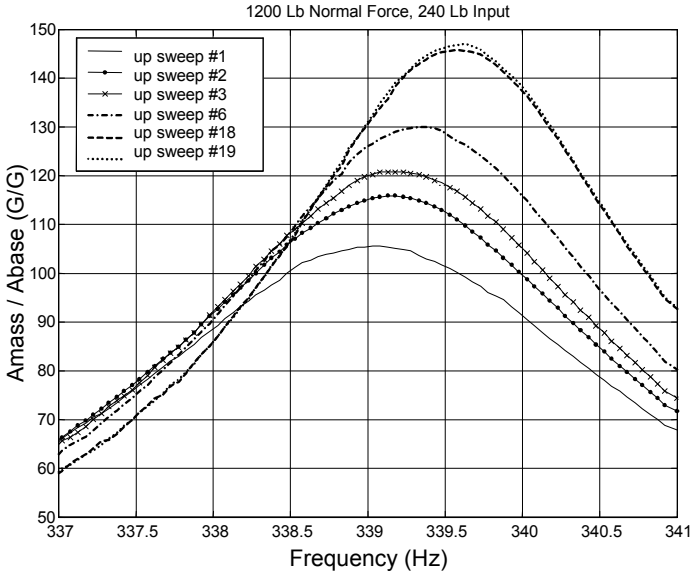

Figure 3.6. Change in Resonance Curves with Sweep Number.

Chapter 4

The Big Mass Device and Related Experiments

Danny L. Gregory and Brian R. Resor

4.1 Big Mass Device Dynamic Sinusoidal Experiments with Rollers

Investigation of the underlying mechanisms involved in the interactions of members of a bolted joint required devising an experimental configuration [46] that would simplify the activity in a simulated joint by removing the bolt from the joint. Referring to Figure 2.1 on page 45, for a single bolt there are four slip interfaces that potentially involve different surface tractions, material types, surface properties, and contact areas. Experimental data gathered for a bolted joint in shear can only measure the resultant energy dissipation, and the actual contributions for each slip interface are unknown. This complexity was the motivation to devise an experiment where the number of slip interfaces could be reduced to one such that the physics could be more easily isolated. A number of concepts were explored to eliminate the presence of a bolt in a preloaded interface; each had advantages and disadvantages. A basic concept that ultimately evolved out of the studies is shown in Figure 4.1 and has become known as the Big Mass Device.

The concept utilizes rollers above and below a simple shear joint to apply a normal load and allow small translations between the members. The rollers apply a line load across the width of the members that reduces the problem to two dimensions. The rollers ideally roll without slipping such that the losses will be small compared with the losses due to friction in the slip interface of interest. This concept has been used in the design of electrodynamic shaker systems in the past to constrain the armature motion to be along the axis of the armature. This roller concept worked well for this application in shakers, generating very little energy loss and introducing small waveform distortion.

The input force, F,is measured with a force transducer attached between the excitation source and the drive member. A concept to apply the normal load and aid in the alignment of the rollers through the use of steel cables attached to a top half “roller” and a bottom roller with tensioning cables linked through force gages, as shown in Figure 4.1, was developed.

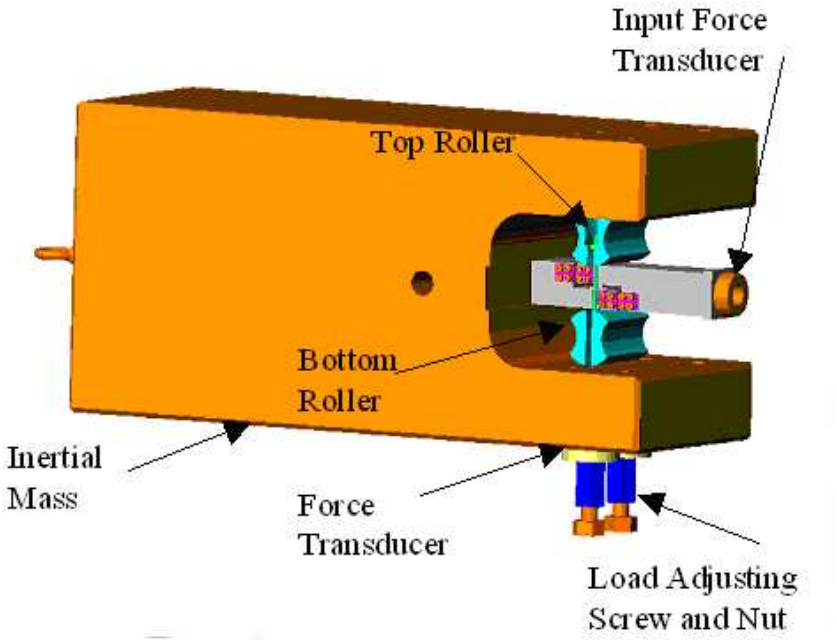

Figure 4.1. Basic Concept for a Single Friction Interface.

A slot machined into the rollers keeps them aligned and accommodates the cables. The slot width in the rollers is slightly larger than the cable diameter to prevent any rubbing and potential friction losses. Cable tension is adjustable from 0 to 2,000 lb through a load-adjusting screw and nut assembly incorporating force transducers to measure tension. The range of tension was selected to provide the range of preload typical for bolts up to 3/8-in diameter. The cable is anchored near the center of rotation of the top half roller so that for the very small linear motions the change in tension in the cables is very small for a load cycle. The surface and material characteristics of the specimens can be varied to investigate their influence on the resultant energy dissipation.

4.1.1 Installation and Alignment of Specimens

One of the critical design issues is the alignment of the contact surfaces of the specimens. It was originally envisioned that the block would be attached to a rigid foundation, but this concept did not allow for fine adjustment to align the contact surfaces. To address the alignment issues, we decided to softly support the experimental apparatus and use the inertial mass of the system to react the input forces. The total weight of the inertial block is 205 lb. The soft supports are springs with the stiffness selected to give a natural suspension frequency of approximately 2 Hz. The selection of a low suspension frequency allows the suspension resonances to be well below the desired test frequency range of 10-3,000 Hz. The soft supports allow small misalignments between the two specimens to be accommodated, as shown in Figure 4.2.

One of the pieces of each specimen pair is designed to attach to the exciter through a force transducer. The second piece is attached to the inertial mass in a centering slot with a bolt to preload the specimen. The inertial block is lowered over the specimen attached to the exciter, and small adjustments for alignment are performed with four turnbuckles between the springs and top attachment plate. The position of the top attachment plate is adjusted with the use of four set-screws. When the desired position is achieved, the top attachment plate is secured with a clamping plate. The roller and cable assemblies are then installed, and the tension in each cable is set by monitoring the force gage for each cable. The tensioning of the cables is performed incrementally while alternating between cables up to the desired load value. The tension in the cables was very stable and very little drift was noted even after a load cycle was performed with the system.

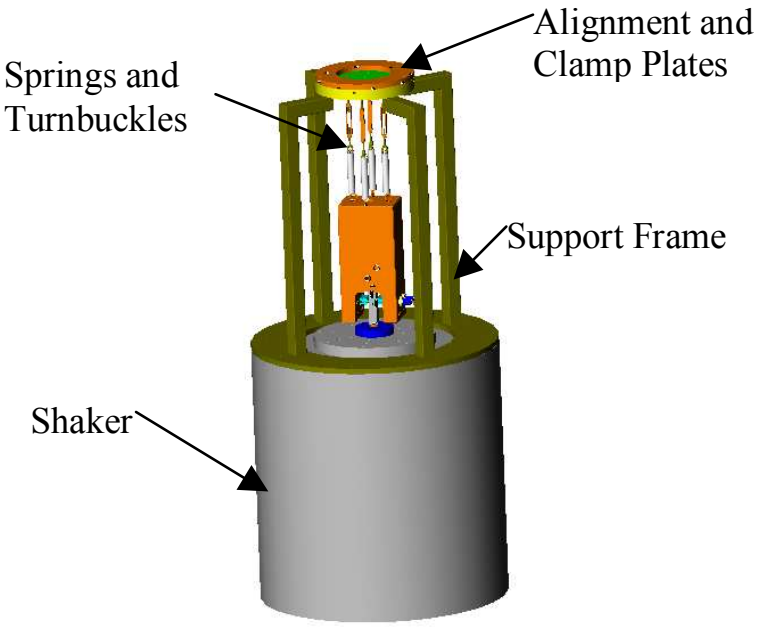

Figure 4.2. Overview of Setup with Soft Supports.

The rollers are made of AISI 4340 steel, heat treated to a Rockwell hardness of 53. Extremely tight tolerances were specified for the rolling surfaces of the rockers, which had a 32-μin rms surface finish. Solid geometry images of the rockers are shown in Figures 4.3 and 4.4. These pieces were made using the EDM (Electric Discharge Machining) technique to maintain the required tolerances with hardened steel. The rollers are designed to roll on the specimen surface to minimize losses at the roller specimen interface. The bottom roller was also machined with a large radius along the axis of the applied load to generate essentially a point load between the roller and the inertial mass. This feature was necessary to correct for any alignment problems between the inertial mass and the fixed portion of the test specimen. Upon tensioning the rollers, a line load will be applied to the external side of each of the two pieces of the test specimen.

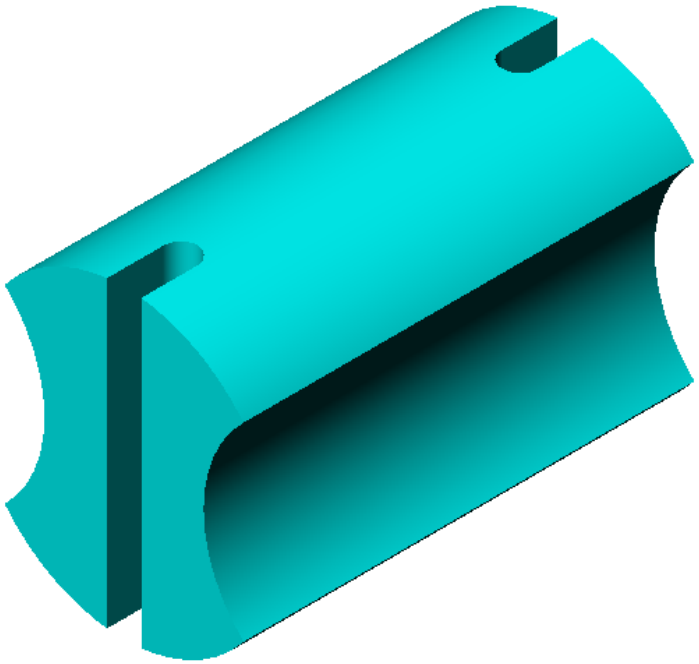

Figure 4.3. Bottom Roller.

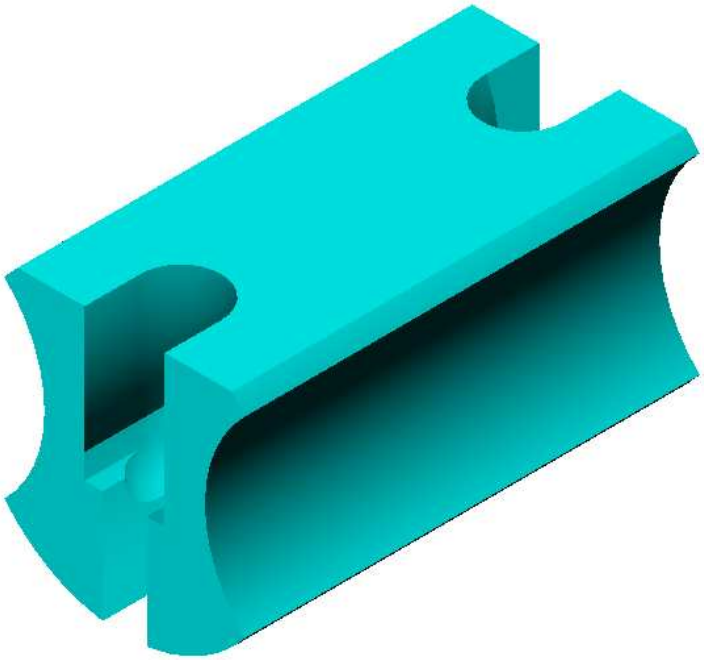

Figure 4.4. Top Roller.

4.1.2 Quantification of Roller Properties

Experiments to obtain an estimate of the magnitude of the forces required to move the rollers by measuring the force required to move a solid bar clamped in the rollers at various preloads were performed. This test configuration is shown in Figure 4.5. Accelerometers were mounted in-axis with the excitation on the solid bar and on each of the rollers. The solid bar and accelerometer were weighed to establish the total moving weight above the force gage. The accelerometer on the end of the bar was used with a digital vibration control system to control the input motion of the bar. The force to acceleration transfer function is calculated and yields the dynamic mass of the system.

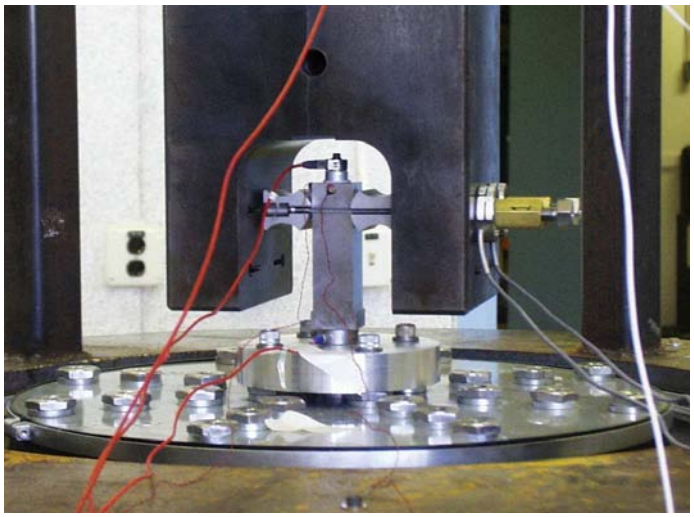

Figure 4.5. Roller Dynamics Investigation.

The total dynamic weight of the calibration bar and rollers is shown in Figure 4.6 for a single pair of rollers with a cable preload of 800 lb per cable at three input levels of random vibration. There is a small resonance of the top roller at frequencies below approximately 250 Hz, depending on the cable preload. As the preload increases, the frequency of the resonance also increases. This resonance exists because the top roller is not constrained on both sides, unlike the bottom roller. The dynamic weight associated with this resonance is small, (less than 20 lb), and can be eliminated from the total force by using the calibration curve. Above this frequency the dynamic weight approaches a constant of approximately 2.0 lb per g, which is independent of the cable preload. The results show that the dynamic mass is very repeatable, is not sensitive to the changes in input level, and can be accounted for with a single calibration curve. The dynamic weight was also measured as a function of preload and found to be very insensitive to changes in preload. These results are very encouraging because ultimately the energy loss factor associated with the rollers will not have amplitude dependence on either the normal force or input force.

The static weight of the calibration bar and accelerometer totaled 1.582 lb. Subtracting this value from the dynamic weight of 2.0 lb yields the very small dynamic weight of the rollers of

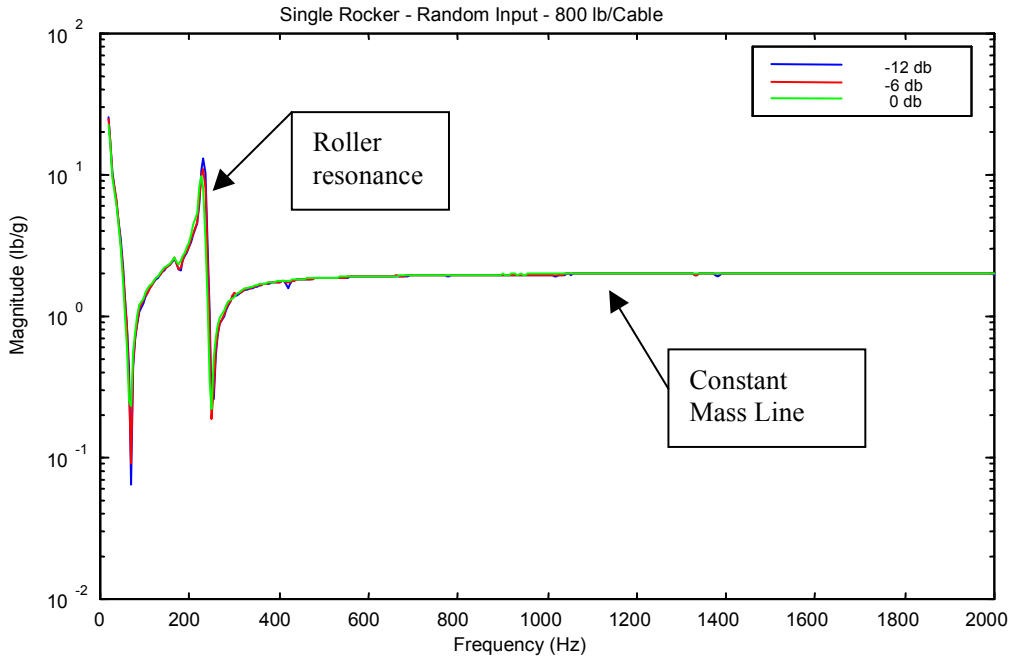

Figure 4.6. Dynamic Mass Measurement of Rollers.

0.418 lb. This amount represents the total force required to move both rollers with a rigid bar and can be subtracted from the total input force to solve for the friction force, which includes both the inertia of the rollers, rolling resistance forces, and any cable interaction forces. For practical purposes, this force could be neglected as it represents only a very small portion of the total force for an actual friction experiment. For simplicity, experiments should be configured at frequencies in the bandwidth of constant roller force. Otherwise, at lower frequencies where the dynamic weight is not constant, the roller force can still be accounted for, if necessary, by using a calibration curve that can be established for each setup.

4.2 Experiments with the Big Mass Device

The BMD has proven to be a very useful means of investigating microslip in a simple interface. The test specimens can be manufactured to vary a number of material parameters found in real bolted joints. These parameters include material types, surface roughness, surface hardness, and surface lubrication. The contact pressure distribution can be modified by changing the geometry of the two halves of the test specimens. Examples of different geometries are shown in Figures 4.7 - 4.9. Three basic configurations were investigated at Sandia National Laboratories. These included a "flat" specimen with both sides of the interface machined flat to provide a continuous contact pressure distribution with moderate edge effects. A second configuration was the "stepped" specimen that provided a localized contact with strong edge effects. The third configuration was the "curved" specimen, which consisted of one half of the specimen machined with a 10-in radius while the other half was kept flat, allowing a localized contact condition with minimal edge effects. Drawings for the test specimens are included in Appendix A.

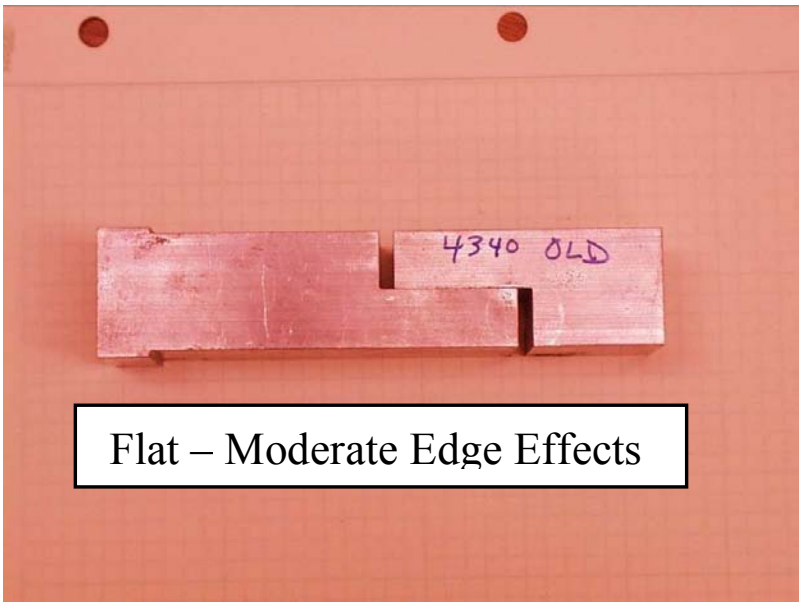

Figure 4.7. Flat Specimens.

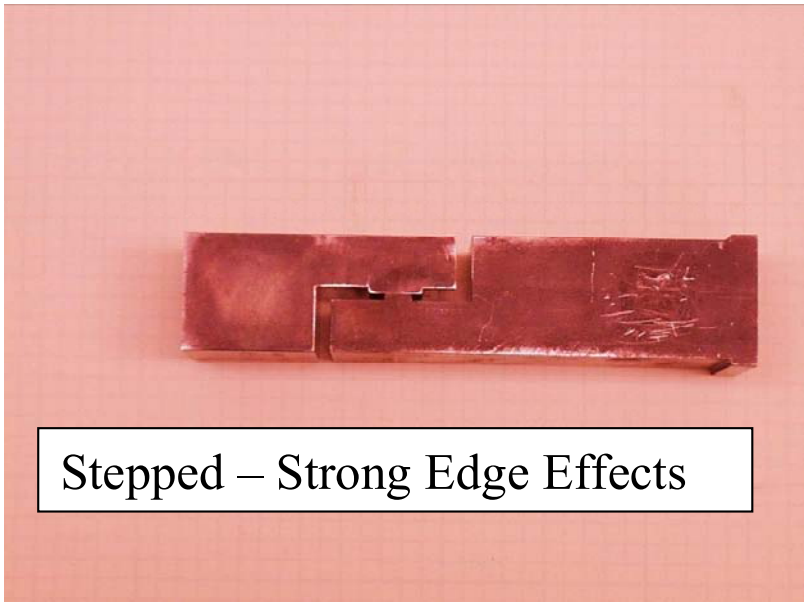

Figure 4.8. Stepped Specimens.

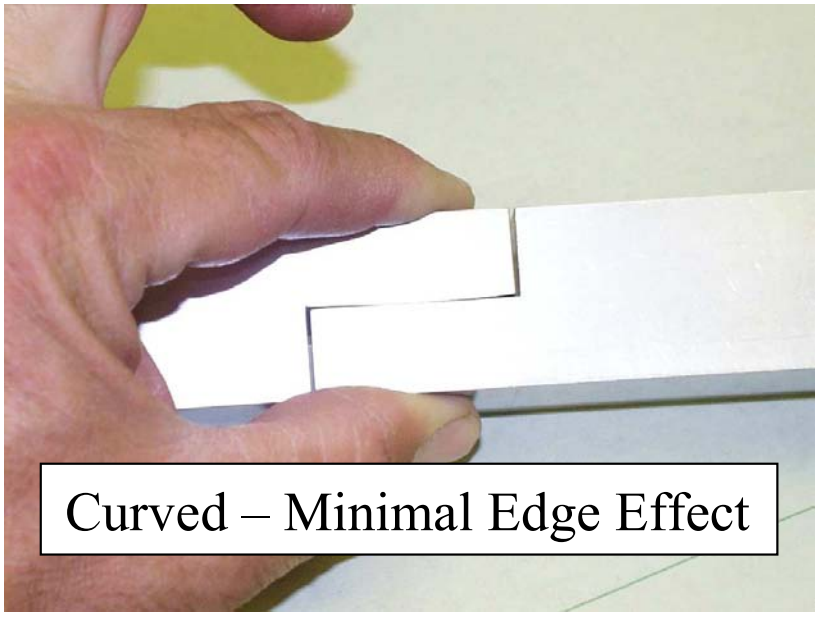

Figure 4.9. Curved Test Specimens.

A typical setup including the rollers and the flat, stepped, and curved test specimens is shown in Figures 4.10 - 4.12. The BMD, coupled to an electrodynamic shaker, provides a very good approximation to a base-driven SDOF system at the first axial resonance, and all of the analysis tools for sinusoidal vibration described in the previous section are applicable.

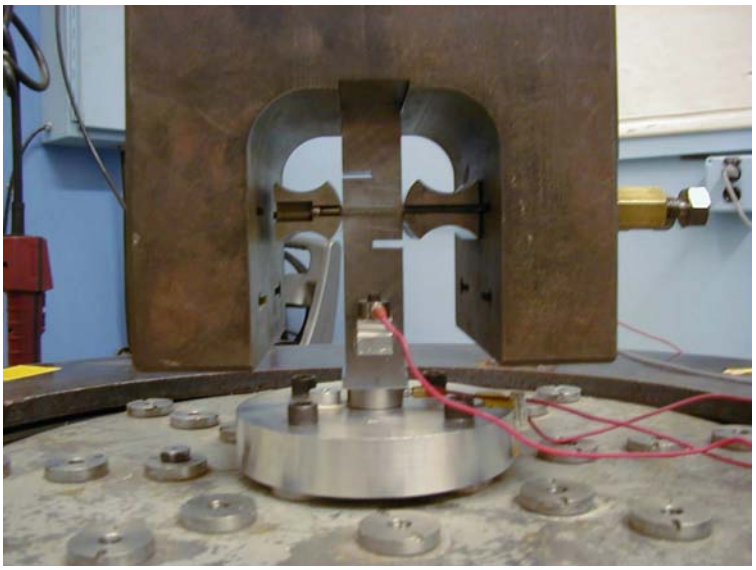

Figure 4.10. Setup with Flat Test Specimens.

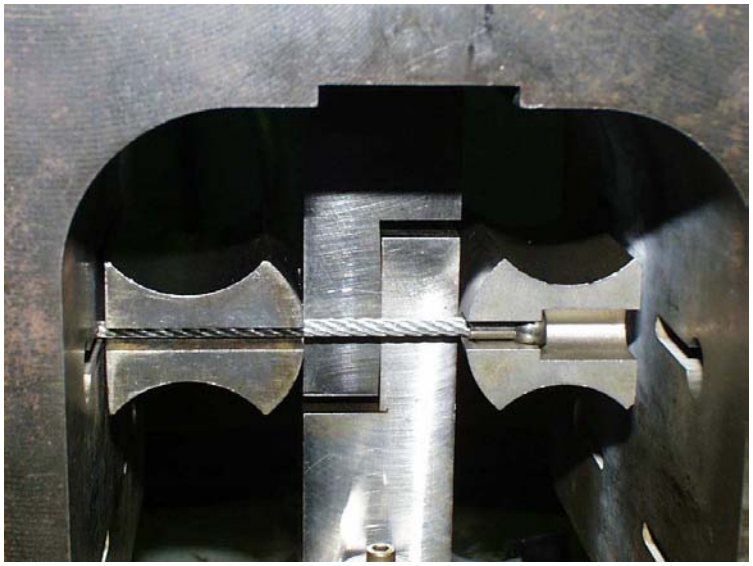

Figure 4.11. Curved Specimen Setup.

Figure 4.12. Stepped Specimen Setup.

4.2.1 Flat Lap Joint Experiments

The initial experiments [47] with the BMD and rollers were performed on flat test specimens to measure the energy loss per cycle for a sinusoidal input force over a range of loads of 60-, 120-, 180-, 240-, and 320-lb peak, and with a range of normal forces of 800-, 1200-, 1600-, and 2000-lb. The experimental apparatus was configured on an Unholtz-Dickie T1000, electrodynamic shaker system. A Spectral Dynamics 2560, vibration control system was used to control the input for the experiments. The overall setup of the BMD on the shaker system is shown in Figure 4.13.

Figure 4.13. Overall Test Setup of BMD.

The specimens were machined out of AISI 4340 steel with a surface roughness of about 32-μin rms. Data were also collected for a geometrically identical solid bar with no frictional interface to establish a lower limit for the unaccounted loss mechanisms in the setup. The energy loss per cycle was experimentally determined by first performing a sine sweep controlling the force at a constant value over a frequency bandwidth encompassing the fixed-base resonance of the test apparatus, which ranged from 330- to 340-Hz depending on the normal clamping load and excitation level. The amplitude ratio (transmissibility) of the acceleration of the mass and the acceleration of the base was then calculated to determine the amplification factor (Q). A constant bandwidth (10 Hz), digital tracking filter was used with a linear sweep rate of 0.50 Hz/s in the signal processing to compute Q. The amplification factor was established at the frequency where the phase was measured to be 90°.

As discussed in Section 3, the experiments revealed a load-history effect where the amplification factor would change with subsequent sweeps. A test repeated at a lower force level always indicated a Q much higher than for the first test at that level. We chose to use the initial sine

sweep after reestablishing the surfaces for the primary data. The surfaces were initially cleaned with alcohol and compressed air during each reset of the surfaces.

A special assembly fixture, shown in Figure 4.14, was designed to assist in aligning the rollers with the test specimen and inertial mass. By inserting locating rods through the assembly fixture and inertial mass, the correct alignment could be achieved. A gage block was machined to set the longitudinal gap between the test specimens.

Figure 4.14. Assembly Fixture for Rollers.

The amplification factors were measured for each load sequence for a given normal force, which was established by tensioning the cables while observing the load in each cable by means of force transducers. Amplification factors were used to compute the equivalent viscous damping ratios, and the results are shown in Figure 4.15, plotted as a function of the input force. The data plotted on a log-log scale approaches a straight line, and the slope of a straight-line fit, denoted by "s" on the plot legends, was computed, with variation ranging from 0.59 to 0.83. The slope of the solid-bar damping ratio is essentially zero, indicating a linear system response over the measured force ranges.

The amplification factors, Q, are next used in Equation (3.9) in Section 3 to compute the energy loss per cycle, and the results are shown in Figure 4.16. Here, the data show the anticipated straight line on a log-log plot, indicating a power-law relationship between the energy loss per cycle and the input force for a given normal force, $D = kF^n$. The data are fit with straight lines, and the slopes vary from 2.56 to 2.86. Note that the slope of the solid bar data is almost exactly 2.0, which is what is expected for a linear system. As a side note, the solid bar data support the hypothesis that bolted interfaces under tension and compression loadings dissipate very little energy, so the damping can be modeled as linear, an important outcome.

The data for the energy dissipation are also shown plotted on a linear scale in Figure 4.17,

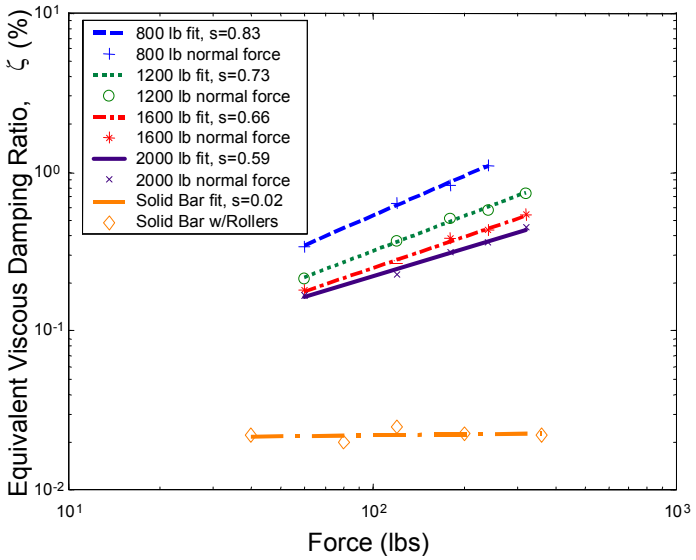

Figure 4.15. Equivalent Viscous Damping Ratio vs Force.

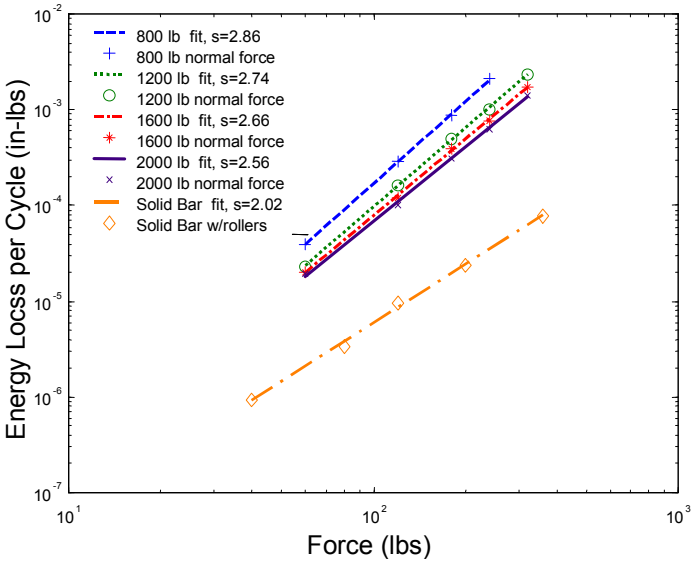

Figure 4.16. Energy Dissipation per Cycle vs Force.

which emphasizes the relative amplitudes of the energy loss per cycle as a function of input force level. In addition, they show the dramatic increase in energy loss created by the presence of the friction interface when compared to the solid bar data. The data are also plotted in Figure 4.18 as a function of the nondimensional force, F/N, obtained by dividing the input shear force by the normal force. The data lie within a band, but do not collapse to a single curve, indicating that the data are not simply a function of the nondimensional force and that other parameters are required in the relationship between the input force, normal force, and energy loss per cycle. It is desirable to gain more understanding of this relationship with further study in the future.

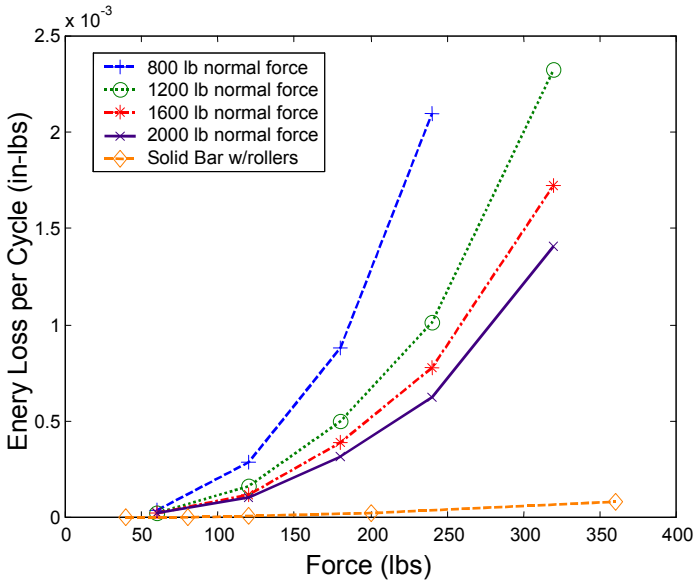

Figure 4.17. Energy Dissipation per Cycle vs Force on a Linear Scale.

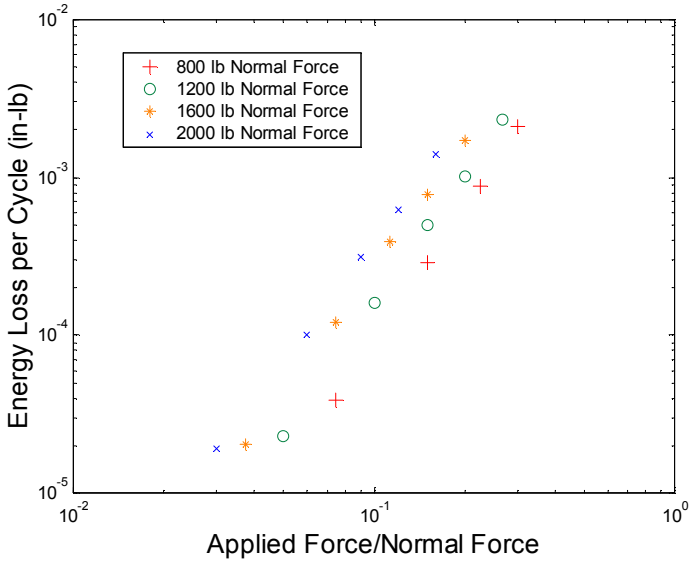

Figure 4.18. Comparison of Energy Dissipation Calculations, 1200-lb Normal Force.

Time history data were also collected for sinusoidal dwells at resonance. Waveform data were used to compute the energy loss per cycle through reconstruction of the classical hysteresis curves. Using techniques discussed earlier in Section 3, the accelerometer data were fit with the fundamental and seven harmonics. The reconstructed waveform was integrated to obtain the velocity and displacement. Figure 4.19 shows the traditional hysteresis curve of force vs relative displacement for 1200-lb normal force and an input force of 320-lb. The hysteresis curve shows most of the dissipation occurs near the center of the curve while the ends are very compressed, indicating small dissipation in these regions. Integration of this curve yields an energy loss of almost exactly the same value obtained using the amplification factor in Equation (3.9) in Section 3.

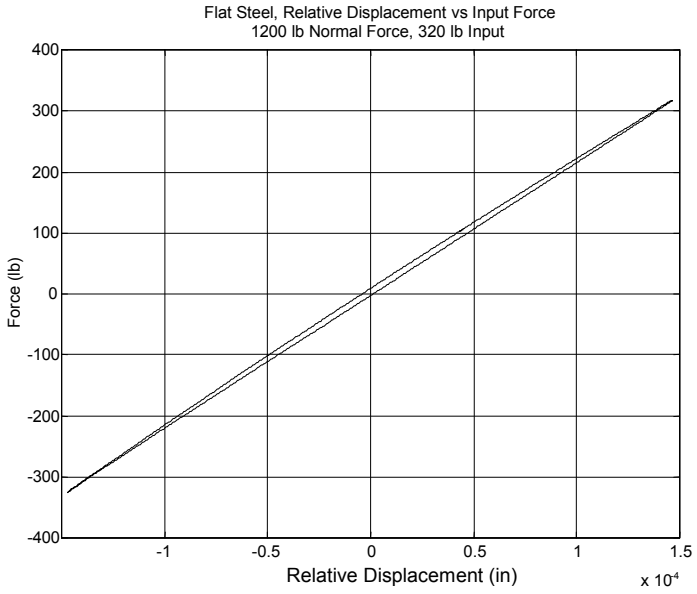

Figure 4.19. Relative Displacement Hysteresis Curve at Resonance.

For the base excited system, another hysteresis curve can be constructed by plotting the force vs the absolute motion of the base. As discussed earlier, this hysteresis curve should yield the same energy loss per cycle as the hysteresis curve generated for the relative motion, because the motion of the mass is in phase with the force and the only out-of-phase response is the base motion. The energy dissipation per cycle calculations by the three methods show very close agreement, as Table 4.1 clearly indicates.

At the fixed-base resonance, the motion of the base to maintain a steady state response with a prescribed force is very small for a lightly damped system. Without an analytical fit of the experimental data, the hysteresis could not be constructed due to signal-to-noise challenges. Utilizing the analytical fit, the force vs base motion hysteresis curves, shown in Figure 4.20, demonstrate some intriguing qualities. As discussed earlier, a linear response would exhibit an ellipse. However, as seen in the plot the curves deviate significantly from the expected ellipses. The deviation from a linear response is shown in Figure 4.21, where the data for 1200-lb normal force and an input

Table 4.1. Energy Dissipation per Cycle as a Function of the Non-Dimensional Force.

Input Force (lb)	Q Method (in-lb)	Relative Hysteresis (in-lb)	Base Hysteresis (in-lb)
120	1.3426×10^{-4}	1.3045×10^{-4}	1.2889×10^{-4}
180	3.6580×10^{-4}	3.5980×10^{-4}	3.6247×10^{-4}
240	8.3285×10^{-4}	8.1720×10^{-4}	8.1645×10^{-4}
320	2.0817×10^{-3}	2.0417×10^{-3}	2.0428×10^{-3}

force of 320-lb are plotted with only the component at the fundamental frequency yielding an ellipse compared with the data retaining all seven harmonics in the response. The energy dissipated is computed by integrating both curves. Very close agreement is achieved, indicating that almost all of the energy is dissipated at the fundamental frequency. The higher harmonics are a result of, and contain information regarding, the nonlinear response of the system.

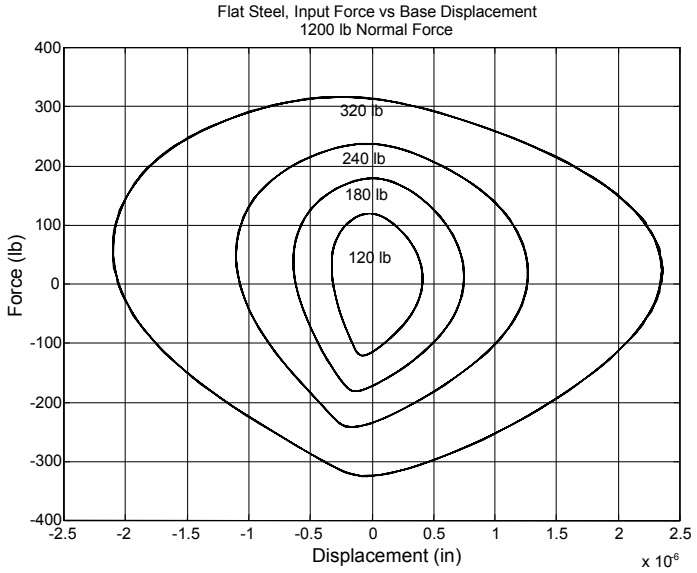

Figure 4.20. Base Motion Hysteresis Curves at Resonance.

The techniques and results from this set of experiments establish the framework for a number of subsequent experiments to study variations of the test specimens to investigate the energy dissipation due to microslip in mechanical interfaces. These experiments demonstrated that the BMD provided an effective and accurate means for determining the energy dissipation in a frictional joint in shear.

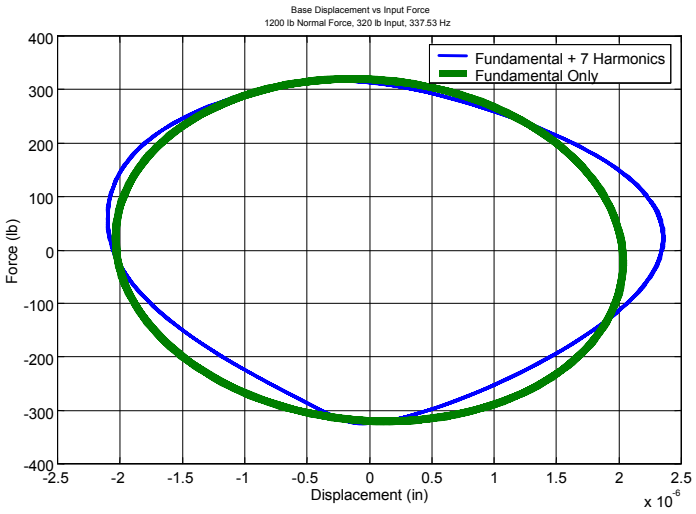

Figure 4.21. Comparison of Hysteresis with only Fundamental and with Harmonics.

4.2.2 Flat Lap Joint - Stainless Steel on Titanium

Two materials of interest to Sandia National Laboratories in a component bolted connection are titanium and stainless steel. The BMD was configured with flat test specimens, and a very similar set of tests as with the AISI 4340 steel specimens was performed to measure the energy dissipation per cycle as a function of normal and applied shear forces. Experiments were performed to measure the energy loss per cycle for a sinusoidal input force over a range of loads of 60-, 120-, 180-, 240-, and 320-lb peak with a range of normal forces of 800-, 1200-, and 1600-lb.

Data were collected on a set of specimens that were machined to the same specifications as the 4340 steel specimens in the previous section. After each load cycle, the joint was assembled and disassembled a total of five times to investigate variability of the results.

The fixed-base resonant frequency of the system varied from 292 to 295 Hz depending on the normal clamping load and excitation level. Energy dissipation vs shear force curves are shown in Figures 4.22 - 4.27 for each normal force level, along with a least-squares, log-log line. The slopes with the mean and standard deviation are also shown in Table 4.2.

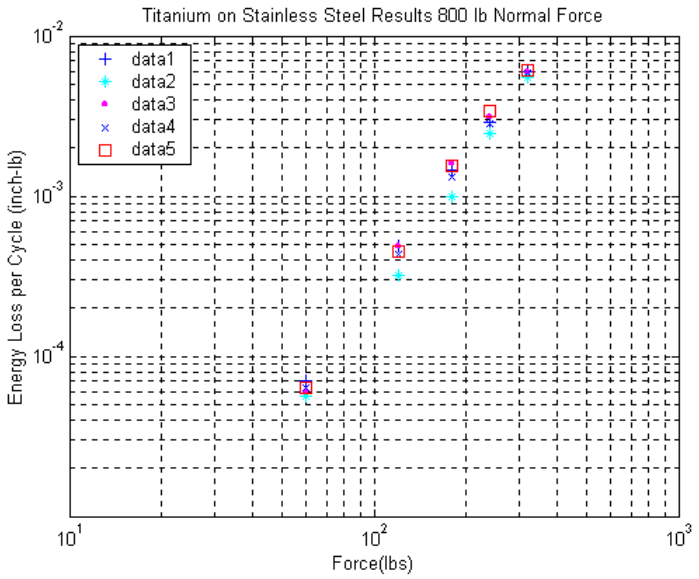

Figure 4.22. Energy Dissipation of Titanium on Stainless Steel with 800-lb Normal Force.

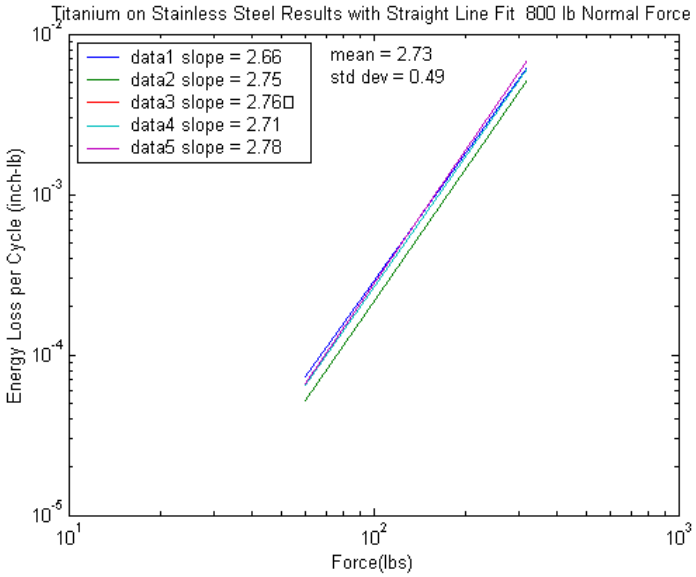

Figure 4.23. Straight Line Fit of Titanium on Stainless Steel with 800-lb Normal Force.

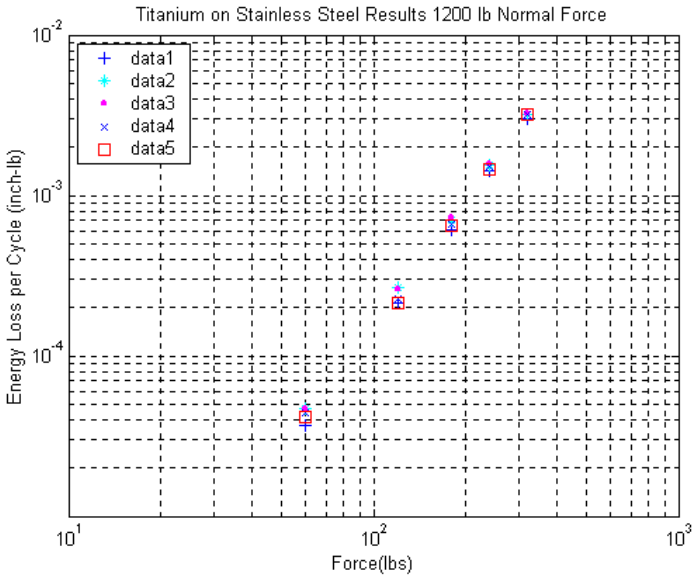

Figure 4.24. Energy Dissipation of Titanium on Stainless Steel with 1200-lb Normal Force.

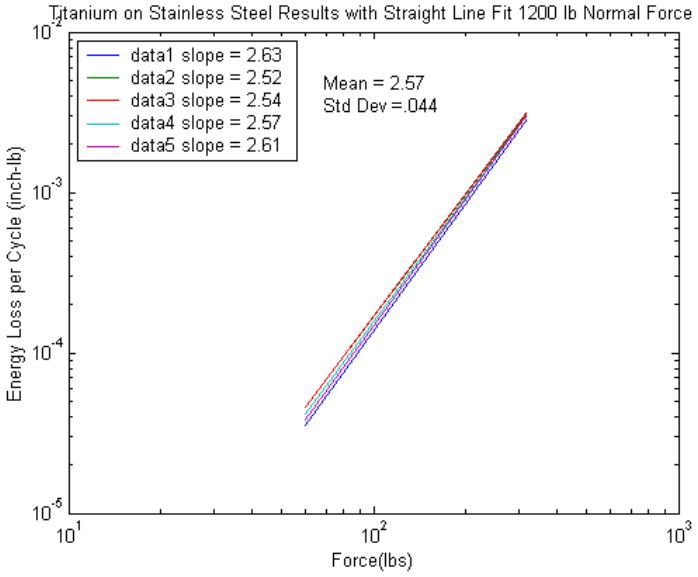

Figure 4.25. Straight Line Fit of Titanium on Stainless Steel with 1200-lb Normal Force.

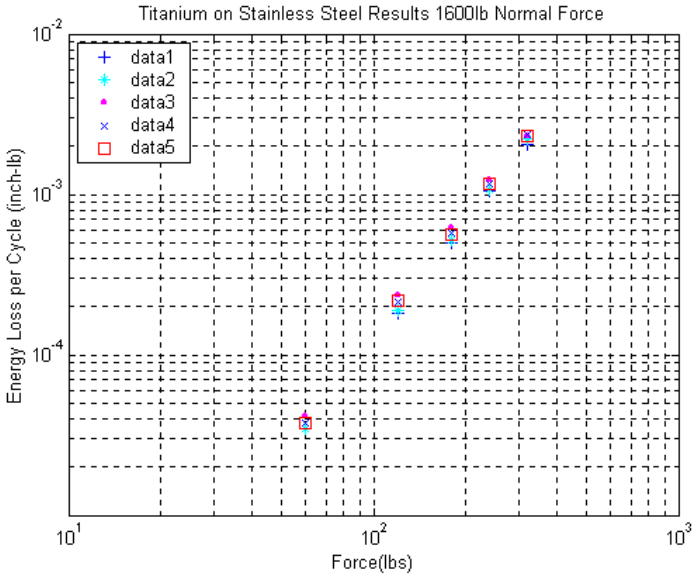

Figure 4.26. Energy Dissipation of Titanium on Stainless Steel with 1600-lb Normal Force.

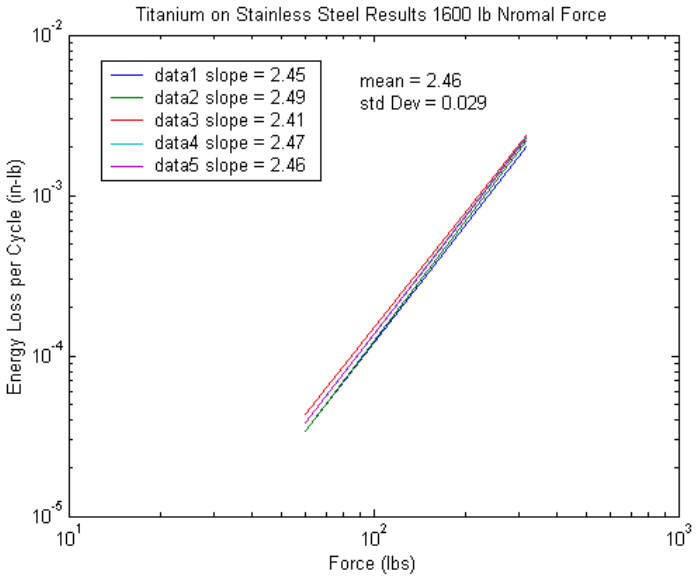

Figure 4.27. Straight Line Fit of Titanium on Stainless Steel with 1600-lb Normal Force.

The data were very repeatable at each of the normal force levels, as illustrated by the small standard deviations that resulted. For the titanium and stainless steel specimens, the data show similar behaviors to the AISI 4340-steel specimens. The slopes of the energy dissipation curves for both experiments showed a slight increase with decreasing normal force. The measured slopes for the Ti-SS data are slightly less than those for the AISI 4340 steel specimens, likely due to the difference in frictional characteristics between the different materials.

Table 4.2. Comparison of Slopes of Energy Dissipation vs Force for Steel and Titanium.

Normal Force (lbs)	Ti-SS Mean Slope	Ti-SS Slope Std. Dev.	AISI 4340 Steel Slope
800	2.73	0.490	2.86
1200	2.57	0.044	2.74
1600	2.46	0.029	2.66

4.2.3 Stepped Specimen Experiments

The stepped specimens were originally designed to provide an almost constant contact pressure in the interface. This intent was not realized, however. The specimens are not rigid bodies, but instead are elastic structures where the localized contact at the corners of the step in the geometry creates a very sharp increase in the contact pressure. A contact analysis with ABAQUS in Figures 4.28 and 4.29 illustrate the interaction of the two halves of the stepped test specimen when loaded with the rollers.

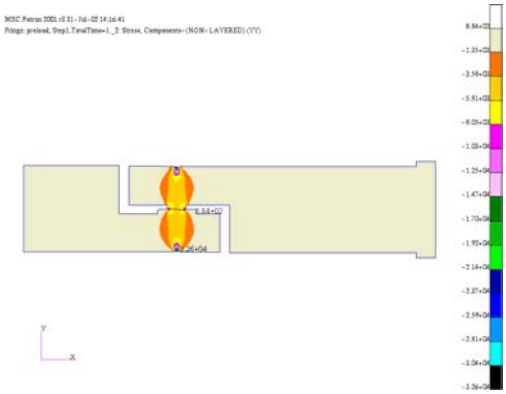

Figure 4.28. Contact Stresses in Stepped Specimen.

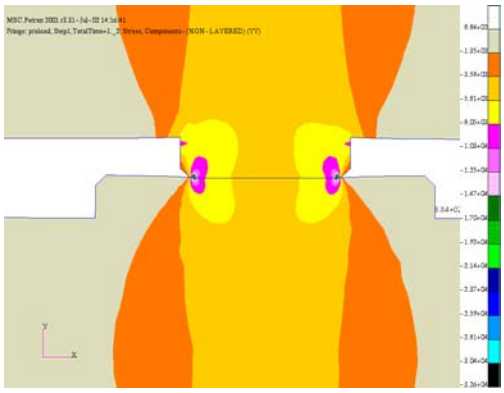

Figure 4.29. Expanded View of Contact Stresses in Stepped Specimen.

The stepped specimen does not give a constant contact pressure, but provides a complex pressure distribution that may provide insight into the behaviors of threaded and tape joints. As shown in Figure 4.30, the thread engagement in a threaded joint shares the feature that the contact patch terminates at an edge.

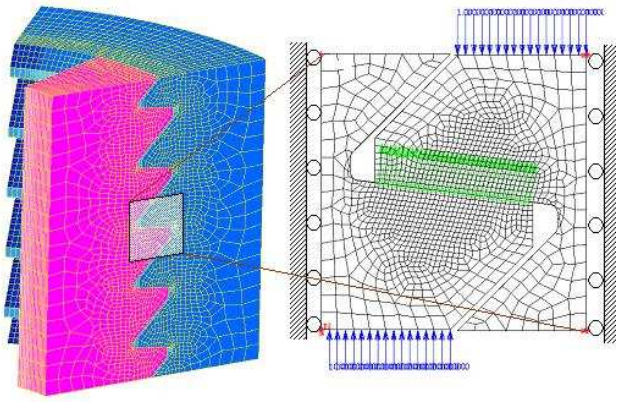

Figure 4.30. Illustration of Localized Contact in a Threaded Joint.

The same normal force and input shear force load levels were used for tests on the stepped specimens as for the previous experiments with the flat specimens. After each load cycle the joint was assembled and disassembled five times to investigate variability of the results, which are shown in Figure 4.31. The range of the resonant frequency was from 252 Hz to 270 Hz, depending upon the normal and input force levels. The slopes of the energy dissipation curves, approximately 2.8, are clearly higher for the stepped steel specimen than for the flat steel specimen, approximately 2.5. Presumably this is due to the dramatically different normal traction distributions in their respective contact patches.

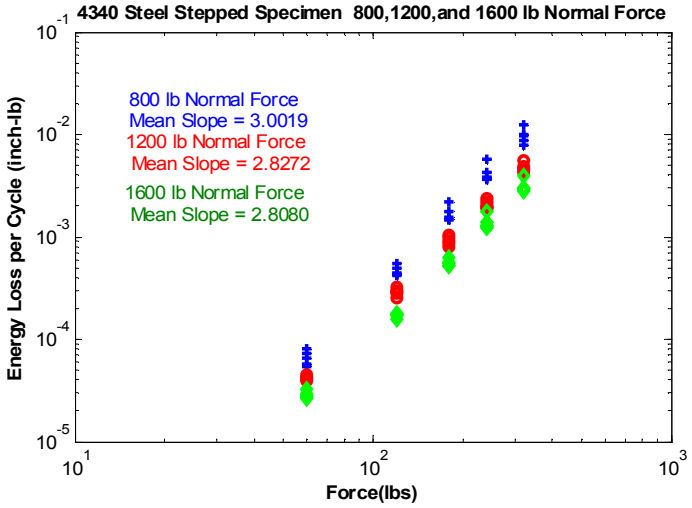

Figure 4.31. Stepped Specimen Results.

4.2.4 Curved Specimen Experiments

The curved specimen was designed to provide a different type of contact pressure that would minimize edge effects and approach a classical, Hertzian, contact condition. Half of the specimen was machined with a 10-in radius while the other half was flat. The special assembly aid to position the rollers proved critical in the alignment of the rollers with the curved specimens. As on the previous experiments with the flat and stepped specimens, the same normal force and input shear force load levels were used in the tests on the curved specimens. Similarly, after each load cycle the joint was assembled and disassembled five times to investigate variability of the results. The resonant frequency ranged from 270 Hz to 285 Hz, depending upon the normal and input force levels. The results, shown in Figure 4.32, demonstrate the anticipated trend of increased energy dissipation with decreasing normal load. The slopes of the energy dissipation curves for the 1200-lb and 1600-lb normal forces were the same (3.06), while there was a substantial decrease for the 1600-lb normal force (2.48).

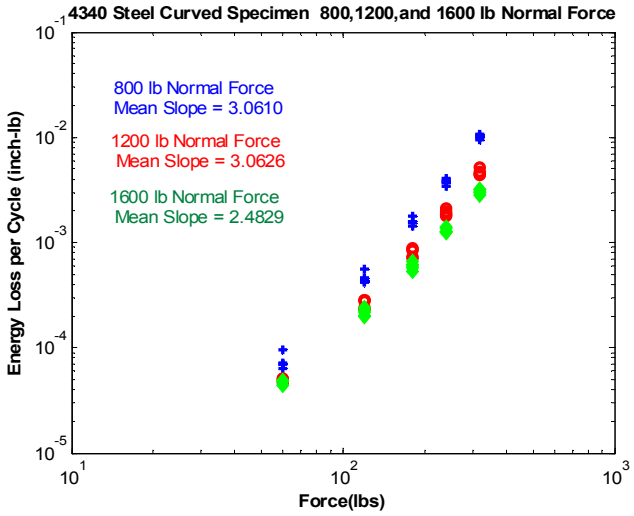

Figure 4.32. Curved Specimen Results.

4.2.5 Comparison of Flat, Stepped, and Curved Test Specimens

One of the objectives of the experiments on the BMD with rollers was to change the parameters of the joint and observe changes in the energy dissipation as a function of normal force and input shear force. Comparisons of the results from the previously described experiments for the AISI 4340 steel, flat, stepped, and curved test specimens are shown in Figures 4.33 - 4.36. The energy dissipation for the flat specimen is substantially less than for the curved and stepped specimens. Note that the computed slopes of the energy dissipations are also different, which is likely a result of the different contact pressure distributions, even though the total normal force is the same in each of the joint geometries.

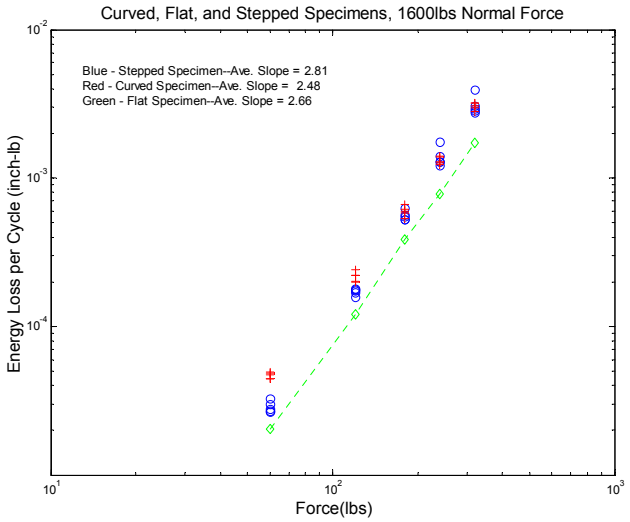

Figure 4.33. Curved, Flat, and Stepped Specimen Results with 1600-lb Normal Force.

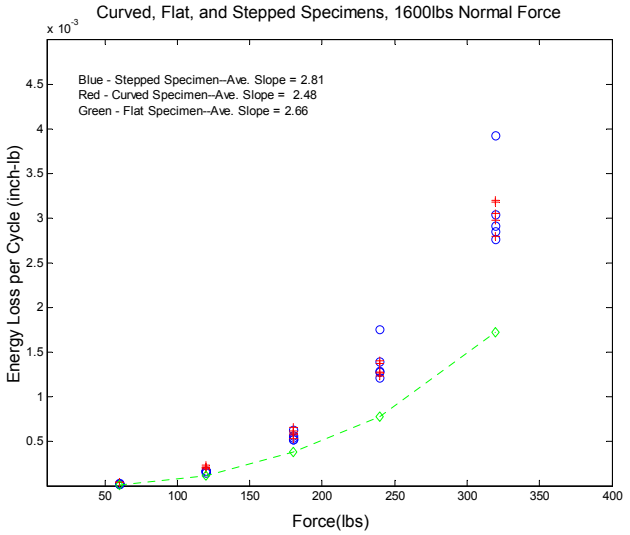

Figure 4.34. Curved, Flat, and Stepped Specimen Results with 1600-lb Normal Force Linear Plot.

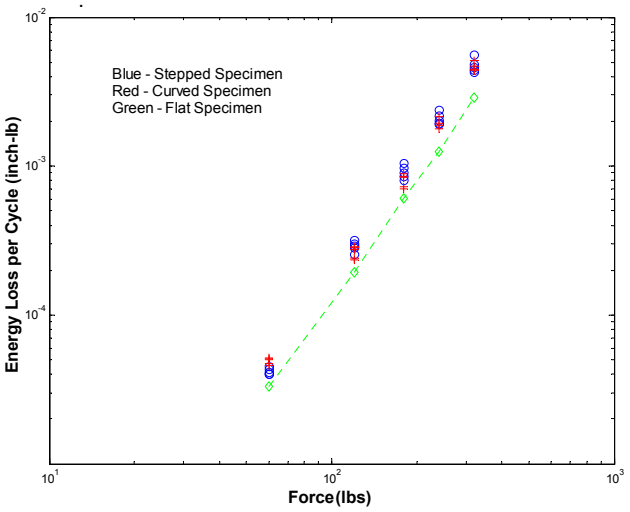

Figure 4.35. Curved, Flat, and Stepped Specimen Results with 1200-lb Normal Force.

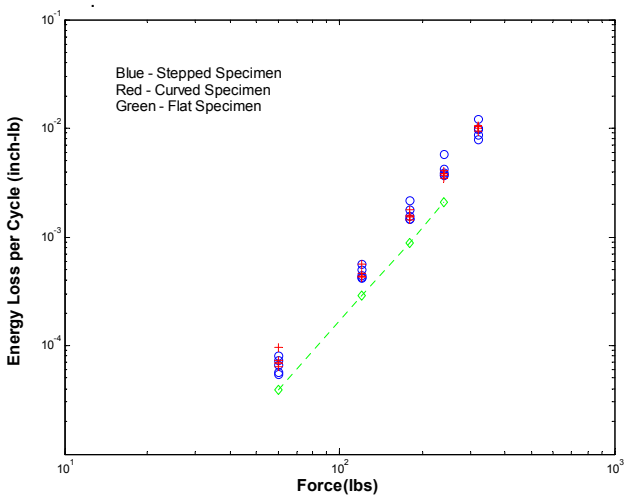

Figure 4.36. Curved, Flat, and Stepped Specimen Results with 800-lb Normal Force.

Table 4.3. Comparison of the Slopes of Energy Dissipation Curves vs Force.

Normal Force	Flat Specimen	Stepped Specimen	Curved Specimen
800	2.86	3.00	3.06
1200	2.74	2.83	3.06
1600	2.66	2.81	2.48

The results are somewhat puzzling because it was initially anticipated that the flat lap joint would dissipate more energy than the more localized contact conditions of the stepped and curved specimens. We hypothesized that the asymptotically decreasing normal pressure for the flat specimen in regions removed from the normal force line load provided by the roller would allow more microslip to occur per unit of shear force.

During assembly of the specimens, we noticed that the localized contact for the stepped and curved specimens provided less bending stiffness of the joint so that the inertial mass could more easily rock. We speculate that there may be more bending actions occurring in these joints that can modify the contact conditions and lead to increased energy dissipation. Further investigations through models and experiments are needed to reconcile the differences. We recommend that in the future, accelerometers should be used to measure the lateral accelerations of the mass that would generate moments in the joint.

The results for the computed slopes are listed in Table 4.3.

4.2.6 Dynamic Stiffness Calculations

Frequency measurements of an SDOF system such as the BMD can yield an effective global stiffness of the test specimen, jointed interface, and the specimen attachments to the mass and the shaker, by using the frequency equation $\omega = (k/m)^{1/2}$. The change in the frequency as a function of the input shear and/or normal force can allow the change in stiffness to be calculated. Experiments with the solid equivalent structures have shown that the stiffness of the specimens and attachment interfaces (tension/compression) to the mass and the shaker are linear and do not change appreciably with input force. Therefore, the change in stiffness as a function of the normal and input shear force is associated with the interface joint itself. An example of this effective stiffness calculation is shown in Figure 4.37. Knowledge of the solid equivalent specimen frequency allows the stiffness of the joint itself to be calculated by subtracting the difference compliances of the jointed and non-jointed specimens. The decrease of effective stiffness with shear load is illustrated for the cases of stepped and curved specimens in Figure 4.37. The response of flat specimens (not shown here) is similar to that of curved specimens.

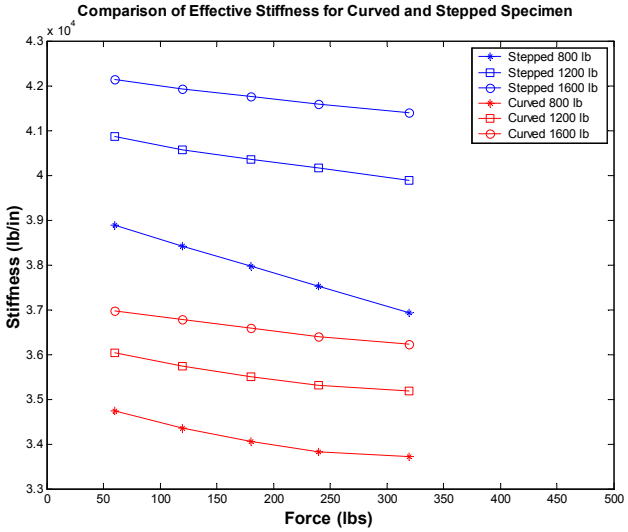

Figure 4.37. Effective Stiffness Calculations.

4.2.7 Surface Roughness Studies

We configured a series of experiments with the BMD to investigate the effect of surface roughness on the energy dissipation of a simple shear interface. A technique to provide a uniform (isotropic) roughness in the contact region was desired. Typical machining and grinding operations leave variations and directionality across the machined surface that might create further unknowns in the contact conditions.

After some research we determined that the Electric Discharge Machining (EDM) technique could provide a very uniform surface roughness. Furthermore, the roughness could be changed over a large, selectable range by adjusting the EDM process for the material of interest. Stepped test specimens were prepared with three target roughness levels termed as “fine”, “medium”, and “rough”. Subsequent laser profilometer measurements determined that the surfaces were indeed uniform in all directions. The measured average roughness values were 75-, 180-, and 385-μin rms for the fine, medium, and rough specimens, respectively. These roughness values were higher than planned, but still provided a large range for study. A typical stepped specimen with the “rough” surface is shown in Figure 4.38.

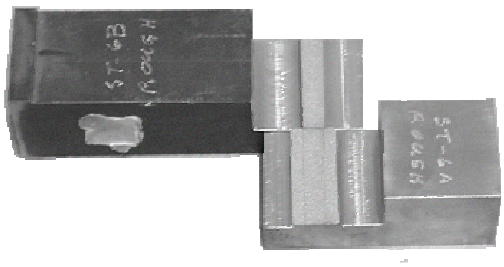

Figure 4.38. Stepped Steel Specimen with EDM Generated Roughness.

The stepped steel specimens with the roughened surfaces were configured and tested in the BMD over the same range of inputs and normal forces used for the previous experiments. Results from the experiments are shown in Figures 4.39 - 4.41. As anticipated, the energy dissipation increased with decreasing normal force for all the surface roughness values, but was more pronounced for the roughest surface. The comparison of the energy dissipation curves for the three roughness levels at 1600-lb normal force is shown in Figure 4.41. The “rough” specimen, as expected, dissipated substantially less energy at all input force levels. The comparison between the “medium” and “fine” results show that at low force levels the medium roughness specimen dissipated less energy than the fine, but at the highest force level (320 lb) the dissipation is essentially equal.

The experiments with the BMD provided some interesting experimental results comparing EDM-processed test specimens at three levels of roughness. We recommend that flat specimens be used in the future for similar surface roughness evaluations. The stepped specimens have local contact conditions with strong edge effects that could possibly obscure the effects of the surface roughness. Future work in this area that may prove valuable would be to perform similar experiments with the surfaces prepared with various machining and grinding operations. These operations will leave various types of anisotropy of the resulting surfaces, which will modify the effective contact area/pressure between the surfaces of a joint. Contact pressure film measurement techniques (see Section 9) can be used to understand the resulting contact between the specimens after the machining operations. Subsequent measurements of the energy dissipation as a function of input shear force and normal force along with the measurement of the effective joint stiffness could provide valuable insight into the constitutive model development for bolted joints.

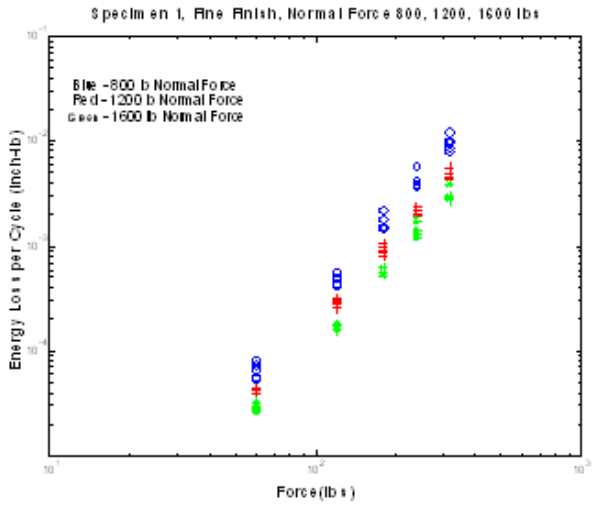

Figure 4.39. Experimental Results for Fine Finish Specimen.

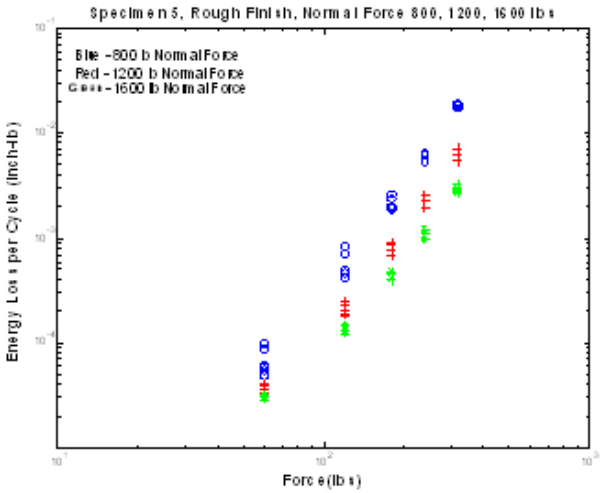

Figure 4.40. Results for Rough Finish Specimen.

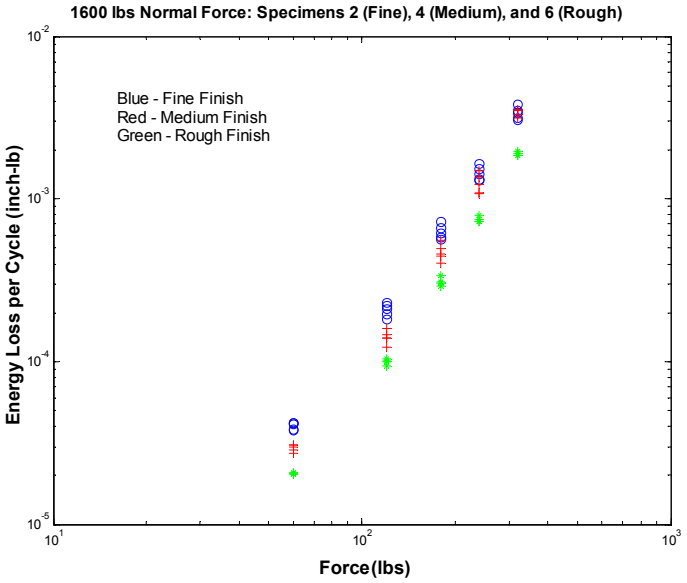

Figure 4.41. Comparison of Three Roughness Levels at 1600-lb Normal Force.

4.2.8 Aluminum-on-Aluminum Lap Joint Experiments

Similar experiments on aluminum-aluminum lap joint specimens were attempted using the BMD with rollers, but were not successful. The aluminum specimens would quickly gall and, on some occasions, would completely lock together. An example of surface galling is shown in Figures 4.42 and 4.43. Steady state testing with sine wave excitation that introduces thousands of cycles of load to the interface will always be prone to complications of galling. We recommend that if aluminum on aluminum joints are to be explored, transient loadings in a dumbbell test configuration, as discussed in Section 5.1, be used because estimates of the energy dissipation can be provided with fewer loading cycles in the joint.

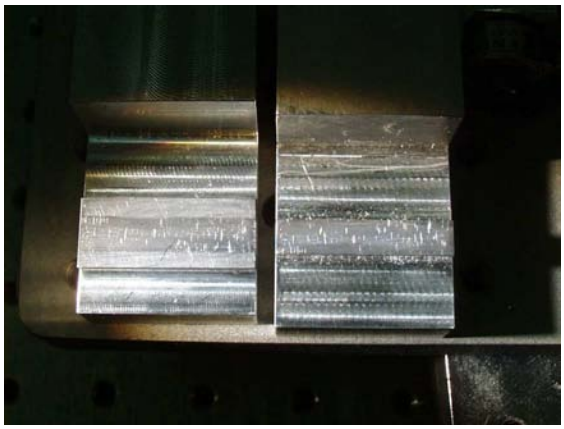

Figure 4.42. Example of Galling of Stepped Aluminum Specimens.

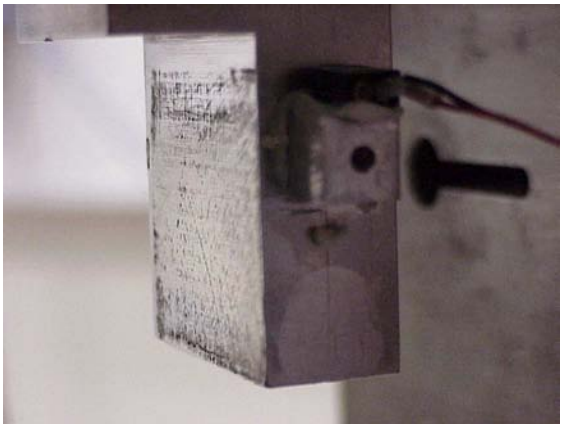

Figure 4.43. Example of Galling of Flat Aluminum Specimens.

4.3 Lessons Learned

As with any experimental research project, lessons learned along the way illuminate previously unknown issues and correct assumptions made at the beginning of the project. Some of the lessons learned with the BMD testing with rollers are listed below.

4.3.1 Inadequately Sized Shaker for the BMD

For the BMD experiments a small 400-lb force rated shaker with a small 10-lb armature (moving element) was used initially (Figure 4.44). The assumption at that time was that the lighter moving element and its suspension system would have less effect on the experiment than a larger shaker with a 100-lb moving element and a 25,000-lb force rating. At the resonance of the BMD, the dynamic mass of the system overwhelmed the smaller shaker's suspension and trunion system, causing side loading of the moving element and vibration of the shaker body and base. This combination created undesired boundary conditions at the shaker attachment and led to very inconsistent results. Upon configuring the support frame for the BMD with a large shaker that is designed to test items weighing a few hundred pounds, we obtained far superior test results. If a concept similar to the BMD is employed, then we recommend that a shaker of sufficient size be used to manage the dynamic response of the BMD.

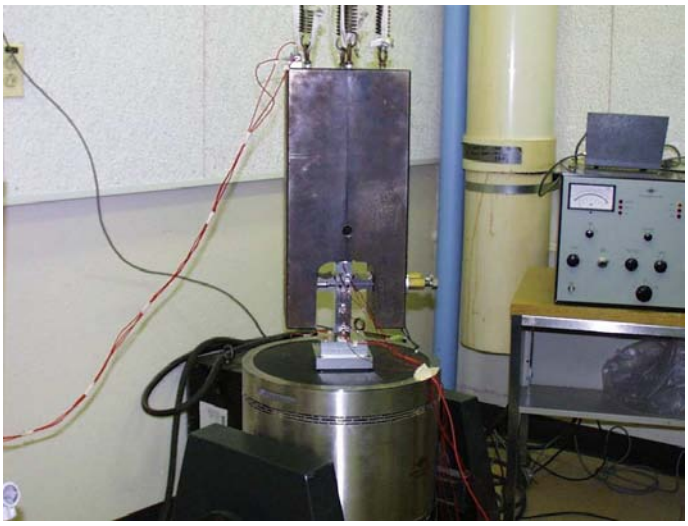

Figure 4.44. BMD on Small Shaker.

4.3.2 Test Control Errors

Test control anomalies utilizing sine wave excitation on large shakers can lead to damaged test specimens before system shutdown. If the input shear force exceeds the macroslip force in the joint, then many cycles of macroslip can occur, creating intense internal heating and wear.

In closed-loop, feedback control systems, the control transducer sensitivity must be correctly established or the control system will run the test at the wrong level. An example of the results of the control system increasing the drive beyond the desired level into the macroslip regime is shown in Figure 4.45. As seen the surfaces of the very high strength AISI 4340 steel were severely damaged. The specimens are expensive to fabricate so we recommend a thorough check of the instrumentation and the channel sensitivities provided to the control system before testing.

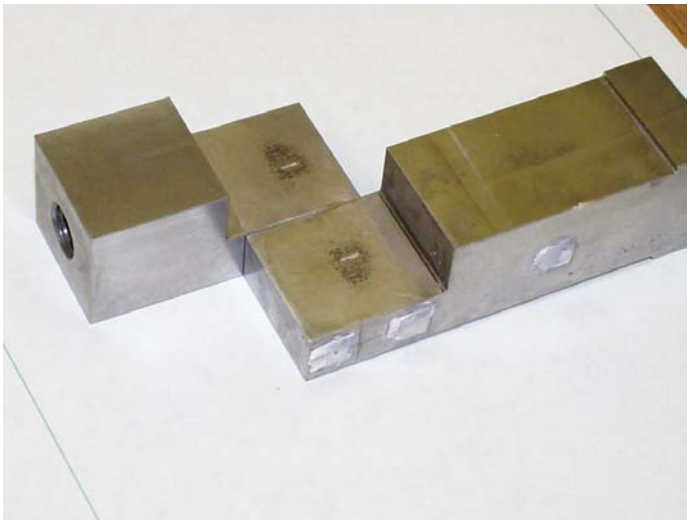

Figure 4.45. Damaged Test Specimens.

4.3.3 Test Specimen Alignment

The alignment of the test specimens in the BMD is critical to achieving accurate and repeatable results. As discussed in the description of the BMD, we used soft springs to support the inertial mass and to account for small misalignment errors between the two halves of the test specimen. If a more crude alignment is made before loading the cables on the rollers then asymmetric suspension forces will be in play and can affect the results. We recommend that assembly fixtures and alignment aids be employed with the use of the BMD concept.

4.3.4 Differencing Raw Accelerometer Signals

Several unsuccessful attempts were made to measure the relative displacement across the joint by placing accelerometers on either side, computing their difference and then integrating the result. The accelerometer arrangement consistent with this approach is shown in Figure 4.46, where accelerometers are identified by the twisted pair wires attached to them. The uncertainty in the calibration values (approximately 5%) and the alignment errors of the accelerometers create bias errors in the computed relative accelerations that can become very large errors during integrations. The instrumentation noise is also problematic, particularly for small acceleration measurements. Also, phase differences between channels (includes accelerometer, signal conditioning amplifiers, and digitizers) can create large errors in the calculations of the relative displacements.

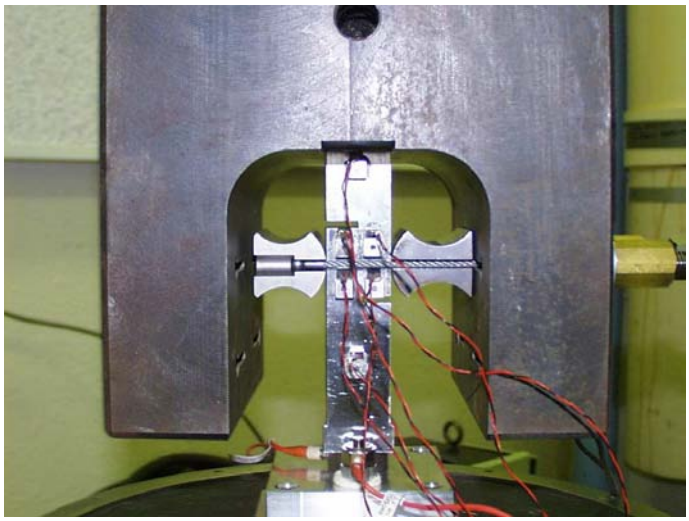

Figure 4.46. Relative Acceleration Measurements.

4.3.5 Utilize Contact Pressure Film to Measure Interface Pressure Distribution

We recommend that as part of any experimental program investigating microslip in mechanical interfaces, the actual contact pressure realized in the joint be measured. As will be discussed in Section 9, the assumptions regarding the contact condition can be very misleading. The use of pressure sensitive film can easily provide insight and guidance in the test setup to establish the desired pressure distribution, and can also be very valuable to assist in the development of models for a particular joint. This information would be very useful in the experiments utilizing the rollers with specimens of different geometry to aid in the interpretation of the results and the diagnosis of improper test setup alignments.

4.3.6 Summary of Lessons Learned

The BMD with rollers has been demonstrated to be a versatile test apparatus to investigate microslip in a single interface without the presence of a bolt. Experiments can be configured to change many parameters of interest in the interface such as normal force, contact geometry, surface roughness, lubrication, etc. The use of the BMD at the fixed-base resonance allows the well known properties of mechanical resonance of an SDOF system to calculate the energy dissipation per cycle and the effective stiffness of the joint. The use of a solid equivalent test specimen (non-jointed specimen) allows the other contributions to the energy dissipation and stiffness to be identified so that contributions of the joint can be isolated. The BMD can also be configured without the rollers to test bolted specimens, as discussed in Section 4.4.

4.4 Big Mass Device Dynamic Sinusoidal Experiments with Bolted Specimens

The BMD can be configured to test bolted test specimens (without rollers) and has proved to be very useful in bolted joint investigations. The bolted joint, test specimen hardware can be designed to attach to the inertial mass and the shaker adapter plate. The intent of the test configuration is to design a test that approximates a base-driven SDOF system at the first resonance. Subsequently, all of the analysis tools for sinusoidal vibration described in the previous sections are applicable. Variations of the BMD concept can be tailored to the type of bolted connection(s) being investigated. For example, the mass and geometry can be selected to provide a particular frequency and/or force level of interest. Concepts to put an additional spring between the shaker and the shaker adapter plate can also be used to tune the frequency while keeping the mass constant. The applications of the BMD described thus far in this document were designed to provide the cleanest possible, axial motion of the mass to preserve one-dimensional loading of the joint. The experiment can be configured to provide more complex loadings by designing the geometry of the test specimens so the joint interface is not coincident with the line of action of the force. An example of this arrangement is discussed later for an inclined lap joint. Use of a solid-equivalent joint can be very successful in isolating the energy dissipation and the stiffness of the joint from the rest of the system.

4.4.1 Flat Specimens with a Single Bolt

A logical extension of the flat lap joint studies without bolts is to repeat the experiments, but incorporate an actual bolt. The flat lap joint used in the previous study is modified to include a drilled clearance hole for a 3/8-in bolt so that the fastener in the test specimen would be centered at the same location where the rollers had been. An instrumented bolt (3/8-24 UNF) is then used to bolt the two halves of the test specimen together with a known preload. The experimental setup in the BMD with the bolted connection is shown in Figures 4.47 and 4.48. The instrumentation remained the same as earlier studies, with a piezoelectric force gage and a piezoelectric accelerometer (not

shown because it was on the bolt head beneath the force gage) collocated on the centerline beneath the test specimen. A piezoelectric accelerometer is also placed on top of the mass near the center. An additional accelerometer for monitoring purposes is attached near the bottom of the test specimen.

Figure 4.47. The BMD with Bolted Flat Steel Specimens.

Experiments similar to the previous experiments with the rollers are performed to measure the energy dissipation per cycle for a sinusoidal input over a range of loads of 60-, 120-, 180-, 240-, and 320-lb peak. In the first set of experiments, the bolt is tightened without a washer beneath the head or nut of the bolt, and is adjusted at two preload levels of 1200- and 1600-lb. The frequency of the first axial resonance ranges from 318 Hz to 332 Hz, depending upon the input force level and the bolt preload. The energy dissipation per cycle vs force results for 1200- and 1600-lb bolt preloads are shown in Figure 4.49. The energy dissipation curves with the bolt look very similar to those developed for the test specimens with the rollers as it follows a similar power-law relationship $F = kD^n$, evidenced by the straight-line fit with a slope of n when plotted on a log-log scale. The energy dissipation is very sensitive to changes in the bolt preload and significantly increases with decreasing normal force (bolt preload). This is obvious when the data are plotted on a linear scale in Figure 4.50, where at 320 lb of input force the energy dissipation for the 1200-lb bolt preload is more than twice that for the 1600-lb bolt preload. The similar character of the results between the bolted and bolt-free joints is evidence that the underlying character of the microslip process remains the same whether the microslip is occurring in a single interface or simultaneously in multiple interfaces with varying contact conditions.

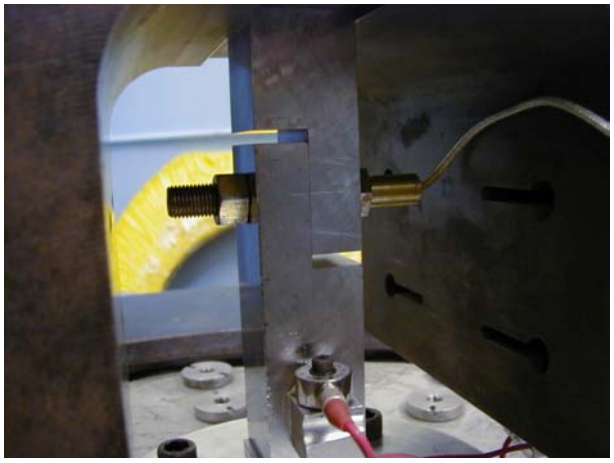

Figure 4.48. Close-Up View of a Bolted Specimen in the BMD.

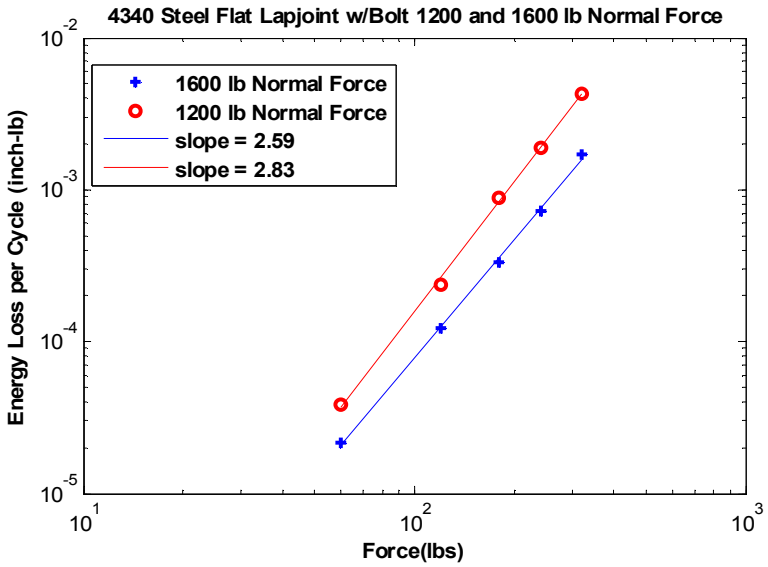

Figure 4.49. Bolted Flat Specimen with 1200-lb and 1600-lb Bolt Preload.

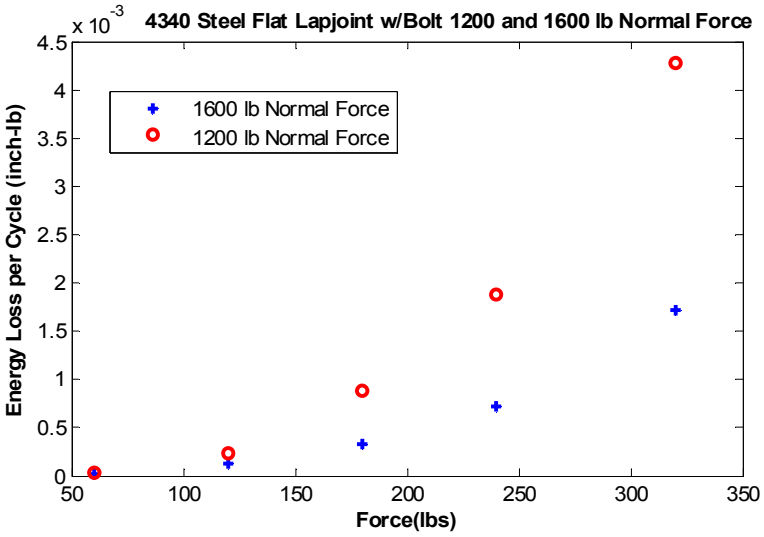

Figure 4.50. Bolted Flat Specimen at 1200-lb and 1600-lb Bolt Preload with Linear Scale.

4.4.1.1 Effects of the Addition of a Washer

To further explore the effect of multiple interfaces in the bolted joint, a plain flat washer is inserted beneath the nut, and the experiment is repeated with a bolt load of 1600 lb. As seen in Figure 4.51, the addition of a single washer substantially increases the energy dissipation and the slope of the fitted line. To further illustrate the substantial effect of the washer, the energy dissipation curves are plotted on a linear scale in Figure 4.52. The presence of the washer provides two additional slip interfaces that participate in the microslip process, causing increased microslip per unit of applied input force while maintaining the preload constant. While this limited study does not widely address the effects of bolts/nuts/washers, the results do show that the BMD provides an effective tool for quantitatively investigating dissipative and other effects.

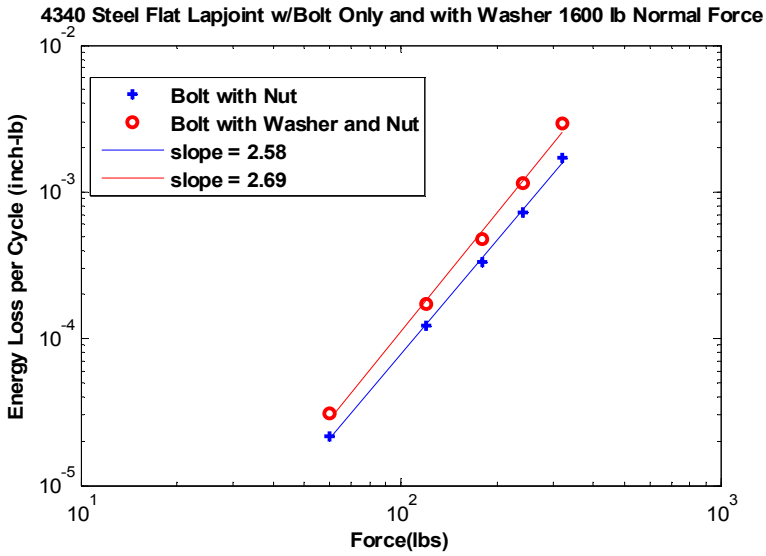

Figure 4.51. Bolted Flat Specimen at 1600-lb Bolt Preload with and without a Washer.

In future studies, the analysis techniques discussed in the previous sections might prove to be very useful to explore the effects of various washers (flat, lock, coated, etc.) and nuts (hex, flanged, etc.) on the loading response of different joints. In particular, the computation of the nonlinear restoring force for various configurations and evaluation of changes to the shape of the function could provide insight into methods of modeling bolted joint behaviors.

4.4.1.2 Comparison Between BMD with Rollers and with Bolts

To further explore the effects on the energy dissipation of a bolted joint, the results of the previous study with the rollers providing the normal force are compared with the results with the bolt. The energy dissipation curves shown in Figures 4.53 and 4.54 display some interesting results

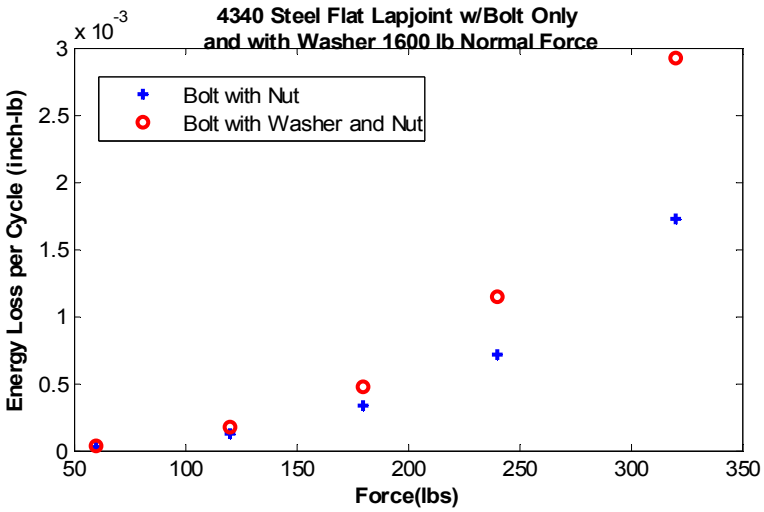

Figure 4.52. Bolted Flat Specimen at 1600-lb Bolt Preload with and without a Washer - Linear Scale.

considering the contact pressure differences of the rollers and of the simple bolted joint. The energy dissipation curves at 1200-lb normal force are similar, but with slightly different slopes, showing that the bolted joint dissipated more energy at higher input force levels. The energy dissipation curves are surprisingly close to each other, with the roller-loaded joint dissipating slightly more energy at higher force levels, and the bolted joint slightly more energy at the low force levels. These experimental results confirm that the microslip process seems to be similar in all interfaces regardless of the contact conditions and number of interfaces. The magnitudes and slopes of the resulting energy dissipation curves may vary as a function of the joint properties but the underlying power-law behavior appears to be a characteristic of the joints studied thus far.

4.4.1.3 Summary

The success of the experiments with the BMD with the bolted, flat lap joint specimens provided the framework to investigate other bolted connections. This test technique is demonstrated to be robust, reliable, and repeatable, while providing valuable details in the dynamic behavior of the bolted joint.

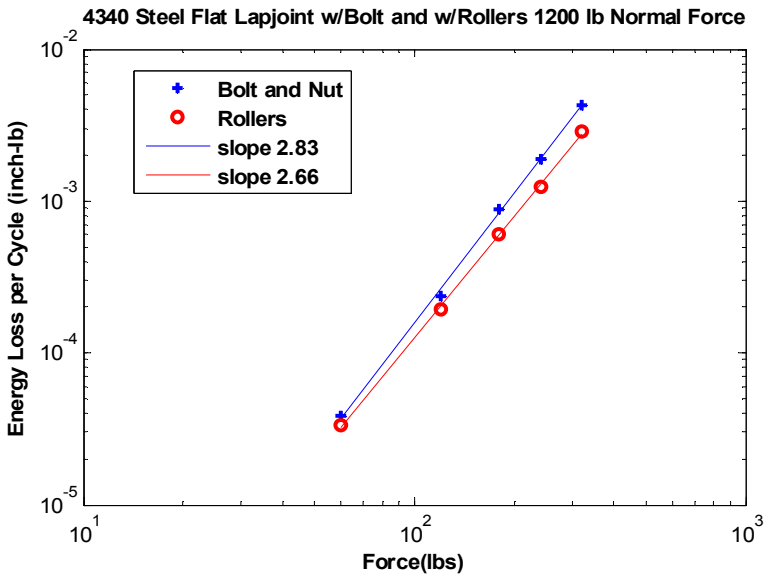

Figure 4.53. Flat Specimen with Rollers and with Bolt and Nut for 1200-lb Normal Force.

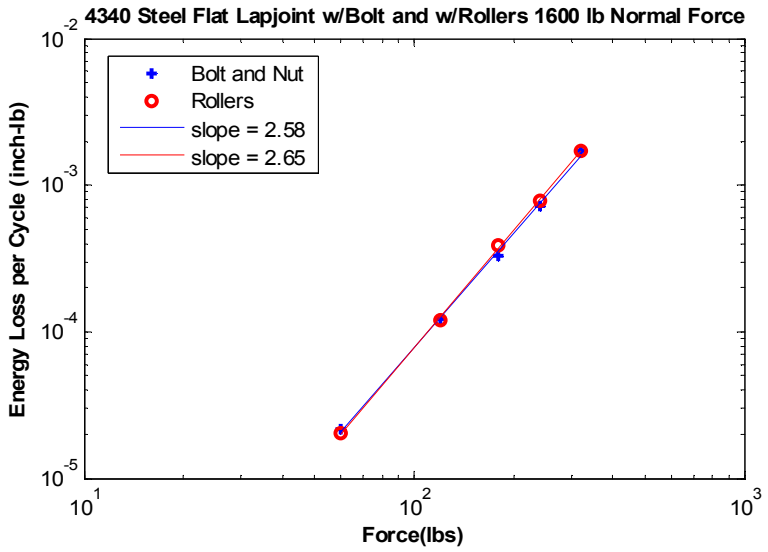

Figure 4.54. Flat Specimens with Rollers and with Bolt and Nut for 1600-lb Normal Force.

4.4.2 AOS, Single-Leg, Bolted Joint - Inclined Lap Joint

4.4.2.1 Motivation

A particular bolted joint of interest at Sandia is the connection of the System A, AOS unit to the base attachment location of System A. The AOS is connected to the base attachment location by three, discrete, inclined lap joints. These connections provide the only mechanical load paths to the AOS, so its dynamic response is strongly dependent on these bolted joints. Two separate experimental studies analyze these joints. The first [49] presents scoping experiments for evaluating the joint with the BMD and the sinusoidal techniques developed in the previous sections. These experiments establish the experimental approach for the second project, which is the first step (calibration) in an integrated model calibration and validation demonstration for a whole-joint model (Chapter 12) for System A, AOS bolted joint. The second step (validation) in the calibration and validation project is discussed in Section 5.2.12.

4.4.2.2 Energy Dissipation Experiments

The initial series of experiments involves the investigations of a single set of hardware that incorporates the local geometry of the AOS bolted joint and attaches to the BMD. Because the hardware for this joint experiment represents one leg of the three-legged attachment of the AOS, it is titled the “single-leg” test specimen. The materials of the two members of the joint are titanium and stainless steel for the lower and upper portions respectively, and the alloys are the same as those used in the actual component hardware. The two pieces of the single-leg hardware disassembled and assembled are shown in Figures 4.55 and 4.56. A 1/4-32 UNF x 3/8-in long mil-spec bolt (MS9566-06) is used. This fastener is a special, flanged stainless steel bolt that does not require a washer. During the assembly of System A, AOS parts to the forward mount hardware, measurements of the vertical gap between the base of the AOS and the legs of the base attachment location could range from a few thousandths of an inch to a light contact condition. This vertical gap is shown in an expanded view in Figure 4.57. Experiments are performed with a gap of 0.010 in and with the gap closed to investigate the effect on the energy dissipation. The over-sized hole in the base attachment location allows significant variation in alignment to occur unless efforts are made to minimize the effect. The over-sized hole in the leg and the interaction of the interface and the bolt head with the hole is the suspected major source of variation in the response of the system from assembly-to-assembly of the same joint.

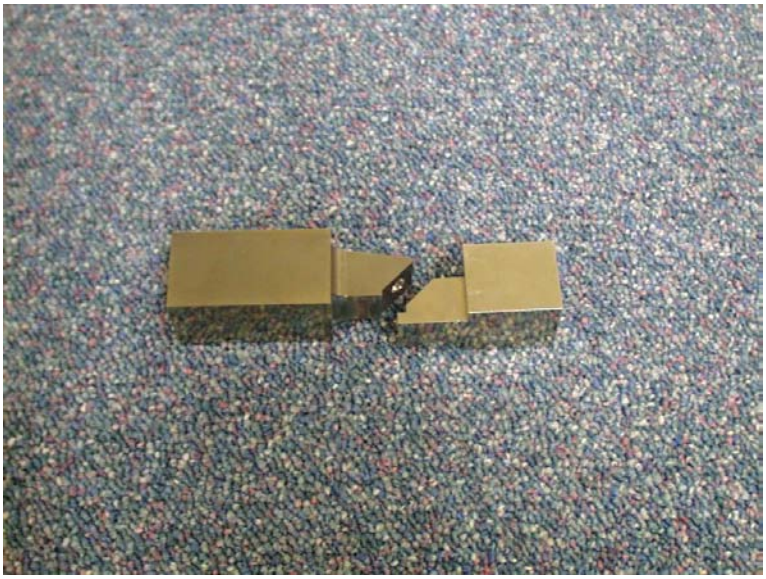

Figure 4.55. AOS Single-Leg Test Specimen.

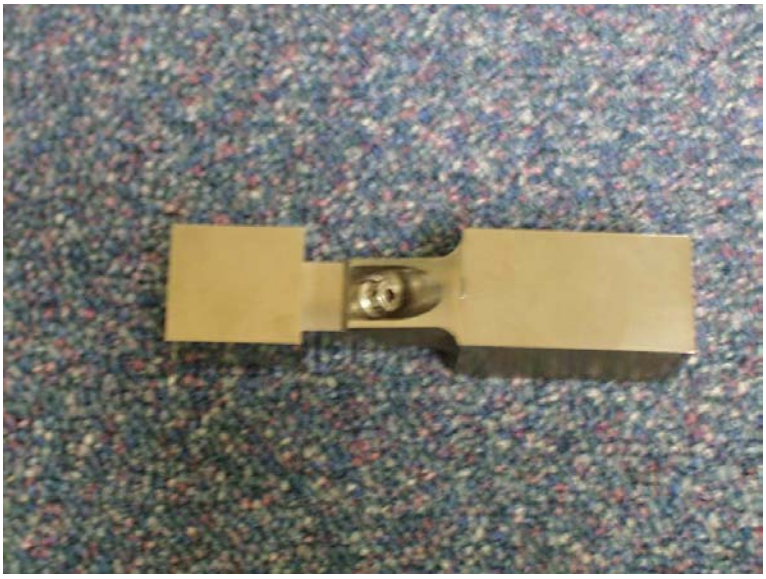

Figure 4.56. AOS Single-Leg Test Specimen with a Bolt.

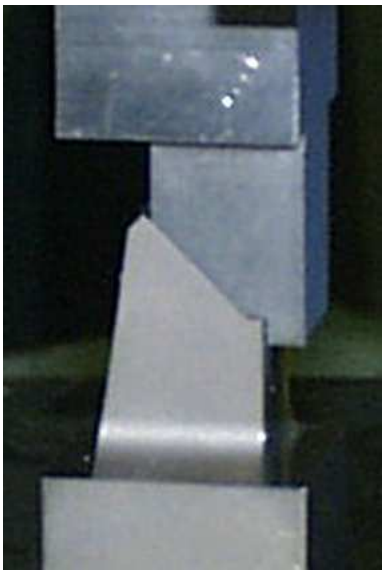

Figure 4.57. Expanded View of the Vertical Gap.

The experimental setup with the single-leg specimen assembled into the BMD is shown in Figure 4.58. The same instrumentation, shaker, and control system are used as in previous BMD experiments. A piezoelectric force gage is used beneath the test specimen to measure the input force, and piezoelectric accelerometers are used to measure the accelerations of the base and the mass. The excitation for the experiments is provided with a Model T1000, Unholtz-Dickie, electrodynamic shaker. A Spectral Dynamics, Model 2552, Vibration Control System is used to generate and control the excitation waveforms used in the experiments.

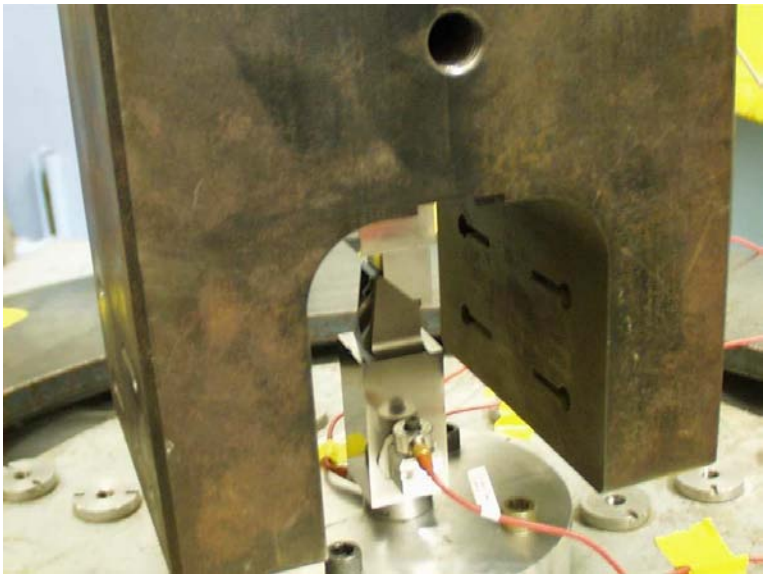

Figure 4.58. Experimental Setup in the BMD.

Experiments are performed to measure the energy loss per cycle for a sinusoidal input force over a range of loads of 60-, 120-, 180-, 240-, and 320-lb peak, with the specified torque of 85 in-lb resulting in a calculated normal force of approximately 1700-lb. The fixed-base resonant frequency of the system ranges form 269 to 278 Hz, depending on the excitation level, and varies slightly for each assembly of the bolted connection. The amplitude ratio (transmissibility) of the acceleration of the mass and the acceleration of the base is then calculated to determine the amplification factor (Q). A constant-bandwidth (10Hz), digital tracking filter is used with a linear sweep rate of 0.50 Hz/s in the signal processing to compute Q. The amplification factor was established at the frequency where the phase angle is measured to be 90°.

Data are collected for a total of nine load cycles, each of which involves cleaning the contact surfaces, reassembling the joint, and then performing sweeps at each of the five force levels. The graph of energy loss per cycle data vs force for the nine experiments is shown in Figure 4.59 in a log-log plot that highlights the straight-line character of the data. This straight-line relationship indicates that there is a power-law relationship between the energy loss per cycle and the input force, $D = kF^n$. The data are also shown on a linear plot in Figure 4.60 that illustrates the strong dependence of the energy dissipation on input force.

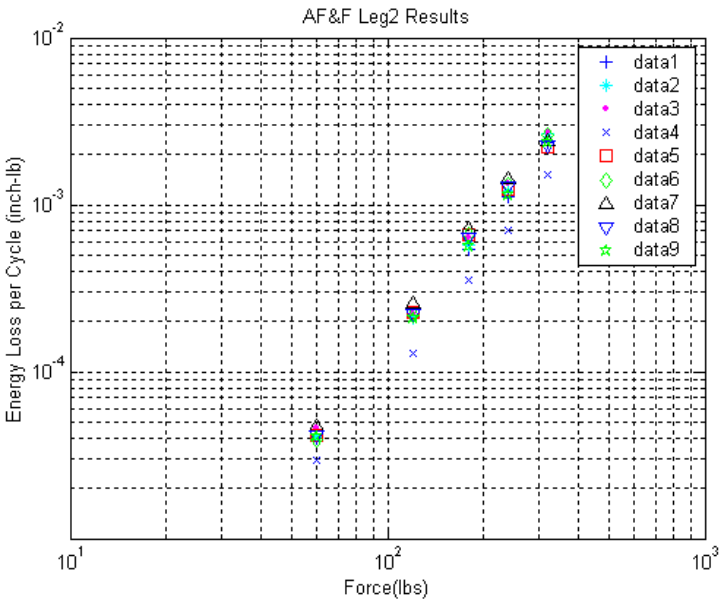

Figure 4.59. Energy Dissipation vs Force Data on Log-Log Scale.

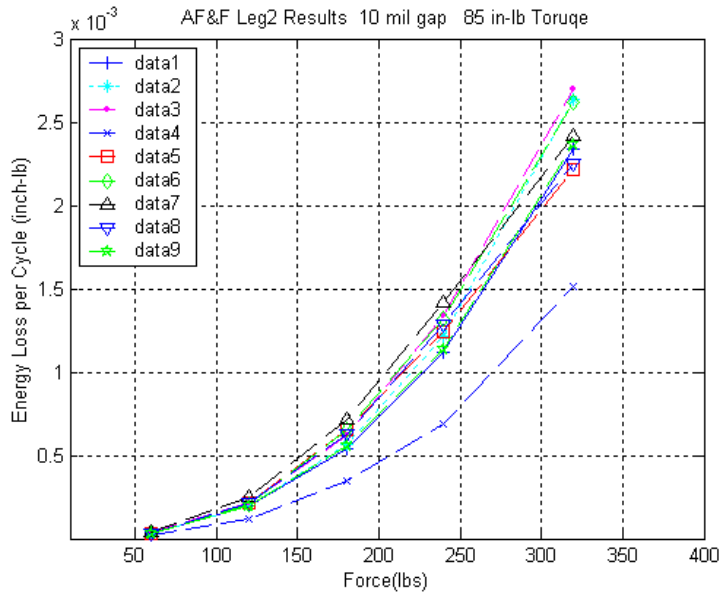

Figure 4.60. Force vs Energy Dissipation on Linear Scale.

At each force level that energy loss is measured, a 20 - 30 % variation is observed (when experiment number four, which shows much less dissipation than the other experiments, is neglected). It appears that the system was “locked-up” for the fourth trial, but for subsequent experiments returned to similar levels as previously measured. The data show that even though the same set of hardware is used in all experiments, variations due to repeated disassembly and assembly can comprise a significant amount of variation in the energy loss. Further, experiments with multiple test specimens, as discussed in the next section, show that part-to-part variability of the energy dissipation for test specimens machined to the same specifications is typically much larger than the assembly variation of one set of hardware. The slopes of the energy curves in Figure 4.61 are determined by a least-squares linear regression to each set of the log-log data, and are found to be very repeatable: the average slope is 2.429 with a standard deviation of 0.05218. This indicates that although the overall amplitude of the energy loss may vary 20 - 30 %, the slope of each energy curve is very repeatable.

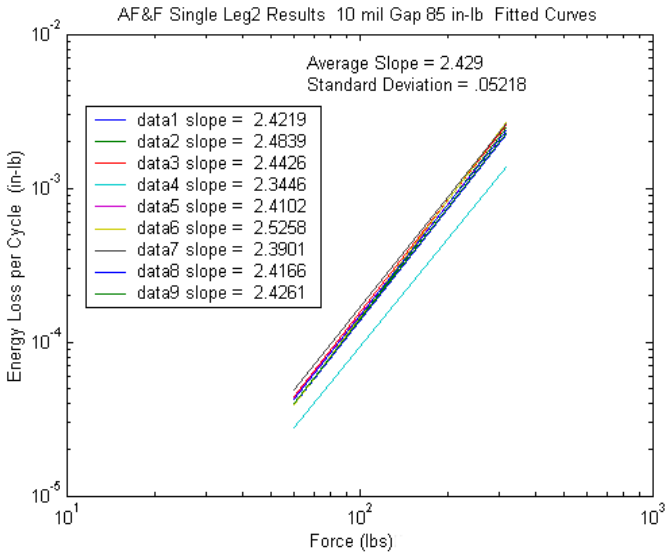

Figure 4.61. Slopes of a Straight Line Fit to the Energy Dissipation Data.

4.4.2.3 Solid Single-Leg Experiments

A similar set of experiments is performed for a geometrically identical, solid-leg made of stainless steel with no frictional interface. (Figure 4.62) The purpose of the experiments is to establish a lower limit for the unaccounted loss mechanisms in the experiment and to allow the contribution due to the joint to be identified. The solid-leg will not have the same stiffness as a single, solid-leg composite (both titanium and stainless steel - physically impossible to construct), but the internal material damping character of both stainless steel and titanium is very low and well below the damping introduced by a bolted interface. The effective stiffness of the joint becomes more difficult

to compute, as the stainless steel, solid-leg does not have the same stiffness as would a solid specimen of titanium and stainless steel. Because the linear portion of the stiffness is due to the elastic behavior of the two members of the specimen, a finite element representation of the two members could help provide an estimate of the linear stiffness that would then allow the contribution of the stiffness of the joint to be estimated. In the future, a technique needs to be developed so that the contribution of the joint to the energy dissipation and the effective joint stiffness can be calculated when the joint members are different materials.

Figure 4.62. Experimental Setup of the Solid, Stainless Steel Leg.

The results for the solid single-leg are shown in Figure 4.63 for five load cycles. The measured natural frequencies for the solid-leg experiment range from 362 to 364 Hz, considerably higher than the (softer) jointed single-leg whose natural frequencies range from 273 to 278 Hz. These frequency differences illustrate the reduction in stiffness in a bolted joint vs a solid geometry. The data for the solid single-leg are very repeatable, as might be expected from a linear structure without the uncertainty of a bolted connection. The data closely follow a straight line with a slope of two, as seen in previous testing of solid equivalent, linear structures. The solid and jointed single-leg data are plotted together in Figure 4.64. The data show the significant increase in energy dissipation introduced by the presence of the bolted connection, and the difference in slopes of the energy curves between the two systems, resulting in much increased energy dissipation for the jointed connection as the input force increases.

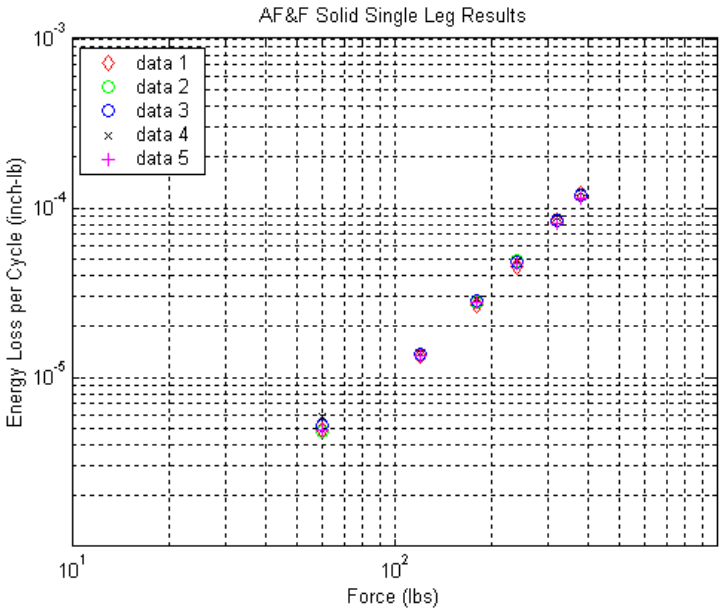

Figure 4.63. Solid, Stainless Steel, Single-Leg Results.

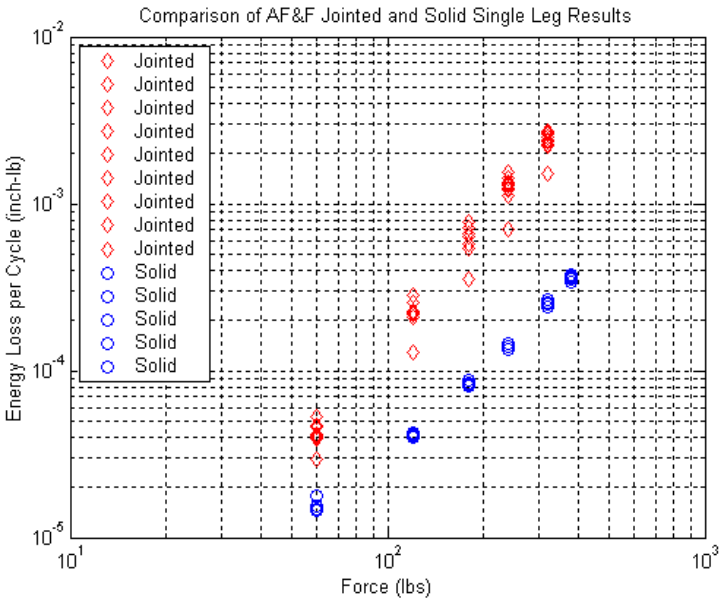

Figure 4.64. Comparison of Solid and Jointed Single-Leg Results.

4.4.2.4 Load History Effects

The experiments demonstrate load history effects that are also noted in simple, lap joint experiments discussed previously. The amplification factor, Q, increases with the number of vibration cycles. When the bolted joint is disassembled and reassembled with the same torque, the system returns to a similar starting point with a lower amplification factor (higher damping) and then follows a similar trend of decreasing damping. A total of seven experiments are performed with an input force of 120 lb. For each experiment, a total of four sinusoidal sweeps are performed, and the equivalent viscous damping ratio $\zeta \approx \frac{1}{2Q}$ is computed and plotted as a function of the cumulative number of vibration cycles in Figure 4.65. The equivalent damping ratio decreases asymptotically as the number of cycles of vibration increases. The mean of the data decreases from approximately 0.4 to 0.3% of critical damping over approximately 28,000 cycles of vibration (approximately 2 minutes at 275 Hz). This is a change of approximately 25% in the damping ratio.

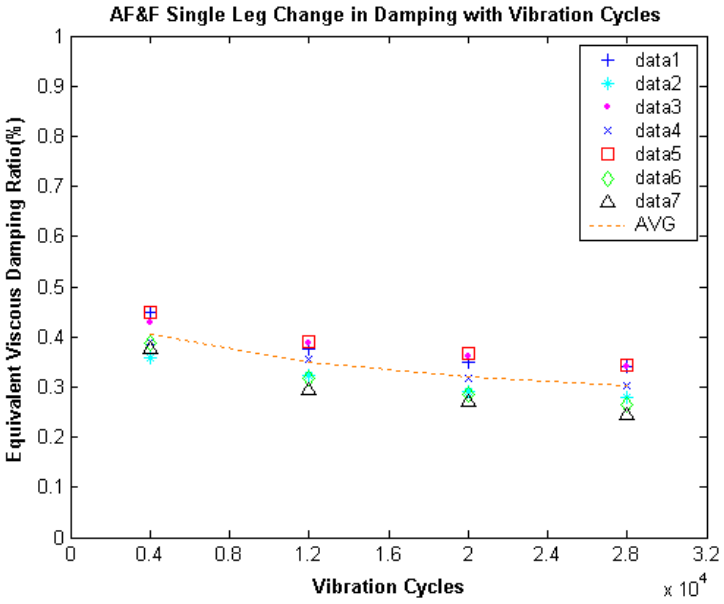

Figure 4.65. Load History Dependence of Single-Leg Damping.

It should be noted that the change in damping associated with the first few thousand cycles is not captured in this data due to the vibration control system's delay in bringing the excitation to the desired level before starting the sine sweep through resonance. There are thousands of load cycles provided to the joint before the first sweep is completed. The transient experiments in the dumbbell configuration discussed in Section 5.3 for a similar joint show a more dramatic decrease in the energy dissipation after the first few transient ring-downs of the structure. The energy dissipation data reported in this section is based on the response during the first sweep through resonance.

4.4.2.5 Base Hysteresis Measurements

The nonlinear response of the single-leg experiment is further investigated by computing the force vs base hysteresis curves. As discussed in Section 3, the base hysteresis curve developed at resonance provides a sensitive measure of the nonlinear response of the system.

The Fourier coefficients of the base acceleration, input force, and inertial mass acceleration are obtained by fitting a best, least-squares fit with a sum of phase-shifted sinusoids at the fundamental frequency and higher harmonics. It is found that maintaining the fundamental and five harmonics is sufficient to represent the accelerations and the input force. Very little is gained by including yet higher harmonics. The Fourier coefficients indicate that the second harmonic is very strong in the base motion, which is an indication of asymmetrical motion between tension and compression of the joint. Asymmetrical waveforms tend to require the addition of even harmonics for their Fourier series representation, in contrast to symmetrical waveforms that may require only odd harmonics. A typical set of Fourier coefficients for the base acceleration is shown in Table 4.4. Note that the amplitude of the second harmonic (twice the frequency of the fundamental) is higher than the fundamental amplitude. Due to the inclined interface with respect to the line of action of the input force, the asymmetry between tension and compression arises from at least two effects: the difference in the joint stiffness between tension and compression, and the normal traction is significantly higher on the compression part of the cycle, thereby increasing the resisting frictional force in the interface. (These two effects may actually be two aspects of one phenomenon.) The corresponding Fourier coefficients for the input force and acceleration of the mass are given in Table 4.5 and Table 4.6.

Table 4.4. Fourier Coefficients of Typical Base Acceleration for the 60-lb Force Input.

Harmonic #	**Frequency (Hz)**	**Acceleration Amplitude (g)**	**Phase (Radians)**
1 (Fundamental)	2.79E+02	1.60E-03	-9.23E-01
2	5.57E+02	3.08E-03	-2.49E+00
3	8.36E+02	4.74E-04	3.84E-01
4	1.11E+03	4.74E-04	-2.86E+00
5	1.39E+03	1.73E-04	-2.84E+00
6	1.67E+03	3.17E-04	-2.37E-01

Table 4.5. Fourier Coefficients of Typical 60-lb Force Input.

Harmonic #	**Frequency (Hz)**	**Force Amplitude (lb)**	**Phase (Radians)**
1 (Fundamental)	2.79E+02	6.02E+01	6.43E-01
2	5.57E+02	7.13E-01	2.98E+00
3	8.36E+02	2.11E-02	-2.15E+00
4	1.11E+03	5.08E-03	3.88E-01
5	1.39E+03	2.85E-03	3.45E-01
6	1.67E+03	1.81E-03	9.95E-02

Table 4.6. Fourier Coefficients of Typical Mass Acceleration for the 60-lb Force Input.

Harmonic #	**Frequency (Hz)**	**Acceleration Amplitude (g)**	**Phase (Radians)**
1 (Fundamental)	2.79E+02	3.21E-01	-2.50E+00
2	5.57E+02	3.81E-03	-1.64E-01
3	8.36E+02	1.00E-04	6.72E-01
4	1.11E+03	2.51E-05	2.37E+00
5	1.39E+03	2.85E-05	-1.77E+00
6	1.67E+03	3.10E-05	-2.78E+00

The reconstructed time histories using the Fourier coefficients are calculated by summing the harmonic components

$$a(t) = \sum_{k=1}^{N} A_k \sin(2\pi k f_0 t + \phi_k) \tag{4.1}$$

where A_k is the amplitude of k^{th} component,
f_0 is the fundamental frequency,
and ϕ_k is the phase of k^{th} component.

The reconstructed time histories for the force, mass acceleration, and the base acceleration are shown in Figures 4.66 - 4.68. Note that the harmonic distortion of the force and mass acceleration are minimal, while the harmonics in the very small base acceleration are very pronounced. The nonlinear behavior of the joint experiencing microslip is much more apparent in the small base acceleration than in the mass acceleration or force where the linear portion of the response dominates the small, nonlinear component. The harmonic distortion in the displacement decreases rapidly with increasing frequency because, for a given acceleration, the corresponding displacement decreases as a function of the square of the frequency.

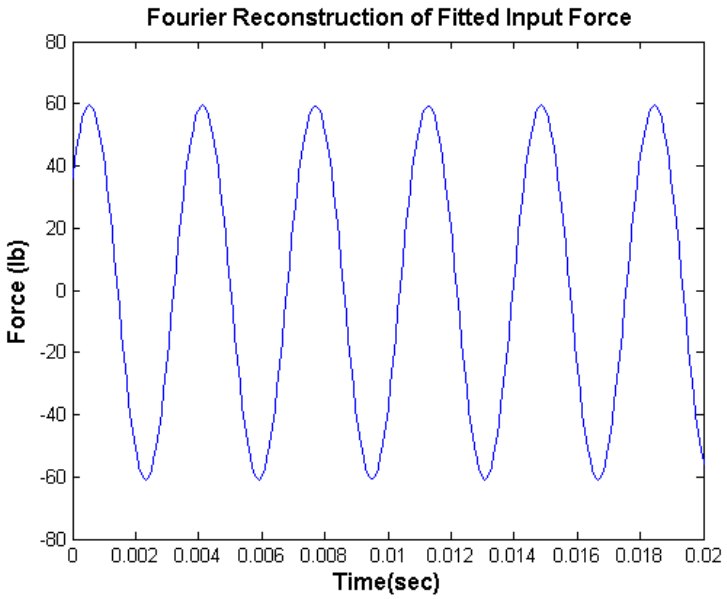

Figure 4.66. Reconstructed Input Force.

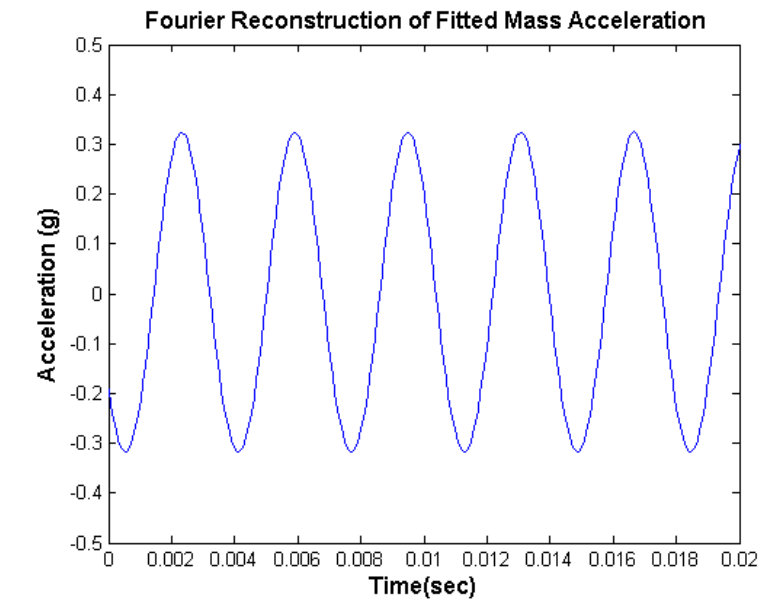

Figure 4.67. Reconstructed Mass Acceleration.

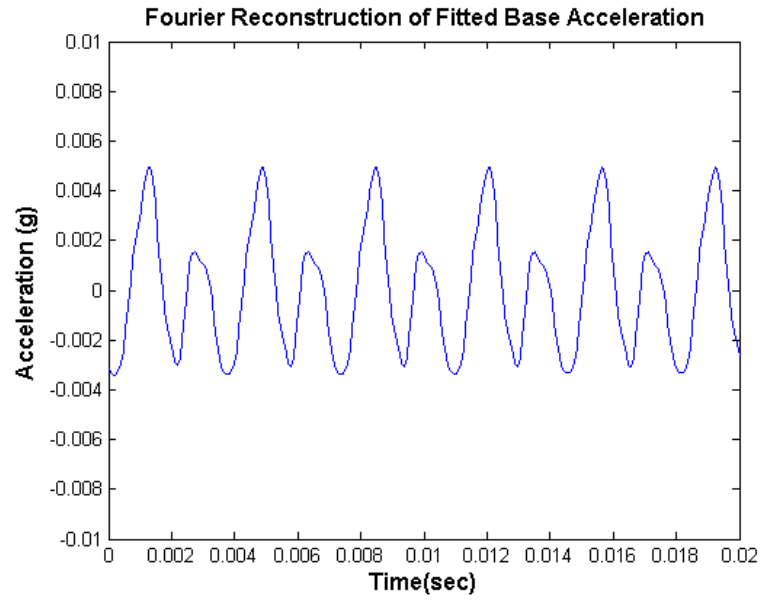

Figure 4.68. Reconstructed Base Acceleration.

Utilizing the analytical fit to the measured signals, the force vs base motion, hysteresis curves were computed for both the solid and jointed legs for selected experiments. Because the linear portion of the response to a harmonic input is contained in the response at the fundamental frequency, the force vs linear portion of the base displacement should plot as an ellipse for a linear system. Deviations from the ellipse are an indication of the nonlinear response. Typical force vs base motion, hysteresis curves are shown for 60- and 320-pounds of force in Figures 4.69 and 4.70. The solid-leg hysteresis curves are much more elliptical than those for the jointed leg. The area within each curve is a measure of the energy dissipated per cycle. Note the significant difference in area for the jointed leg compared to the solid-leg. The asymmetry of the response between compression and tension is also very evident in the plot. The loop shown in the hysteresis curve for the 320-lb input force level is due to the large, second harmonic component that increases with increasing input force level. This loop indicates that energy is actually being recovered during this part of the response cycle and is further indication of a nonlinear mechanism in the experiment.

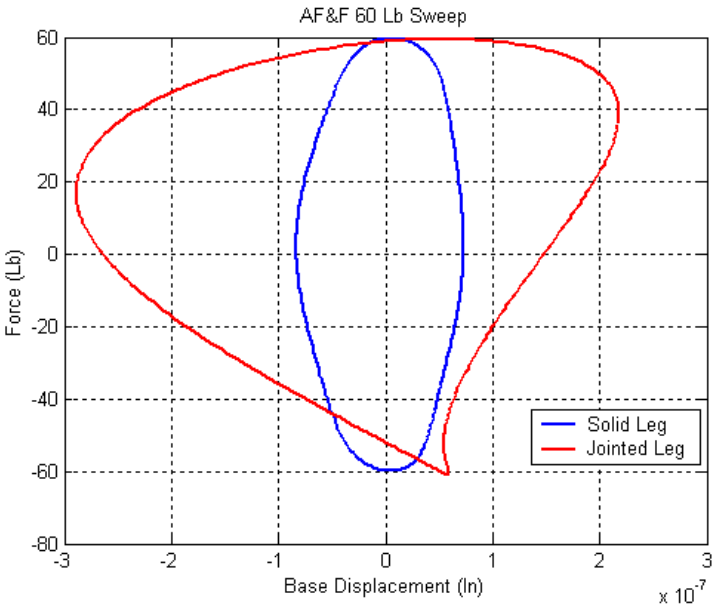

Figure 4.69. Force vs Base Displacement Curves for a 60-lb Sine Input.

The energy loss per cycle was computed three ways for selected load cycles. The first technique utilizes the measured Q at resonance. The second uses the derived Fourier coefficients for the mass and base accelerations to compute the relative displacement, and integrates the force vs relative displacement, hysteresis curve. The third technique uses the derived Fourier coefficients of the base acceleration to integrate the area under the force vs base displacement, hysteresis curves. A typical comparison of the computed energy loss per cycle from these techniques is shown in Table 4.7. The calculations using Q at resonance yield numbers that differ by as much as 12% at the higher force levels, compared to those computed by the methods that involve fitting the force and acceleration signals and computing the hysteresis curves. The method utilizing the amplifica-

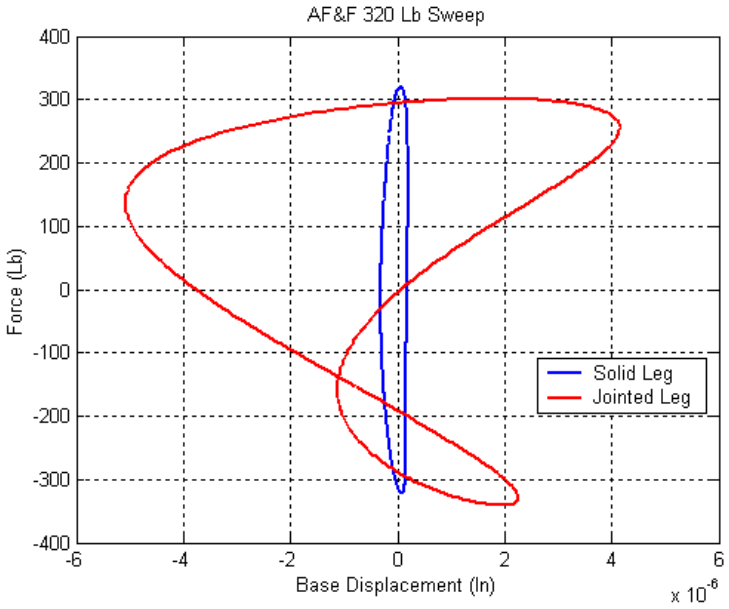

Figure 4.70. Force vs Base Displacement Hysteresis Curves for 320-lb Sine Input.

Table 4.7. Comparison of Energy Dissipation per Cycle Calculations.

Input Force (lb)	**Resonance (*Q*) (in-lb)**	**Force vs. Relative Displacement (in-lb)**	**Force vs. Base Displacement (in-lb)**
60	3.805E-05	3.683E-05	3.768E-05
120	1.956E-04	1.893E-04	1.893E-04
180	5.207E-04	4.907E-04	4.905E-04
240	1.066E-03	9.759E-04	9.755E-04
320	2.242E-03	1.958E-03	1.957E-03

tion (Q) at resonance assumes all of the energy is dissipated at the fundamental frequency of the excitation. As discussed in Section 3, if harmonic distortion exists on both the base acceleration and the force, then energy can be dissipated (or recovered) by the higher harmonics. The loop that occurs in the hysteresis curves represents energy being added to the system and must be subtracted from the total energy calculated by using only the fundamental frequency. The results for the flat lap-joint discussed in Section 4.1 with a much more symmetrical stiffness, did not show this loop, and all three techniques yielded much closer results for the energy dissipation.

4.4.2.6 Further Investigations of Nonlinear Response of Single-Leg Joint

The results of the AOS single-leg bolted joint studies prompted additional analysis by Hunter [56] to investigate the nonlinear behavior observed in the response of the system. The approach expanded upon the techniques discussed in Section 3.1 to calculate the nonlinear restoring force of a bolted joint. A least-squares estimate, utilizing the analytical representations of the base acceleration, force, and mass accelerations of the linear portion of the restoring force was computed and removed from the total restoring force. The computed nonlinear restoring force at the five input force levels for a typical set of single-leg data is shown in Figure 4.71.

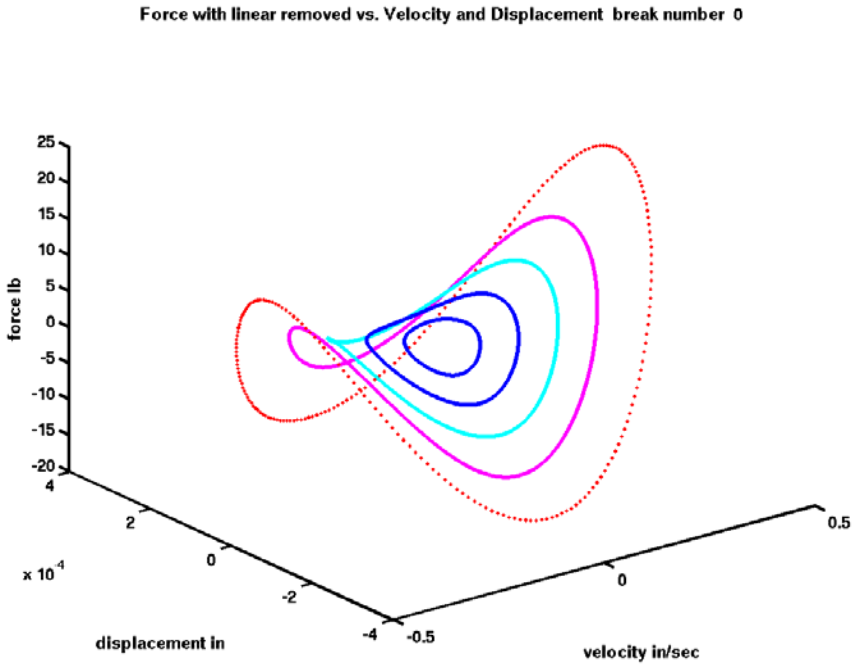

Figure 4.71. Nonlinear Restoring Force of a Single-Leg.

Based on the orbital nature of the restoring force curves, Hunter converted the curves to polar coordinates and fit the restoring force surface using a linear combination of five harmonic terms as given in Equation (4.2). The resulting surface fit to the restoring force is shown in Figure 4.72. This surface fit interpolates the measured trajectories and fully defines the nonlinear restoring force that

can allow candidate joint constitutive models and numerical simulations of the nonlinear restoring force and system response to be evaluated.

$$F_m est = \sum_{n=1}^{n=5} c_n(r)\sin(n\theta) + d_n(r)\cos(n\theta) \tag{4.2}$$

where $r =$ radius of query velocity, displacement.
$\theta =$ angle of query velocity, displacement.
$c_n(r)$, $d_n(r) =$ Fourier coefficients as a function of radius.
$c_n(r) = c_n(1) + c_n(2)\,r + c_n(3)\,r^2 + c_n(4)\,r^3$
and $d_n(r) = d_n(1) + d_n(2)\,r + d_n(3)\,r^2 + d_n(4)\,r^3$

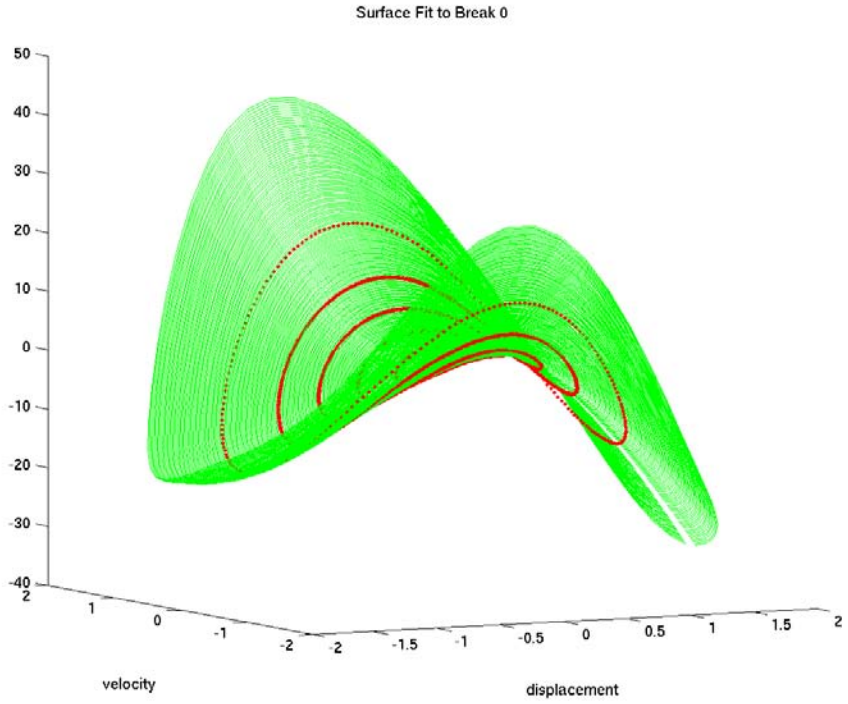

Figure 4.72. Surface Fit of the Nonlinear Restoring Force.

4.4.2.7 Summary

The results for the AOS bolted joint in the BMD allows for the nonlinear damping of the joint to be isolated and measured. This joint represented an inclined lap joint with the interface not coincident with the applied force, providing substantial stiffness nonlinearity between tension and compression. The joint demonstrates similar energy dissipation behavior as seen in the previous lap joint experiments, and the energy dissipation vs force curves demonstrates a similar power-law relationship. In this study the bolt load is maintained constant (as measured by bolt torque) and

the repeatability of the joint behavior evaluated after repeated assemblies. The results indicate for this joint the assembly-to-assembly variation of the magnitude of the energy dissipation is on the order of 20-30%, but the slopes are very repeatable. This series of experiments provided the experimental approach to extend the study of the AOS joint to evaluations of multiple joints machined to the same specifications. The purpose is to develop calibration data with known and unknown uncertainties for parameterizing joint constitutive models. These experiments are discussed in the next section.

4.4.3 AOS Single-Leg, Bolted Joint - Model Calibration Experiments

An integrated model calibration and validation project is performed at Sandia to demonstrate the process for a finite element, structural dynamic model. The AOS bolted joints are a key part of the project, as they represented a nonlinear element of the model with significant variability in their energy dissipation and stiffness properties. These experiments are performed to generate a statistically significant data set for purposes of calibration of an Iwan whole-joint model with known uncertainties associated with the parameters. The validation experiments are discussed in Section 5.3.

To develop a statistical estimate of the variability of the bolted joints, multiple sets of joint hardware are fabricated. Three top pieces and three bottom pieces of the AOS single-leg hardware are used to create nine single joint configurations shown in Figure 4.73. Each of the nine configurations is assembled and disassembled five times, yielding forty-five independent data sets. Actual mating components of a full-scale system consist of both titanium (bottom) and stainless steel (top), but both halves for this study are made from stainless steel. Utilizing stainless steel for both halves of the bolted connection allows for a monolithic “reference” structure to be fabricated to isolate the behavior of the joint and allow computation of attachment compliances of external interfaces. This is the same bolt type discussed in Subsection 4.4.2.2 (1/4-32 UNF x 3/8-in long, MS9566-06).

The single-leg specimens are assembled into the BMD in the same manner as discussed in the previous section, and are shown in Figure 4.74. In this series of experiments, a different range of input forces is selected to span a larger range of forces. The experiments were performed to measure the energy loss per cycle for a sinusoidal input force over a range of loads of 100-, 200-, 300-, 400-, 500-lb peak, with the specified bolt torque of 85 in-lb resulting in a calculated normal force of approximately 1700 lb.

4.4.3.1 Solid-Leg Baseline Experiments

Since this series of experiments is being performed for calibration purposes, it is important to establish a lower limit for the unaccounted energy loss mechanisms in the experiment with the single-leg specimens. It is also important to establish effects of the boundary conditions, repeatability, and other unknowns in the experiment. To accomplish this, a similar set of experiments is

Figure 4.73. Single-Leg Specimens.

Three pairs of jointed specimens (top A, B, C and bottom 1, 2, 3), and one monolithic solid specimen.

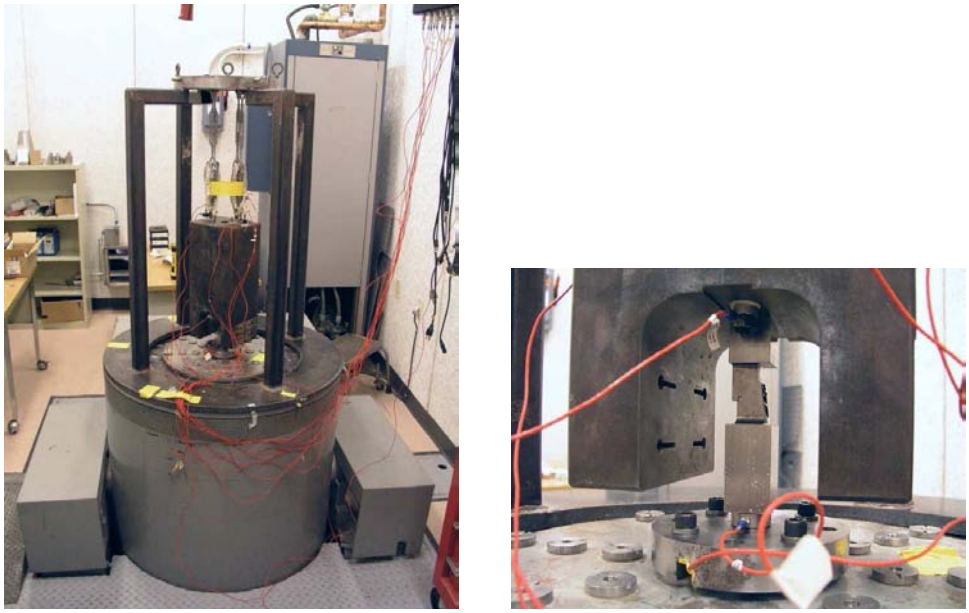

Figure 4.74. Single-Leg Setup in the BMD.

performed on the solid-equivalent single-leg with no frictional interface. In the first series of tests, the solid hardware is disassembled and assembled between each set of tests. This test is intended to evaluate the sensitivity of the responses to uncertainty in the portions of the experiment setup that have nothing to do with the jointed interface under study, such as fixture bolts, mounting bolts, support flexures of the large mass, etc. Between each test, the fixture base is rotated to a new position, the force gage is removed and rotated, and the fixture bolts and washers are exchanged. This test is repeated sixteen times and the results are shown in Figure 4.75. The measured natural frequencies for the solid-leg experiment ranged from 362 to 367 Hz with a mean of 365 Hz.

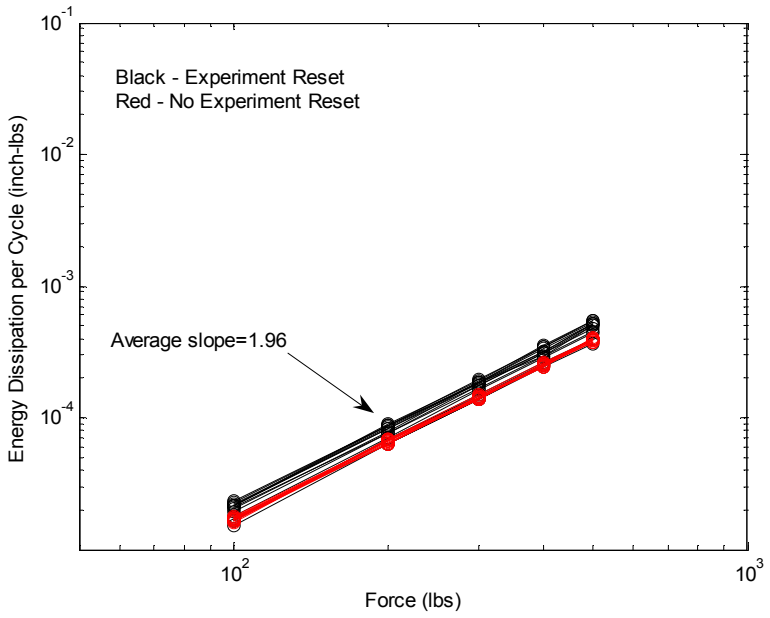

Figure 4.75. Solid Hardware under Steady-State, Sinusoidal Excitation.

In the second test series, the hardware is not disturbed between tests. This series of tests is intended to evaluate the sensitivity of the responses only to signal measurement accuracy. By leaving the experiment setup undisturbed for each test, it could be determined whether there are any variations in the measured response due to variations in the data acquisition and vibration control system. This test is repeated twelve times and the results are also shown in Figure 4.75.

The tests performed on the solid hardware indicate that measurement repeatability is acceptable. The scatter in the energy dissipation data acquired for the hardware with no experiment resetting can be quantified with a coefficient of variation (COV), defined as the standard deviation divided by the mean, of 3% at most. The variation in energy dissipation due to disturbances in the experiment assembly is higher. The scatter in the data when the experiment is reset can be quantified with a COV of no more than 13%. The average slope of a linear fit through the solid data on a log-log scale is 1.96. Recall that a slope of 2.0 indicates linear behavior.

4.4.3.2 Experiments on Multiple-Jointed Single-Leg Configurations

Next, response data is gathered on all combinations of jointed hardware, and energy dissipation is calculated as a function of the five force levels. The fixed-base resonant frequency of the system ranges from 298 to 342 Hz, depending on the excitation level, and varies slightly for each assembly of the bolted connection. The average is approximately 320 Hz, considerably less than that measured for the solid-leg (365 Hz), with the frequency difference indicating the reduction in stiffness caused by the bolted interface. After gathering data at each of the five different loads, the joint was reset. Resetting the joint is defined as taking the bolt out then assembling the joint with bolt again. Energy dissipation measurements are included for all runs in Figure 4.76.

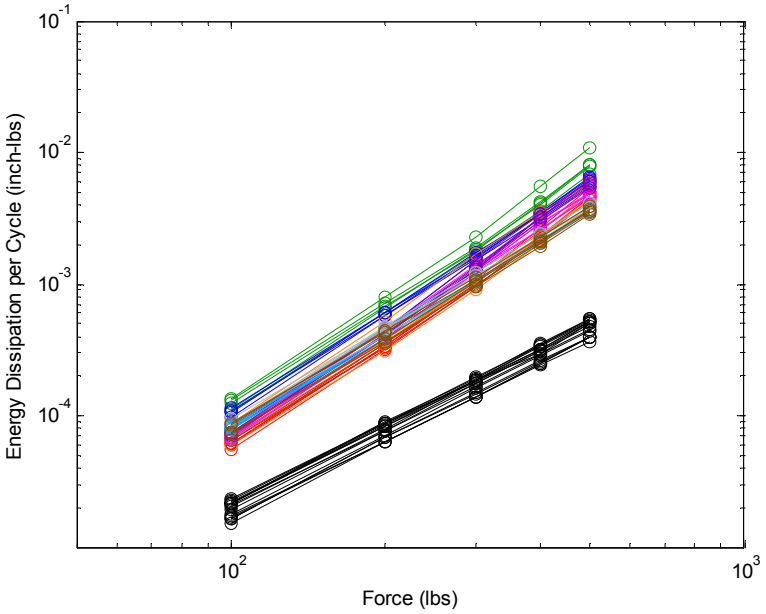

Figure 4.76. Bolted (Color Curves) and Solid (Black Curves) Specimen Dissipation.

The average slope of the energy dissipation curves for the jointed hardware is 2.55, which indicates significant nonlinear behavior in the joint interface. The variation in the jointed energy dissipation represented by COV is as high as 30%. The variation in energy dissipation ranges from as high as 150% of the mean to as low as 95% of the mean. Histograms of calculated energy dissipation values at each load level are shown in Figure 4.77. In general, a larger portion of energy dissipation values falls toward the lower end of each distribution. The average log-log slope of the jointed specimen energy curves is 2.55 and the histogram of the calculated slopes are shown in Figure 4.78. Data from these experiments are transmitted to analysts and uncertainty engineers for use as calibration data and as the basis of a probabilistic model of the fundamental parameters of the Iwan joint model for the inclusion in the structural dynamic model.

The BMD is shown to provide a very repeatable experiment through the evaluations with the

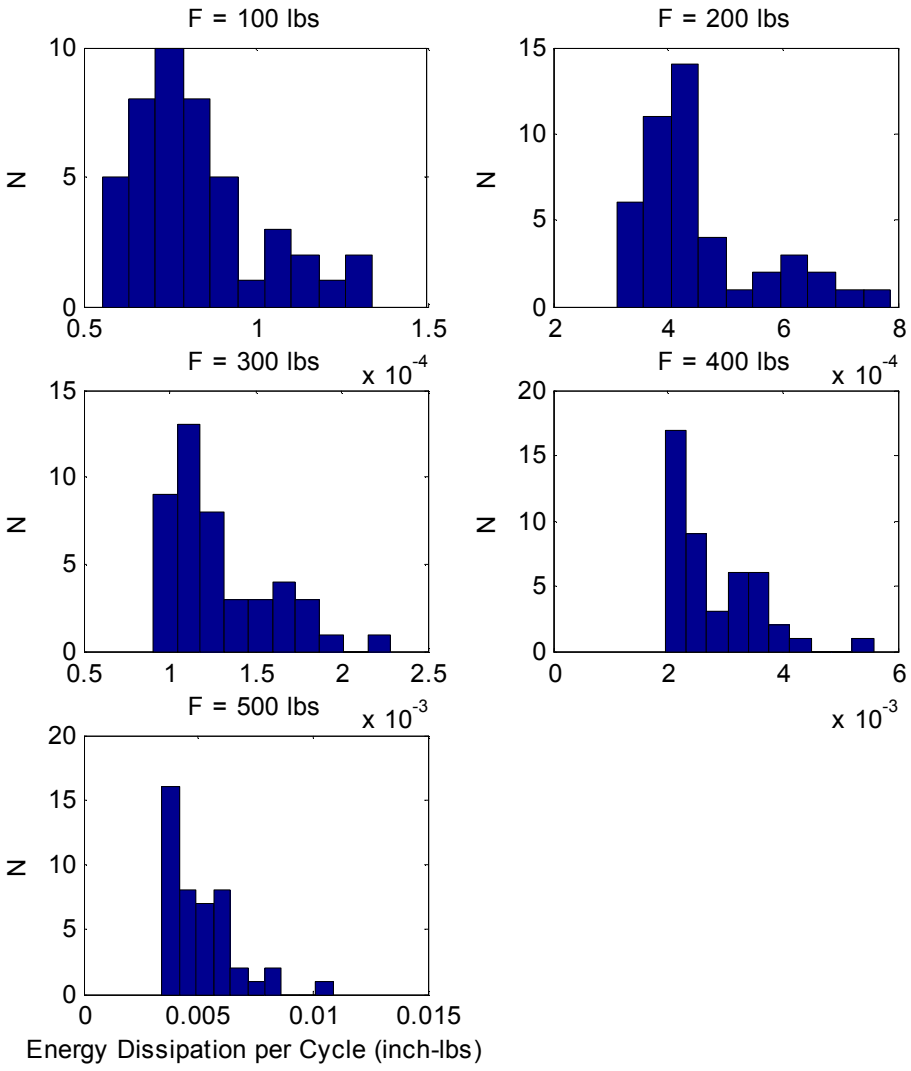

Figure 4.77. Energy Dissipation Values at Five Load Levels.

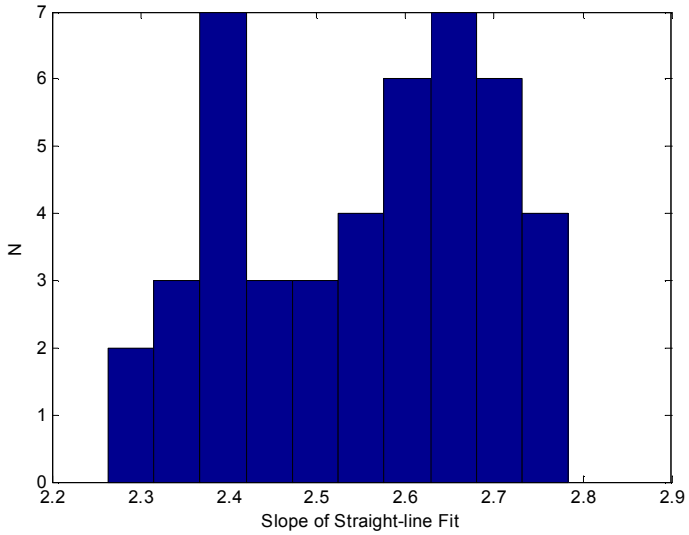

Figure 4.78. Slopes of Energy Dissipation Curves.

solid specimen. The data from the experiments show that there are two basic types of variability for the bolted connections. The first is the assembly variability for a specific joint. The experiments show that there is a 20-30% variability that occurs when the joint is reassembled several times. The second is the part-to-part variability that comes from the slight differences in the geometry of specimens machined to the same specifications. This is particularly true for the contact region of the joint as discussed in Section 9. The range of the variation in energy dissipation is as high as 150% of the mean and as low as 95% of the mean. This clearly indicates that the part-to-part variability dominates the uncertainty of a particular bolted joint geometry.

4.4.4 Summary of BMD Dynamic Experiments on Bolted Joints

The experiments discussed in this section show that the BMD concept is a very versatile experimental method for bolted joints research. The results for the bolted specimens demonstrate very similar behaviors as the experiments in the BMD with the rollers and bolt-free specimens. Several measures of response can be generated from the experiments that give insight into the nonlinear behavior of bolted joints. The techniques for computing the nonlinear restoring force appears to offer a very valuable approach for future research.

Chapter 5

Dumbbell Joints Experiments

Brian R. Resor, Danny L. Gregory,
Michael D. Jew, and James P. Lauffer

5.1 The Dumbbell Technique For Dynamic Axial Loading

A two mass dumbbell arrangement is one of the cleanest experiments for the measurement of energy dissipation and stiffness of simple, nonlinear, jointed interface elements. The dumbbell is well isolated from other experiment hardware because it utilizes free-free boundary conditions. The only connections to other hardware are the relatively soft bungees that suspend the masses. Additionally, the axial mode of the dumbbell is easily excited, while at the same time keeping participation of other dumbbell modes minimized. Upon excitation of the dumbbell axial mode with an instrumented hammer, the transient loads in the joint interface sample during ring-down are dominated by motions that induce tension and compression in the hardware. If desired, the dumbbell can also be excited in other manners to force participation of other modes, and therefore more complicated loads in the joint interface.

The transient response of the dumbbell to the hammer input data is collected and then post processed. Post processing can reveal the effective joint element stiffness and the damping. For jointed interfaces, the damping is typically nonlinear. A modified, logarithmic decrement, analysis technique is used in the simplest cases to understand the time varying properties of the jointed interface.

This section will describe the experimental technique and the simple data analysis using logarithmic decrement. Later sections will show several examples of dumbbell experimental results. The experimental data will give the reader a reasonable appreciation for nonlinear, bolted joint behavior in axial loading.

5.1.1 Experiment Setup

Figure 5.1 shows the setup of a typical dumbbell hardware and hammer. In this case, each stainless steel dumbbell mass weighs approximately 30 lb and contains a $\frac{1}{4}$-in tapped hole for eye bolts. The dumbbell is suspended by soft bungees. Lap joint specimens are each held to the masses with a single $\frac{1}{2}$-in bolt, torqued to 80 ft-lb.

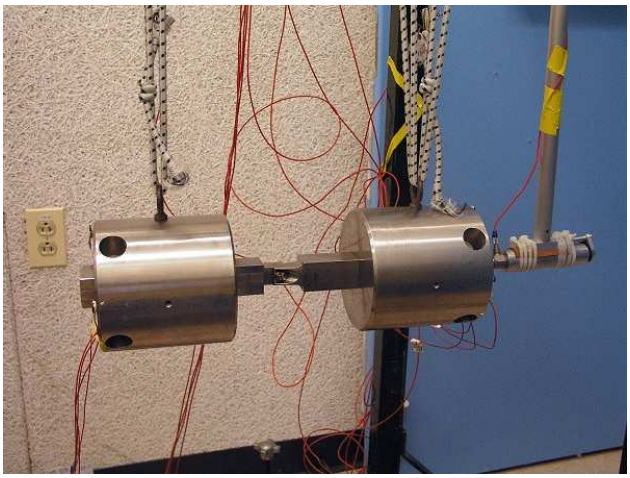

Figure 5.1. Dumbbell Experiment Setup.

The bolt holes have been tapped for a short length to allow the installation of a threaded plug in the outside end of each dumbbell mass. This configuration, shown in Figure 5.2, ensures that the hammer tip can strike the dumbbell at the center of its radius.

5.1.1.1 Dumbbell Excitation

A 5,000-lb force gage and nylon hammer tip are used to measure and provide the near-Haversine input to the dumbbell. Additionally, the use of a pendulum arrangement enables the inputs to be consistent in impact location, direction, and amplitude across all hits. In typical hammer excited experiments, the hammer tip and hammer size are both chosen carefully to excite specific frequency ranges.

5.1.1.2 Force Measurement in the Dumbbell Specimen

Axial Force Measurement Early dumbbell experiments were conducted with a ring-type, piezo-electric, force gage installed in-line with the joint specimen. Figures 5.3 and 5.4 (shown again later as Figures 5.25 and 5.26) show an example of a dumbbell with two axial force gages in-line with

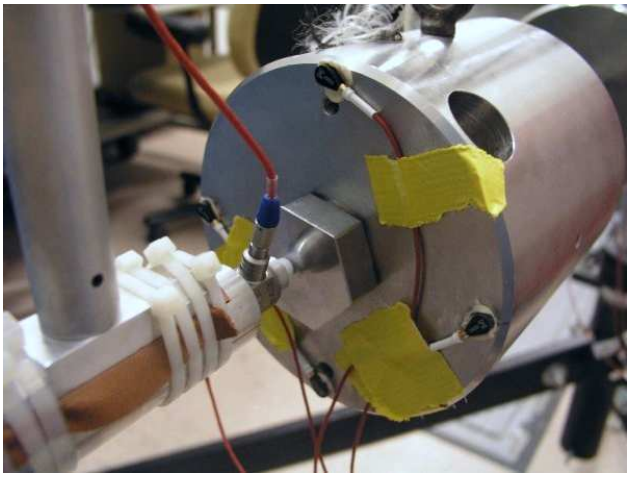

Figure 5.2. End View of the Dumbbell and Threaded Plug.

the hardware. The force gage provides a direct measure of axial force in the joint specimen. Investigations quickly revealed that the force in the joint interface is truly the product of one dumbbell mass and the acceleration of the center of mass of the dumbbell. The axial motion of the dumbbell center of mass can be approximated quite well by time synchronous averaging of two or more appropriately placed, single-axis accelerometers on the end of the masses, eliminating the need for the force gage and simplifying the experiment. Removing the in-line force gages is desirable because their compliance significantly changes system dynamics.

Without a force gage installed, a very effective instrumentation scheme for response measurement includes four accelerometers on the end of at least one dumbbell. Figure 5.2 shows an example of four, single-axis accelerometers spaced evenly around the end of a dumbbell for axial motion measurement. By performing time synchronous averaging one can indirectly determine the force exerted in the joint during ring-down. Four accelerometers (two on each end mass) are sufficient to describe the axial motion of the dumbbell center of mass.

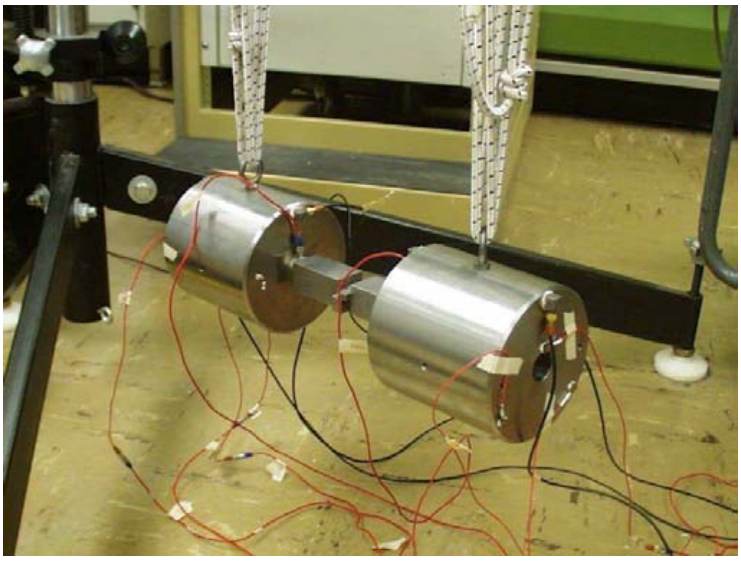

Figure 5.3. Dumbbell with Force Transducers In-Line With The Specimen and Tri-Axial Accelerometers On The End Masses.

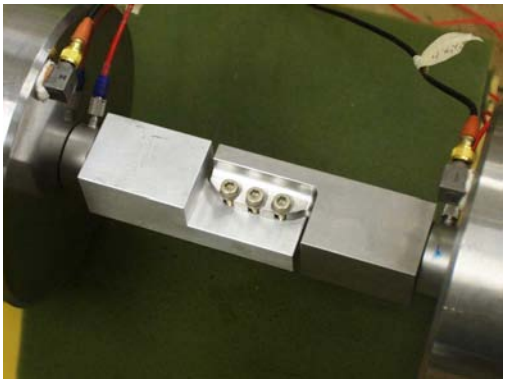

Figure 5.4. 3S-Jointed Specimens Installed with Two In-line Force Gages.

Time Synchronous Averaging of Response Waveforms Prior to averaging in the time domain it is important to remove any offsets that may be present in the signals. Typically, the average of the pre-trigger data is used to remove the offset in each measurement channel. Next, time synchronous averaging is applied to the signals from evenly spaced gages around the perimeter of the end of one of the dumbbells. The resulting discrete waveform represents the average motion of its mass.

$$a_{avg}[i] = \frac{\sum_{k=1}^{N} a_k[i]}{N}, i = (1, 2, ...n) \tag{5.1}$$

where N is the number of response channels being averaged
and n is the number of points in the discretized time history.

The average acceleration can then be multiplied by the mass of a single dumbbell to determine the time varying force in the specimen.

$$F = ma_{avg} \tag{5.2}$$

Lateral Force Measurement Force gages that measure all three axes of force are available. These gages can also be used at the locations shown in Figures 5.25 and 5.26 to determine the shearing forces in addition to the axial force in the specimen. These measurements have been made at Sandia. Accurate and meaningful interpretation of the lateral shearing forces, which probably are realized in the joint interface as a moment, is an area for future work.

5.1.1.3 Use of Monolithic Hardware

To understand the response of the jointed specimens , it is essential also to test monolithic elements in the experimental fixturing.

5.1.1.4 Expected Mode Shapes

The mode shapes described in this section were derived from a finite element model of the dumbbell setup. The modal frequencies and mode shapes calculated from the finite element model generally agreed well with the modes identified and fitted from test data. There are six flexible-body modes that are of primary interest to the experimentalist beyond the six, rigid body modes of the dumbbell on the bungee supports. The first six flexible-body modes for the dumbbell are pictured in Figures 5.5 - 5.8. Though there appear to be two pairs of orthogonal bending modes, asymmetries of the test specimen result in significant differences in natural frequency. Frequencies of the modes will vary depending on whether the hardware is monolithic or contains a joint.

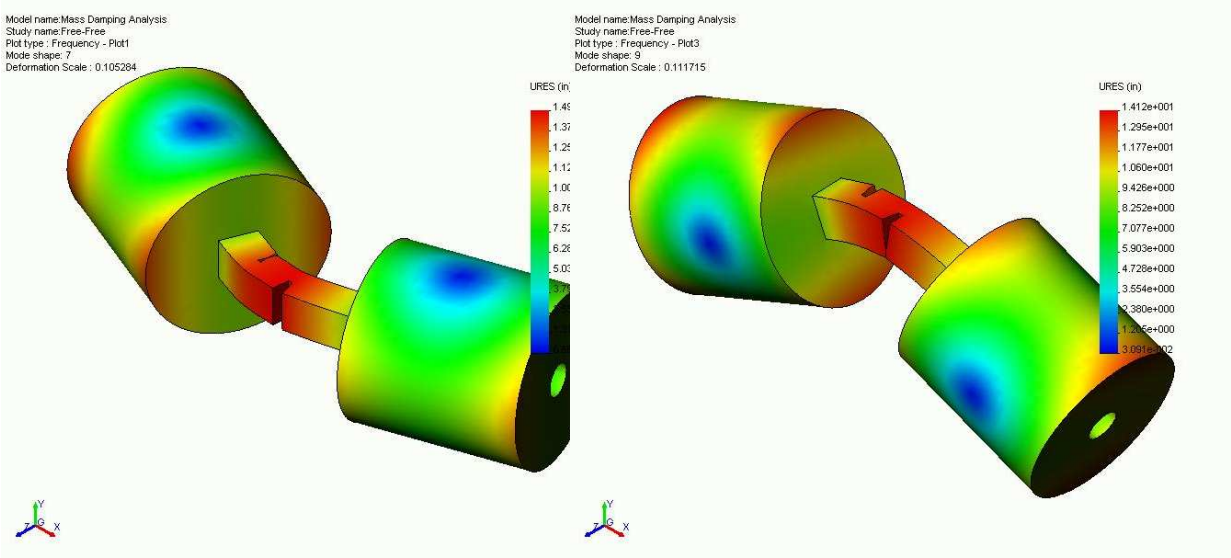

Figure 5.5. Modes 1 & 2 - Dumbbell, Orthogonal, First Bending Modes.

The jointed hardware frequencies are lower than the monolithic frequencies. Regardless, the mode shapes of both monolithic and jointed dumbbells are similar.

Generally, the first two flexible-body modes are lowest in frequency, and modes three and four are the next higher pair of modes. Occasionally, as shown in Figures 5.5 - 5.8, the frequency of the first torsional mode lies between the first two (superficially) orthogonal bending modes. (We drop the word “superficially” in the following but its presence is to be understood.) The closeness in frequency of these orthogonal modes is related to the nature of the joint specimen under test. Indeed, the mode ordering may change for one specimen type to another, depending on the stiffnesses in the two bending directions.

The first two orthogonal bending modes have the ability to exercise the joint interface in simple bending. Study of the structural response at these modes would yield information regarding the joint interface with application of moments.

The dumbbell axial mode is generally the fifth mode. The axial mode is the mode that provides the most useful loading of the joint specimen for axial loading. The experimental setup should be designed so the axial mode is spaced sufficiently far from any other structural modes, assuring that analysis of the axial mode is as straightforward as possible, with little influence of response by adjacent modes.

Generally, the torsional mode of the dumbbell is not easily excited by the inputs described in this chapter. It is not typically present in any significant amount in these experiments. However, the experimentalist should understand the mode to keep it from adversely influencing the data in an unknown manner.

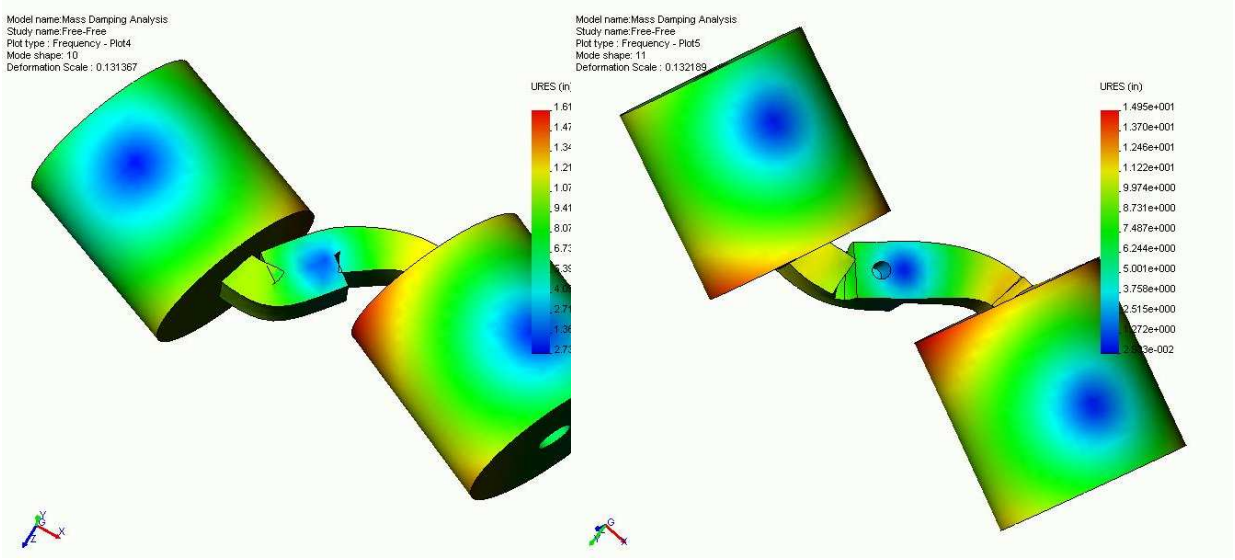

Figure 5.6. Modes 3 & 4 - Dumbbell, Orthogonal, Second Bending Modes.

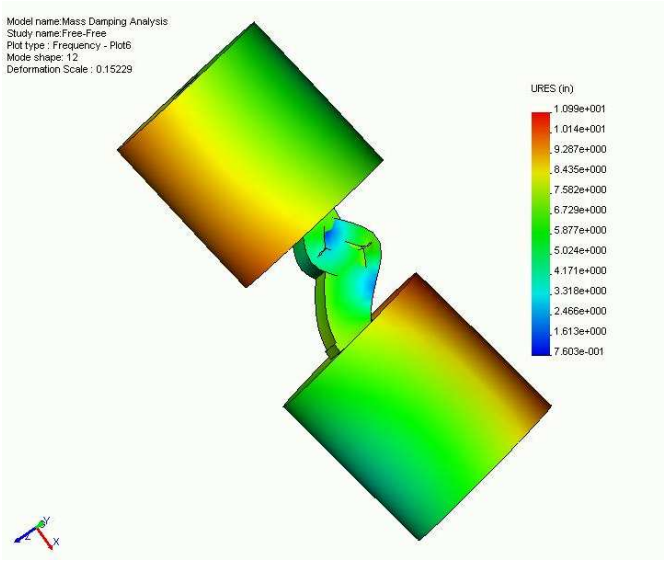

Figure 5.7. Mode 5 - Dumbbell Axial Mode.

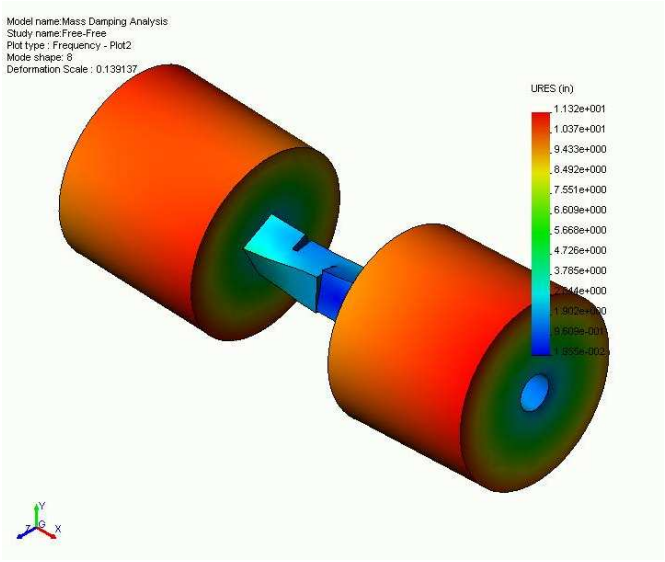

Figure 5.8. Mode 6 - Dumbbell Torsional Mode.

Beyond the modes shown here, there are many more local modes of the joint specimen. Their shapes and frequencies are highly dependent on the geometry and material of the individual specimens. Examples are shown in Figure 5.9. These modes occur at relatively high frequencies. Therefore, their displacements are very small when they happen to be excited. As far as is understood now, they have little effect on the behavior of the joint interface experiment response.

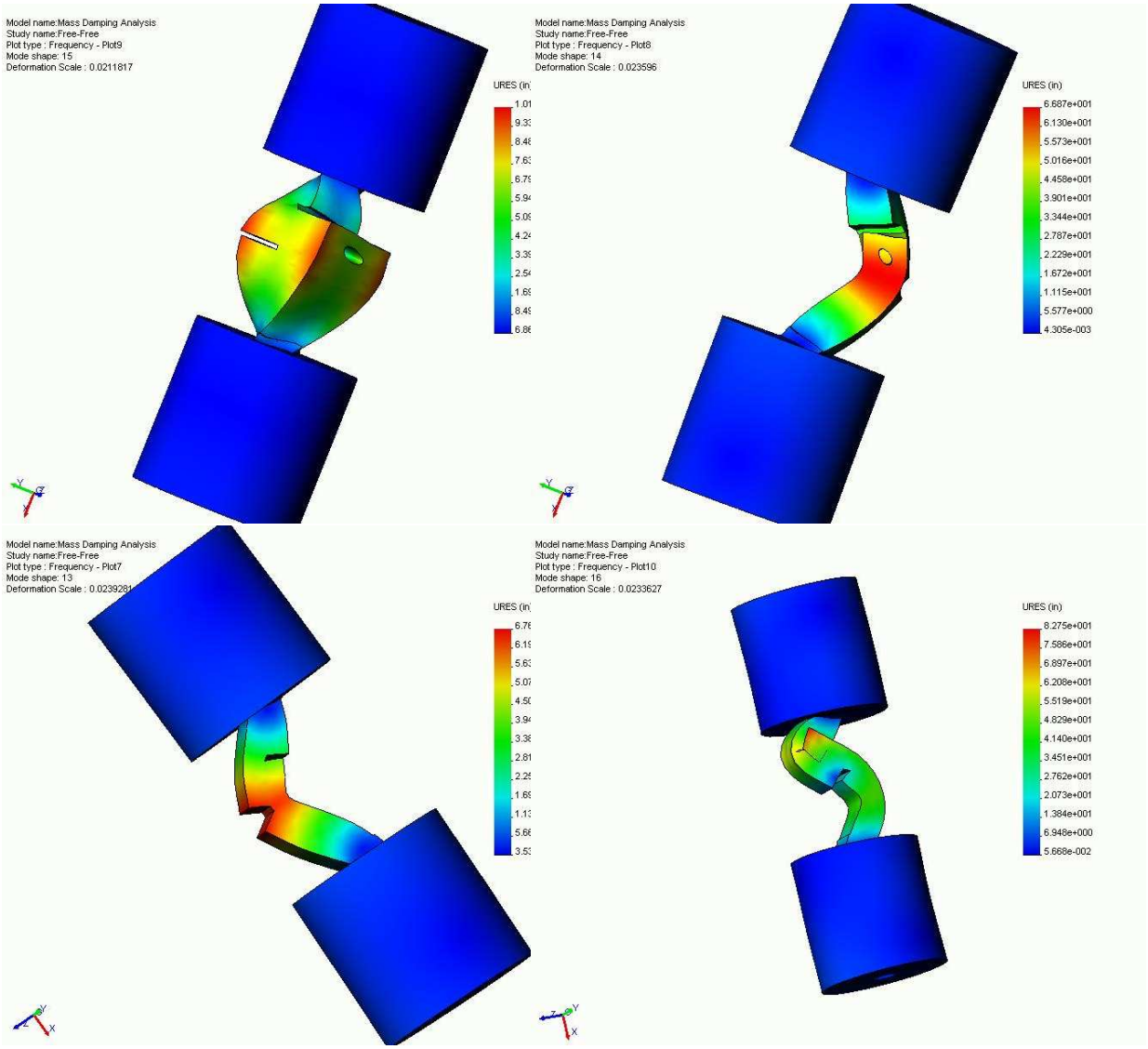

Figure 5.9. Higher Frequency Dumbbell Modes.

5.1.2 Basic Analysis of Transient Ring-Down

The waveform decays of the transient responses are postprocessed to derive a curve describing the energy dissipation dependence of damping on force amplitude. An advantage of this technique is that a single impact with the hammer exposes the joint to a wide range of force amplitudes during ring-down.

The rate of decay of the transient response is related to the damping in the structure, and the damping is related to the energy dissipation. In a nonlinear jointed interface, the rate of decay, the damping, and the energy dissipation per cycle appear to vary with time because they are governed at least partly by the force in the joint at any particular time. The following basic derivation explains how a time varying, instantaneous value for damping and energy dissipation can be approximated.

5.1.2.1 Derivation of Damping and Energy Dissipation Measurement Techniques

Consider the free decay of a *linear* SDOF system,

$$x(t) = x_o e^{-\zeta \omega_n t} \cos(\omega_d t) \tag{5.3}$$

where $x(t)$ is the time history of the system response (restoring force, acceleration, velocity, or displacement),
ω_n is the natural frequency of the SDOF: $\omega_n^2 = K/M$
ω_d is the damped natural frequency,
ζ is the instantaneous damping factor,
and x_o is the initial amplitude of the response.

The envelope of the peaks in the waveform is

$$x(t) = x_o e^{-\zeta \omega_n t}$$

Taking the logarithm of both sides,

$$\log(x) = -\zeta \omega_n t + \log(x_o)$$

Then, differentiating with respect to t,

$$\frac{\mathrm{d}(\log(x))}{\mathrm{d}t} = -\zeta \omega_n \tag{5.4}$$

The equivalent damping factor, ζ, is the slope of the envelope ($\log(x)$ as function of t) divided by the resonance frequency.

Though the above derivation presumed a linear system, we demonstrate in the following that the log decrement technique can be used to deduce the energy dissipation per cycle even in nonlinear systems.

The envelope of $\log(x)$ is linear for a linear system. A higher order polynomial can be used to approximate the points that define the envelope for nonlinear jointed structures, such as the bolted joint. The polynomial order applied to yield the best fit depends on the shape of the envelope. Typically a fourth or fifth order polynomial is used to fit envelopes of the dumbbell responses, such as was done to fit the curve in Figure 5.10.

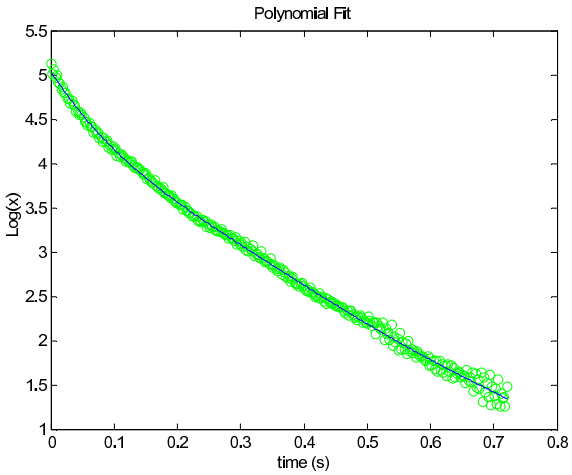

Figure 5.10. Peak Amplitude Fit.

Fifth order polynomial fit to the logarithm of peak amplitudes.

The instantaneous value of the equivalent viscous damping ratio at any time during transient decay, $\zeta(t)$, is obtained by computing the slope of the polynomial fit to the logarithm of the peak amplitudes and dividing by the natural frequency, ω_n, per Equation (5.4). Example results are given in Figures 5.11 - 5.12, indicating the decrease in damping with time as the amplitudes decay during the transient response.

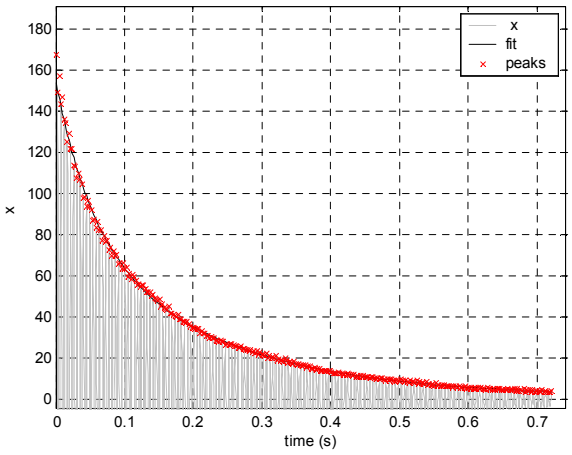

Figure 5.11. Polynomial Fit and Actual Response.

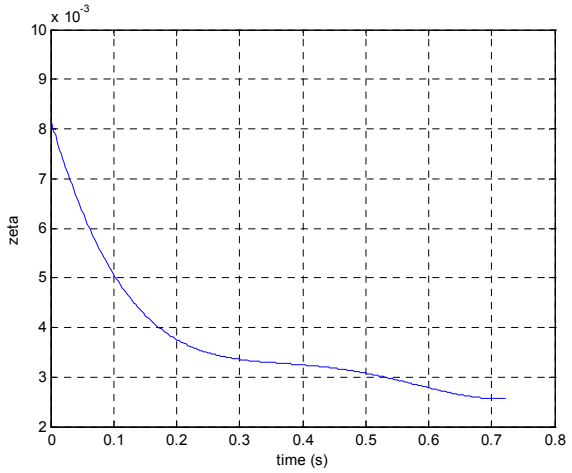

Figure 5.12. Time Evolution of Zeta.

Zeta plotted as a function of time. Zeta is proportional to the slope of the fit seen in Figure 5.10.

To estimate energy dissipation for a nonlinear system, we presume that the ring-down has the same form as in Equation (5.3), but with ζ slowly varying in time. The decrease in potential energy from one cycle to the next is

$$D = \Delta P = (1/2)KX^2\left(1 - e^{-4\pi\zeta\omega_n/\omega_d}\right) \approx 2\pi\zeta KX^2 = 2\pi\zeta M\omega_n^2 X^2 \tag{5.5}$$

where K is the linearized system stiffness,
M is the system sprung mass,
and X is the amplitude of oscillation.

Because it is generally accelerations rather than amplitude that is measured, a more convenient form of the above is

$$D = \frac{2\pi\zeta K}{\omega_n^2}A^2 = 2\pi\zeta MA^2 \tag{5.6}$$

where A is the amplitude of measured acceleration: $A = \omega_n^2 X$.

Several assumptions have gone into the above.

1. The relation $\omega_d = \omega_n\sqrt{1+\zeta^2}$ holds even for our nonlinear system,
2. ζ is small enough that we can ignore terms higher than the first order in ζ,
3. $2\pi\dot{\zeta}/\omega_d << \zeta$

The dumbbell may be considered as the composite of two SDOF systems, each oscillating about the mid-plane of the specimen. The energy dissipation of the dumbbell is now

$$D(t) = 2\left(2\pi\zeta K_{1/2}A^2/\omega_n^2\right) = 2\left(2\pi\zeta M_{1/2}A^2\right) \tag{5.7}$$

where A is the amplitude of acceleration of each end mass with respect to the specimen center,
$M_{1/2}$ is the mass of each of the end masses,
and $K_{1/2} = M_{1/2}\,\omega_n^2$

Of course, if using inch-pound-second units, one must be especially careful to use units of mass rather than weight in the above.

Log-log plots of energy dissipation per cycle vs force amplitude have become a very common method of exploring the nonlinearity of joint response. The force terms are obtained either from in-line force transducers or from a use of $F = MA$. Such log-log plots are often nearly linear and one looks to the parameters of the fitted line for insight into the dissipation properties of the joint.

An example plot of energy dissipated vs force together with its straight-line fit is shown in Figure 5.13. The straight-line fit is used to estimate the gain and slope of the curve in log-log space. These parameters provide some insight into the damping and nonlinearity of the response. Gain is a measure of the overall damping, and the slope is a measure of the nonlinearity. A slope

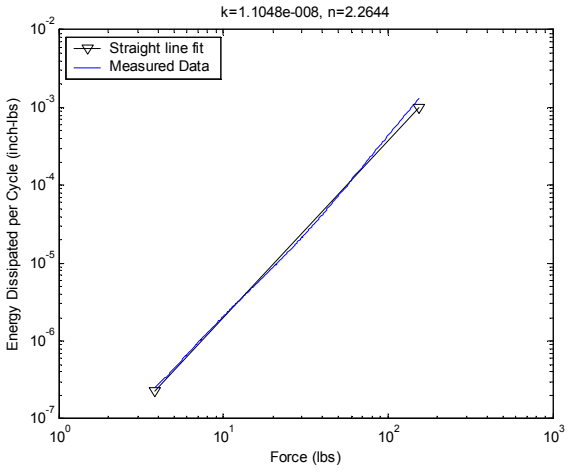

Figure 5.13. Fit to Energy Dissipation Curve.

of 2.0 indicates a linear damping. A slope greater than 2.0 indicate high magnitudes of nonlinear damping.

5.1.3 Digital Filtering

Often the desired axial dumbbell response actually is contaminated by structural dynamic modes of the experiment that can either be detrimental to the desired data or can simply complicate post processing of the data. There are several reasons why a single, axial, dumbbell mode may actually include more modes:

- The input to the end of the dumbbell is not well-centered, and therefore bending modes of the dumbbell are excited.
- The line of action of the axial force through the jointed interface is not centered about the interface. Thus, the primary axial mode shape includes some bending.

If multiple modes are unavoidable, then there are ways to deal with them:

- Use a pendulum hammer or pneumatically charged hammer for input to the end of the dumbbell. Either tool typically enables the input location and amplitude to be extremely repeatable, relative to a manual hammer input by the experimentalist.
- Digital bandpass filtering around the mode of interest to remove influence of other resonances in the postprocessing steps (the subject of this subsection).

- Modal filtering of the dumbbell response data (explained in a later section of this handbook).

The purpose of this section is to verify and illustrate that accurate damping estimations can be made of a single mode that is embedded within several modes during a transient response. Estimation requires use of a digital band-pass filter at the frequency of interest. Discrete, analytical responses are generated and their decay rates are determined.

Not only does this exercise verify the correctness of applying filters to the data and measuring the correct damping values, but it also serves as a verification of the accuracy of the transient decay rate measurement discussed directly above.

5.1.3.1 SDOF Numerical Example

Matlab is used to calculate responses of an SDOF system. As verification of the accuracy of the routine, one compares a response from the numerical scheme to the analytical equation for the response of a linear system. The transient response of an initially quiescent SDOF system to an impulse can be described as follows:

$$x(t) = e^{-\zeta \omega_n t} \frac{\dot{x}(0)}{\omega_d} \sin(\omega_d t) \tag{5.8}$$

where $\dot{x}(0)$ is the velocity induced by the impulse and, as usual, $\omega_d = \omega_n \sqrt{1-\zeta^2}$.

The physical parameters chosen in this exercise are

$$k_1 = 1.2 \text{ x } 10^9$$
$$c_1 = 3.0 \text{ x } 10^4$$
$$m_1 = 100$$

where m_1 is the mass of the SDOF,
k_1 is the spring stiffness,
and c_1 is the damping coefficient.

Therefore, $\omega_n = \sqrt{\frac{k_1}{m_1}} = 200 \text{rad/sec}$ is the natural frequency of the system and $\zeta = \frac{c_1}{2\sqrt{k_1 m_1}} = 0.0433$ is the damping factor.

The Matlab function ode45.m uses the state-space representation of the equations of motion to solve for the response. The state-space representation for free vibration of a single mass, spring and damper is written as

$$\dot{x} = Ax \tag{5.9}$$

where x is the vector of state variables

and

$$A = \begin{bmatrix} 0 & 1 \\ \frac{-k_1}{m_1} & \frac{-c_1}{m_1} \end{bmatrix}$$

An initial value for the velocity is used to simulate the impact. Figure 5.14 shows the analytical response of Equation (5.8) and the numerically calculated response together. The logarithmic decrement technique described above is used to calculate the damping of both the numerical and analytically generated responses. A straight line can easily be used to fit the logarithm of the peaks in the response because the responses are linear. Damping values of 0.0434 and 0.0433 were calculated from decay of the numerical solver generated response and analytical formula, respectively. The difference corresponds to a 0.25% variation in measured damping. This shows that the technique is very accurate for simple, linear responses.

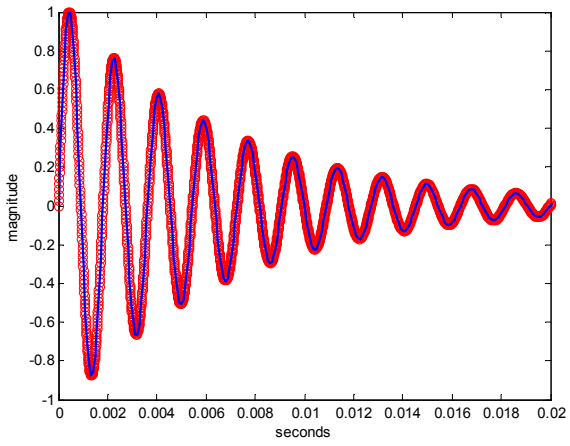

Figure 5.14. Transient Response Comparison.

Comparison of transient responses generated using the analytical formula and generated using a numerical solver with state equations.

5.1.3.2 Two DOF System

Next, an analytical 2DOF system was created in order to generate a response that contains multiple modes. Once the response is calculated, the response of each mode will be filtered out of the overall response and compared to the analytical predictions of the modal responses. An example of the 2DOF system is shown in Figure 5.15.

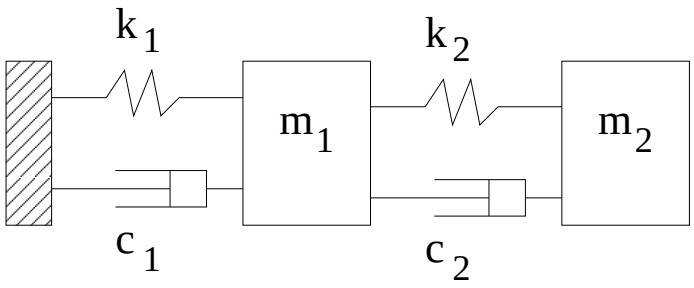

Figure 5.15. Simple 2DOF System.

The equations describing the free vibration this system are

$$M\ddot{x} + C\dot{x} + Kx = 0 \tag{5.10}$$

with

$$M = \begin{bmatrix} m_1 & 0 \\ 0 & m_2 \end{bmatrix}, C = \begin{bmatrix} c_1 + c_2 & -c_2 \\ -c_2 & c_2 \end{bmatrix}, K = \begin{bmatrix} k_1 + k_2 & -k_2 \\ -k_2 & k_2 \end{bmatrix} \tag{5.11}$$

or in state equation form

$$\frac{d}{dt}\begin{Bmatrix} x_1 \\ x_2 \\ \dot{x}_1 \\ \dot{x}_2 \end{Bmatrix} = \begin{bmatrix} 0 & 0 & 1 & 0 \\ 0 & 0 & 0 & 1 \\ \frac{-(k_1+k_2)}{m_1} & \frac{k_2}{m_1} & \frac{-(c_1+c_2)}{m_1} & \frac{c_2}{m_1} \\ \frac{k_2}{m_2} & \frac{-k_2}{m_2} & \frac{c_2}{m_2} & \frac{-c_2}{m_2} \end{bmatrix} \begin{Bmatrix} x_1 \\ x_2 \\ \dot{x}_1 \\ \dot{x}_2 \end{Bmatrix} \tag{5.12}$$

The response of the system to an initial condition is determined numerically two ways. First, the state-space matrix is used with the numerical differential equation solver ode45.m to calculate a response. Then, the modal matrix, formed from mode shape vectors, is used to calculate both the modal response and overall system response. Physical parameters are added to those of the SDOF model above for the 2DOF case: k_2=k_1, c_2=c_1, and m_2=m_1.

First, calculate the modal responses. Define the modal coordinates,

$$q = [\phi]^{-1} \cdot x$$
$$\dot{q} = [\phi]^{-1} \cdot \dot{x}$$

where ϕ is the transformation (modal) matrix formed from the mass-normalized mode shape vectors.

Initial conditions for q and $\dot{q}$ can be determined based on the actual physical initial conditions. Also, the transformation matrix is used to transform Equation (5.10) into a set of uncoupled differential equations. These equations in state-space form are written as

$$\dot{q} = Aq \tag{5.13}$$

with

$$A = \begin{bmatrix} 0 & 0 & 1 & 0 \\ 0 & 0 & 0 & 1 \\ -k_{11} & 0 & -c_{11} & 0 \\ 0 & -k_{22} & 0 & -c_{22} \end{bmatrix}$$

where k_{11}, k_{22}, c_{11}, and c_{22} are the diagonal terms in the decoupled matrix coefficients of Equation (5.10) (diagonal terms in the decoupled mass matrix are 1).

Matlab is used to calculate the modal matrix and then to decouple the coefficient matrices so that the state matrix A can be used again along with the numerical differential equation solver ode45.m to calculate responses q to initial conditions q_0 and $\dot{q}_0$. Using initial conditions of

$$x_0 = \begin{bmatrix} 0 \\ 0 \end{bmatrix} \qquad \dot{x}_0 = \begin{bmatrix} 100 \\ 0 \end{bmatrix}$$

The modal responses are as shown in Figure 5.16. A by-product of the modal response calculation is the parameter set for each mode, shown in Table 5.1. The modal responses can then be combined using the modal matrix (mass normalized) to obtain overall system responses, x. The system responses are shown in Figure 5.17a. The system responses calculated using the original state Equations (5.10) are shown in Figure 5.17b, and are in good agreement.

Table 5.1. Analytical Modal Parameters of the 2DOF System.

	Zeta	Frequency (Hz)
Mode 1	0.0268	341
Mode 2	0.0701	892

5.1.3.3 Compare Filtered and Modal Responses

Estimates of the modal responses are obtained by applying a digital, bandpass, Chebyshev filter to the system response x_1. Figure 5.18 shows the transfer function of response x_1 to a perfect impact

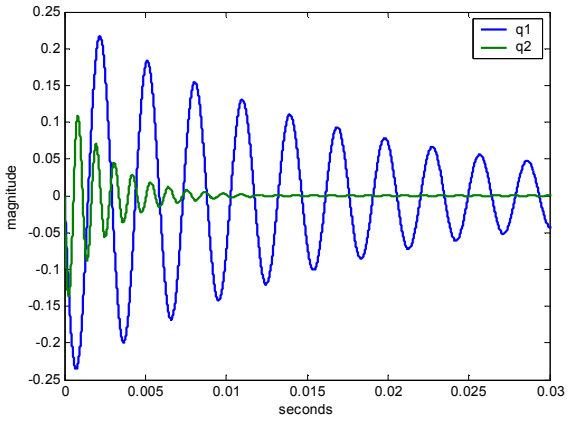

Figure 5.16. 2DOF Modal Responses.

Modal responses of 2DOF system to initial condition with physical parameters defined above.

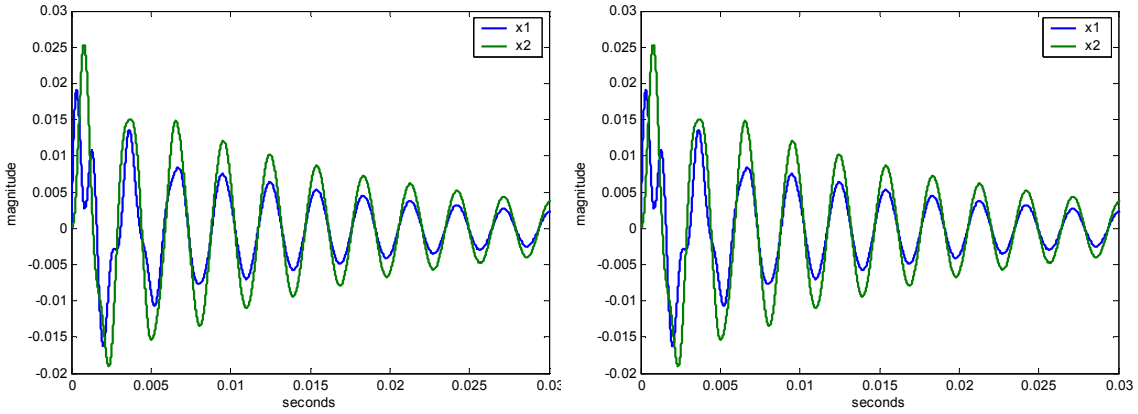

Figure 5.17. Calculations of System Response.

(a) System responses calculated as a linear combination of individual modal responses. (b) System responses calculated from state equations.

on mass m_2. The natural frequencies determined from this plot are 341 Hz and 892 Hz.

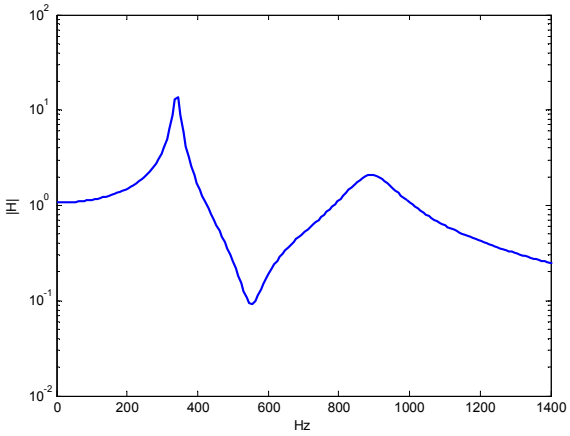

Figure 5.18. Transfer Function of Response x_1 to a Perfect Impact Input.

A 300-Hz-wide fourth-order, digital, bandpass, Chebyshev filter was applied to each mode. The filtered responses are seen in Figure 5.19 and Figure 5.20 along with the modal responses from Figure 5.16.

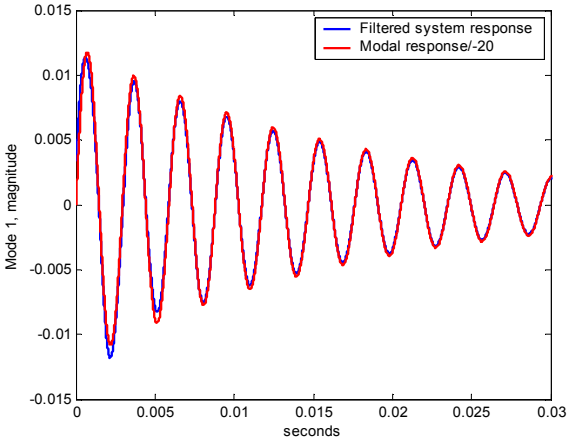

Figure 5.19. Filtered and Modal Response - Mode 1.

The evolution equations for the modal coordinates are obtained by substituting the modal expansion back into the governing equation, Equation (5.12). The resulting nodal predictions are then independent of any modal scaling or normalization.

The linear damping of each filtered response is again estimated using the transient decay-rate technique with a straight-line fit of the logarithm of the peaks in the response. A straight line is

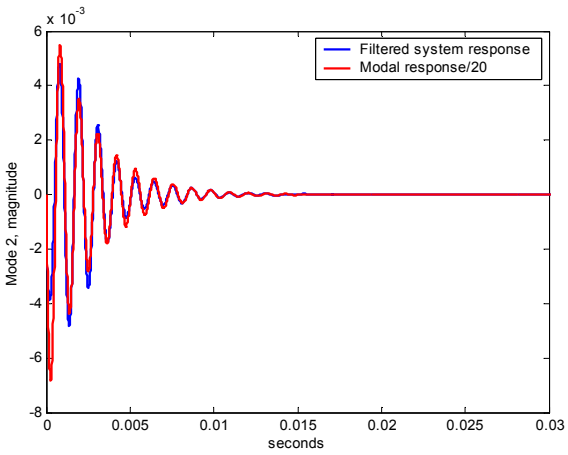

Figure 5.20. Filtered and Modal Response - Mode 2.

Table 5.2. Comparison of Zeta for Each Mode

	Mode 1	Mode 2
From modal transformation calculation	0.0268	0.0701
Measured using logdec technique	0.0267	0.0722

used because the analytical model is linear. Table 5.2 compares the calculated and estimated ζ for each mode.

The estimated ζ in the Mode 1 filtered response is an accurate representation of the actual damping of that mode as determined by the modal transformation calculation. The contribution of Mode 1 dominated the overall response, and therefore the decay rate of the filtered signal is easy to measure because there are many peaks and few end effects due to startup and ending of the digital filter. Figure 5.21 shows the high quality fit of the envelope to the filtered signal.

The estimate of the Mode 2 damping is not as accurate. Gibbs phenomena in the filtered response make data at the beginning and end of the interval unusable. Also, Mode 1 dominates the response. Even after filtering, Mode 1 response remains a complication in extracting Mode 2 response until very long times, when Mode 1 has nearly decayed to zero. The effects of Mode 1 contamination and Gibbs phenomena, do not leave very many peaks in the filtered Mode 2 response that are clean enough to fit in the damping measurement. In the end, an estimate of the Mode 2 damping is not as accurate as desired. Figure 5.22 shows the linear fit to the transformed amplitude data.

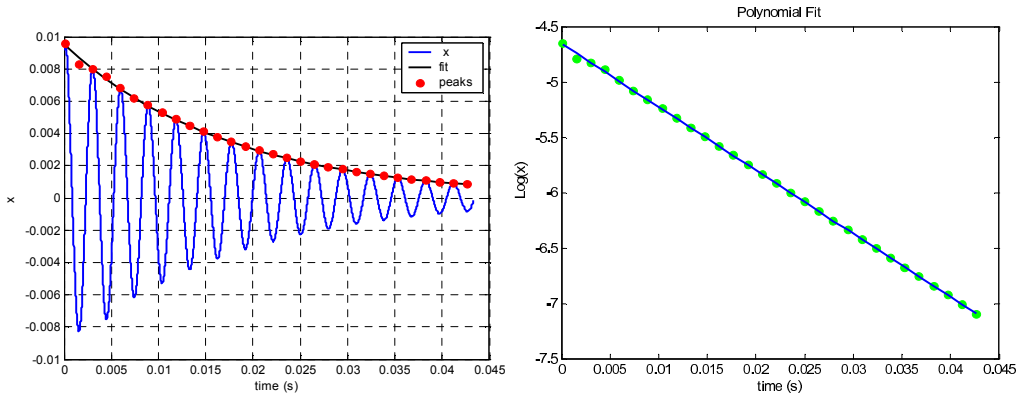

Figure 5.21. Mode 1.

(a) Fitted peaks in the filtered signal. (b) Energy curves for all configurations.

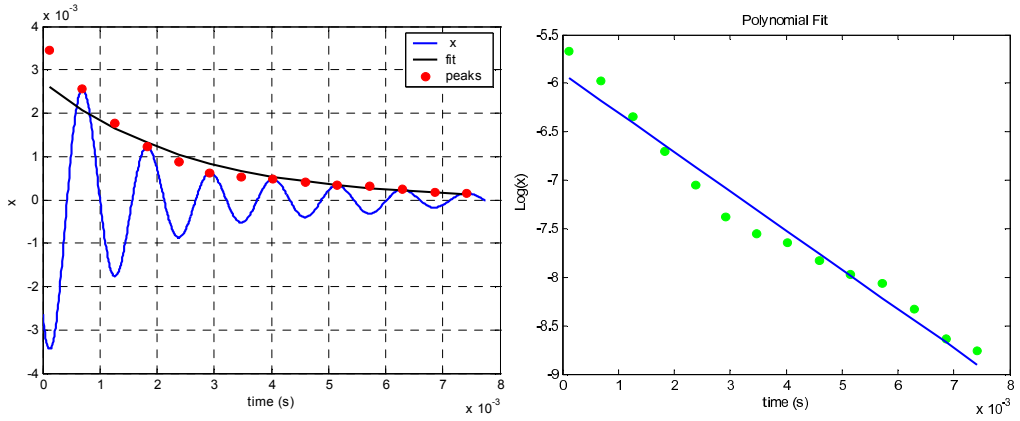

Figure 5.22. Mode 2.

(a) Fitted peaks in the most acceptable portion of the filtered signal and (b) straight-line fit through the logarithm of the peaks.

5.1.3.4 Summary of Digital Filtering

This simple investigation shows that accurate damping measurements can be obtained, with certain limitations, for the response of a single mode by applying a digital bandpass filter to the overall time-history. Digital bandpass filtering is a useful tool when damping measurements of a single, specific mode are desired and the experimental transient response is just slightly contaminated by other modes.

It is still best to try to ensure that the mode of interest does dominate the dumbbell response, though. As long as the mode of interest dominates, and the mode of interest is spaced sufficiently far from other strong modes, then a low order, relatively wide, digital filter can be used to filter the response. Such a filter minimizes the effects in the filtered response due to filter startup, thereby allowing a wider range of amplitudes in the response to be utilized for the damping, and energy dissipation, calculations.

This study has shown that the modified logarithmic decrement routine used to determine damping by measuring the decay rate of a transient response is accurate.

5.2 Dumbbell Experiment Examples System B Bolted Joint Specimens

5.2.1 Motivation

Early dumbbell experiments were performed using joint specimens that replicated the geometry and materials found at the tab-like bolted connections of System B, Laterally Oriented Subsystem (LOS) housing. This experiment was unique for a few reasons:

- The joint specimens were created in a way that simulated two different orientations of shear loading for a given tab.
- The hardware under investigation utilized joints that contained both two and three bolts in a single tab. (See Figure 5.24.)
- The materials used in the joint specimens were not the same: aluminum was on one side and stainless steel on the other.

The goal of this particular project was to provide experimental data and insight to develop and validate structural dynamics models for System B, LOS bolted joint. The finished, whole-joint element was to be included in a Salinas, structural dynamics model of System B.

Some jointed interfaces contain a load path through the joint that is in a single preferred direction relative to the overall system. Because the LOS housing connections carry loads from multiple directions, test specimens were designed to represent the bounds of the joint orientation with respect to the incoming load.

Differences were observed in the energy dissipation of the bolted joint depending on the configuration. This variability suggests a need for joint models that have the capability to utilize more than one set of parameters, depending on the orientation. Similarly, the variation in physical tolerances and assembly procedures of the LOS housing bolted connections create variability and uncertainty in their responses. Studies were performed to investigate the sensitivity of the response to this assembly variability. We learned that a range of jointed interface model parameters can be determined based on the experimentally observed variability.

5.2.2 Dumbbell masses

The setup of System B hardware experiments was exactly as described in Section 5.1.

5.2.3 Hammer input

The dynamic load input to System B hardware came from a manually applied, modal hammer.

5.2.4 Bolted Joint Specimens

The LOS housing had six tabs oriented at various angles around its circumference. Lateral loads into the housing were the environment of greatest interest for this hardware. A lateral load can enter an individual tab from any direction. Two primary orientations defined the bounds of how this lateral load can enter as a shear force into an individual tab (Figure 5.24). The loading direction is indicated by arrows in Figure 5.24a.

We used a simple nomenclature to distinguish the specimens. When three bolts were in series with the applied load, the specimen is named a 3S-specimen; when two bolts were in parallel with the applied load, the specimen is named a 2P-specimen.

Solid specimens, without joint interface, were used to provide a controlled measurement of unknown sources of damping. The difference in energy dissipation per cycle between the solid data and the corresponding jointed data approximates the energy dissipation due to the joint interface.

The specimens were made of materials representing the actual system hardware. The housing is stainless steel and the cylindrical case into which the housing attaches is aluminum. For the simplified specimens, the half of the joint that contains the tab was made of stainless steel and the half that represents the mounting surface of the case was aluminum. The solid specimens were made of stainless steel. The difference in internal damping of stainless steel vs aluminum is very small, and well below that introduced by the joint. Bolts and washers that were used in the real hardware were also used for the simplified joints: bolts, MS16997-33 (cap screw with #8-32 UNF threads) and #8 washers, NAS620-8.

5.2.5 Dumbbell Design

After the joint specimens for this investigation were designed, the dumbbell masses were modeled along with the specimens using a relatively simple, linear model (Cosmos within Solidworks). (Resulting hardware is shown in Figure 5.25.) The frequencies of the axial and bending modes of the dumbbell were estimated. Using the simple model, the size of the dumbbells could be varied until the modes were adequately spaced. A primary goal was to ensure that the frequency of the axial mode was not near any of the dumbbell bending modes. Additionally, the axial frequency was targeted for the 500-1000 Hz range to simplify data acquisition and postprocessing. With a dumbbell weight of about 30 lb at each end, the axial mode for both S and P specimens was in the vicinity of 800 Hz. The exact weight of each of the dumbbells after fabrication was 29.4 lb.

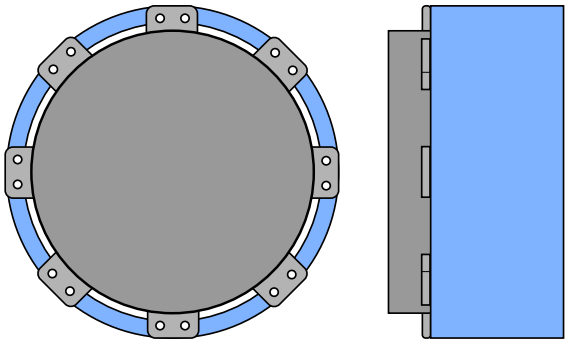

Figure 5.23. LOS Housing (grey) , Aeroshell (blue) with Tabular Bolted Joints.

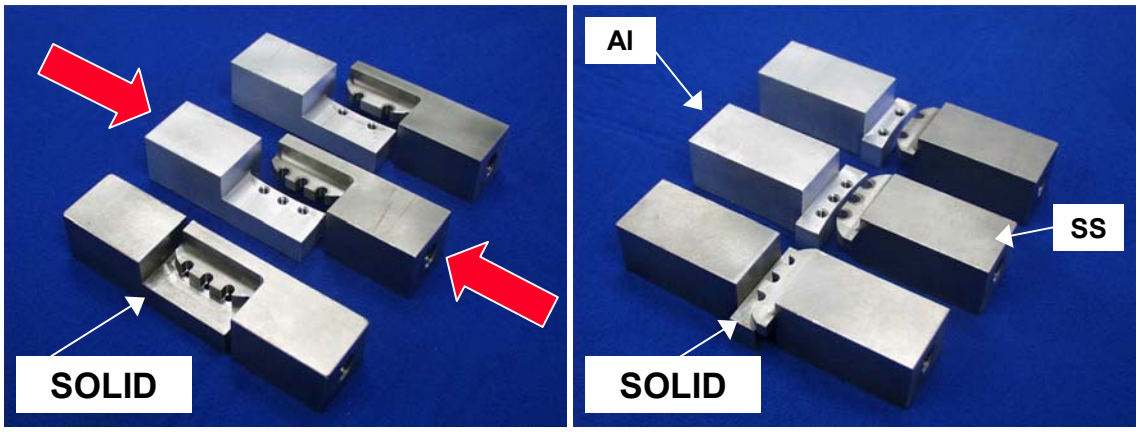

Figure 5.24. Specimen Nomenclature.

(a) S-specimens with arrows indicating direction of force application, and (b) P-specimens.

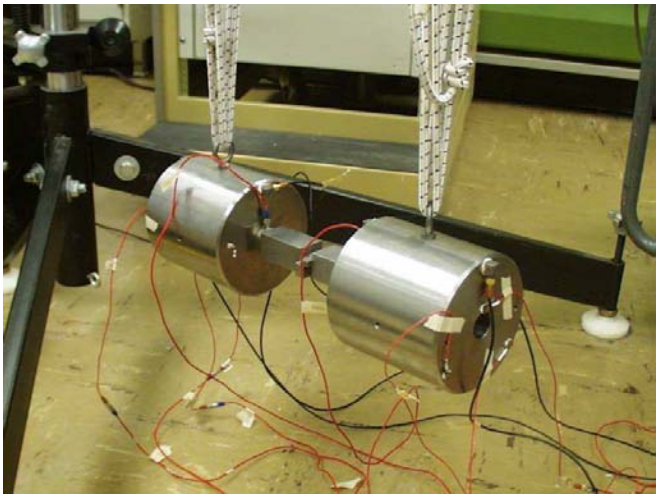

Figure 5.25. Hardware Setup for the Dumbbell Experiment.

5.2.6 Dumbbell Excitation

Hardware was excited by careful taps with the hand-held modal hammer, which was a PCB Model 086D05 with a plastic tip. Excitation was done in two ways: 1) axial tap applied at the end of one dumbbell mass and 2) lateral tap applied to the top surface of one dumbbell (S-specimens, only). The axial input exercised the specimens in axial tension/compression. The lateral input exercised the S-specimens in bending similar to that experienced by the joints when the overall housing responded in a drum-like mode. More information on analysis of bending response of this hardware is found later in this section.

5.2.7 Force Measurement in the Dumbbell

The dumbbell responded primarily in its first axial mode upon hammer impact or tap at the end of the mass in the longitudinal direction. As the response of the axial mode rings down, the joint is exposed to varying amounts of shear loading, starting at an initial peak and decaying to zero. The transient decay force response was measured by force gages in-line with the specimens (Figure 5.26). Two force gages and eighteen accelerometer channels were used both to measure the axial force in the specimen and to determine mode shapes. Axial mode shapes for both S- and P-specimens demonstrated that the specimens were exercised in tension/compression, while the joint interface was exercised in shear.

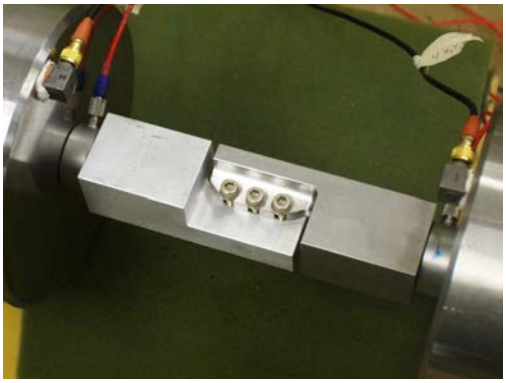

Figure 5.26. 3S-Jointed Specimens Installed with Two In-line Force Gages.

5.2.8 Data Analysis

Each measured transient force time history was processed to yield an energy dissipation per cycle vs force curve. The modified logarithmic decrement technique described in detail earlier in this section was used to calculate energy dissipation per cycle for various loads in the joint specimens when the transient response ring-down was dominated by a single mode.

The dumbbell was not perfectly symmetrical and it was impossible to apply the hammer input in the exact center of the dumbbell end. Therefore, multiple modes are present in the response of this structure. It becomes difficult to process the data accurately if their magnitudes are significant enough to contaminate the axial response and cause an unclean decay envelope. Therefore, the raw responses were bandpass filtered around the axial mode of the structure. Bandpass filtering is described in detail earlier in this section

Considerable thought was given to the choice of the order of the polynomial fit, n, to the peaks of the waveform in log-log space. Findings for this data are as follows: When n is about 2.2-2.4 and the dumbbell axial response is uncontaminated by other modes, a fourth or sixth order fit works well. Figure 5.27 shows the fit of a fifth order polynomial to the logarithm of peak amplitudes for a medium level hit. Figure 5.28 shows the same polynomial fit and peaks superimposed with the positive amplitudes of the transient response. The fit to the peaks is quite good.

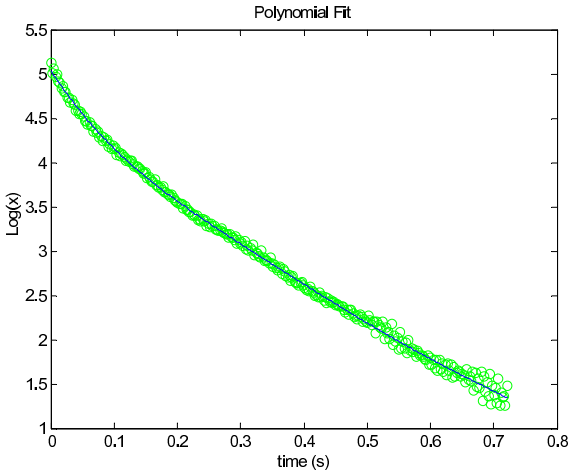

Figure 5.27. Fifth-Order Polynomial Fit to the Logarithm of Peak Amplitudes for Medium Level Impact.

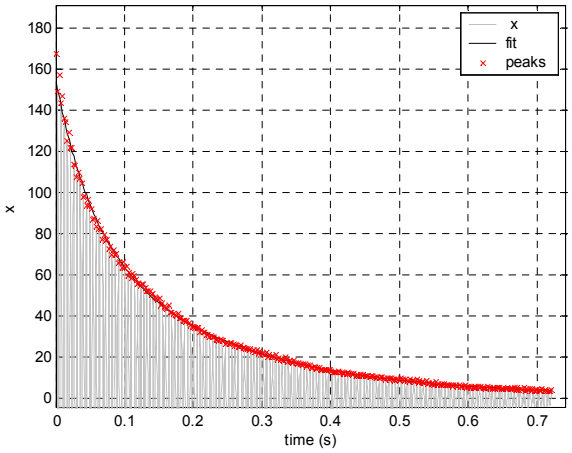

Figure 5.28. Polynomial Fit and Actual Response.

5.2.9 Application of Filters to Experimental Data

The stiffness of P-type joint specimens is nearly symmetrical. When a hammer input is applied to the end of the mass in the axial direction, the response that is observed is a clean decay that is dominated by the axial mode (Figure 5.29a). However, the stiffness of an S-type joint specimen is not as symmetrical. When a hammer input is applied near the center of the mass in the axial direction, the response that is observed is contaminated by the first bending mode of the system (Figure 5.29b). It is difficult to determine a clean envelope and measure the decay rate of a single mode from such a response using the technique described above. Digital filtering of these responses is desired.

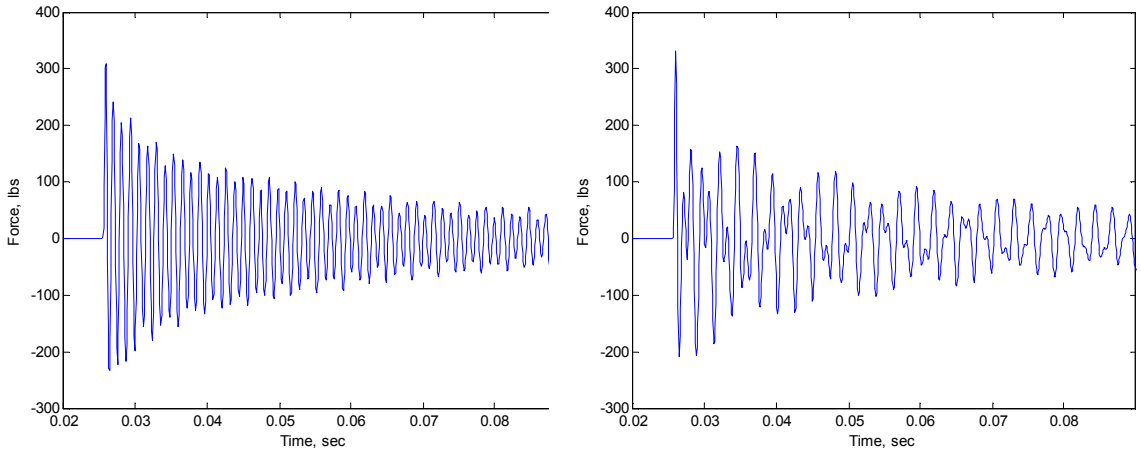

Figure 5.29. Comparison of Measured Responses.

(a) P-type joint specimen and (b) S-type joint specimen.

The presence of the bending mode in the response of the S-specimen is obvious in the plot of the restoring force in Figure 5.30. The peak at 800 Hz is the axial mode, and the peak at about 435 Hz is the first bending mode.

A second order, Butterworth, digital bandpass filter is applied to the data to extract a clean axial response. Several filters were tried. Each worked equally well, but the lower order, Butterworth filter tended to create lower magnitude start and less end effects. The filter is centered on 800 Hz and is 300 Hz wide. The resulting discrete, Fourier transform magnitude is seen in Figure 5.31 and the filtered time history is seen in Figure 5.32.

A few of the first peaks in the filtered time history of Figure 5.32 must be ignored because they are contaminated by the filter end effects. Overall, the filtered transient decay is clean and can be easily analyzed to determine energy dissipation per cycle for the axial mode.

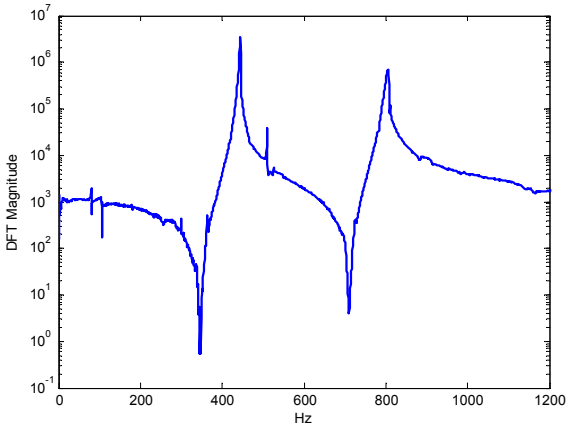

Figure 5.30. Discrete Fourier Transform Magnitude of S-Type Specimen Response.

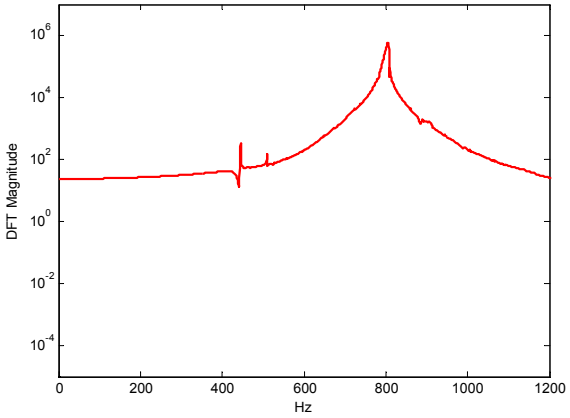

Figure 5.31. Discrete Fourier Transform Magnitude of S-Type Specimen Filtered Response.

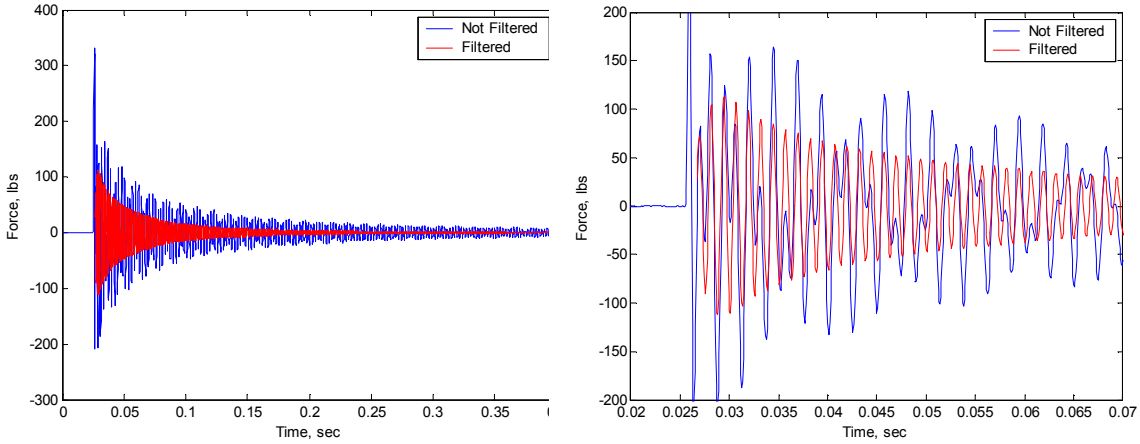

Figure 5.32. Comparison of Filtered and Unfiltered Time Histories of an S-Specimen.

5.2.10 Experiment Results

The experiments performed here subjected the joint specimens in Figure 5.24 to tension and compression forces using hammer excitation at the end of one of the masses in Figure 5.25. The hammer inputs were sufficiently high to cause peak force levels of 200-300 lb in the joints at initiation of the transient.

Figure 5.33 shows an example of some measured responses and illustrates the difference in response decay rate of a jointed and a solid specimen. Clearly, the jointed specimen exhibits amplitude dependent damping. It also exhibits more overall damping.

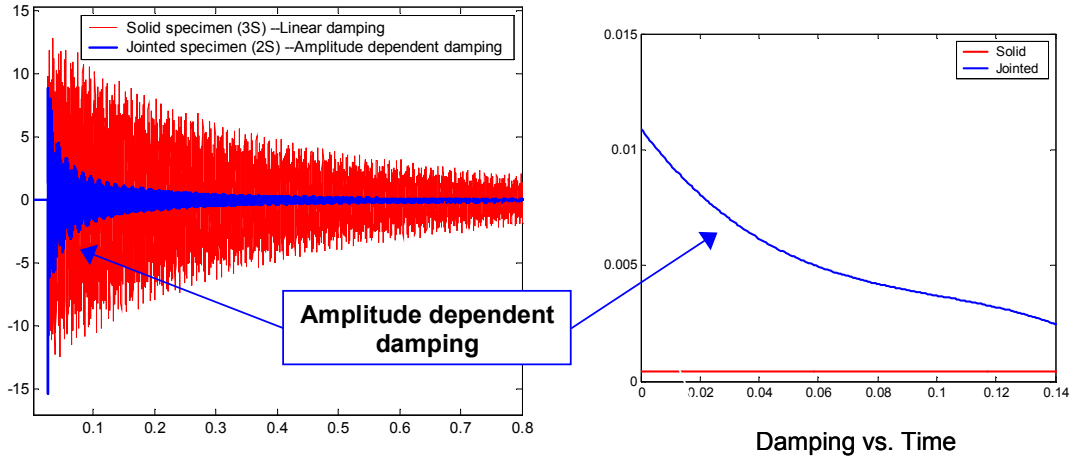

Figure 5.33. Comparison of Linear and Nonlinear Damping.

5.2.10.1 Comparison of Series and Parallel Configurations

Figures 5.34 and 5.35 provide a comparison of measured energy dissipation per cycle for series and parallel configurations. Each plot also contains energy dissipation curves for the solid specimens. The slope of the solid specimen curve is approximately 2.0, indicating the solid specimens exhibit linear damping. The differences between the solid and jointed curves represent the energy dissipation due to microslip in the joint interface. In both cases, series specimens dissipate more energy than the parallel specimens. The vast majority of variability in the results occurs because of differences in response due to assembling and disassembling the joint interface.

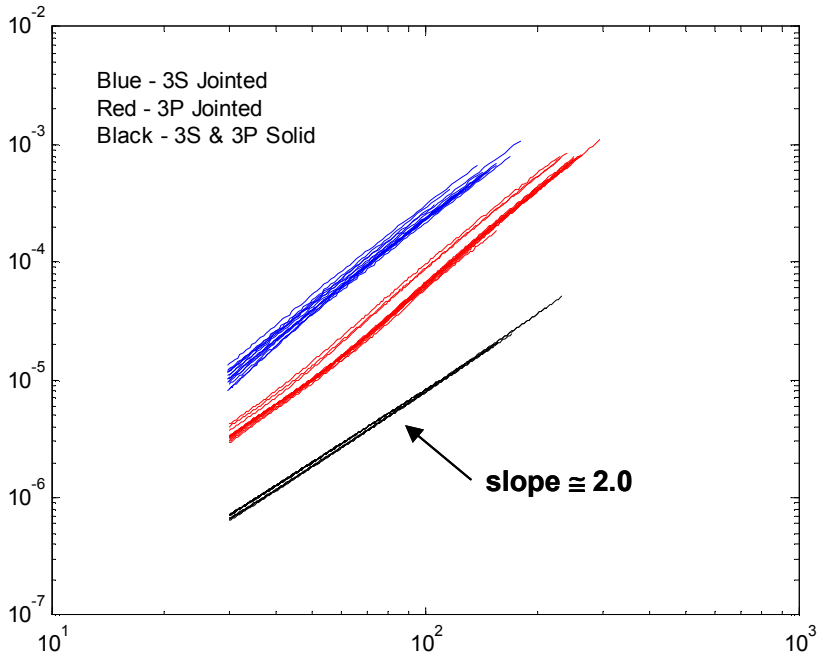

Figure 5.34. Comparison of Joint Orientations.

Examples: Three bolts in series and three bolts in parallel, 18 in-lb bolt torque preload.

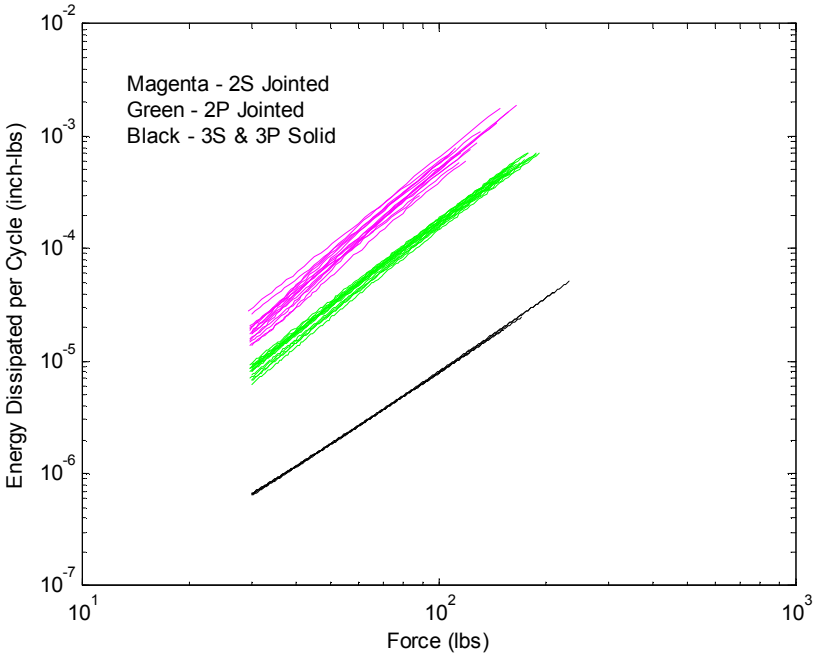

Figure 5.35. Comparison of Joint Orientations.

Examples: Two bolts in series and two bolts in parallel, 18 in-lb bolt torque preload.

5.2.10.2 Comparison of Two and Three Bolt Configurations

Figures 5.36 and 5.37 compare energy dissipation curves for similar bolt orientations and varying number of bolts. In both cases, specimens with only two bolts exhibited more energy dissipation than specimens with three bolts. When there are only two bolts, there is less contact pressure generated in the joint interface. Therefore, more microslip occurs when shear loading is applied to the interface.

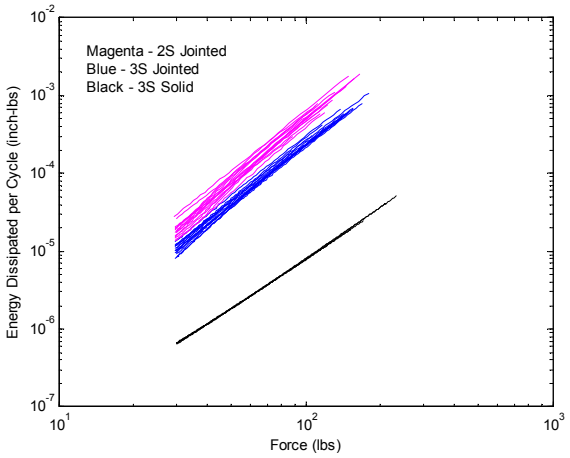

Figure 5.36. Comparison of Energy Dissipation for Two and Three Bolts in Series.

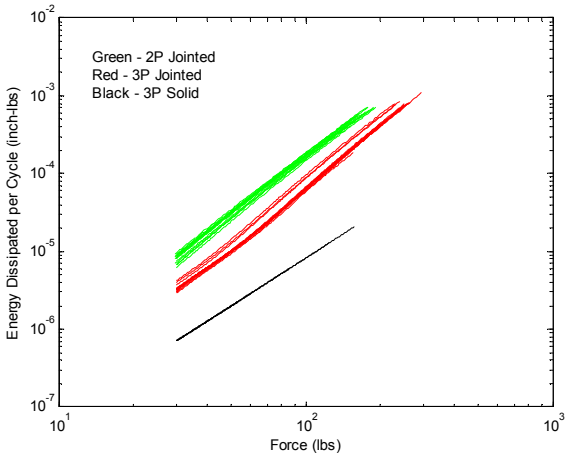

Figure 5.37. Comparison of Energy Dissipation for Two and Three Bolts in Parallel.

5.2.10.3 Comparison of Bolt Torque

The assembly procedures for attachment of System B housing to its mating counterpart call for a bolt torque of 18-22 in-lb. Data were gathered during this investigation using bolt torques of both 18 and 22 in-lb. Figures 5.38 - 5.40 contain families of energy curves for all specimens with bolts torqued to both 18 and 22 in-lb. In all cases, the average energy dissipation per cycle is higher with a bolt torque of 18 in-lb. Lower torque and lower bolt preload encourage less contact pressure in the joint interface and allow more microslip to occur when the interface is loaded.

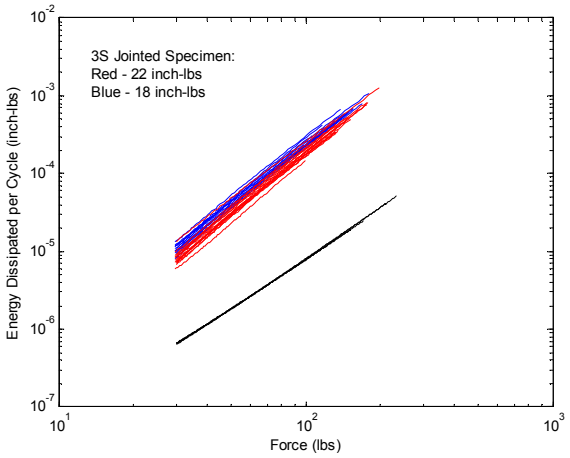

Figure 5.38. Effect of Preload on Energy Dissipation per Cycle in the 3S-Jointed Specimen.

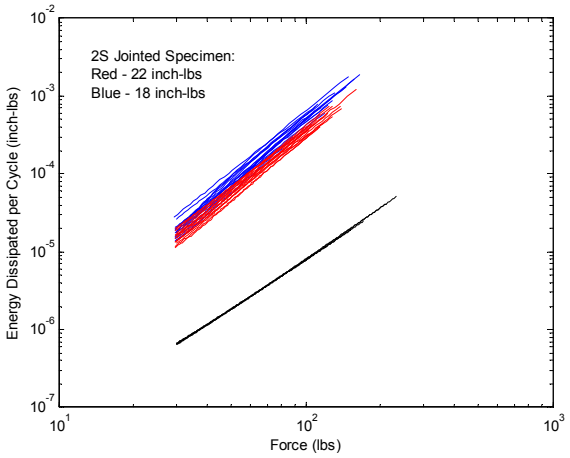

Figure 5.39. Effect of Preload on Energy Dissipation per Cycle in the 2S-Jointed Specimen.

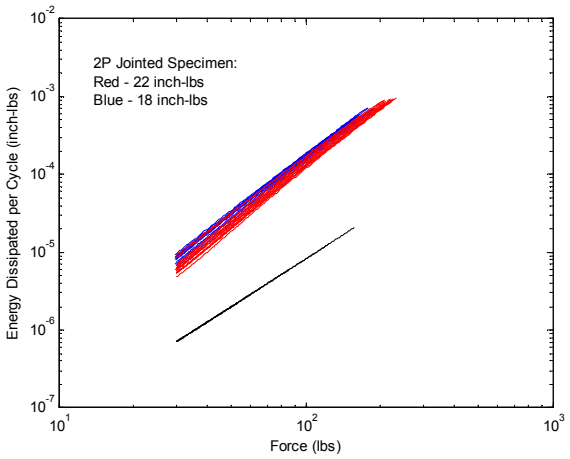

Figure 5.40. Effect of Preload on Energy Dissipation per Cycle in the 2P-Jointed Specimen.

In one case, a set of data was gathered with a bolt torque of 14 in-lb to observe the effects on energy dissipation outside the specified range. Figure 5.41 contains energy curves for preloads of 14, 18, and 22 in-lb. Figure 5.42 is a plot of the average energy dissipation at 90-lb external load for each bolt torque setting. Figure 5.42 demonstrates a linear relationship between bolt torque and energy dissipation in this range of bolt torques with the 3P-specimen.

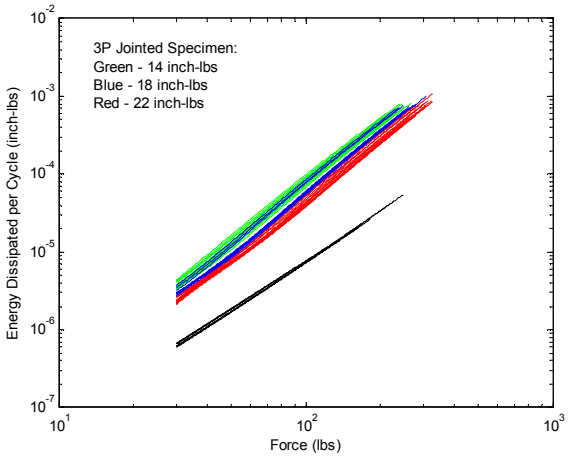

Figure 5.41. Effect of Preload on Energy Dissipation per Cycle in the 3P-Jointed Specimen.

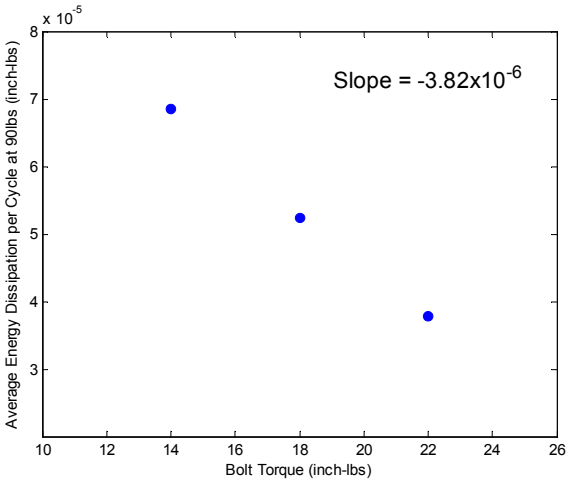

Figure 5.42. Average Energy Dissipation at 90 lb for Varied Bolt Preloads on the 3P-Jointed Specimen.

5.2.10.4 Investigation of Bending in the Joint

Shear loading at the jointed interface is suspected as the overwhelming cause of microslip and therefore, energy dissipation. Typically, when a bolted joint is loaded so that only the local normal force in the joint is varying (such as a bolted pipe flange in pure tension), then practically no microslip occurs at the interface and very little energy is dissipated due to the bolted joint. However, when a joint is loaded in such a way that there is local shear at the interface, microslip still occurs and additional energy is dissipated during the response.

If the LOS housing was excited in its longitudinal direction, and the housing responded strongly with drum-like modes, then each of the attachment tabs would be exercised in some amount of bending. The bending action is a potentially significant source of additional energy dissipation in the structure.

Excitation from a hammer tap to the top of the dumbbell was shown in Figure 5.25, along with the measured dumbbell responses. P-type specimens are the best representation of the tabs in bending in the case of the LOS housing deforming in response to a drum mode in the housing. The first bending mode of the dumbbell is excited by the input and the responses are measured.

Figure 5.43 shows how a joint in bending might be approximated by a simple SDOF system so that the equivalent energy dissipation per cycle vs generalized force (moment) amplitude curves can be generated for the joint in bending in a similar manner as for a joint in shear. Figure 5.44 is a side-by-side comparison of energy dissipation curves of joints in shear and joints in bending.

There is a small amount of additional energy dissipation measured for the P-series joint in bending relative to the solid joint in bending. However, the difference appears to be insignificant

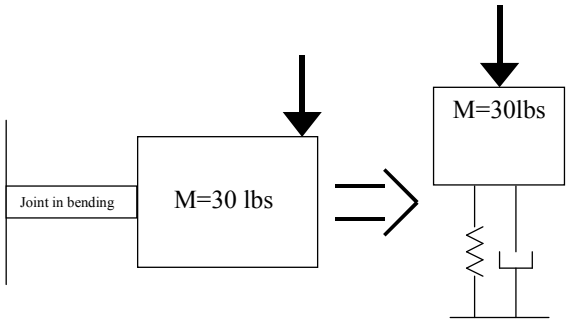

Figure 5.43. Approximate Representation of a Joint in Bending to an SDOF System.

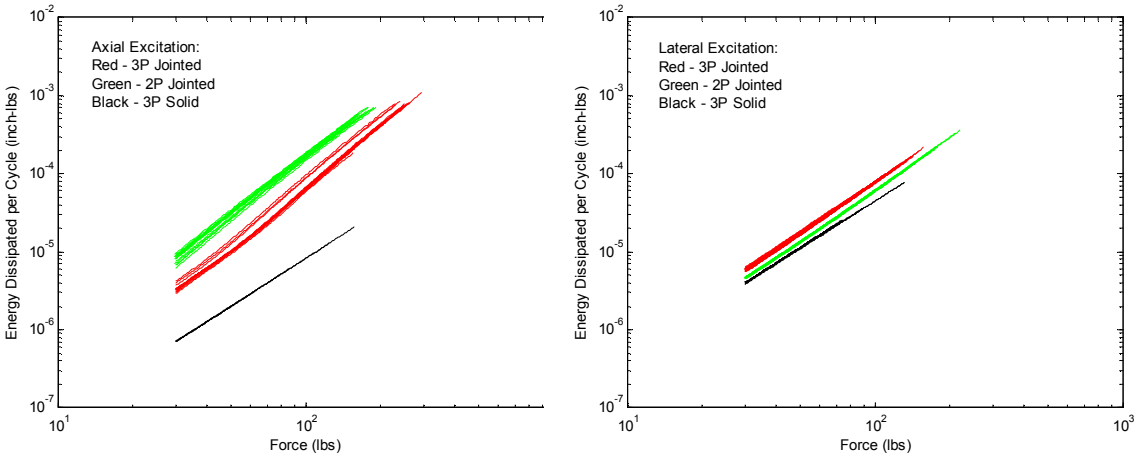

Figure 5.44. Energy Dissipation per Cycle for the P-Series Specimens.

Examples in (a) shear and (b) bending. Generalized force in subfigure (b) is moment.

compared to the difference that is observed for a joint in shear. This result tends to support the hypothesis that bending can introduce additional energy dissipation, but local shear in the interface is likely the major contributor to overall energy dissipation.

5.2.10.5 Energy Dissipation Curves Characteristics

There are two main characteristics that can be used to simply describe an energy dissipation curve for a bolted joint: slope of the curve and overall gain (vertical position) of the curve. The slope of a straight line fit through the energy curve on a log-log plot is an indication of the nonlinear dependence of damping on amplitude. The energy dissipation curve for a perfectly linear, viscous damped system would have a slope of exactly two. Figure 5.46 is a plot of the slope of a straight line fit through the average energy dissipation curve of each assembly/disassembly that was performed during the experiment. These points represent data for all jointed specimens with both 18 and 22 in-lb of bolt torque. The average slope is 2.576. Also, there does not appear to be an obvious dependence of slope on the tab orientation, number of bolts, or bolt torque.

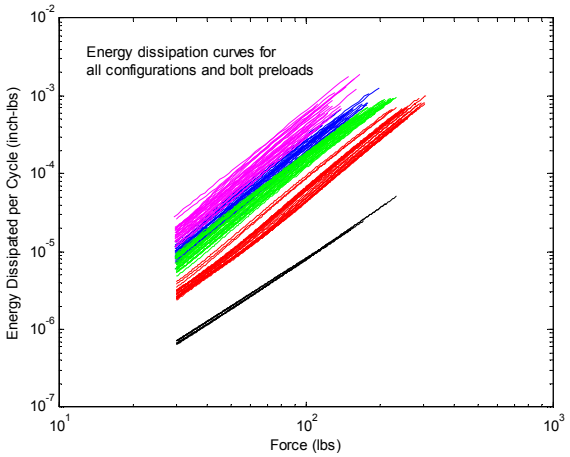

Figure 5.45. Energy Dissipation Curves for All System B Configurations.

Figure 5.47 is a plot of the average energy dissipation at 90-lb for each assembly/disassembly that was performed during the experiment. This plot illustrates the strong dependence of average energy dissipation on tab orientation and number of bolts.

5.2.11 Derivation of Whole-Joint Model Parameters

Each configuration does exhibit a different amount of energy dissipation, and it would make sense to characterize each uniquely in a system model that contains these joints. The best representation of this joint in all its configurations would be obtained by using separate joint elements, each of which has its own independent parameters. Parameters determined for series specimens would be representative of the behavior of a housing tab when the load enters the interface in the housing circumferential direction. Parameters determined for parallel specimens would be representative of the behavior of a housing tab when the load enters the interface in the housing radial direction.

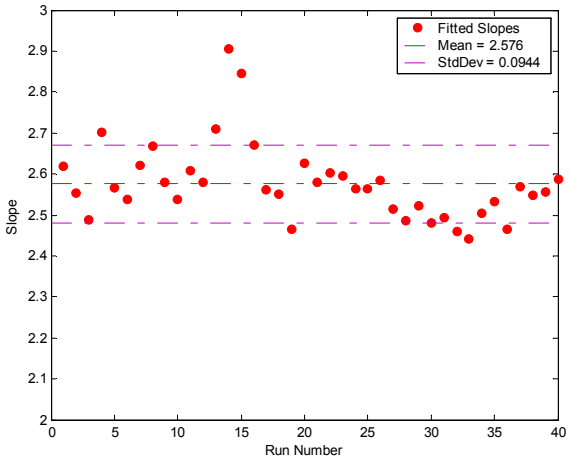

Figure 5.46. Slope of the Straight Line Fit Through Energy Curves on a Log-Log Plot for Each Set of Data.

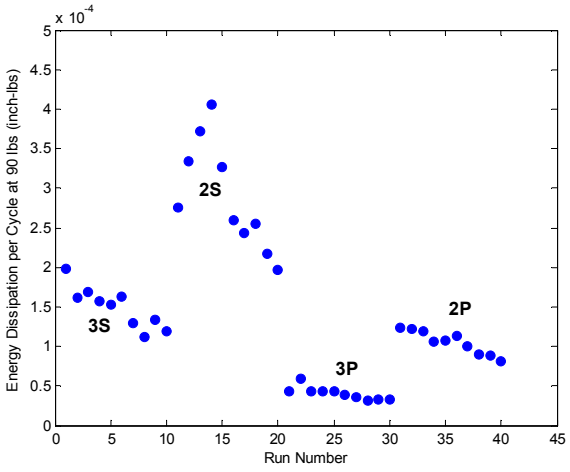

Figure 5.47. Average Energy Dissipation per Cycle at 90-lb for Each Set of Data.

5.2.12 Conclusion

Experiments were performed to quantify the effects of nonlinear energy dissipation due to attachment tabs of System B, LOS housing. Hardware was fabricated to capture the various configurations of attachment tabs around the housing and to measure the isolated effects of the joint interfaces. Experiments were performed to evaluate the effects of bending in the attachments tabs of the LOS housing. As expected, local shear in the interface was the major contributor to energy dissipation, and bending effects were insignificant. Internal force levels in the joint during experiments are representative of what will be encountered in actual environments. Sufficient data were gathered to assess the variability and uncertainty in the measured responses and the final metric energy dissipation per cycle.

5.3 Dumbbell Experiment Examples System A, AOS, Single-Leg Joint

This investigation was performed as a second step in a model calibration and validation exercise for derivation of whole-joint parameters. The model parameters were intended for use in a larger, component level model. The transient nature of the dumbbell input and response was a desired characteristic in the validation. The combination of dumbbell and pendulum hammer input provided a very efficient and clean experiment for gathering useful joint interface response information.

5.3.1 Experiment Setup

The setup of this dumbbell investigation is similar to that of System B investigation, as the dumbbell was suspended from a sturdy support by soft bungees. (See Figures 5.48 and 5.49.) However, there were differences between the two investigations. First, no force gages were placed inline with the joint specimen. Second, the hammer tip was placed at the end of a pendulum arrangement, as shown in the figures, better to control accuracy of both the input location and magnitude. Both differences helped to enable a very clean and effective experiment to measure energy dissipation in the joint due to axial motion in the specimen.

5.3.2 Dumbbell Masses

Dumbbells used for this investigation were 30-lb each. Connections between masses and joint specimens used a $\frac{1}{2}$-in bolt that torqued to 80 ft-lb.

5.3.3 Specimens

There were three pairs of AOS, single-leg, joint hardware. Each pair consisted of a top and bottom, both fabricated from stainless steel. Tops are designated A, B and C while bottoms are designated 1, 2 and 3. A combination of top and bottom is referred to as A2, B3, C1 and so on. Multiple pieces of the same hardware were created to evaluate variability in response due to slight manufacturing differences. (See Figure 5.50.)

The local geometry of the joint interfaces was exactly the same as for the joints of the actual System A. The bolt used to load the interfaces was the same bolt as used in the real system. Assembly torque applied to the bolt was the same as for the real system, 85 in-lb. Again, there was a monolithic joint specimen. (Figure 5.51.) The monolithic specimen in this case included every detail of the interface geometry, including the small gaps expected to appear in the real, assembled, component level connection.

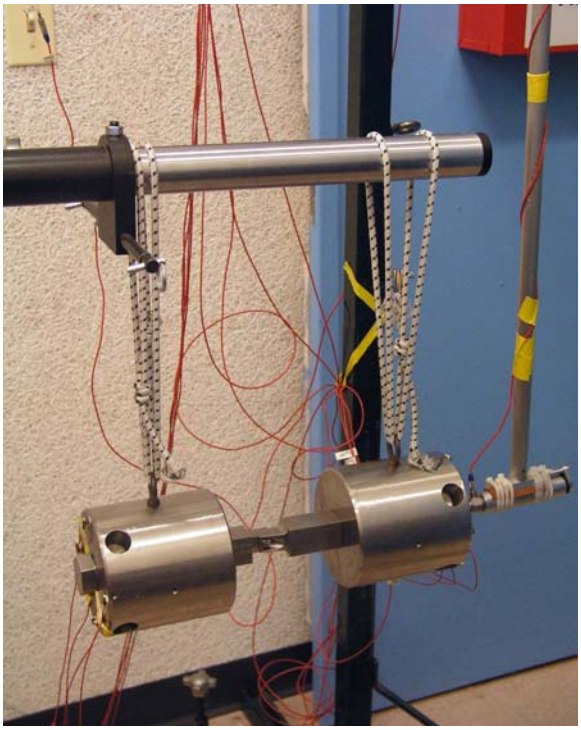

Figure 5.48. AOS Single-Leg Dumbbell Setup.

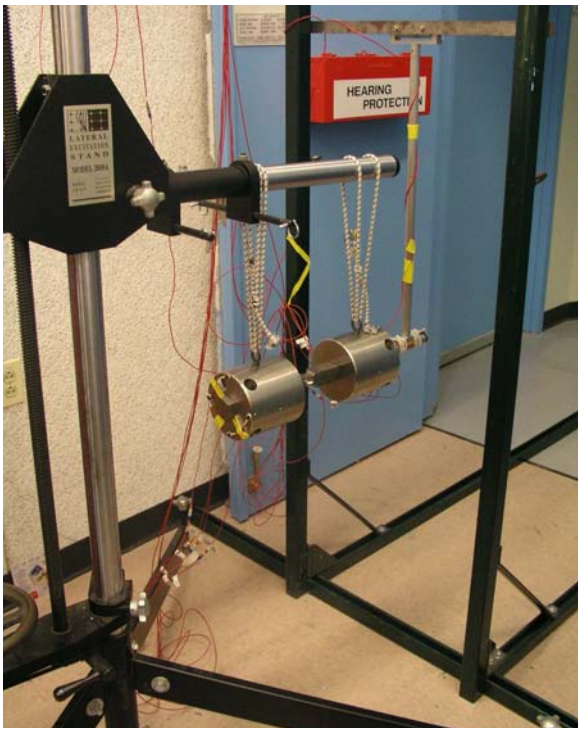

Figure 5.49. AOS Experiment Setup, Showing Pendulum Input Structure.

Figure 5.50. AOS Single-Leg Specimens.

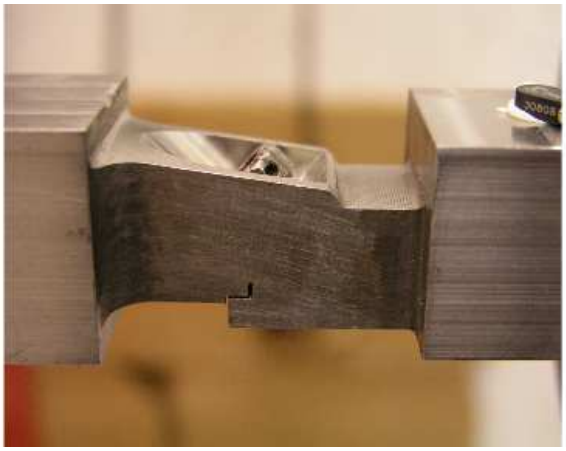

Figure 5.51. Monolithic AOS Single-Leg Specimen - Side.

5.3.4 Force Measurement

Axial force in the joint specimens were determined indirectly with Equation (5.2). There were four accelerometers on the end of the dumbbell mass that were used in the time synchronous average.

5.3.5 Experiment Results

The solid-leg was again used to quantify issues related to baseline energy losses in the experiment and boundary conditions. The characteristics of the solid hardware were also used to calculate the unknown attachment compliances at the boundaries. The nine combinations of jointed hardware were each exercised a total of five times to yield a set of forty-five responses that capture the inherent variation in dynamic response due to the bolted joint assembly/disassembly and variation in hardware.

Hammer inputs were sufficiently high to create peak force levels of 400-500 lb in the joints during response ring-down. These levels were representative of the levels at which the joint was initially calibrated for use in steady state, harmonic input experiments (up to 500 lb). Higher levels in this case were not practical with the combination of hammer and tip that was used.

5.3.6 Solid-Leg Baseline Experiments

Information about the solid-leg in the dumbbell arrangement was provided to analysts for initial calibration of the linear dumbbell model. The dumbbell dynamics are simple. There were six rigid body modes and five major structural modes. Table 5.3 lists rigid body frequencies that were

Table 5.3. Dumbbell Rigid Body Modes.

Mode	Frequency, Hz
Vertical translation	2.2
Axial translation	0.71
Transverse translation	0.63
Rotation about vertical axis	0.72
Rotation about transverse axis	Not measurable
Rotation about axial axis	Not measurable

measured manually using a stopwatch and direct observation. The time required for ten cycles of vibration in each mode was measured, and then the frequency was calculated.

Figure 5.52 shows the other structural resonances of interest for the dumbbell configuration. The axial responses reported are due to a slightly off-center axial input. The solid-leg was assembled into the dumbbell arrangement and responses measured. The leg was then removed and reassembled a total of five times. Energy curves from the exercise are shown in Figure 5.53.

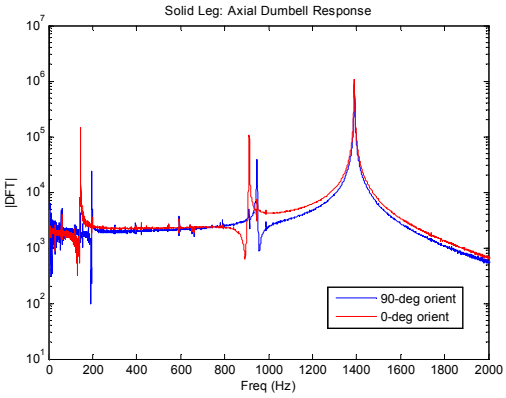

Mode	Frequency (Hz)
1st Bending - Rocking	145
1st Bending - Shearing	195.6
2nd Bending - Rocking	912.2
2nd Bending - Shearing	948
Axial	1390.6
Axial mode damping = 0.0589%	

Figure 5.52. Solid Dumbbell Response Information.

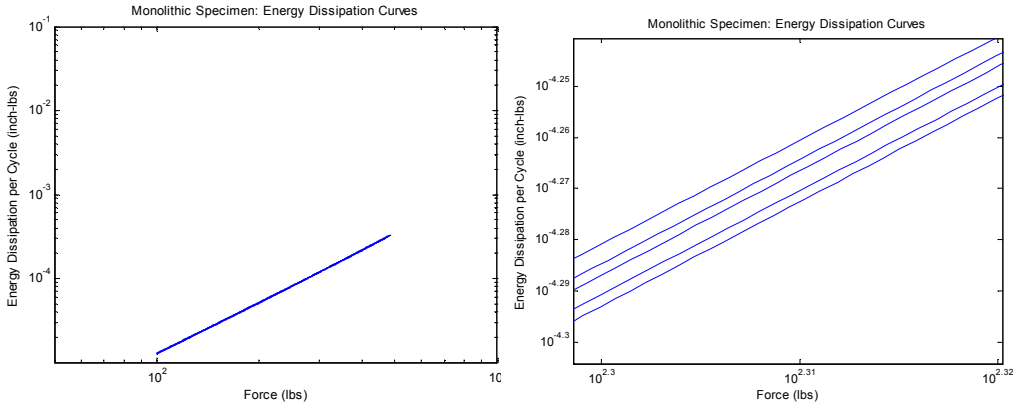

Figure 5.53. Energy Dissipation Curves.

Energy dissipation curves for the solid specimen in the dumbbell arrangement: (a) Five different curves that appear indistinguishable and (b) Extreme zoom on curves.

The dumbbell experiment was a very clean experiment, for there was virtually no variation in the measured responses of the solid-leg. Figure 5.54 compares energy dissipation curves from the solid calibration (steady state sinusoidal) and monolithic validation (transient dumbbell) experiments. The baseline dissipation of the solid dumbbell is low compared to the steady state experiment. The close agreement between calibration (harmonic excitation; BMD) and validation (transient excitation; dumbbell) experiments for solid-leg dissipation indicates that they are both "clean" experiments with the latter being "cleaner" and more repeatable. (See Section 5.1.1.3 for a discussion of this issue in the context of dumbbell experiments.)

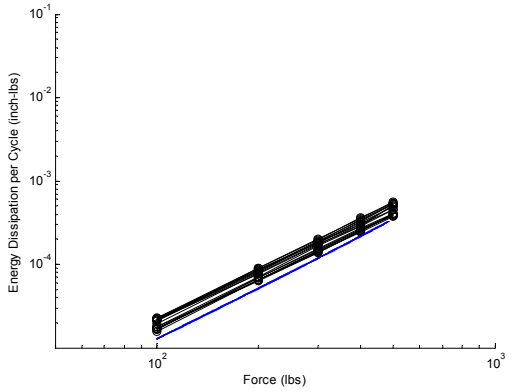

Figure 5.54. Solid-Leg Energy Dissipation Curves.

Comparison of calibration (black) and validation (blue) solid-leg energy dissipation curves.

The high quality of the data is partly due to the simplicity of the dumbbell experiment. There were only two bolted connections, each using $\frac{1}{2}$-in bolts torqued to 80 ft-lb. Also, the only boundary conditions that provide a path for additional energy dissipation are the two elastic support bungees.

5.3.7 Load History Effects

Very large variations in energy dissipation, along with a large offset in dissipation from the expected range, were observed in the jointed dumbbell specimens during early stages of testing. The source of the variation was finally attributed to the load history of the joints. This effect was quantified using the pendulum hammer as a consistent input. Figure 5.55 demonstrates the variation in responses for the same specimen with practically the same inputs.

The number and magnitude of hammer inputs were tightly controlled using the pendulum setup so that the breaking-in effect could be carefully observed for each specimen. Figure 5.56 illustrates the progression of energy dissipation curves as a single specimen experienced increasing numbers of hammer inputs.

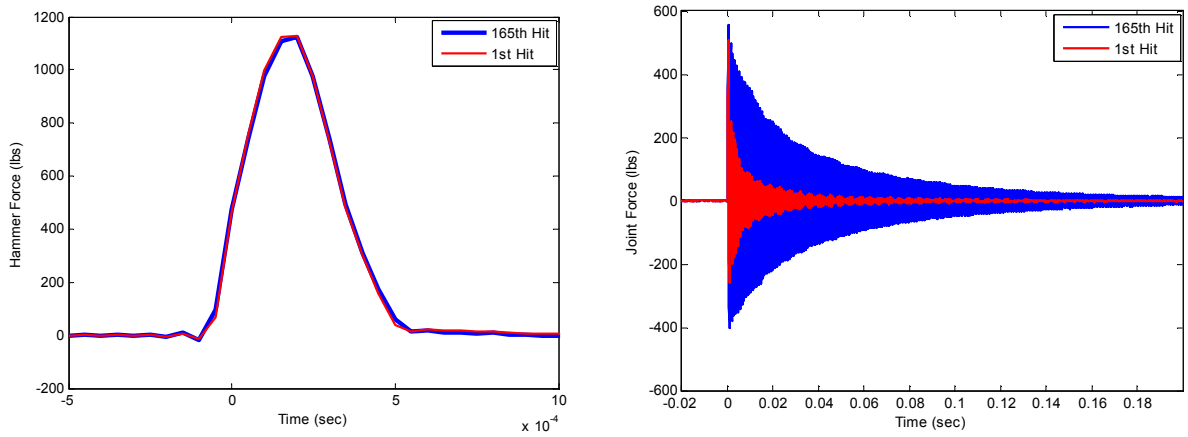

Figure 5.55. Break-in Effect.

(a) Hammer force waveform for first and 165th inputs and (b) dumbbell axial response for first and 165th hammer inputs.

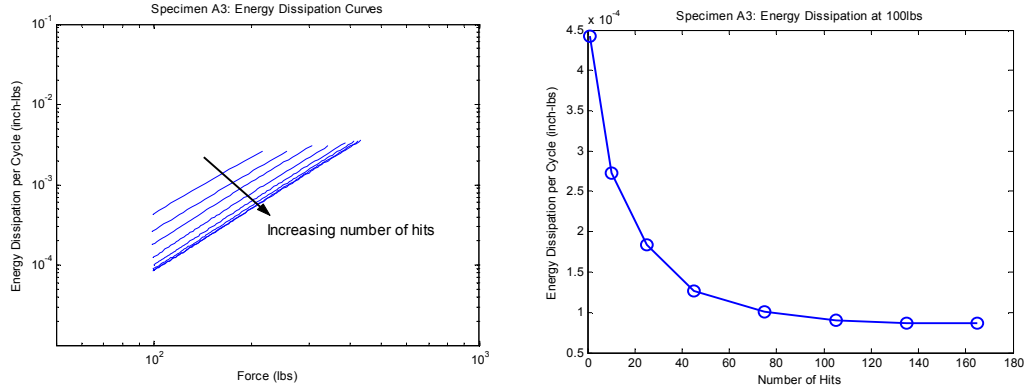

Figure 5.56. Energy Dissipation Evolution.

(a) Example of the progression of energy dissipation curves with increasing hammer inputs. (b) Energy dissipation at an arbitrary force level as a function of number of hammer inputs.

After a large number of inputs, the energy dissipation converges on a stable value. Examples of more convergences are seen in Figure 5.57 for a single specimen sequence. Each time the joint was taken apart and reassembled, the asymptote for a large number of hits was slightly different, but the convergence behavior is clearly similar.

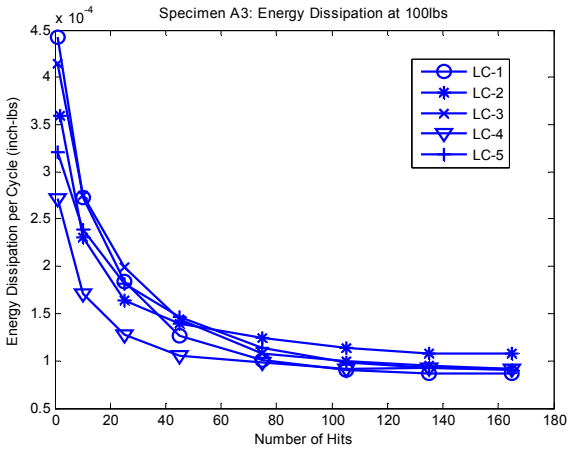

Figure 5.57. Energy Dissipation Convergence.

Example curves showing energy dissipation convergence at a single force level for five load cycles of one specimen combination.

A similar load history effect has been observed in the past on single-leg joint experiments in an SDOF experiment under steady state, sinusoidal loading [47, 49]. During those experiments, the equivalent damping ratio also decreased in an asymptotic fashion with increasing vibration cycles. Changes of about 25% were observed over approximately 28,000 cycles of sinusoidal vibration.

Changes in energy dissipation values by an approximate factor of four (a range of 300%) were observed for most jointed dumbbell, transient experiments. The discrepancy in the variation between transient and steady state experiments is easily explained. Many thousands of cycles occur in the specimen during a sinusoidal test before the test control is equalized and accurate response measurements can be made. The transient experiment has the advantage that the dissipation for a freshly assembled joint interface can be measured with the first hammer input. Therefore, the transient technique does a better job of capturing the total variation in energy dissipation due to the "break-in" effect from a fresh interface to a "well-used" interface.

Figure 5.58 illustrates a postulated mechanism for the break-in effect. As the interface is exposed to more vibration cycles, asperities engagement increases. As the interface becomes more constrained, the damping goes down.

Energy dissipation measurements for both the sinusoidal and transient tests are compatible for purposes of direct comparison because they both were made on the hardware after it had converged to its asymptote. The dumbbell for every transient test was submitted to at least 165 controlled hammer inputs (with the pendulum hammer) and the SDOF experiment for every sinusoidal test

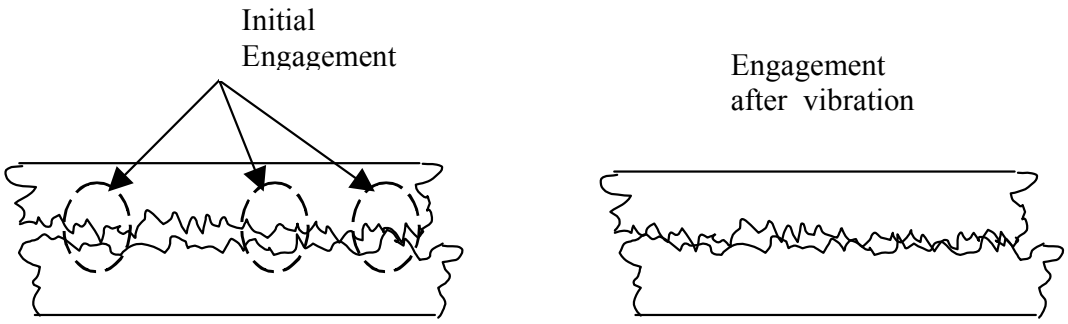

Figure 5.58. Load History Effect - Postulated Asperity Engagement Mechanism.

was submitted to thousands of vibration cycles in the process of system equalization and the subsequent sweep through resonance.

5.3.8 Jointed Experiments

The nine different combinations of hardware were each assembled and disassembled five times yielding forty-five responses from which energy dissipation curves were determined using the technique previously explained. The force input from the pendulum hammer was very repeatable. The average peak force input was 1,126 lb, with a standard deviation of 2% of the mean. Pulse durations were 0.6 ms.

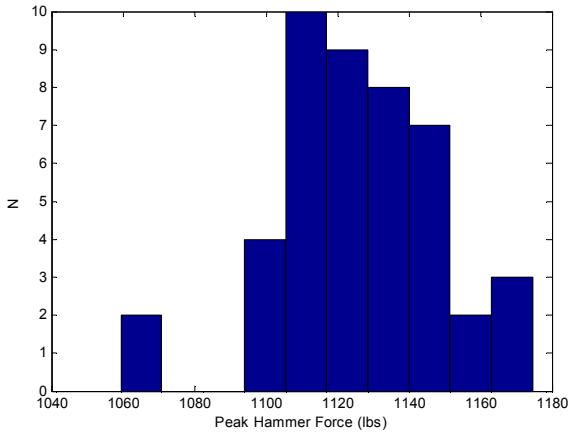

Figure 5.59. Peak Hammer Input Forces.

Mean = 1126 lb, Standard Deviation = 22 lb.

The magnitude of the input force was chosen to transmit almost 500 lb of peak force into

the joint during the initial peak. The actual achieved, peak joint force levels varied due to slight differences in joint behavior, and did not quite reach 500 lb in all cases. More force could have been applied by the hammer, but would have been at the cost of decreased consistency in peak input level and input location, because a bungee cord would have been required to accelerate the pendulum through the required additional velocity.

The use of the pendulum to apply an input that was consistent in both amplitude and location at the end of the mass, mitigated any significant, dumbbell, bending mode contamination in the responses. Still, the motion of each of the four accelerometers on the far end of the dumbbell (away from the hammer input) was averaged to yield the cleanest possible single-mode ring-down. The data were easily processed by the log decrement technique. Responses were gathered at a sample rate of 12.8 kHz and a specified number of data points were used to perform the analysis. The first 2,500 or 8,000 points, beginning with the initial response peak for the jointed and solid specimens, respectively, were used to make the energy dissipation measurements. A fifth order polynomial was used to fit the peaks of the ring-down as an estimate the envelope. All the energy curves from each hardware combination are shown in Figure 5.60.

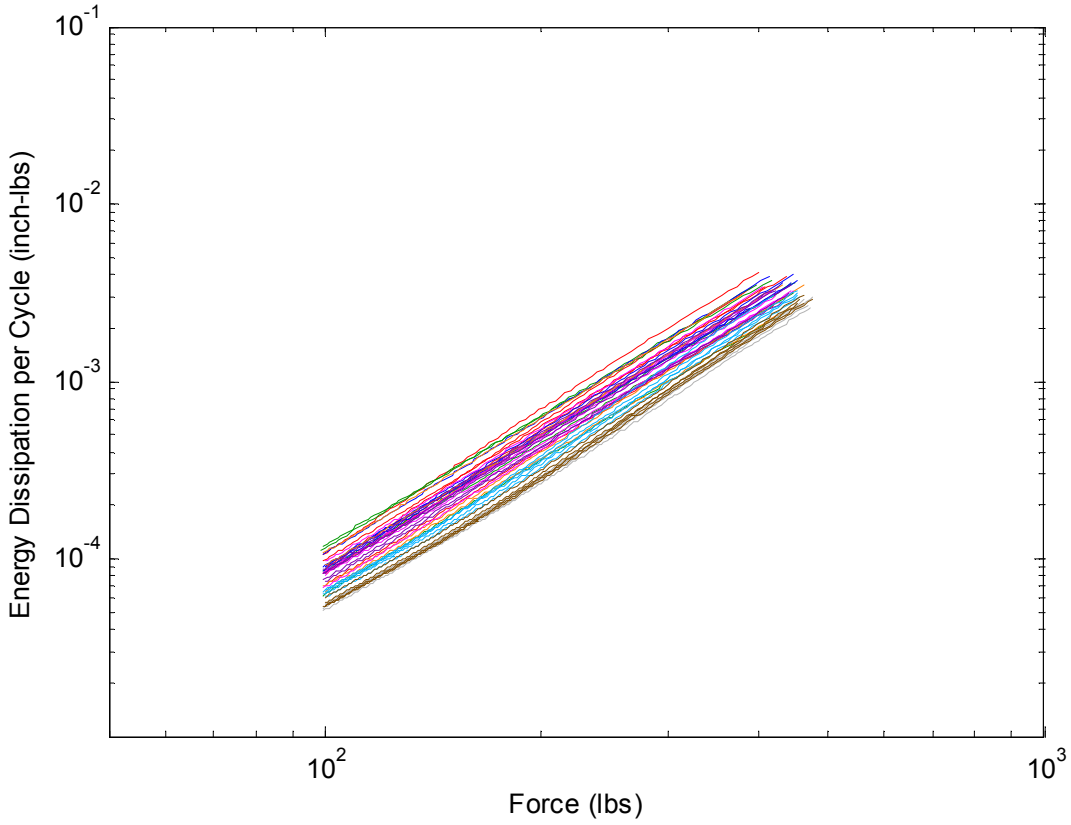

Figure 5.60. Transient Dumbbell Validation Data.

The energy dissipation curves from the transient dumbbell experiments were overlaid with the energy dissipation measurements from the steady state calibration experiments in Figure 5.61. The

agreement in both overall magnitude and variation in the data between calibration and validation experiments is very good.

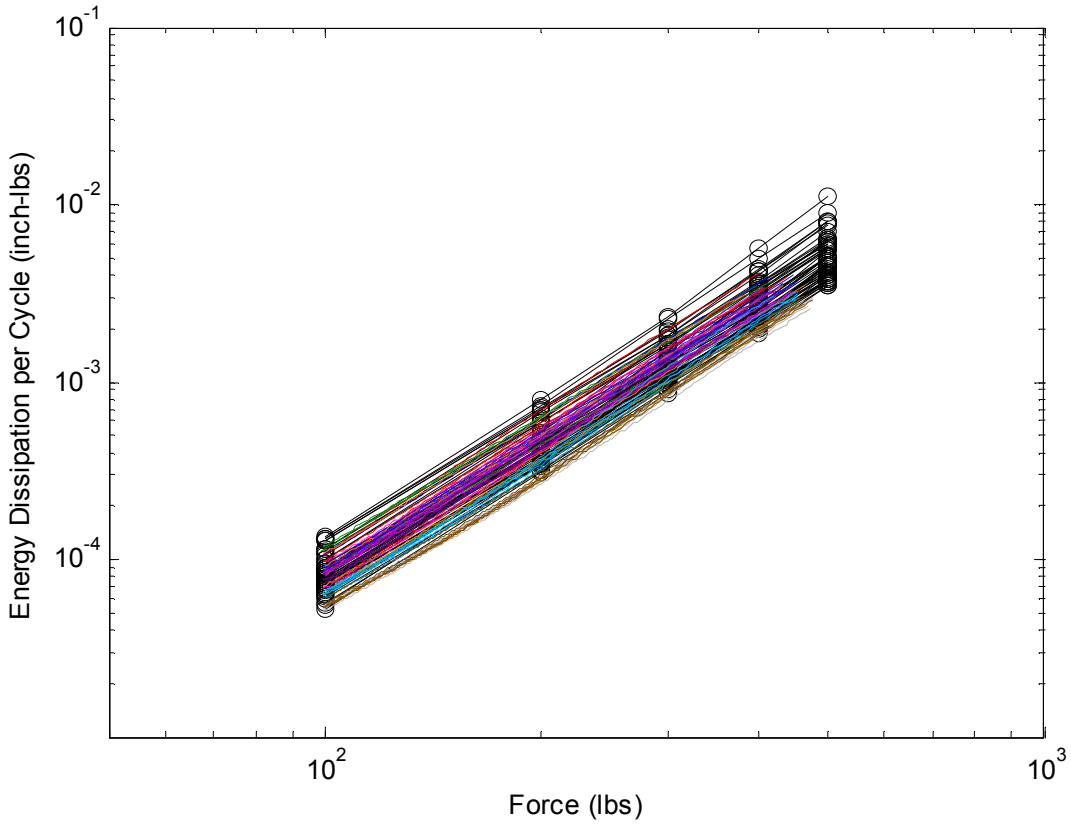

Figure 5.61. Transient Validation Curves Superposed on Steady State Calibration Curves.

5.4 Dumbbell Experiment Examples A Generic Interface Parameter Study

5.4.1 Motivation

This series of experiments was an effort to understand jointed interfaces that are held together by some of the more common small bolts. These types of bolted interfaces are used at the component and subcomponent level of hardware assemblies.

Bolted joint experiments shown thus far have been designed to understand a single and specific type of interface, one that is in the only mechanical load path to a component of specific interest, such as an AOS. Often such an interface is unique and benefits from careful assessment. The quantification of its behavior experimentally can be relatively straightforward. Then, implementation of the bolted joint element in an analytical model can proceed with relative ease.

It is not always true, though, that the majority of energy dissipation in a real structure comes from a single set of jointed interfaces that are in the mechanical load path of some input energy. Much energy dissipation can occur within a component if it contains many smaller, bolted connections distributed within it. This is especially true for hardware that is not dynamically rigid and therefore experiences notable amounts of relative displacement and strain throughout its structure. Examples of such hardware are shown in Figures 5.62 and 5.63.

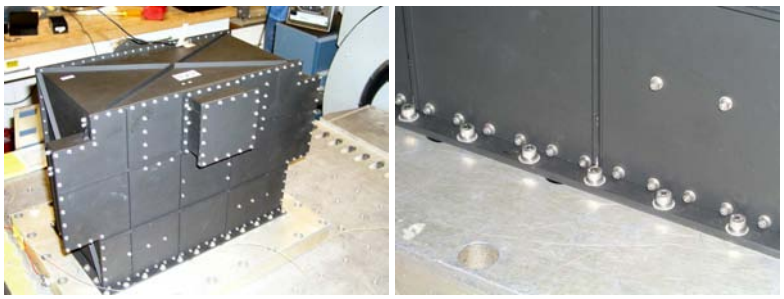

Figure 5.62. Example of Space Flight Hardware.

This component has a relatively simple metal framework containing electrical components held together and connected to the next assembly by numerous small bolts with washers.

Figure 5.62 shows an example of hardware containing numerous interfaces held together by small bolts. Also, the component itself is attached to the next level of assembly by a large number of small bolts distributed in some fashion. Bolts and interfaces in this hardware provide a large majority of the energy dissipation to the structure. The abundance of interfaces serves as a desirable mechanism to keep the responses of the box to a minimum, and also protect internal electronics.

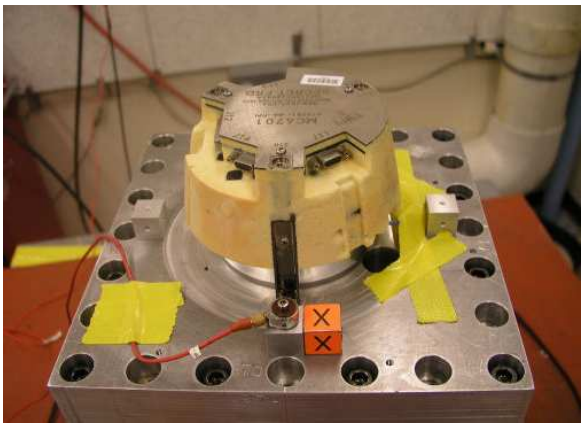

Figure 5.63. Mock Weapons Component.

Collection of circuit boards and foam potting fastened together at key locations and connected to next assembly with small bolts.

The hardware in Figure 5.63 is an example of a component with a minimal metal skeleton that supports several stacked circuit boards. The circuit boards are intrinsically rugged partly because of the foam potting compound supporting them. In the final assembly, the mechanical energy into this hardware arrives through both the top and bottom of the three-legs of the metal support structure, which contains a small number of carefully designed, small bolt connections.

In addition to studying very specific jointed interfaces that are well-known energy dissipaters along a mechanical load path, it is beneficial to study and begin to understand the contribution towards overall energy dissipation in the structure the smaller bolted joints may provide.

5.4.2 Experiment Setup

The dumbbell experiment was chosen over other experimental possibilities to exercise the joints specimens for this study. The dumbbell experiment is desirable for the following reasons:

- Captures the nature of dynamic behavior in a true transient environment
- Easily performed by most well trained laboratory personnel with basic knowledge of accelerometers, conditioning, hammer input, and data acquisition. Experiments involving electrodynamic shakers require detailed understanding and availability of the proper vibration control system.
- Efficient and effective application of simple pendulum, hammer, and dumbbell technique to gather large data sets provided that several tens of hammer impacts are not needed to "condition" the joint to account for effects of accumulated loading.

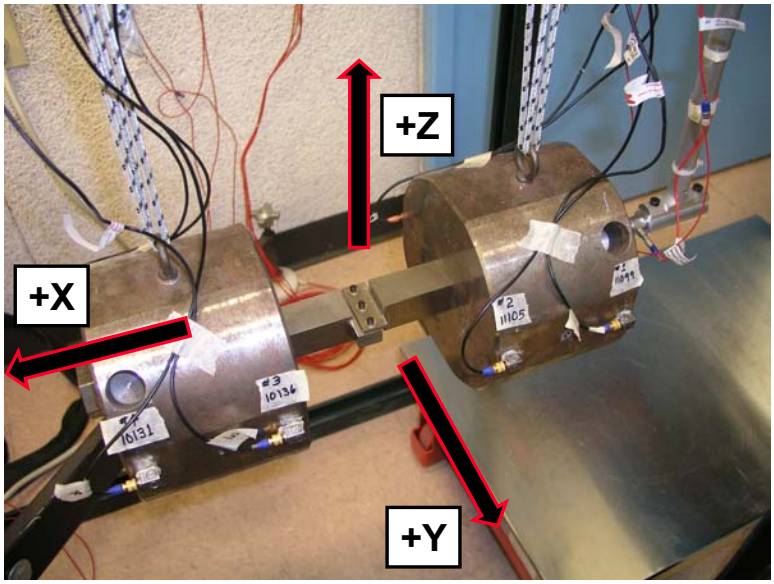

Figure 5.64. Experimental Setup.

- Most importantly, the experiment is supported freely and often is “clean” enough to distinguish the effects of deceptively small features in the jointed hardware, dynamic response

This experiment was performed later in the time line of SNL, bolted joints work. The setup seen in Figure 5.64 shows a rather large number of response measurements. These response measurements are arranged so that the first six major structural modes of the dumbbell can be studied. The hope for future work in this area is to gain the ability to analyze and then describe the behavior of the jointed interfaces due to coupled loading in the interface as a result of any combination of modes.

This section will describe only the lessons learned from analyzing the axial motion of the dumbbell, or pure shear loading in the bolted joint. This experiment was performed in accordance with all the preparations, procedure, and attention to details as described earlier in this section.

5.4.3 Dumbbell Masses

The weight of each dumbbell in this arrangement was 60 lb, including the plugs that are installed during tests. When installed and torqued tightly, the threaded plugs provided a convenient, solid surface for the hammer to strike the dumbbell in a way that excited primarily the axial mode of the system.

5.4.4 Hammer Input

A pendulum hammer arrangement was again used to provide repeatable, transient inputs to the end of the dumbbell. The amplitude was controlled by the release height and was measured by a force gage at the end of the hammer. The input amplitude was kept constant, within 5%, for the entire range of tests shown here.

The hammer tip for these experiments was again white plastic. The repeatable location of impact was also well controlled by the use of the pendulum technique. For inputs meant to excite primarily the axial mode of this hardware, the impact location was limited to the center of the threaded plug.

5.4.5 Time History Effects

Unlike the AOS single-leg hardware, there were practically no effects from multiple hits on the energy dissipation of this hardware. Still, to be sure that any small effects or inconsistencies are effectively minimized, the data sets shown here are for the tenth hit applied to the experimental assembly.

5.4.6 Specimens

There were three pairs of jointed hardware and one piece of monolithic hardware. (See Figure 5.65.) The specimens were made from stainless steel. All specimens received up to three bolts each. Each of the three pairs had different sizes of bolts: #6-32 UNF, #8-32 UNF, and #10-32 UNF. The monolithic specimen was made the same geometry as the jointed specimens, and was drilled and tapped for #8-32 UNF bolts.

The purpose of the specimens was to allow investigation of a variety of bolt parameter variations with all other factors remaining constant.

- Bolt size - affects preload in the joint when nominally recommended bolt torque is applied.
- Washers vs no washers - affects the number of potential individual microslip interfaces in the overall interface.
- Bolt torque - affects preload in the joint, which is also related on bolt diameter
- Number of bolts, or bolt spacing - affects the character of pressure distribution in the interface.

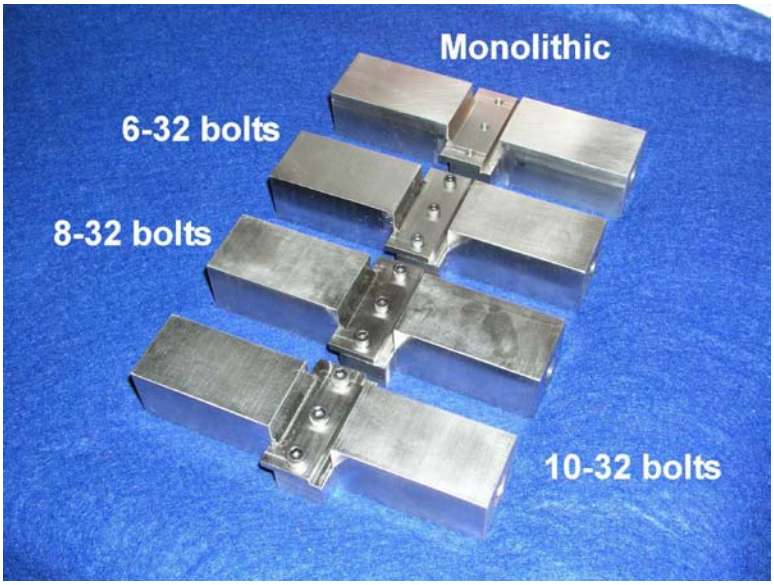

Figure 5.65. Generic, Small Bolt Specimens.

5.4.7 Force measurement

No joint specimen forces were measured in this particular activity. For axial loading in the specimens, force is the product of mass and axial acceleration of the dumbbells.

5.4.8 Test Matrix

Three torque values were chosen for use with each size bolt (Table 5.4.) First, a nominal torque for each bolt had to be chosen. The recommendations for installation torque can vary widely based on materials and applications. The nominals listed here may not agree exactly with those listed elsewhere, but they do represent values that are representative of typical recommendations. Lowest torques were chosen to be approximately 0.75 times the nominal torque for the given bolt size. High torque values were chosen at approximately 1.25 times the nominal torque. The other consideration in choice of nominal torque was to avoid exceeding the recommended maximum torque for any of the bolts and possibly inducing undesirable brittle failures of the bolt material.

A huge variety of parameter combinations was possible during this study. Table 5.5 shows the space of possibilities and shows the data that was actually gathered and that has been archived. Due to practical and cost limitations, the entire matrix of possible parameter combinations was not tested.

Table 5.4. Bolt Torque Definitions, in-lb.

Bolt size	Low	Nominal	High
6-32	6	8	10
8-32	12	16	20
10-32	18	24	30

Table 5.5. Full Test Matrix and Availability of Data.

	TORQUE>>	**Low**			**Nominal**			**High**		
	BOLTS>>	**1**	**2**	**3**	**1**	**2**	**3**	**1**	**2**	**3**
6-32	**Axial input**	A	A	A	A	A	A	A	A	A
	Washers				N	A	A			
	Y-bending				N	A	A			
	Z-bending				N	A	A			
8-32	**Axial input**	A	A	A	A	A	A	A	A	A
	Washers				A	A	A			
	Y-bending				A	A	A			
	Z-bending				N	A	A			
10-32	**Axial input**	A	A	A	A	A	A	A	A	A
	Washers				A	A	A			
	Y-bending				A	A	A			
	Z-bending				N	A	A			

Note: A = Data acquired and archived. N = Either 1) specimen damping was too high, and reasonable measurement not practical or 2) interface pressure was low and therefore abundant macroslip in the interface suppressed almost all structural response.

5.4.9 Investigation Results

The study provided numerous examples, many of them intuitively obvious, regarding how the parameters combine to yield various energy dissipation curves. The following subsections will adequately illustrate typical post processed data.

In all cases, five energy dissipation curves were gathered, analyzed, and plotted to illustrate variability due to assembly and reassembly of the joint interface. Reassembly consists of removal of bolts, realignment of joint interface, reinstallation of bolts, and application of desired torque.

5.4.9.1 Analysis

Again, analysis of dumbbell responses was in accord with the mathematical approaches described earlier in this section. The transient response envelopes of the filtered dumbbell axial modes were all fitted with fifth order polynomials, unless otherwise noted.

5.4.9.2 Monolithic Specimen

Every jointed interface experiment performed has benefited from companion testing of a monolithic solid specimen with replicate geometry and materials, but without the actual joint interface. This very useful practice was followed here. The results of the monolithic tests, in terms of energy dissipation, are shown in Figure 5.66.

Purely Monolithic Specimen, Figure 5.66 The following plot of energy dissipation contains the five tests of the dumbbell with the monolithic hardware installed. Notice how closely the five curves agree with each other. The close agreement proves that 1) assembly variability in this case is low, because there was no reassembly needed and 2) the experiment, both input and dumbbell, and the analysis algorithm as a whole provided a consistent testbed for these tests.

The average slope for all curves is 2.00, which is consistent with the expectation of a linear structure with linear damping limited to the material damping. The average linear damping for the five tests of the monolithic hardware was 0.035% of critical.

Monolithic Specimen with Bolts, Figure 5.67 The monolithic hardware lacked the joint interface, included threaded holes for three #8-32 UNF bolts. Installation of the three bolts, at nominal torque, actually increased the energy dissipation per cycle by an almost imperceptible amount.

The blue curves, for the monolithic hardware including bolts, in Figure 5.67 are only slightly higher in overall energy dissipation per cycle than the black (no bolt) curves. The difference certainly is apparent upon close examination. Addition of the bolts allowed a small amount of extra energy dissipation due to interactions of the bolt thread and bolt head with the monolithic

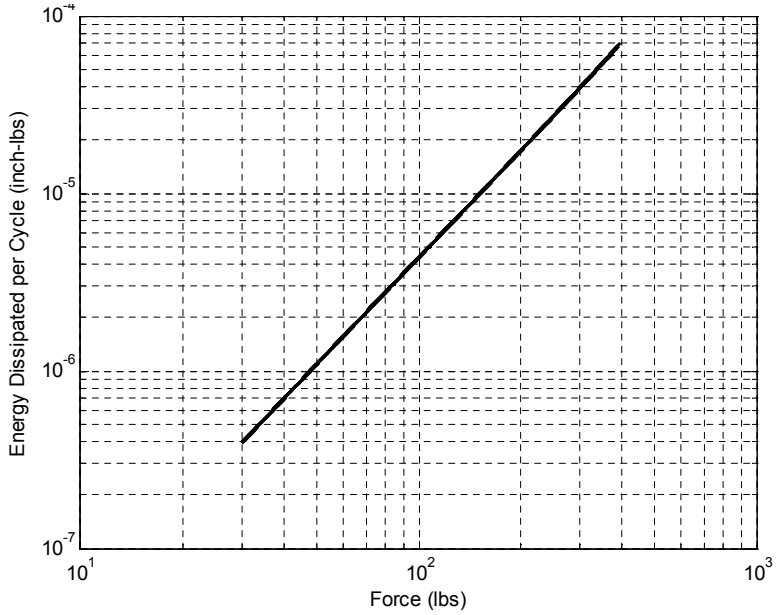

Figure 5.66. Solid Monolithic Hardware. Average slope = 2.00.

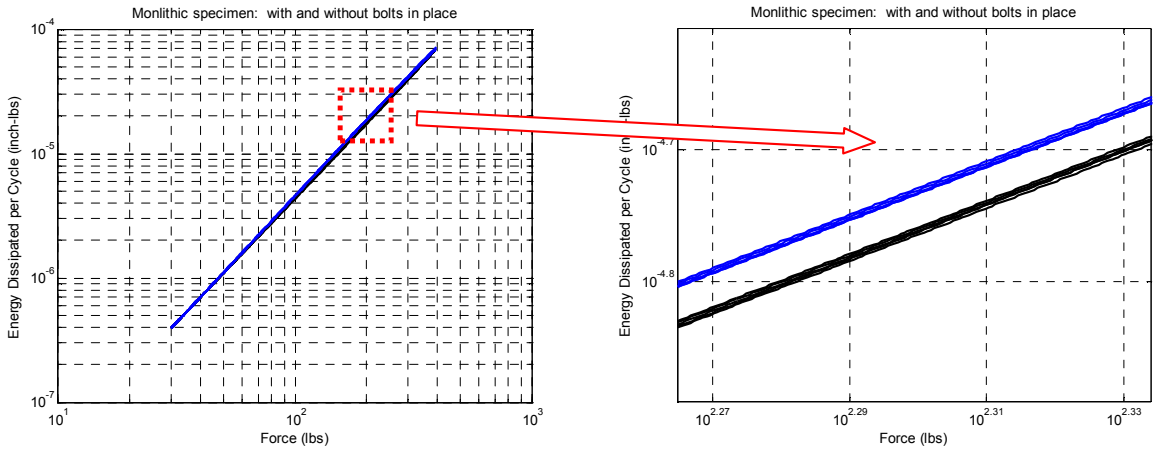

Figure 5.67. Energy Dissipation, Purely Monolithic Joint.

(a) No bolts (black) vs monolithic with #8-32 UNF bolts in place at nominal torque (blue). (b) Magnified view of curve set.

specimen. The addition of the tiny amount of extra interface is not enough to cause the dissipation to behave nonlinearly. The average slope of the blue curves is 2.00.

5.4.9.3 Jointed Specimens

Each of the following brief subsections illustrates the effect of small bolt parameter combinations on the overall energy dissipation in the jointed interface. Each energy dissipation plot shows five curves for each of the parameter combinations to illustrate variability due to reassembly. Typically, the plots include three variations on a parameter with all other parameters held constant. Each plot also shows the energy dissipation per cycle curves for the plain, monolithic hardware. All the data have been plotted on the same scales for comparative purpose. A final plot of all the data on one axis concludes the plot display.

While studying the following sections, the reader should keep in mind the relationship of bolt preload to the bolt size and the applied torque.

$$\tau = 0.2PD \tag{5.14}$$

where 0.2 is a bolt factor chosen for basic estimations of preload force in the limited range of bolt sizes used. Table 5.6 lists the calculated preloads for the parameters used in this study.

Table 5.6. Bolt Torque Variation, #6-32 UNF

Low (red), nominal (green), high (blue) torques along with Solid (black).

Bolt size	Diameter (in)	Preload (lb) Low	Preload (lb) Nominal	Preload (lb) High
6-32	**0.14**	**214**	**286**	**357**
8-32	**0.16**	**375**	**500**	**625**
10-32	**0.19**	**474**	**632**	**789**

Vary: Bolt Torque

Three #6-32 UNF Bolts, Figure 5.68 Variation of the installation torque for the #6-32 UNF bolts illustrates a consistent trend toward lower energy dissipation for the highest torque. The lowest torque also exhibits slightly more variability in dissipation. (See Figure 5.68.)

Three 8-32 Bolts, Figure 5.69 Variation of the installation torque of the #8-32 UNF bolts also demonstrates a steady trend toward lower energy dissipation for the highest torque. The lowest torque still exhibits slight more variability in energy dissipation.

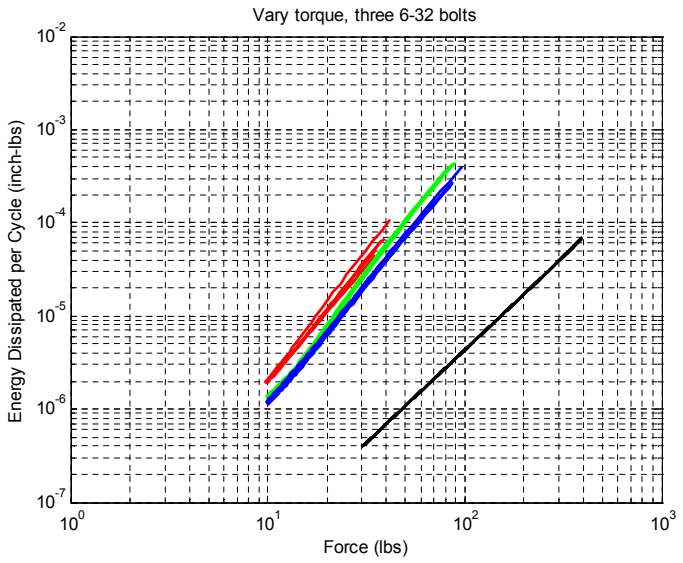

Figure 5.68. Bolt Torque Variation, #6-32 UNF.

Low (red), nominal (green), high (blue) torques along with Solid (black).

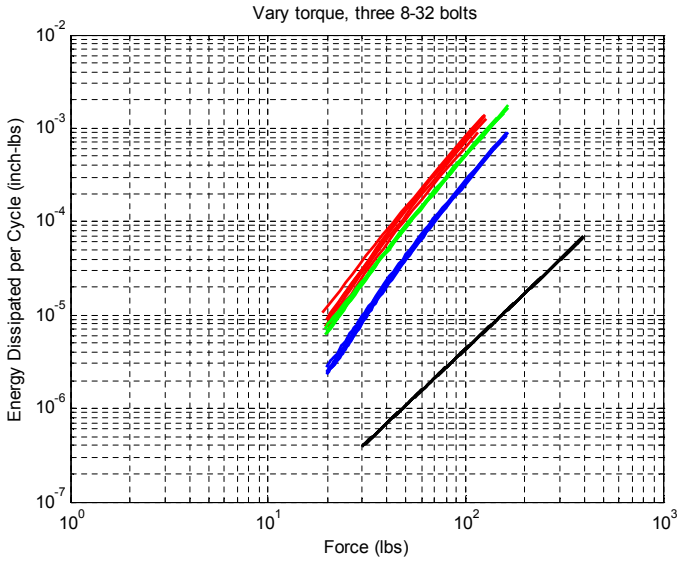

Figure 5.69. Bolt Torque Variation, #8-32 UNF.

Low (red), nominal (green), high (blue) torques along with Solid (black).

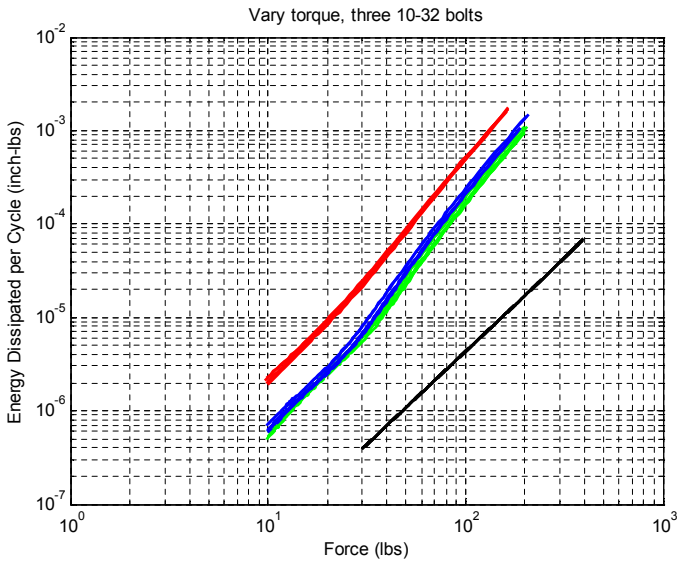

Figure 5.70. Bolt Torque Variation, #10-32 UNF.

Low (red), nominal (green), high (blue) torques along with Solid (black).

Three #10-32 UNF Bolts, Figure 5.70 Variation of the installation torque of the #10-32 UNF bolts again illustrates a steady trend toward lower energy dissipation for the highest torque. In this case, the lowest torque exhibits equal amounts of variability in dissipation.

There appears to be a type of asymptotic convergence of energy dissipation when the torque is high because the nominal and high torque data are very similar, but much lower than the dissipation for the low torque cases.

Notice also in this case that the lower amplitudes of the nominal and high torque energy dissipation curves are showing a slope that is fairly close to that seen in the linear, monolithic hardware. It is likely that below a certain force threshold, some bolted joint interfaces can exhibit linear damping rather than damping arising from microslip. Microslip damping leads to energy dissipation curve slopes greater than two.

Vary: Number of Bolts (Bolt Spacing)

Nominal Torque, #6-32 UNF Bolt, Figure 5.71 When #6-32 UNF bolts are torqued to the nominally recommended value, the data show that three bolts allow less dissipation than the case of two bolts. When only one #6-32 UNF bolt was used, the data could not be analyzed with the logarithmic decrement technique because the dissipation was simply too much. The axial mode would dampen out almost as soon as it was excited.

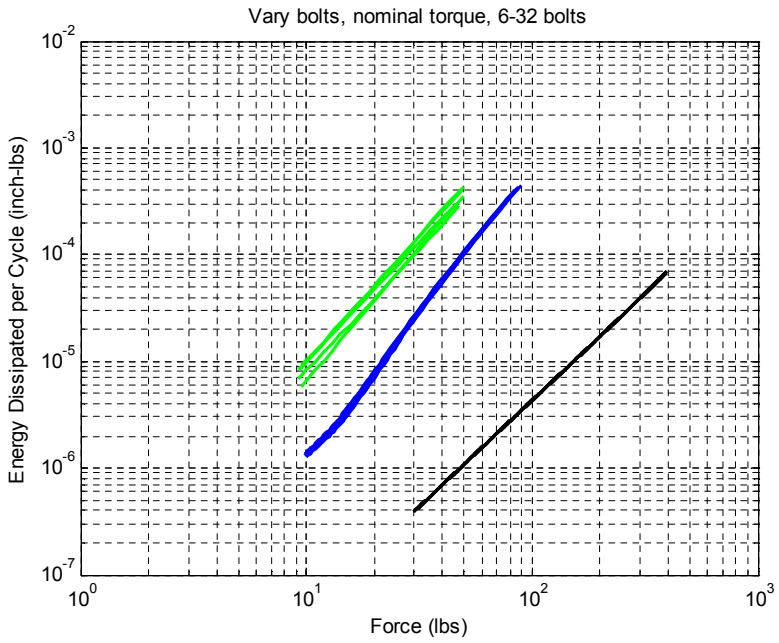

Figure 5.71. Energy Dissipation Variation for #6-32 UNF Bolts.

Two bolts (green), three bolts (blue), along with solid (black).

Note here that the case with two bolts also exhibits slightly more variability in energy dissipation, probably due to the likelihood of a more variable contact patch. Three closely spaced bolts are more likely to have less of a microslip boundary at the edge of the contact patch than the case of two bolts that are spaced further apart, with everything else remaining constant.

Nominal Torque, #8-32 Bolt, Figure 5.72 Variation of the number of #8-32 UNF bolts, torqued to the nominally recommended value, demonstrates again that three bolts allow less dissipation than only two bolts. Similarly, two bolts allow less dissipation than only one bolt. The case with two bolts exhibits much more variability in energy dissipation than both the single bolt or three bolts. Currently, we have no plausible explanation for this behavior.

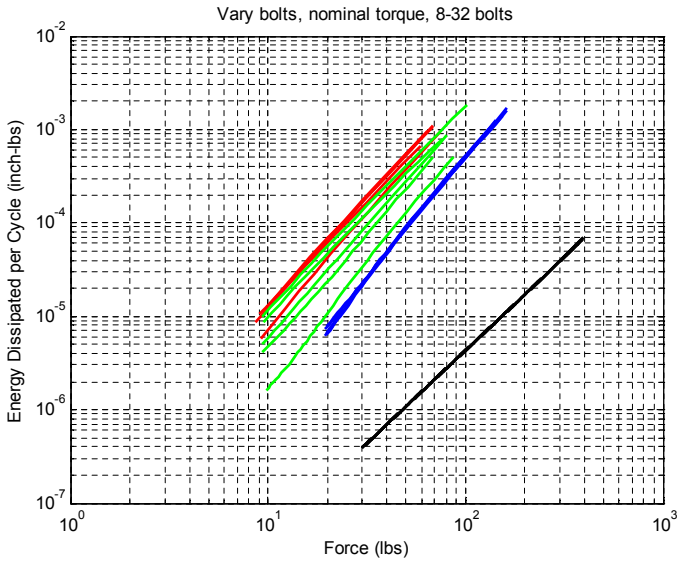

Figure 5.72. Energy Dissipation Variation for #8-32 UNF Bolts.

One bolt(red) Two bolts (green), three bolts (blue), along with solid (black).

Nominal Torque, #10-32 Bolt, Figure 5.73 The character of these responses was slightly different. The above data were generated using a fourth order polynomial fit to the envelopes.

Variation of the number of #10-32 UNF bolts, torqued to the nominally recommended value, clearly shows that three bolts allow less dissipation than only two bolts or a single bolt.

The variability seen in each case was relatively low. Perhaps the load generated by a nominal torque of a #10-32 UNF bolt in this hardware allowed a repeatable contact patch boundary to be achieved in all cases.

Note that as previously seen, there is a tendency for the case with three bolts to exhibit linear damping and a dissipation slope of two, below a certain force threshold.

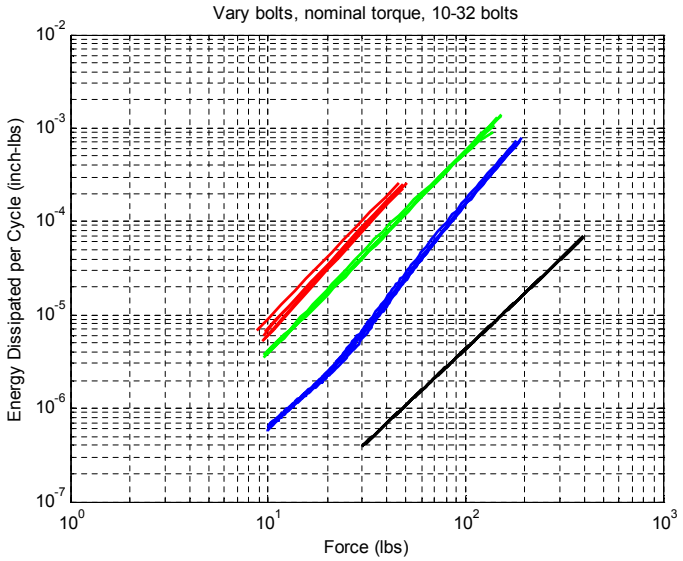

Figure 5.73. Energy Dissipation Variation for #10-32 UNF Bolts.

One bolt(red) Two bolts (green), three bolts (blue), along with solid (black).

Vary: Washers

Three #6-32 UNF Bolts, Nominal Torque, Figure 5.74 When plain washers were added to the three, nominally installed, #6 bolts, the overall energy dissipation increased slightly, as did the variability in the energy dissipation. This observation makes sense because the washers add more interfaces that contribute both damping and variability.

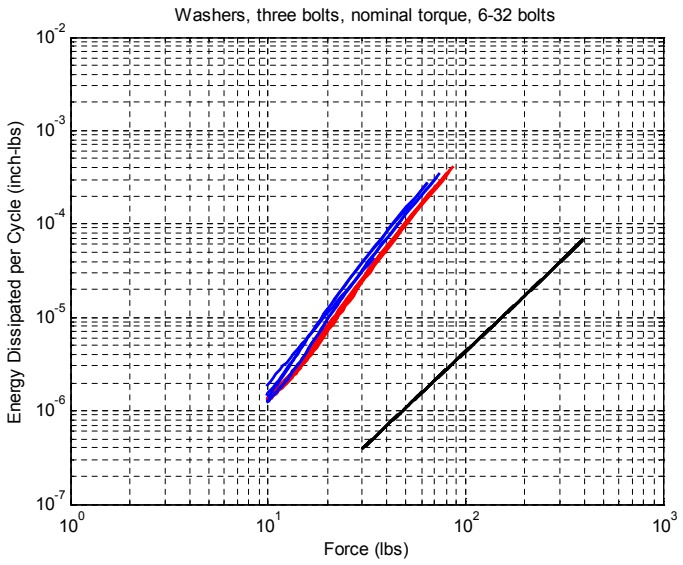

Figure 5.74. Effect of Washers.

Nominal torque, #6-32 UNF bolts: no washers (red) and washers (blue), along with solid (black).

Three #8-32 UNF Bolts, Nominal Torque, Figure 5.75 When plain washers were added to the three, nominally installed, #8-32 bolts, overall energy dissipation decreased slightly, but for reasons that remain unclear. The variability in the energy dissipation did increase slightly with the addition of washers, which is consistent with the observations for #6 bolts and washers.

Three #10-32 UNF Bolts, Nominal Torque, Figure 5.76 When plain washers were added to the three, nominally installed, #10 bolts, the overall energy dissipation increased slightly. The variability in the energy dissipation also increased by a very small amount. This observation, again, makes sense due to the additional interfaces that contribute both damping and variability.

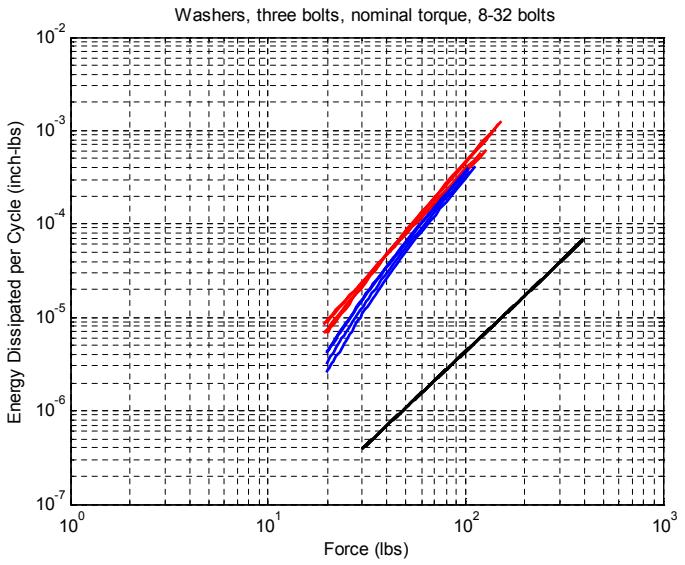

Figure 5.75. Effect of Washers.

Nominal torque, #8-32 UNF bolts: no washers (red) and washers (blue), along with solid (black).

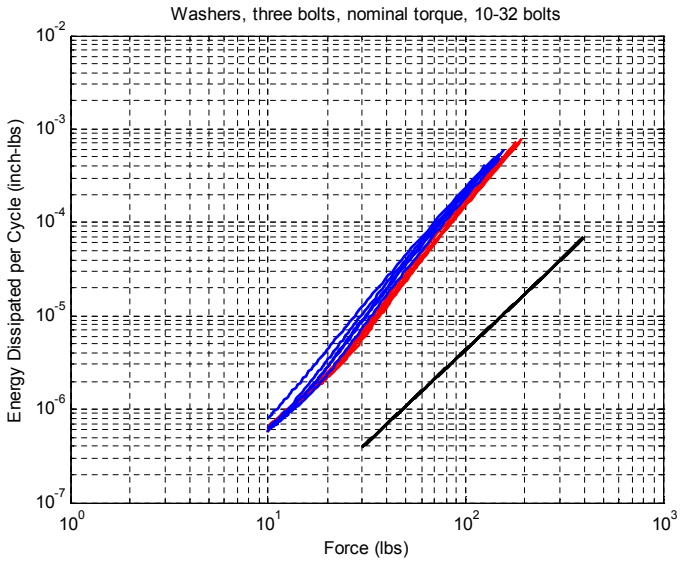

Figure 5.76. Effect of Washers.

Nominal torque, #10-32 UNF bolts: no washers (red) and washers (blue), along with solid (black).

Vary: Bolt Size

Nominal torque, three bolts, Figure 5.77 The load in the bolt is related directly to both applied torque and bolt diameter (Table 5.4). In general, the nominally installed bolts should exhibit higher preload for larger sizes. In this case, the trend appears almost as predicted, except for the fact that the #6 and #8 bolts yield very similar dissipation curves.

Different bolt sizes also have different bolt-head diameters, which may influence contact patch shapes and pressure distribution more than is realized in the interface. In turn, these differences may have a more complicated effect on the energy dissipation than is experimentally observed.

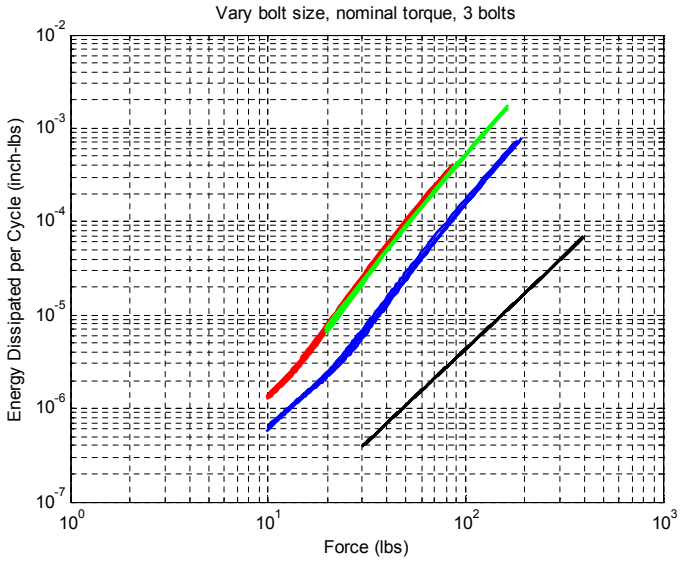

Figure 5.77. Nominal Torque, 3 Bolts.

#6-32 UNF (red), #8-32 UNF (green), #10-32 UNF (blue), along with solid (black).

Presentation of all data, Figure 5.78 When all of the above curves are plotted on a single-axis, the amount of variability in the energy dissipation curves is rather significant. The amount of variation demonstrated is the most dramatic of all collections of data presented in this handbook. However, except for the case of the two, nominally installed, #8 bolts, no single combination of parameters has shown a large amount of assembly-to-assembly variation, especially when compared to that observed in the earlier experiments, such as the AOS single-leg joints or System B specimens.

It can be important to note that large amounts of experimentally observed variation in energy dissipation per cycle for bolted joints actually might have straightforward explanations. In this

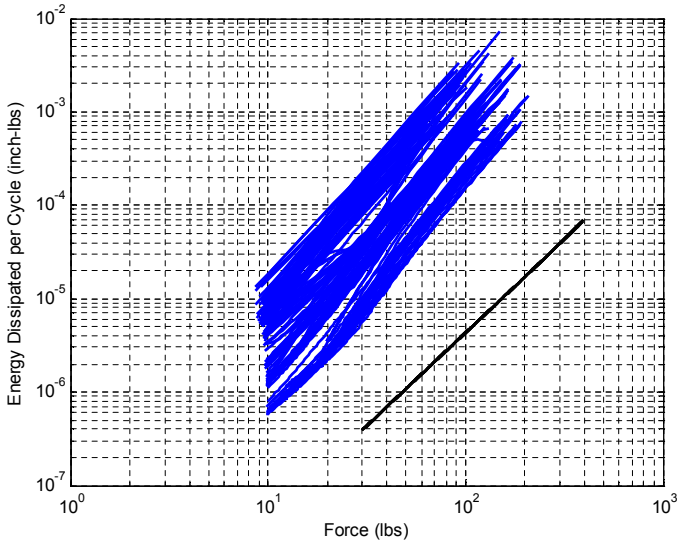

Figure 5.78. Complete Bolt Data Set.

particular case, the energy dissipation differences in the overall collection of data can be easily explained by the relatively large parameter space of torques, bolt size, bolt spacing and washers. It is conceivable that large amounts of variation in other joints can be explained by unexplored variations in similar parameters that are simply not as yet understood or quantified.

The data in Figure 5.78 have a bit of a banded appearance to it. There might be a way to group and differentiate (color) the data in a way that would point to an underlying relationship. One possibility might be coloring the data according to bolt size as shown in Figure 5.79.

The organization of data in Figure 5.79 does not show any obvious trends. However, when the data are arranged and colored according to the preload per bolt, one can readily see an emerging relationship.

Figure 5.80 illustrates the relationship between preload and overall energy dissipation. All data shown are for parameter combinations including only three bolts using preloads from Table 5.6. The red curves are from experiments with the lowest bolt preload, and they consistently appear at the top of the overall collection of curves. The green curves lie in the middle of the curve collection, almost perfectly dividing the low and high preload data. The blue curves consistently make up the lower portion of the curve collection. There is clearly a relationship between bolt preload and overall energy dissipation.

Figure 5.81 shows the energy dissipation per cycle at 30 lb of input for each of the parameter combinations shown in Table 5.7. Energy dissipation at 30 lb is plotted against approximate bolt preload as calculated by Equation (5.14) using information from Table 5.6.

In general, the energy dissipation decreases as the preload is increased. The data for parameter

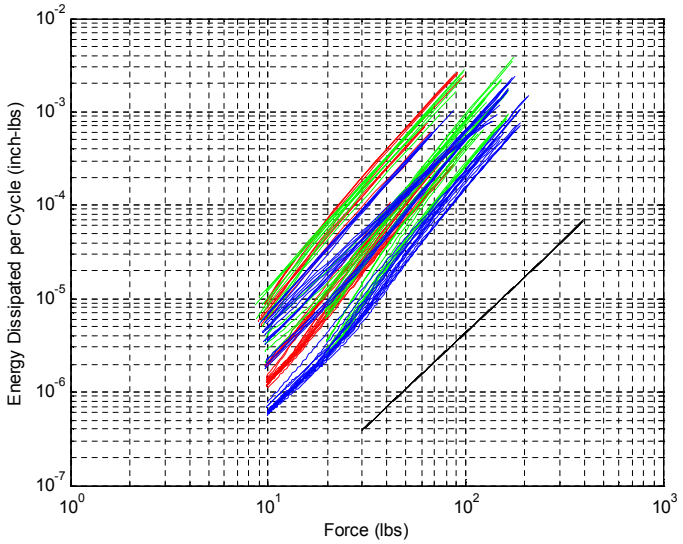

Figure 5.79. Energy Dissipation Data Summary.

#6 bolts (red), #8 bolts (green), #10 bolts (blue), and solid (black).

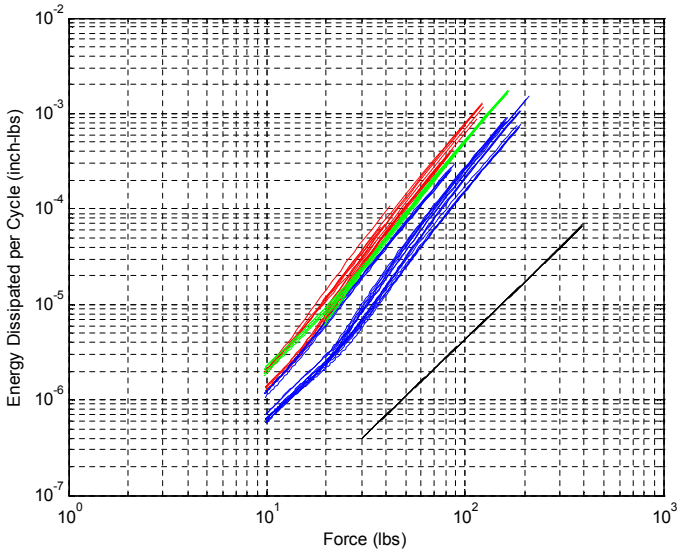

Figure 5.80. Energy Dissipation Data with Three Bolts, No Washers.

Color according to bolt preload: 200-400 lb (red), 400-600 lb (green) and 600-800 lb (blue).

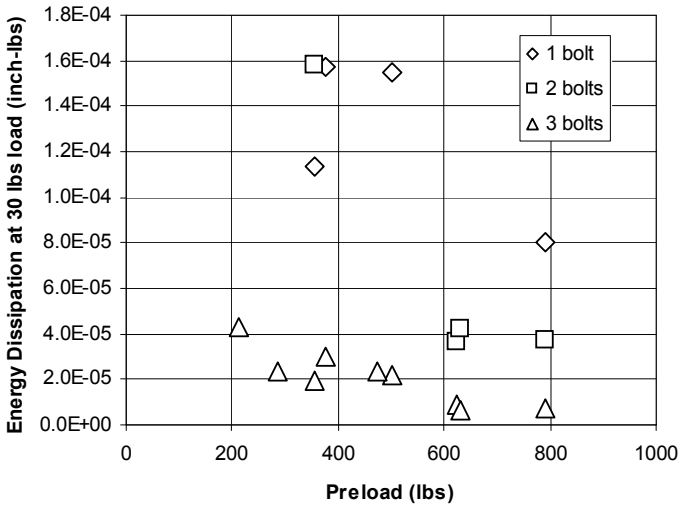

Figure 5.81. Energy Dissipation per Cycle vs Bolt Preload.

combinations including three bolts show less energy dissipation than the cases with one or two bolts because the three bolts generate the highest normal force in the interface.

Similarly, Figure 5.82 shows that the frequency of the axial mode of the dumbbell goes up with increased preload (given same number of bolts, again), which is logical. As the load in the joint is increased, the interface becomes more rigid and more closely approximates the stiffness of the monolithic specimen, which had an axial mode frequency of 906 Hz.

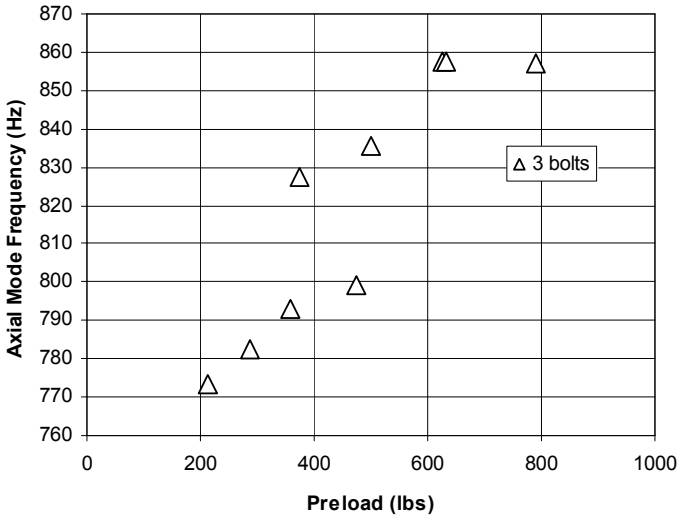

Figure 5.82. Dumbbell Axial Mode Frequency vs Bolt Preload.

Table 5.7. Summary of Average Slopes from the Parameter Study.

Bolt Size	Number of Bolts	Bolt Torque	Washer	Average Slope
6-32	1	10	N	2.43
6-32	2	10	N	2.55
6-32	3	6	N	2.61
6-32	3	8	N	2.77
6-32	3	10	N	2.56
6-32	3	8	Y	2.82
8-32	1	12	N	2.57
8-32	1	16	N	2.31
8-32	2	20	N	2.42
8-32	3	12	N	2.72
8-32	3	16	N	2.63
8-32	3	20	N	2.87
8-32	3	16	Y	3.07
10-32	1	30	N	2.37
10-32	2	24	N	2.15
10-32	2	30	N	2.09
10-32	3	18	N	2.41
10-32	3	24	N	2.48
10-32	3	30	N	2.57
10-32	3	24	Y	2.58
8-32 solid	NA	NA	N	2.00

5.4.9.4 Energy Dissipation Curve Slopes

The previous subsection has shown that there is potential for understanding the relationship between overall energy dissipation and preload in a bolted interface.

Another number used to describe the character of a nonlinear bolted joint is the slope of the energy dissipation-per-cycle curve as plotted in log-log space. As indicated earlier, this number is an indication of the degree of damping nonlinearity that is present in the interface. A slope of exactly two indicates linear, viscous damping. Slopes greater than two indicate damping that is amplitude dependent, with higher slopes indicating higher amplitude dependency. Typically, slope values top out at, or slightly above, three.

Shown in Table 5.4.9.4 are average energy dissipation curve slopes for all the data that was utilized in this section.

Data not included in Table 5.7 was not conducive to analysis by the modified logarithmic decrement technique for one of the two following reasons: 1) the specimen exhibited very high amounts of damping at the axial mode, or 2) envelopes of peaks were hard to fit due to proximity of an adjacent mode, even with digital bandpass filtering.

The average of all the slopes in Table 5.7 is 2.55. The median value of these slope data is also 2.55. The conclusion from this limited illustration is that we can assume a slope of about 2.5 or 2.6 even if we did not have other detailed knowledge of the particular bolted joint. In all the experimental work that has been done at Sandia on bolted joints, a slope of 2.5 has generally been very close to the experimentally determined slope values.

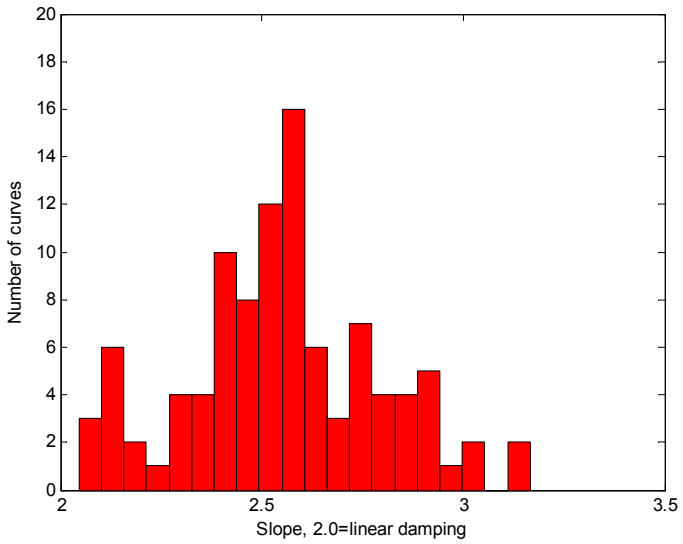

Figure 5.83. Slope Histograms for Table 5.7 Data.

Figure 5.83 shows a histogram of the slope values found in Table 5.7. The slope values do vary within the entire space from two to three. This statistical picture of the distribution might help the experimentalist decide whether detailed experiments are needed or simply choosing an average value of 2.55 would suffice.

5.4.9.5 Summary

The purpose of this section is to provide some general background as to the overall behavior of a very simple and generic, bolted joint interface as the most basic parameters affecting the joint are changed. Lessons learned from this study include the following:

- Interface preload, in the form of bolt tension, is a major factor in the overall energy dissipation in a bolted joint.

- The presence of washers under bolt heads tends to raise both the overall energy dissipation of the interface and the variability in the dissipation.
- Compared to other, more complicated specimens, the variability of energy dissipation in these specimens is low, suggesting that the simple geometry of these interfaces does not offer as much opportunity for variability in the way the surfaces mate together. The AOS single-leg joint, shown earlier, is an example of a complicated interface with more opportunity for assembly-to-assembly variation.
- With rare exceptions, for all of the bolted joint data collected and presented in this handbook, the slopes of the energy dissipation curves are between 2.0 and 3.0. In those exceptional cases, (similar to other experimental observations occasionally seen in the literature), only a few experimental observations involve power-law slopes that exceed 3.0. *Typically, one expects power-law slopes lying between 2.3 and 2.9.*

5.4.9.6 Future Work Using these Data

Much data was collected in the process of this investigation (Table 5.5 on page 195) but not all the data has been fully analyzed. The lessons learned presented here are limited in the following ways that also suggest areas appropriate for future work:

- Imaging and analysis of interface contact patches for one, two, and three bolt arrangements. The shape and distribution of contact patch probably varies substantially among the three cases.
- Analysis and understanding of more than the simple axial loading action in the interface. Data was also gathered, but not presented, in this 1st Edition Handbook, that will allow thorough analysis of energy dissipation in the interface due to bending modes in the joint. Bending modes are expected to affect the behavior by modification of the contact patch due to the moment in the interface.

5.5 Analysis of Dumbbell Interface Data Using Spatial Filtering Techniques

5.5.1 Data Analysis

There is no direct way to measure the energy dissipation within a joint. The measured acceleration waveforms are complex and require some decomposition to understand their character. The dumbbell design assumption is that the dominant energy dissipation occurs by the axial sliding of the joint. Because of the coupling between bending and axial motion, it was necessary to isolate the effects of axial motion. Axial effects within the dumbbell can be isolated using spatial filtering. Spatial filtering was investigated using modal filtering and over-parameterization.

For these studies, a joint representative of the primary connection between the Laterally Oriented Subsystem (LOS) and the exterior aeroshell of the System C system was selected. This interface is a flanged, screwed lap joint. Any loads applied to the exterior of the system must be transferred across this bolted interface to excite the LOS. Based upon previous research done at Sandia/NM [49], it was conjectured that the primary energy dissipation mechanism would be slippage in the joint - both microslip and macroslip. Consequently, the experimental test bed was developed to facilitate the sliding of the facing surfaces past one another, exciting the mechanism of interest. Because of the aluminum-to-aluminum interface it was important to minimize the number of large amplitude cycles that could cause damage and variability in the results. It was decided that a "dumbbell" impact experiment would best excite the sliding dynamics of the system while minimizing the damage to facing surfaces. Examples of the interfaces specimens are shown below in Figures 5.84 and 5.85.

5.5.1.1 Dumbbell Specimen Experiment

The initial concept of the dumbbell experiment was that the dumbbell would represent an idealized 2-DOF spring, mass, dissipation model as shown below in Figure 5.86.

In the model, K represents the stiffness of the joint, M is the mass of each end element and D is nonlinear energy dissipation term. The response of the system to an axial excitation would be the rigid body acceleration of the system and the ring-down of the elastic mode. The characterization of the energy dissipation across the joint could be determined by the physical parameters of the experiment and the ring-down of the axial mode.

Unfortunately, the physics of the dumbbell test specimen are somewhat more complicated than the idealized 2-DOF system above. The actual hardware approximates a twelve DOF system: six rigid body modes and six elastic modes (ignoring the higher frequency local modes). The six rigid body modes are the system translations and rotations, and the six elastic modes are the axial, torsion and four bending modes. So, even in an idealization of the hardware, an experiment must be careful to excite and measure only the axial mode of interest that represents the sliding of the

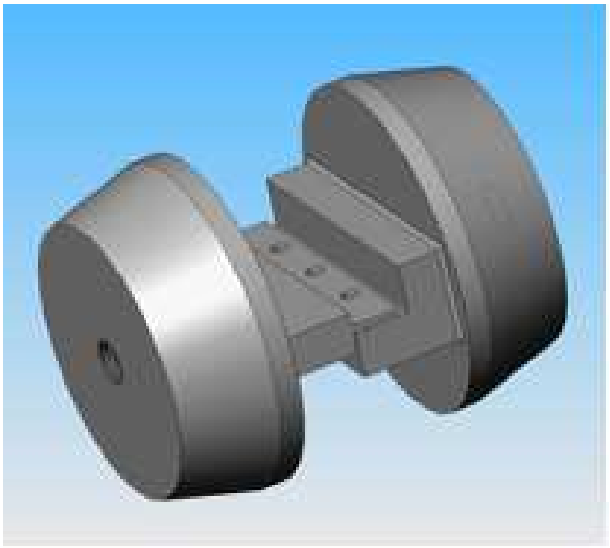

Figure 5.84. Interface Specimen.

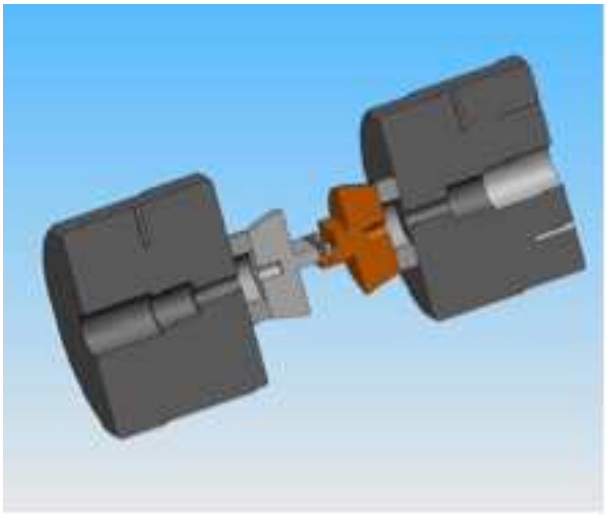

Figure 5.85. Cross-Section of Dumbbell Test Specimen.

facing surfaces. This is a controllability/observability problem in which the aim is to only excite and observe the axial mode.

The actual hardware does not behave like the idealized 12-DOF system described above. The jointed test specimen is not symmetric and cannot be designed to be symmetric. Consequently, the lack of symmetry causes modes that are coupled axial and bending modes and are closely

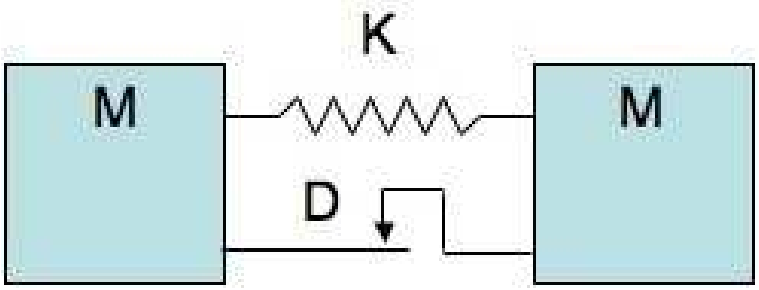

Figure 5.86. Idealized 2-DOF Dumbbell System

spaced. The resulting response cannot be analyzed directly. The response of the system must be decomposed to track the individual modal responses of the system (at this stage consider only the mild nonlinearities associated with microslip). The methods considered for this decomposition are: temporal filtering (including wavelets), and spatial filtering. As other efforts (Section 5.1.3) addressed the temporal filters, this investigation is focused on spatial filtering.

5.5.1.2 Spatial Filtering

A spatial filter, allows observation of the contributions to the acceleration waveforms of the dynamics of interest and exclusion of the information from other, less important dynamics. The first attempt at spatial filtering was to use a modal filtering approach using a pseudo-inverse method to derive the modal filter parameters.

$$\{X(t)\} = [\phi]\{\alpha(t)\} \tag{5.15}$$

$$\{\alpha(t)\} = [\phi]^{\dagger}\{X(t)\} \tag{5.16}$$

Because of the limited frequency bandwidth associated with the impact hammer and the use of anti-aliasing filters, only the first twelve modes of the system were retained in the modal filter. The rigid body modes were derived from the geometric definition of the test hardware, and the elastic modes were determined from test data: low-level impact testing and at-level testing with the pendulum. As shown in Equation (5.16) the modal filter is the pseudo inverse of the mode shape matrix, $[\phi]^{\dagger}$.

As stated earlier, due to the inherent asymmetry of the joint, a pure axial mode does not exist. The axial and bending response is coupled. There are two closely spaced modes that contain contributions from the sliding mode and a bending mode. These modes can be seen in the acceleration response as a “beat” in the waveform in Figure 5.87 and more clearly in the Fast Fourier Transform

(FFT) of the response in Figure 5.88. The contributions of these two modes were isolated using the modal filter with varying degrees of success. Ultimately, the filtered response was very sensitive to small changes in the mode shapes and the nonlinearity of the system precluded using the modal filter to isolate the desired response. A different approach that was not as sensitive to small changes in mode shape was needed to extract the ring-down of the coupled modes.

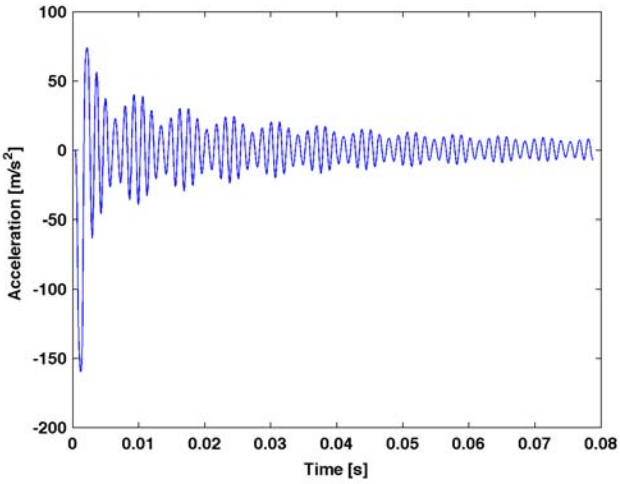

Figure 5.87. In-Axis Acceleration Response of Dumbbell Specimen.

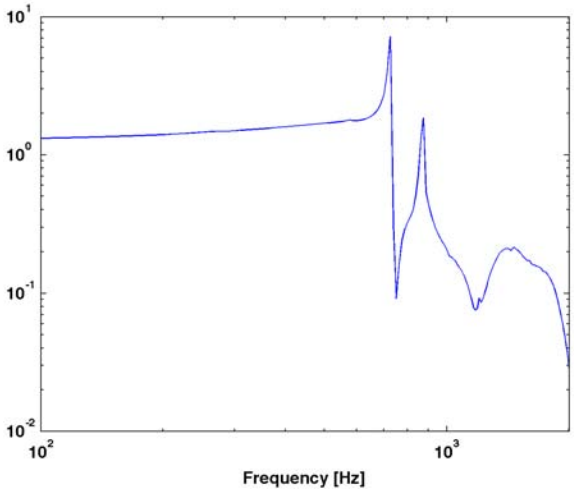

Figure 5.88. Fast Fourier Transform of Acceleration Response.

Over Parameterization and Modal Subtraction Those familiar with using time domain methods to extract modal response of real structures understand its difficulty and the frustration in using it. In the frequency domain, the peaks that correspond to the modes of interest are clearly observed, but the time domain solution results in multiple modes being estimated to properly fit the ring-down of the individual modes. The cause of this is due to mild system nonlinearities and signal processing effects such as leakage. This observation is so widespread that modal processing codes like I-DEAS generate convergence/stability plots allowing the user to pick the "best" modal representation.

For this analysis the time domain code was used to curve fit the data by including multiple modes at the resonant frequency of interest. This approach does not result in a predictive input/output model of minimum order. It is simply a curve fit to the data using a series of decayed sinusoids of approximately the correct frequency that minimizes the error between the measured data a series of analytical curves. The modes not associated with the dynamics of interest are removed and the remaining decayed exponential responses are used to define the decay of the mode(s) of interest. This method appears to work well; however, because of the closely spaced nature of the modes in question, there are some issues with mode separability.

Eigensystem Realization Algorithm Because of its familiarity, the Eigensystem Realization Algorithm (ERA) [57] time domain code was used to process the individual acceleration waveforms. The output of ERA is in state-space form. The state-space equations are manipulated to determine the nonlinear mode decays. Initially, the curve fitting calculations were performed interactively; however, because of the large number of individual data sets being processed (over 400 data sets), software was developed to process the data in a batch mode. Many of the parameters used in the batch process were selected based upon experience "fitting" the data interactively.

ERA falls in the general category of system identification techniques referred to as generalized block Hankel decomposition. A principal input parameter is the number of time points to use in forming the rows and columns of the Hankel matrix. Ultimately, the row space of the Hankel matrix is the limiting factor, limited by computer memory, on how long a data record can be used in the curve fitting process. The number of poles selected in the curve fitting process is based upon a unity normalized cumulative sum of singular values of the Hankel matrix. The number of poles retained is determined by a user specified parameter relating to the value of the cumulative sum of singular value curves. The value used in these analyses was set to 0.9995.

Error Checking in ERA Because the data was processed in batch mode, it was important to have an error metric associated with the quality of fit. To calculate this error metric, all responses from the ERA state-space model were resynthesized. Next, a singular value decomposition of both the resynthesized data and the original experimental data was performed. Because the response of the system is dominated by the two coupled axial/bending modes, the first two singular values of the response matrices are expected to correspond to the axial dynamics. Correspondingly, the first two columns of the left hand singular vectors will reflect modal-like response of the principal axial modes.

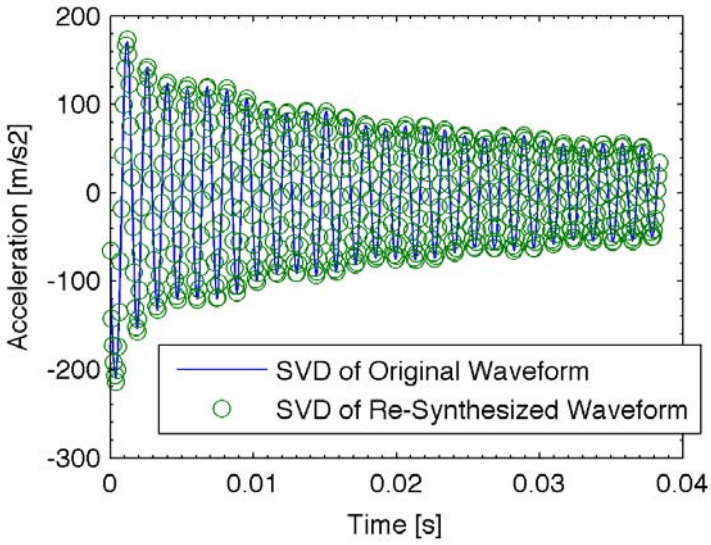

Figure 5.89. Resynthesized ERA Response Fit for First Singular Value Vector.

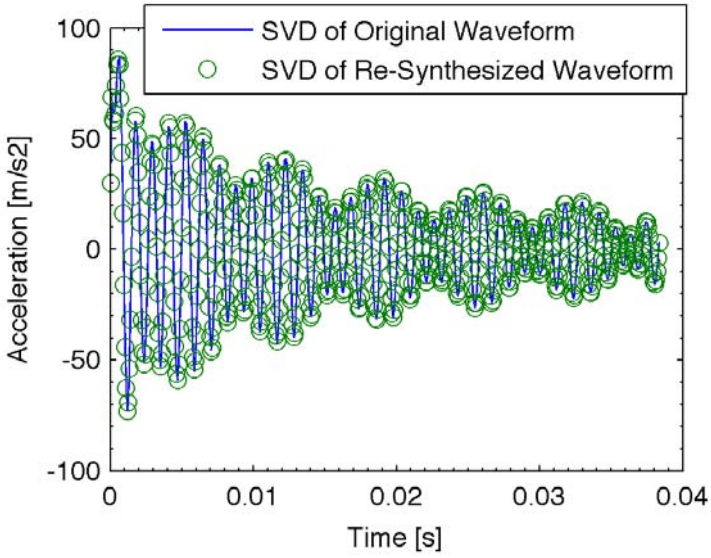

Figure 5.90. Resynthesized ERA Response Fit for Second Singular Value Vector.

Consequently, natural error metrics are the normalized differences between the experimental and analytical left-hand singular value vectors. These error metrics reflect the ability of the

state-space model to reproduce the dominant axial dynamic response. Figures 5.89 and 5.90 are examples of the comparison of the experimental and ERA resynthesized singular value vectors demonstrating the ability of the state-space model to capture the desired dynamics. Interestingly, these responses are very similar to the results obtained through the use of the pseudo-inverse modal filter.

The responses of over-parameterized modes of interest can be resynthesized using the model. Figures 5.91 and 5.92 show the resynthesis of the two over-parameterized modes with their corresponding Hilbert transform envelopes (HTE). Ripple in the early time response of the HTE precludes using it directly to extract the energy dissipation. A better approach is to fit the HTE with a series of monotonically decaying basis functions. The functions selected are the decay envelopes of the damped sinusoids that approximate the nonlinear response of the mode of interest. Figures 5.93 and 5.94 show the HTEs and the basis functions for the two nonlinear modes of interest. It is apparent that the early time response corresponds, almost exactly, to the heavily damped sinusoid (Basis function) and late time response corresponds to a more lightly damped sinusoid (Basis function).

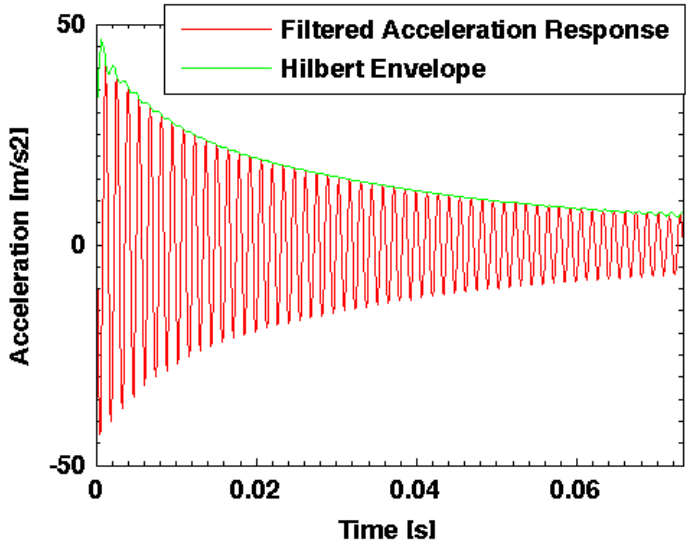

Figure 5.91. Filtered Acceleration Response for Mode 1.

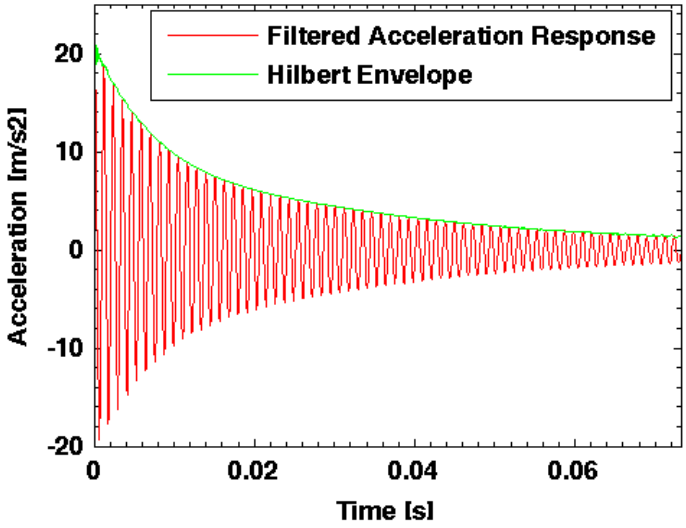

Figure 5.92. Filtered Acceleration Response for Mode 2.

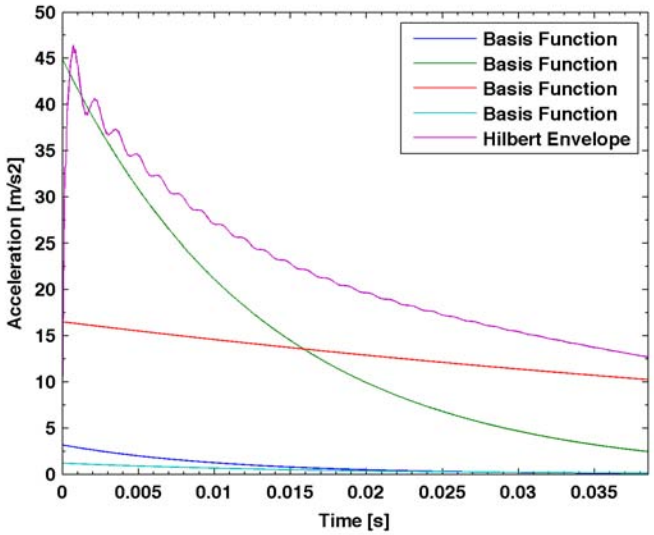

Figure 5.93. Basis Functions and Hilbert Envelope for Mode 1.

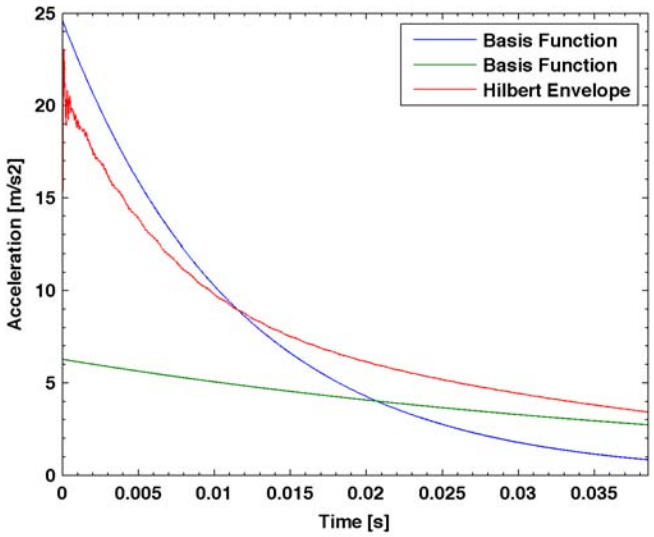

Figure 5.94. Basis Functions and Hilbert Envelope for Mode 2.

With the HTEs and the basis functions determined, a least squares fit of the basis functions to the HTEs gives a smoothed version of the HTE. Figures 5.95 and 5.96 show the resynthesized nonlinear mode responses, their HTEs and the smoothed versions of the HTEs which are described in the figures as fits to the Hilbert envelope. The next step is the extraction of the damping factors from the smoothed HTEs.

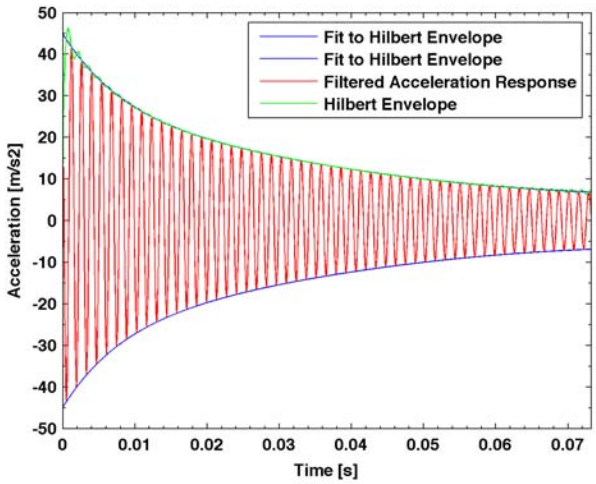

Figure 5.95. Fit to Hilbert Transform Envelope for Mode 1.

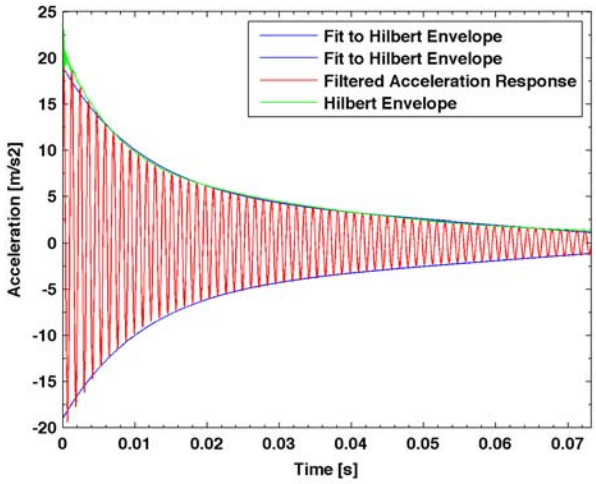

Figure 5.96. Fit to Hilbert Transform Envelope for Mode 2.

The following derivation extends the work by Resor [58], allowing the recursive extraction

of the amplitude dependent critical damping ratio from an evenly sampled decay envelope. The decayed response of a SDOF system is

$$X(t) = \mathrm{X} e^{-\varsigma(t)\omega_n t} \sin(\omega_d t) \tag{5.17}$$

with a decay envelope

$$X_e(t) = \mathrm{X} e^{-\varsigma(t)\omega_n t} \tag{5.18}$$

Taking the logarithm of both sides

$$\log(X_e(t)) = \log(\mathrm{X}) - \varsigma(t)\,\omega_n t \tag{5.19}$$

and discretize by looking at the discrete time points

$$k\Delta t = t,\, for: k = 0,1,2,\ldots n \tag{5.20}$$

The difference of the logarithm of the envelope for times k and $k+1$ yields

$$\log(X_e((k+1)\Delta t)) = \log(\mathrm{X}) - \varsigma((k+1)\Delta t)\,\omega_n((k+1)\Delta t) \tag{5.21}$$

Rearranging Equation (5.21) to solve for $\varsigma(k+1)$ results in the following recursion equation

$$\varsigma(k+1) = \frac{\log(X_e(k)) - \log(X_e(k+1))}{\Delta t\,\omega_n(k+1)} - \varsigma(k)\frac{k}{k+1} \tag{5.22}$$

The starting point for the recursion equation at $k = 0$ is

$$\varsigma(1) = \frac{\log(X_e((k))) - \log(X_e(k+1))}{\Delta t\,\omega_n} \tag{5.23}$$

The derived recursion equation allows estimation of the damping ratio from the smoothed HTE for each of the n time points. Figure 5.97 displays the calculated critical damping ratios for the two nonlinear modes for a particular system input.

Calculation of Energy Dissipation The energy dissipation per cycle for each of these single mode responses can then be calculated from the decay envelope. From Thompson [52], the energy

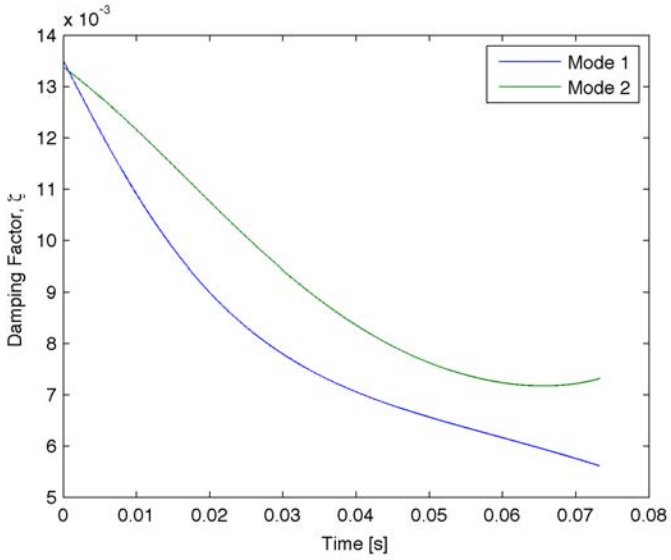

Figure 5.97. Critical Damping Factor.

dissipation per cycle for an SDOF spring mass damper system can be approximated as

$$D = 2\zeta\pi kX^2 \tag{5.24}$$

For the system with two masses, the dissipation is doubled

$$D = 4\zeta\pi kX^2 \tag{5.25}$$

where ζ is the time varying critical damping ratio,
k is the dynamic stiffness,
and X is the amplitude of sinusoidal displacement of one of the masses.

Assuming that the natural frequency of the system is constant for a particular mode, and that the acceleration amplitude can be determined from the second time derivative of the displacement leads to Equation (5.26).

$$X \approx \frac{A}{\omega^2} \tag{5.26}$$

A further assumption is that the response frequency is the natural frequency of the system.

$$\begin{aligned} \omega &= \sqrt{\tfrac{k}{m}} \\ k &= m\omega^2 \end{aligned} \tag{5.27}$$

Substituting Equations (5.26) and (5.27) into Equation (5.25) gives an expression for the energy dissipation per cycle expressed as a function of the acceleration envelope and critical damping ratio.

$$D = \frac{4\zeta\pi m A^2}{\omega^2} \tag{5.28}$$

Plotting energy dissipation per cycle as a function of the force across the joint on a log-log plot (Figure 5.98) shows curve slopes between 2.3 and 2.5 indicating a nonlinear damping mechanism consistent with the results by Gregory and Resor [49]. While the procedures described herein are complex, it does eliminate distortions caused by temporal filters and uncertainty associated with wavelet transforms.

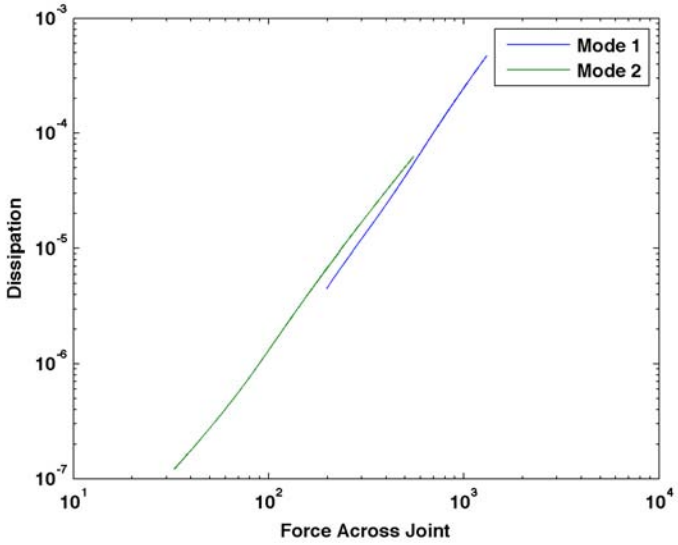

Figure 5.98. Energy Dissipation per Cycle vs. Force Amplitude.

Chapter 6

Performing Controlled, Bolted Joint Transient Experiments on Electrodynamic Shakers

Danny L. Gregory and Brian R. Resor

The purpose of this section is to discuss issues that arise in controlling transient inputs to hardware for the purposes of model validation.[1] The challenge is to impose a prescribed acceleration to the test specimen so that the resulting system response can be compared that of a computer model for the structure subject to the same imposed acceleration.

Tests were performed on an Unholz-Dickie, T2000, electrodynamic shaker in which tests were controlled either by a Spectral Dynamics, Jaguar, shock and vibration control system, or by an in-house control package. (The hardware arrangement is shown in Figure 6.1). The test method was first approached the same as in a typical shaker shock test in which it is acceptable to control the chosen input location only to the given Shock Response Spectrum (SRS). Normal guidelines for shaker shock testing proved inadequate for this work. Several lessons are shown to demonstrate the intricacies of shaker shock testing and associated tools to control the test input in a way that acceptable hardware responses can be gathered for model validation purposes.

6.1 Test Background

The test of interest is a shock consisting of various exponentially decaying, sinusoidal components designed to match a desired SRS. The overall level of the acceleration input was scaled to exercise the bolted joints over an approximate force range representative of an intended application. The level of the input that reproduces the intended loads in the joints is different for the mock hardware than it is for actual hardware due to differences in actual stiffness and damping values between the two systems. The desired input for the mock hardware is pictured in Figure 6.2.

The objective of the experiments is to provide a prescribed acceleration input to the base of

[1] This chapter is taken largely from [59].

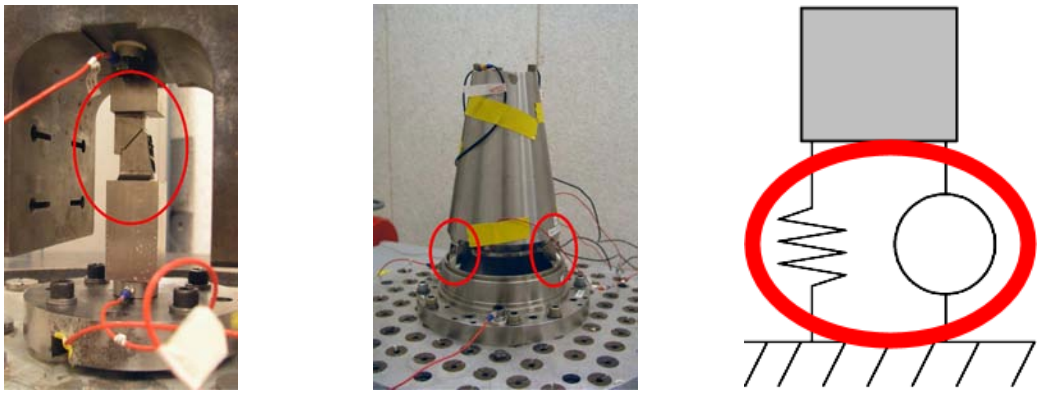

(a) (b) (c)

Figure 6.1. Test Hardware with Bolted Joints Circled.

(a) Single bolted joint on a shaker head with large reaction mass, (b) three bolted joints as attachments for a piece of mock aerospace hardware on the head of an electrodynamic shaker, and (c) an SDOF lumped mass, stiffness and damping simplification of either system (a) or (b).

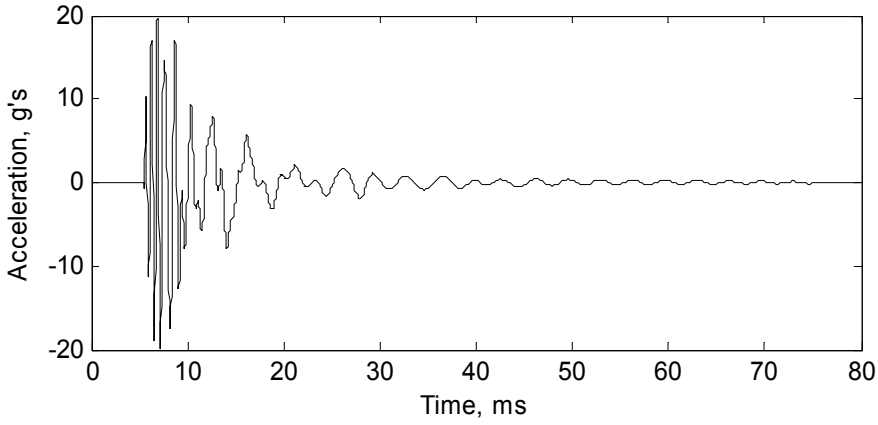

Figure 6.2. Reference Shock Input for Mock Hardware.

the test hardware that is independent of the dynamics of the hardware configurations placed on the shaker. Furthermore, the input must be accurate and repeatable so that meaningful statistics regarding randomness associated with the joints for the multiple hardware configurations and their assembly can be quantified. The enforcement of acceleration at the base of the test hardware provides a close approximation of a fixed-base condition that allows the boundary conditions for the computational model to be realized.

This hardware exhibited properties that made it a very challenging test. A basic shaker shock control algorithm is open loop and assumes a linear system. The algorithm also assumes only one control location, and so choosing that location can be very important. From the beginning, the nonlinear nature of the test item was well known, as was the sensitivity of reference locations defined at the base.

Regardless, there are advantages to performing this experiment on a shaker. The true input for this environment does actually look like a waveform composed of decaying sinusoids, so measuring responses to a different input, such as a haversine, was not as appealing for model validation in this case. Shock inputs as seen in Figure 6.2 cannot be reproduced exactly with any other shock test method (e.g., drop table or resonant plate). The electrodynamic shaker also easily allows high input levels to be achieved in a repeatable manner.

6.2 Basic Shaker Shock Control

A simplified representation of a shaker and test item is shown in Figure 6.3. To calculate a drive signal, the system must be accurately characterized with a transfer function that relates the control system drive voltage signal for the power amplifier to the acceleration that is created and measured at the control location. There are several dynamic features in the system that can contaminate the inputs and responses if they are not properly controlled: the first axial resonance of the armature, back electromagnetic force (EMF) damping in the coils, the free-free resonant mode of the test item and armature, and the nonlinearity of the test item.

The estimated system transfer function is calculated during the system characterization simply as

$$H(\omega) = \frac{R(\omega)}{C(\omega)} = \frac{\text{response}}{\text{calibration pulse}} = \frac{\text{g}}{\text{V}} \tag{6.1}$$

Next, the drive is calculated in the frequency domain using

$$S(\omega) = \frac{D(\omega)}{H(\omega)} = \frac{\text{desired pulse}}{\text{FRF}} = \frac{\text{g}}{\text{g/V}} = \text{V} \tag{6.2}$$

The drive pulse, $s(t)$, in Equation (6.3) , can be found by performing the convolution between

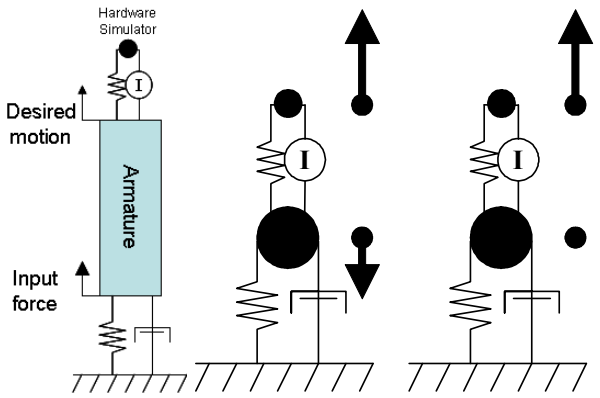

Figure 6.3. Shaker and Test Item.

(a) Simplified representation of a shaker and test item and illustrations of two important modes of the shaker system: (b) free-free resonance of the armature and test item and (c) fixed-free resonance of the test item. Arrows represent an estimate of motion in each resonance.

the desired pulse, $d(t)$, and the inverse impulse response of the system, $IIR(t)$, with IFT denoting the inverse Fourier transform. Note that in the actual application of this theory, the discrete Fourier transforms are used and issues of aliasing, periodicity, and spectral leakage must be addressed.

$$s(t) = \text{convolution}\,(d(t), IIR) \text{ where } IIR(t) = IFT\left(\frac{1}{H(\omega)}\right) \tag{6.3}$$

Problems arise in calculating $s(t)$ when the IIR cannot be calculated cleanly. As seen in the above equation, the estimate of $H(\omega)$ is in the denominator. Frequency intervals where the amplitudes are very small (i.e., notches) amplifies any noise in $H(\omega)$ in the calculation of the $IIR(t)$. Dividing by $H(w)$ in the range of the noisy notches is similar to dividing by a number close to zero in that it yields large amplitudes in IIR. The IIR can be contaminated by notches and noise in the transfer function, and can lead to a poor estimate of the drive signal.

6.3 Test Control Issues

The hardware in this test has little material damping (on the order of 0.2% of critical). Most of its damping is generated by the joint under investigation. This scenario can be desirable so that the effects of the joint damping tend to dominate the response and are more easily detected and measured.

Amplification of the axial mode associated with the hardware is high in this case. It causes a

deep notch in the system characterization transfer function at a frequency that represents the fixed-base mode of the test item relative to the control location. Additionally, the nonlinear nature of the joint causes low coherence in the transfer function in the vicinity of the fixed-base mode of interest, and results in a noisy estimate of transfer function in the vicinity of the notch. These features lead to difficulties in controlling the shaker shock test well enough that it can provide useful information for model validation because clean and repeatable acceleration inputs are desired.

6.3.1 Baseline Tests

Figure 6.4 shows the transfer function, the calculated drive, and the measured response for a first round of tests. The noisy notch in the transfer function at 1400 Hz is associated with the fixed-base, axial mode of the test item, the primary mode of interest for exercising the joint interfaces. (Note that base-driven resonance occurs at the frequency of the fixed-base modes.) The problematic notch causes frequency smearing in the IIR which, in turn, creates a non-causal (meaning that the input begins before zero time) drive calculation during the convolution operation (Figure 6.5.) The end result of the contamination is obvious in Figure 6.5 when the response actually initiates prior to zero time. The fact that the contamination frequency occurs at the 1400-Hz, axial mode of the test item makes matters worse. A small amount of drive at that frequency will cause a significant response in the structure. This type of behavior is not desired in model validation experiments because the model will not include those effects.

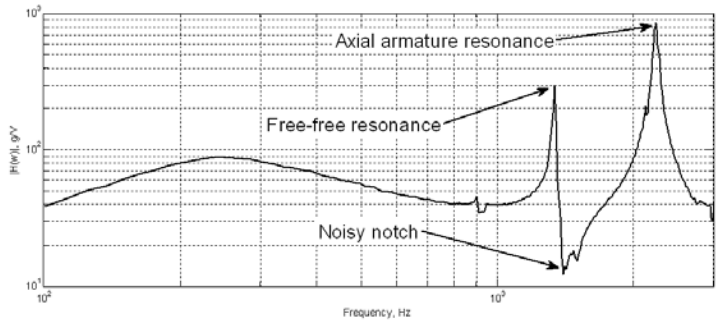

Figure 6.4. System Characterization Transfer Function, $H(w)$.

6.3.2 Hanning smoothing

Having smoothing of the transfer function near the problem frequencies can be used to fix the frequency smearing in the drive signal [60]. The smoothing operation can be done several times to achieve desired results. For this test, approximately 20 smoothing operations were performed to

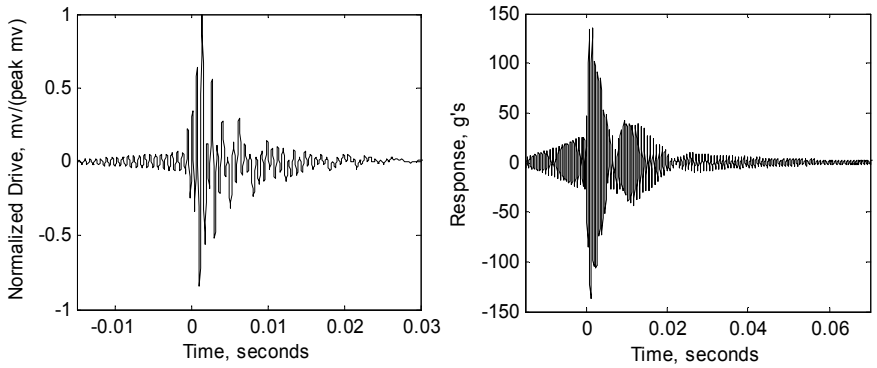

Figure 6.5. Input and Output Signals.

(a) calculated drive signal, $s(t)$ and (b) measured response on the test item.

arrive at the transfer function seen in Figure 6.6. The smoothing operation is defined as

$$F = \frac{1}{4}F_{m-1} + \frac{1}{2}F_m + \frac{1}{4}F_{m+1} \tag{6.4}$$

where F is the quantity that is smoothed.

Amplitude and phase of the transfer function are the smoothed quantities in this case.

Figure 6.7 shows the new drive signal and measured response, respectively. Notice the lack of any contaminating frequency components. Smoothing greatly improved the apparent quality of this test by eliminating the artificial drive at the frequency of the notch. Considering the typical shaker shock test metric, the shock response spectrum, this test was well behaved and the input specifications were realized.

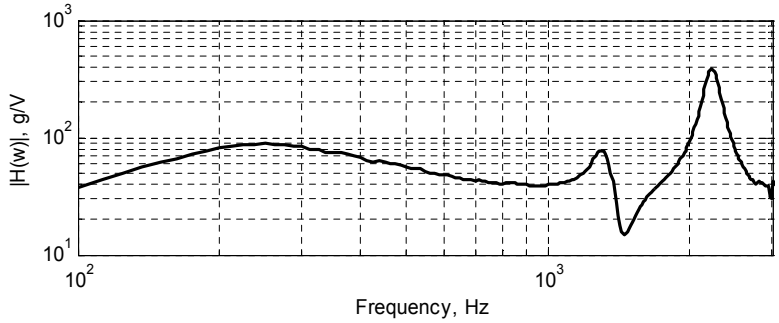

Figure 6.6. Hanning-Smoothed Transfer Function, $H(w)$.

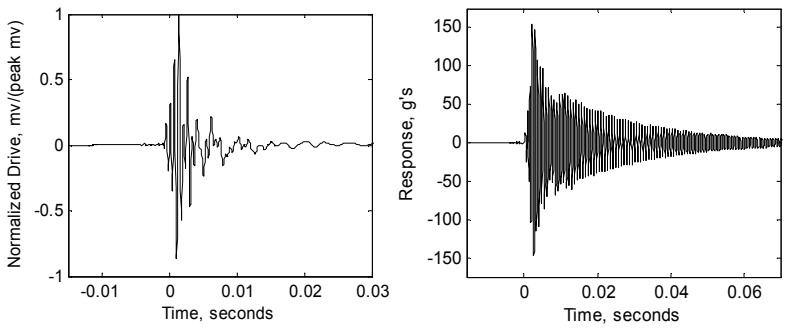

Figure 6.7. Improved Input Signal and Response.

(a) New drive signal, $s(t)$ and (b) measured response on the test item using the drive signal that has been corrected.

Upon closer examination, it is apparent that modifications to the transfer function due to the smoothing operation also changed it at other frequencies, introducing other errors in the drive calculation that make the drive unable to fully control the unwanted modes of the test item and shaker system. Figure 6.8 illustrates the issues. First, the fixed-base mode at 1400 Hz was not fully excited. There is a notch in the input spectrum at that frequency. Second, the armature resonance at 2200 Hz was present in both the input and response. Third, the free-free mode of the shaker armature and test item at 1330 Hz is significant in both the input and response. This mode is easily identified by measuring the response of the system to a hammer input when the shaker is at rest and supported by its flexures. The additional damping that can be introduced into the response of the hardware due to the action of these resonances combined with the presence of extra damping from electromagnetic forces on the armature is not acceptable in a model validation that is designed to evaluate the energy dissipation due only to the joints.

6.3.3 Issues

The responses measured from the above described experiments, which include information about the shaker system, cannot be used for input to a model that does not model the actual shaker system. The model under validation is likely a true, driven-base model of only the test item and its fixture, and has been designed to isolate effects of the physics of interest - the bolted joints.

There are problems in recreating the proper stiffnesses in this setup in an associated analytical model. The variability in stiffness of the bolted joints causes the driven-base axial mode of the experimental hardware to vary by as much as 10%. This variability is quantified experimentally by performing tests on multiple hardware combinations, and then also including it in the analytical model of the hardware. The input that is reproduced in the experiments must match exactly the reference input that is applied to the model so that in both cases there is no contamination due to shaker structural dynamics. High quality test input control is highly desired for the purposes of

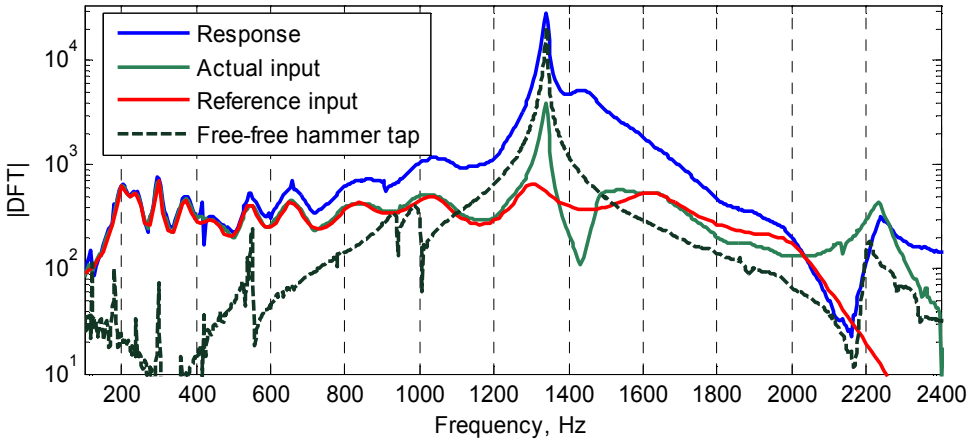

Figure 6.8. Frequency Domain Representation of Test Response.

Domain elements show achieved input, reference input, and hammer tap.

model validation.

6.4 Dealing With Test Control Issues

During subsequent testing, certain aspects of the test setup were modified. The initial testing revealed that the fixed-base mode of interest was close in frequency to the undesired free-free mode of the shaker armature/test item combination. Lack of mode frequency distinction creates difficulties calculating the correct drive signal.

Measurements also indicated that the base of the test item was not rigid at these frequencies. Acceleration gradients were present around the base of the fixture. These gradients created difficulties in picking the location to define as the input, because a different input would be calculated depending where the control accelerometer was located on the base.

Adapter plate To address these issues, an 18-in wide adapter plate 1.5-in thick and weighing approximately 70 lb was added to the top of the armature. The armature weighs 100 lb, while the test item and fixture weigh a total of 25 lb. The addition of the adapter had two major effects. First, it shifted the complete system fixed-base mode and axial armature resonance in a manner that allowed more separation from the fixed-base mode.

Once the peaks and notches are better separated, the estimate of $H(w)$ is more closely matched in the vicinity of the fixed-base modal frequency and noisy notch shown in Figure 6.4 on page 231.

Average Control Scheme The test also was controlled by the average response of three different locations at the fixture base. This was accomplished by feeding the response signals through a summing amplifier. Most shaker shock control algorithms are based on a single input, single output model using only one signal as a desired pulse, $d(t)$. Through use of the summing amplifier, the controlled signal is the average of three individual measurements, equally spaced around the fixture base. This scheme worked well largely because the experimental setup was axisymmetric. One must be careful and thoughtful when performing time-synchronous averaging of structural motion to avoid undesirable results. In the end, averaging the control locations in this axisymmetric setup is an excellent way to provide consistent inputs to each different test item.

Drive Update A form of drive update can be the final tool used to ensure good reproduction of the reference input. Updating the drive after each pulse is a way to add a kind of feedback loop to the normally open-loop shock control algorithm.

There are two ways to update the drive [60]. One method involves correcting the drive based on an error signal derived from the difference between the actual return waveform and the desired waveform. The correction factor is derived in the frequency domain based on the error spectrum, and then applied in the time domain to the drive signal. However, if much of the error comes from nondeterministic sources, then this drive update technique can go unstable, causing a highly erroneous drive calculation. Even though the hardware in this test is nonlinear, it behaves in a fairly consistent manner during each pulse and the experiments benefited from this technique. A second method is to update the system transfer function with each pulse. This tends to account for nonlinearities in the structural response, especially those that are amplitude dependent and cause changes in the system transfer function from initial low-level tests to the final full level tests.

The Jaguar control software that was used for this test utilizes a combination of these two techniques. Because this test is performed on mock hardware there is little risk of damage by multiple pulses applied at nominal levels. By applying multiple pulses to the structure and updating the drive after each pulse, the input can be recreated very accurately. Figure 6.9 shows an example of the quality of repeatability.

Final results In the end, nine combinations of hardware were each tested three different times using the techniques described here. The inputs were repeatable in each separate test, and the effects of unwanted modes of the shaker system were eliminated each time. Figure 6.10 shows the quality of reference pulse reproduction for all tests.

6.5 Conclusion

This section has addressed several issues that arise in the effort to gather high quality shock responses for the purposes of model validation using electrodynamic shaker input. To run the best test possible, one must first understand the basics of the particular shaker shock control algorithm.

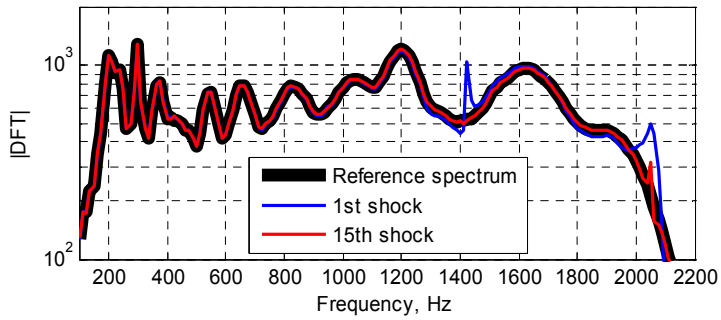

Figure 6.9. Example of Benefits with Drive Updates.

Pictured is the reference input spectrum along with the initial pulse (after system characterization) and 15th pulse (utilizing drive update).

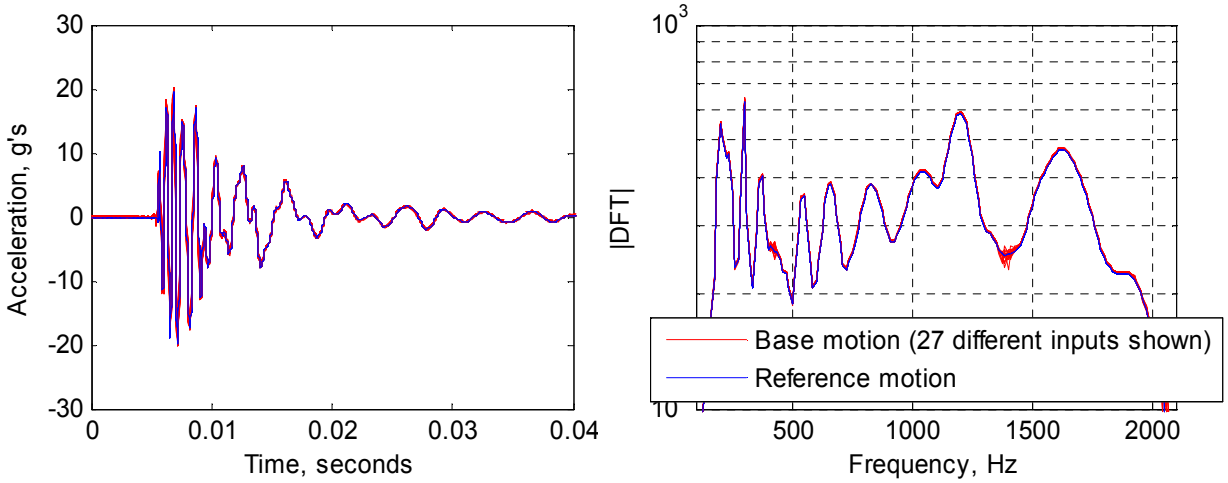

Figure 6.10. Time and Frequency Domain Plots.

Shown are the reference pulse and all 27 controlled inputs.

This hardware exhibits properties that caused problems in the calculated transfer function. The notch causes frequency smearing in the drive and generally created inconsistent controllability between different test hardware.

The variability in stiffness of the bolted joints causes the base-driven axial mode of the hardware to vary. The variability is also included in the model and is one of the important features of interest when trying to understand or model jointed interfaces. Inputs that are reproduced in experiments must exactly match the reference input that is applied to the model with no contaminating effects from test equipment structural dynamics.

Chapter 7

Quasistatic Load Testing of Bolted Joints

Brian R. Resor and Brendan R Rogillio

7.1 Background and Introduction

Experiments utilizing quasistatic loading of jointed interfaces, in theory, can yield much useful data describing the important parameters of a jointed interface. Quasistatic loading often can be a useful experimental technique because associated modeling can be relatively easy to accomplish. Characteristics that have been studied, and that are included in this chapter, include elastic bilinear stiffness, macroslip force, bolt pinning behavior, and relationships with bolt preload. Attention to detail is essential in the design and implementation of the experimental measurements to ensure that the results are useful and meaningful.

This section illustrates examples of quasistatic experimental investigations on two, simple, single, bolted joint elements that yielded useful insight into the quasistatic loading regime. The first is a simple flat lap joint that has the joint interface inline with the applied load. The joint also includes an instrumented bolt so that the preload in the interface due to the bolt can be known. The second is an inclined lap, bolted joint, including a rather complicated geometry. The complex nature of this bolted joint gives rise to load displacement curves with a much more complicated character.

7.2 Quasistatic Experiments

Attention to detail is also important in the design and implementation of the experimental measurements associated with quasistatic load testing of bolted interfaces. Often, load frames are utilized for characterization of material properties for loads up to and including failure of the material. Forces and displacements, as well as associated strains, are typically rather large. Instead, the majority of tests performed on bolted interfaces and discussed in this section are performed at low loads and with very small displacements.

7.2.1 Choice of Load Frame

The experiments shown in this section were all performed on a 22,000-lb force, MTS, servo hydraulic uniaxial load frame. Smaller load frames are superior to very large load frames for this work. It will be shown later in this section that the loads associated with initiation of macroslip and bolt pinning are, relatively, very small. Small capacity equipment is desirable for single joint element testing.

7.2.2 Force Measurement

Because the forces associated with these experiments are very low, it is also important to use a force transducer with a full range that is not excessive so that the force measurements are not below the noise floor of the measurement. A 3,000-lb force gage was used in all the experiments shown in this section.

7.2.3 Displacement Measurement

Often it can be hard to find a clean and robust method to instrument the joint specimens to yield useful and accurate data. When testing singular joint interface elements as described here, the installation is relatively straightforward because there is adequate space around the region of interest for extensometer installation. It is important to note the attachment locations of the displacement transducer for future reference. The measured displacement or strain can be very sensitive to transducer location if large strain field gradients are present in the hardware.

The displacement measurements for this investigation were made by two different methods: 1) a mechanical extensometer and 2) a Linear Voltage Displacement Transducer (LVDT). The earlier experiment utilized the mechanical extensometer. It yielded useful information, but there was a noticeable amount of noise in the measurement. Later experiments utilized the LVDT. The LVDT yielded very clean, low noise, measurement signals.

7.2.4 Fixtures

It is important to install these specimens into the load frame in a way that promotes natural alignment of the two mating sides of the interface. As discussed in other sections of this handbook, interface behavior can be very sensitive to side loading or tilting of the surfaces relative to one another. In this case, spiral washers were used in line with the specimens and the force gage to enable the best possible fit.

7.3 Quasistatic Load Tests of a Flat Lap Joint

The simple flat lap joint has a joint interface that is in line with the applied loads from the load frame. The joint also includes an instrumented bolt so that the preload in the interface due to the bolt tension can be known and also varied. Figure 7.1 shows the experimental setup for the flat lap joint experiments.

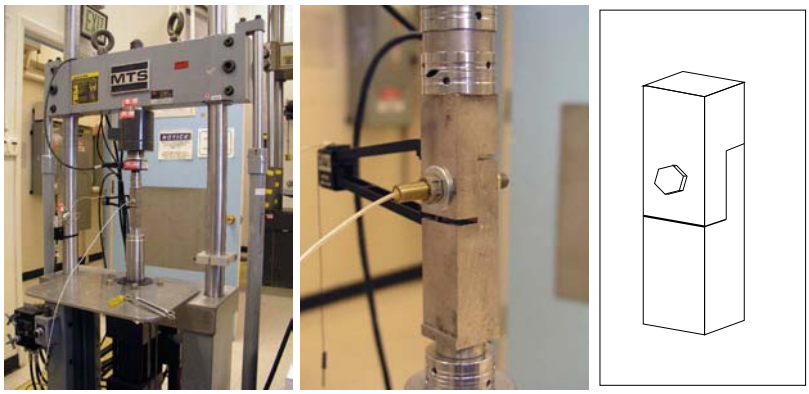

Figure 7.1. Quasistatic Load Test Frame Setup.

Shown are the flat lap joint, instrumented single bolt (including force transducer), and mechanical extensometer. The graphic on the right highlights the orientation of the specimen.

7.3.1 Demonstration of Bolted Joint Interface Behavior at High Loading

Most work in this handbook deals with understanding of microslip and macroslip in jointed interfaces. However, if a bolted joint is loaded with enough force, more extreme effects occur on the load curve. Figure 7.2 shows actual experimental data illustrating the various types of bolted joint behavior. Starting with no load and zero displacement, the region of microslip is relatively small and stiff (high slope) compared to other types of behavior that are seen in this plot. This hardware then moves into a rather distinct region of macroslip, where the contact patch in the interface begins to reach a point where it is mostly slipping. As the shear force in the contact patch become high enough that friction is fully overcome, the whole interface begins to slip. Within the region of macroslipping, there are relatively large increases in displacement for small increases in force. It should be noted that experiments invoking large amounts of macroslip will quickly deform the surfaces of the interface in an adverse manner. Such experiments should be done only after other data is gathered at lower forces. Finally, as the empty space between the edge of the bolt hole and the edge of the actual bolt comes to a close, the surfaces contact and a new force enters into the picture. At this point, the stiffness of the load curve is governed primarily by the effective shear stiffness of the bolt.

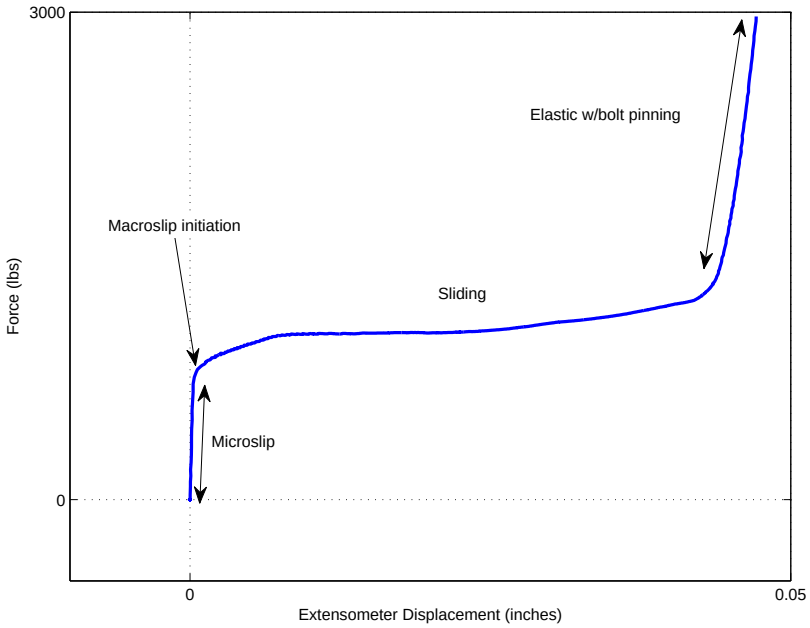

Figure 7.2. Applied Load vs Extensometer Displacement.

Example is a flat lap joint undergoing all stages of behavior (microslip, macroslip/sliding and bolt pinning.)

7.3.2 Macroslip Force Threshold

The threshold of macroslip force depends on the preload that the bolt is applying to the interface. Figure 7.3 shows load curves for eight different bolt preloads. In all cases the initial linear elastic stiffness is relatively consistent. The occurrence of macroslip is at a distinctly different level for each preload. Also notice on this plot the apparent measurement noise in the displacement measurement of the mechanical extensometer.

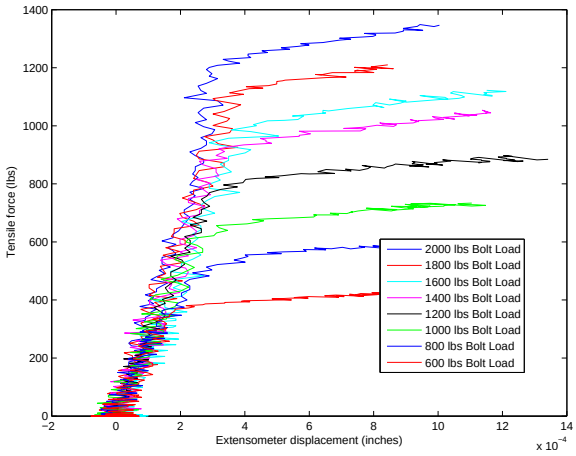

Figure 7.3. Tensile Force vs Extensometer Displacement.

Example is a flat lap joint with instrumented bolt; plots include several bolt preloads.

The macroslip forces for each bolt preload can be determined and the data plotted to show the relationship. Figure 7.4 shows the data along with a straight line fit of the data, which passes through zero. The slope of this curve, 0.63, is the effective friction coefficient for the interface.

7.4 Single-Leg, AOS, Quasistatic Load Tests

The inclined lap bolted joint, known in this handbook as the AOS single-leg, contains a rather complicated geometry, and so the contact in the joint interface is not as simple and straightforward as for a simple flat joint. Similar tests were performed on the nine combinations of stainless steel, AOS, single-leg specimens to help us understand the behavior of each. The tests utilized the same equipment and setup as the flat lap joint tests, and are seen in Figure 7.5. The AOS, single-leg tests utilized an LVDT for displacement measurement. Compared to the mechanical extensometer, the LVDT yields cleaner and higher quality measurements of the small displacements.

Figure 7.6 shows the load curves for selected, AOS, single-leg hardware combinations. In

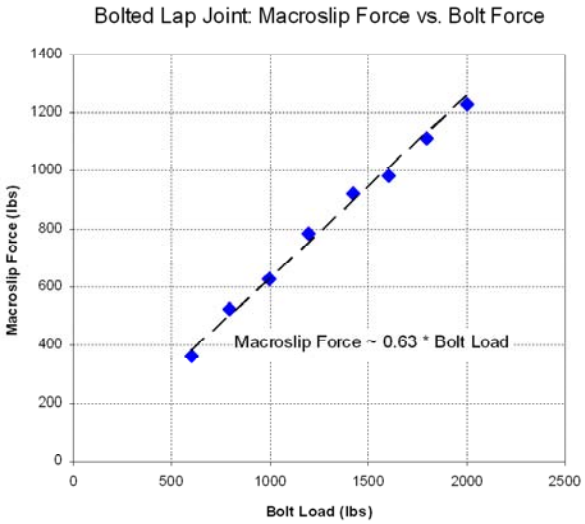

Figure 7.4. Force (tension) at Macroslip Initiation vs Bolt Preload.

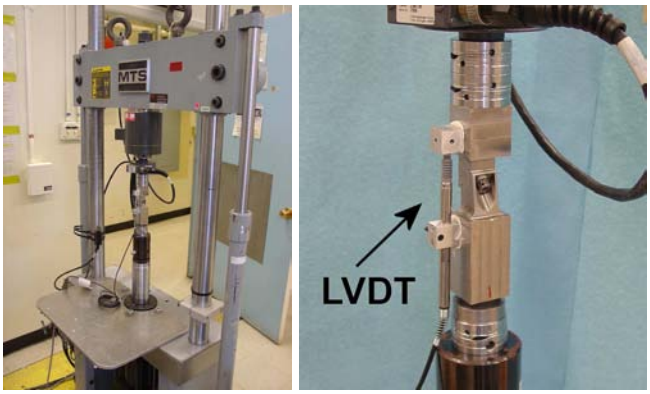

Figure 7.5. Test Setup for Quasistatic Loading of AOS, Single-Leg Joint.

keeping with typical recommended practice, each combination was disassembled and reassembled multiple times to aid our understanding of assembly variability. The parts were taken apart and reassembled three times.

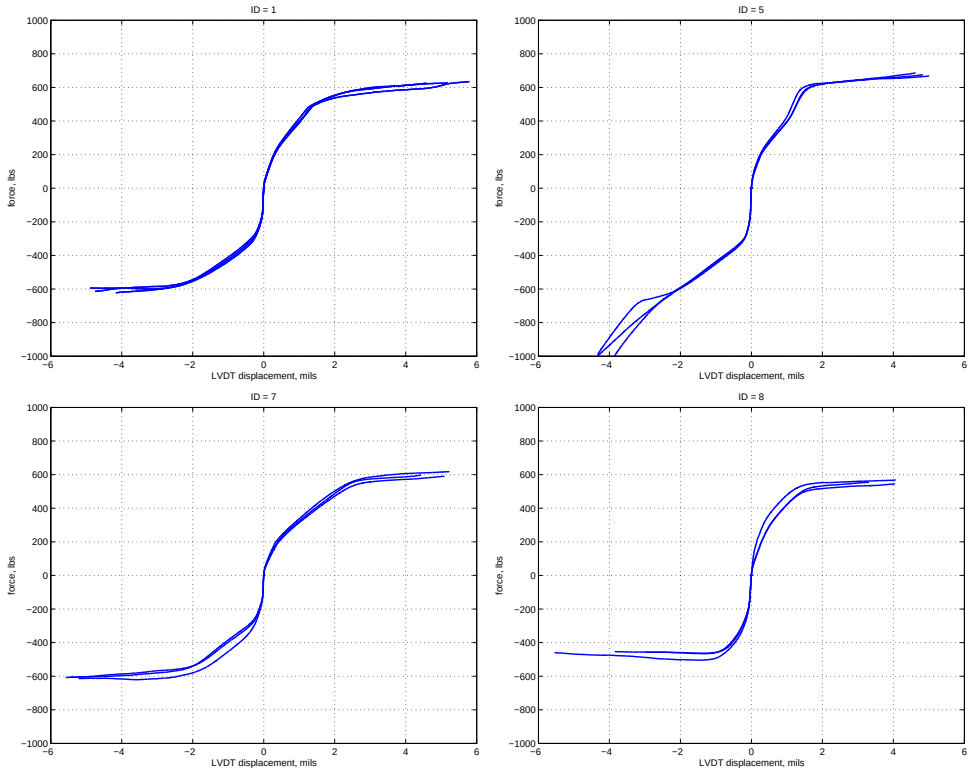

Figure 7.6. Tension and Compression Quasistatic Load Curves for AOS, Single-Leg Combinations A-1, B-2, C-1 and C-2.

It is rather important to also note that these plots were generated by combining the data from tension tests and compression tests on one axis. The tension and compression test were performed independently because of the issues that variability in the fixture introduces as the load passes through zero between tension and compression.

Figure 7.6 shows that the different combinations of hardware can exhibit rather different load curves. Each of the hardware combinations behave basically as one might expect, with some differences that are due to part-to-part and assembly variations. These specimens do not exhibit the apparently clean and simple linear stiffness that was shown for the flat lap joint. Also, these specimens clearly exhibit a bilinear stiffness and are stiffer in compression. Higher stiffness in compression is reasonable due to the fact that the interface is inclined relative to the applied load. There is a coupling effect between applied load and interface preload, and as a result the interface pressure in this specimen tends to increase in compression and decrease in tension.

In almost all cases, the threshold of macroslip in the joint is fairly obvious, with the exception

of hardware combination B-2 where the macroslip threshold is not visible in compression. This is likely due to lack of alignment of the experiment hardware.

Figure 7.7 contains load curves for all nine combinations of hardware. The variability arising from different parts and assemblies influences the results.

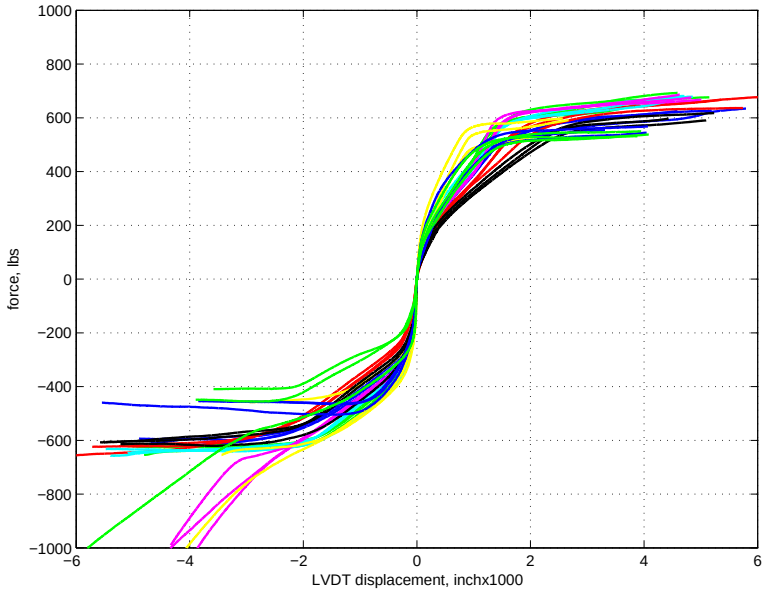

Figure 7.7. All Tension and Compression Quasistatic Load Data for AOS, Single-Leg Combinations.

As always, it is good practice with jointed interface experiments to also test a monolithic specimen having the exact geometry as the jointed hardware. Figure 7.8 shows the load curve data for these test runs, and these indicate possible issues with the experiment setup.

The tension data, after a small initial displacement realignment, is very linear and repeatable. The compression data indicates potential problems with the test setup. The stiffness of this hardware should be linear in compression as well as tension, but the data indicate otherwise. This hardware is known to be linear so it is likely that there was a problem with either the instrumentation or the hardware alignment for this test. One possibility is that there was bending motion in the specimen that was unaccounted for and that was affecting the measurement.

Neglecting the other potential imperfections in this test, the slope of the solid load curve in tension is linear and easily measurable: 4.0146×10^6 lb/in. Keep in mind that this measured stiffness applies only to the material that is between the gage length of the LVDT. A different stiffness value would be measured if the gage length was larger or smaller because this hardware contained rather large strain field gradients.

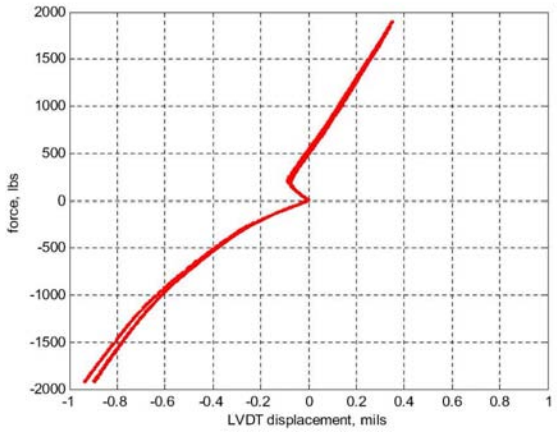

Figure 7.8. Monolithic, AF& F Single-Leg Load Data.

Load vs force curve for tension and compression of the solid, monolithic, AOS, single-leg. The tests were each performed separately.

7.5 Other Work

Other quasistatic test work has been pursued at Sandia in the form of multi-axis loading of slightly larger structures. Figure 7.9 shows a picture of a three-axis load frame that has been designed and manufactured. This load frame is able to apply simultaneous quasistatic loads to component level hardware in an effort to understand coupled loading of multiple joint interfaces.

7.6 Summary

With these techniques, basic information about the jointed interfaces can easily be obtained. Perhaps the most valuable measurement of bolted joint behavior that can be accurately determined using quasistatic loading is the threshold of macroslip. Macroslip threshold is very difficult to measure directly during dynamic experiments.

Little time has been allocated to the development of clean and robust techniques for quasistatic loading of jointed hardware, and opportunities for improvement are numerous. There is a need for better, more robust fixtures for the experiment setup. Ideally, the scheme should show success first by making sensible measurements of a monolithic specimen in both tension and compression. Then, there would be more trust in the other measurements that are being made with jointed hardware.

With a clean, robust and gap free experimental setup, one could also measure the hysteretic behavior of the joint loading through both tension and compression. This information would allow

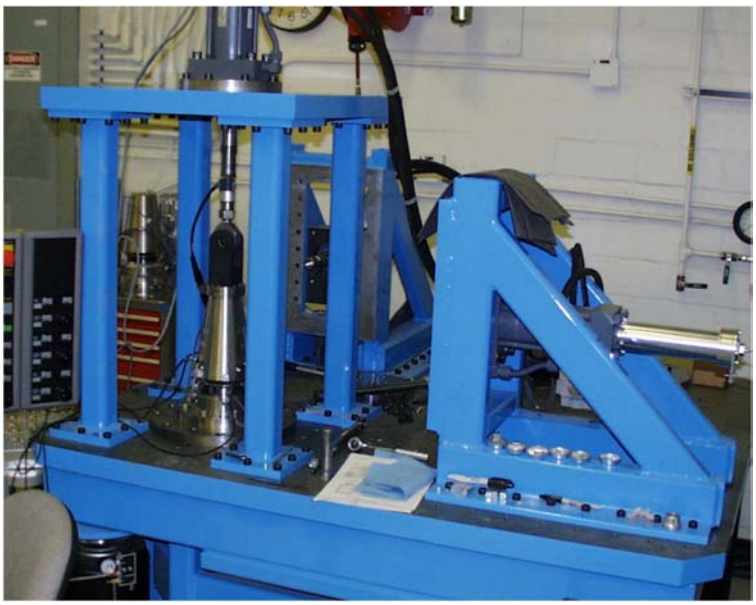

Figure 7.9. Multiaxis Quasistatic Load Frame.

more accurate measurement of quasistatic energy dissipation.

Since analytical modeling of the interface contact patch is coming into wider use, validation of models with quasistatic load are valuable for this purpose. Often the models are actually exercised with quasistatic loads, rather than dynamic loads. A clean and robust quasistatic experiment would serve as a valuable model validation tool in the future.

Chapter 8

Experiments on Component Hardware

Danny L. Gregory and Brian R. Resor

This section describes a bolted joints experiment that involves multiple, discrete joints employed in a single component level simulation. The joints under investigation in this structure are System A, AOS joints - the same joint that was discussed extensively when studied individually in Section 5.3. That hardware is shown in Figure 8.1 and discussed in detail later in this chapter.

A series of experiments is performed on the three-jointed structure to gather a variety of data describing nonlinear structural dynamics of a component mock representing System A-1 AOS. The first set of data consists of a sinusoidal, steady state dynamic input into the mock hardware. The input is achieved by performing sine sweeps over a bandwidth encompassing the fixed-base axial resonance. (Corresponding investigation of individual joints in Chapter 3 of this report required the used of a large reaction mass on the end of the specimen opposite to the shaker.)

Next, transient excitation tests are performed on an electrodynamic shaker. Two types of transient experiments are performed. Each used the same equipment and means of control, but each was meant to reproduce different input waveforms.

The first waveform is generically called a tailored transient.The purpose of the tailored transient is to excite the physics of interest in the mock hardware. In this case, the nonlinear behavior of the bolted joints are tested by tuning the energy in the pulse in a manner that excites the first axial mode of the hardware. A wavesyn component accomplishes the excitation, where the amplitude and number of wavesyn half cycles were chosen in a manner that optimizes response levels of the hardware for validation.

The second transient test is representative of a waveform that more closely resembles an actual shock that might be seen by hardware in a real test or in actual use. The second transient is called a blast simulation because the pulse contains components at multiple frequencies. The levels are scaled such that approximate loads in the joints do not exceed those required for macroslip.

Multiple hardware realizations and combinations are tested once again in both transient tests. Nine configurations of hardware are tested and each assembled/disassembled three times. This combination resulted in 27 sets of response data. The bolted joints were reassembled after each transient. For the tailored input, response ring-downs were postprocessed to determine energy

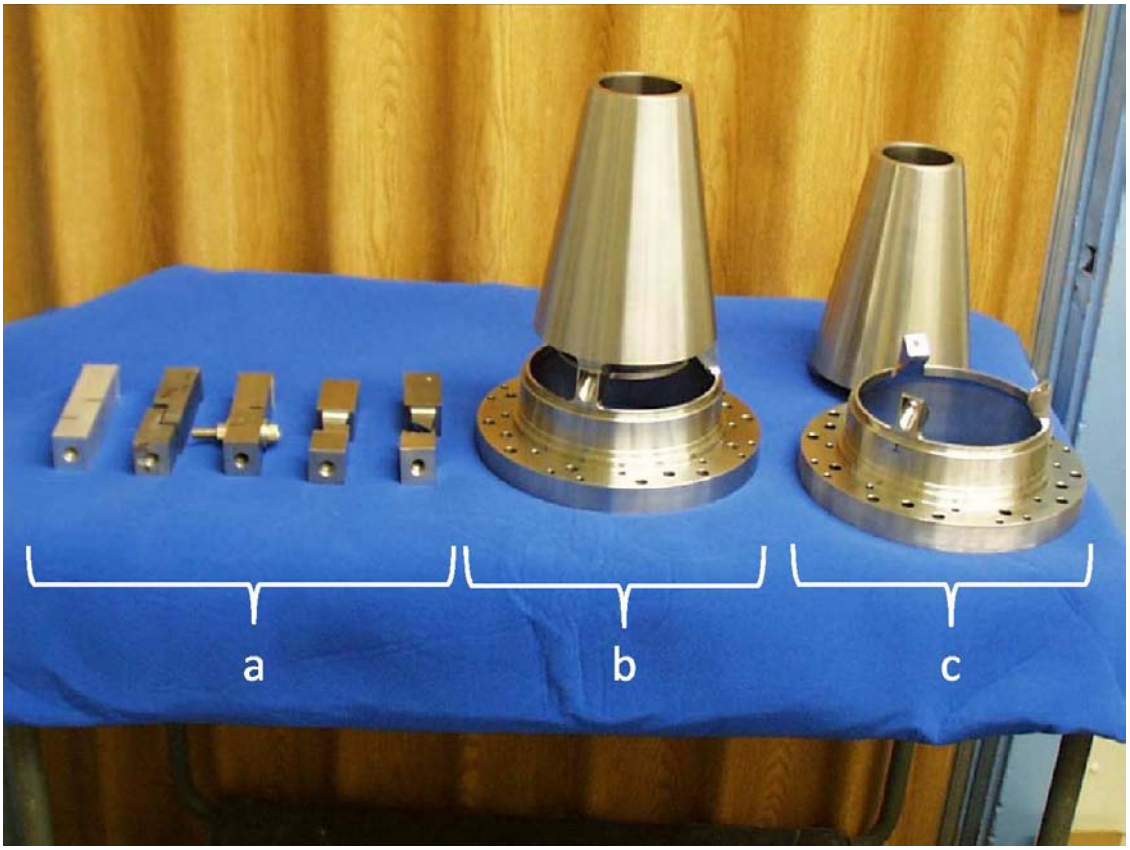

Figure 8.1. Mock Hardware.

Mock hardware from left to right: (a) Single-leg solid and jointed, (b) Three-leg solid (monolithic) hardware representing a mock AOS and truncated base attachment location, and (c) One pair of jointed mock hardware.

dissipation of the axial mode.

As an exercise, the response of this structure was predicted using a finite element model with joint models populated by parameters deduced from single-leg experiments. Blast simulation was performed with the knowledge that joints of the three-legged, statically indeterminate structure were preloaded differently than the single-leg experiments used to parameterize the joint models. The single-leg specimens were conformal and self-aligning, while the three-legged structure had to be compressed mightily to close the joints. The test sequence was chosen such that combinations of hardware were sampled evenly to prevent bias in results due to wear on the parts.

Finally, it is important to point out that all data in this section are calculated to yield energy quantities *per leg*. It is an important distinction because the hardware contains three discrete joints.

8.1 Hardware

Test specimens capturing the local geometry and overall mass of the connection and actual hardware for System A-1 AOS were fabricated as shown in Figure 8.1. Actual mating components of a full scale system consist of both titanium (bottom) and stainless steel (top), but both halves for this study are made from stainless steel so that a monolithic specimen could be fabricated and used for baseline dissipation experiments and to quantify unknown attachment compliances at the base.

The oversize hole in the base attachment location along with a lack of a positive alignment feature,such as a locating pin, enables significant variation in installation alignment to occur unless special care is taken. The oversize hole in the leg and the interaction of the interface and the bolt head with the hole is a suspected major source of variation in the response of the system for different assemblies of the same joint. For this reason, the AOS is assembled randomly each time and the bolts are tightened in a random order. Random assembly means in this case that the alignment of the AOS mock on the legs is made to look good to the naked eye, the same process that would be used in regular production assembly. Afterwords, the bolts were tightened in random order. First, they were each tightened snugly. Then, they were tightened to the specified torque of 85 in-lb.

The three-leg specimens with bolted joints approximately represent an SDOF system. The three joints of the specimen represent an equivalent nonlinear spring in the system while the AF&F mass mock represents the rigid mass (Figure 8.2).

8.2 Joint Force Determination

The axial force in each of the three joints is assumed to be equally distributed and directly proportional to the mass times the axial acceleration of the AOS mass. For example, a sine dwell where the 12-lb AOS mock is controlled at 100 Hz and 100 g, the force in each leg would be

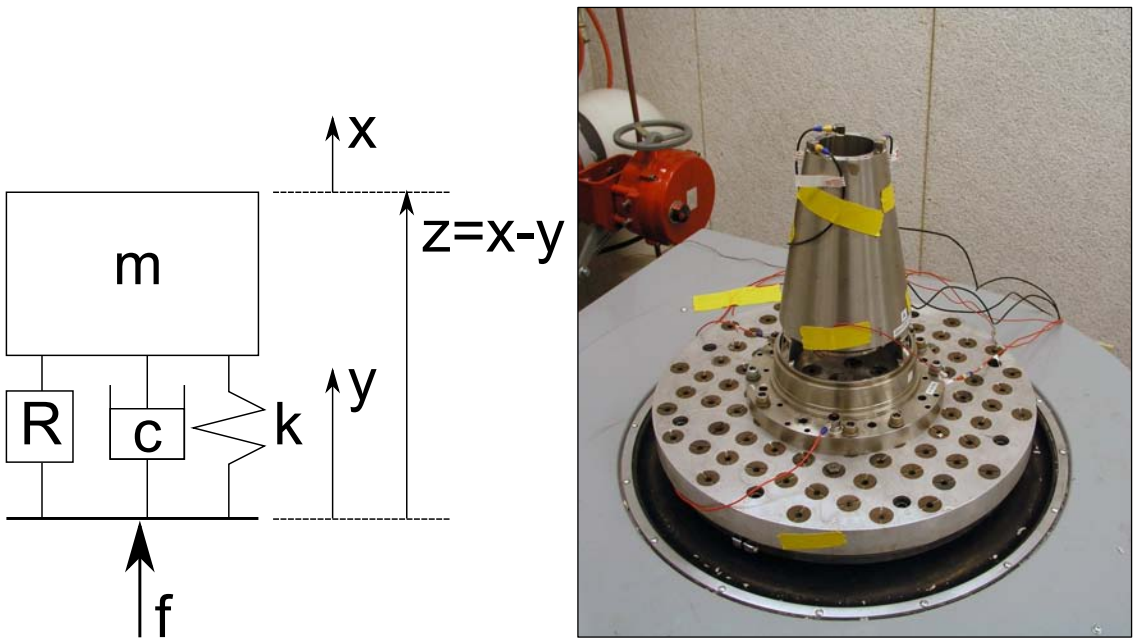

Figure 8.2. Simplified Model of SDOF Experiment.

approximately $100 \times 12/3 = 400$ lb.

8.3 Response Measurements and Energy Dissipation

An expression (Equation (5.6)) for energy dissipation per cycle of a single degree of freedom system with mass m when the frequency of forced harmonic motion is $\omega = \omega_n$ was derived in Section 5.1.2.1 and is repeated here as Equation (8.1).

$$D = 2\pi\zeta KA^2 = 2\pi\zeta M\omega_n^2 A^2 \tag{8.1}$$

where ζ is the fraction critical damping,
M is the system sprung mass,
K is the linearized system stiffness
A is the amplitude of oscillation acceleration
and $\omega_n^2 = K/M$.

The three-leg hardware is not perfectly axisymmetric. The simplified model implies that for a perfectly axial input to the base of the AOS the response will also be perfectly axial in nature. The small geometric asymmetry of the structure results in at least a small amount of bending deformation from axial excitation. Also, Equation (8.1) assumes a rigid mass mock. Because the deformation - and hence the kinetic energy - is distributed along the height of the specimen, the

hardware is not perfectly representative of a true SDOF with rigid mass. In fact, measurements indicate that there is a seven percent difference in operating displacements between the bottom surface and top surface of the AOS mock at the axial mode of the jointed assembly. Though the mass mock is not perfectly rigid, the approximation an SDOF is still pretty close and will be used in this investigation.

With all the above in consideration, the overall acceleration waveform of the mass, A_m, is determined by time synchronous averaging of six separate gages: three placed on the top surface of the AOS mock and three on the bottom surface. All gages are oriented to measure in the axial direction. Also, all the gages are located either right next to or right above an AOS leg. Each individual axial acceleration measurement contains a component of acceleration from the elastic deformation of the mock AOS and also from bending effects due to asymmetry. Averaging of all six gages helps eliminate the contributions due to the elastic and bending effects and to ensure that the averaged motion of the mock AOS represents the acceleration of its center of mass.

8.4 Excitation

The excitation for the experiments is provided with a T2000 Unholtz-Dickie electrodynamic shaker. A Spectral Dynamics 2560 Vibration Control System is used to generate and control the excitation waveforms used in the experiments. The control system was also used to acquire the magnitudes of the sinusoid fundamental through the use of an on-board bandpass filter. The techniques for data acquisition and analysis are similar to that described in Chapter 3.

8.5 Experimental Results Steady State Sine Vibration Experiments

Experiments are performed to measure the energy loss per cycle for a sinusoidal input force over a range of loads: 100, 300, and 500 peak pounds with the specified bolt torque of 85 in-lb.

8.5.1 Solid-Leg Baseline Experiments

As a standard practice in this program, a solid (no bolted joints) piece of hardware is manufactured. It looks exactly the same as the jointed hardware, but is monolithic. It is used to baseline repeatability of the three-leg experiment attachment boundary condition as well as to quantify miscellaneous dissipation mechanisms.

The dissipation measurement results for the solid three-leg hardware are shown in Figure 8.3 for four different runs through the set of loads. The data for the solid single-leg is very repeatable, which is what one expects from a linear structure without the uncertainty of a bolted connection.

The average slope of the solid specimen energy curves is 1.99, indicating that their behavior is linear. Linear behavior is exhibited by energy dissipation curves with slopes of exactly 2.0.

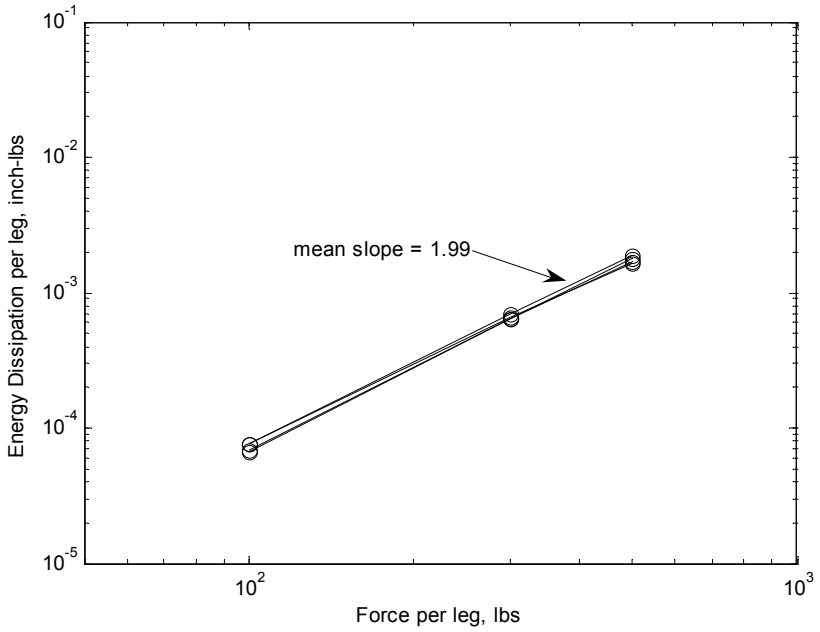

Figure 8.3. AOS Solid, Three-leg Hardware, Steady State Energy Dissipation.

8.5.2 Jointed Experiments

Figure 8.4 shows a plot of all 27 energy curves from the jointed three-leg hardware experiments along with energy dissipation curves for the three-leg solid hardware. Note that the jointed hardware exhibits greater variability in energy dissipation. The jointed hardware also exhibits increased average slope, averaging 2.30, indicating nonlinear behavior.

The population of calculated slopes is illustrated in Figure 8.5, showing the power-law dissipation sloped to lie, fairly evenly, between 2.2 and 2.4. Of interest to note is that a slope of 2.30 is lower than all previous experiments on the AOS inclined lap joint (including single-leg steady state and single-leg dumbbell experiments). Previous experiments at the single joint level yield slightly higher slopes closer to 2.6. The difference should not be too surprising: the single-joint experiments were designed to cause a flush contact across the joint interface while it would be very surprising to have that kind of contact among the three joints in the statically-indeterminate, three-legged structure.

Figure 8.6 shows a comparison of jointed three-leg dissipation (energy dissipation per leg) and jointed single-leg dissipation. When the three-leg hardware energy dissipation is compared to the

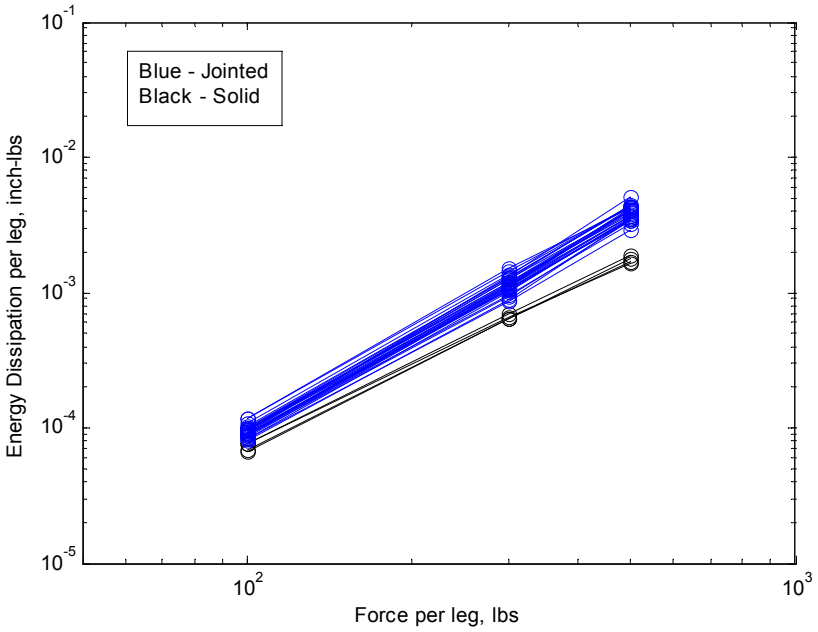

Figure 8.4. Jointed and Solid Calibration Data.

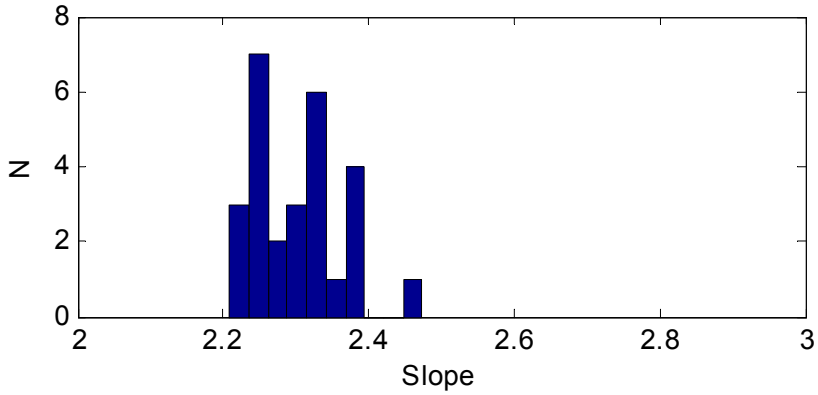

Figure 8.5. Three-Leg Fits.

single-leg they are generally similar. Upon close examination, the three-leg hardware tends to have less variation in dissipation. The three-leg data also tends to exhibit an overall lower slope than the single-leg data. The mean slope of the three-leg hardware data is 2.30 while the mean slope of single-leg hardware data is 2.55.

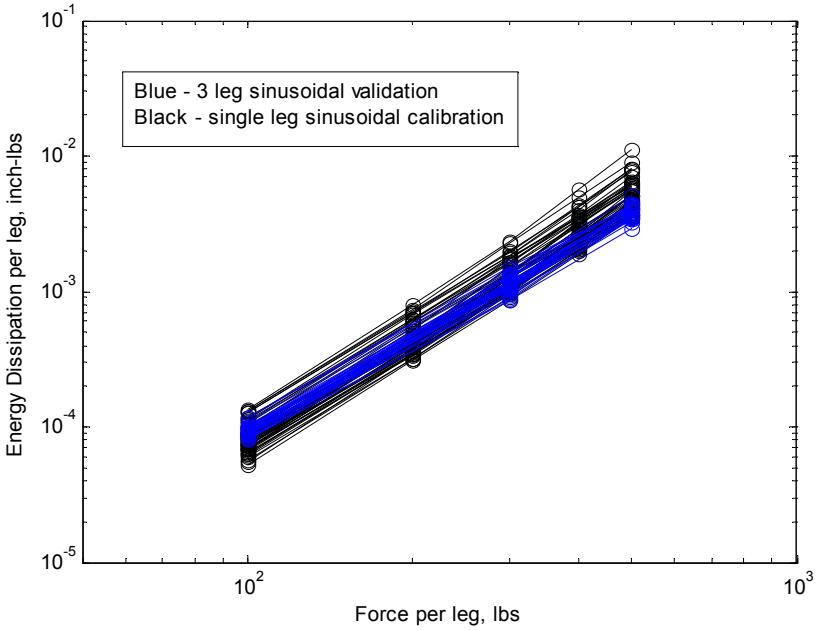

Figure 8.6. Leg Configuration Hardware Comparisons.

Comparison of energy dissipation data for three-leg hardware steady state experiments to single-leg hardware steady state dissipation experiments.

8.5.3 Use of The Sinusoidal Dissipation Data

This energy dissipation data is stored for potential use as whole-joint model calibration data. However, something is disturbing about this data set. In order to calculate ζ at each load, a single reference point had to be chosen. The chosen point was at the shaker armature center insert. This location was chosen after discovering the high sensitivity of measured ζ and resonant frequency to reference locations. While the armature center insert is a logical location to choose due to its symmetric nature and due to the fact that it is below all bolted joints, the authors believe that there might still be unknown dynamics affecting the measurement of ζ when referencing the data to this point.

Basically, the fact that the overall slope of the energy dissipation curves is low is unsettling because it tends to hint at the presence of an extra linear dissipation mechanism in this setup that is not present in other experiments. Discussions in the next sections describe energy dissipation

measured during transient excitation tests. Those data are more sensible to the authors and also happen to agree more closely with data from the single-leg experiments.

8.6 Experiment Results Transient Experiments

Transient tests are performed on the electrodynamic shaker in order to gather response data at elevated bolted joint loads. (See Figure 8.7.) Two different controlled, transient inputs are applied to the base of the mock AOS base attachment location fixture: 1) a tailored wavesyn pulse with a single frequency component and 2) a frequency rich pulse composed with decayed sinusoids.

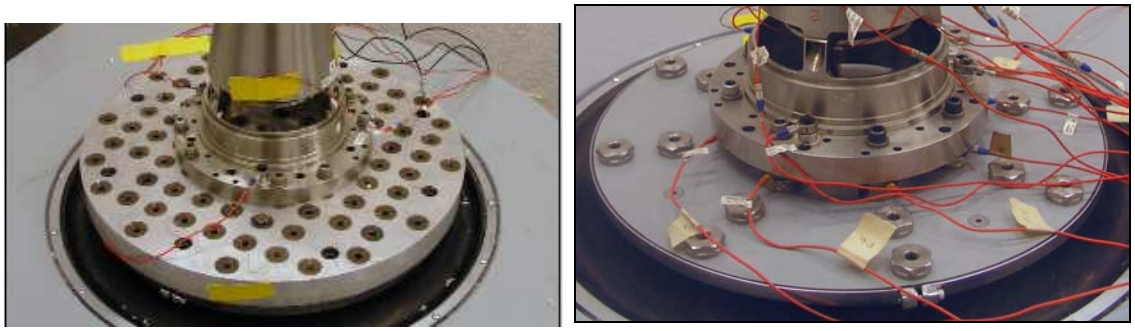

Figure 8.7. Test Fixture Arrangement.

Photo of test fixture setup both with (left) and without (right) extra adapter plate.

Vibration shakers provide a versatile and controllable excitation source for validation experiments but there can be challenges in gathering high quality model validation responses from these tests. This subsection will discuss the challenges and then will show the results from each type of transient input.

8.6.1 Shaker Shock Control Issues

The issues that have been described in Chapter 6 are directly applicable to this experiment. This test hardware exhibited properties which made it a very challenging shaker-shock test for electrodynamic shakers. There are three significant reasons for the difficulties: 1) shaker shock control is achieved using open loop control, 2) the control algorithm is based on linear assumptions, and 3) the control algorithm gets feedback from a single point.

8.6.2 Structural Tuning and Control Location

Initial tests reveal that the frequency of the fixed-base mode of interest, the axial mode, is near the undesired free-free mode of the shaker armature and test item. This creates difficulties calculating the correct drive signal. Measurements also indicate the base of the test item is not rigid at these frequencies and there are acceleration gradients around the base. These gradients created difficulties in picking the location to define as the input because a different input would be calculated depending where the control accelerometer was located on the base.

To address these issues an 18-inch adapter plate with a 1.5-in thickness weighing approximately 70 lb was added to the top of the armature. The armature weighs 100 lb and the test item and fixture weigh a total of 25 lb. The addition of the adapter shifted the system free-free mode and axial armature resonance in a manner that enabled more separation from the fixed-base mode.

With the peaks and notches separated, the estimate of $H(\omega)$ is better in the vicinity of the fixed-base modal frequency and the noisy notch associated with armature resonance. The addition of the adapter plate also provides a more desirable boundary condition in that it enforces a more fully fixed surface at the bottom of the fixture. The more rigid base reduces the acceleration gradients making the assumption of uniform base acceleration more realistic. Previously, the surface was not fully supported because it rested on discrete points at each armature insert and so the base flange was unsupported between the inserts. The extra plate creates a more consistent boundary condition for the computational model, which assumes a fully rigid surface at the base.

8.6.3 Input Averaging

Second, the test was controlled on the average response of three different locations at the fixture base using a summing amplifier. (See Figure 8.8.) The shock control algorithm is based on a single-input and single-output model. It expects only one signal as a desired pulse, $d(t)$. Using the summing amplifier, the controlled signal is the average of three individual measurements, equally spaced around the fixture base. The effect is the same as averaging in the time domain of the analog signals.

This fixture exhibits sensitivity in the quality of the control to the control location that is chosen. In other words, as one moves the control location around the base the notch associated with the fixed-base mode of the hardware shifts slightly due to the fact that the fixture base is not totally rigid, even with the addition of the adapter plate. Controlling on the time average of multiple locations tends to average out these effects and, in this case, enables the calculation of a very good drive signal. The calculated drive signal does a nice job of controlling the test.

Additionally, also because of the the large gradients around the base of the fixture and the nature of part-to-part variability, it is impossible to choose one control location that works well for all the different hardware combinations. Averaging the control locations proved to be an excellent way to provide consistent inputs to each different test item.

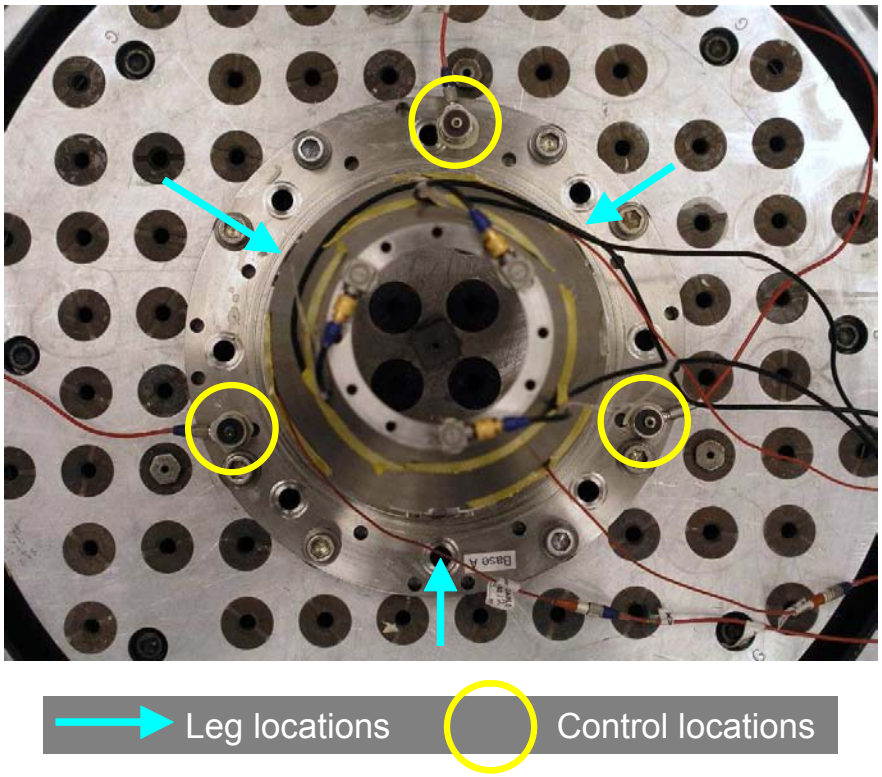

Figure 8.8. Transient Testing Control Locations.

8.6.4 Drive Update Algorithm

The final tool used to ensure good reproduction of the reference input was a form of drive updating. Updating the drive after each pulse is a way to add a type of feedback loop to the normally open loop shock control algorithm.

There are two ways to update the drive [60]. One method involves correcting the drive based on an error signal derived from the difference between the actual return waveform and the desired waveform. The correction factor is derived in the frequency domain based on the error spectrum and then applied in the time domain to the drive signal. However, if much of the error comes from non-deterministic sources, then this drive update technique can go unstable and can cause a highly erroneous drive calculation. Even though the hardware in this test is nonlinear, it behaves in a fairly consistent manner during each pulse and the experiments benefited from this technique. Another method is to update the system transfer function with each pulse. This tends to account for nonlinearities in the structural response, especially those that are amplitude dependent and cause changes in the system transfer function from initial low level tests, to the final full level tests.

The Spectral Dynamics Jaguar^R control software that was used for this test uses a combination of these two techniques. Usually in vibration testing an over test results from subjecting the test hardware to multiple full level pulses in order to get a perfect drive pulse. However, this test was performed on mock hardware so there was little risk of damage. By applying multiple pulses to the structure and updating the drive after each pulse the input was recreated extremely well. Figure 8.11 shows an example of the quality of repeatability.

8.6.5 Experiment Setup

There were six gages on each mock AOS during transient testing: three on the bottom surface of the mock (single-axis gages) and three on the top surface of the mock (triaxial gages). All gages were installed in the vicinity of a leg location. The gages at the top of the mock were installed such that the lateral measurements were made in directions corresponding to radial and tangential alignment. Three axial gages were also installed at the base of the base attachment location fixture. (See Figure 8.9.)These base waveforms were processed such that the average of all three was used as the control variable.

The three base gages were not installed close to the legs. Instead, they were installed at locations mid-circumference between each leg. Doing so reduced contamination of the lightly damped axial mode of the hardware in the control waveform.

The base accelerometers are averaged using an analog summing amplifier. The three signals were combined with weighting factors of 0.33 and the output signal from the summing amplifier was used for the control signal.

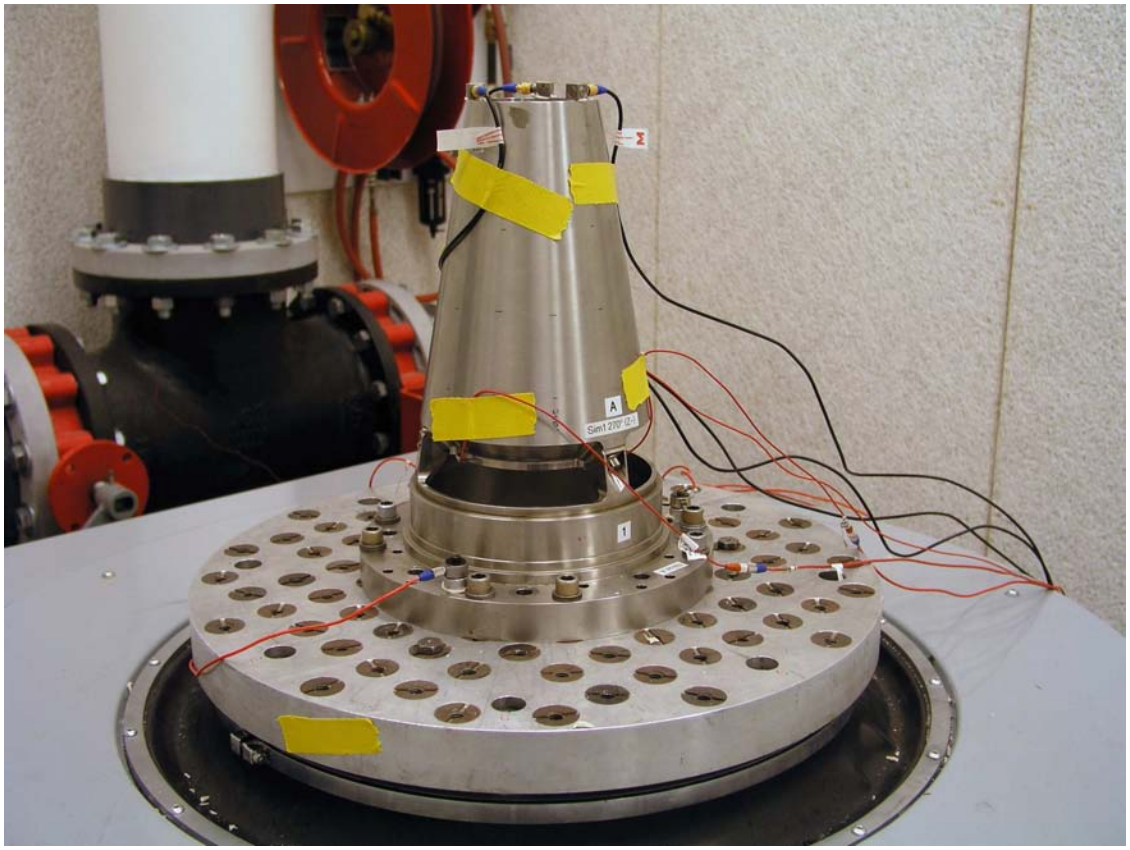

Figure 8.9. Transient Testing Hardware and Instrumentation.

8.6.6 Transient Experiments on Monolithic Hardware

Damping of the monolithic three-leg specimen is extremely low. As a result, the challenges faced in running acceptable shaker shock inputs discussed in the previous sections were magnified. No acceptable tests could be performed on the monolithic three-leg hardware due to the inability to compute a clean drive waveform with the inherent lack of damping. For this reason, response data of the three-leg hardware to the transient environments is not available and is not discussed here.

8.6.7 Wavesyn Pulse Excitation

It is often desirable to selectively excite specific dynamics of a structure in order to study specific behaviors. Almost all the techniques earlier in this Chapter are designed with that goal in mind. The harmonic excitation experiment is a very nice technique to excite a single frequency of a structure in a controlled manner.

In the case of this three-leg hardware we have shown above how harmonic experiments can again be used to selectively excite the axial mode of the hardware. Figure 8.10a shows how focused the energy in a single tone sine wave can be. Example shown is actually a sine waveform with a rectangular window (no window). A steady state harmonic input is even more focused.

The goal is to design a transient input that can be applied to the structure by the electrodynamic shaker and will also excite only the axial mode of the hardware. Neither a half-sine or a haversine input, as would be generated by a hammer or other impact excitation, would be acceptable. These inputs contain a rather broad distribution of input energy throughout frequency. Figure 8.10b shows how the energy in the frequency domain of the half-sine input waveform is widely distributed. Such an input to the three-leg hardware would definitely excite all the additional bending modes of the structure. Their participation is unwanted in this investigation.

A combination of two waveforms works well. A simple wavesyn pulse with only one frequency component will focus the energy at a desired frequency. The number of half cycles in the wavesyn determines the width of the energy band in the frequency domain. Increasing the half cycles approaches an approximation of a steady state sine wave. Decreasing the number of half cycles approaches an approximation of a single half-sine pulse.

Figure 8.10c shows the reference waveform for the single frequency wavesyn pulse used in this test series. The chosen pulse has five half cycles. Five cycles focuses the energy on a particular bandwidth, but at the same time is wide enough to adequately excite the axial mode of various hardware combinations that demonstrate noticeable variation in axial mode resonant frequency.

The energy in this pulse is focused around 1400 Hz to excite the fixed-base axial mode of the mock AOS hardware. The response of the hardware to this input is almost entirely composed of transient ring-down of the fixed-base axial mode. The pulse was controlled for 80 milliseconds so that the responses could decay to a low level. Maximum joint forces were in the range of 200 to 500 lb during the ring-down. Response waveform data occurring outside the controlled pulse

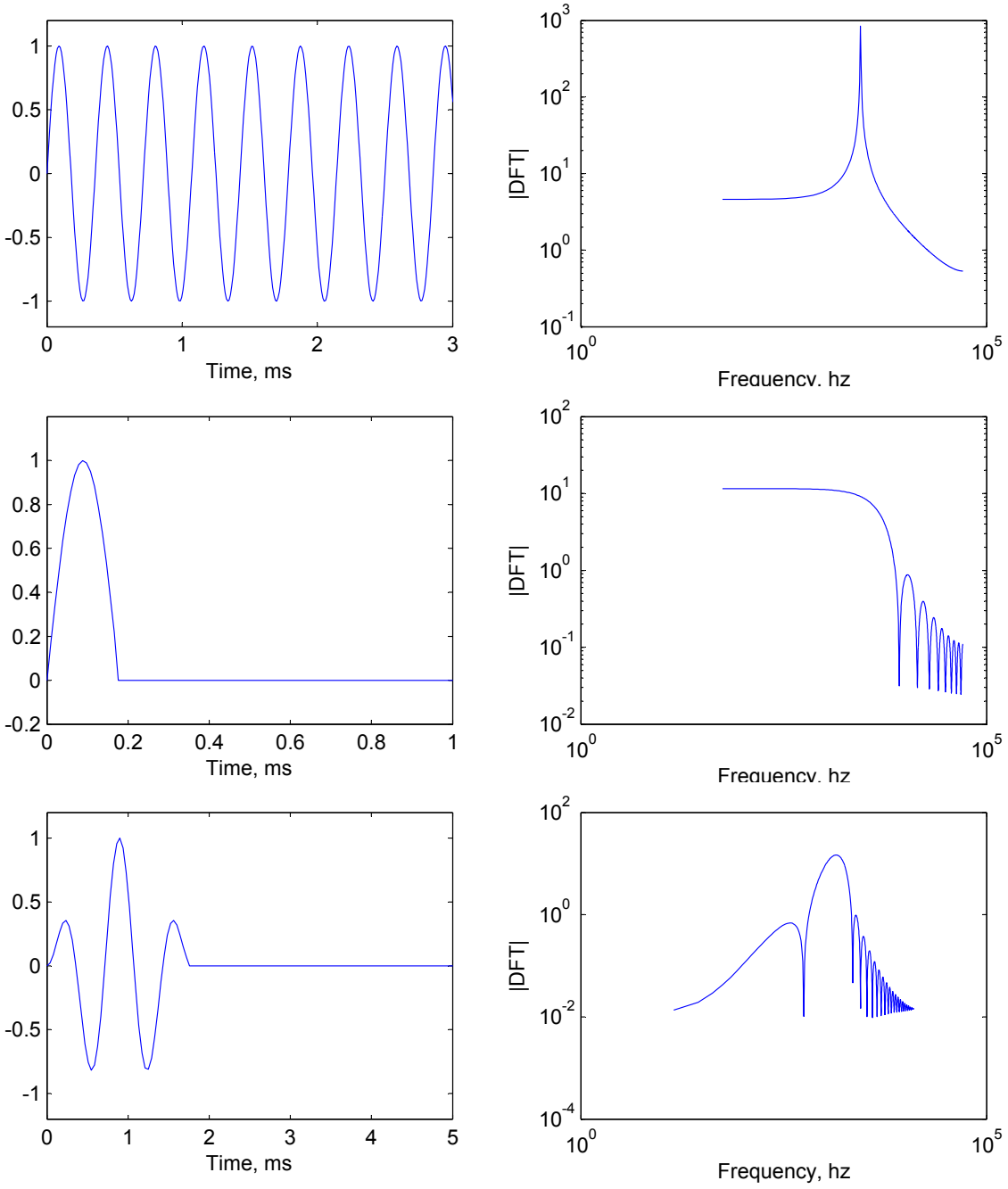

Figure 8.10. Time and Frequency Domain Representation of Transient Pulses.

(a) sine wave with rectangular window, (b) half-sine pulse and (c) five half cycle wavesyn pulse; the chosen reference waveform for input to the three-leg hardware. Overall amplitude is arbitrary and was scaled to achieve desired response levels.

duration of 80ms are not applicable to model validation because they include stiffness and damping effects of the free-free mode of the test item and shaker armature.

Three assemblies each of nine hardware combinations were tested to this input. A total of twenty seven response ring-down data sets were gathered for analysis. The shaker transient tests were conducted according to practices in Section 6. The repeatability and accuracy of the input was very good. (See Figure 8.11.) These response data were representative of a true fixed-base boundary condition.

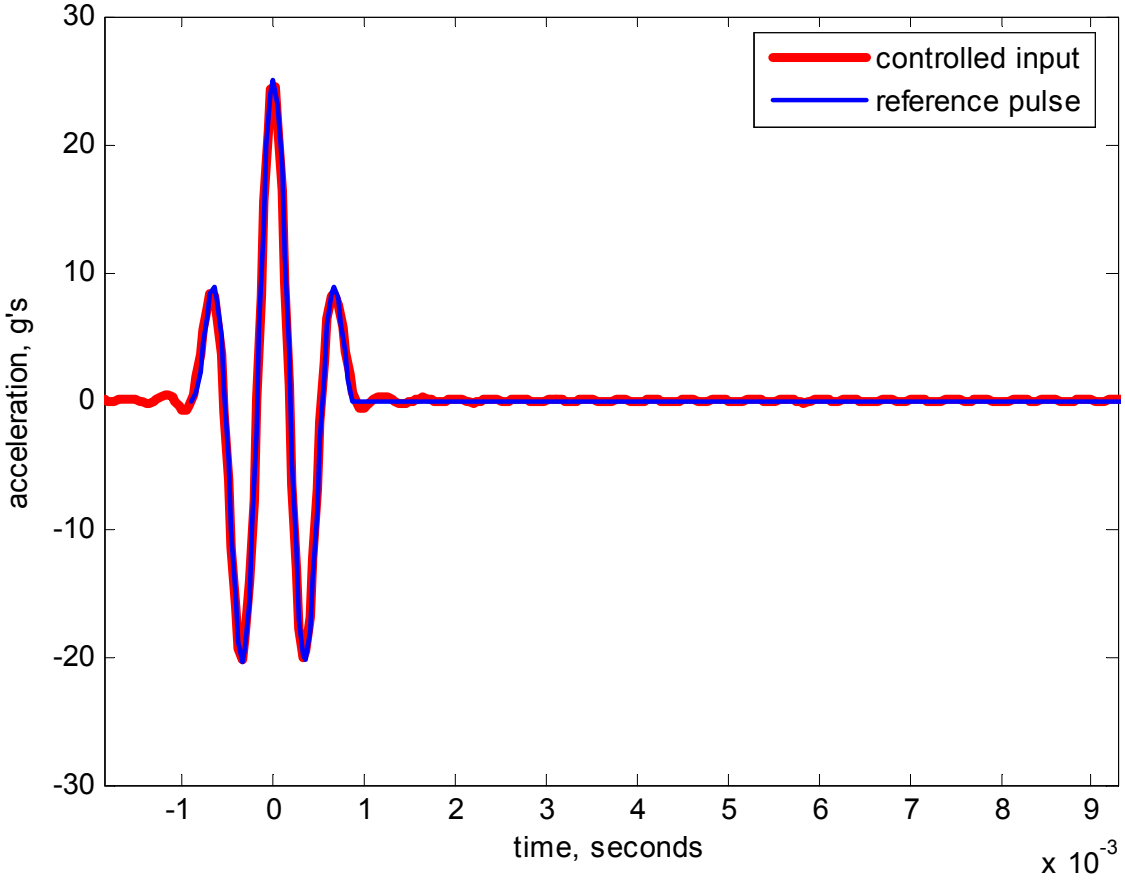

Figure 8.11. Reference Wavesyn Pulse Reproduction.

The repeatability of the peak input level for the test was excellent. Figure 8.12 shows a histogram of peak input level. The average peak input level was 24.9 g and the desired reference peak input was 25 g.

Figure 8.13 shows an example response of the mock AOS to a wavesyn pulse input. Note that the response level is very high compared to the input level due to the fact that the energy in the pulse is tuned to a frequency that is very close to the fixed-base axial mode of the hardware resulting in significant amplification.

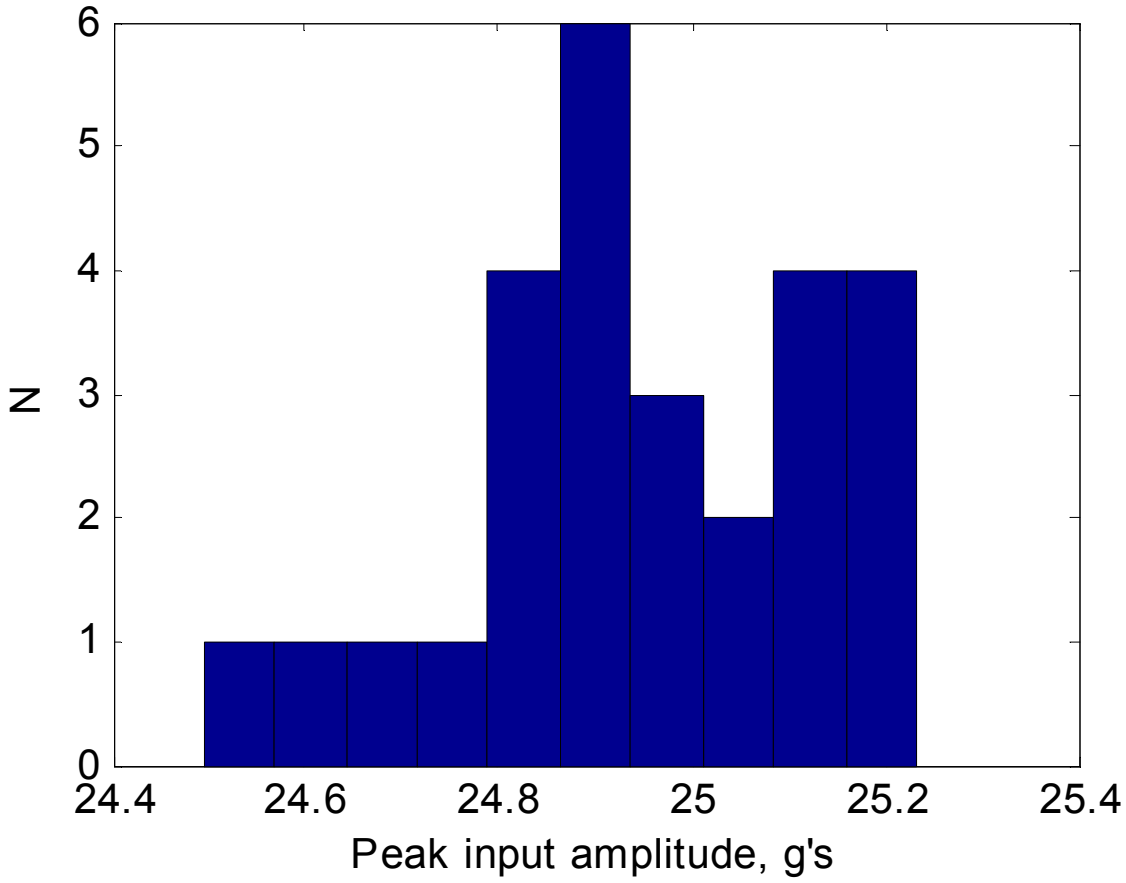

Figure 8.12. Wavesyn Peak Input. (Avg. = 24.9 g.)

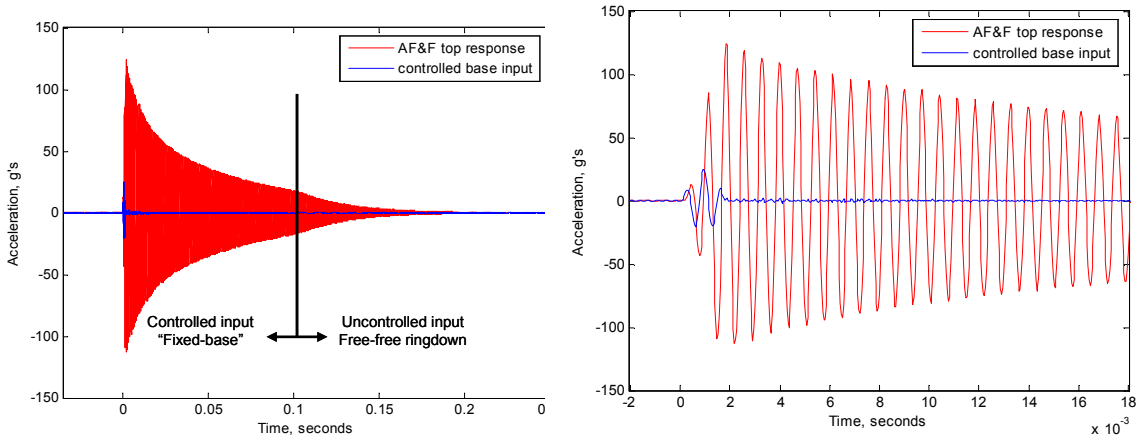

Figure 8.13. Mock AOS Response.

(a) Example of a response of the mock AOS to wavesyn pulse input and (b) Zoom in on example response.

The effect of the control algorithm's ability to enforce the driven-base boundary condition is readily visible. After a pulse duration of approximately 100 ms, the damping of the response increases. The higher damping is associated with additional energy dissipation due to backwards electromagnetic forces working against the shaker armature in the field as the armature and test item resonate in the free-free mode of vibration.

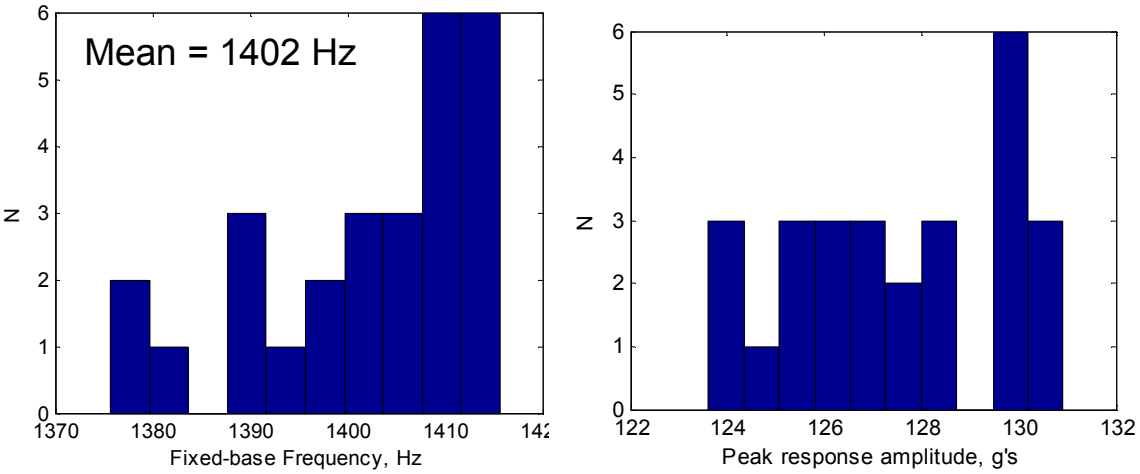

Figure 8.14. Mock AOS Response.

(a) Histogram of axial driven-base frequency and (b) Histogram of achieved peak mock AOS response amplitudes.

Figure 8.14 illustrates the variability in the driven-base axial frequency that was measured for each run of the hardware. The average frequency of the driven-base axial resonance is 1402 Hz. Also notice that the variation in response amplitude varies quite a bit more that the input amplitude. This is partly due to variation in damping and stiffness in the hardware realizations. The response of the mock AOS to this input was very clean. The response data contained little influence from modes other that the driven-base axial mode of the hardware. This enables use of the modified logarithmic decrement techniques mentioned in Section 5.1 for calculation of energy dissipation data (Figure 8.15).

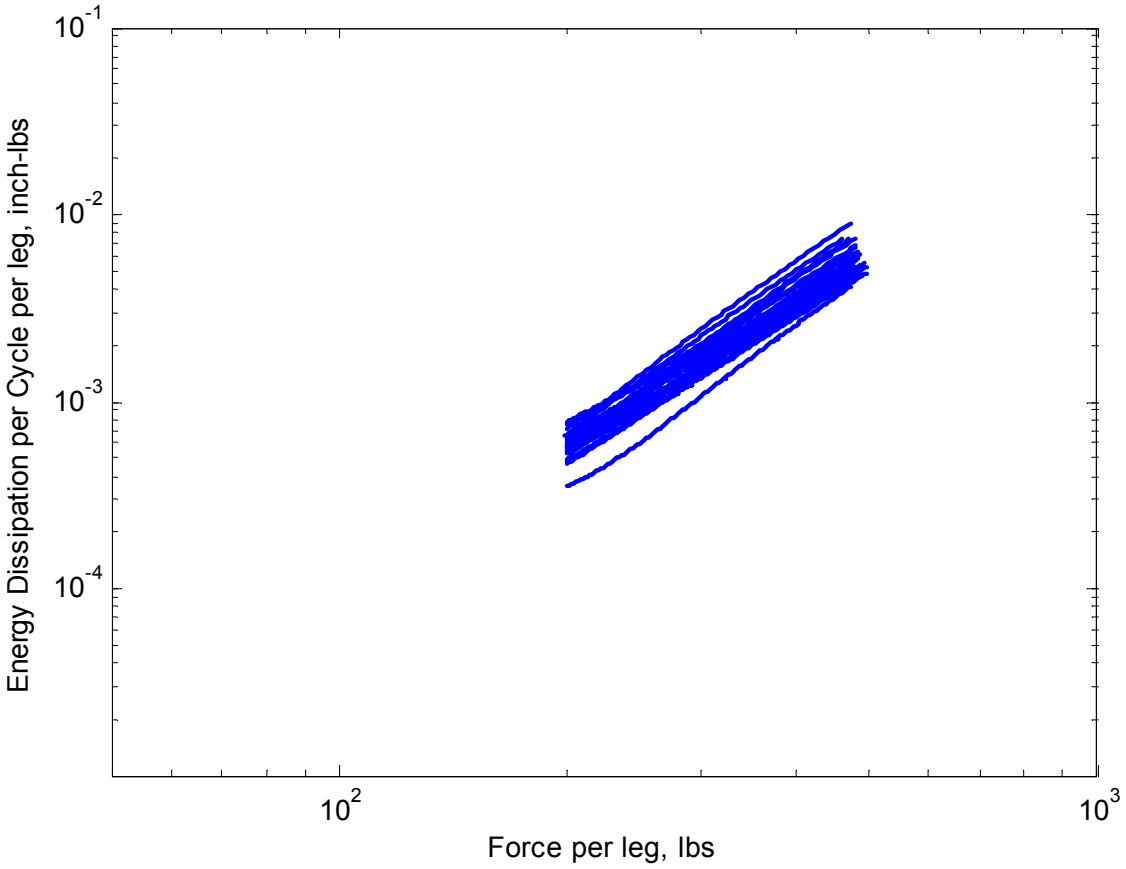

Figure 8.15. Three-Leg Transient Ring-down.

Energy dissipation curves of the three-leg hardware transient ring-down to wavesyn input. Only loads between 200 and 500 lb per joint are shown.

Figure 8.16 illustrates the variation in dissipation curve slopes. The mean slope of all curves is 2.65. This value is a little higher than the single-leg experiment results and also higher than seen in the three-leg sinusoidal experiments.

As stated earlier, the quality of the steady state sinusoidal energy dissipation data that were

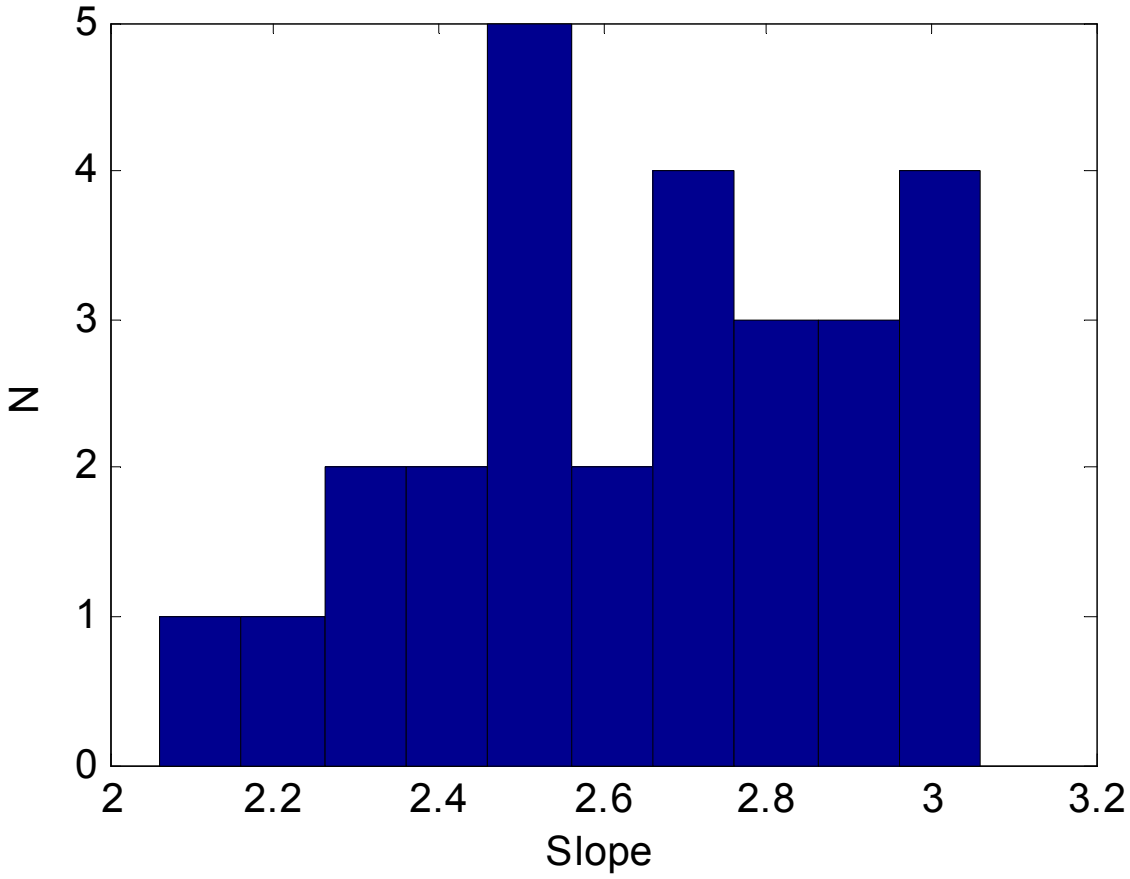

Figure 8.16. Wavesyn Energy Dissipation Slopes (Avg. = 2.65)

gathered from the three-leg hardware on the shaker are slightly questionable. The three-leg transient data, on the other hand, agree better with energy dissipation expectations. This test appeared to control well and accurately represent a fixed-base boundary condition with no apparent additional damping or stiffness contamination from the shaker system. The authors believe that the wavesyn ring-down energy dissipation data are more accurate than the sinusoidal energy dissipation data.

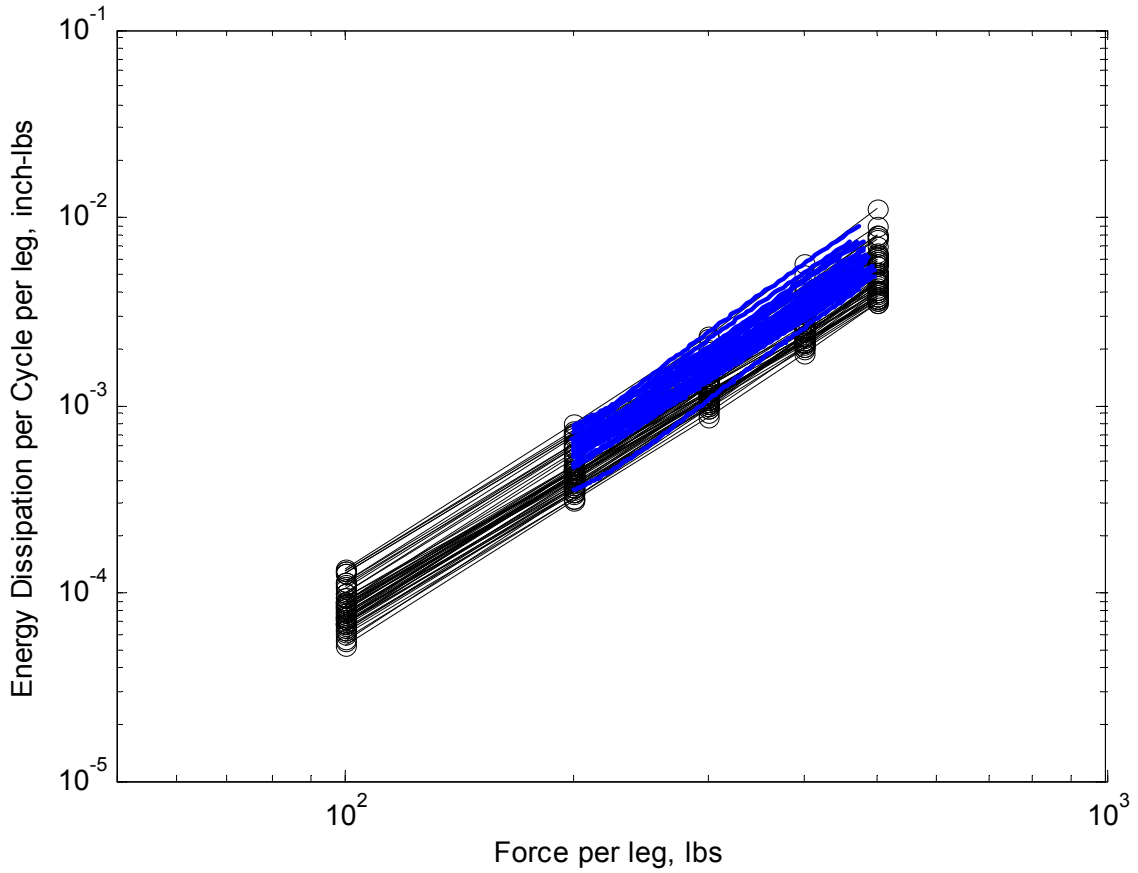

Figure 8.17. Single-Leg Sinusoidal and Three-Leg Transient Wavesyn Comparison.

When compared in Figure 8.17, the range of three-leg ring-down curves are within the range of the single-leg curves. This is reassuring since two different tests provide consistent results. As seen previously, the damping and stiffness of the shaker and electromagnetic field can contaminate the response if the test is not controlled accurately (Figure 8.13).

8.6.8 Simulation of a High-Amplitude Transient

The tailored transient wavesyn input was designed to gather energy dissipation data of the multiple jointed mock hardware for the purposes of model validation of the single joint element in a three joint configuration. The next input to the mock three-leg hardware is meant to serve purely as a model validation activity in which the input environment is rather generic.

The input is representative of a short, high-amplitude transient ("bang") and the simulation contains components of decayed sinusoids at multiple frequencies. The energy distribution in the pulse is meant to approximately represent the profile that might be expected in System A-1 system. The overall level of the input is chosen to generate approximate peak loads in the joints that corresponded to the levels at which the joints had been calibrated and validated. Levels are not meant to exceed 500 lb per leg. Joint forces higher than 500 lb are expected to induce macroslip in the joint, a phenomenon that was not yet meant to be part of this particular experimental activity. Figure 8.18 shows the reference input for the "bang" simulation.

Using all the same transient shaker test techniques described in Section 6, all nine combinations of hardware are each tested three different times (the bolted joints were reassembled three times for each hardware combination) using the techniques described here. The inputs are repeatable for each separate test and the effects of unwanted modes of the shaker system are eliminated in each case. Figure 8.19 shows the high quality of the reference pulse reproduction for all tests for this shock.

Figure 8.20 shows the range of responses to this input. In early time, the waveforms actually overlay quite well. However, what is not obviously visible are the differences at later time due to the varying stiffness and damping found in the different hardware realizations. This should be anticipated due to the inherent variability in each system configuration. Each hardware realization will have a slightly different frequency and damping and these differences will cause the response time waveforms to be increasingly different as time increases.

Figure 8.21 shows the range of responses in the frequency domain. The variation in frequency and amplitude for the axial mode of each hardware realization is visible at about 1400 Hz.

The average axial frequency for this test was 1403 Hz (compare to 1402 Hz for wavesyn transient input). The fact that both the wavesyn and decayed sine testing frequencies agree is nice positive confirmation both tests were controlled well and the driven-base boundary condition was properly enforced.

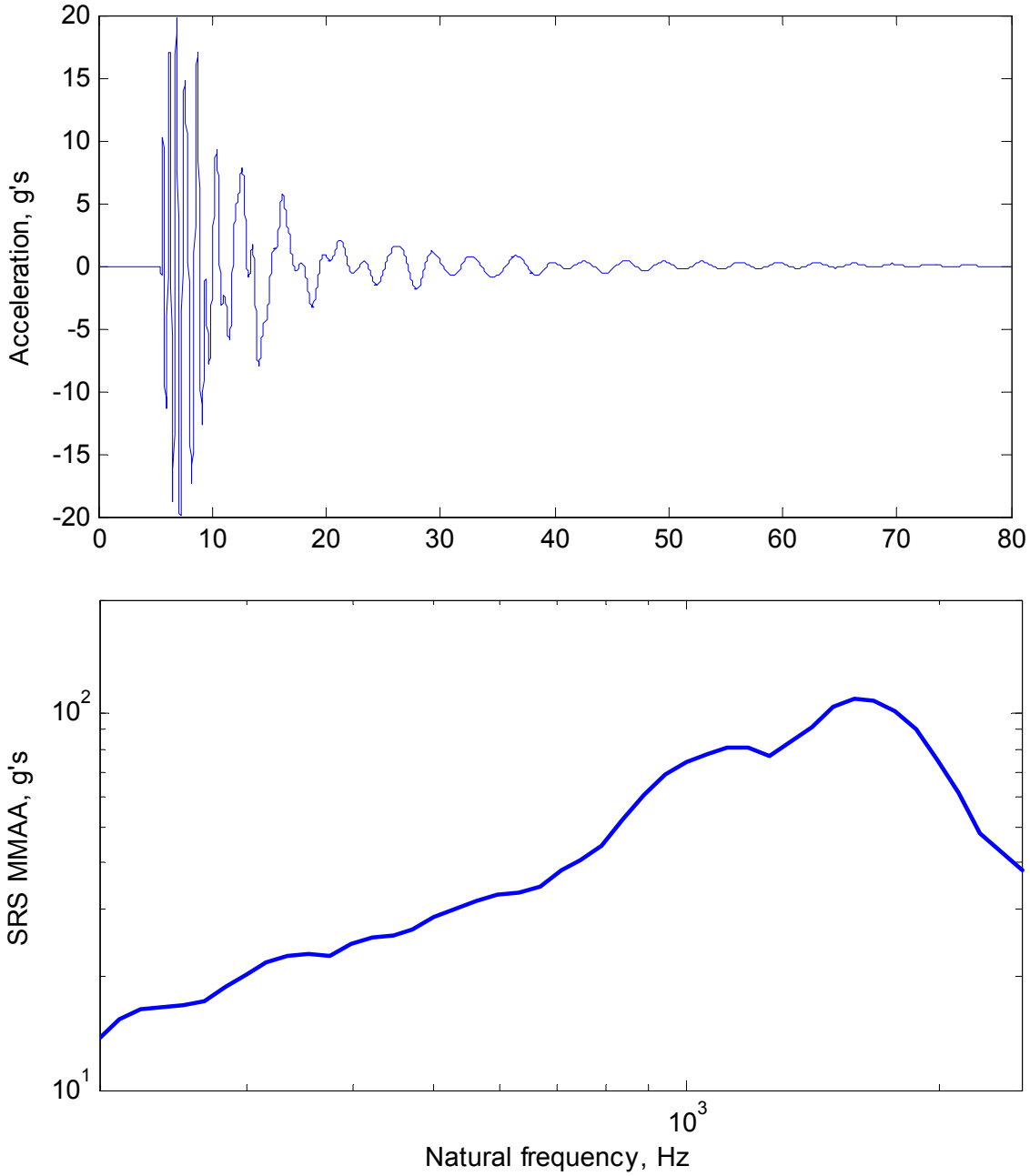

Figure 8.18. Reference "Bang" Waveform Input.

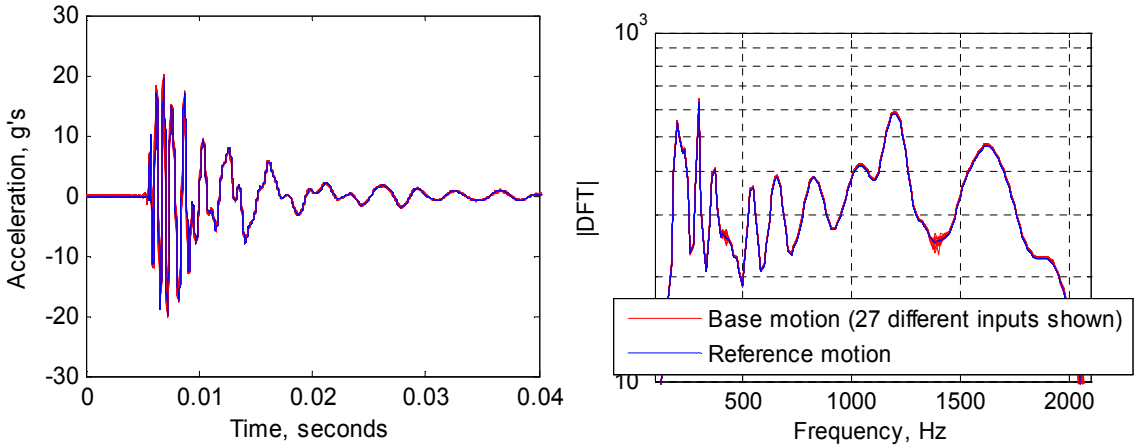

Figure 8.19. Time and Frequency Domain Reference Pulse (27 Controlled Inputs).

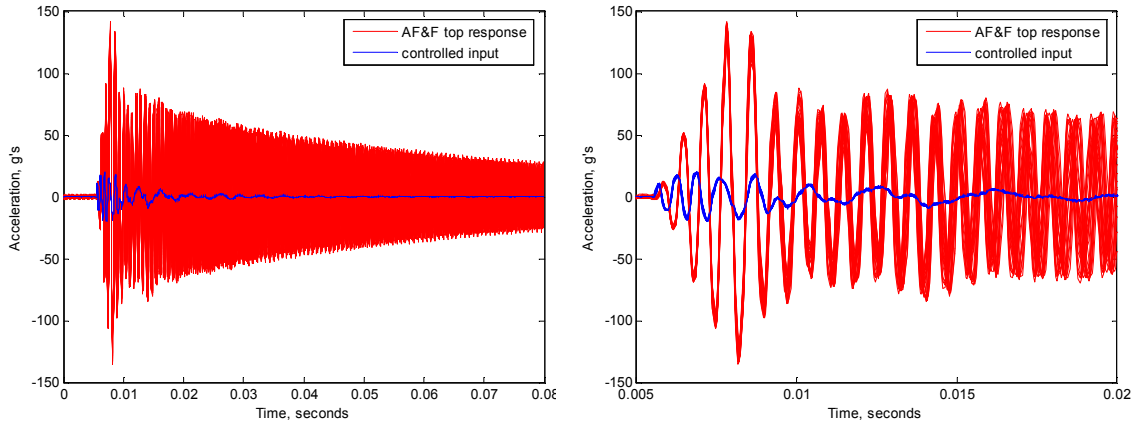

Figure 8.20. Mock AOS Response to "Bang" Simulation Input.

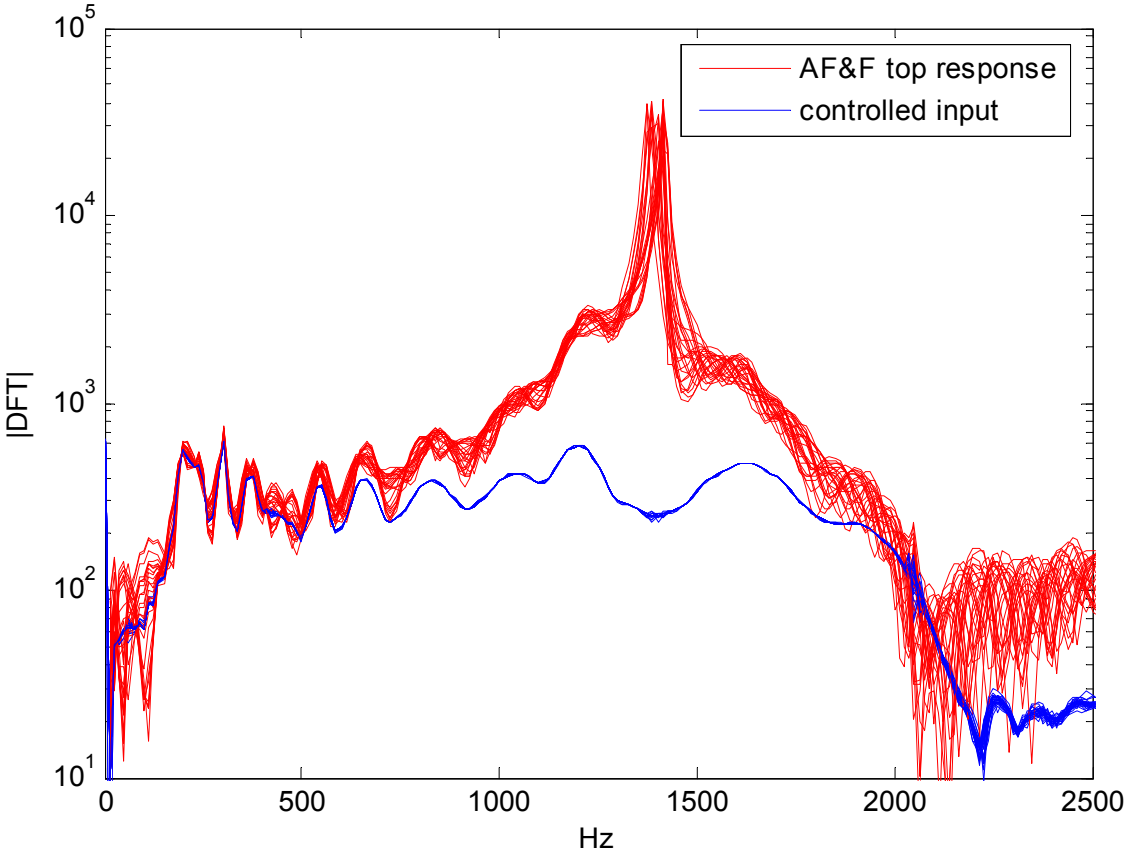

Figure 8.21. "Bang" Simulation Input and Response - Frequency Domain.

8.7 Summary

This section has summarized the experiments and data used for calibration and validation of a System A-1 AOS three-leg bolted model for extension of the single-leg model into a multiple joint configuration.

The first set of calibration experiments consisted of a sinusoidal, steady state dynamic input into the mock hardware. Nine configurations of hardware were tested, each was assembled and disassembled three times, and three load levels were used. This combination resulted in 81 sets of energy dissipation data, or 27 different energy dissipation curves.

Subsequent tests consisted of transient excitation and response on an electrodynamic shaker. Two types of transient experiments were performed. Each used the same equipment and means of control, but each was meant to reproduce different input waveforms. Again for both transient tests, nine configurations of hardware were tested and each assembled/disassembled three times. This combination resulted in 27 sets of response data.

These calibration and validation data provide the statistical foundation from which probabilistic bolted joint models can be calibrated, validated, and deployed into system models to predict the response of System A-1 AOS to modest and very high loads.

Chapter 9

Influence of Contact Pressure on Response

Brian R. Resor

Geometric features with characteristic lengths on the order of the size of the contact patch interface are partly responsible for the variability observed in experimental measurements of structural stiffness and energy dissipation per cycle in a bolted joint[1]. The behavior of bolted interfaces is known to be nonlinear and highly variable and has a large effect on the overall energy dissipation of a structure during dynamic response. Experiment responses of nominally identical hardware show that the structural stiffness of the tested specimens varies by up to 25% and the energy dissipation varies by up to nearly 300%.

A pressure sensitive film can be assembled into interfaces of jointed structures to gain a qualitative understanding of the distribution of interfacial pressures. The resultant pressure distributions suggest that there are misfit mechanisms that may influence contact patch geometry and as well as structural response of the interface. These mechanisms include local plateaus and machining induced waviness. The mechanisms are not consistent across nominally identically machined hardware interfaces. The proposed misfit mechanisms may be partly responsible for the variability in energy dissipation per cycle of joint experiments.

9.1 The System A, AOS Bolted Joint

The first bolted joint under investigation in this section is pictured in Figure 9.1. Nonlinear behavior unique to this bolted joint comes largely from the nature of its inclined interface and its varying contact patch during loading. The joint is also unique in that its surface is not flat because its interface has a small amount of curvature corresponding to the cylindrical shape of the component level hardware. The bolted joints are the major load path into the hardware that they support. Behavior of the bolted joints should be understood and modeled accurately to adequately predict the response of internal subcomponents due to external inputs.

Several experiments have been devised at Sandia National Laboratories to provide data for model development and have been discussed earlier in this text. The specific data used in this

[1]This chapter is taken largely from [51].

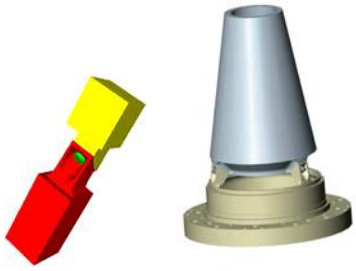

Figure 9.1. Joint Interfaces.

(a) Example of a single bolted interface and (b) Example of multiple joints in a single experiment.

discussion are found in [50]. The experimental techniques used to gather the response data shown later in this section are all described in this handbook. The first is performed on an electrodynamic shaker and uses harmonic forcing to excite the structure at the desired frequency. The second consists of a simple dumbbell configuration, while the third incorporates multiple joints into a single experiment and is discussed in another section of this text. Bolted joints tend to exhibit two types of variation in response: 1) part-to-part, or machining variation, and 2) assembly variation, which comes from taking hardware apart and realizing slightly different response behavior upon reassembly. Throughout this bolted joint, model calibration and validation process, several realizations of nominally identical hardware were machined and tested so we could understand variability in response character due to part-to-part differences. Three pairs of single-leg tops and bottoms were fabricated. By combining pairs, we prepared a total of nine hardware combinations for testing. In this section, one top and three different bottoms of three-leg hardware are also examined for a total of three hardware combinations, all made from stainless steel.

A pressure sensitive film was assembled into the interfaces of the jointed structures to provide insight into the distribution of contact pressure in the nominally conformal surfaces. See Figure 9.2. The resultant pressure distributions definitely suggest that there are misfit mechanisms influencing contact patch shape and magnitude, as well as structural response of the interface. These mechanisms include local plateaus and machining induced waviness, but are not consistent across nominally machined hardware interfaces.

A calibrated torque wrench was used to apply a nominally consistent preload to the bolt during each assembly through torquing each of the 1/4-in diameter bolts to 85 in-lb. The Pressurex® pressure film used in this study is sensitive to pressures from 1,400-7,100 psi and is manufactured by Sensor Products, Inc.

Figure 9.2. Pressure Sensitive Film.

(a) Pressure sensitive film installed in joint interface and (b) as viewed immediately after removal from joint interface.

9.2 Interface Pressure Imagery

The pressure sensitive film was scanned into electronic form in a controlled manner so that the image data could be analyzed electronically. Figure 9.3a shows the raw scanned image, as viewed in Matlab. Pink dye darkness is basically directly related to magnitude of contact pressure in the interface. Figure 9.3b shows the spatial distribution of pressure intensity with pressure magnitude in the third dimension. For this qualitative study the exact pressure values have not been determined.

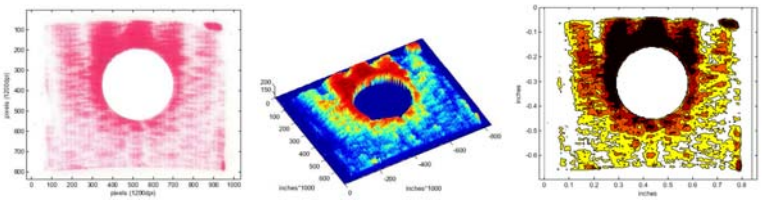

Figure 9.3. Contact Patch Imagery.

(a) Raw scanned image, (b) mapping of color intensity in three-dimensions and (c) filtered and simplified image of contact patch.

Representative interface prints for each of the nine hardware combinations are shown in Figure 9.4 below. The three tops are labeled A-C, while the bottoms are labeled 1-3.

Even though all the pieces were manufactured using the same techniques and to the same drawings, there is a difference in part C that has caused its contact patch to take on a different shape with more pressure toward the outside edges of the interface. Simple bolted joint concepts would suggest that the contact patch in the vicinity of the material directly underneath the bolt head is annular for mating surfaces that are nominally conformal. Even parts A and B exhibit variations

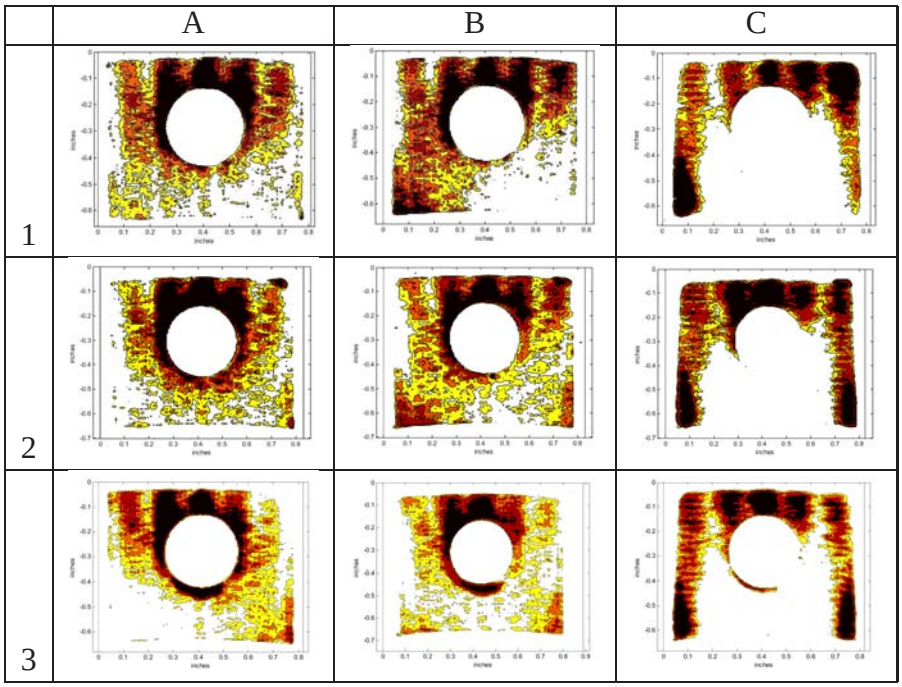

Figure 9.4. Interface Prints for Nine Combinations of Single-Leg Hardware.

in contact patch shape from what might be expected theoretically because the center of the contact patch is generally shifted toward the top of the bolt hole instead of being centered about the bolt hole.

Figure 9.5 shows a close-up view of one of the interfaces. In this image the waviness of the surface due to machining can be seen. At a much smaller scale, though not as visible in this image, are also actual machine tool marks from the cutting of the surface. The roughness of the surface was specified on the drawing for all these joints, and the final hardware did meet specification. Therefore, one might assume that the variation seen in this paper might be representative of typical part-to-part variation.

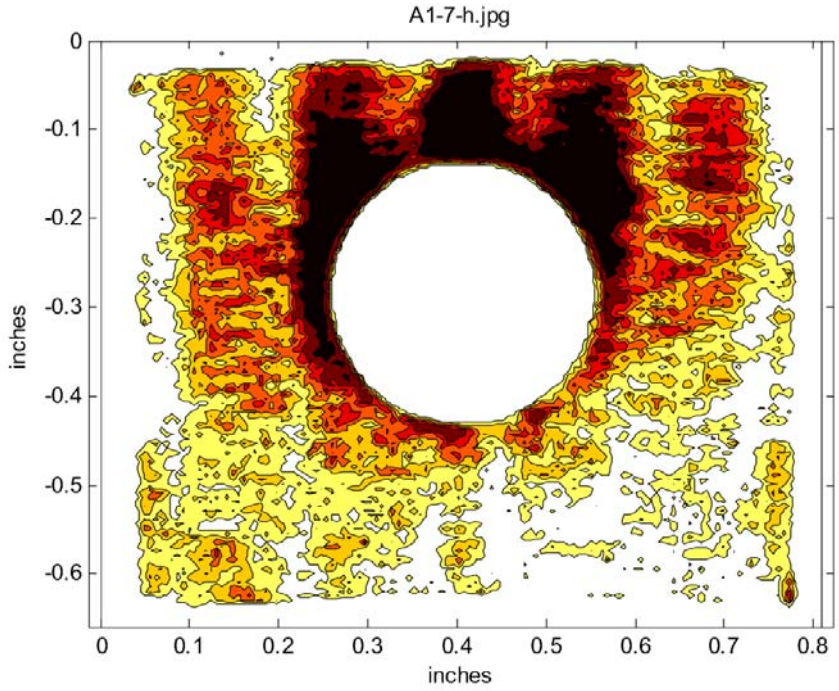

Figure 9.5. Interface Print for Hardware Combination A1.

Most of the joint combinations exhibit qualitatively similar contact patches when the joint is taken apart and reassembled. Sometimes, though, upon reassembly the interface comes together inconsistently. Hardware combination A3 is an example of a pair that did not tend to assemble together in a repeatable manner as seen in Figure 9.6.

9.3 Structural Dynamic Experiments on the AOS Leg

The hardware of Figure 9.2 has been used extensively at Sandia National Laboratories in many experimental activities. The ability to view the qualitative image of the contact patch motivated

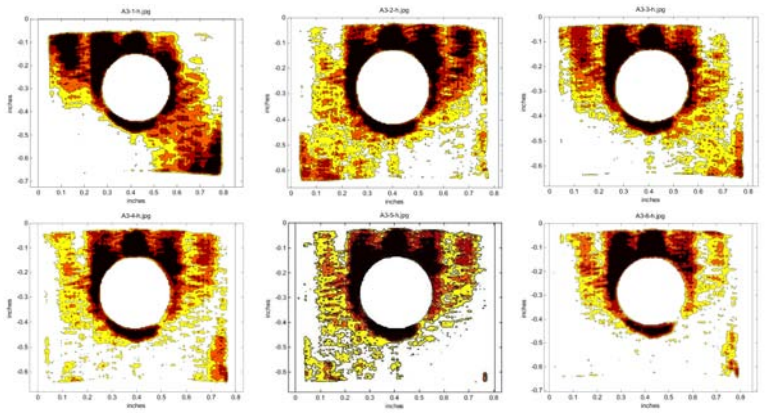

Figure 9.6. Assembly Variation in Hardware Combination A3.

us to investigate effects or anomalies observed in the structural dynamic response that might be attributable to certain features in the contact patch. The findings are very revealing.

9.3.1 Harmonic Excitation and Stiffness Observations

Harmonic excitation experiments were performed on the single-leg hardware so we could collect data for possible use in calibration of a whole-joint model. This experiment very accurately simulates an SDOF system with nonlinear damping and stiffness elements. As a part of the process, the resonant frequency of the experiment was determined at specified peak interface load levels. The experiment was repeated five times with all nine combinations of hardware. All curves are shown in Figure 9.7.

As expected, the bolted joint interface for combinations including tops A and B exhibit amplitude nonlinearity with stiffness decreasing as load increases in the joint. Note that all hardware combinations including top C clearly exhibit a qualitatively different behavior than the rest.

Until the interface prints were viewed, there was no explanation for the discrepancy in behavior that top C was exhibiting. All hardware was machined to the same drawings using the same techniques. The unique behavior was attributed to part-to-part variability (which is still arguably a good assumption). It is common for stiffness measurements of nominally identical bolted joint hardware to vary by as much as 25%.

9.3.2 Transient Excitation and Energy Dissipation Observations

Transient excitation experiments were also performed using the same hardware combinations [49, 50]. A final product of transient ring-down postprocessing of all the experiments is a set of 45

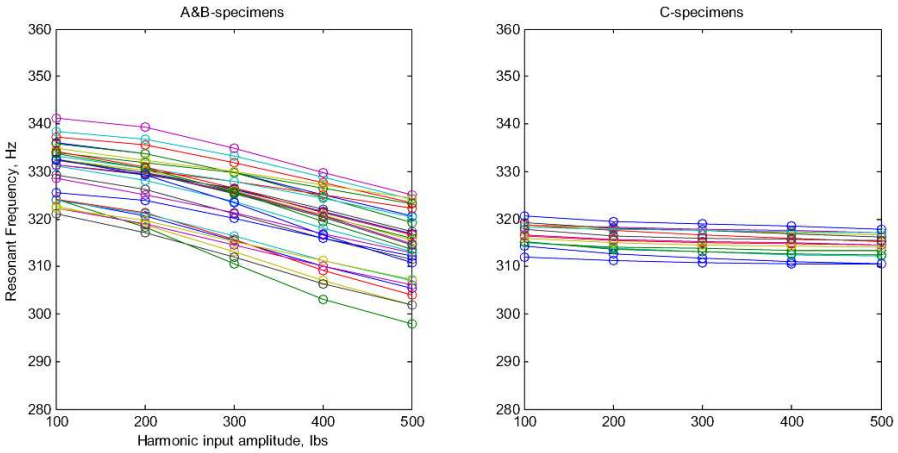

Figure 9.7. Single-Leg Resonant Frequency.

The plot shows the complete data set of 45 individual curves.

energy dissipation curves that are plotted as a function of force in the joint interface. See Figure 9.8. The data is organized into two colors: black are the 30 curves associated with single-leg tops A and B and red are the 15 curves associated with single-leg top C.

The overall energy dissipation for the hardware combinations that include single-leg top C is lower than energy dissipation of combinations that include tops A and B. In fact, there is very little overlap between the two clusters of curves.

Again, until the contact patch images could be viewed, there were no reasonable explanations for the energy dissipation differences in those combinations of hardware. It is common for energy dissipation measurements on nominally identical bolted joint hardware to vary by as much as 300%.

An attempt is made here at explanations of the observations that are being made with respect to energy dissipation. When top C is used, the contact patch consists of a much smaller contact area than the other assemblies. Given equal preloads, the contact pressures will be significantly higher when top C is included. The extent of the microslip (and hence dissipation) could be much reduced. Also, the kinematics on the interface will be significantly different than the other assemblies. Highly localized contact pressures may constrain the interface in such a manner that different modes of deformation occur within the structure. For example, stronger coupling between the lateral loading and bending response could result, or there might even be special participation of torsional modes.

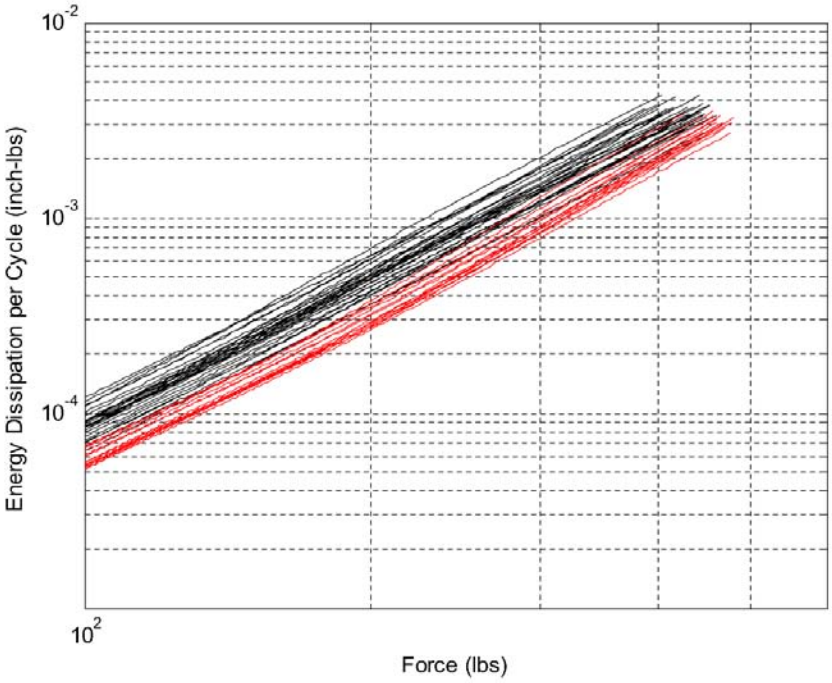

Figure 9.8. Single-Leg, Transient, Dumbbell Energy Dissipation.

9.3.3 Observations of Energy Dissipation Curve Slopes

When a straight line is fit to an energy dissipation curve, such as that in Figure 9.8 in log-log space, the slope of the line is indicative of the magnitude of nonlinear behavior that is exhibited by the joint. A slope of 2 indicates a perfectly linear joint element, as is the case when monolithic steel specimens are tested. Slopes as high as 3 are commonly observed, depending on the nature of the joint interface.

Table 9.9 illustrates the average slope value for each of the nine hardware combinations as measured from the energy dissipation curves obtained in the harmonic excitation experiment. This experiment is slightly different from the transient excitation experiment in that a single load level can be exercised at one time as opposed to a whole range of loads.

The slopes of energy dissipation curves associated with top C are generally not as high, but still are well above 2.0. This information would suggest that the degree of damping amplitude nonlinearity in hardware that includes top C is not as high. As mentioned earlier, Figure 9.7 suggests the same conclusion because stiffness is not as dependent on input forces.

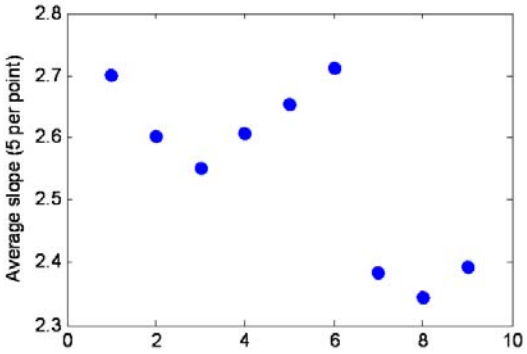

Figure 9.9. Power-Law Slope.

Average slope of energy dissipation curve for the nine hardware combinations in the dumbbell experiment. (A1=1, A2=2, A3=3, B1=4, etc.)

9.3.4 Recalibration of Stiffness for Multiple Joint Experiments and Modeling

When researching the intricacies of jointed interfaces, it is extremely valuable to also analyze hardware that has exactly the same geometry in the vicinity of the joint, but without the interface. In other words, fabricate a monolithic specimen that exhibits linear elastic behavior with the same nominal geometry. The interface is only added to the experiment once the properties of the monolithic hardware are quantified. Using this technique, it is easier to understand the specific contributions of the nonlinear joint interface to the overall behavior of the hardware. Monolithic hardware is available for both the single-leg and three-leg examples used in this study.

The monolithic hardware is especially useful for understanding the overall elastic stiffness of the joint element. Figure 9.10 illustrates simplified dynamic representations of the single-leg and three-leg hardware. When focusing on the axial mode of each, the latter can be approximated very well using equations of SDOF systems with appropriate equivalent stiffness values. The equivalent stiffness depends on whether springs are in series or in parallel with each other.

Stiffness values, k_1 and k_{j1}, in the single-leg calibration hardware can be determined when the resonant frequencies are known. An assumption of the whole-joint modeling approach used to date is that the calibration stiffness of the joint, k_{j1}, can be used in the multiple joint component model in the place of k_{j3}. One would hope that a validation of that multiple joint model against a corresponding multiple joint experiment would then be successful. However, during the validation exercises with this particular hardware a large discrepancy in joint stiffness (Table 9.1) was discovered.

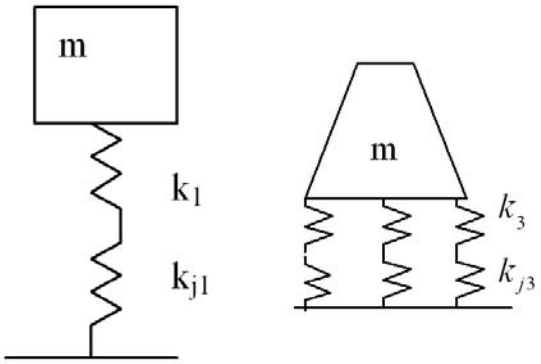

Figure 9.10. Experimental Schematics.

Simplified representations of the (a) single-leg and (b) three-leg experiments including stiffness elements.

Table 9.1. Experimentally Determined Joint Stiffnesses

Approximate Single-Leg Harmonic Experiment Joint Stiffness: k_{j1}=8.8 x 10^6 lbs/inch
Approximate Three-Leg Hardware Joint Stiffness: k_{j3}=4.9 x 10^6 lbs/inch

It is clear that using the parameters derived from the single-leg calibration experiments would yield a three-leg model that would be much stiffer than the actual three-leg experiment. At the time of the initial experimental work there was, again, no good explanation or obvious correction for the discrepancy. Instead, a recalibration of the stiffness in the three-leg hardware was done so that the validation exercise could continue without too much error. It is more desirable to have the ability to accurately predict the stiffness of a multiple joint interface by performing experiments, or simple analysis, on single joint elements. The use of the pressure sensitive film to image the contact patch in this hardware helps to explain the differences in joint interface stiffness that have been observed and that have caused issues around validation exercises. Figure 9.11 shows the interface prints for three-leg, hardware top A2 with three-leg bottom 2. (Prints for hardware combinations including bottoms 1 and 3 are very similar to those shown and so are not shown here.)

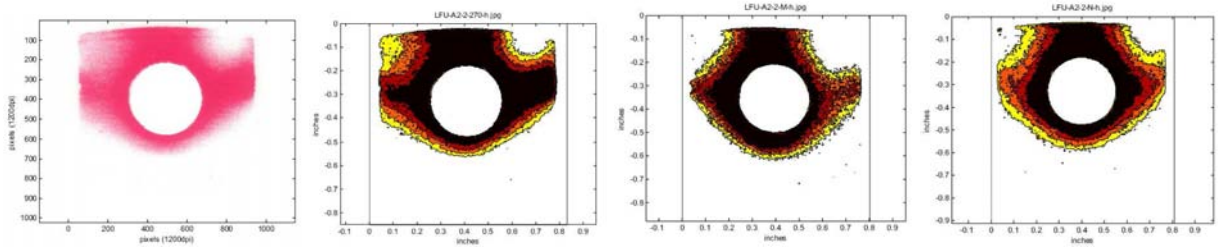

Figure 9.11. Three-Leg Interface Print.

Example interface print from three-leg hardware: (a) raw image of Leg 1, (b) processed image of Leg 1, (c) Leg 2 and (d) Leg 3.

Comparison of interface prints in Figures 9.4 and 9.11 shows conclusively that the contact patches are not similar for the two cases. Again, the joint and interface geometry for both single-leg and three-leg hardware are nominally the same, and yet the details of the contact patch are very different. Also notice that the machined surface for the three-leg hardware is much smoother than was achieved for the single-leg hardware.

With this insight available, one would not necessarily expect a stiffness value derived from a single-leg calibration experiment to successfully apply in a model validation of a three-leg configuration.

9.4 Flat Lap Joint Interface

The flat lap specimen under line loading is a seemingly simple joint interface (Figure 9.12). One would expect the contact patch to be centered under the load line, with decreasing pressure away from the line of application. However, measurement of the contact pressure distribution shows that reality is quite different from theory.

Figure 9.12. Flat Lap Joint Pressure Film Assembly.

Application of force in the interface to generate this imagery was challenging because there are two cables, one on each side of the specimen, that are preloaded one at a time. The pressure film used in this investigation records peak pressure. Therefore, the experimentalist must use care to ensure that one side of the interface does not experience excessive load due to uneven torquing during preload application and removal.

Figure 9.13 shows the distribution of pressure in this interface for one assembly. Note that the majority of contact pressure is actually not directly underneath the line of application of load. Instead, the majority of contact pressure is at one end and at one side. The extra pressure at the side could be due partly to uneven distribution of load between the two cables. Regardless, the fact that the sides of the specimen can experience such high pressure contradicts the theory or assumption that the contact pressure is concentrated below the load.

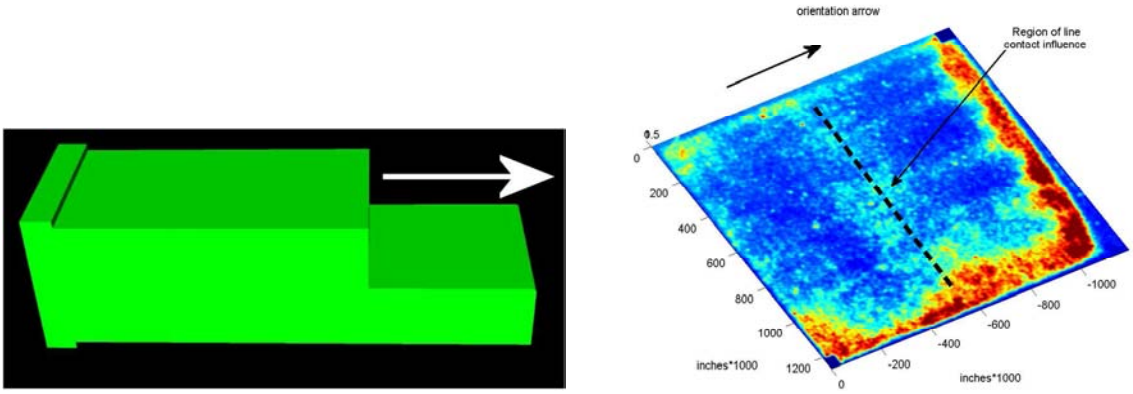

Figure 9.13. Contact Patch Imagery.

Contact patch imagery of the flat lap joint combination A1. White arrow and black arrow point in same directions, for orientation purposes.

Even though this joint specimen was designed to be flat, imperfections cause a majority of pressure to actually be away from the loading line. The slightly higher pressure under the loading line is faintly visible and is marked with the dotted line. Also notice faint indications of machining marks that run perpendicular to the load application line.

9.5 Conclusion

The AOS bolted joint has been a useful specimen for studying the nonlinear behavior of the interface because of the complex nature of its geometry. This paper has shown the dramatic effects that the subtle differences in interface contact patches can have on structural dynamic response properties of nominally conformal surfaces. The variations that are observed in the cases studied here are

truly caused by part-to-part variation in identical manufacturing processes. One could argue that the variations are real and need to be accounted for in the development of a model that can predict the corresponding variability in structural response.

An example pressure image of the flat lap joint is shown, again demonstrating how actual contact pressure can vary from what is assumed or theoretically anticipated. Only two examples of joint interface geometry were shown in this section: one with a simple geometry and one with a complex geometry. Inside both, there are important hidden details describing the interface interactions. Imagery of the contact patch is a valuable tool in helping researchers understand the nature of both contact and micro- or macroslip in the interface.

Future work with respect to contact patch imagery will be discussed within the next chapter.

Chapter 10

Experimental Work: Closing

Danny L. Gregory

10.1 Summary of Experimental Work

In addition to the traditional quasistatic load frame testing, three dynamic experimental approaches for investigating mechanical interfaces and bolted joints have been discussed with representative data for several experiments. The first approach is to use the Big Mass Device (BMD) concept to configure an experiment that can be modeled as an SDOF and the behaviors of the system at resonance exploited to measure the energy dissipation and effective stiffness of the joint. Utilizing properties of sinusoidal excited structures, the harmonics of the forcing frequency have been shown to contain the information about the nonlinear mechanisms in the joint. The second approach is to use the transient response of the two mass (dumbbell) concept to exercise the joint and use the free decay of the system to measure the energy dissipation and stiffness of the joint. The instantaneous rate of the free decay of a particular mode of the dumbbell system can be used to evaluate the nonlinear response of the joint. The third is shaker driven transient excitation to a structure with bolted connections. The shaker driven excitation can allow a multitude of candidate excitations to be applied to the structure for the purposes of bolted joint characterization as well as for model validation. All techniques have been shown to provide valuable insight and measures of response for investigations of bolted joints.

Measurement and signal processing techniques to isolate and quantify key measures of joint behavior have been discussed. These techniques include the traditional techniques for development of hysteresis curves for harmonic excitation as well as techniques to estimate the nonlinear restoring force in a mechanical joint. A modified logarithmic decrement technique, applied to the free decay envelopes from transient excitation, to estimate the instantaneous rate of energy dissipation was also demonstrated. Spatial filtering techniques to isolate the response of each of the modes of the system participating in the system ring-down have also been introduced.

Techniques for contact pressure measurements using pressure sensitive film have been discussed with example results. The results are very revealing and demonstrate the large variability in the contact pressure for nominally identical structures fabricated to the same specifications. The film images can be post processed to provide rapid full-field qualitative information and with

careful processing, quantitative data for the contact pressure in a mechanical interface. It is recommended the use of this or similar techniques become an integral part of any bolted joints research effort.

The solid equivalent joint has proven to be invaluable in our investigations. It has enabled the experiments to be evaluated for repeatability, assessment of the boundary conditions, and quantification of sources of energy dissipation without the presence of the joint. The solid equivalent joint results allow the energy dissipation due to the joint to be isolated. Similarly, the effective stiffness of the joint can be estimated by measuring the frequency differences between the solid and jointed interface results.

These experimental techniques provide useful results but certainly are not the only way of experimentally investigating the behavior of mechanical interfaces, bolted or otherwise. Many variations on the basic techniques described here can be envisioned as well as completely different approaches. The myriad of possible bolted joint configurations provides endless opportunities to develop new experimental approaches, measurement and signal processing techniques, and analysis tools to gain insight into the complex physics associated with the dynamic behavior of mechanical joints.

10.2 A View for Future Experimental Work

As discussed in the introduction to the handbook, the physics associated with microslip behaviors in mechanical joints span several length scales, from molecular to the full assembled structure. To fully capture the physics and to develop constitutive models that span the inherent range of length scales, experiments are needed at all these length scales. Advanced measurement techniques and strategies are needed to obtain enhanced information to allow the complex interface mechanisms to be observed or inferred. New signal processing and analysis tools need to be developed to provide measures of the joint behaviors that can help reveal and define the underlying physics of the interface dynamics. Some future areas of work prompted by the current research are discussed below.

10.2.1 Experiments at the Asperity Level

Experiments at the asperity level might be useful to determine the constitutive behavior of mating surfaces . Experiments and measurement techniques at this scale are difficult and expensive to devise and use of such data to deduce continuum-level interface constitutive models would be problematic, but success of this enterprise could lead to prediction of joint behavior at the macro-level without the need for calibration experiments at the same length scales. Perhaps emerging Micro-electro Mechanical Systems, (MEMS) technologies can be exploited for the purposes of these difficult experiments.

10.2.2 Improved Measurement Techniques

The inherent inability to directly observe the contact zone(s) in the interface requires the use of indirect measurements to infer the physics in the interface. In the current research described in the handbook, point measurements were employed and the global response (total energy dissipation and total stiffness) of the joint were measured. The ability to obtain improved spatial definition of the external deformations in the vicinity of the joint could improve the inference of deformations internal to the contact region(s). Some measurement techniques that may provide enhanced spatial information include: (1) Full field relative displacement measurement techniques such as Holographic Interferometry (Holometry) and Electronic Speckle Pattern Interferometry (ESPI) [61, 62] can be used directly for quasistatic loadings or can be applied in a time average mode for harmonic vibration loadings. (2) LDV [63] can also be used to obtain the velocity field in the vicinity of the joint under harmonic vibration loadings. (3) Thermoelastic Imaging [64] might be used to measure the stress patterns in the vicinity of the joint under harmonic loading. These optical techniques provide enhanced spatial resolution but must have line of sight available to the area of interest and special steps must be used to resolve three dimensional measurements.

10.2.3 Macro-Scale Multi-Dimensional Loadings

The macro-scale experiments described in the handbook were configured to very selectively introduce a one-dimensional shear loading into the joints while maintaining a near constant normal force. In real field environments the normal force in a mechanical joint is time varying depending upon the dynamic modes participating in the response of the structure and the resulting forces realized in the joint. The microslip in the joints are created by shearing forces that generate the slip zone(s) in the interface for a given surface pressure field in the contact region(s). Simultaneous bending and transverse loadings of the interface will modify the contact region(s) and the resulting contact pressure distribution in the interface, and thus change the slip zone(s) and the microslip occurring in the joint.

Experiments are needed to provide more generalized loadings to simple joints to guide development of more generalized joint constitutive models that account for time varying normal forces in the joint. Experiments that can introduce controlled (and measurable) combinations of loadings (shear, bending, normal, etc.) are desired to provide the basis for model development and validation.

The dumbbell configuration can provide multi-dimensional loading to the joint by selectively exciting certain vibration modes of the system. The modal participation in the response can be adjusted by selecting the excitation location. For example, an axial hammer impact applied off center of one of the masses will excite the axial and certain bending modes depending upon the impact location. The free decay of the system then becomes a superposition of the modal responses participating in the ring-down. Special signal processing techniques are required (such as the spatial filtering discussed in Section 5.5) which can isolate the response of each of the modes of the dumbbell.

Multi-axis shaker systems are becoming more common for environmental simulations and research purposes. These systems can be used to provide controlled combinations of shear, bending, and torsion loadings into an experimental structure. Joint experiments configured with an inertial mass, similar to that used for the BMD experiments, can be envisioned with the multi-axis shaker systems. By properly controlling the inputs to the test structure, selected combinations of loadings can be applied and the response of the structure measured to characterize the behavior of the joint(s) under coupled loadings. Creative measurement and signal processing techniques will be required to capture the multi-dimensional loading(s) and dynamic response of the structure and to isolate the contribution of the joint(s).

10.2.4 Piezoelectric Actuators and Washers

Experiments incorporating piezoelectric devices might be configured to provide complex time varying loads into a mechanical interface to simulate the generalized loadings of a joint in a built-up structure. Piezoelectric washers have been used in experiments by Nitsche and Gaul [65] to actively control the damping in a bolted joint by varying the normal force. This concept could be extended to purposely provide a time varying normal pressure in the joint at selectable frequencies and levels. The addition of piezoelectric actuators could provide excitation forces/moments to the joint through various configurations. This could simulate the generalized loading effects at a local level in a joint without the complexity of multi-axis loadings in built-up structures. Techniques to minimize and account for the additional interfaces introduced by the inclusion of the piezoelectric devices must be considered.

10.2.5 Advanced Signal Processing and Data Analysis Tools

The traditional time and frequency domain measurement and signal processing techniques can provide valuable information about the dynamics of mechanical interfaces. However, further signal processing or calculating other measures of the response can provide additional insight into the underlying physics in an interface. As discussed in Section 5.5, the use of spatial filtering techniques can decompose the transient response of the experimental structure into each of the participating modal responses. Further processing of the free decay envelopes of the individual modal responses and measures of response in these generalized coordinates may provide further insight into the joint dynamics.

Another signal processing technique that seems to hold promise for investigating mechanical joints is the Harmonic Wavelet Transform (HWT) [66, 67]. The HWT provides a time-frequency domain measure of the response of a structure. The frequency resolution is approximately logarithmic and variable, the frequency resolution – time resolution product is almost constant. Integration along a frequency line at all times results in an estimation of the magnitude squared of the Fourier spectrum at the specified frequency. Integration along a time line at all frequencies yields an estimate of the instantaneous mean square time value. The resulting spectrum is a discrete approximation of the instantaneous spectrum. When HWT is applied to the transient response of a

structure, the instantaneous spectrum allows the nonlinear response to be observed as the response decays. The time-frequency map of the response of a jointed structure provides a unique measure of the response to provide insight into the development and validation of future joint models.

Further exploration of techniques, discussed in previous chapters, to estimate and characterize the nonlinear restoring force of a joint seems to hold promise for future joints research. By isolating the nonlinear restoring force for various mechanical joint configurations, candidate constitutive model forms can be hypothesized and compared to those measured. Varying parameters of a joint, such as preload, contact geometry, or surface finish, and observing changes in the nonlinear restoring force can provide insight into the underlying physics governing microslip in mechanical interfaces.

10.2.6 Experiments on Multi-Jointed Structures

Experiments on various configurations of multi-jointed structures are also needed to provide experimental results to assist in the development of modeling approaches for built-up structures. As constitutive models are developed at the various length scales they must ultimately provide useful results in real engineering applications. This will require model predictions for the response of structures with a multitude of mechanical joints. These experiments will provide benchmark data to test robustness, computational efficiency, and accuracy of candidate joint models integrated into a full structural dynamic model. Experiments on assembled structures will add size, complexity and challenges for the experimentalist to perform controlled experiments and acquire meaningful data.

Part II

Joint Models

Chapter 11

Whole-Joint Models

Daniel J. Segalman

Once enough experiments are performed to characterize the joints of interest, and once a constitutive form is selected and parameters are found that reproduce the data, there is still the issue of integrating that constitutive model into a structural dynamics model.

The challenge here is connecting a one dimensional equation with the FE kinematics - an essentially three dimensional world. This is the same problem that is encountered regularly in connecting spring elements to plates, shells, and solids. Another flavor of this problem is that regularly addressed by analysts in connecting plates and shells to three dimensional element blocks.

The mathematics of this problem are still challenging after over twenty years of concerted effort in the mathematics and applied mechanics worlds. The issues of nonphysical stress singularities and retarded mesh convergence appear important to those communities more for philosophical than practical reasons. The singularities are integrable, and the uncertainty in loads and boundary conditions, along with the intrinsic variability in joint response, so dwarf discretization error that engineering analysts do not mind living with a few mathematical anomalies, if they notice them at all.

The approach employed in this handbook for coupling one dimensional joint models with three dimensional, FE, component models is comfortably within the class of tools used by the general analysis community, though care must be taken to use the approach consistently.

We refer to this class of constitutive model, coupled with the kinematics defined in this chapter, as a *whole-joint model* because the whole-joint is represented by a single equation for each of the six degrees of freedom available to the joint.

11.1 Whole-Joint Kinematics

For the sake of discussion, consider the measured properties of System A, AOS, base attachment location joint shown in Figure 11.1. The specimen is sandwiched between a shaker and a large mass. A force transducer is placed in line and an accelerometer is placed on the reaction mass.

As indicated in the experimental sections, energy dissipation can be deduced from the effective damping at resonance, and the specimen stiffness can be deduced from resonance frequency. How are these properties to be introduced to the FE formalism?

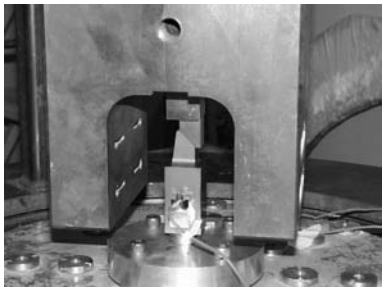

Figure 11.1. System A Single-Leg Assembled Into the BMD.

Joint properties specimens are obtained using the BMD. Comparison of data from jointed specimens with data from corresponding measurements on monolithic specimens yields dissipation and compliance properties that are attributed to the joint.

Unfortunately, the two key difficulties here are substantial:

1. The experiments yield integrated properties of the whole system - the joint, the rest of the specimen, and the compliances of attachments. How the joint properties can be deduced for these experiments and others conducted on monolithic specimens is discussed in the experimental chapters of this handbook.
2. The joint properties that are measured are scalar mappings of force and displacement, while FE descriptions of the components are intrinsically three dimensional. Some method is required to bridge the one-dimensional joint models and the three dimensional FE meshes.

It is this second issue that is the focus of this section.

11.2 Rigid Surface Kinematics

The approach described here and employed in the rest of this document is common in FE modeling of large structures with small contact patches. The technique is to define a rigid surface (geometric patch) on each side of the interface and to slave each rigid surface to a single representative node. This concept is suggested in Figure 11.2. The joint constitutive model then couples the forces (and moments) and displacements (and rotations) of those two representative nodes. In commercial FE code, one usually defines the rigid surfaces using rigid elements (such as RBE3) or multi-point constraints (MPCs).

The solution presented here degrades the field kinematics of the finite elements in the neighborhood of the interface so that it is consistent with the scalar nature of the joint constitutive model. These two rigid surfaces are connected by six, scalar, constitutive equations (one for each relative degree of freedom) relating displacement and conjugate forces. In general, we have experimental data along only one axis, so we employ the associated constitutive model along just those degrees of freedom. The remaining degrees of freedom are connected by whatever constitutive behavior seems plausible or appropriate.

Note that the approach presented here is more rigorous than what is often done in practice by FE analysts. When dealing with coarse meshes, the analyst will just spring connect two nodes on opposite sides of the interface. If the analyst has no intention of refining that mesh and plans to tune the spring anyway, then the analyst will ignore that computed result of applying a point load on a surface because it will not converge as the mesh is refined. In the method discussed in this section, because a geometric patch is treated as rigid, nodes of any refined mesh that are on that surface will also be connected rigidly, so a unique problem of linear elasticity is defined and the numerical solution should converge to the exact solution of the elasticity problem as the mesh is refined.

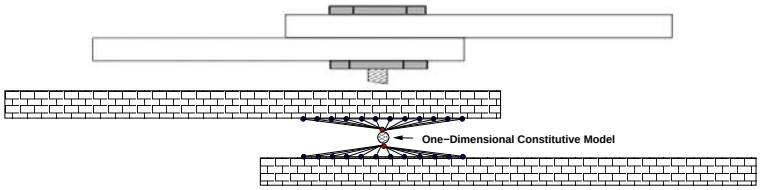

Figure 11.2. Schematic of Nodal Constraint in the Whole-Joint Method.

The scalar constitutive behavior is coupled to the FE displacement and traction fields by constraining the FE nodal displacements on each side of the interface to move rigidly.

11.3 Definition of Joint Properties

It is important that the simplified kinematics employed for our FE analysis are used consistently. In the following, the use of these kinematics in dynamics of jointed structures is illustrated by showing how they are employed in FE analysis to reproduce the experiments from the joint properties that are deduced.

The experimental sections demonstrated the manner in which data collected on jointed specimens can be compared with that collected on corresponding monolithic specimens to deduce joint properties. These comparisons yield values for effective joint stiffness and joint energy dissipation, each as a function of force amplitude. There will be substantial discussion in later chapters

on how to identify appropriate constitutive models and then deduce model parameters from the experimental data.

Consider the monolithic specimen shown in Figure 11.3.

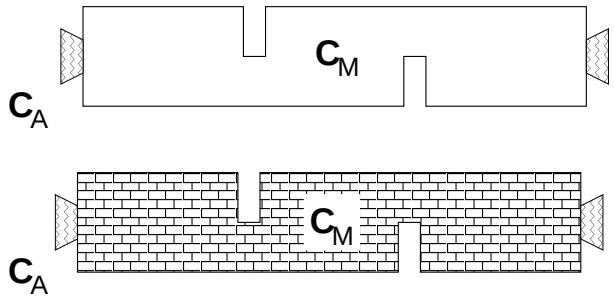

Figure 11.3. Schematic of Monolithic Specimen.

The use of an FE model for the monolithic specimen is employed to deduce the connection compliances.

The net compliance C_N of the specimen is that intrinsic to specimen C_M and that due to its connections to the testing device C_A. Compliance C_N is known from experiment. C_M is calculated from FE analysis, yielding repeatable estimates for the attachment compliance $C_A = C_N - C_M$. C_A will be used later.

Next, consider the representation of the monolithic specimen as an assemblage of lap joint components whose contact surfaces are made rigid (Figure 11.4). The rigidization of those opposing surfaces adds constraints that stiffen the system, so an additional compliance C_R must be placed between the representative nodes to recover the compliance of the monolithic specimen. Fortunately, FE analysis of the half-lap components yields compliance C_{L1} and C_{L2} for the left and right components. The compliance that must be placed between the two surfaces to recover the compliance of the monolithic specimen is $C_R = C_M - C_{L1} - C_{L2}$.

Now an FE model is constructed for the jointed specimen by inserting the joint constitutive model in the bipartite model for the monolithic specimen.

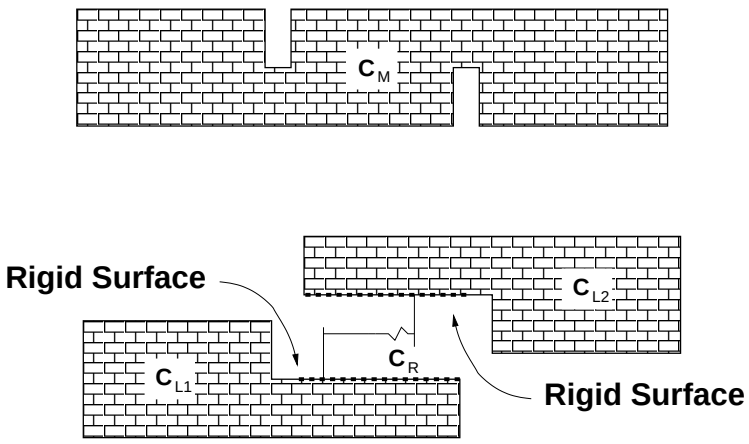

Figure 11.4. Rigid Interface Construction.

A compliance C_R is placed across the rigid surfaces to compensate for the stiffening due to rigidization of the surfaces.

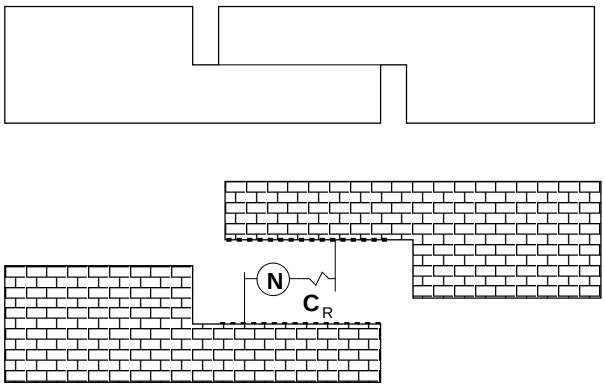

Figure 11.5. Inclusion of the Interface Constitutive Model.

The joint properties are incorporated in the FE model for the specimen by inserting the joint constitutive model into the model for the monolithic specimen.

11.4 Verification

To verify that all of the parameters have been derived correctly and to assess how well the constitutive equation captures the properties of the joint, the deduced compliances, the constitutive model, and the FE models for the two halves of the joint are used to reproduce the original laboratory experiment. First, the test on the monolithic specimen is reproduced. This demonstrates that compliances C_A and C_R have been computed correctly. Performing the corresponding test on the jointed specimen next provides some measure of fidelity by which the joint constitutive model captures the joint response.

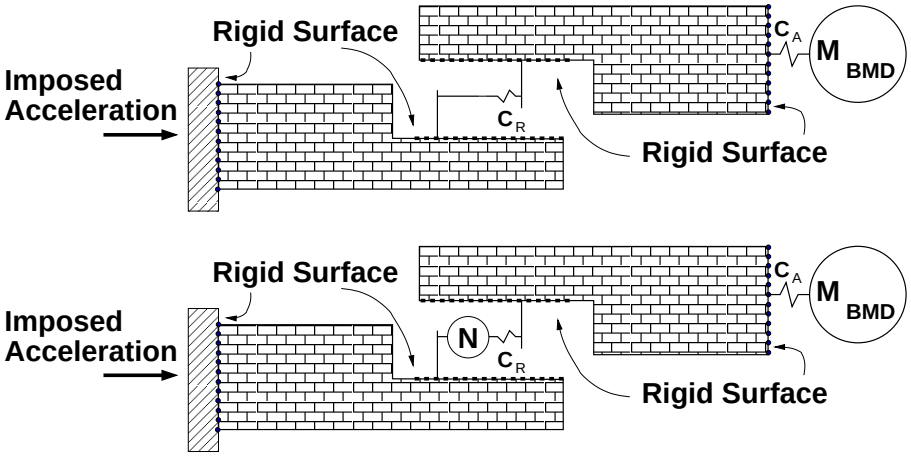

Figure 11.6. Adequacy Test for the Compliance Estimates.

The adequacy of the estimates for C_A, C_R, can be obtained by performing an FE analysis of the original experiment on the monolithic specimen. Some estimate of the adequacy of the constitutive model results when the corresponding calculation for the jointed specimen is performed.

11.5 Other Possible Kinematic Assumptions

The kinematic simplification employed here has advantages of simplicity and clear definition. As mentioned above, a unique solution to the FE problem can be expected as the mesh is refined. There are some disadvantages that should be noted as well.

One disadvantage is that as the mesh is refined near the joint, the rigid boundary condition results in the nonphysical stress singularity mentioned above. This singularity appears to be common to all problems when attempting to connect one dimensional components to two or three

dimensional structures. Although these anomalies are not significant in terms of the engineering calculations, it is worthwhile exploring other strategies.

There are analogous tools devised for simulation of spot welds ([68] for instance), and these might merit investigation for what they can provide in terms of ease of use and computational efficiency. Also, there has been some work at Sandia recently in relaxing the constraint on rigidization on each side of the interface. It is still to be determined whether any of these alternative approaches, when applied to a monolithic specimen can be guaranteed to yield finite C_R.

This area is still a fertile field for investigation.

Chapter 12

Constitutive Modeling for Joints

Daniel J. Segalman[1]

12.1 Introduction

The constitutive behavior of mechanical joints is largely responsible for the energy dissipation and vibration damping in built-up structures. For reasons arising from the dramatically different length scales associated with those dissipative mechanisms and the length scales characteristic of the overall structure, the interface physics cannot be captured through Direct Numerical Simulation (DNS) of the contact mechanics within a structural dynamics analysis. The difficulties of DNS manifest themselves either in terms of Courant times that are orders of magnitude smaller than that necessary for structural dynamics analysis or as intractable conditioning problems.

The only practical method for accommodating the nonlinear nature of joint mechanisms within structural dynamic analysis is through constitutive models employing degrees of freedom natural to the scale of structural dynamics. In this way, development of constitutive models for joint response is a prerequisite for a predictive structural dynamics capability.

A constitutive equation is required that maps arbitrary inputs (histories forces or displacements) into the energetically conjugate quantities (displacements or forces). In general the parameters of that model must be deduced from a small number of physical or numerical experiments of narrowly defined sorts. In the SNL experience, these calibration experiments have been primarily harmonic excitation (on such equipment as the BMD) or ring-down experiments on a dumbbell configuration.

There are many admissible constitutive model forms that could reproduce the available experimental data to within the inherent uncertainty. However, there are a few measures of merit to cause us to prefer one constitutive equation over another:

1. How well is it able to reproduce simultaneously the most important qualitative properties of joints? In most engineering problems, the most important properties are the strongly

[1]Much of this chapter was taken from Reference [69].

nonlinear dependence of energy dissipation on the amplitude of harmonic loading, the significant but less dramatic decrease in joint stiffness with load amplitude at small loads, and the manifestation of macroslip at very high loads.

2. Is the numerical evaluation of the constitutive equation efficient and stable?

3. How many parameters must be deduced from experiments? Fewer is better; it is highly desirable that those parameters should be deduced from a small number of experiments so that other data remains for comparison with model predictions.

4. Is there a well conditioned process for deducing the model parameters from limited experimental data? This last feature requires that a unique parameter set be deduced from a set of data.

5. Is model integration into a structural level FE code practical?

Only one class of constitutive model is explored to any depth in this handbook. This constitutive model satisfies all the above conditions reasonably well and additionally lends itself to mathematical analysis. Certainly other researchers will find other models just as good as the one presented in this handbook, but the value of those models can be demonstrated only after thorough testing against experiment and implementation in simulations of real structures. The editor, having experience in constitutive modeling of several flavors, has already asserted that the community quest for constitutive equations should emphasize quality over quantity.

12.2 Iwan Models

The class of model that is employed here is that of Bauschinger [29], Prandtl [30], Ishlinskii [31], and Iwan [33, 32] model. For convenience, it is referred to in this handbook as the Iwan model. This class of model is mathematically equivalent to a parallel system of Jenkins elements. 12.1. Though Iwan introduced his constitutive models for metal elasto-plasticity, they have since been used to model joints [70, 71], and the work reported here addresses how that model-form can be exploited in a systematic manner to capture the important responses of mechanical joints.

Mathematically, the constitutive form of the model is [33, 72]

$$F(t) = \int_0^\infty k\tilde{\rho}(\tilde{\phi})\,[u(t) - \tilde{x}(t,\tilde{\phi})]\,\mathrm{d}\tilde{\phi} \tag{12.1}$$

where u is the imposed displacement,
$F(t)$ is the applied force
$\tilde{\rho}(\tilde{\phi})$ is the population density of Jenkins elements of strength $\tilde{\phi}$
k is the stiffness common to all of the Jenkins elements
and $\tilde{x}(t,\tilde{\phi})$ is the current displacement of sliders of strength $\tilde{\phi}$

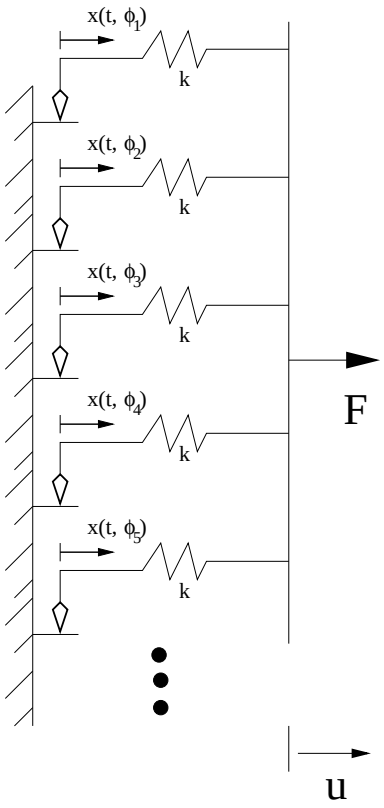

Figure 12.1. Parallel-Series Iwan System.

A parallel-series Iwan system is a parallel arrangement of springs and sliders (Jenkins) elements.

The slider displacements, $\tilde{x}(t,\tilde{\phi})$ evolve from the imposed system displacement, $u(t)$:

$$\dot{\tilde{x}}(t,\tilde{\phi}) = \begin{cases} \dot{u} & \text{if } \|u-\tilde{x}(t,\tilde{\phi})\| = \tilde{\phi}/k \text{ and } \dot{u}\,(u-\tilde{x}(t,\tilde{\phi})) > 0 \\ 0 & \text{otherwise} \end{cases} \tag{12.2}$$

It is assumed $\tilde{x}(0,\tilde{\phi}) = 0$ for all $\tilde{\phi}$. Note that Equation (12.2) guarantees that $\|u-\tilde{x}(t,\tilde{\phi})\| \leq \tilde{\phi}/k$ at all times.

Noting that all Iwan models - even those without uniform k - are Masing models, and all Masing models can be represented by Iwan models with uniform k, there is no loss in generality in employing identical stiffnesses among the Jenkins elements [73].

The parameter k can be removed from the above equations through the following changes of variable:

$$\phi = \tilde{\phi}/k \tag{12.3}$$

$$\rho(\phi) = k^2\tilde{\rho}(k\phi) \tag{12.4}$$

$$x(t,\phi) = \tilde{x}(t,k\phi) \tag{12.5}$$

Equations (12.1) and (12.2) now become

$$F(t) = \int_0^\infty \rho(\phi)[u(t)-x(t,\phi)]\,\mathrm{d}\phi \tag{12.6}$$

and

$$\dot{x}(t,\phi) = \begin{cases} \dot{u} & \text{if } \|u-x(t,\phi)\| = \phi \text{ and } \dot{u}(u-x(t,\phi)) > 0 \\ 0 & \text{otherwise} \end{cases} \tag{12.7}$$

which guarantees that $\|u-x(t,\phi)\| \leq \phi$.

The new quantities have different dimensions than the original ones. Though $\tilde{\phi}$ has dimensions of force, ϕ has dimensions of length. Similarly, $\tilde{\rho}$ has dimensions of $1/\text{force}$ but ρ has dimensions of $\text{force}/\text{length}^2$. The dimensions of the external loads and displacements applied to the joint remain unchanged.

Two overall parameters for the interface can be expressed in terms of the above integral system. The force necessary to cause macroslip (slipping of the whole interface) is denoted F_S, and the stiffness of the joint under small applied load (where slip is infinitesimal) is denoted K_T. Macroslip is characterized by every element sliding:

$$u(t)-x(t,\phi) = \phi \tag{12.8}$$

for all ϕ, so Equation (12.6) yields

$$F_S = \int_0^\infty \phi \rho(\phi)\, \mathrm{d}\phi \tag{12.9}$$

Because no elements have slipped at the inception of loading, (at $t = 0$) Equation (12.6) yields

$$K_T = \int_0^\infty \rho(\phi)\, \mathrm{d}\phi \tag{12.10}$$

12.3 Response of Iwan Models to Small and Large Force

Experiments involving large monotonically applied forces can indicate the force necessary to initiate joint macroslip but, for reasons explained below, it is very difficult to obtain any other meaningful detail on joint response from quasistatic experiments. On the other hand, resonance experiments do enable the measurement of dissipation per cycle with reasonable precision even at relatively small loads [46, 7]. Additionally, with proper calibration, those experiments can be used to obtain effective stiffness as a function of load amplitude. It is shown below how each sort of experimental data can be used to determine the parameters of a parallel-series Iwan model that can capture both quasistatic and dynamic behaviors.

12.3.1 Small Amplitude Oscillatory Loads

When a joint is subject to small amplitude oscillatory lateral loads, the dissipation appears to behave as a power of the amplitude of the applied load. Generally, the exponent of that relationship is a number lying between 2.0 and 3.0. Goodman [74] pointed out that the Mindlin solution [11, 75] for the energy dissipation resulting from oscillatory lateral loads imposed on two spheres pushed together yields a power-law slope of 3.0 in the regime of small lateral loads.)

In Figure 12.2, that power-law slope is represented as $3+\chi$ where χ is a negative number of small magnitude ($-1 < \chi \leq 0$). Mathematically, this is expressed as the following:

$$D(F_0) = \upsilon F_0^{3+\chi} \tag{12.11}$$

where D is the dissipation per cycle resulting from a harmonic load of amplitude F_0

and χ and υ are selected so that Equation (12.11) matches experimental data collected at small force amplitudes.

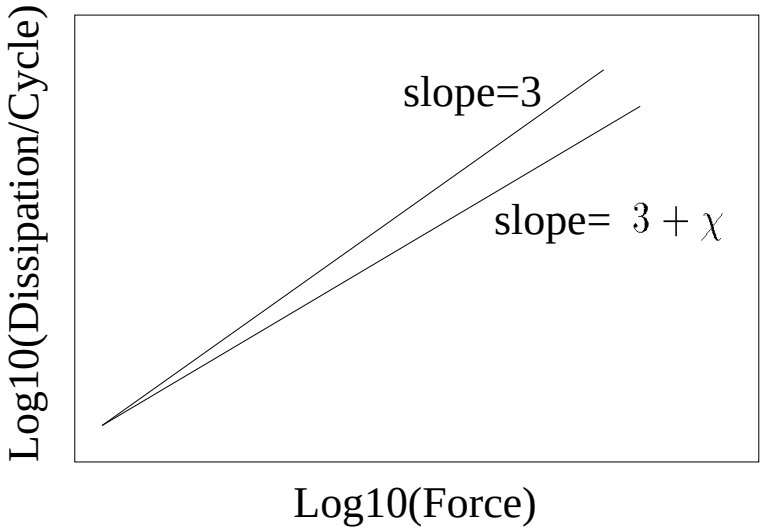

Figure 12.2. Energy Dissipation Under Harmonic Loading.

The dissipation resulting from small amplitude harmonic loading tends to behave as a power of the force amplitude.

The dissipation per cycle associated with oscillatory displacements ($u(t) = u_0 \sin(t)$) applied to a Jenkins element of strength ϕ is the area within a parallelogram shaped hysteresis loop having height 2ϕ and base $2(u_0 - \phi)$. The dissipation integrated over all Jenkins elements is:

$$D = \int_0^{u_0} 4[u_0 - \phi]\phi\rho(\phi)\,\mathrm{d}\phi \tag{12.12}$$

One major simplification made possible for histories where the displacement is bounded by a small value $u_{\max}$ (i.e. $|u(t)| < u_{\max}$) is that the integral of Equations (12.6) and (12.7) can be simplified to

$$F(t) = \int_0^{u_{\max}} \rho(\phi)[u(t) - x(t,\phi)]\,\mathrm{d}\phi + u(t)\int_{u_{\max}}^{\infty} \rho(\phi)\,\mathrm{d}\phi \tag{12.13}$$

$$= K_T u(t) + O({u_{\max}}^2) \tag{12.14}$$

where $O()$ is the notation for quantities that are on the order of their argument as the argument goes to zero [76].

Expanding $\rho(\phi)$ as a

$$\rho(\phi) = \phi^{\chi}\left(a_0 + a_1\phi + a_2\phi^2 \ldots\right), \tag{12.15}$$

and substituting Equations (12.11), (12.14), and (12.15) into Equation (12.12), and matching leading terms, we find

$$\rho(\phi) = \frac{\upsilon(K_T)^{3+\chi}(2+\chi)(3+\chi)}{4}\phi^{\chi} + O(\phi^{1+\chi}) \tag{12.16}$$

for small ϕ [72]. This approach provides something of the character of the population distribution that is necessary to yield a power-law-type dissipation behavior.

12.3.2 Large Monotonic Loads

Considering large monotonic pulls ($0 < \dot{u}$), Equations (12.6) and (12.7) show that

$$F(t) = \int_0^{u(t)} \phi\rho(\phi)\mathrm{d}\phi + u(t)\int_{u(t)}^{\infty} \rho(\phi)\mathrm{d}\phi \tag{12.17}$$

The tangent stiffness is

$$\frac{\partial f}{\partial u} = u(t)\int_{u(t)}^{\infty} \rho(\phi)\mathrm{d}\phi \tag{12.18}$$

from which Iwan derived

$$\frac{\partial^2 F(u)}{\partial u^2} = -\rho(u) \tag{12.19}$$

Because the second derivative of force cannot be measured with any resolution for most joints at small displacements, the above is at best useful only for large displacement experiments.

Figure 12.3 sketches the monotonic force-displacement curve for a canonical lap joint. We anticipate that the force saturates at F_S and interface displacement u_S, corresponding to complete breaking of interface bonds.

Some comment should be made about why it is necessary to guess at the force displacement curves for joints in structures that we typically encounter. The key is that the interface mechanics cannot be viewed directly. The interface region is acted on by external loads conveyed through an

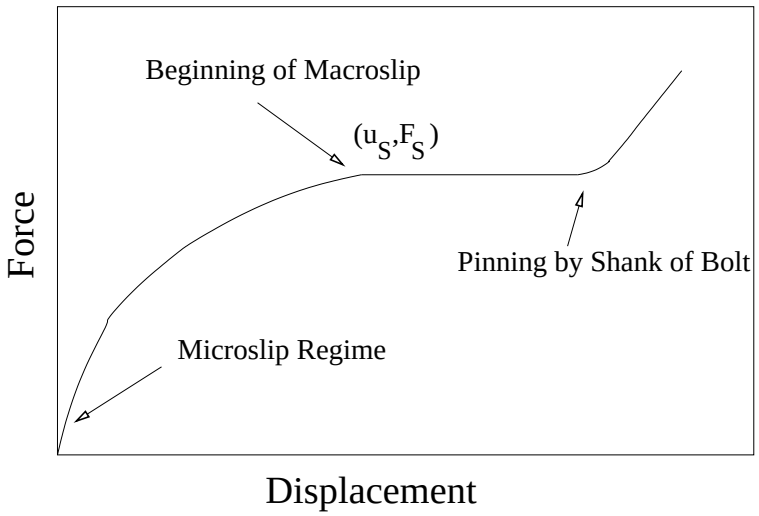

Figure 12.3. Monotonic Pull of a Lap Joint.

The monotonic pull of a simple lap joint shows the force saturates at F_S as the displacement passes a critical value.

elastic structure. Additionally, kinematic measurements are of the net displacements of that composite system - not of the joint. Particularly vexing is that the elastic subsystem is generally much more compliant than the interface until the latter has been forced into the vicinity of macroslip.

This insight is illustrated in Figure 12.4, showing large elastic deformations taking place in a lap joint specimen long before serious slip occurs at the joint. As suggested by the drawing in Figure 12.5, the force-displacement plot looks nearly linear until the applied force almost reaches the level necessary to induce macroslip of the joint. The nearly linear region is dominated by the compliance of the elastic part of the system and the response of the interface is almost entirely obscured. Once the force is nearly sufficient to cause macroslip, it is the (near infinite) compliance of the interface which dominates. Though such experiments do identify the force necessary to initiate macroslip of the joint, they are not very useful to achieve resolution on the force-displacement response of the interface itself.

It should be said that for some structures in which joints represent a major source of stiffness degradation of the structure, Levine and White [70] were able to deduce Iwan parameters by examining distortion of nominal frequency response curves as excitation frequency increased. This technique is an illustration of deducing joint properties indirectly through observation of the integrated behavior of the full structural dynamic response.

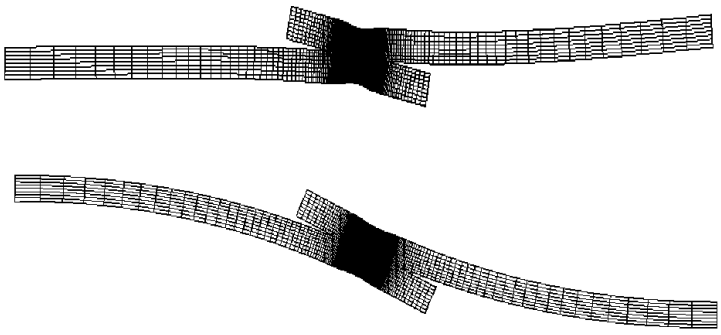

Figure 12.4. Single Lap Joint Deformed Meshes.

The numerical predictions of a finely meshed system containing a single lap joint illustrate how interface displacements are obscured by the large compliance of the elastic response of the attached members. In the figure at top, both sides of the system are clamped, as well as being stretched horizontally. In the figure below that, the left side is clamped and a zero slope boundary condition is imposed on the right.

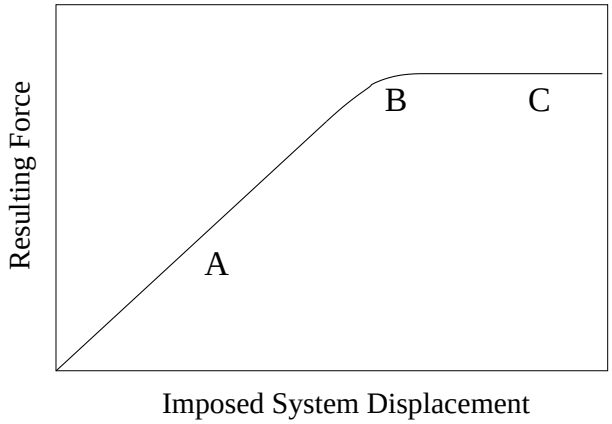

Figure 12.5. Constitutive Response of a Jointed Elastic System.

Typically the force displacement conditions on elastic systems containing joints are dominated at low loads by the elastic compliance (Region A). As the applied load approaches that necessary to initiate macroslip, the force-displacement curve begins to flatten (Region B). In macroslip the force-displacement curve is exactly flat (Region C). The only useful information about the joint available from such experiments is identification of the force necessary to initiate macroslip.

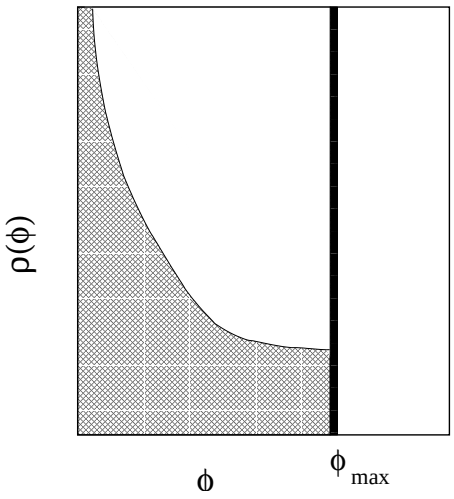

Figure 12.6. Lap Joint Density Distribution Function.

A spectrum that is the sum of a truncated power-law distribution and a Dirac delta function can be selected to satisfy asymptotic behavior at small and large force amplitudes.

12.4 The Four Parameter Iwan Model

The above observations may be summarized:

- at small displacements the population density $\rho(\phi)$ behaves as in Equation (12.16);
- initiation of macroslip occurs at finite displacement, indicating that $\rho(\phi)$ has finite support;
- Equation (12.19) implies that a discontinuous slope of the force-displacement curve at the initiation of macroslip corresponds to a delta function in ρ;

motivating us to consider parallel Iwan systems having a power-law population distribution terminated by a Dirac delta:

$$\rho(\phi) = R\phi^{\chi}[H(\phi) - H(\phi - \phi_{\max})] + S\delta(\phi - \phi_{\max}) \tag{12.20}$$

where $H()$ is the Heaviside step function and $\phi_{\max}$ is numerically equal to u_S. The coefficient S accounts for the potential discontinuity in the slope of the force displacement curve at the inception of macroslip: S is the slope of the force-displacement curve just before macroslip. This form of population distribution is shown graphically in Figure 12.6.

Substitution of Equation (12.20) into Equation (12.6) yields

$$F(t) = \int_0^{\phi_{\max}} [u(t) - x(t,\phi)] R\phi^{\chi} \, \mathrm{d}\phi + S[u(t) - x(t,\phi_{\max})] \tag{12.21}$$

Referring to Equation (12.9), the macroslip force for the system becomes

$$\begin{aligned} F_S &= \int_0^{\phi_{\max}} \phi \rho(\phi) d\phi && (12.22) \\ &= \frac{R\phi_{\max}^{\chi+2}}{(\chi+2)} + S\phi_{\max} && (12.23) \\ &= \phi_{\max} \left(\frac{R\phi_{\max}^{\chi+1}}{\chi+1} \right) [\frac{\chi+1}{\chi+2} + \beta] && (12.24) \end{aligned}$$

where

$$\beta = S / \left(\frac{R{\phi_{\max}}^{\chi+1}}{\chi+1} \right) \tag{12.25}$$

The dimensionless quantity β is the ratio of the joint stiffness due to the ϕ^{χ} term in Equation (12.20) to that due to the δ function term. It will be shown below that β does strongly influence the shape of the log-log curve of dissipation vs force amplitude in harmonic loading, and the shape of the force-displacement curve in monotonic loading.

It is notable that R and S each have fractional dimension - not desirable qualities in constitutive parameters. On the other hand F_S does have the desirable features of having integral dimension and being measurable. Equation (12.24) can be inverted to solve for R by employing Equation (12.25) to express S in terms of F_S:

$$R = \frac{F_S(\chi+1)}{\phi_{\max}^{\chi+2}(\beta + \frac{\chi+1}{\chi+2})} \tag{12.26}$$

and

$$S = \left(\frac{F_S}{\phi_{\max}} \right) \left(\frac{\beta}{\beta + \left(\frac{\chi+1}{\chi+2} \right)} \right) \tag{12.27}$$

Referring to Equation (12.10), the interface stiffness could be computed as

$$K_T = \int_0^{\infty} \rho(\phi) \mathrm{d}\phi = \frac{R\phi_{\max}^{\chi+1}}{(\chi+1)} + S = \frac{R\phi_{\max}^{\chi+1}}{(\chi+1)}(1+\beta) = \frac{F_S(1+\beta)}{\phi_{\max}(\beta + \frac{\chi+1}{\chi+2})} \tag{12.28}$$

The stiffness K_T can be estimated from resonance experiments in a manner described below. Because K_T can be estimated from experiment and involves no fractional units, it is also a desirable parameter.

Equation (12.28) can be solved for $\phi_{\max}$:

$$\phi_{\max} = \frac{F_S(1+\beta)}{K_T\left(\beta + \frac{\chi+1}{\chi+2}\right)} \tag{12.29}$$

which is substituted in to Equations (12.26) and (12.27) to define our model completely in terms of a preferred system of parameters: $\{F_S, K_T, \chi, \beta\}$. The first two of these are measurable and of integral dimension, while the last two are dimensionless.

12.4.1 Monotonic Pull and Hysteresis

Though, as discussed above, performing meaningful monotonic pull experiments on a jointed structure is not feasible, it is worthwhile to express the force-displacement curve that would result if the experiment could be performed on the joint alone. This is particularly true because the original parallel-series Iwan model was presented in terms of the properties of such a curve.

Substituting the equations for monotonic pull into Equations (12.20) and (12.21), transforming to the preferred parameter set, and normalizing by F_S obtains

$$f(s) = F(s\,\phi_{\max})/F_S = \frac{s\left(\beta\,\chi + 2\,\beta + \chi + 2 - s^{\chi+1}\right)}{\beta\,\chi + 2\,\beta + \chi + 1} \tag{12.30}$$

where $s = u/\phi_{\max}$. Note that the only parameters of this dimensionless curve are χ and β, themselves dimensionless. The above function is plotted for $\chi = -1/2$ and for three values of β in Figure 12.7. This figure shows that smaller values of β correspond to larger amounts of curvature prior to macroslip, but greater discontinuity in slope as the imposed force approaches that necessary to initiate macroslip. In fact, examination of Equation (12.21) shows that as $\beta \to \infty$ the response of the model to monotonic load approaches that of a single Jenkins element.

The smoothness - or lack of smoothness - of the transition from partial slip to macroslip is indicated by

$$f'(s=1) = \frac{\beta\,(\chi+2)}{\beta\,\chi + 2\,\beta + \chi + 1} \tag{12.31}$$

and the transition is sudden unless $\beta = 0$.

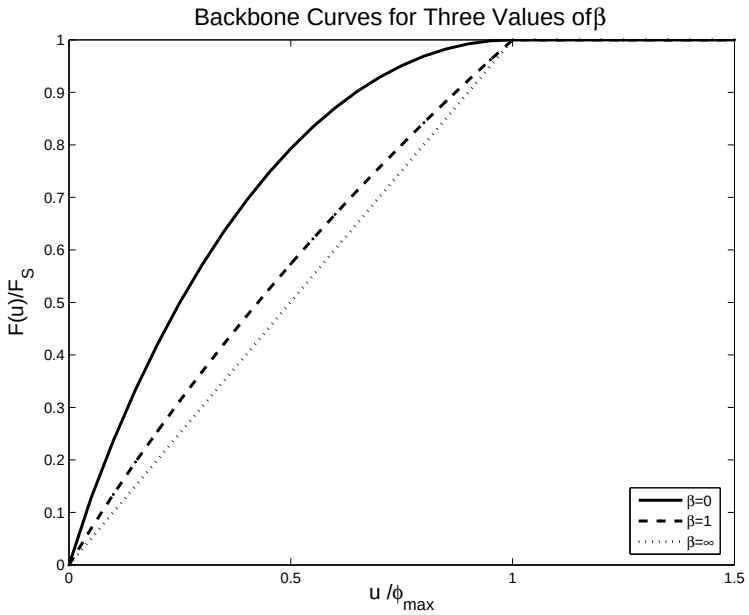

Figure 12.7. Dimensionless Four-Parameter Monotonic Force-Displacement Curve.

The dimensionless force-displacement curve for monotonic pull for the four-parameter model for $\chi = -1/2$ and for three values of β.

As Peng [71] points out, parallel-series Iwan models satisfy the Masing conditions postulated for plastic materials. The first Masing condition, which actually is due to Masing, is that if the virgin material is monotonically deformed to some state and then subject to cyclic deformation at that same amplitude, the following symmetries will exist:

- the "forward" part of the hysteresis curve will look like the loading ("backbone") curve, but stretched along each of the displacement (strain) and force (stress) axes by a factor of two, and translated to terminate at the tip of the backbone curve.
- the "return" part of the hysteresis curve will look like the forward part, but be reflected along each of the displacement (strain) and force (stress) axes.

The second condition states that the equation of any hysteretic response curve is obtained by 1) applying the Masing hypothesis using the latest point of loading reversal and 2) requiring that if an active curve crosses a curve described in a previous cycle, the current curve follows that of the previous cycle. These two conditions constitute the extended Masing rules[77]. With these rules, the response to any load history can be computed from the backbone curve and a record of all load reversals. (Among the ramifications is that K_T is twice the slope of the hysteresis curve just after reversal.)

Mathematically, if the joint is cycled between dimensionless extensions $u/u_{\max} = s_0$ and $-s_0$, then on the extensional branch, the force-displacement curve will behave as:

$$f_e(s) = -f(s_0) + 2f(\frac{s+s_0}{2}) \tag{12.32}$$

and will behave on the compression branch as:

$$f_c(s) = f(s_0) - 2f(\frac{s_0-s}{2}) \tag{12.33}$$

Using the extension curve for the four parameter Iwan model of Equation (12.30), maximum extension $s_0 = \frac{3}{4}$, $\chi = \frac{1}{2}$, and two values of β, one obtains hysteresis loops indicated in Figure 12.8.

12.4.2 Oscillatory Response

For reasons discussed above, quasistatic experiments alone do not provide adequate data to characterize joints. Good supplemental data can be obtained by dynamic resonance experiments [46, 7]. In these experiments, a jointed specimen is anchored on one end by a large sprung mass, and is excited on the other end by an electromagnetic shaker acting through a force transducer. The shaker is driven to excite the system through resonance and to do so at various levels of force amplitude. Because this is a resonance experiment, the energy dissipation per cycle can be deduced from the

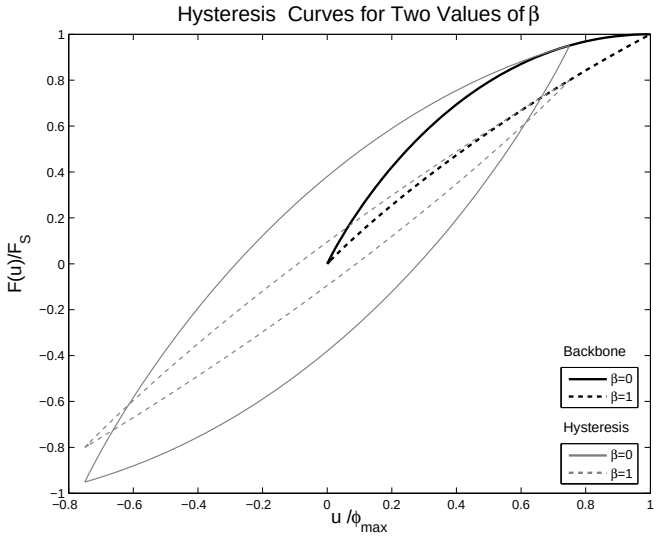

Figure 12.8. Dimensionless Four Parameter Hysteresis Curves.

The dimensionless hysteresis curves for the four parameter model for $\chi = -1/2$ and for two values of β are shown in gray. The maximum and minimum extensions are set to $3/4$ of that associated with the inception of macroslip. The corresponding curves for the unidirectional extension of a virgin material (backbone curves) are shown in black.

force amplitude measured at the force transducer and the acceleration measured at the reaction mass [46].

Additionally, the joint stiffness at each force amplitude can be estimated in the following manner. From the resonance frequency and the known mass, one may deduce an effective compliance of the mechanical system. That compliance is the sum of the compliance of the force transducer, the compliance of the elastic part of the specimen, various attachment compliances, and the compliance of the joint. The sum of all but the joint compliance is deduced by performing a resonance experiment on a nearly identical, unjointed specimen (machined from a single piece of metal). The compliance measured with the unjointed (monotonic) specimen is nearly always force independent and is assumed to be elastic. One subtracts that elastic compliance from the effective compliance measured with the jointed specimen to identify the compliance of the joint:

$$1/K(F_0) = C_{\text{exp.}}(F) - C_E \tag{12.34}$$

where $K(F_0)$ is the effective joint stiffness at force amplitude F_0,
$C_{\text{exp.}}(F)$ is the compliance deduced for the system with the jointed specimen,
and C_E is the compliance deduced for the system with the unjointed specimen.

The parameter K_T is the stiffness of the joint under zero load and is approximated in a practical manner by the $K(F_0)$ found at the lowest driving force employed.

Direct solution of Equations (12.21) and (12.7) for a problem specified by $F = F_0 \sin(t)$ would involve solution of a difficult, nonlinear integral equation. An alternative approach is to specify $u(t) = u_0 \sin(t)$ and then to solve for the resulting dissipation and peak force.

Noting that the maximum displacement of Jenkins elements of strength ϕ is $x(t,\phi) = u_0 - \phi$, we observe that for $u_0 \leq \phi_{\max}$ the dissipation per cycle of such elements is $4(u_0 - \phi)\phi$. The net dissipation per cycle is exactly that given by Equation (12.12). For the density function of Equation (12.21) and for $u_0 \leq \phi_{\max}$, the dissipation per cycle is

$$D = \frac{4R{u_0}^{\chi+3}}{(\chi+3)(\chi+2)} \tag{12.35}$$

$$= 4r^{\chi+3}\left(\frac{F_S^2}{K_T}\right)\left(\frac{(\beta+1)(\chi+1)}{(\beta+\frac{\chi+1}{\chi+2})^2(\chi+2)(\chi+3)}\right) \tag{12.36}$$

where $r = u_0/\phi_{\max}$.

Next, observing that the maximum force seen in each cycle is that force current during the maximum displacement in the cycle:

$$F_0 = \int_0^{u_0} \phi\rho(\phi)\mathrm{d}\phi + u_0\int_{u_0}^{\phi_{\max}} \rho(\phi)\mathrm{d}\phi \tag{12.37}$$

$$= u_0(S + R\frac{{\phi_{\max}}^{\chi+1}}{\chi+1}) - \frac{R{u_0}^{\chi+2}}{(\chi+1)(\chi+2)} \tag{12.38}$$

Equation (12.38) is nondimensionalized by dividing by F_S

$$F_0/F_S = r\frac{(\beta+1) - r^{\chi+1}/(\chi+2)}{\beta + (\chi+1)/(\chi+2)} \tag{12.39}$$

The experimental quantity most easily measured is dissipation , D, as a function of applied, lateral-load amplitude, F_0. Examination of Equations (12.36) and (12.39) affords the following observations:

- As $u_0 \to 0$,
  $F_0 \to r\frac{(\beta+1)}{\beta+(\chi+1)/(\chi+2)} = u_0K_T$, and
  $\partial\log(D)/\partial\log(F_0) \to \chi+3$.

- As $u_0 \to \phi_{\max}$,
  $F_0 \to F_S$, and
  $\partial\log(D)/\partial\log(F_0) \to (\chi+3)(\beta+\frac{\chi+1}{\chi+2})/\beta$.

A plot of dimensionless dissipation per cycle, DK_T/F_S^2, vs normalized force amplitude, F_0/F_S, is shown in Figure 12.9 for $\chi = -1/2$ and three values of β. As expected, we see that for small force amplitudes , $F_0 < F_S/2$, and all values of β the dissipation per cycle behaves as a power-law. Also for values of β substantially greater than 1, the dissipation appears to have power-law behavior over the full range of force amplitude. Asymptotic analysis of Equations (12.36) and (12.39) as $\beta \to \infty$ shows that this should be the case.

Equation (12.38) helps express the secant stiffness at large amplitude oscillation:

$$K(r) = \frac{F_0}{u_0} = K_T\left(1 - \frac{r^{\chi+1}}{(\chi+2)(\beta+1)}\right) \tag{12.40}$$

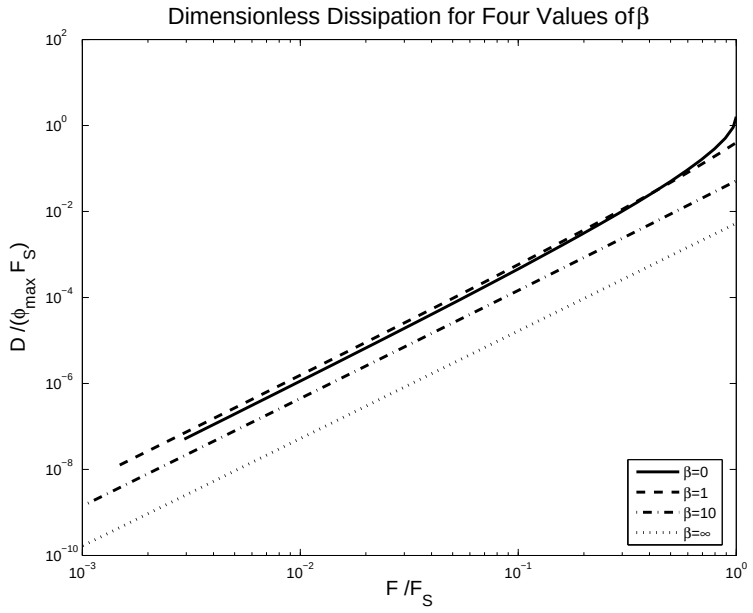

Figure 12.9. Dimensionless Four Parameter Dissipation Per Cycle.

The dimensionless dissipation per cycle as a function of normalized force for the four-parameter model for $\chi = -1/2$ and for three values of β.

12.5 Identifying Parameters

Of the four parameters F_S, K_T, χ, and β, the first can be determined experimentally or estimated via statics and an assumed value for Coulomb friction. The second, K_T, might be estimated by extrapolating specimen stiffnesses obtained from resonance down to a zero load state, though that approach magnifies the experimental uncertainty. It is the determination of χ and β that is particularly challenging.

The following approach is the most robust and most reliable at giving unique parameters. In this approach the dissipation data is simultaneously fit over the whole experimental range in a least squares sense, and the measured stiffness is matched at some point in the midst of the range of applied load. This result is achieved by employing inner and outer iteration loops. The inner loop employs Equations (12.36) and (12.39), F_S, and an estimate for K_T to deduce $\chi(K_T)$ and $\beta(K_T)$ that will reproduce the measured dissipation per cycle over the experimental load range. This is done most easily with a canned optimization technique, such as that available with Matlab's *fminsearch* tool [78]. (One subtlety is that each comparison of the four-parameter model with the experimental data requires solution for $r(\chi,\beta,F_0/F_S)$.) The outer loop consists of a Newton iteration to identify K_T so that when the parameters F_S, K_T, $\chi(K_T)$, and $\beta(K_T)$ are employed in Equations (12.39) and (12.40), the stiffness $K(F_0)$ is correctly predicted at some load in the middle of the experimental data.

Figures 12.10 and 12.13 show reasonable fits to experimental dissipation when the automated method is exploited. In the first case, (Figure 12.10) the fit is to data from a bolted leg of a component mass mockup (Figure 12.12) of a System A substructure. The dissipation data appear to lie on a straight line when plotted in a log-log manner. The parameters used to fit that data are indicated in the figure caption. The value of F_S employed was deduced from statics and a postulated coefficient of friction of 0.5.

The log-log plot of dissipation vs lateral force for the AFF leg problem is nearly linear, but that is not the case for the stepped specimen shown in Figure 12.11. Though this is a geometrically simple specimen, the dissipation data (shown in Figure 12.13) show substantially more curvature. The qualitatively different response might be due to the nearly singular normal tractions at the edges of the contact patch. In this case, there was no unjointed specimen constructed, and it as impossible to know how much of the specimen compliance to ascribe to the joint, so K_T was arbitrarily assumed to be three times the specimen stiffness, with only the inner iteration being employed. The joint parameters of the fitting curve are indicated in the figure caption.

In the case that all data has been collected well below the macroslip force, the dissipation behavior will appear to be power-law in nature. A good fit to that dissipation can be obtained with any value for F_S substantially above the experimental loads and appropriate values of β and χ. Of course, when using a joint model for loads that may approach macroslip, it is appropriate to employ the best possible estimate for F_S.

A listing of the Matlab code developed for the purpose of extracting parameters for this four parameter model, along with an example of running the code is provided in the appendix.

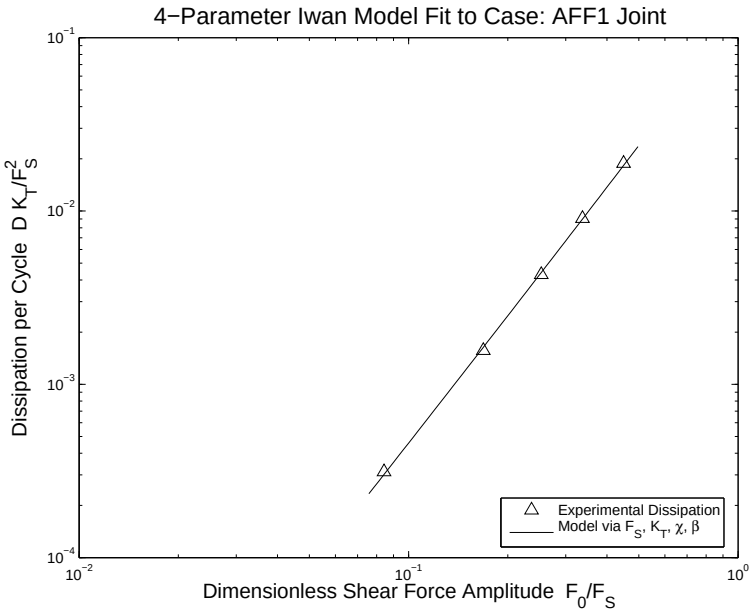

Figure 12.10. Four-Parameter Model Fit to Dissipation Data.

Dissipation data was gathered from a single-leg of a component mass mockup. In this case, there is almost no curvature in the log-log plot of dissipation per cycle vs force amplitude, consistent with a power-law relationship. The dimensionless parameters employed were: $\chi = -0.632$ and $\beta = 3.68$.

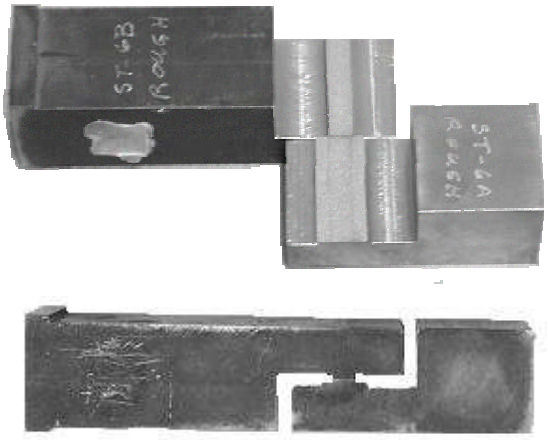

Figure 12.11. Stepped Lap Joint Hardware.

A stepped specimen shows qualitatively different dissipation than a simple half lap joint. The difference may be due to the near singular traction that develops at the edges of the contact patch.

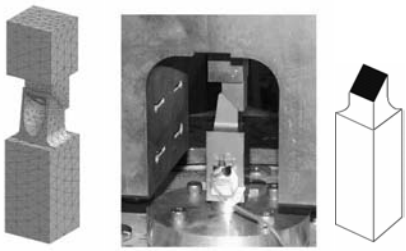

Figure 12.12. Leg Section of the Mock AOS.

To the left is an FE mesh of the full leg section, in the middle is the actual leg section in the test apparatus, and to the right is a sketch indicating the interface being modeled by the four parameter model.

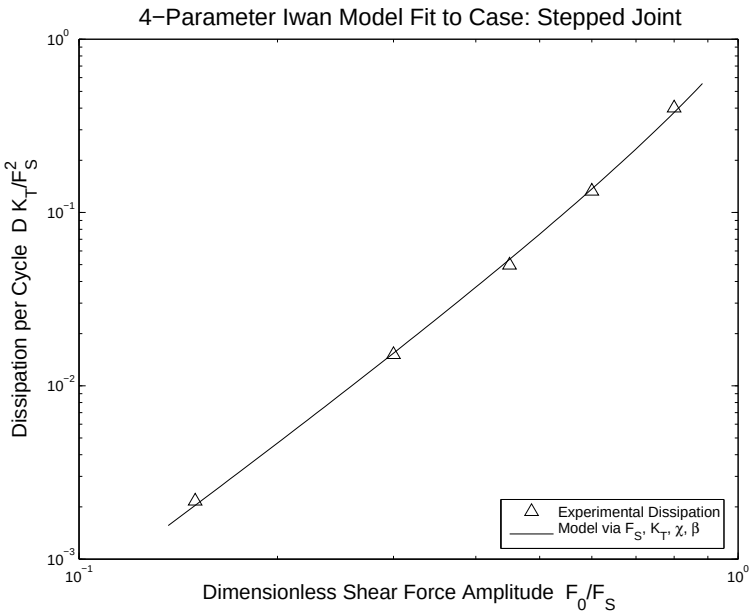

Figure 12.13. Four-Parameter Model Fit to Stepped Specimen Dissipation Data.

In this case, there is appreciable curvature in the log-log plot of dissipation per cycle vs force amplitude. The dimensionless parameters employed were: $\chi = -0.304$ and $\beta = 0.613$.

12.6 Alternate Iwan Formulations

Restricting the model to only four parameters requires sacrificing fidelity in reproducing experimental data. This problem is illustrated in Figures 12.14 and 12.15. Those figures show the joint energy dissipation and joint stiffnesses of nine nominally identical specimens of the kind shown in Figure 12.10. The identification method outlined in the previous section was employed to deduce parameters to match the data of specimen B-2. The dissipation curve is matched very well qualitatively and quantitatively. The model's plot for stiffness as a function of load amplitude does go through the data point employed in the parameter identification, but the model's curve is much flatter than most of the experiments.

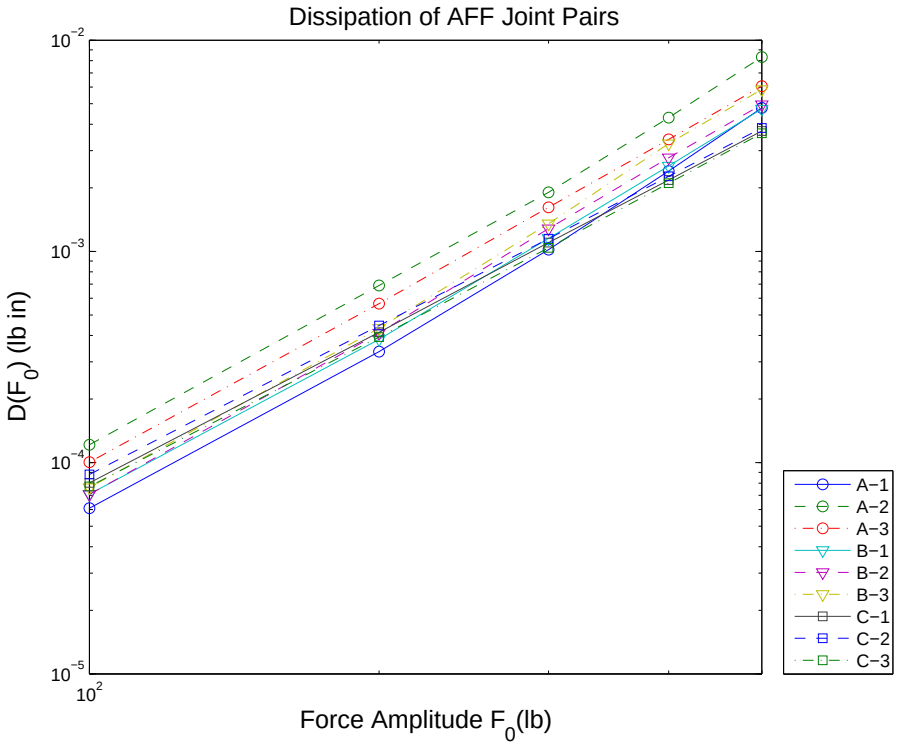

Figure 12.14. Dissipation of AOS Joint Pairs.

The thick dotted line is the dissipation of the four parameter Iwan model, calibrated to reproduce the dissipation curve with fidelity and to match the stiffness of a load of 400 lb.

The inability of the four parameter model to capture the shape of the stiffness vs load curve is a result of restricting the model to four parameters. In our four-parameter model the stiffness declines at a modest slope and drops suddenly to zero when the delta function in Equation (12.20) kicks in. This can also be seen in monotonic pull (Eq (12.18)) where the tangent gradually decreases with displacement u until u exceeds $\phi_{mboxmax}$, and the tangent stiffness instantaneously drops to zero.

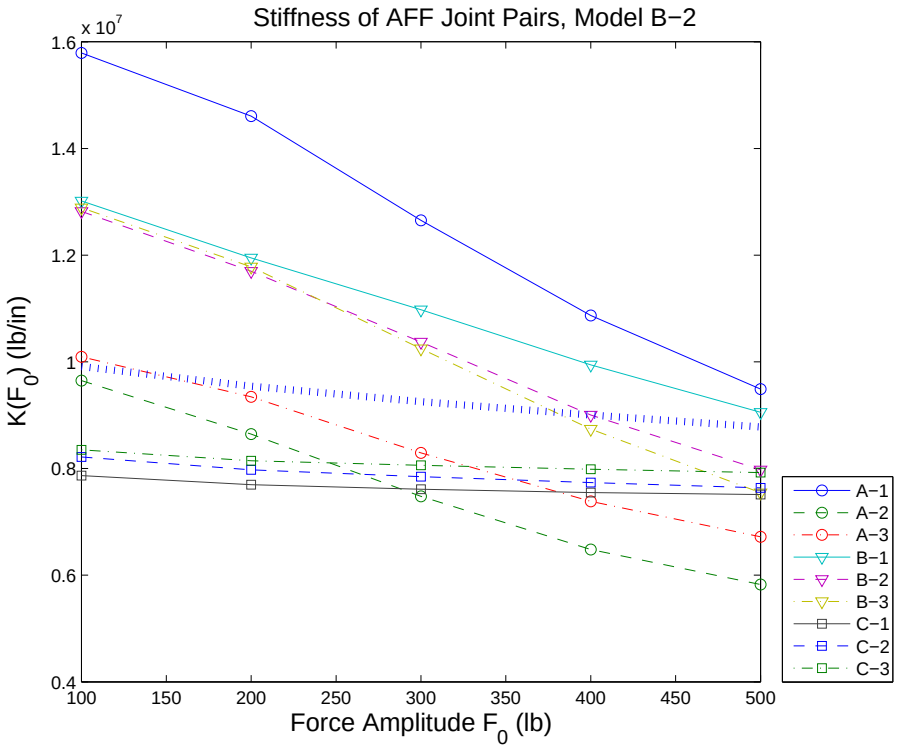

Figure 12.15. Stiffness of AOS Joint Pairs.

The thick dotted line is the stiffness of the four-parameter Iwan model, calibrated to reproduce the dissipation curve with fidelity and to match the stiffness of a load of 400 lb.

Reconsideration of Equation (12.18) suggests that a smoother stiffness vs load curve, one consistent with a continuous tangent stiffness, would be obtained using an expression for $\rho(\phi)$ such as the following.

$$\rho_5(\phi) = [H(\phi) - H(\phi_{\max} - \phi)] \left[R\phi^{\chi} + S(\phi_{\max} - \phi)^{\lambda} \right] \tag{12.41}$$

The above equation, which has been studied recently by the author and Jerry Rouse of Sandia, demonstrates very favorable properties in terms of matching both dissipation and stiffness curves. The cost of the additional parameter (λ) is that there is no clear mapping between model parameters and characteristic features of the experimental data, and that one must devote much more of the experimental data to parameter identification, leaving less for validation.

Many other density functions for parallel-series Iwan models can be suggested, and the author encourages the reader to explore other low parameter distributions.

12.7 Discretization

Equations (12.6) and (12.7) are sufficient to solve for the force response of the above Iwan system once one has the constitutive parameters (F_S, K_T, χ and β). It is useful to discretize the integral in Equation (12.6) in the following manner. One breaks up the interval $(0, \phi_{\max})$ into N intervals whose lengths form a geometric series:

$$\Delta\phi_{m+1} = \alpha \Delta\phi_m \quad \text{for all } m+1 < N \tag{12.42}$$

where α is a number slightly greater than one ($1 < \alpha$) and $\phi_{\max}$ is determined from Equation (12.29). That the sum of the intervals must be the whole interval:

$$\sum_{m=1}^{N} \Delta\phi_m = \phi_{\max} \tag{12.43}$$

permits us to solve

$$\Delta\phi_m = \alpha^{m-1} \Delta\phi_1 \tag{12.44}$$

where

$$\Delta\phi_1 = \left[\phi_{\max} \frac{\alpha - 1}{\alpha^N - 1} \right] \tag{12.45}$$

Consider one sample point, characterized by slide strength ϕ_m, at the midpoint of each interval $\Delta\phi_m$. At that sample point, the evolution of $x_m(t)$ is computed per Equation (12.7). For quadrature purposes, the coordinates of the left and right hand of each subinterval are $\phi_{l,m}$ and $\phi_{r,m}$ respectively.

The force is evaluated by a discrete version of Equation (12.6).

$$F(t) = \sum_{m=1}^{N} F_m(t) + F_\delta(t) \tag{12.46}$$

where

$$F_m(t) = \begin{cases} R\dfrac{\phi_{r,m}^{2+\chi} - \phi_{l,m}^{2+\chi}}{2+\chi}\,\mathrm{sgn}[u(t) - x_m(t)] & \text{if } \|u(t) - x_m(t)\| = \phi_m \\ R\dfrac{\phi_{r,m}^{1+\chi} - \phi_{l,m}^{1+\chi}}{1+\chi}\,[u(t) - x_m(t)] & \text{if } \|u(t) - x_m(t)\| < \phi_m \end{cases} \tag{12.47}$$

$$F_\delta = S\phi_{\max}[u(t) - x_\delta(t)], \tag{12.48}$$

$\phi_\delta = \phi_{\max}$, and x_δ and each $x_m(t)$ evolve per Equation (12.7). Appropriate values for R and S are determined from Equations (12.29) and (12.26) and Equations (12.29) and (12.27), respectively.

Note that the above quadrature reproduces the values for F_S in Equation (12.23) exactly.

The discretization discussed here is illustrated by the results of a C++ code that imposes cyclic deformation on a four parameter Iwan system, and calculates the energy dissipation once steady state is achieved (always on the second cycle). Those numerical calculations are compared with the analytic expressions of Equation (12.36). In Figure 12.16, for the amplitude range $0.1F_S < F_0 < F_S$, integration over the responses of as few as 10 Jenkins elements ($N = 10$) appears to be sufficient. Satisfactory results were achieved in all exercises using values of $\alpha = 1.2$ and $N = 50$. This choice is certainly overly conservative.

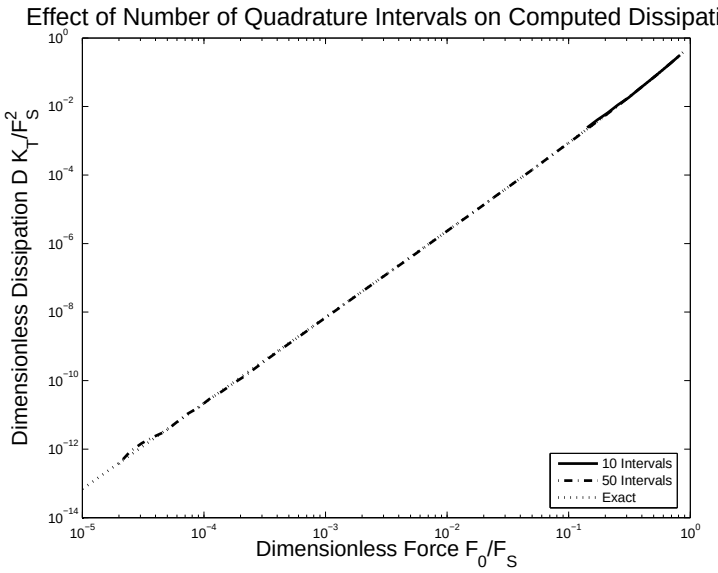

Figure 12.16. Dissipation Prediction Comparison.

Comparison of dissipation prediction of Equation (12.36) with the quadrature of Equations (12.46) - (12.48).

The question arises as to whether there is analytic guidance on how many Jenkins elements are necessary. The simplest criteria are:

- In a monotonic pull, the stiffness degradation from K_T down to zero at macroslip should occur without too much discontinuity in the stiffness slope:

$$\max_m \{\rho(\phi_m)\Delta\phi_m\} \ll K_T \tag{12.49}$$

The maximum term in the above sequence is that associated with the last increment, so the condition is

$$R\left[\frac{\alpha^{N-1}(\frac{1+\alpha}{2})-1}{\alpha^N-1}\right]^{\chi}\frac{\alpha^{N-1}(\alpha-1)}{\alpha^N-1}\phi_{\max}^{1+\chi} \ll K_T \tag{12.50}$$

For large N, this condition becomes

$$\left(\frac{\chi+1}{\beta+1}\right)\left(\frac{(\alpha+1)^{\chi}(\alpha-1)}{2^{\chi}\,\alpha^{\chi+1}}\right) \ll 1 \tag{12.51}$$

For ranges of χ and β considered above ($0<\chi<1$ and $0<\beta$), values of α on the order of 1.1 or 1.2 appear to cause Equation (12.51) to be satisfied adequately.

- The sliding forces associated with the weakest element should slide at a force well below the smallest increment of force $\Delta F_{\min}$ between the reversals to be captured:

$$R\frac{\phi_{r,1}^{2+\chi}-\phi_{l,1}^{2+\chi}}{2+\chi} \ll \Delta F_{\min} \tag{12.52}$$

This becomes a condition that

$$R\left(\phi_{\max}\frac{\alpha-1}{\alpha^N-1}\right)^{\chi+2}/(\chi+2) \ll \Delta F_{\min} \tag{12.53}$$

The quantity on the left goes as $\alpha^{-(\chi+2)N}$, explaining why Equation (12.53) appears to be satisfied with fairly modest values of N.

12.8 Conclusion

The four parameter model presented here appears to be capable of capturing the dissipation behavior found from harmonically loaded experiments on lap joints conducted so far. Further, the tools have been demonstrated to deduce the necessary model parameters with only modest effort.

Though the results presented here provide some reason for optimism, comparison with more sophisticated experiments should be made. Among those experiments could be multi-frequency experiments such as discussed by Segalman [72] or random vibration experiments as performed by Smallwood for his hysteretic model [79]. Such experiments would be necessary to validate this four parameter model in ranges and types of loadings other than those used to calibrate it.

The delta function in Equation (12.21) causes the force-displacement curve to have a discontinuity in slope as the joint approaches macroslip. Because there does not appear to be any precise

data on this transition, it is unclear whether the slope discontinuity is a problem. The discontinuity can be removed by replacing the delta function by an integrable singularity at the expense of adding one more parameter. A model of this type has been suggested in [73].

Finally, constitutive equations of the kind developed here are “whole-joint” models. Such models may capture the response of the joint for the class of loads from which model parameters were deduced, but they give little insight into the micro-physics taking place. Also, it is not yet clear how to integrate joint data taken from qualitatively different load types - such as tension and moment loads - into models of this sort.

Over that longer term, more sophisticated approaches must be developed that better incorporate the distribution of tractions and displacements that develop dynamically around the joint, and that do not presume a specific nature to the joint loading.

Chapter 13

Modeling of Threaded Joints using Anisotropic Elastic Continua

Daniel J. Segalman and Michael J. Starr[1]

13.1 Introduction

This chapter is different from the previous ones in that it discusses a modeling effort that preceded any significant experimental program. The theme of this work was to assess whether the threaded region of a threaded connection could be approximated by a block of equivalent anisotropic material. Results of this modeling effort are intended to provide guidance in simulating threaded connections within large structures. Also this modeling effort is intended to provide guidance on future experimental efforts on threaded connections.

Studies of threaded connections have become ubiquitous in recent technical literature due to the advancing capabilities of FE tools. In most cases, these analyses are validated through comparison to the broadly accepted theoretical work of Sopwith [81] and the experimental work of Goodier and Hetenyi [82, 83].

Finite element models have become accepted tools for the design of screw threads and the development of design codes for mechanical and structural applications [84]. Implicit in the appropriateness of such analyses is sufficient discretization of the model mesh to capture the physics of contact between adjacent threads and to capture adequately the singular behavior at the thread root.

Threaded joints are not only a major component of the mechanical integrity of the structure, but they are also a major path for mechanical energy flow through the system. From the perspective of structural dynamics, the energy flow through a threaded joint is generally a more important consideration than mechanical energy dissipation because it is believed that there is very little energy dissipation in tightened threaded connections. (See [85] for an example.) Very finely meshed, quasistatic FE analysis of joints can lend insight into joint mechanics, but fine meshes are

[1]Much of this chapter has been taken from Reference [80].

impractical for direct use in structural dynamics modeling, typically requiring impractically small time steps [86].

Rather than using finely meshed individual threads, a recourse is to replace the threaded region with an equivalent medium that captures the manner in which statically indeterminate equilibrium is achieved in the joint and quantitatively represents the manner of mechanical energy transmission through the joint. Bretl and Cook [87] employed an axisymmetric technique to replace the thread zone with a layer of elements with orthotropic properties. Their numerical results agreed well with theoretical and experimental results, but required an *a priori* assumption of zero normal stress in an assumed direction.

In this paper, a simple, low order modeling approach that captures the general behavior that would be manifest by a very finely meshed FE model of the threaded region is explored. The approach is similar to that of Bretl and Cook in that a narrow region including opposing thread pairs is replaced by a homogeneous, continuous material with fictitious material properties. However, rather than assuming a principal direction and normal stress condition to employ an orthotropic model, anisotropic elastic properties are deduced by performing a set of FE simulations involving homogeneous boundary conditions on a finely meshed, characteristic thread pair unit. This systematic method of arriving at effective material properties leads to easy implementation within an FE code. The resulting linear model provides an otherwise missing link in the linear structural dynamic analysis of systems connected by threaded assemblies.

The next section explains the motivation and theoretical development of this approach. The remainder of this chapter illustrates the technique through a set of two dimensional, numerical, bolt-pull simulations.

13.2 Theoretical Construction of Equivalent Homogeneous Material

When performing failure analysis, highly discretized geometries may be inescapable, although engineering judgment may be used to concentrate investigation on local regions of expected high stresses and strains. Structural dynamics analysis, on the other hand, endeavors to capture the manner in which the local geometries and physics yield a global response. Complex interfaces, notably threaded connections, require significant numbers of elements to capture the physics of the mechanical interaction. The core problem of integrating micro-mechanical analysis of thread interactions with structural dynamics lies in the fundamentally different spatial (and temporal) scales associated with each. This difficulty manifests itself in two ways.

1. The myriad tiny elements needed to capture the geometry and detailed mechanics of each thread pair define a time scale through the Courant-Friedrichs-Levy condition that is orders of magnitude smaller than those characteristic of the dynamics of the structure as a whole [88]. Regardless of the number of processors available to the analyst, time integration associated with each joint element domain will involve time steps that are orders of magnitude

greater in number than dynamic analysis of similar structures without joints. If this difficulty is addressed through implicit integration, the problem manifests itself through prohibitively bad matrix conditioning. In this sense the problem has more to do with the size of the elements than with the number of elements.

2. Attempting to capture the full unilateral contact mechanics of each joint pair during the structural dynamics analysis requires solving the coupled, nonlinear, contact problem across each opposing element surface pair. Such problems are particularly difficult, because they converge slowly and in a manner exacerbated by the number of potential contact pairs involved.

In the method presented here, the above difficulties are eliminated by replacing the whole threaded region by a continuous equivalent material. Finite element modeling of this equivalent material could involve elements roughly on the scale of the thread pairs rather than on the scale necessary to micro-model such pairs, thus obviating the first issue raised above. If some of the nonlinearity intrinsic to thread mechanics (such as frictional energy dissipation) are to be captured, an appropriate, equivalent nonlinear material would be devised. In that context, the nonlinearity would be embodied in the nonlinear properties of a small number of finite elements representing the threaded region. For example, an anisotropic, elastic-plastic, constitutive model might be employed for this purpose. In this manner the second of the above difficulties is circumvented. If, however, the primary interest is the elastic behavior of the threaded zone as it affects structural dynamics, an equivalent, anisotropic, elastic medium is sufficient. This is the approach presented here.

The theoretical construction of equivalent material properties begins with the definition of the thread pair unit cell. Figure 13.1 shows a cell of the representative thread pair, the associated fine FE mesh of the cell, and an equivalent material mesh of the same cell. The micro-meshed thread pair is placed in a large mesh containing an array of similar thread pairs (Figure 13.3). The boundaries of this large periodic mesh are then subjected to a number, N, of different displacements consistent with homogeneous deformations. Here, St. Venant's principle is assumed to assert that the resulting deformation field in the middle thread pair is similar to that which would result if the thread pair were part of an infinite array of such thread pairs. (Note that St. Venant's principle is applied to the far-field, elastic portion of the problem, not to the inelastic near field.) From the static solutions of each of the N displacements, equivalent homogeneous stresses and strains are deduced. The mathematics of these calculations are discussed in Appendix sections C.0.1 and C.0.2, respectively. Finally, the constitutive parameters of an equivalent, anisotropic, elastic material most consistent with the above ensemble of stress and strain pairs are deduced. The manner in which this optimization is achieved can be found in the Appendix section C.0.3.

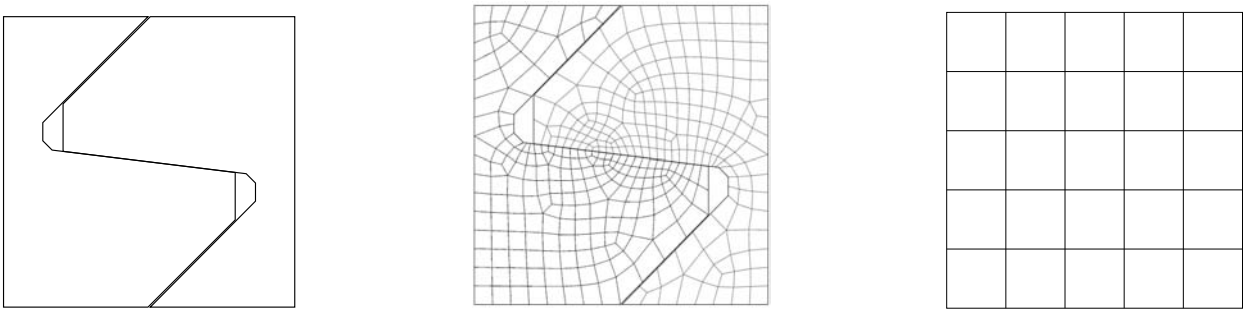

Figure 13.1. Unit Cell for a Representative Thread-Pair.

13.3 Applications in Two Dimensions

13.3.1 Constitutive Formulations

The general approach introduced in this manuscript is illustrated in this section for a problem of two dimensional, plane elasticity (plane stress or plane strain). In the most general case of elastic anisotropy, there are 21 material parameters to identify, but in the case of two dimensional plane elasticity, there are only 3 significant stress components and 3 significant strain components, so the number of necessary parameters reduces to 6:

$$\begin{bmatrix} \sigma_{xx} \\ \sigma_{yy} \\ \sigma_{xy} \end{bmatrix} = \begin{bmatrix} C_1 & C_3 & C_5 \\ C_3 & C_2 & C_6 \\ C_5 & C_6 & C_4 \end{bmatrix} \begin{bmatrix} \varepsilon_{xx} \\ \varepsilon_{yy} \\ \varepsilon_{xy} \end{bmatrix} \tag{13.1}$$

Though it may be that the equivalent material response is nearly orthotropic, further reducing the number of parameters, the use of general anisotropy permits us to avoid having to identify the principal directions.

The quasistatic, FE code JAS3D [89] was used in the calculations discussed here, with its three dimensional, orthotropic, material model extended to accommodate full anisotropy. The choice of plane stress or plane strain elasticity is implemented through the choice of boundary conditions applied to surfaces normal to the x, y plane.

Axisymmetry is accommodated at the cost of just a little more complexity. The thread pitch is assumed small relative to the distance of the thread zone from the axis of symmetry and the circumferential direction is assumed to be a principal material direction. The equilibrium equations involve the three stresses discussed above and the stress $\sigma_{\theta\theta}$ in the circumferential direction. Given

the above assumptions, the elastic constitutive model is of the following form:

$$\begin{bmatrix} \sigma_{xx} \\ \sigma_{yy} \\ \sigma_{xy} \\ \sigma_{\theta\theta} \end{bmatrix} = \begin{bmatrix} C_1 & C_3 & C_5 & \\ C_3 & C_2 & C_6 & \\ C_5 & C_6 & C_4 & \\ & & & C_7 \end{bmatrix} \begin{bmatrix} \varepsilon_{xx} \\ \varepsilon_{yy} \\ \varepsilon_{xy} \\ \varepsilon_{\theta\theta} = u_x/r \end{bmatrix} \tag{13.2}$$

For simplicity of presentation, the rest of this article focuses on problems of plane elasticity, but the methods employed apply similarly to problems of axisymmetry.

13.3.2 Plane Elasticity Threaded Bolt Experiments

The ability of the equivalent material to replace threaded models was explored for the two, canonical, threaded bolt configurations in Figure 13.2. The geometry on the left, Case 1, approximates the case of a bolt in an infinite substrate. The geometry on the right, Case 2, is similar to the "classical" bolt/nut geometry that is frequently reported in the literature. The threads are of the buttress variety with the assumed material properties of an aluminum alloy ($E = 69$ GPa and $\nu = 0.33$) and the boundary conditions are those of plane strain ($\varepsilon_{zz} = 0$).

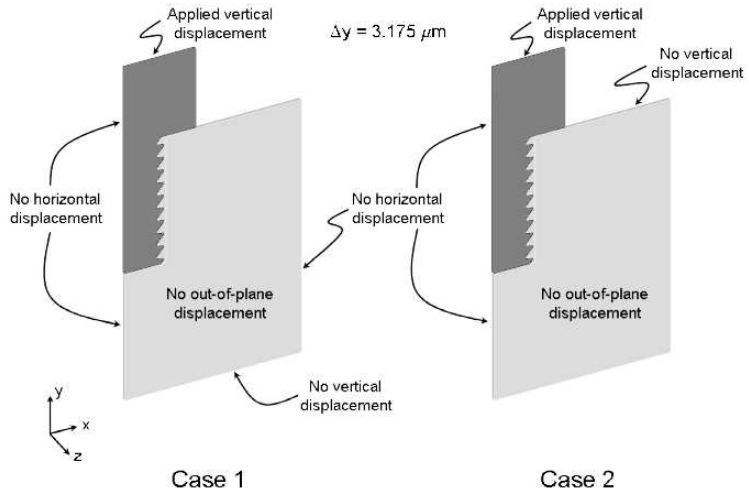

Figure 13.2. Simple, Plane Strain, Bolt-Pull Test.

Configuration of test designed to exercise the equivalent material model. Case 1 approximates that of a bolt in a large block. Case 2 is consistent with the boundary conditions of a tightened bolt/nut system. The model is cut along its plane of symmetry.

This geometry has a large number of threads, making an approximation of periodicity plausible. Thread dimension is small compared to the distance from the axis of symmetry, supporting the

plane strain geometric assumptions. In applying this method, a unit thread pair (or unit cell) is defined so that the identified thread region can be treated as an assembly of stacked, unit thread pairs. A unit thread pair is highlighted in its test matrix in Figure 13.3. The associated FE analysis of the unit thread pair requires sufficient geometric resolution to contain all of the pertinent features necessary to capture the important interactions among the teeth.

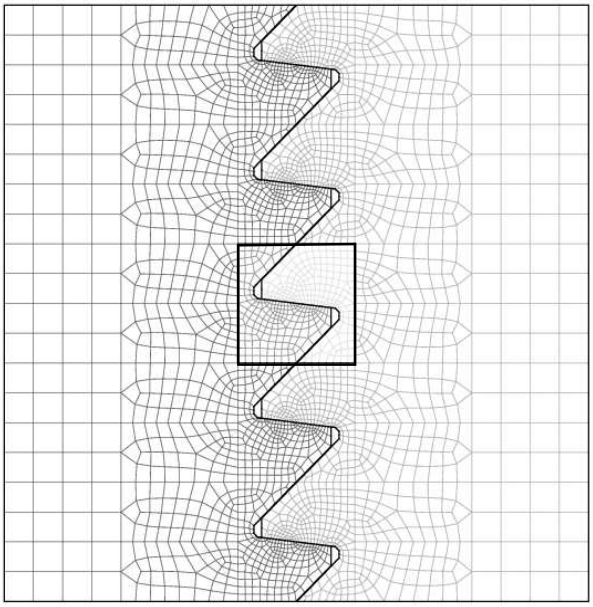

Figure 13.3. Thread Test Model.

The finely meshed, thread test model for determining material properties in plane strain. The center thread pair is the cell on which the material parameters are calculated.

The thread pair is loaded by applying displacements upon the boundary surfaces of the matrix. Figure 13.4 shows the four loading cases considered for developing the material constants: two extensional cases and two shear cases. For each case, the FE code is employed to find the stress and displacement fields over the whole structure from which the equivalent (mean) homogeneous stress and strain fields are deduced in the region of the representative thread pair. Equivalent elastic constants are then calculated in the manner discussed in the previous section, assuming perfect adherence (welded conditions) on each screw thread interface.

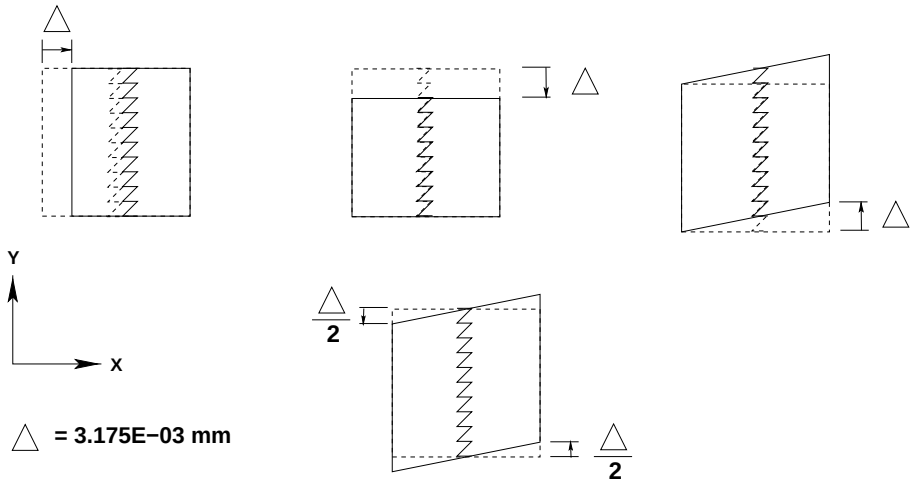

Figure 13.4. Thread Load Cases.

The four load cases employed to develop the equivalent material parameters.

With the equivalent elastic properties now defined, a displacement- controlled experiment, where the top surface of the bolt head depicted in Figure 13.2 was displaced upward 3.175 μm, was performed for three, unique, thread representations for both sets of boundary conditions. Two of the thread representations employed identical meshes (Figure 13.5) and the actual screw thread geometry, but differed in the application of the contact condition across adjacent threads. The two contact conditions were: frictionless across contacting interfaces, and welded across contacting interfaces. These two cases serve as bounds to the stiffness response of the bolt/block system. The number of elements employed in the mesh for these cases was 6309 hexagonal elements, of which 1219 were located in the thread region. Most of the 5090 elements outside the thread area were required to accommodate the transition from the very fine mesh used in the threads.

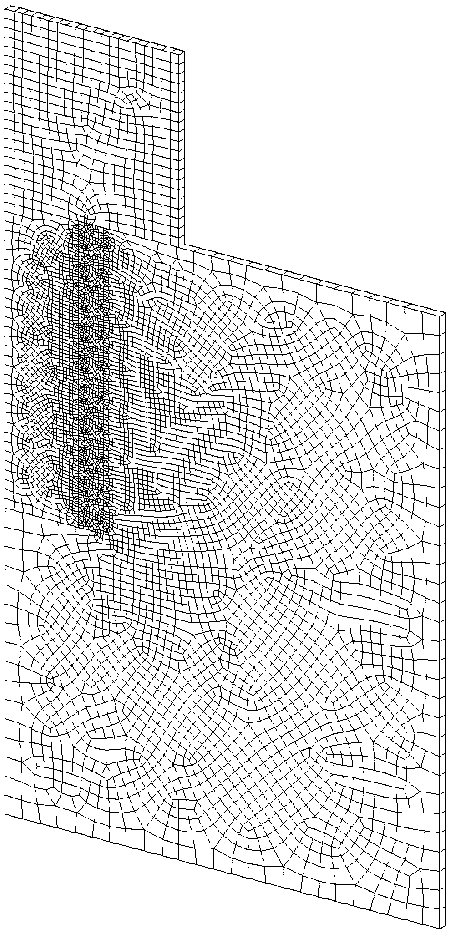

Figure 13.5. Finely Meshed Thread Model.

The finely meshed, thread model employs 6309 hex elements, with 1219 of those elements located in the thread region.

The third thread representation was that of an equivalent, continuous, homogeneous, anisotropic, elastic material. Several different meshing schemes, with increasing degrees of coarseness (de-

creasing degrees of fineness), were employed for comparison to the screw thread geometry results. Figure 13.6 shows a mesh of intermediate coarseness, which has 1754 hexagonal elements, with 230 of these elements located in the thread zone.

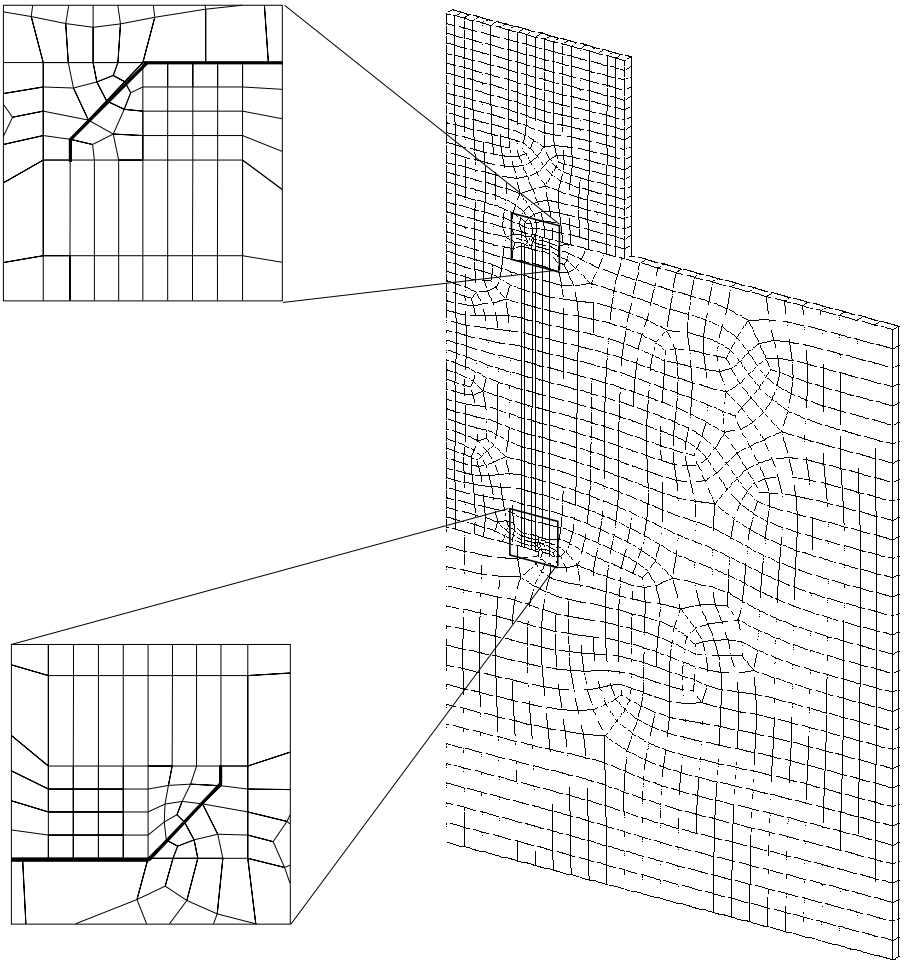

Figure 13.6. Equivalent Material Model Mesh.

The coarsely meshed, equivalent material model used for comparison in the following plots employs 1754 hex elements, with 230 of those elements located in the thread region. The thick solid lines in the insets are planes of discontinuity within the equivalent material.

An important feature of this equivalent, anisotropic, material mesh is shown in the insets of Figure 13.6. The equivalent material approximation is only good where the thread loads are nominally periodic. This assumption breaks down at the extreme boundaries of the threaded region, and the voids between the threads must be accommodated explicitly. This result is achieved by introducing "cuts" in the mesh at physical locations of non-contact that precede the first thread interface and that follow the last thread interface. These cuts are indicated in the insets with solid black lines.

Discontinuous displacements are admitted across the cuts, approximating the free surfaces around the voids.

For the boundary conditions of Case 1, a comparison of the predictions associated with each of the three, described, thread representations is shown in the next five figures. The mesh of Figure 13.6 was used for the equivalent material model. Figure 13.7 shows the resultant vertical reaction force for each thread representation as the top of the bolt head is subjected to an imposed vertical displacement. For the small displacements imposed, the response in each instance appears linear with effective stiffness values of (10^6 N/m) 12.17, 12.96, and 12.90 for frictionless screw threads, welded screw threads, and the welded, equivalent-material model, respectively. The latter underestimates the effective stiffness of the welded screw threads by less than 0.05%. The welded equivalent material and the frictionless interface were not expected to agree as well, and indeed, these two sets of predictions differ on the order of 6%. The difference in effective stiffness values for the screw thread meshes with different contact conditions appears to be broadly consistent with those numerical results reported by Chabaan and Jutras [84].

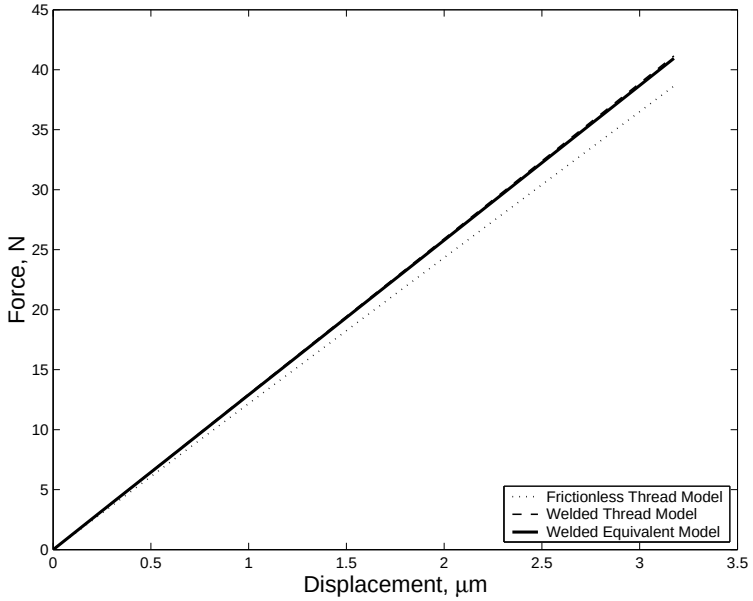

Figure 13.7. Force vs Displacement Plot.

Three material cases are shown: finely meshed, welded threads; finely meshed, frictionless threads; and coarsely meshed, welded, equivalent material. The displacement is measured at the nodes where the displacement is imposed.

These results raise the intriguing possibility of devising an appropriate, nonlinear, constitutive model to capture the behavior of the frictionless simulations. Development of such a nonlinear model could be the topic of future study.

Figure 13.8 shows a plot of the shear stress along the mid-line of the mated screw threads and through the middle of the equivalent material. The origin is positioned at the bottom of the thread stack. Of course, for the meshed screw thread cases, the shear stress trace necessarily passes through an interface, whereas the equivalent material is continuous. The oscillatory period of the shear stress along the screw threads corresponds to the geometric period of thread pairs. The shear stress in the equivalent material appears to match the trends of the shear stress at the top and bottom of the thread stack. The shear stress also matches well in the mean sense along the interior thread region. Figure 13.9 illustrates this matching more directly as the shear stress is integrated along the length of the thread stack. Again, the origin is located at the bottom of the thread stack. The equivalent material model matches well with the welded, screw thread case. The oscillations in the screw thread models reflect the periodic nature of the geometric discontinuities along the thread stack.

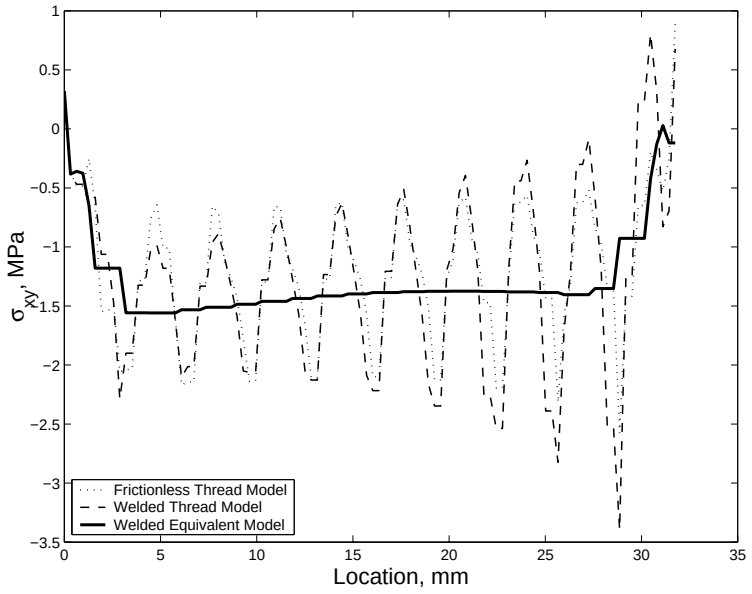

Figure 13.8. Shear Stress Comparison.

Shear stress along the mid-line of the thread region for three material cases: finely meshed, welded threads; finely meshed, frictionless threads; and coarsely meshed, welded, equivalent material.

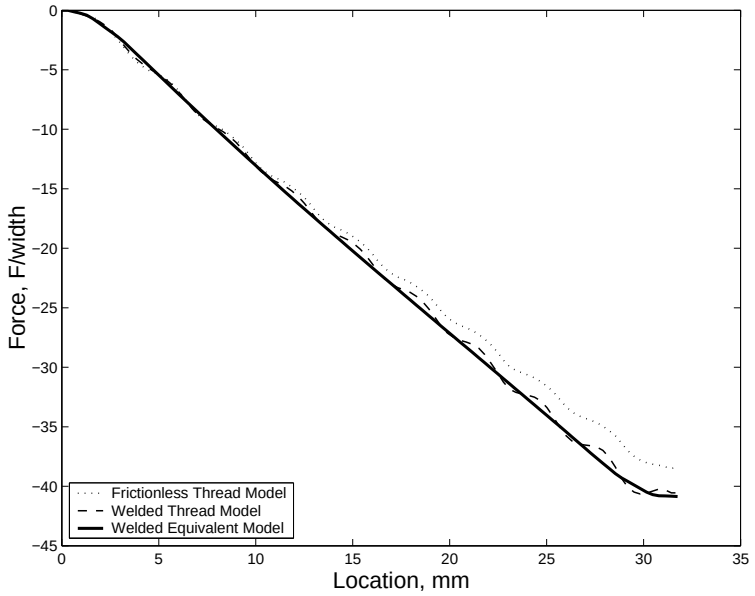

Figure 13.9. Integrated Shear Stress Comparison.

Integrated shear stress along the mid-line of the thread region for three material cases: finely meshed, welded threads; finely meshed, frictionless threads; and coarsely meshed, welded, equivalent material.

The next two figures show results along the mid-line of the bolt shaft, the plane of symmetry in the model. Figure 13.10 shows the vertical displacements as a function of axial coordinate. Figure 13.11 shows the normal stress along the bolt shaft as a function of axial coordinate. In both figures, the origin is located at the bottom of the bolt and the vertical dashed line at 31.5 mm indicates the position of the top of the threads. In both figures there is good matching between the welded screw thread case and the equivalent material model.

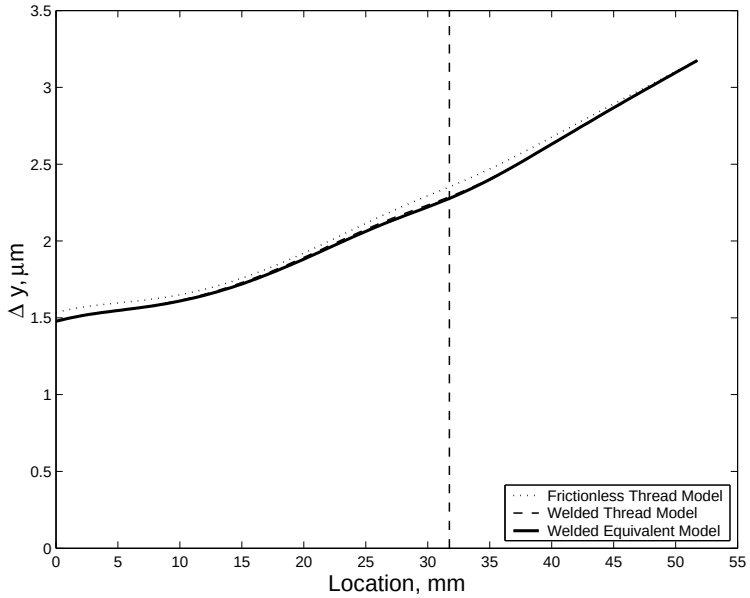

Figure 13.10. Vertical Displacement Comparison.

Vertical displacement along the symmetry plane of the bolt model for three material cases: finely meshed, welded threads; finely meshed, frictionless threads; and coarsely meshed, welded, equivalent material. The vertical dashed line corresponds to the location of the bottom of the bolt cap.

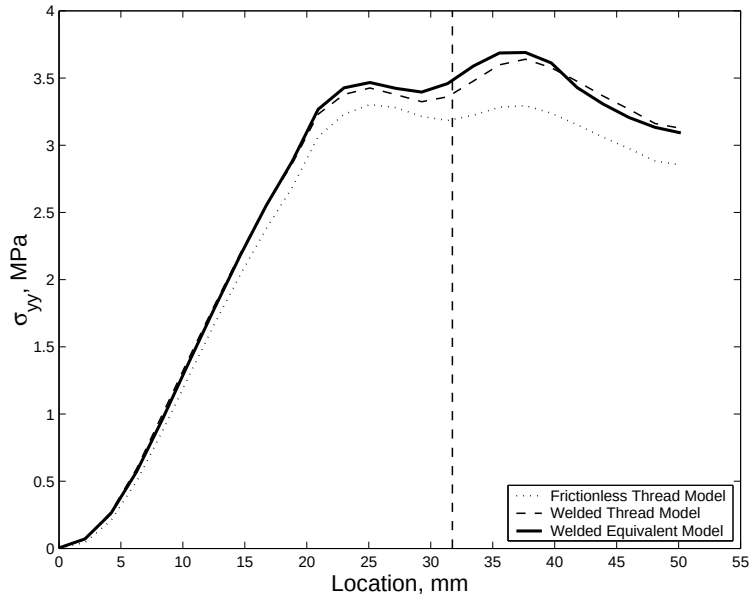

Figure 13.11. Normal Stress Comparison.

Normal stress along the symmetry plane of the bolt model for three material cases: finely meshed, welded threads; finely meshed, frictionless threads; and coarsely meshed, welded, equivalent material. The vertical dashed line corresponds to the location of the bottom of the bolt cap.

Figure 13.12 shows a comparison of the calculated force-displacement results between the welded thread model and three realizations of the welded equivalent material with different levels of mesh coarseness. The legend on the right hand side of the figure shows the unit cell associated with each line style used in the figure. From top to bottom, the unit cells are: the welded thread model, fine equivalent mesh (4330 total elements, 803 in the thread region), intermediate equivalent mesh, and the coarse equivalent mesh (436 total elements, 63 in the thread region). It is apparent that the force vs displacement curves for all four cases are quantitatively similar. The effective stiffnesses (10^6 N/m) for the four meshes are, respectively, 12.96, 12.87, 12.90, and 13.00. As expected, the reported stiffness increase for the more coarsely meshed cases is due to discretization error. However, the stiffness difference is less than 0.5% between the threaded model and the coarsest equivalent model, despite a reduction of the number of elements in the threaded region by a factor of nearly 20.

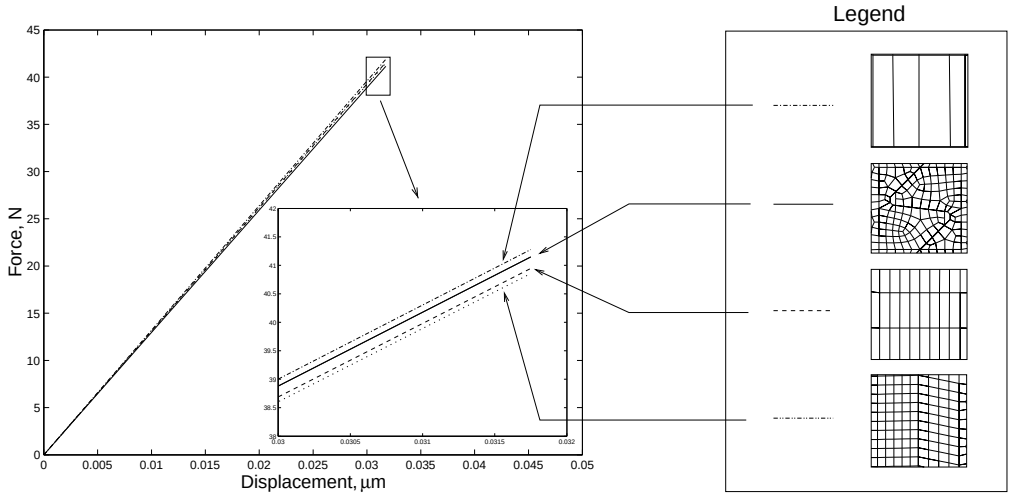

Figure 13.12. Force vs Displacement Plot.

Four different mesh cases: welded thread model; fine equivalent material; intermediate equivalent material; and coarse equivalent material. The legend associates each case with a corresponding line in the force vs displacement plot.

For the boundary conditions of Case 2, the shear stress distribution through the center of the thread stack is shown in Figure 13.13. This shear stress distribution, as compared to that of Case 1, (Figure 13.8) suggests substantially different load distributions along the threads. It is often reported as a "rule-of-thumb" that the first several threads of a screw carry the majority of the load. This is indeed true for the boundary conditions illustrated for Case 2.

It was Sopwith's [81] examination of threaded joints subject to boundary conditions similar to those of Case 2 that led to the often repeated "rule-of-thumb". Ironically, conditions for which the rule is in error are implicitly stated and theoretically supported in that same paper. Indeed, general

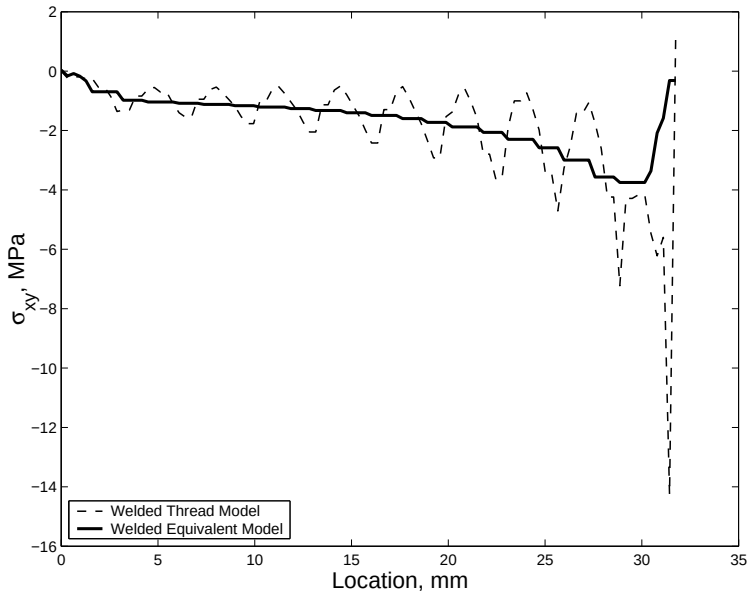

Figure 13.13. Mid-line Shear Stress Comparison.

Shear stress along the mid-line of the thread region for two material cases: finely meshed, welded threads and coarsely meshed, welded equivalent material.

applicability of the "rule-of-thumb" is clearly contradicted in Figure 13.14. This figure plots the fraction of the total load carried by the threads for the boundary conditions of Figure 13.2, where the first thread is that closest to the bolt head. The figure compares the results for the welded thread model and the welded equivalent model for both boundary condition cases. For Case 1, the load is distributed essentially linearly along the length of the bolt, while for Case 2, the majority of the load is carried by the first several threads. The load distribution agrees, quantitatively, very well with similar results reported by Chaaban and Jutras [84]. Figure 13.14 also includes an overlay of Sopwith's theoretical result. There is good agreement between Sopwith's result and Case 2, provided that the appropriate triangular thread parameters are used within Sopwith's derivation.

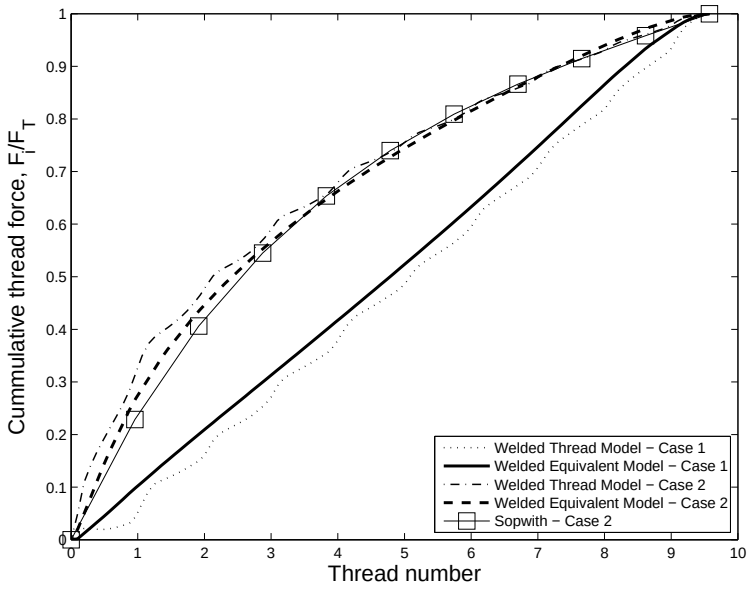

Figure 13.14. Screw Thread Load Distribution.

Fraction of the load carried by the threads along the thread stack for the two boundary condition cases illustrated in Figure 13.2. The welded thread model and welded equivalent model are shown for both cases. Sopwith's derivation overlays the results for boundary condition Case 2.

13.4 Conclusions

A technique has been introduced in this paper for deriving equivalent material models to represent threaded connections. The illustrations have centered on planar elastic response of simple geometries, but the technique can be applied in direct manners to more complex materials and geometries.

It should be noted that it is not necessary to assume that the equivalent material is elastic. In particular, by accommodating the elastic/hardening-plastic nature of the metals that make up the thread cell, appropriate numerical experiments employing incremental deformations can be performed to deduce the parameters of an equivalent elastic/hardening-plastic material. This inelastic model suggests a systematic method for predicting ductile failure loads of threaded joints. Specifically, the kinematics deduced from the coarse equivalent model could be mapped onto the nonlinear, finely meshed, thread pair unit cell. A quasistatic simulation employing those kinematic boundary conditions could then be compared against a set of local failure criteria.

Three dimensional analyses similar to the two dimensional ones performed here would be necessary to accommodate large thread depth-to-radius problems. Such work is planned for a future study. Because these are relatively small problems, the associated three dimensional, FE analyses and post processing of the results would not be prohibitive. The resulting axisymmetric material would have one more material parameter than was the case in the two dimensional problems discussed above.

Additionally, if experimental data indicate that significant energy dissipation can take place in a threaded joint - FE calculations on this issue were inconclusive - dissipative models may be employed. Iwan models could be considered since they have worked well in other contexts ([72], [69]). The suitability of this approach is still an open question.

Finally, it is important to emphasize that the analysis presented here provides linear approximations for threaded connections. Though it has value in linear structural dynamics, it cannot be employed in problems of load reversals sufficient to overcome preload nor will it be helpful in problems of torsion (finite rotation).

Part III

Finite Element Modeling of Joints

Chapter 14

Verification Test Suite for a Candidate Nonlinear Quasistatic Contact Code

Daniel J. Segalman and Michael J. Starr

14.1 Introduction

Even though there is no resolution on the most appropriate frictional constitutive equations and there is little experience using advanced frictional constitutive models in finite element contact analysis, one still looks to using finite element packages to obtain insight into interface mechanics. Of course, obtaining meaningful insights is contingent on those packages being able to provide mathematically correct solutions.

Verification of finite element code with respect to a class of problems addresses two issues: 1)are the algorithms employed in the code capable of producing the correct approximations to the solutions of governing equations of that problem class? and 2) how fine must problem meshes be in order for the numerical solution to approximate the exact solution? An affirmative answer to the first question is necessary for the finite element code to be useful at all in investigating frictional contact. Understanding of the second issue is necessary to use the code effectively.

The calculations presented in this chapter were performed using a version of the SIERRA [90] code Adagio [91], developed under the Department of Energy's Advanced Computing Initiative (ASC)[92]. Similar calculations were performed with two commercial code and results of those calculations are presented in the Chapter D of the Appendix.

Included in the following is a listing of six essential contact problems that any quasi-static code must be able to solve in order to engender confidence in its ability to solve other, more difficult, contact and sliding friction problems. Additionally, the results are included for each problem from computational analyses run using Adagio-Legacy contact in a serial environment (runs in the massively parallel environment are still underway.) For our purposes, the solutions to these problems must also be captured by any candidate, distributed-interface model. This list is not intended to be all inclusive, but should serve as a template for the minimum set of solvable problems. All of the problems have either analytical or semi-analytical solutions for traction and

displacement fields. Further, all of these problems are directly related to the types of contact and interface geometries and boundary conditions that are commonly encountered in built-up systems. Many of these problems are presented in Johnson's Contact Mechanics text [93].

14.2 Indentation by a Rigid, Flat Punch

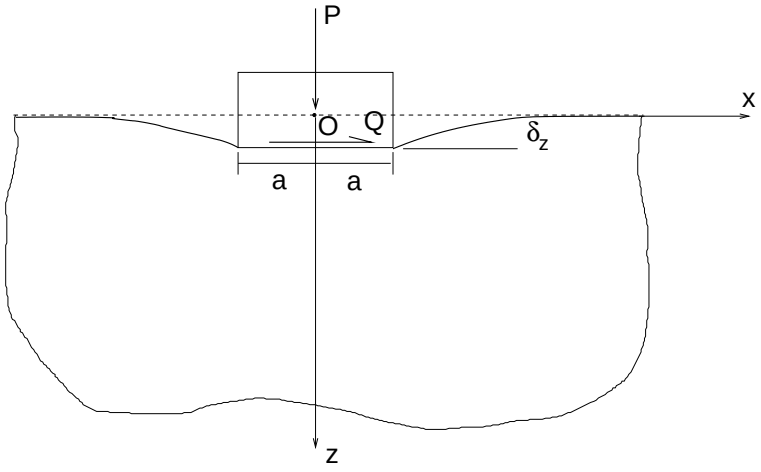

Figure 14.1. Flat, Rigid Punch Pressed into an Elastic Half Space.

14.2.1 Static, Frictionless Punch

14.2.1.1 Analytical Formulation

A rigid punch is pressed into an elastic half space ([93] pp. 36-38). The punch has a flat base and a width of $2a$. Because this is a two-dimensional problem, conditions of plane strain are assumed. The contact is assumed frictionless, so the boundary conditions are $\overline{u}_z(x) = \text{constant} = \delta_z$ and $q(x) = 0$. The pressure distribution for this problem is

$$p(x) = \frac{P}{\pi \left[a^2 - x^2\right]^{1/2}} \tag{14.1}$$

The displacement outside the contact zone is given by

$$\overline{u}_z(x) = \delta_z - \frac{2(1-\nu^2)P}{\pi E} \ln \left\{ \frac{x}{a} + \left(\frac{x^2}{a^2} - 1 \right)^{1/2} \right\} \tag{14.2}$$

where the displacement, δ_z is determined with respect to an arbitrarily chosen datum. The tangential displacements under the punch are given by

$$\overline{u}_x(x) = -\frac{(1-2\nu)(1+\nu)P}{\pi E} \sin^{-1}(x/a) \tag{14.3}$$

where ν is Poisson's ratio,
and E is the elastic modulus.

This problem may be difficult to solve numerically due to the strong singularity at the corners of the punch, as well as the assumption of an infinite half space.

14.2.1.2 Numerical Results

The numerical solutions show good matching to the analytical results. As expected, achieving good numerical results required very refined meshes at the substrate location immediately adjacent to the corner of the punch. Figure 14.2 shows the extent to which the mesh was refined.

It should also be stated that the numerical solution was not strictly two-dimensional, but also involved a three-dimensional geometry that was subjected to plane strain boundary conditions. The following three figures show a comparison between the analytical results and the numerical solutions for the three solutions given by Equations (14.1), (14.2), and (14.3). The parameters employed for the analysis are $a = 0.5$ m, $E = 3.0 \times 10^7$ MPa, $\nu = 0.30$, and $P = 1.0$ N. Figure 14.3 shows excellent agreement between the analytical and numerical results.

Figures 14.4 and 14.5 show the long-range nature of the punch solution. Both figures plot the displacement fields for two different representations of an "infinite" half-space. A convergence study showed that the analytical solution could be reached with an appropriately large representation of the substrate.

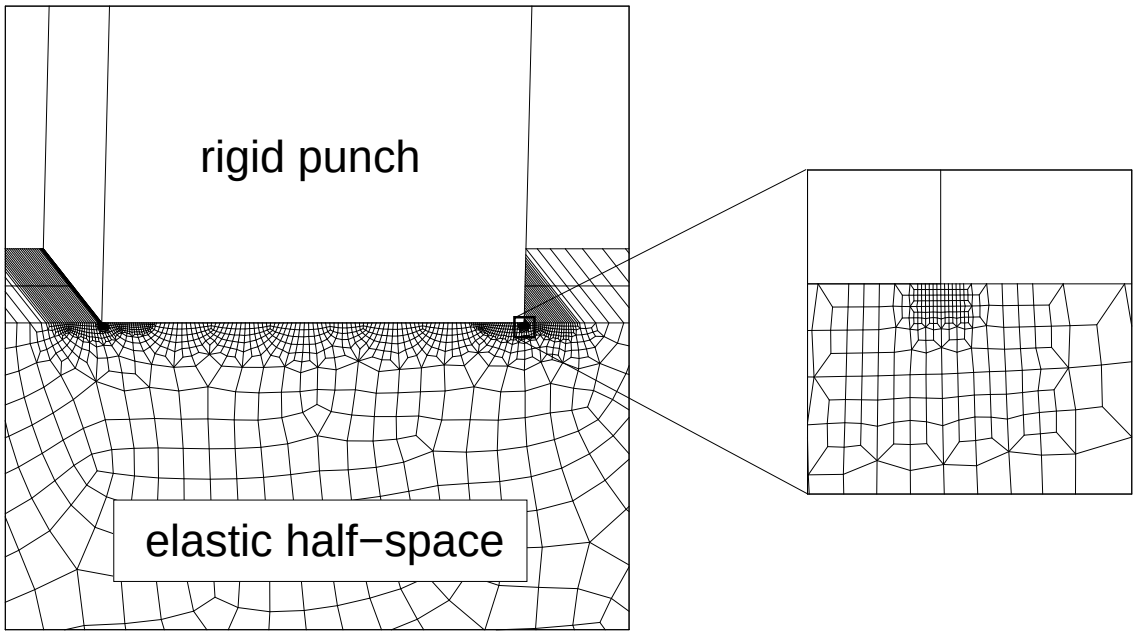

Figure 14.2. Mesh Arrangement.

Significant mesh refinement was required in the substrate adjacent to the punch corners to capture the stress singularity. The long range nature of the solution required a large substrate.

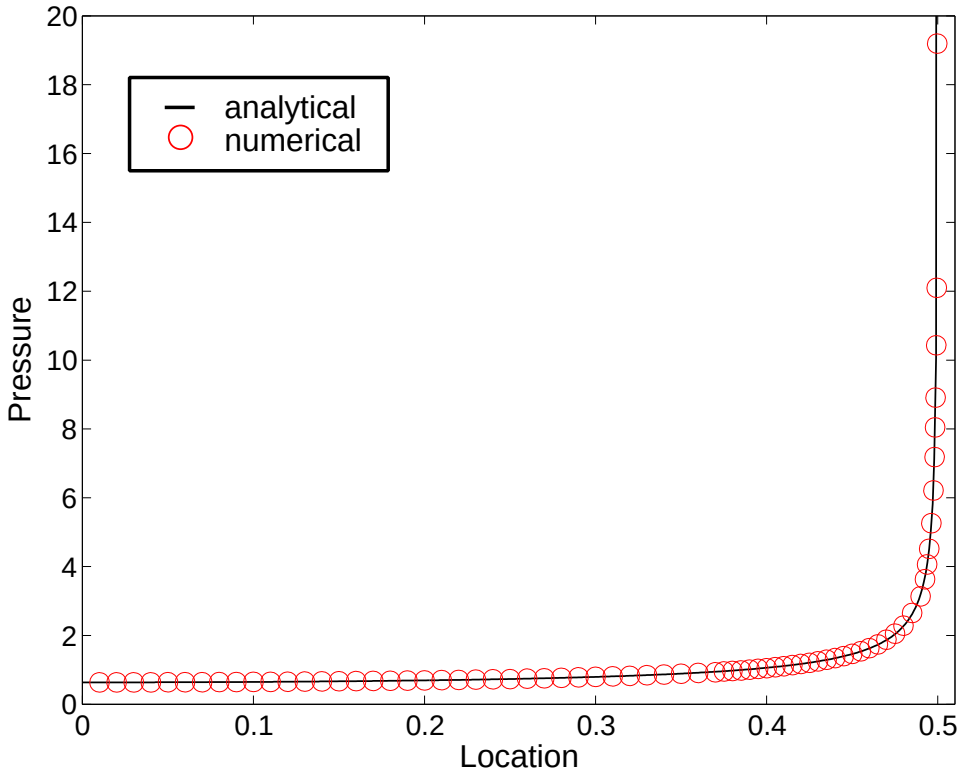

Figure 14.3. Punch Pressure Profiles.

Comparison of normal pressure profiles under the punch over a half-width of the punch. The parameters employed for the analysis are $a = 0.5\ m$, $E = 3.0 \times 10^7\ MPa$, $\nu = 0.30$, *and* $P = 1.0\ N$.

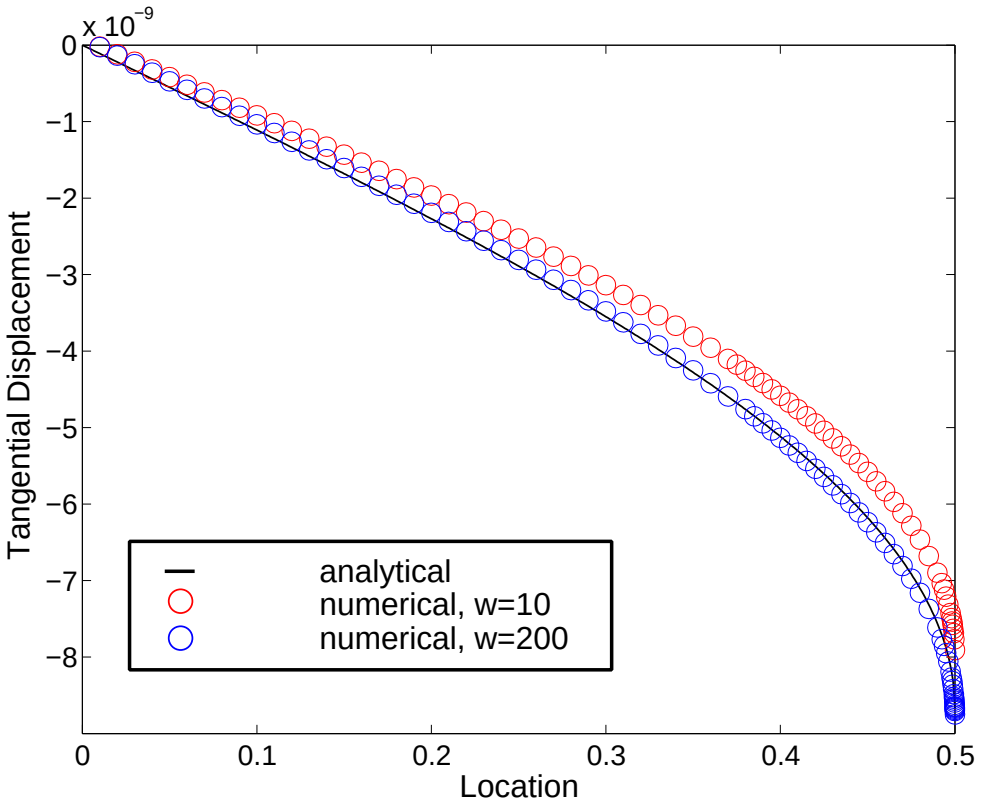

Figure 14.4. Elastic Body Displacements.

Comparison of the lateral displacement of the elastic body under the punch with frictionless contact. Numerical convergence to the analytical solution required a half-space width much larger than the punch width, $2a$*. The parameters employed for the analysis are* $a = 0.5$ *m,* $E = 3.0 \times 10^7$ *MPa,* $\nu = 0.30$*, and* $P = 1.0$ *N.*

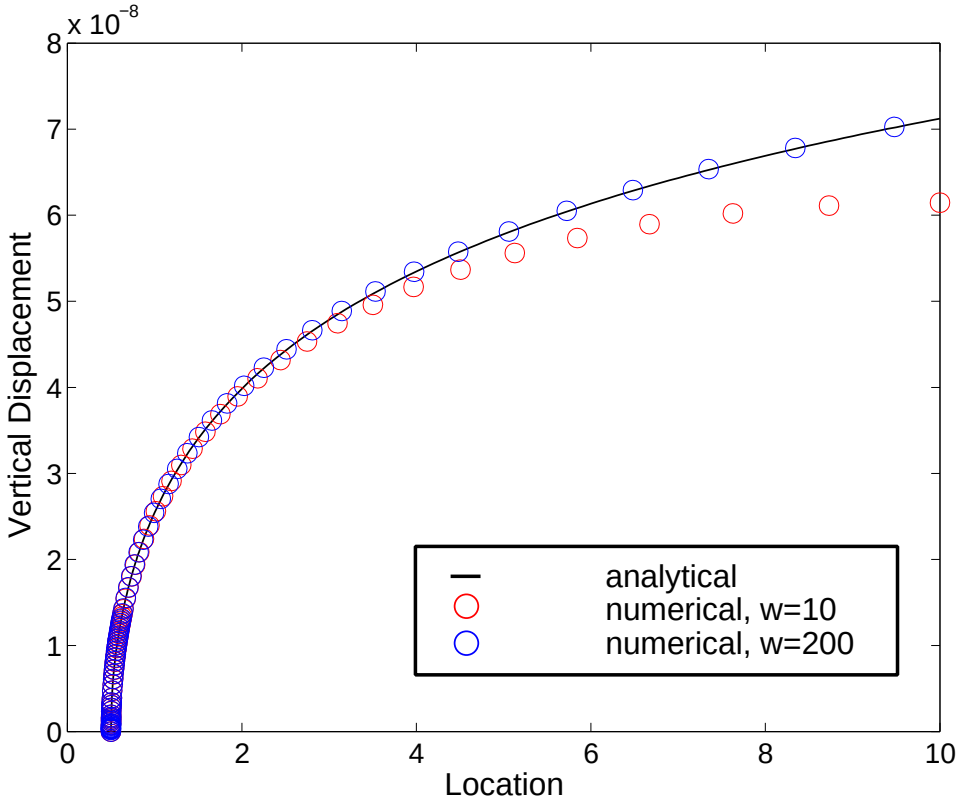

Figure 14.5. Normal Displacement of Elastic Body.

Comparison of the normal displacement of the elastic body outside of the punch contact zone. Numerical convergence to the analytical solution required a half-space width much larger than the punch width, $2a$*. The parameters employed for the analysis are* $a = 0.5$ *m,* $E = 3.0 \times 10^7$ *MPa,* $\nu = 0.30$*, and* $P = 1.0$ *N.*

14.2.2 Steady-State Sliding Punch

14.2.2.1 Analytical Formulation

If the punch from the previous problem slides over the half space at a speed sufficiently low for inertial forces to be neglected, and friction is introduced, $q(x) = \mu p(x)$, the traction distribution under the punch can be given by ([93] pp. 41-42)

$$p(x) = \frac{P \cos \pi\gamma}{\pi \left(a^2 - x^2\right)^{1/2}} \left(\frac{a+x}{a-x}\right)^{\gamma} \tag{14.4}$$

where the exponent γ satisfies

$$\cot \pi\gamma = -\frac{2(1-\nu)}{\mu(1-2\nu)} \tag{14.5}$$

where ν is Poisson's ratio,
and μ is the coefficient of friction.

14.2.2.2 Numerical Results

The same mesh was used for the sliding punch problem. For this problem, the Poisson's ratio used was, $\nu = 0.3$ and the friction coefficient was $\mu = 0.30$. Using Equation (14.5) these parameters lead to a value of $\gamma = -0.0272$, so the skewing in the pressure profile is minimal. The remaining parameters employed for the analysis are $a = 0.5$ m, $E = 3.0 \times 10^7$ MPa, and $P = 1.0$ N. Figure 14.6 shows excellent agreement between the analytical and numerical results.

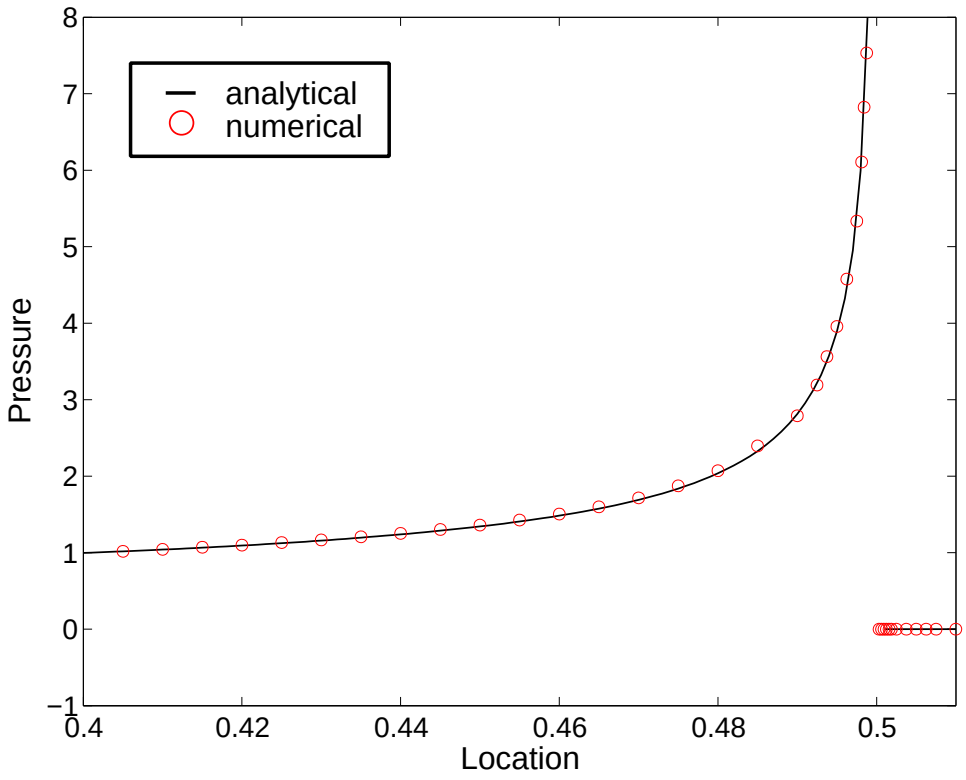

Figure 14.6. Pressure Profiles.

Comparison of normal pressure profiles under the punch over a half width of the punch, for $\mu = 0.30, \nu = 0.30$. *The other parameters employed for the analysis are* $a = 0.5$ *m,* $E = 3.0 \times 10^7$ *MPa, and* $P = 1.0$ *N.*

14.3 Hertzian Contact of Spheres

14.3.1 Static Contact

14.3.1.1 Analytical Formulation

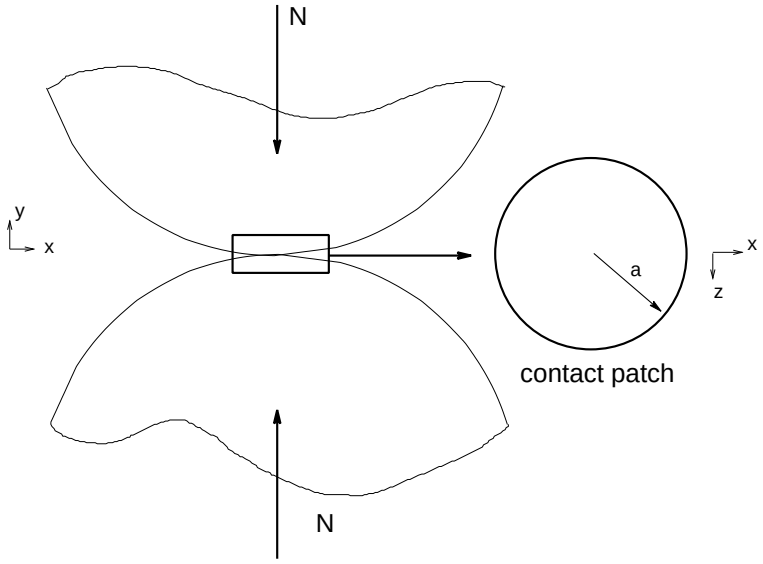

Figure 14.7. Spheres Pressed Together.

For the classical Hertzian problem of two spheres pressed together with a normal force of magnitude N, the interfacial traction distribution is given by ([93] pp. 84-93)

$$p(r) = \frac{3N}{2\pi a^2}\left\{1-(r/a)^2\right\}^{1/2} \tag{14.6}$$

The radius of the contact patch is

$$a = \left[\frac{3NR}{4E^*}\right]^{1/3} \tag{14.7}$$

where

$$\frac{1}{R} = \frac{1}{R_1} + \frac{1}{R_2} \tag{14.8}$$

and

$$\frac{1}{E^*} = \frac{1-\nu_1^2}{E_1} + \frac{1-\nu_2^2}{E_2} \tag{14.9}$$

NOTE: If solving a problem involving contact of identical spheres ($E = E_1 = E_2, \nu = \nu_1 = \nu_2, r = R_1 = R_2$), then

$$\frac{1}{E^*} = \frac{2(1-\nu^2)}{E}$$
$$R = r/2$$

14.3.1.2 Numerical Results

The mesh and geometry used for the problem is shown in Figure 14.8. The degrees of freedom of the numerical solution can be greatly reduced by replacing the contact of two spheres with that of a sphere and a rigid surface. This is an equivalent elasticity solution, provided that appropriate scalings for moduli and effective sphere radius are employed. A further reduction in the size of the problem can be achieved by further assuming that the contact patch radius will be a small fraction of the sphere radius. In this instance, it is appropriate for the sphere to be represented as a hemisphere without the introduction of significant error. The numerical solution has reasonable agreement with the analytical solution with respect to the pressure distribution expressed in Equation (14.6). The parameters employed for the analysis are $N = 5.0 \times 10^7$ N, $R_1 = 1.0$ m, $R_2 = \infty$, $E_1 = 68.9 \times 10^9$ MPa, $E_2 = \infty$, and $\nu_1 = \nu_2 = 0.33$. Figure 14.9 shows this comparison. In the vicinity of the contact boundary, the normal pressures are not captured very accurately. This is to be expected due to mesh discretization error. In general, the contact patch size will not be known *a priori*, so the mesh will not be compatible with the exact extent of contact. Although the test suite meshes were engineered problems, with precisely determined loads and meshes, minor deviations between the solved boundary value problems and the intrinsic assumptions that allow analytical solutions were significant enough to introduce small, but acceptable errors. This result is illustrated in Figure 14.10. For this problem a different normal load was used and applied to a finely discretized mesh. The figure shows the mesh designed to capture precisely the contact patch size as calculated using Equation (14.7), with $N = 5 \times 10^6$ N and all other parameters identical to those previously listed. This theoretical contact patch is shown as the shaded red patch, $a = 0.0376$ m. The numerical solution calculated a contact patch illustrated with the solid black line, $a = 0.0368$ m, exactly one radial element short of the expected contact patch radius.

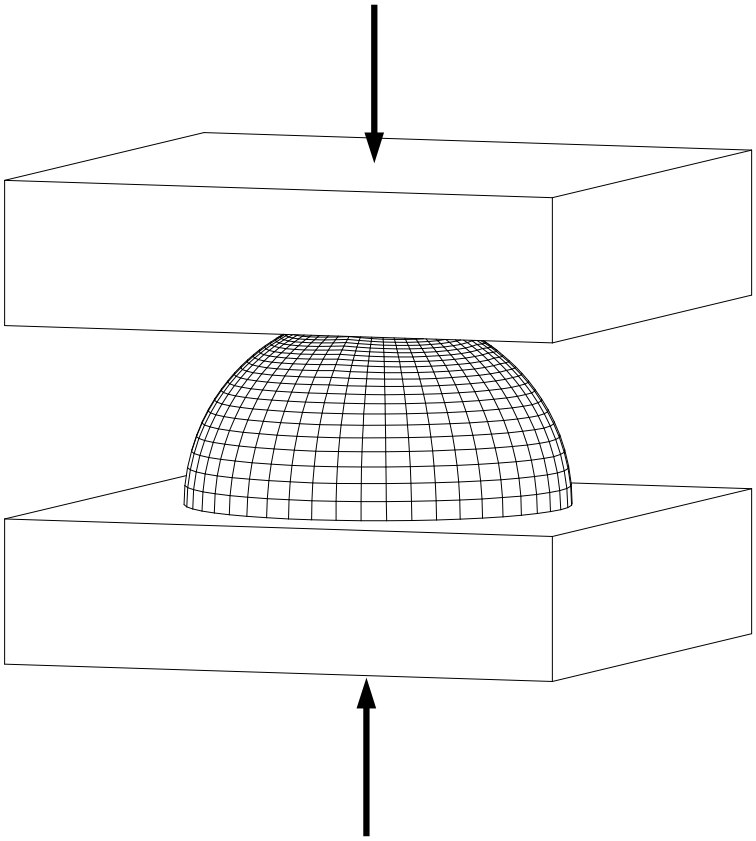

Figure 14.8. The Two Sphere Problem.

Symmetries and small normal forces can be exploited to reduce the problem degrees of freedom.

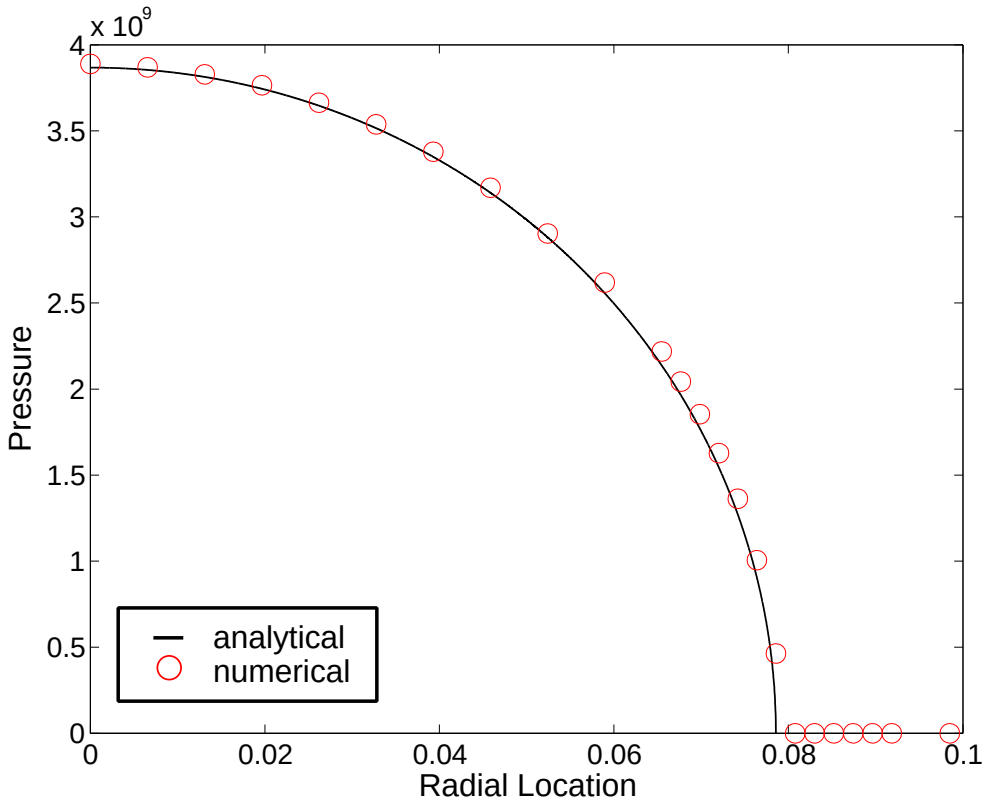

Figure 14.9. Hertzian Contact Comparison.

The pressure distribution is adequately captured, but the contact radius is not captured exactly despite a priori *knowledge of the theoretical, contact patch radius. The parameters employed for the analysis are* $N = 5.0 \times 10^6$ *N,* $R_1 = 1.0$ *m,* $R_2 = \infty$*,* $E_1 = 68.9 \times 10^9$ *MPa,* $E_2 = \infty$*, and* $\nu_1 = \nu_2 = 0.33$*.*

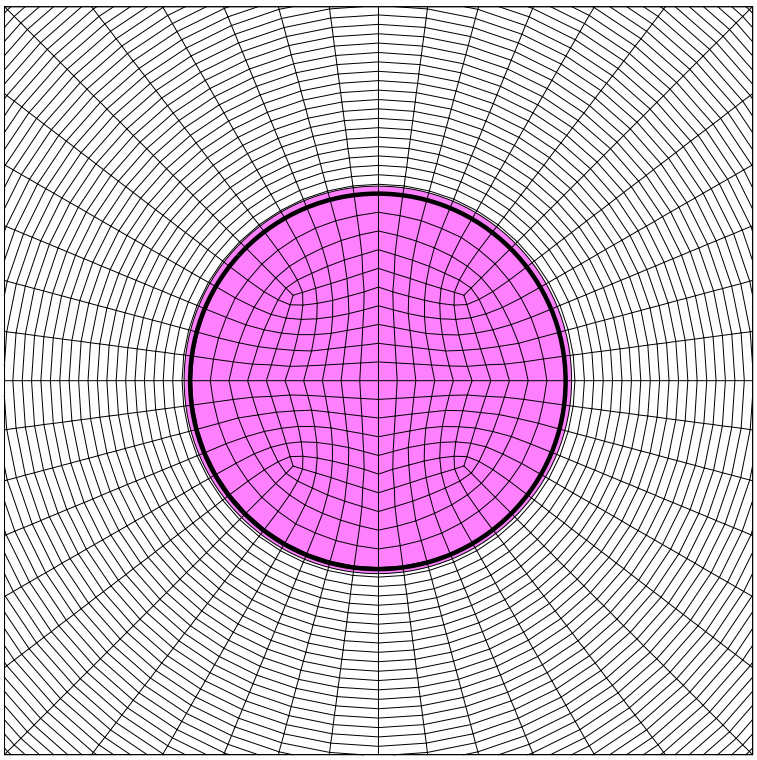

Figure 14.10. Contact Patch Radius.

The numerically calculated contact patch ($a = 0.0368$ m) is one radial element short of the expected contact patch radius ($a = 0.0376$ m). The parameters employed for the analysis are $N = 5.0 \times 10^7$ N, $R_1 = 1.0$ m, $R_2 = \infty$, $E_1 = 68.9 \times 10^9$ MPa, $E_2 = \infty$, and $\nu_1 = \nu_2 = 0.33$.

14.3.2 Oscillating Tangential Forces

14.3.2.1 Analytical Formulation

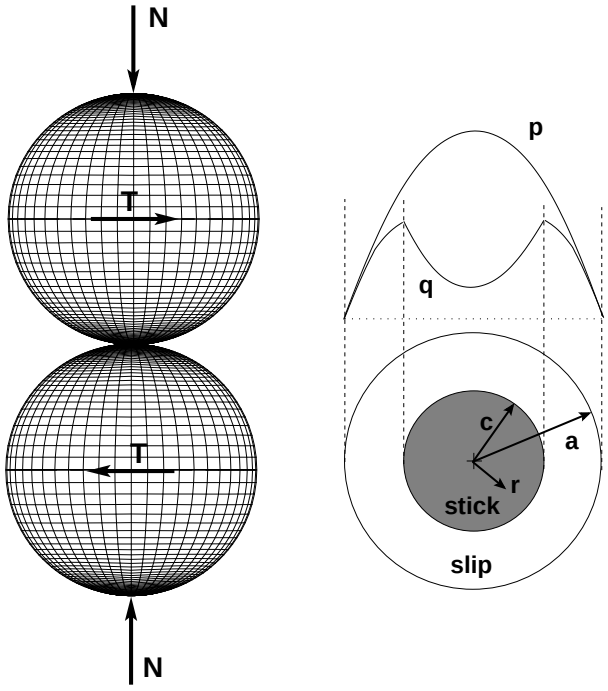

Figure 14.11. Mindlin Problem Configuration.

Spheres pressed together, then subjected to oscillating tangential forces or moments.

One of the few, nontrivial, elasticity contact problems for which analytical results are known is Mindlin's, oscillating, elastic spheres problem (Mindlin, 1949; Mindlin et al., 1962; Johnson, 1955). The geometry for the problem, illustrated in Figure 14.11, involves two elastic spheres pressed together with a normal force, N. An oscillating tangential force of magnitude T acts in the plane of contact.

As predicted in Hertz's solution, an ellipsoidal normal stress distribution will develop. Because the shear stress must satisfy $q \leq \mu p$ in the contact patch, where μ is the friction coefficient, slip will develop in an outer annulus of the contact patch. The relative displacement of the two spheres, at distances far removed from the contact plane is

$$\delta = \frac{3(2-\nu)\mu N}{8Ga}\left[1-\left(\frac{c}{a}\right)^2\right] \tag{14.10}$$

where ν is Poisson's ratio,
G is the shear modulus,
and a is the contact radius.

For the case of partial slip in the contact patch, the radius of the stuck region, c, can be related to the contact radius, a, through ([93] pp. 224-231)

$$c = a\left[1 - \frac{T}{\mu N}\right]^{1/3} \tag{14.11}$$

The tangential components of traction over the contact interface are

$$\mathbf{t}_s = \frac{3\mu N}{2\pi a^2}\begin{cases} \left[1-\left(\frac{r}{a}\right)^2\right]^{1/2} & c \le r \le a \\ \left[1-\left(\frac{r}{a}\right)^2\right]^{1/2} - \frac{c}{a}\left[1-\left(\frac{r}{c}\right)^2\right]^{1/2} & r \le c \end{cases} \tag{14.12}$$

The monotonic loading, or backbone curve (displacement as a function of lateral force), is given by

$$\delta(T) = \frac{3\mu N}{16a}\left(\frac{2-\nu_1}{G_1} + \frac{2-\nu_2}{G_2}\right)\left\{1 - \left(1 - \frac{T}{\mu N}\right)^{2/3}\right\} \tag{14.13}$$

If the spheres are now subjected to an oscillating tangential force with amplitude $\hat{T}$, the energy dissipation per cycle is given by (this equation is given in [93] p. 227 incorrectly, the correct form is shown below)

$$\begin{aligned} \Delta W \;=\; & \frac{9\mu^2 N^2}{10a}\left(\frac{2-\nu_1}{G_1} + \frac{2-\nu_2}{G_2}\right)\left[1 - \left(1 - \frac{\hat{T}}{\mu N}\right)^{5/3}\right. \\ & \left. - \frac{5\hat{T}}{6\mu N}\left\{1 + \left(1 - \frac{\hat{T}}{\mu N}\right)^{2/3}\right\}\right] \end{aligned} \tag{14.14}$$

For small applied tangential loads, this equation can be approximated as

$$\Delta W = \frac{\hat{T}^3}{36a\mu N}\left(\frac{2-\nu_1}{G_1} + \frac{2-\nu_2}{G_2}\right) \tag{14.15}$$

14.3.2.2 Numerical Results

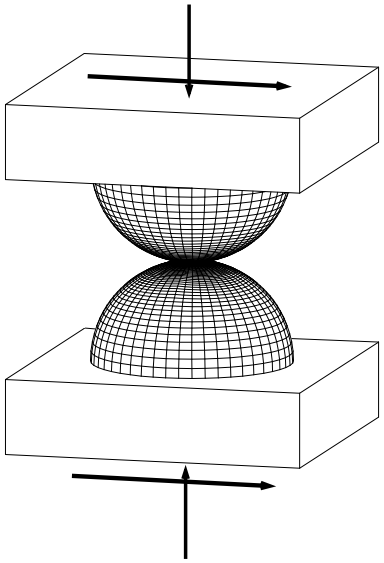

Figure 14.12. Mindlin Problem Mesh.

Geometry and mesh used to solve Mindlin's, oscillating, tangential load problem.

A good deal of time and computing effort has been expended on the Mindlin problem. The reality is that the match between the analytical solution and the numerical results is poor. After a thorough analysis of both the analytics and the numerics, it was determined that the relative strength of the assumptions employed to achieve an analytical solution is the cause of the deviations seen in the comparisons between solutions. The root of the difference lies in Mindlin's assumption that the sphere could be approximated as a plane for small enough normal forces. With that, the comparisons between the solutions are shown below. Figure 14.12 shows the geometry and mesh used for the numerical calculations. The parameters employed for the analysis are $N = 5.0 \times 10^6$ N, $R_1 = R_2 = 1.0$ m, $E_1 = E_2 = 68.9 \times 10^9$ MPa, $\nu_1 = \nu_2 = 0.33$, and $\mu = 0.3$. The simulation was performed under displacement control, where the displacement was applied linearly to a displacement level of $\delta = 1.2 \times 10^{-3}$ m. This displacement is approximately 20% greater than the macroslip displacement calculated using Equation (14.10). Again, for the magnitude of normal loads applied, the spheres were represented as hemispheres, and the boundary conditions were applied at the sphere mid-plane. This treatment is an adequate representation as the mid-plane is sufficiently removed from the contact patch that there is minimal impact on the solution.

Figure 14.13 shows the systematic difference between the analytical and numerical results which was described previously. The analytical expression plotted is that given by Equation (14.13). It should be noted that because the Mindlin problem can be fit within the Masing model

framework, we are guaranteed that the numerically calculated dissipation will also be different from the analytical expressions (either Equation (14.14) or (14.15)). This difference is true because the backbone curve as described in Equation (14.13) completely characterizes the dissipation characteristics of a particular model.

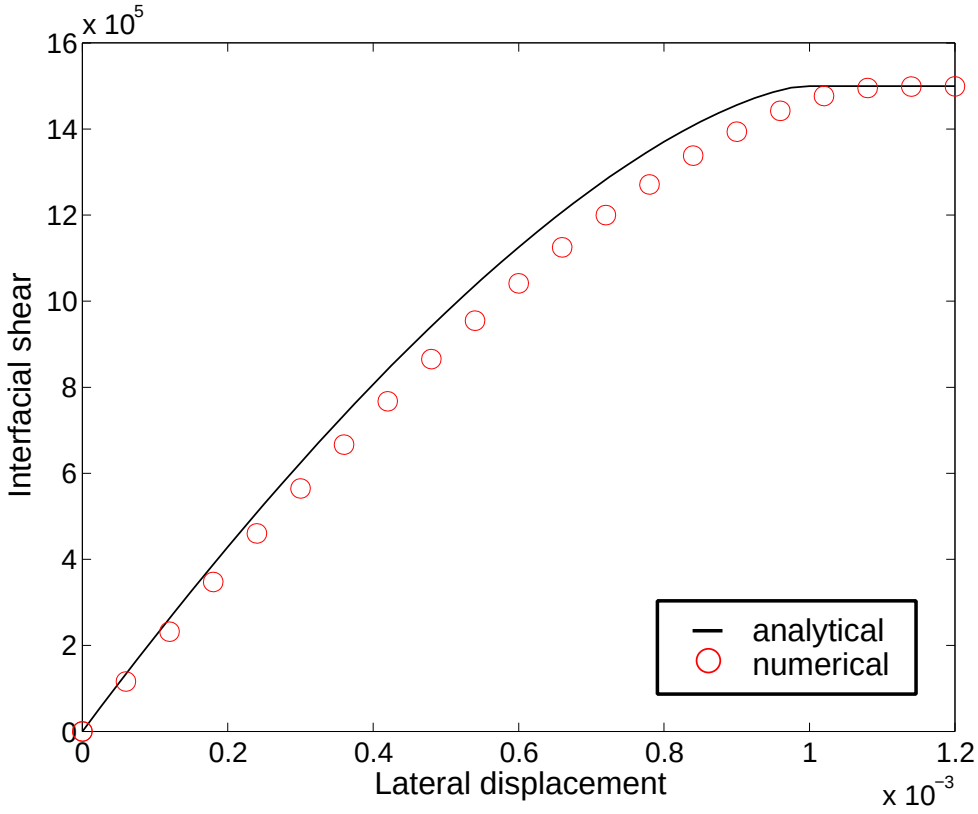

Figure 14.13. Mindlin Backbone Curve Comparison.

Comparison of the backbone curves for Mindlin's problem. The curve illustrates only the monotonic initial loading of the spheres. The parameters employed for the analysis are $N = 5.0 \times 10^6$ *N,* $R_1 = R_2 = 1.0$ *m,* $E_1 = E_2 = 68.9 \times 10^9$ *MPa,* $\nu_1 = \nu_2 = 0.33$*, and* $\mu = 0.3$*.*

Other important measures of comparison can be made between the analytical expressions and the numerical calculations. These comparisons are shown in the following figures. Figure 14.14 shows the evolution of the stick/slip boundary as a function of the far-field displacement of the spheres. Some of the deviation can be explained by the discretization of the contact interface, which only allows discrete nodes to either stick or slip, as opposed to a continuum of allowed interface kinematics. This error will be particularly amplified when the contact patch is small, and consequently it includes only a small number of contact nodes.

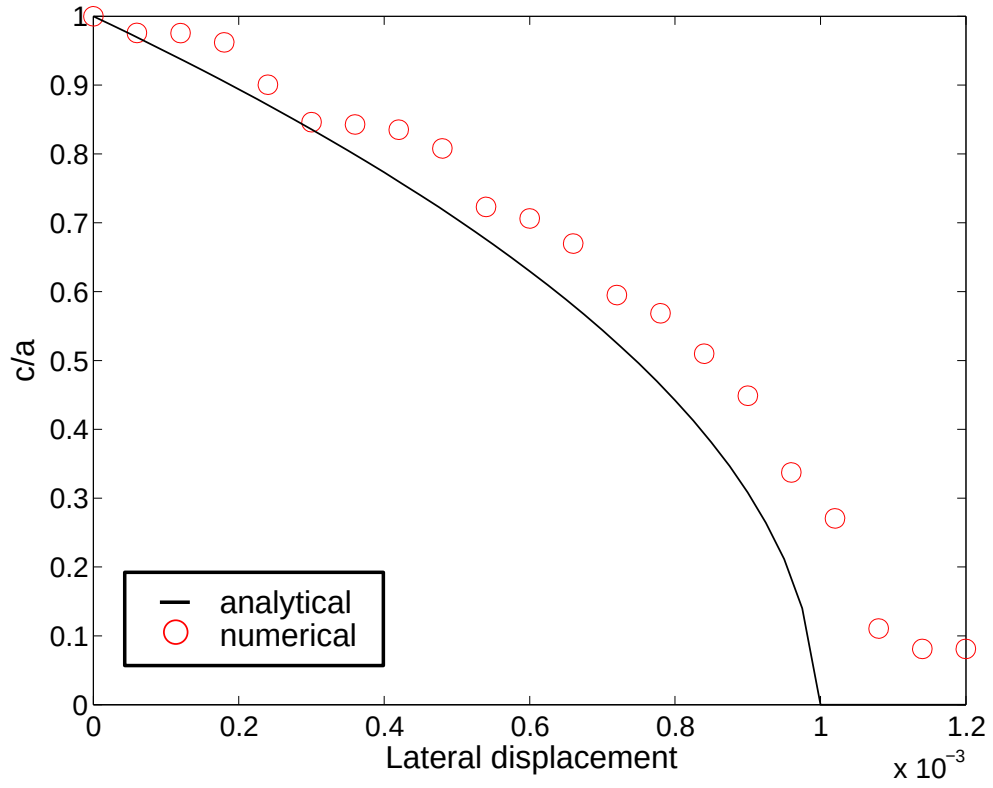

Figure 14.14. Mindlin Stick/Slip Front.

Comparison of the stick/slip front for Mindlin's problem. The parameters employed for the analysis are $N = 5.0 \times 10^6$ *N,* $R_1 = R_2 = 1.0$ *m,* $E_1 = E_2 = 68.9 \times 10^9$ *MPa,* $\nu_1 = \nu_2 = 0.33$*, and* $\mu = 0.3$*.*

Figure 14.15 shows the results of integrating the tangential tractions given in Equation (14.12). Again, these results are strongly dependent on the accuracy of the slip front calculation as characterized in the previous figure.

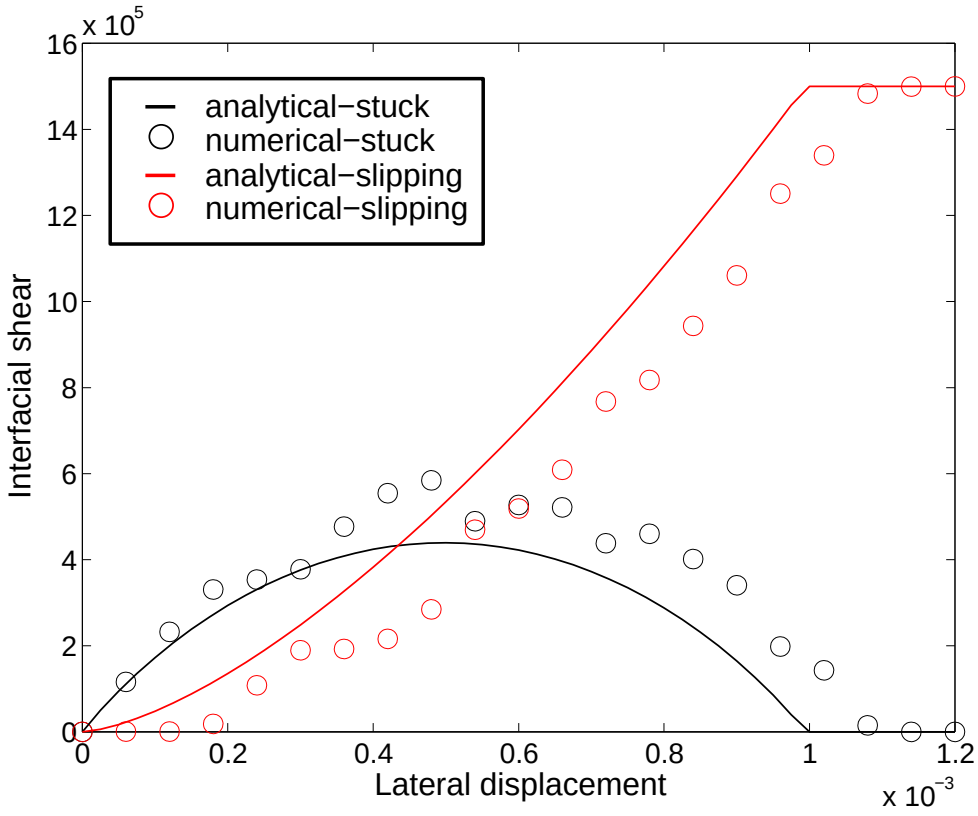

Figure 14.15. Shear Force in the Contact Patch.

Comparison of the amount of shear carried by both the stick and slip regions within the contact patch. The parameters employed for the analysis are $N = 5.0 \times 10^6$ *N,* $R_1 = R_2 = 1.0$ *m,* $E_1 = E_2 = 68.9 \times 10^9$ *MPa,* $\nu_1 = \nu_2 = 0.33$*, and* $\mu = 0.3$*.*

The final comparisons that can be made are secondary in nature, but interesting nonetheless. Johnson [94] extended Mindlin's force-displacement expression (Equation (14.10)) to determine the tangential displacements that occur in the slip annulus. Within the slip zone, $c < r < a$, the following relative displacements occur

$$u_x = \frac{3\mu N r^2}{32Ga^3}\left[2(2-\nu)\left\{\left(1-\frac{2}{\pi}\sin^{-1}\frac{c}{r}\right)\left(1-2\frac{c^2}{r^2}\right)+\frac{2}{\pi}\frac{c}{r}\sqrt{\left(1-\frac{c^2}{r^2}\right)}\right\}\right.$$
$$\left.-\nu\left\{\left(1-\frac{2}{\pi}\sin^{-1}\frac{c}{r}\right)+\left(1-2\frac{c^2}{r^2}\right)\frac{2}{\pi}\frac{c}{r}\sqrt{\left(1-\frac{c^2}{r^2}\right)}\right\}\cos 2\theta\right] \quad (14.16)$$

$$u_y = \frac{3\mu N r^2 \nu}{32Ga^3}\left\{\left(1-\frac{2}{\pi}\sin^{-1}\frac{c}{r}\right)\right.$$
$$\left.+\left(1-2\frac{c^2}{r^2}\right)\frac{2}{\pi}\frac{c}{r}\sqrt{\left(1-\frac{c^2}{r^2}\right)}\right\}\sin 2\theta \quad (14.17)$$

Figure 14.16 shows the comparison between the Johnson expressions (Equations (14.16) and (14.17)) at the onset of macroslip ($c = a$). The results are reasonable, but yet again may suffer from the discretization issues described earlier in the text. Figure 14.17 shows the comparison for the slip direction around the circumference of slip, and also at the onset of macroslip.

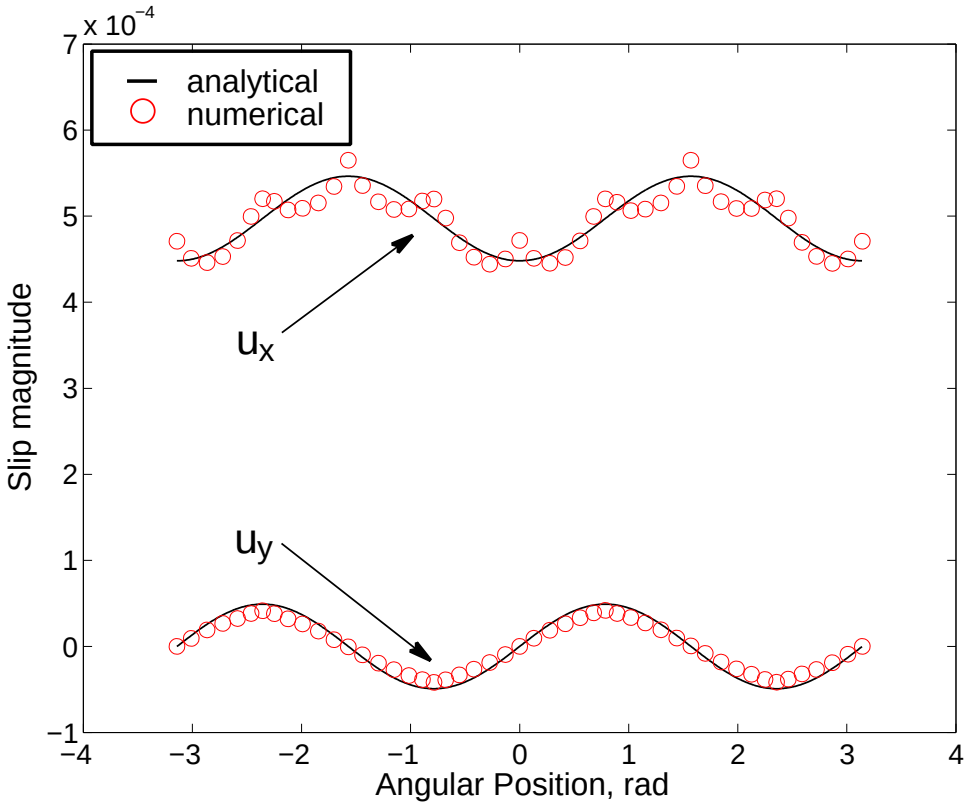

Figure 14.16. Relative Slip Between Spheres.

Comparison of the relative slip between spheres in the slip annulus at the onset of macroslip $c = a$. The parameters employed for the analysis are $N = 5.0 \times 10^6$ N, $R_1 = R_2 = 1.0$ m, $E_1 = E_2 = 68.9 \times 10^9$ MPa, $\nu_1 = \nu_2 = 0.33$, and $\mu = 0.3$.

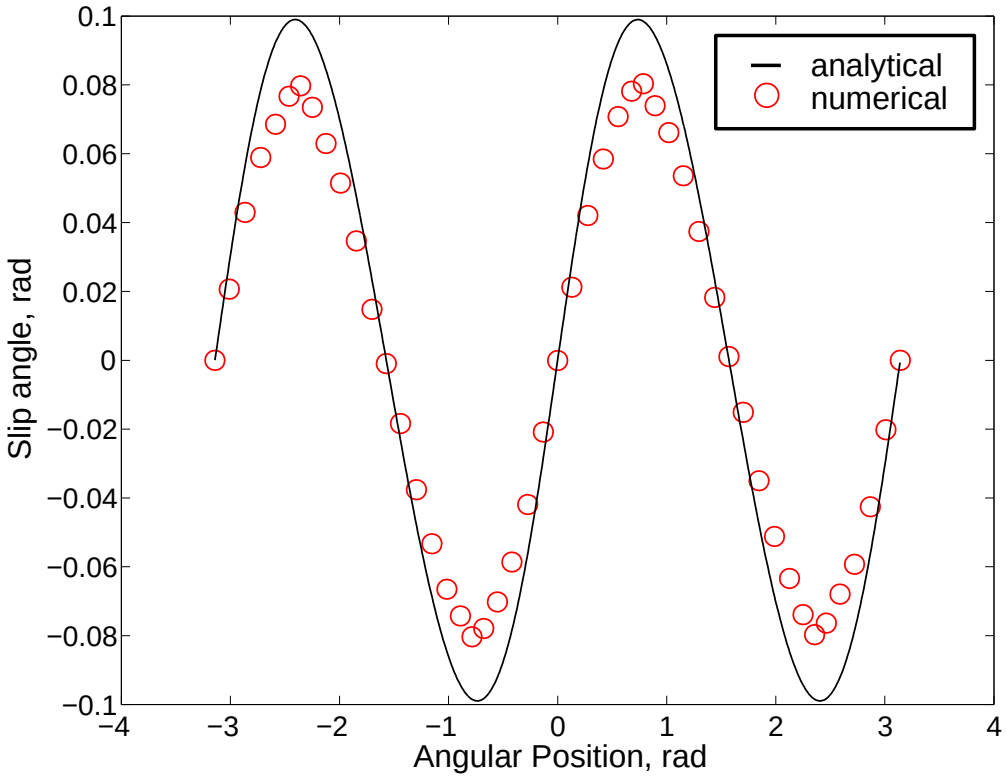

Figure 14.17. Relative Slip on Contact Patch Circumference.

Comparison of the slip between spheres around the circumference of the slip zone at the onset of macroslip $c = a$. The parameters employed for the analysis are $N = 5.0 \times 10^6$ N, $R_1 = R_2 = 1.0$ m, $E_1 = E_2 = 68.9 \times 10^9$ MPa, $\nu_1 = \nu_2 = 0.33$, and $\mu = 0.3$.

14.3.3 Oscillating Torsional Forces

14.3.3.1 Analytical Formulation

A corollary problem to Mindlin's, oscillating, elastic spheres problem is known as Lubkin's torsional sphere problem (Lubkin, 1951, Deresiewicz, 1954). The geometry for the problem is identical to that of Mindlin's, but has an oscillating torsional couple of magnitude M acting in the plane of contact.

For the case of partial slip in the contact patch, the radius of the stuck region, c, can be determined through ([93] pp. 231-233)

$$\frac{3}{4\pi}\left(1-(c/a)^2\right)\left(\frac{1}{G_1}+\frac{1}{G_2}\right)\mathbf{D}(k)=\frac{a^2\beta}{\mu N} \tag{14.18}$$

where $\mathbf{D}(k)=\mathbf{K}(k)-\mathbf{E}(k)$,
$k=(1-c^2/a^2)^{1/2}$,
and β is the relative rotation of the spheres.

For the Lubkin problem, there is no closed-form solution for the backbone curve (torque as a function of angular twist), but a reasonable approximation is

$$T(\beta)=\frac{3\pi\mu Na}{16}\left[1-\exp\left[\left(-\frac{2G_1G_2}{(G_1+G_2)}\frac{a^2\beta}{\mu\pi N}\right)\left(\frac{16}{3}\right)^2\right]\right] \tag{14.19}$$

If the spheres are now subjected to an oscillating torsional moment with amplitude $\hat{M}$, the energy dissipation per cycle is given by

$$\begin{aligned}\Delta W &= \frac{2\mu^2N^2}{a}\left(\frac{1}{G_1}+\frac{1}{G_2}\right)\left[\frac{8}{9}\left\{1-\left(1-\frac{3}{2}\frac{\hat{M}}{\mu Na}\right)^{2/3}\right\}\right.\\ &\left.-\frac{\hat{M}}{\mu Na}\left\{1+\left(1-\frac{3}{2}\frac{\hat{M}}{\mu Na}\right)^{1/2}\right\}\right]\end{aligned} \tag{14.20}$$

For small applied moments, the energy dissipation can be approximated as

$$\Delta W=\frac{3\hat{M}^3}{16a^4\mu N}\left(\frac{1}{G_1}+\frac{1}{G_2}\right) \tag{14.21}$$

14.3.3.2 Numerical Results

Figure 14.18 shows the geometry and mesh used for the numerical calculations. The parameters employed for the analysis are $N = 5.0 \times 10^6$ N, $R_1 = R_2 = 1.0$ m, $E_1 = E_2 = 68.9 \times 10^9$ MPa, $\nu_1 = \nu_2 = 0.33$, and $\mu = 0.3$. Again, for the magnitude of normal loads applied, the spheres were represented as hemispheres, and the boundary conditions were applied at the sphere mid-plane. This is an adequate representation because the mid-plane is sufficiently removed from the contact patch that there is minimal impact on the solution. The numerical simulation was performed under angular rotation control, where the angular rotation was applied linearly to a level of $\beta = 0.05$ radians. This displacement is approximately 20% greater than the macroslip, angular rotation calculated using Equation (14.18).

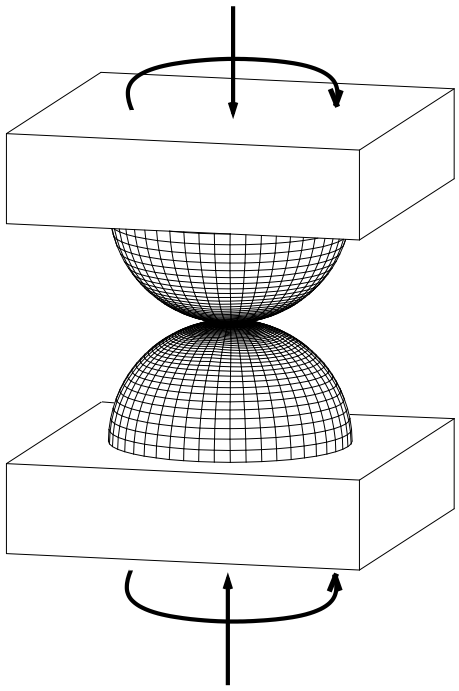

Figure 14.18. Lubkin Problem Configuration.

Geometry and mesh used to solve Lubkin's oscillating torsional load problem.

Figure 14.19 shows the comparison between the semi-analytical expression and the numerical results. The agreement is very good in this boundary value problem because it does not suffer from the same set of restrictive assumptions. The solutions provided by Deresiewicz are a significant improvement over the expansion solutions provided by Lubkin, and are consistent with the manner in which the boundary conditions are applied in the numerical solutions.

Figure 14.20 shows the evolution of stick/slip front. The same limitation that applied to Mindlin

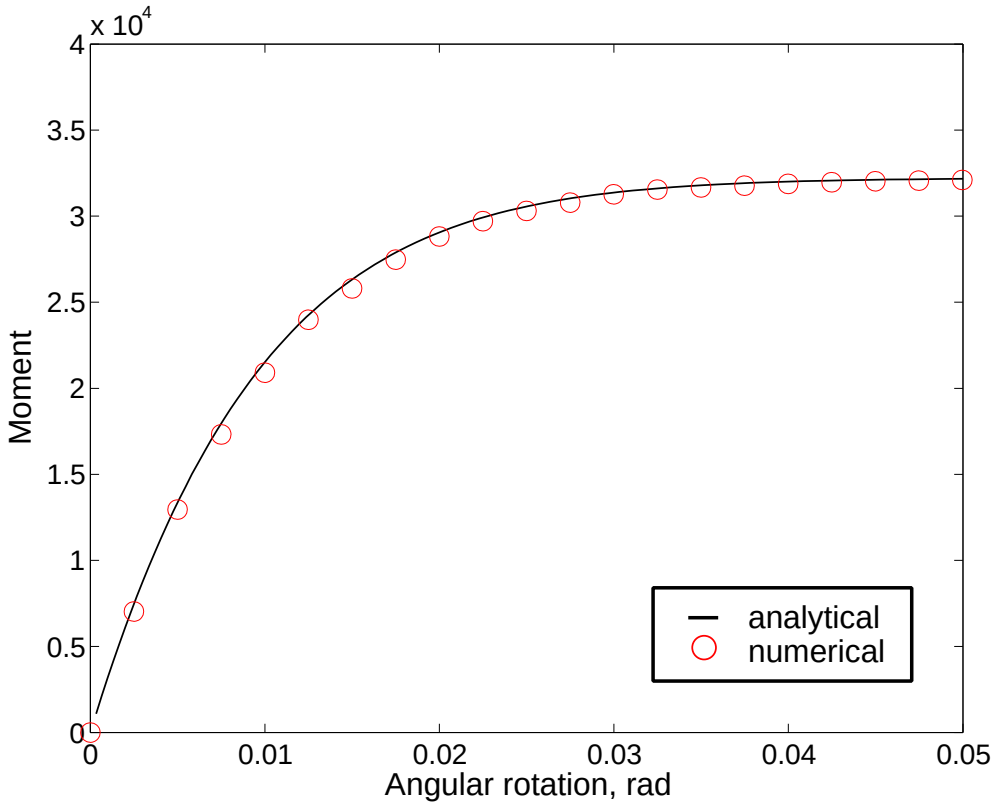

Figure 14.19. Lubkin Problem Backbone Curve Comparison.

Comparison of the backbone curves for Lubkin's problem. The curve illustrates only the monotonic initial loading of the spheres. The parameters employed for the analysis are $N = 5.0 \times 10^6$ *N,* $R_1 = R_2 = 1.0$ *m,* $E_1 = E_2 = 68.9 \times 10^9$ *MPa,* $\nu_1 = \nu_2 = 0.33$*, and* $\mu = 0.3$*.*

applies here as well; discretization of the contact patch can lead to apparently significant errors, especially when the number of nodes in contact is small.

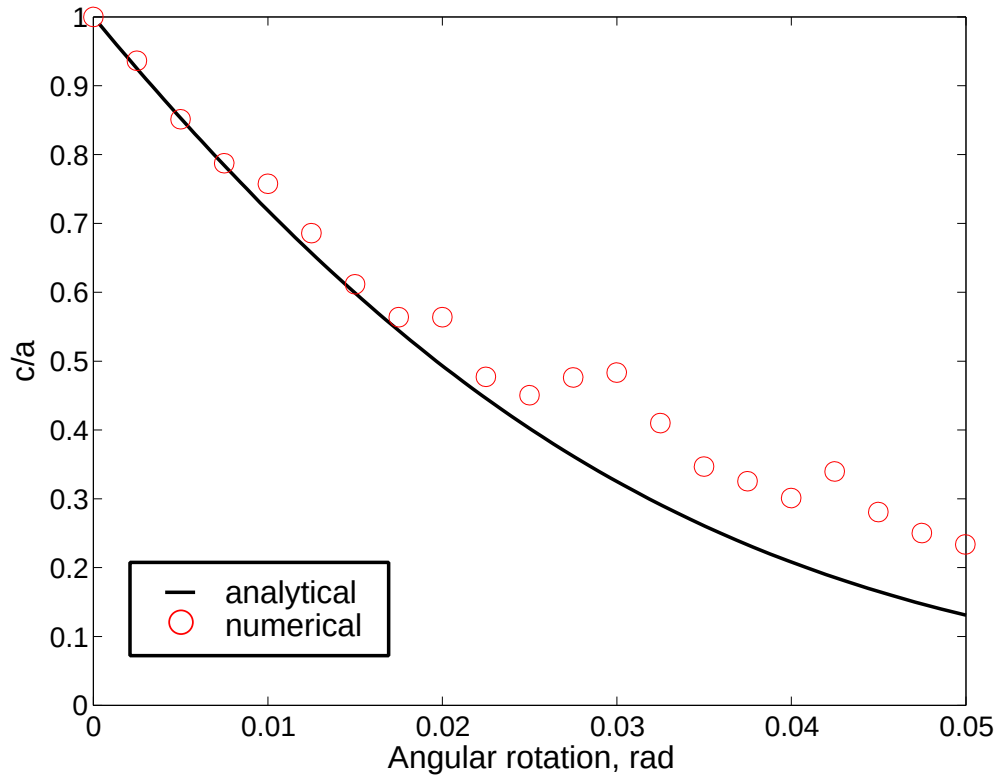

Figure 14.20. Lubkin Stick/Slip Front Comparison.

The parameters employed for the analysis are $N = 5.0 \times 10^6$ *N,* $R_1 = R_2 = 1.0$ *m,* $E_1 = E_2 = 68.9 \times 10^9$ *MPa,* $\nu_1 = \nu_2 = 0.33$*, and* $\mu = 0.3$*.*

14.4 Clamped 2D Strip

14.4.1 Analytical Formulation

A simple, one-dimensional model can demonstrate Goodman's [74] hypothesis that other systems involving slip cause energy dissipation to increase proportionately to the force amplitude, F, to the third power.

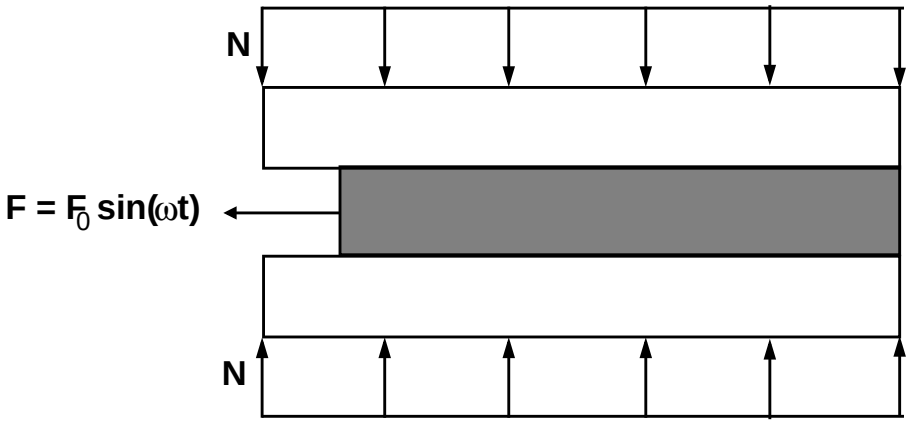

Figure 14.21. Clamped 2D Strip Configuration.

Elastic strip clamped with uniform normal traction and subjected to oscillating applied force.

The strip in Figure 14.21 is assumed to be elastic, and the normal traction applied by the clamps is assumed uniform. When the applied force is maximum in the cycle, the region of slip is also at its maximum. Within the region of slip, the equilibrium equation is

$$EA\frac{\mathrm{d}^2u}{\mathrm{d}x^2} = 2\mu N \tag{14.22}$$

where E is Young's modulus,
A is cross sectional area of the strip,
N is the uniform normal traction,
and μ is the coefficient of friction. (Poisson contraction is ignored).

The energy over a full cycle can be calculated as

$$\Delta D = \frac{1}{3}\frac{F_0^3}{EA\mu N} \tag{14.23}$$

14.4.2 Numerical Results

Figure 14.22 shows the mesh refinement that was required to capture the slip front and adequately capture the energy dissipation in the slip zone. Figure 14.23 shows the evolution of the energy dissipation over time. For this numerical simulation, the elastic strip was subjected to a uniformly imposed deformation, $\delta_h = 0.001$ m. Based on this deformation, and the application of plane strain boundary conditions, the resultant, uniform, normal traction can be calculated as $N = 10.5263$ N/m. The remaining parameters of the analysis are $\mu = 0.1$, $E = 10000$ Pa, $A = 9.0 \times 10^{-5}$ m^2, and $F_0 = 0.09$ N. The numerically calculated energy dissipation per cycle, $\Delta D = 2.503 \times 10^{-4}$ Joule per cycle, compares favorably to that calculated using the the closed-form expression given in Equation (14.23), $\Delta D = 2.565 \times 10^{-4}$.

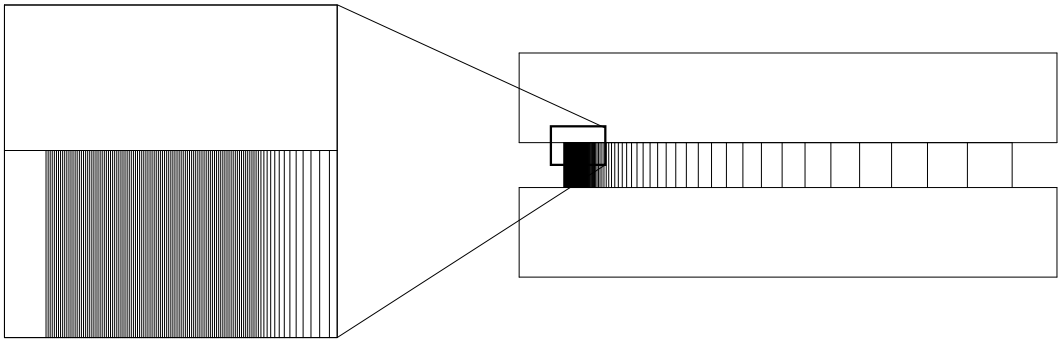

Figure 14.22. Clamped Strip Mesh.

Geometry and mesh used to solve the two-dimensional clamped strip problem.

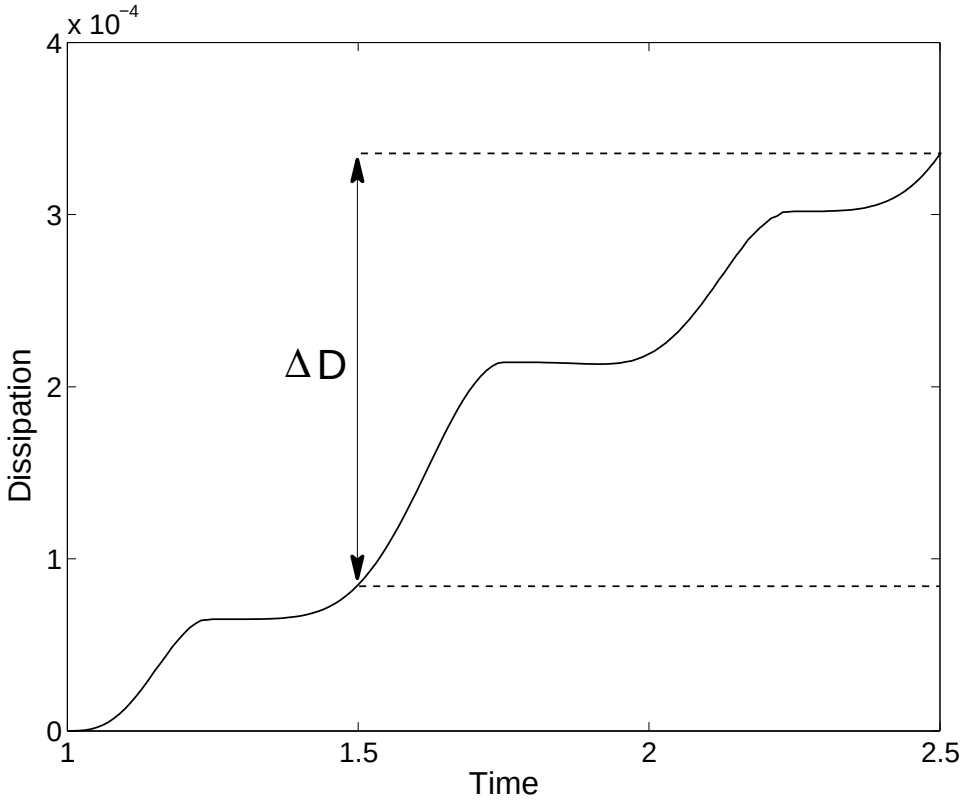

Figure 14.23. Energy Dissipation Prediction.

Energy dissipation prediction from numerical calculations. The dissipation change over one cycle is illustrated. The elastic strip was subjected to a uniformly imposed deformation, $\delta_h = 0.001$ *m. The remaining parameters of the analysis are* $\mu = 0.1$, $E = 10000$ *Pa*, $A = 9.0 \times 10^{-5}$ m^2, *and* $F_0 = 0.09$ *N.*

Chapter 15

A Parameter Study on the Qualitative Dissipation Response of the Simple Flat Lap Joint

Michael J. Starr

15.1 Introduction

Over the course of the five year testing history, a wealth of experimental data has been collected on a variety of joint geometries. This section will focus on a class of specimens that has been termed simple lap joints. The reason for considering these joints "simple" is because they are idealized and do not make use of bolts to put the contact interface into a state of pre-stress. In fact, the loading of the lap joint is accomplished through a fixture that approximates line loading. These lap joints come in three configurations: flat lap joint, radius joint, and stepped joint. The bulk of the data has been collected for the flat lap joint, and, therefore, it will serve as the geometry for comparison.

15.2 Parameter Study

A series of parameter studies was performed to uncover trends in energy dissipation per cycle, and to establish general dependencies of the power-law dissipation parameters on modifications to the boundary conditions. Figure 15.1 shows the free-body diagram of the axially loaded portion of the simple lap joint. Due to deformations and the asymmetry of loading, the actual equilibrium state during a loading sequence is somewhat more complicated than the free body diagram implies. However, deviations from the figure are generally minor.

The following sections each highlight a unique parameter study that was performed to better understand dissipation dependencies and perhaps develop a more complete understanding of the relative importance of correctly modeling boundary conditions and material parameters. Although

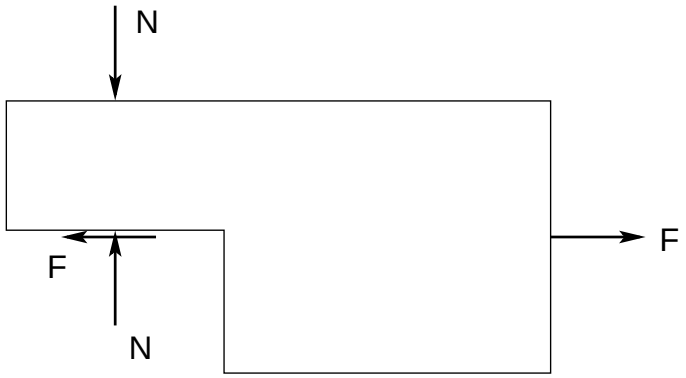

Figure 15.1. Free Body Diagram of the Simple Lap Joint.

there are systematic differences between experimental results and numerical predictions under an assumption of Coulomb friction, a simple Coulomb friction, constitutive model was employed in all of the parameter studies. These studies quantified the dependencies of dissipation per cycle calculations on the following parameters: clamping load, friction coefficient, lateral kinematic constraints, Poisson's ratio, and load coupling on the free end.

15.2.1 Dependence on Clamping Load

Experiments on the simple lap joint are typically performed over a relatively limited range of clamping loads (less than one decade) in a range that is consistent with loads seen in service hardware. For the simple, flat lap joint, data were taken for clamping loads (designated N in Figure 15.1) of $N = 800$, 1200, and 1600 lb. Steady state data were collected at five levels of axially applied, force magnitudes of $|F| = 60$, 120, 180, 240, and 320 lb. These boundary conditions were reproduced in numerical predictions, and the results are shown in Figure 15.2.

Clockwise from the upper left corner, the plots show: the experimental measurements of energy dissipation per cycle for the three clamping load levels, numerical predictions for $\mu = 0.3$, numerical predictions at $\mu = 0.7$, and numerical predictions at $\mu = 0.5$. The numerical predictions were performed at the three discrete levels of clamping load for friction coefficients consistent with measured values for steel-on-steel contact.

Energy dissipation data of this type are typically presented on a log-log scale. That format is repeated here. The value of this form of representation is that the data appear linear as a function of the logarithm of applied force. It is convenient, then, to make comparisons with respect to linear curve fits of the data, where the slope of the curve fit is the exponent of a power-law representation of the data.

It is clear from Figure 15.2, that some qualitative trends seen experimentally are captured in the numerical predictions. Namely, the arrangement of the energy dissipation predictions matches that

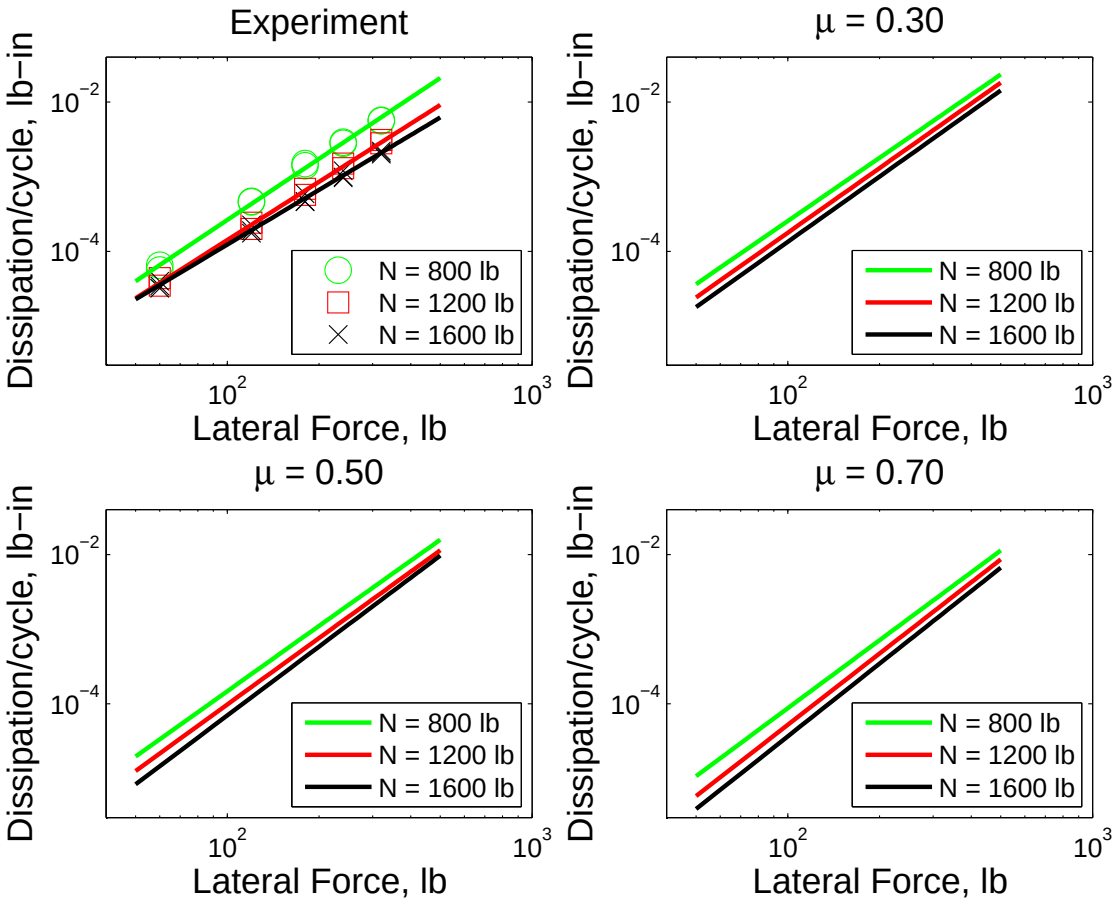

Figure 15.2. Dissipation per Cycle, Normal Clamping Loads.

The upper left figure shows experimental measurements, while the remaining figures are numerical predictions for various realistic values of friction coefficient.

of the experiment. The larger the normal clamping load, the smaller the dissipation per cycle at a given axial load level. A feature that is not captured, however, is the change in dissipation slope. Experimentally, the dissipation slope decreases with increasing clamping load. The numerical predictions appear to exhibit precisely the opposite of this behavior.

15.2.2 Dependence on Friction Coefficient

The data presented in Figure 15.2 can be re-framed to more clearly illustrate the dependence of dissipation behavior on the friction coefficient, as is shown in Figure 15.3. Clockwise from the upper left corner, the plots show: the experimental measurements of energy dissipation per cycle for the three clamping load levels, and numerical predictions for $N = 800$ lb, $N = 1600$ lb, and $N = 1200$ lb. The numerical predictions were performed at the three discrete levels of friction coefficients consistent with measured values for steel-on-steel contact. Experimental results at each respective clamping load are superposed on the numerical predictions.

The figures show the general trend that the smaller the friction coefficient, the larger the energy dissipation per cycle at a given axial load level. This is a physically acceptable result, since the resistance to sliding decreases for lower friction coefficients. The direct comparisons to experimental measurements show that the predictions are quantitatively reasonable, but also highlight a fundamental inadequacy of Coulomb friction, because the predicted dissipation slopes are significantly higher than experiment. This is not simply a matter of unconverged meshes or inappropriate time stepping, as evidenced by numerous such convergence studies.

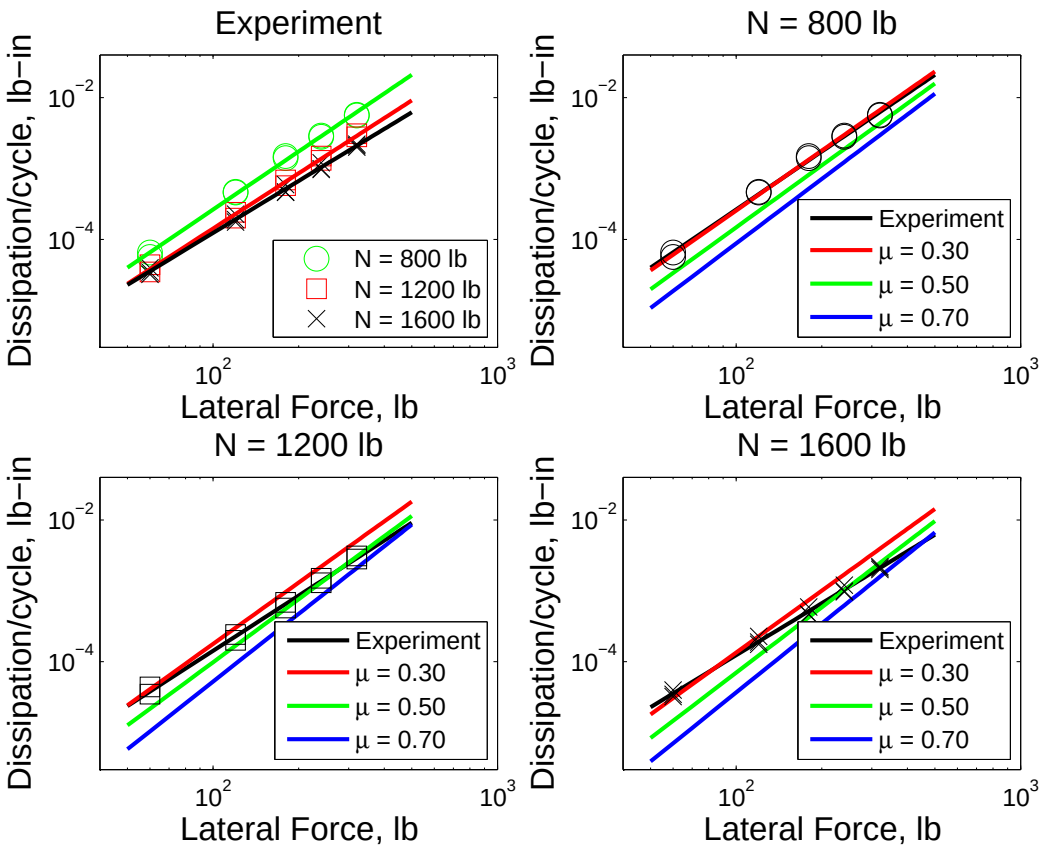

Figure 15.3. Dissipation per Cycle for Various Friction Coefficients.

The upper left figure shows experimental measurements, while the remaining figures are numerical predictions at each of the three, discrete, normal, clamping loads. Experimental results at each respective clamping load are superposed on the numerical predictions.

15.2.3 Dependence on Lateral Constraints

The fixture that holds the simple lap joint is known as the BMD and is typically not included in FE analysis. Consequently, we can question whether the boundary conditions at the attachment points are adequately modeled. The loaded end of the flat lap joint most closely resembles a cantilevered connection, but because the fixturing is not perfectly rigid, the true boundary constraints lie somewhere between simply supported and cantilevered. Figure 15.4 shows the dissipation response under consideration of these two boundary condition extremes. It is interesting to note that although the boundary conditions will lead to significantly different measures of joint stiffness, the dissipation characteristics are essentially the same.

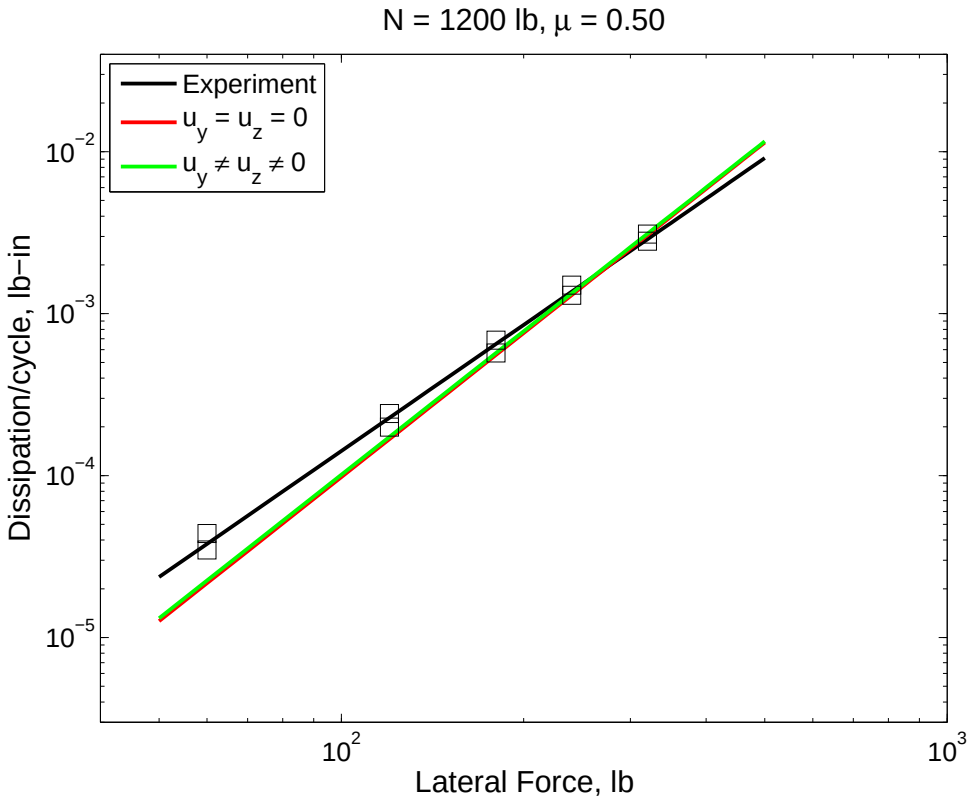

Figure 15.4. Dissipation Prediction Comparisons.

Dissipation results for the two boundary condition extremes of unconstrained, $u_y \neq u_z \neq 0$ and constrained, $u_y = u_z = 0$.

15.2.4 Dependence on Poisson's Ratio

Figure 15.5 shows the dissipation response of the simple lap joint for two different values of Poisson's ratio. The figure shows that the dissipation response is essentially independent of Poisson's ratio in the regime of realistic values for steel.

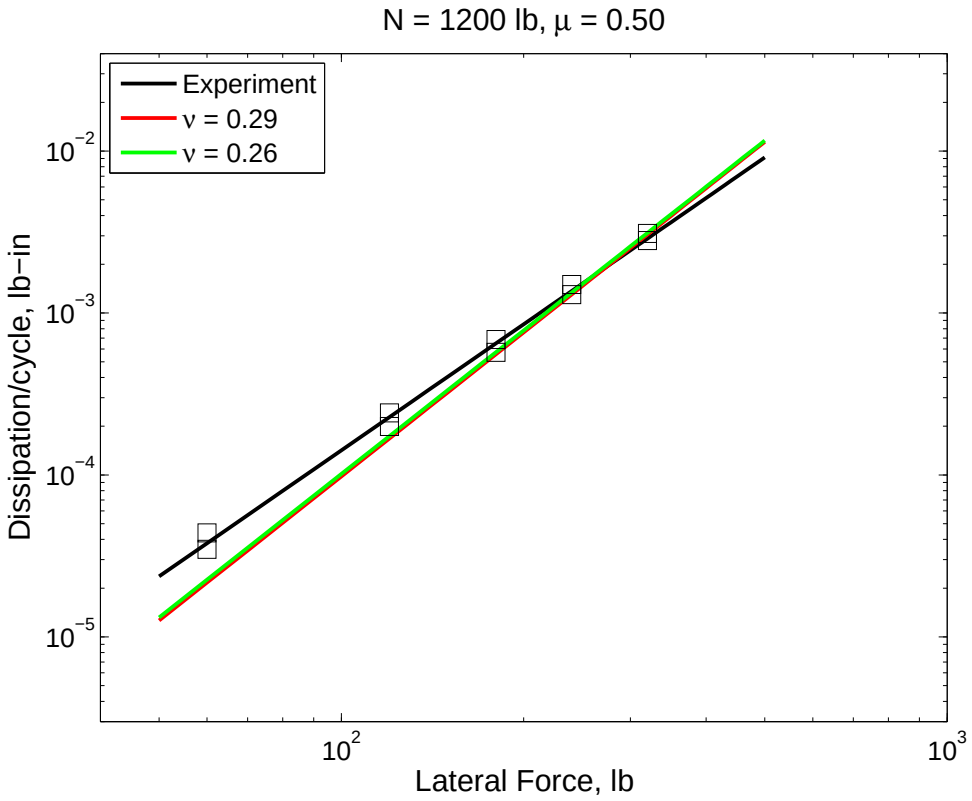

Figure 15.5. Dissipation Predictions for Variable Poisson's Ratio.

Dissipation results for two unique Poisson's values, $\nu = 0.26$ and $\nu = 0.29$.

15.2.5 Dependence on End Shear

As stated previously, the true state of boundary conditions on the loaded end of the lap joint assembly is not perfectly known. Therefore, it has been postulated that the end loading may not be purely axial. The sensitivity of the predicted dissipation response is explored in the following two sections. In the first, the end shear coupled with the axial load is a constant fraction of the applied clamping load. In the second section, two different, time dependent schemes are applied, both of which are in phase with the applied axial load.

15.2.5.1 Constant End Shear

In this section, it is postulated that the presence of a loading eccentricity has induced a coupled loading on the end of the lap joint assembly. Figure 15.6 shows the nature of the loading boundary conditions that have been applied numerically. These conditions pertain while an oscillatory axial load, $F(t)$, is also applied at the free surface. It is important to note that there is no direct evidence in our experimental work that such a loading actually occurs.

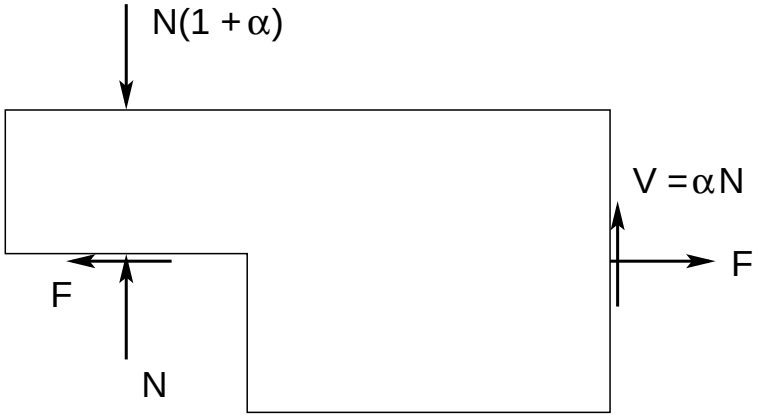

Figure 15.6. Free Body Diagram, Loaded Portion of the Simple Lap Joint.

A constant end shear has been applied to accommodate the presence of a loading eccentricity. The applied shear has amplitude αN, where $-0.10 < \alpha < 0.10$.

Figure 15.7 shows the results of dissipation behaviors over a range of scalings of the coupled shear. In general, the predictions indicate that the amount of dissipation decreases with increasing shear load for a given axial load. The power-law dissipation slopes increase from 0% shear up to 2% shear. At some point between 2% and 5% shear, a local maximum is reached and the predicted power-law slope decreases with increasing amount of coupled shear.

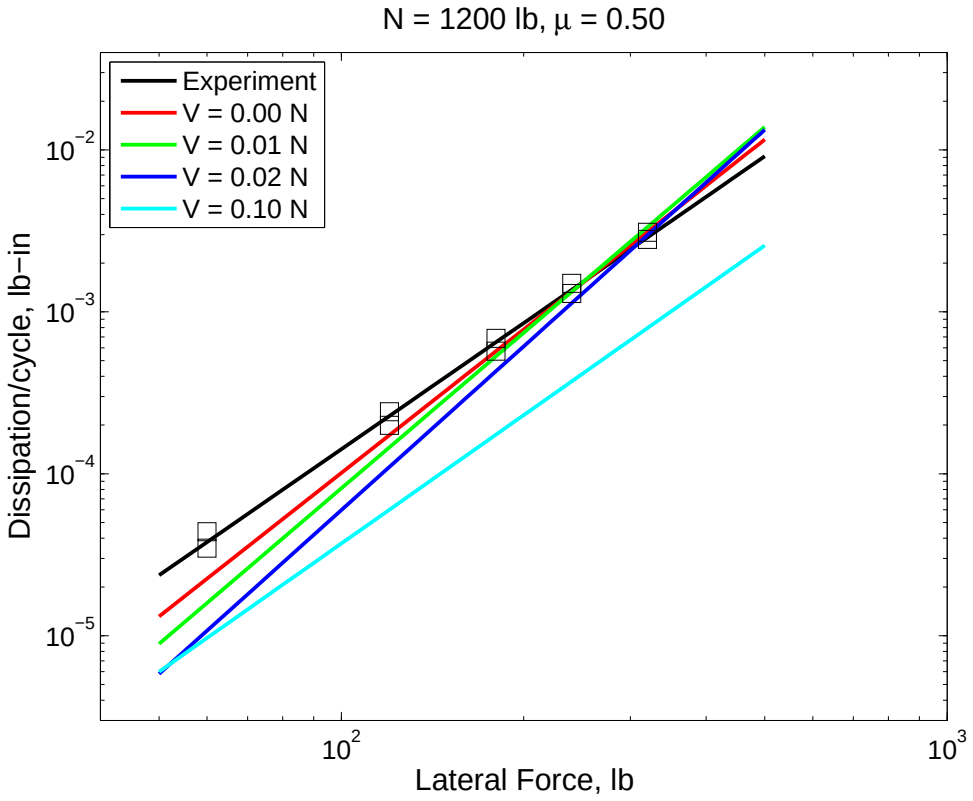

Figure 15.7. Dissipation Predictions With Coupled Shear.

Dissipation response of the simple lap joint for various fractions of coupled shear on the axially loaded end.

As demonstrated in Figure 15.8, reversing the sign of the coupled end shear has essentially no effect on the predicted dissipation value. This holds true for all coupled shear scaling levels explored.

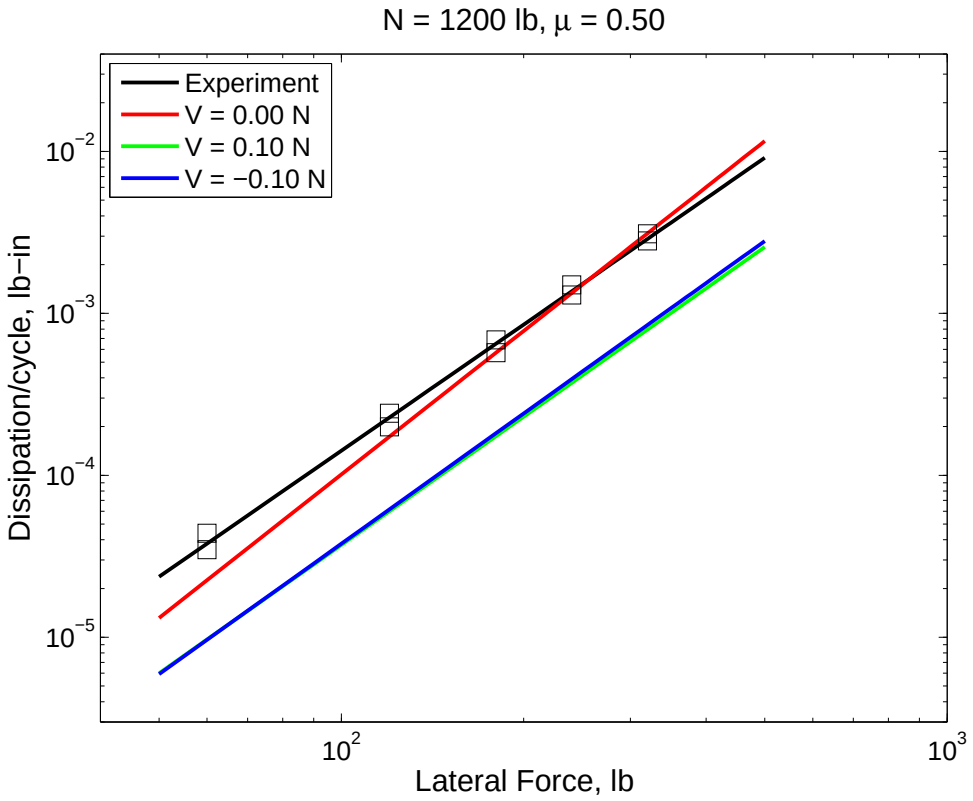

Figure 15.8. Dependence of Dissipation Predictions on Shear.

The dissipation response is essentially independent of the direction of the applied shear load. The dissipation is shown to be virtually identical for V = ± 0.1 N.

15.2.5.2 Time Varying End Shear

Here we consider an oscillatory axial load accompanied by an in-phase oscillatory shear load orthogonal to the plane of the interface (See Figure 15.9).

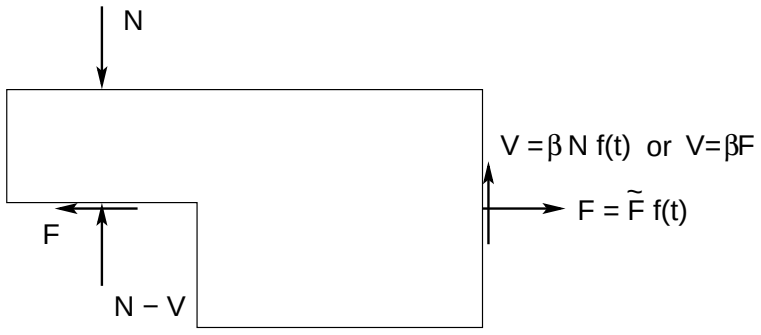

Figure 15.9. Shear Loaded Free Body Diagram of the Simple Lap Joint.

A time varying end shear has been applied to accommodate the presence of a loading eccentricity. The shear has been applied in a manner that is in phase with the applied axial load F(t), and with amplitude $\beta N f(t)$ *or* βF*, where* $0.0 < \beta < 0.10$*.*

The results of application of the time varying shear with amplitude $\beta N f(t)$ are shown in Figure 15.10. Increasing the level of the scaling factor β causes greater dissipation for a given applied load. The effect is dramatic as the ratio of the magnitude of the oscillatory shear load to the magnitude of the oscillatory normal load increases - resulting in orders-of-magnitude increases in dissipation but a decrease in the slope of the power-law relationship.

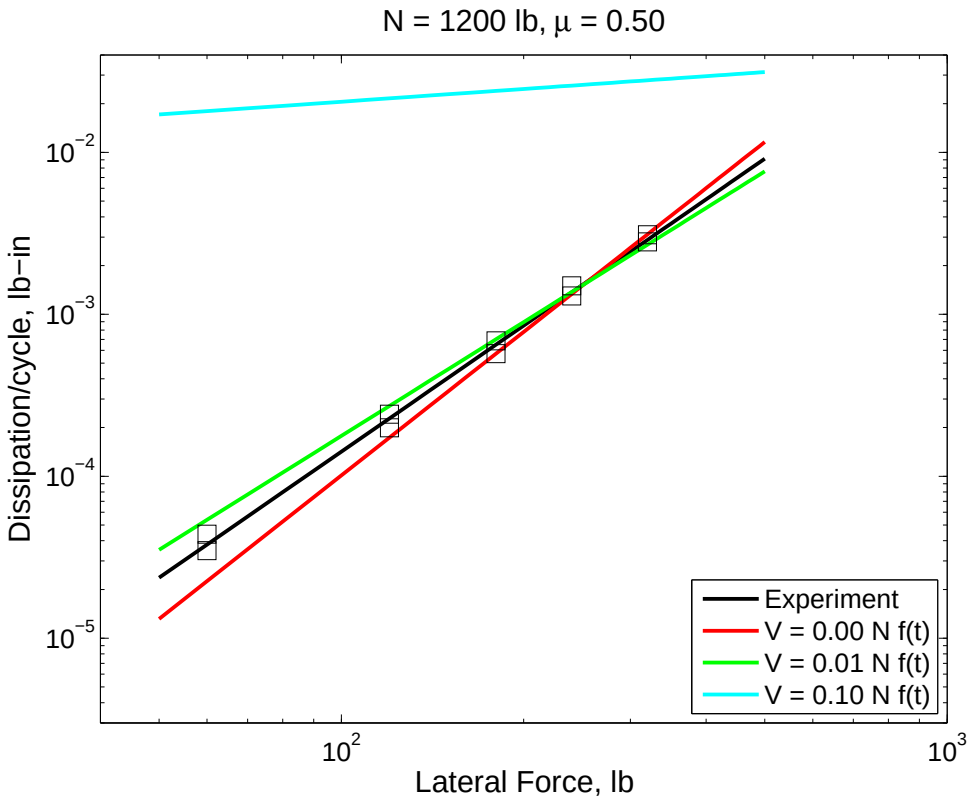

Figure 15.10. Coupled Shear Dissipation Predictions.

Time varying shear has been applied in a manner that is in phase with the applied axial load $F(t)$, and with amplitude $\beta N f(t)$, where $0.0 < \beta < 0.10$.

The results of application of the time varying shear with amplitude βF are shown in Figure 15.11. Increasing the level of the scaling factor β causes greater dissipation for a given applied load, but there is very little change in power-law slope.

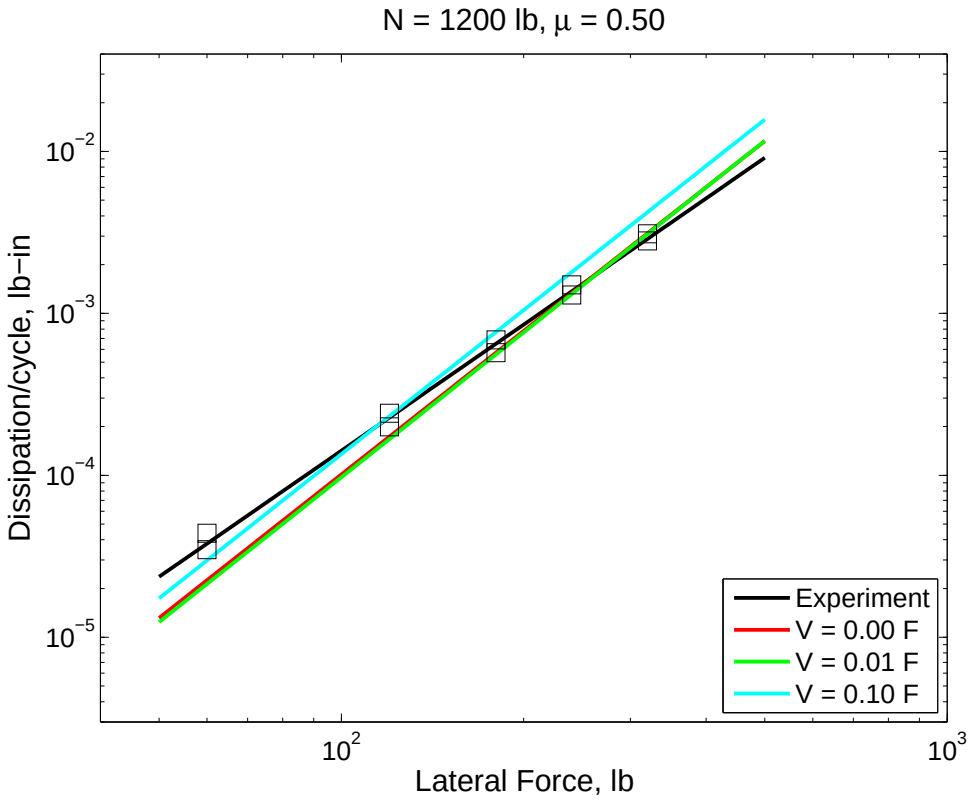

Figure 15.11. Coupled Shear Dissipation Predictions.

Time varying shear has been applied in a manner that is in phase with the applied axial load $F(t)$, and with amplitude βF, where $0.0 < \beta < 0.10$.

15.3 Extrapolation of Joint Parameters

Here the data gathered from the parameter study is used to describe how to calculate joint parameters for structural dynamics analysis.

Four parameters are employed to populate the Iwan model that exists within the structural dynamics code SALINAS. These parameters are: power-law dissipation exponent, C_0, power-law dissipation coefficient, α, joint stiffness, K_J, and macroslip force, F_S.

15.3.1 Power-Law Dissipation Parameters - C_0,α

The two parameters associated with fitting the energy dissipation per cycle predictions with a power-law are easily derived. A common approach to deriving these parameters is to use a straight line least squares fit to the logarithm of dissipation per cycle as a function of the logarithm of the applied lateral load. The dissipation per cycle for a particular flat lap joint configuration will be of the form

$$\mathscr{D} = C_0 F^{\alpha} \tag{15.1}$$

where $\mathscr{D}$ is the energy dissipation per cycle,
C_0 is a scaling coefficient,
F is the amplitude of the lateral load across the lap joint interface,
and α is the power-law exponent.

15.3.2 Joint Stiffness, K_J

Unlike with the experimental data, we need not concern ourselves with the attachment compliances of experimental fixturing. However, a set of reference simulations must be run to deduce the separate contributions to the overall structural compliance from the bulk material and the joint. The joint stiffness, K_J can be deduced from the following expression

$$K_J = \left[\frac{1}{K_S} - \frac{1}{K_{ref}}\right]^{-1} \tag{15.2}$$

where K_S is the calculated tangent stiffness of the jointed specimen at a load level sufficiently removed from the macroslip force level
and K_{ref} is the calculated tangent stiffness for a specimen where the lap joint has been made effectively monolithic, either by merging the opposing sides of the contact patch or mathematically welding the interface using tied contact across the interface.

15.3.3 Macroslip Force, F_S

This parameter is the easiest to calculate because the numerical modeling enforces a Coulomb friction model. So, the macroslip force is typically given by

$$F_S = \mu N \tag{15.3}$$

where μ is the coefficient of friction used in the numerical analysis
and N is the normal force across the contact patch.

For the cases where no shear loads are coupled with the lateral load, it is reasonable to assume that the macroslip force will essentially remain constant during a loading simulation despite the evolution of the normal force due to induced bending. Typically, the normal force will change by a very small fraction of the initial clamping preload. It is also a very simple matter to calculate the macroslip load for the cases of coupled shear and lateral loadings. The free body diagrams shown previously can be used to solve directly for macroslip load. For the case of constant coupled shear loading (Figure 15.6), the clamping load was modified from nominal so that macroslip occurs at

$$F_S = \frac{\mu N_C}{1+\alpha} \tag{15.4}$$

where N_C is the applied clamping load.

For time-varying coupled shear loadings shown in Figure 15.9, for which the shear loading is a function of the clamping load, macroslip occurs at

$$F_S = \mu(1-\beta)N_C \tag{15.5}$$

and for the case where the shear loading is a function of the applied lateral load, macroslip occurs at

$$F_S = \frac{\mu N_C}{1+\mu\beta} \tag{15.6}$$

15.4 Extraction of Iwan Parameters: An Example

In this section, a simple geometry will be used to deduce the Iwan parameters that would be input into a SALINAS structural dynamics analysis. The model chosen is known as the simple, flat lap joint, and was introduced previously in this chapter (shown in experimental fixturing in Figure 15.12). It will be assumed that there is no experimentally gathered data. Further, the example will

demonstrate the mechanics of the process and will not use any experimental source to inform the selection of input parameters.

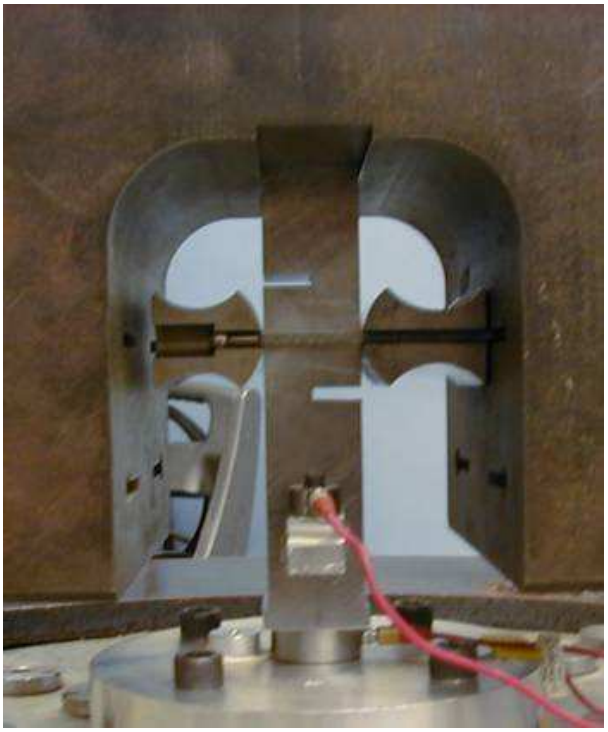

Figure 15.12. Simple Flat Lap Joint Shown in the BMD.

15.4.1 Calculating Reference Stiffness, K_{ref}

The boundary conditions on the loaded end of the experimental specimens are not precisely known. A reasonable assumption is that the boundary conditions are somewhere "between" simply supported and cantilevered. Based on the fixturing, an assumption of cantilevered boundary conditions seems the most appropriate, although both instances are examined. With the coordinate system shown in Figure 15.13, the displacement conditions at the loaded end can be expressed as: simply supported implies $u_y \neq u_z \neq 0$ and cantilevered boundary conditions implies $u_y = u_z = 0$.

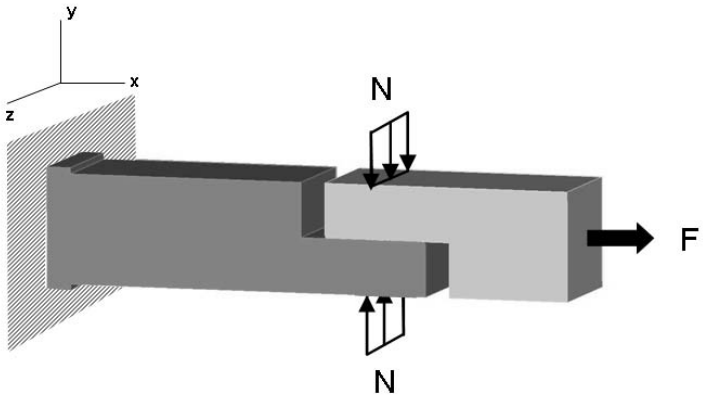

Figure 15.13. Numerical Model Configuration.

Schematic illustrating the boundary conditions and coordinate of the numerical approximation to experiment.

Calculations of reference stiffness employed a tied contact formulation on the interface. This is equivalent to enforcing zero relative displacements on all of the slave surface nodes that were originally in contact with the master surface before the application of external loadings and displacements. For both displacement boundary condition types, monotonic-pull numerical experiments were performed for each of the three possible clamping loads (800, 1200, and 1600 lb.). The maximum load applied in each instance was simply the load at which macroslip would have occurred on a jointed specimen with a friction coefficient of $\mu = 0.5$. (This friction coefficient will be used for all of the jointed-specimen numerical simulations in this section.) The reference stiffness was then calculated as the tangent stiffness over the final loading increment in the monotonic loading sequence. The results are summarized in Table 15.1.

15.4.2 Calculating Structural Stiffness, K_S

The next step is to calculate the structural stiffness by employing whichever interfacial constitutive model is appropriate for the material system. For the simple, flat lap joint in this example,

Table 15.1. Joint Reference Stiffness, K_{ref}

$u_y \neq u_z \neq 0$		$u_y = u_z = 0$	
N(lb)	K_{ref} (lb/in)	N(lb)	K_{ref} (lb/in)
800	2.742 x 10^6	800	3.876 x 10^6
1200	2.740 x 10^6	1200	3.876 x 10^6
1600	2.738 x 10^6	1600	3.875 x 10^6

Coulomb friction is adequate for steel-on-steel contact. A monotonic loading scheme may also be employed for this calculation. The loading should be taken to a level that is sufficiently far removed from macroslip. For example, the maximum load might be to the level at which the induced end displacement matches the level achieved in the reference stiffness calculation. This load should be sufficiently less than macroslip under an assumption that the structural configuration is more compliant than the reference configuration.

The structural configuration was simulated using a Coulomb friction value of $\mu = 0.5$. The results for both boundary condition extremes are given in Table 15.2.

Table 15.2. Joint Structural Stiffness, K_S

$u_y \neq u_z \neq 0$		$u_y = u_z = 0$	
N(lb)	K_S (lb/in)	N(lb)	K_S (lb/in)
800	2.243 x 10^6	800	2.969 x 10^6
1200	2.482 x 10^6	1200	3.164 x 10^6
1600	2.647 x 10^6	1600	3.286 x 10^6

15.4.3 Calculating Effective Stiffness, K_J

Now the effective joint stiffness can be calculated in a straightforward manner by employing Equation (15.2). The results for both boundary condition extremes are given in Table 15.3.

Table 15.3. Effective Joint Stiffness, K_J

$u_y \neq u_z \neq 0$		$u_y = u_z = 0$	
N(lb)	K_S (lb/in)	N(lb)	K_S (lb/in)
800	1.232 x 10^7	800	1.269 x 10^7
1200	2.636 x 10^7	1200	1.722 x 10^7
1600	7.964 x 10^7	1600	2.162 x 10^7

15.4.4 Calculating Power-Law Dissipation Parameters, C_0,α

The next set of parameters can be calculated by performing a quasistatic, cyclic loading sequence. The dissipation per cycle vs lateral force data are fit to a power-law of the form first shown in Equation (15.1). The power-law parameters are independent of the nature of the boundary condition constraints. The data sets from which the parameters are extracted are shown in Figure 15.14, and the parameters are given in Table 15.4.

Table 15.4. Power-Law Parameters, C_0,α

N(lb)	C_0	α
800	2.305 x 10^{-10}	2.9032
1200	1.200 x 10^{-10}	2.9560
1600	5.200 x 10^{-11}	3.0633

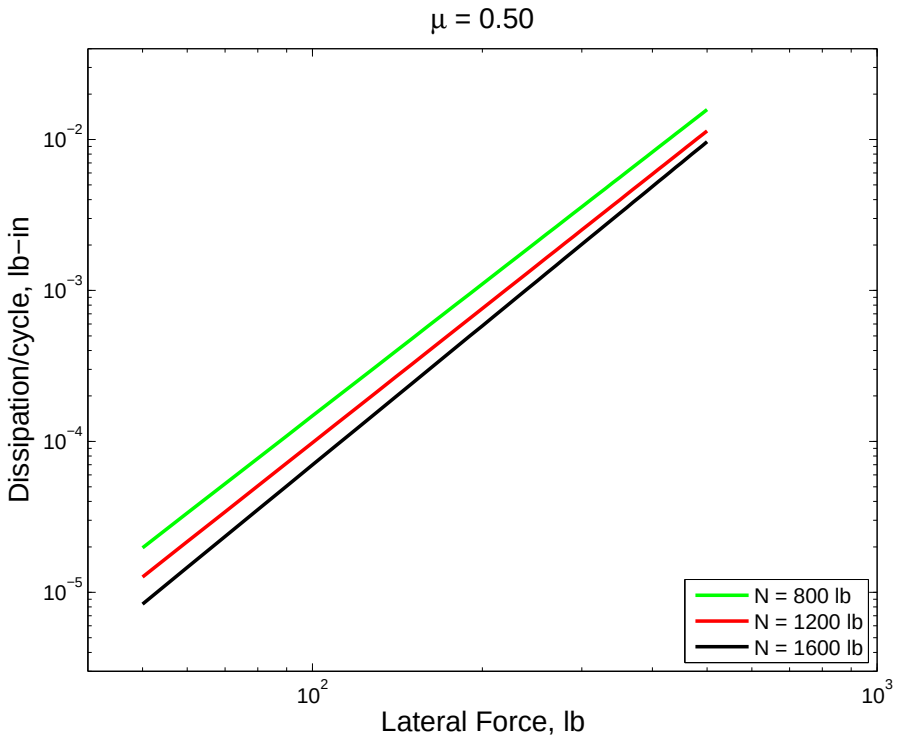

Figure 15.14. Dissipation Predictions.

Power-law dissipation curves for all combinations of F and N with $\mu =$ 0.5.

15.4.5 Calculating the Break Free Force, F_S

It is a simple matter to calculate the break-free force using Coulomb friction as the interface constitutive model. The simple relationship was stated in Equation (15.3), and the results for this example problem are shown in Table 15.5.

Table 15.5. Break Free Force, F_S

N(lb)	F_S (lb)
800	400
1200	600
1600	800

15.4.6 Deducing Iwan Parameters from Calculated Data

Now, with all of the values calculated in the previous several sections, the Iwan parameters can be deduced from Dan Segalman's optimization routine. The results of the optimization are shown in Table 15.6.

Table 15.6. Iwan Parameters Deduced from Numerical Experiments

$u_y \neq u_z \neq 0$				
N(lb)	χ	ϕ_{MAX}	R	S
800	-0.7864	3.2473×10^{-5}	6.542×10^{7}	6.388×10^{6}
1200	-0.9993	2.6638×10^{-5}	1.140×10^{7}	1.123×10^{7}
1600[a]	—	—	—	—
$u_y = u_z = 0$				
N(lb)	χ	ϕ_{MAX}	R	S
800	-0.8162	3.1533×10^{-5}	5.149×10^{7}	6.466×10^{6}
1200	-0.9143	4.1510×10^{-5}	2.021×10^{7}	6.613×10^{7}
1600	-0.9276	8.0552×10^{-5}	2.078×10^{7}	1.449×10^{5}

[a]Could not converge due to $\alpha > 3.0$

The deduced parameters can now be input into a joint definition within a SALINAS input deck.

```
BLOCK 1 // Joint # 1
//RBAR
  nonlinear = yes
  coordinate 4
  joint2G
  kx = iwan 1
  ky = iwan 1
  kz = elastic 1.8e6
  krx = elastic 1.e6
  kry = elastic 1.e6
  krz = elastic 1.e9
END
```

```
PROPERTY 1 // Sample A1 Mean
  chi = -0.7864
  phi_max = 3.2473e-5
  R = 6.542e+7
  S = 6.388e+6
END
```

Chapter 16

Modeling Joint Variability Via Direct and Indirect Numerical Methods

Michael J. Starr

16.1 Introduction

Proponents of micromodeling often make the argument that simply micromeshing a contact interface and applying a Coulomb friction- type constitutive model is the best approach to modeling joints. This philosophy, however, neglects very important issues of scale: some numerical and some physical. The physical issues are addressed here. It is known that on some length scale all apparently smooth surfaces will exhibit roughness of some sort. The source of the roughness may be intrinsic to the nature of atomic packing, introduced during fabrication or machining, or be the result of loading history and wear. The impact of surface features is not well understood as it relates to such global measures as energy dissipation per cycle. An approach to quantifying the impact of surface roughness on the variability seen experimentally can be explored through direct modeling of surface features. A road map for such a study is outlined here in the next section.

An alternative approach, indirect modeling, is described in the third section. The basis for approaches of this nature are the fundamental understanding that there exists a constitutive relationship associated with a length scale. The intrinsic assumption is then that all of the geometric details of smaller length scales are appropriately captured in the constitutive model, and therefore, under some approaches, a perfect, conformal mesh could be employed in an analysis. (Recognize that this is exactly the argument made for the application of Coulomb friction. Coulomb friction is a empiricism, employed for it's simplicity and convenience, which results from more complex physical phenomena on smaller length scales.)

All of the approaches in this section will be motivated through explorations involving the simple flat lap joint.

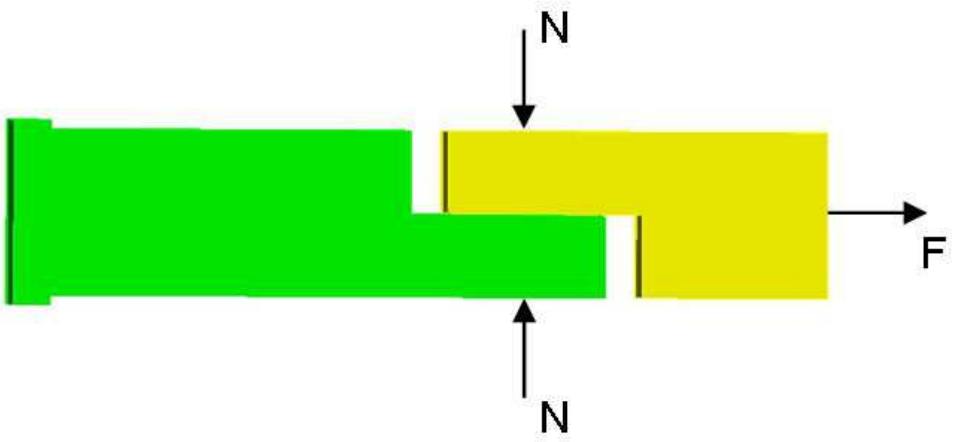

Figure 16.1. Simple Flat Lap Joint Configuration.

The simple flat lap joint will be the focus of the direct and indirect modeling studies.

16.2 Direct Modeling of Surface Characteristics

In this section two direct modeling approaches will be explored. The first approach employs data gathered from imaging the height profiles of the mating contact surfaces. The second approach employs data gathered from the contact surfaces of an assembled joint pair. These data have the benefit of also capturing features of misfit and misalignment where the first approach cannot. However, a considerable effort must be expended to reduce the data to a usable form for FE analysis.

16.2.1 Surface Perturbations From Surface Imaging

The data are presented on the following pages for the available specimens. Figure 16.2 shows the reference local coordinate system for the scans.

16.2.1.1 Profilometry of Joint Interfaces

There are several techniques that could be employed to measure the mating surface profiles of the flat lap specimens. These techniques include, but are not limited to, atomic force microscopy, (AFM), interferometry, and confocal, laser scanning microscopy. Due to the contact patch size and the spatial resolution required, a confocal, laser scanning microscope was used to gather surface profile data from a collection of flat lap joint specimens. The specimens can be broken into two distinct groups. The first group consists of three lap bottoms, designated specimens A, B, and C,

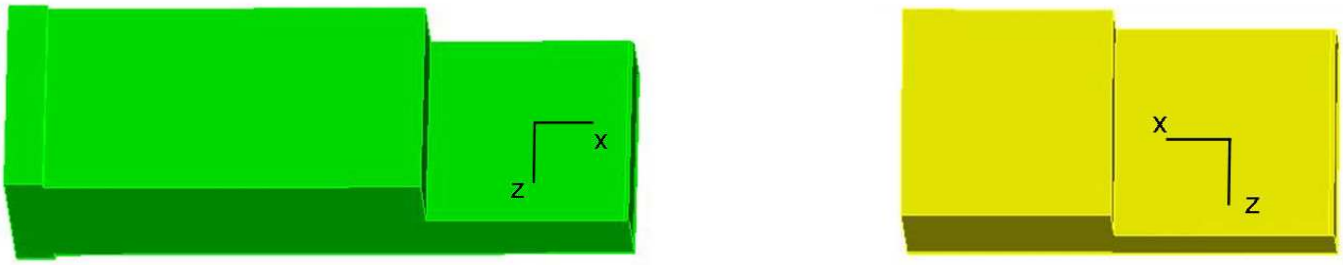

Figure 16.2. Contact Interface Local Coordinate System.

and two lap tops, designated specimens 1 and 2. All of the specimens in this group were machined from AISI 4340 steel with a surface finish specified at 32 μin. Two dimensional projections of the surface heights of these specimens are shown in the following figures. Height data were sampled every 50 μm in the plane of contact, with a vertical resolution on the order of 10 nm. Figures 16.3 through 16.5, below, show the height profiles measured on the bottom specimens A, B, and C. Figures 16.6 and 16.7, below, show the height profiles measured on the top specimens 1 and 2. (All of the dimensions in the figures have been converted to inches.)

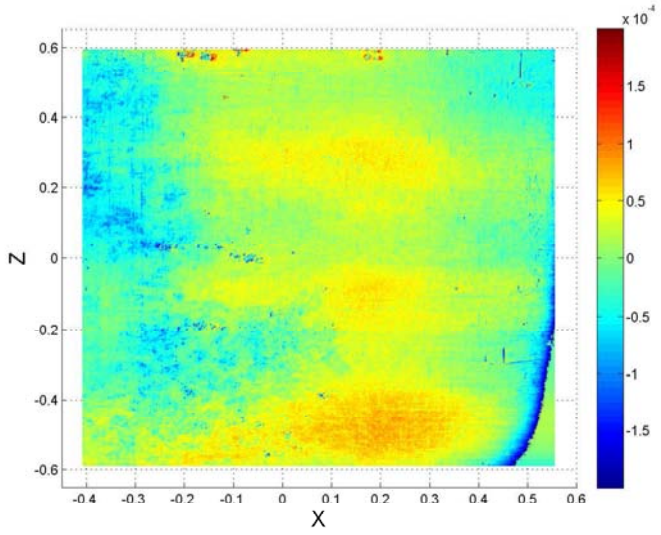

Figure 16.3. Bottom Lap Joint Specimen A.

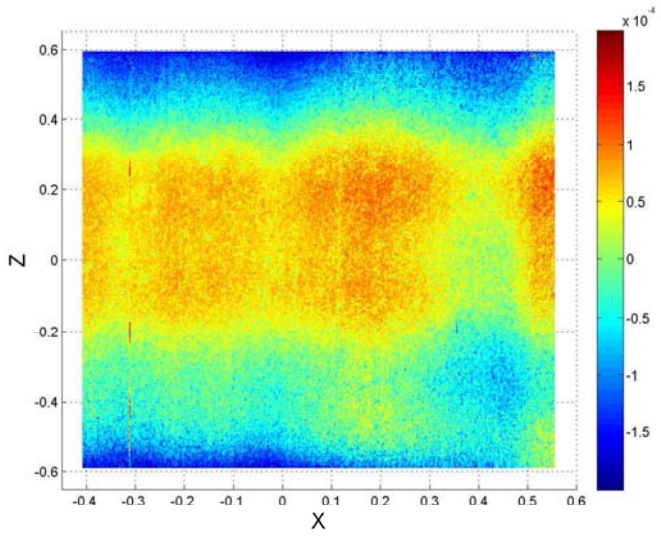

Figure 16.4. Bottom Lap Joint Specimen B.

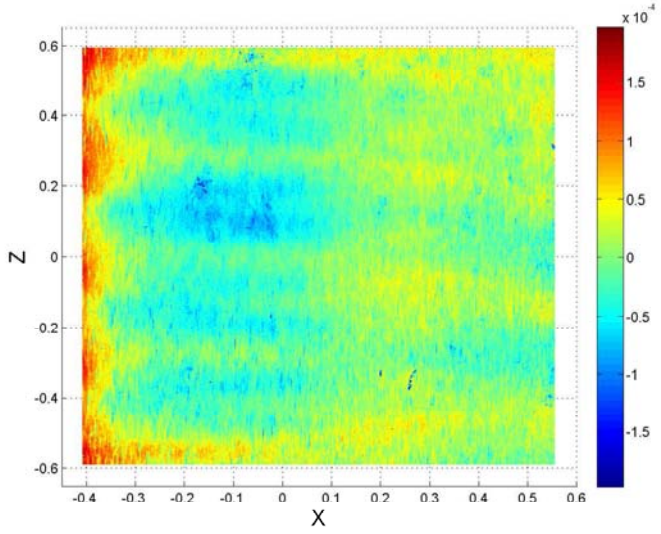

Figure 16.5. Bottom Lap Joint Specimen C.

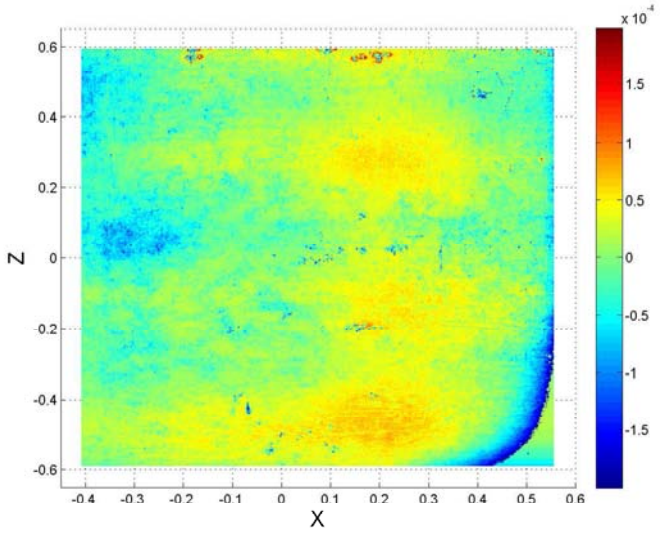

Figure 16.6. Top Lap Joint Specimen 1.

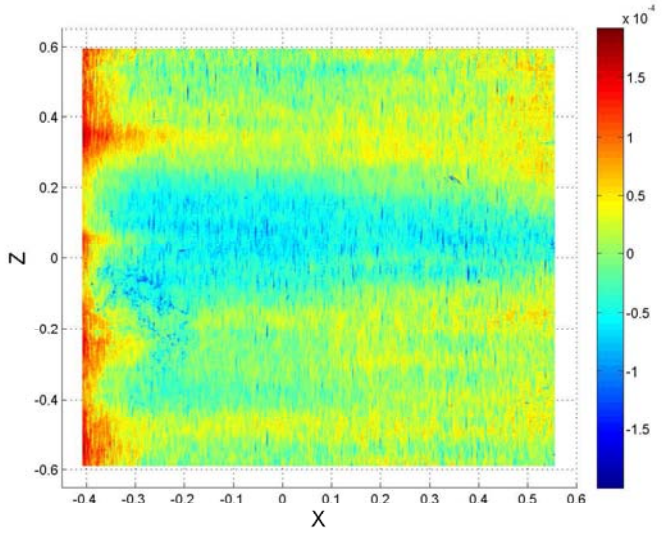

Figure 16.7. Top Lap Joint Specimen 2.

The second group comprises 3 sets of top and bottom specimens. Again, each specimen was machined from AISI 4340 steel, however, each set had a different surface roughness prescribed on the contact patch. Each specimen was machined in a traditional manner, likely with an end milling process. Following this, electrical discharge machining (EDM) was used to impart an "isotropic" surface finish on the contact patch. The surface roughnesses were broadly defined as "rough", "medium", and "fine". Numerical processing of the confocal laser scans yielded the RMS values for each specimen shown in Table 16.1.

Table 16.1. RMS Surface Roughness

Specimen Type	Bottom	Top
Fine	78.5 μin	72.2 μin
Medium	191 μin	174 μin
Rough	412 μin	359 μin

Figures 16.8 through 16.13 show two-dimensional projections of the EDM processed interfaces for the second specimen group where the surface was specifically prepared as a "fine", "medium", or "rough" surface.

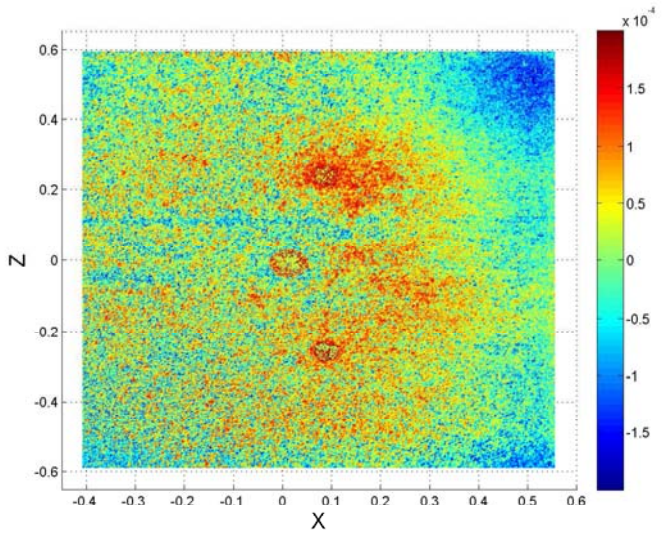

Figure 16.8. Bottom Lap Joint - “Fine” Surface Roughness.

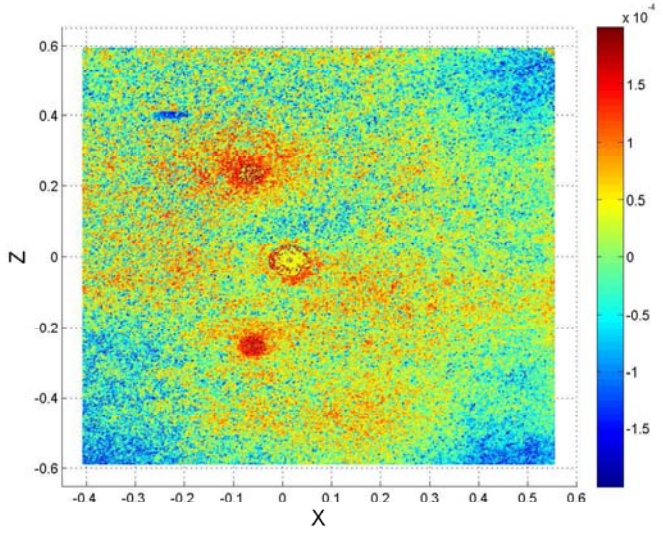

Figure 16.9. Top Lap Joint - “Fine” Surface Roughness.

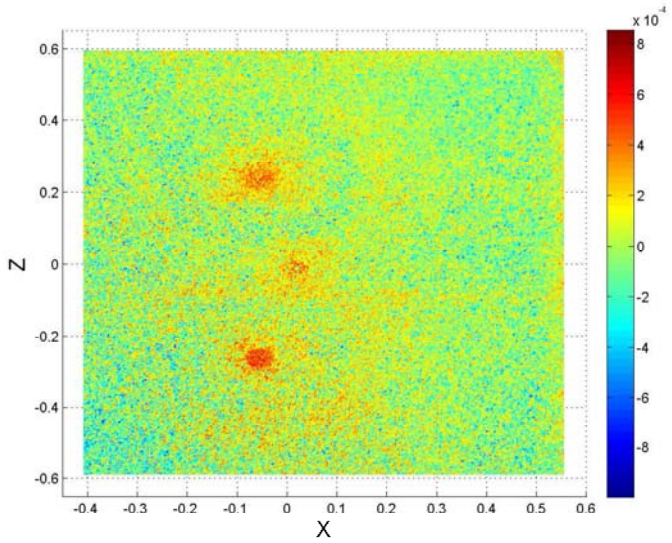

Figure 16.10. Bottom Lap Joint - “Medium” Surface Roughness.

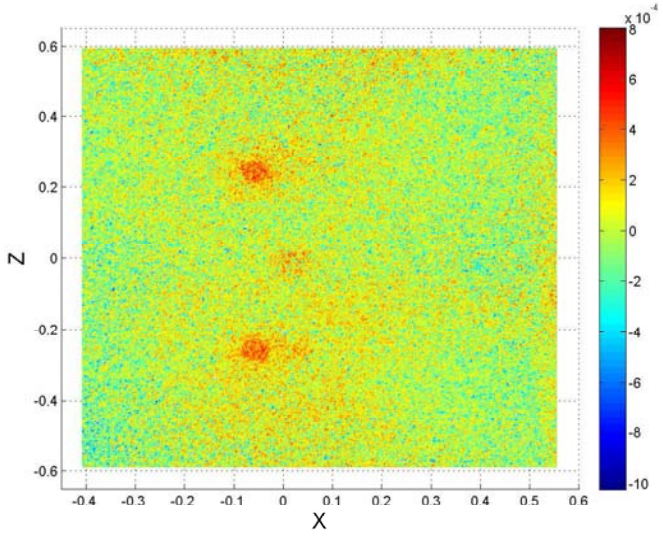

Figure 16.11. Top Lap Joint - “Medium” Surface Roughness.

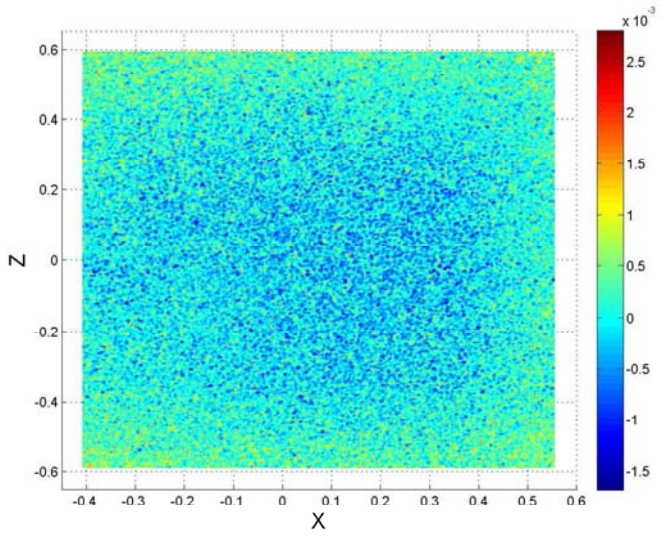

Figure 16.12. Bottom Lap Joint - “Rough” Surface Roughness.

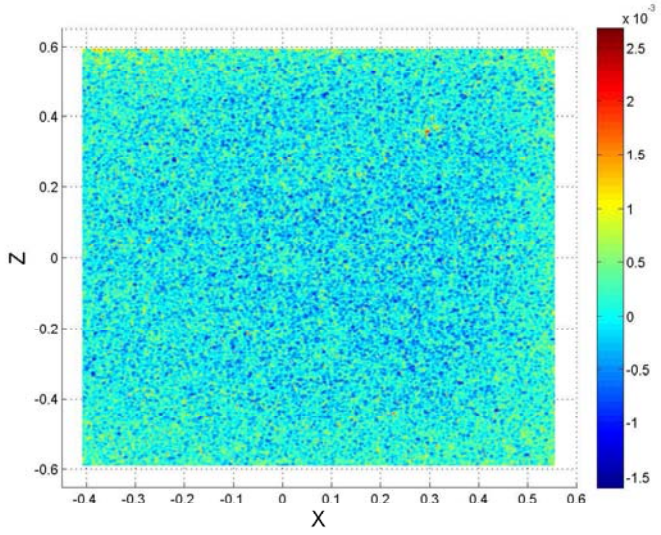

Figure 16.13. Top Lap Joint - “Rough” Surface Roughness.

16.2.1.2 Numerical Processing and Assembly of Surfaces

With the collection of scans taken it is possible to construct 30 unique contact pairs (6 bottom specimens and 5 top specimens). For the purpose of simplifying the modeling, all of the roughness was initially applied to the slave surface by convolving the surfaces together in the appropriate manner. Figure 16.14 shows the result of combining bottom specimen “A” and top specimen “1” to yield the new composite surface “A1”.

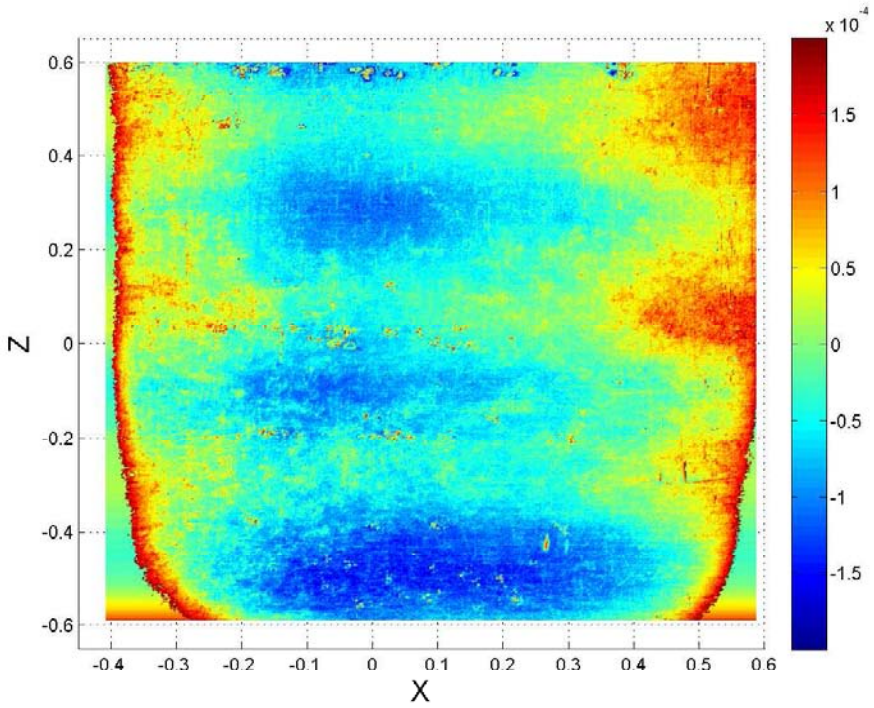

Figure 16.14. Composite Rough Surface.

Two-dimensional projection of the perturbed rough surface obtained by combining specimens ‘A’ and ‘1’.

The modification of the new perturbed surface is a simple matter once the composite surface has been constructed. Given a particular mesh, the initial coordinates of each contact slave node are perturbed from their initial state by interpolating the height values from the composite surface A1. It will typically be the case that the mesh density is significantly coarser than the density of the data taken from conformal microscopy. Figure 16.15 shows the resultant perturbed slave surface on an actual, coarse interface mesh. The mesh is approximately 0.3% of the density of the confocal, microscopy, height data.

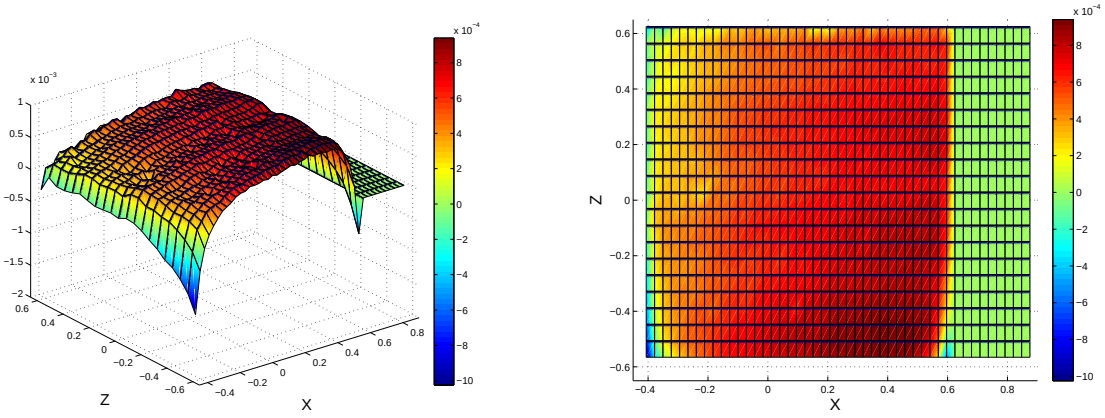

Figure 16.15. Modified Surface Mesh.

Perturbed profile of the slave surface of the meshed geometry for the simple flat lap joint.

16.2.1.3 Validation of Assemblies Against Experiment

A simple but meaningful validation activity is the comparison of the resultant, normal, pressure distributions on the contact interfaces to those that are obtained experimentally. This validation can be accomplished in a semiquantitative manner through the use of calibrated pressure film.

A numerical comparison of the interfacial, normal, pressure distribution is shown in Figures 16.16 - 16.18. In these figures, a preload of 1200 lb has been applied to clamp the two lap components together. Figure 16.16 shows the normal pressure distribution under the assumption that both contact surfaces are perfectly smooth and form a nominally conformal contact. Figure 16.17 shows the pressure distribution after the introduction of roughness with peak-to-valley measures on the order of 1000 μin. The interface is comprised of approximately 1000 elements. Figure 16.18 shows the pressure distribution given the same initial, rough, surface scan, but with a mesh refined in both planar dimensions. The interface for this figure is comprised of approximately 4700 elements. For both rough surfaces, pressure distributions in the contact region is quite localized. The effect of refining the mesh to capture more accurate contact pressures is apparent from these figures.

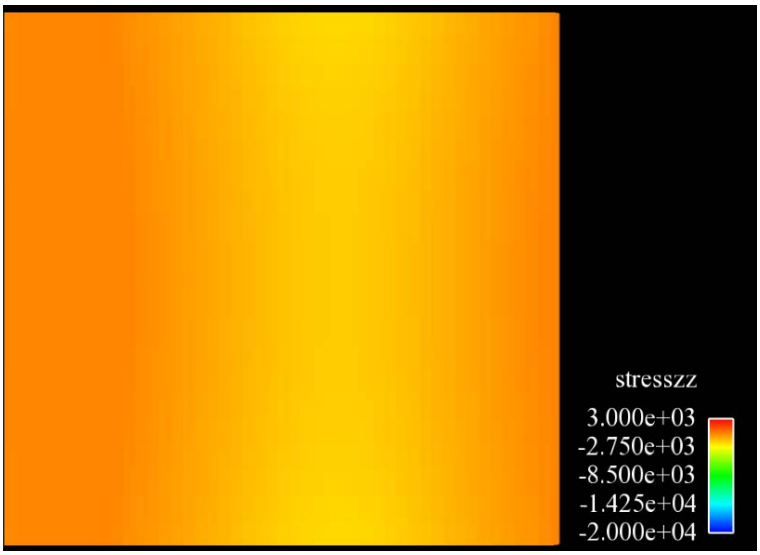

Figure 16.16. Normal Pressure Distribution.

Normal pressure distribution on the contact interface between perfectly smooth lap joints.

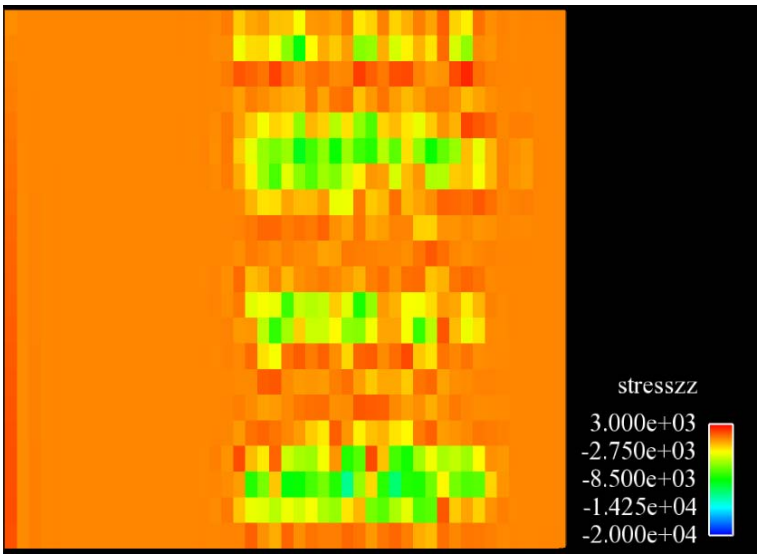

Figure 16.17. Normal Pressure Distribution.

Normal pressure distribution on the contact interface between rough contacting surfaces. The interface is comprised of approximately 1000 elements.

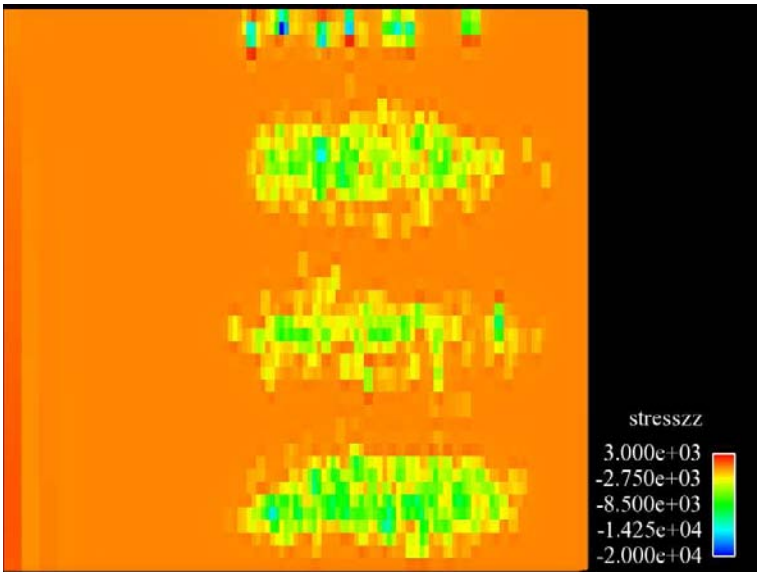

Figure 16.18. Normal Pressure Distribution.

Normal pressure distribution on the contact interface between rough contacting surfaces. The interface is comprised of approximately 4700 elements.

The experiments clamping the different combinations of specimens together have yet to be performed. It is important to note that the numerical calculations performed to date have only considered steel-on-steel contact. A more accurate treatment, for validation purposes, should include a layer of compliant material between the joint faces to capture the compliance of the pressure film.

16.2.1.4 Comparisons of Predicted Dissipations

All of the numerical studies reported in this section have been performed with the understanding that Coulomb friction cannot validate our experimental results. The influence of various sources of variability will be reported while discounting the error of assuming a Coulomb friction based interface model. Therefore, only qualitative conclusions are sought which might help guide modeling decisions.

Figure 16.19 shows the effect of modeling surface roughness features on predictions of energy dissipation. The first observation from this plot is that dissipation predictions from the rough surface simulation is smaller than that of the smooth surface simulation. This is not surprising considering that the true contact area in the rough simulation is significantly smaller than that of the smooth simulation. So, locally, much higher normal stresses will be achieved, and therefore fewer nodes will reach the critical shear sliding force level. A second observation is that the power-law slopes of the rough simulations are actually greater than the smooth simulation. This difference

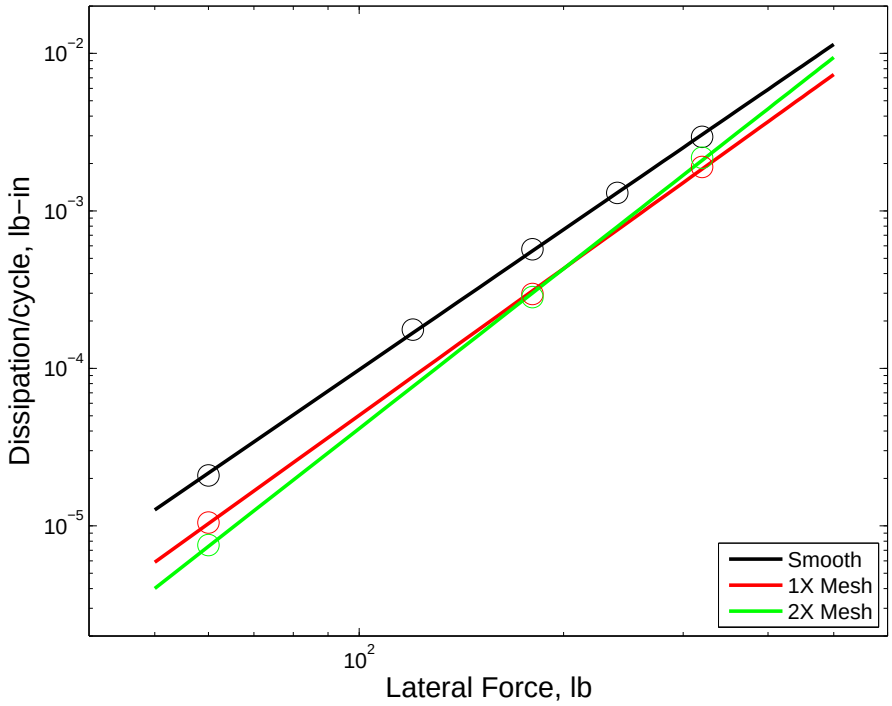

Figure 16.19. Energy Dissipation Predictions.

Comparison of energy dissipation predictions for composite surface A1 for two different levels of mesh refinement.

is an even further deviation from the slopes that are observed experimentally. A final observation is that the mesh refinement produced predictions that were quantitatively similar to the coarser mesh. This result is not a statement related to mesh convergence, but rather a simple statement that the added computational cost did not substantially change the nature of the prediction.

Figure 16.20 shows the effect of modeling the roughness in different manners: smooth-on-smooth contact, composite rough-on-smooth contact, and rough-on-rough contact. Both of the rough contact simulations exhibit the expected decrease in predicted dissipation magnitude. It is interesting to note that the composite rough approximation isn't significantly different than the rough-on-rough representation. This similarity may be due to the fact that the majority of the dissipation is carried by a relatively small number of nodes, and there are only very small nodal displacements during local sliding.

Figure 16.21 shows the dissipation predictions that are obtained by performing simulations of all 6 pairings of the lap joints machined using traditional techniques (A1, A2, B1, B2, C1, C2). The plots also contain the reference curves for the smooth surface simulation as well as the experimental mean. There is a significant spread between the lowest and highest predicted dissipations. In fact, the numerical spread (20 times) is significantly higher than the spread seen experimentally

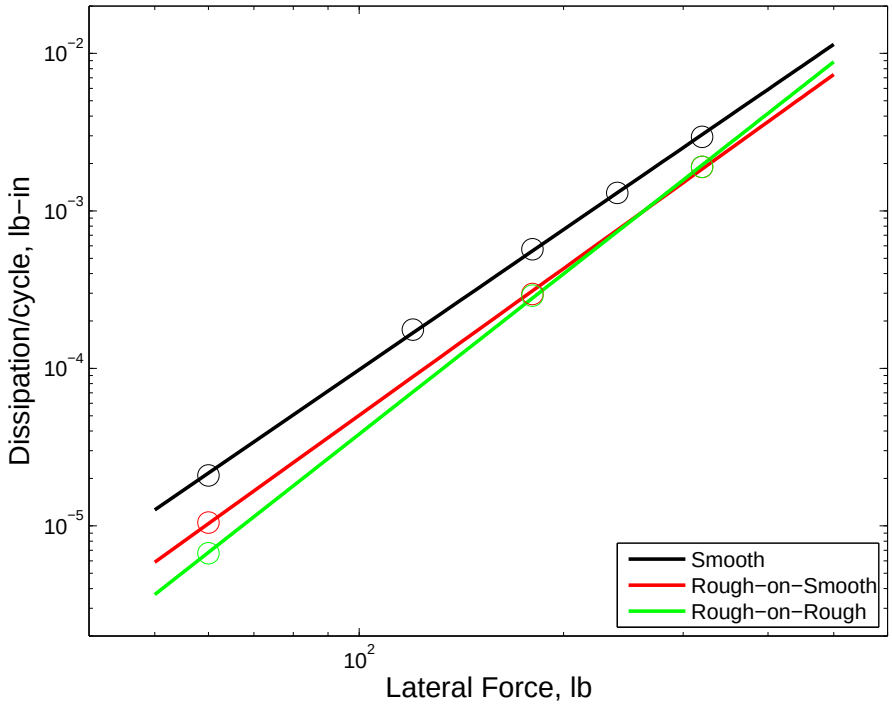

Figure 16.20. Roughness Based Energy Dissipation Predictions.

Comparison of energy dissipation predictions considering three different representations of the interface:smooth, rough composite A1 on smooth, and rough A on rough 1.

for similar lap joints (3 times). Another interesting feature of the predicted dissipations is that the predictions are clustered. All of the composite surfaces that include lap joint "2" predict higher dissipations than composite surfaces that include lap joint "1". This is consistent with data gathered for System A, single-leg configuration, in which one group of data associated with one lap component was systematically different than all other configurations.

The large numerical spread may be due to the manner in which the composite surfaces were mathematically assembled. In all cases, the raw, confocal, microscopy data were not modified. Since the measurements are taken with respect to an arbitrary datum, an artificial tilt may have been introduced into the surface representation. Figure 16.22 shows that surface assembly is the likely cause of the large numerical spread. The raw data was "self-aligned" so that a local, planar, coordinate axis on the rough data was mathematically forced into parallel with its smooth mating surface. This operation essentially reduces the predictions by a factor of approximately 20.

It is not known whether real features of the true contact have been removed by performing this tilt alignment. This question may be answered by a complete study of interfacial pressures employing the pressure film. A more complete study of the impact of the specimen tilt is shown in

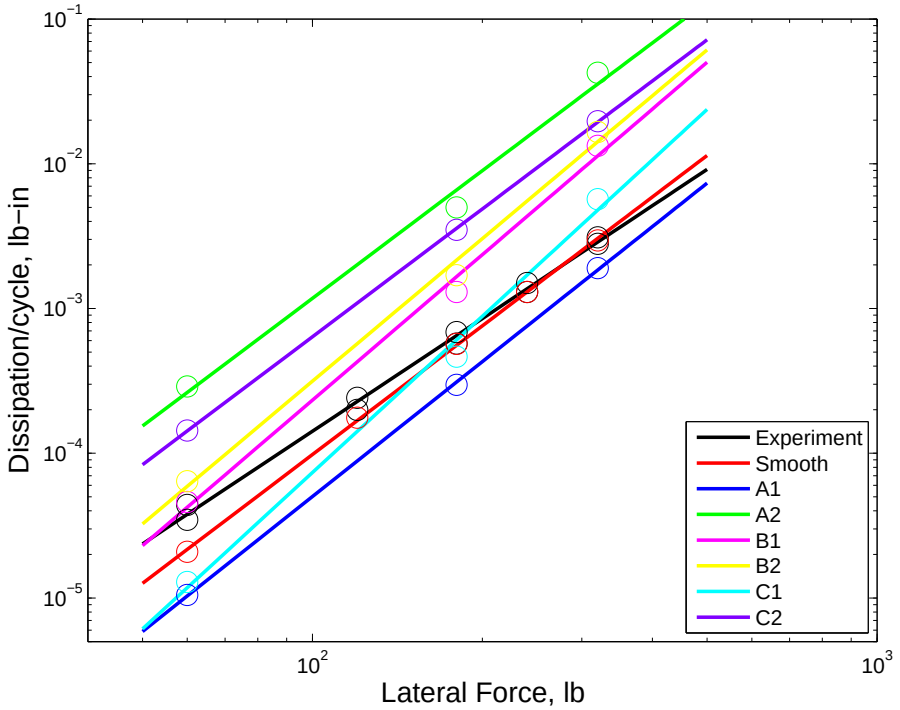

Figure 16.21. Energy Dissipation Predictions of Assemblies.

Comparison of energy dissipation predictions between various assembly combinations.

Figure 16.23. In this figure, the logarithm of energy dissipation per cycle is plotted as a function of the tilt of the assembled, rough, composite surface, A2. A mean planar surface was defined from a linear least squares fit to the rough composite surface along two axes: one parallel to the long axis of the lap joint (longitudinal) and one parallel to the in-plane normal to the longitudinal axis (lateral). Aligning the mean plane defined by these two axes parallel to the smooth opposing surface serves as the datum for the study. A suite of frictional dissipation studies was performed for 0.025° increments for lateral and longitudinal tilts in $[-0.10^\circ, 0.10^\circ]$. For each test performed, the clamping load was $N = 1200$ lb, the axial load magnitude was $F = 60$ lb, and the friction coefficient was $\mu = 0.5$. The energy dissipation appears to be essentially independent of the longitudinal tilt, but exhibits a rather strong quadratic dependence on the lateral tilt. The subsequent figure (Figure 16.24) shows the mean true contact area during the simulations. From the figure, it appears that there is an inverse relationship between true contact area and energy dissipation over the lateral tilt axis.(Compare these results to the case of smooth-on-smooth contact, where the mean true contact area is approximately 1.25 in^2.)

It is clear from this study that the specimen surface characteristics and the mechanics of assembly are potential causes for the energy dissipation spread observed experimentally. At this point, it appears that the tilt misfit plays a much stronger role in establishing the spread in numerical

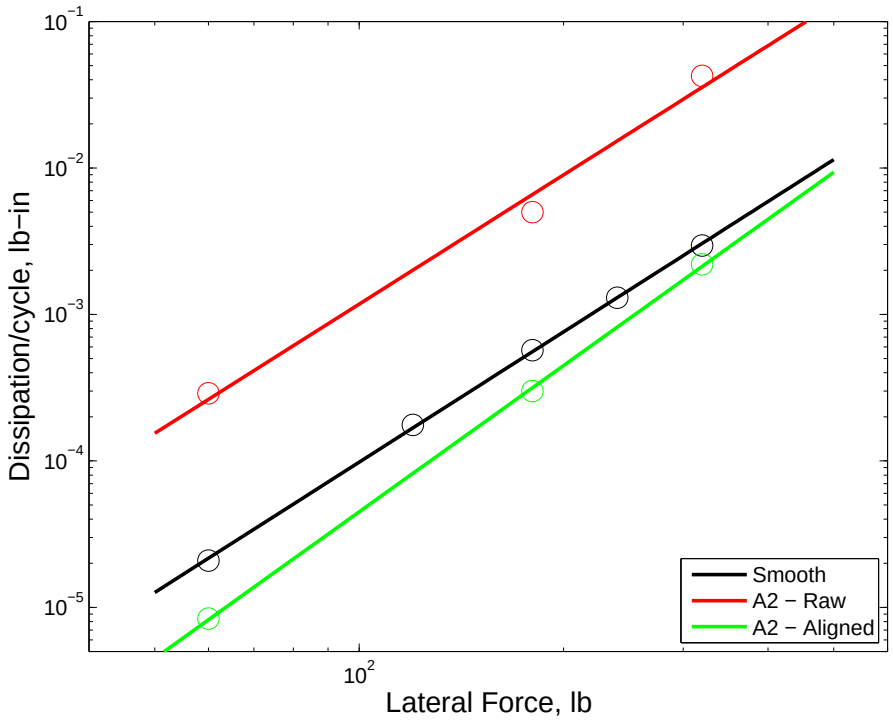

Figure 16.22. Surface Alignment Energy Dissipation Predictions.

Comparison of dissipation predictions using the raw surface scan of composite surface A2 with the case where the surfaces have been aligned.

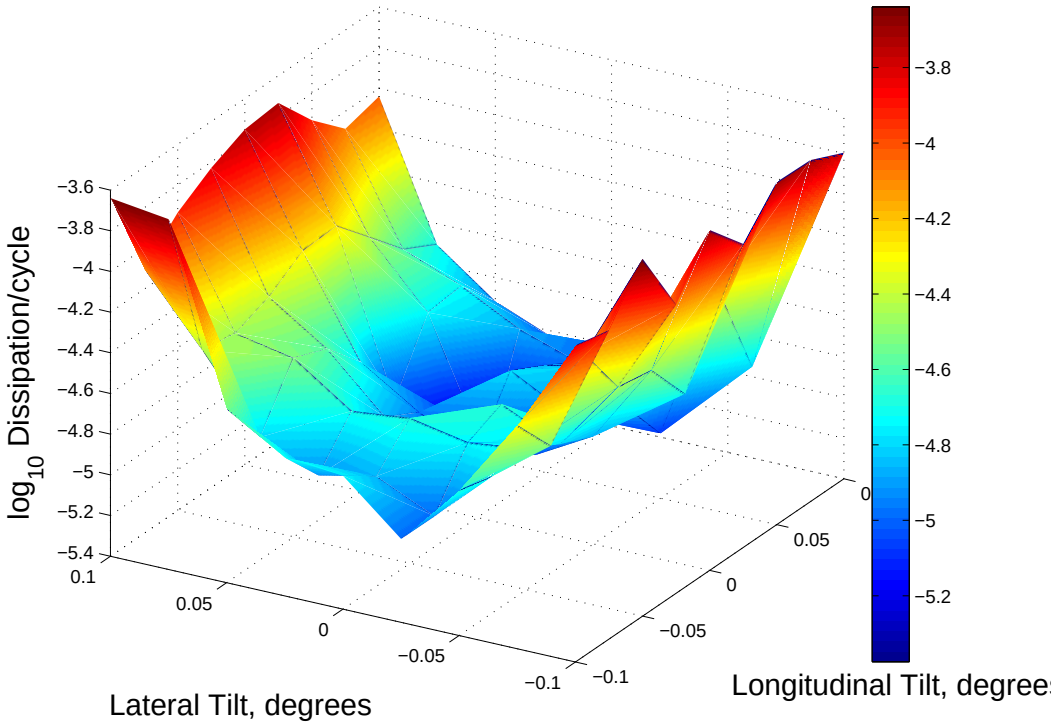

Figure 16.23. Tilt Misalignment Dissipation Predictions.

Energy dissipation per cycle is shown plotted as a function of tilt misalignment of the mean composite rough surface, A2, and smooth opposing surface, for $N = 1200$ *lb,* $F = 60$ *lb, and* $\mu = 0.5$.

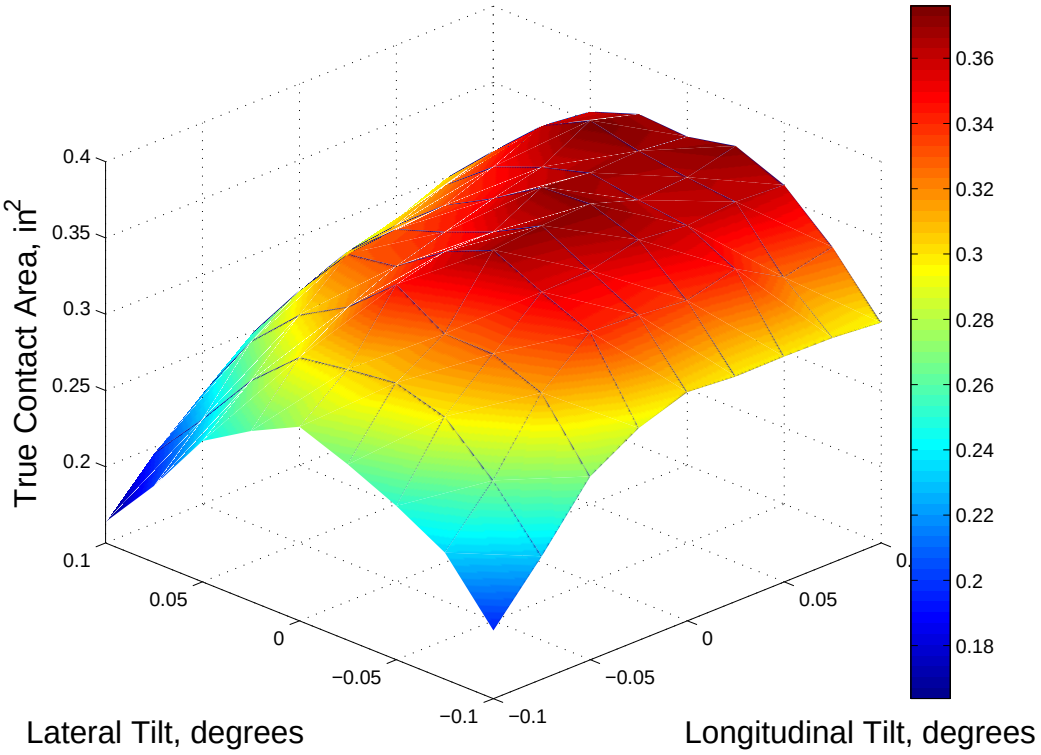

Figure 16.24. Tilt Misalignment True Contact Area Predictions.

True contact area is shown plotted as a function of tilt misalignment of the mean composite rough surface, A2, and smooth opposing surface, for $N = 1200$ *lb,* $F = 60$ *lb, and* $\mu = 0.5$.

predictions, but it is clear that the effect is intrinsically linked to surface roughness and machining variabilities.

16.2.1.5 Extending Analysis to Probabilistic Study

We would like to extend the analysis by performing probabilistic modeling. Given a set of experimentally measured height distributions for the flat lap joint, it is possible to generate realizations for the spatial distribution of surface heights on each interface

$$Z(x,y) = \mu(x,y) + U(x,y)\sigma(x,y) \tag{16.1}$$

where $\mu(x,y)$ is the mean height at spatial location (x,y),
$U(x,y)$ is to be determined,
and $\sigma(x,y)$ is the standard deviation at spatial location (x,y).

A more complete treatment of this topic will be given in the subsequent section on indirect modeling techniques.

16.2.2 Solving the Inverse Problem From Pressure Film

Another direct method of joint modeling is through the use of the pressure sensitive film. One of the compelling reasons to use pressure sensitive film to guide the modeling of an interface is that the film reports a resultant state of equilibrium of an assembled component. The pressure distribution recorded on the film is the direct result of surface roughness, imperfections, machining features, component misfit, and variations introduced through assembly. This is in fact a richer set of data than that provided by profilometry.

The application of the results, then, requires the solution of the inverse problem of what surface perturbations, away from perfect conformality, are required to arrive at the measured pressure distribution. This process is not a trivial matter, as there is no unique solution, and it is somewhat complicated by the fact that the pressure film is introducing a compliance that would not be present in the joint during actual assembly. For this reason, an indirect modeling technique using this data will be described in the next section.

16.3 Indirect Modeling of Surface Characteristics

The focus of this section will be the generation of joint models assuming that the only available data for characterization of the lap joint contact interface is given in the form of three dimensional pressure profiles of an assembled joint (or perhaps a collection of pressure profiles that represent a number of unique profiles generated from a number of unique combinations of different, but nominally identical, components.)

16.3.1 Modeling From Pressure Film Data

It is clear that representations of contact interfaces as perfectly flat and/or conformal entities is incorrect. An illustration of the departure from this idealization is shown in Figure 16.25. In this image, a pressure sensitive film was assembled into a joint interface. Contact is indicated by the red dye, where regions of higher color intensity correspond to locally higher pressures. In an ideal contact, the pressure would look paraboloidal, and centered about the bolt hole (although the distribution will be skewed somewhat due to the proximity of the upper boundary.) The pressure plot clearly shows this not to be the case. The two corners on the right side appear to have very high pressure (perhaps a tilt misalignment) and a periodic waviness exists on the entire surface.

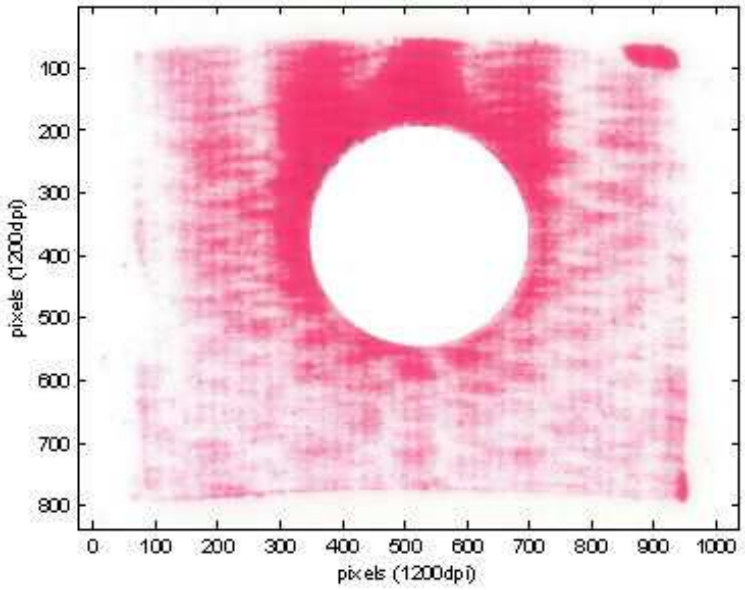

Figure 16.25. Interface Pressure Profile.

A pressure profile gathered by assembling a pressure- sensitive film into the joint interface. The joint was designed to be conformal in nature.

It is important to recognize that data in this form cannot be considered a boundary condition, but it is rather a representation of an equilibrium state. There is no direct way of applying the gathered data to generate an elasticity model for the purposes of performing numerical simulations.

An approach to generating a serviceable model for representing the interface is to solve the "inverse" problem. This approach is not a trivial matter, as it requires building a pair of rough mating surfaces so that the manner of the non-smoothness leads to the measured pressure distribution. A single or several such inverse solutions can be performed. However, if an ensemble of pressure distributions is generated as part of a larger uncertainty study, the time required for solving each inverse problem of each pressure realization becomes prohibitive.

The remainder of this section will lay out what should be considered a reasonable alternative approach to solving the indirect problem, which necessarily avoids the inverse solution and leverages the current solution capabilities of the quasistatic elasticity code, ADAGIO. The important feature of the proposed solution technique is that it retains all of the fundamental physics of elasticity theory in conjunction with a Coulomb friction interface model. There are no guarantees of kinematic equivalence between this method of model generation and a model that accounts explicitly for rough surface geometries. However, there is an explicit guarantee that both models will achieve macroslip at the same force level.

16.3.1.1 Numerical Processing of Data

Because there currently are no pressure profiles for the simple flat- lap joint, we will employ pressure data obtained from simulations of rough-on-rough contact generated from confocal, laser microscopy scans of the surfaces described previously.

The method relies on an *a priori* knowledge of the macroslip load, the simple relationship between normal pressure and tangential pressure at macroslip, the ease of calculating the interfacial pressure distribution for an ideal, conformal lap joint, and the ability within ADAGIO to prescribe friction coefficients spatially.

Simply stated, the method transfers the modifications of the ideal interfacial pressure to the friction coefficient. At a local contact node, during slip, the following relationship always holds

$$T^i = f_s S_N^i a^i \tag{16.2}$$

where T^i is the tangential force at a node,
S_N^i is the normal pressure at that node,
and a^i is the area associated with the node.

The ideal pressure, at a node on the contact interface, s_{ref}^i can be calculated easily in a numerical simulation. With this value and a particular assembly of the interfacial pressure, Equation (16.2) can be rewritten as

$$T^i = f_s \Omega^i s_{ref}^i a^i \tag{16.3}$$

where Ω^i is a pure number that scales the reference pressure at each spatial location.

$$S(x,y) = \Omega(x,y) s_{ref}(x,y) \tag{16.4}$$

The net effect of this operation is the apparent transfer of the perturbed, normal, pressure

distributions onto the friction coefficient

$$F_s(x,y) = \Omega(x,y)\, f_s \tag{16.5}$$

where F_s is now a spatially representation of the friction coefficient.

Applied in this manner, it is clear that the friction coefficient is scaled deterministically, informed by the perturbed pressure profile. If the reference pressure is calculated at the onset of macroslip, then the macroslip force will be reproduced identically by a model that employs the spatially varying, friction-coefficient formalism. The reason for this construction is simply to leverage the currently existing capabilities of the quasistatic code ADAGIO and avoid the intermediate step of constructing new, perturbed, solid-model geometries to capture the pressure distribution variability.

An example of normal interface pressure distributions are shown in Figures 16.17 and 16.18. Figure 16.26 shows the distribution $F_s(x,y)$ that results when the normal pressure profile of composite surface A1 (Figure 16.17) is compared to a perfect surface idealization (Figure 16.16)

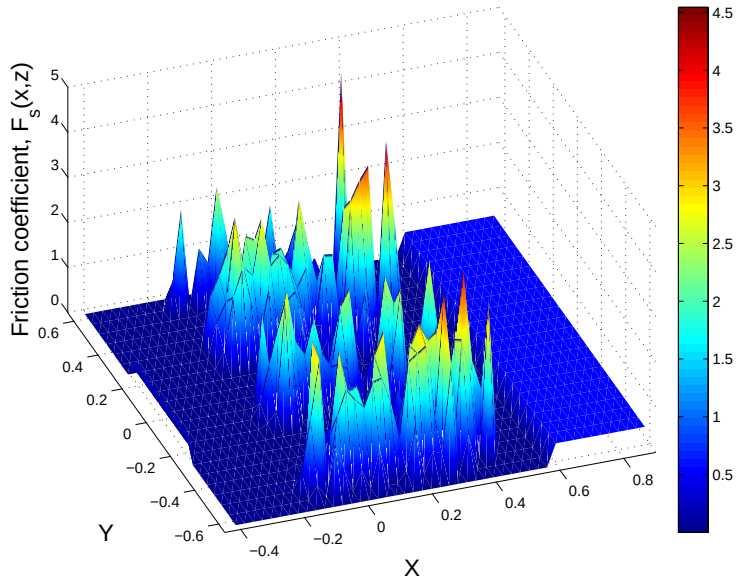

Figure 16.26. Spatial Friction Coefficient.

Spatial friction coefficient, $F_s(x,y)$ derived from composite surface A1 using constant friction coefficient, $f_s = 0.5$.

The spatial friction map that was constructed and shown in Figure 16.26 was employed in a numerical simulation. The results are shown in Figure 16.27. This figure shows a comparison

between the spatial, friction-coefficient formulation and the corresponding direct simulation of a composite rough surface. The predictions are quantitatively very similar. Although the local kinematics are expected to be very different, the friction scaling has produced results that match well with the direct modeling technique. It is expected that this will likely be the case in instances when local, nodal displacements are very small, the normal pressure distribution does change significantly during a loading cycle, and the joint is sufficiently far removed from a macroslip condition.

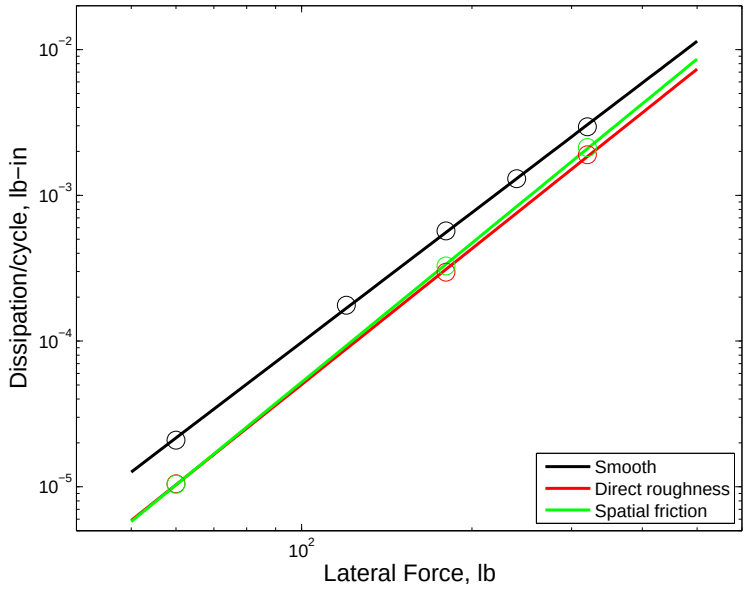

Figure 16.27. Spatial Friction Energy Dissipation Predictions.

Comparison of direct roughness modeling with the spatial friction representation.

16.3.1.2 Extending Analysis to Probabilistic Study

The measurements taken on the interfacial pressure distributions, with the pressure film, give direct evidence of joint misalignment, machining variability, and material surface characteristics. It is hoped that accounting for these features within an FE analysis could help to quantify the extent to which these mechanisms contribute to the systematic variability in predictions for energy dissipation in the flat lap joint.

Given a set of experimentally measured, interfacial, pressure distributions for the flat lap joint, it is possible to generate realizations for the spatial distribution of normal pressure on the interface

$$S_N(x,y) = \mu(x,y) + U(x,y)\sigma(x,y) \tag{16.6}$$

where $\mu(x,y)$ is the mean height at spatial location (x,y),
$U(x,y)$ is to be determined,
and $\sigma(x,y)$ is the standard deviation at spatial location (x,y).

It is important to recognize that each random realization must always satisfy equilibrium, therefore

$$N_{clamp}^{(k)} = \int S_N^{(k)}(x,y)\mathrm{d}A \qquad\qquad k = 1,2,\ldots \tag{16.7}$$

Now, if a numerical simulation is run in which the friction coefficient is applied globally to the contact interface, the simulation would provide a meaningful comparison to the experiment provided the friction coefficient was selected so that

$$T_{min} < f_s \int S_N(x,y)\mathrm{d}A < T_{max} \tag{16.8}$$

where T_{min} is the minimum macroslip force measured experimentally,
T_{max} is the maximum macroslip force measured experimentally,
and f_s is the static friction coefficient.

(No distinction will be made here between the static and dynamic friction coefficient.) It should also be noted that, in general, the interfacial pressure distribution is not a stationary function, but will evolve as a result of applied boundary conditions, e.g. the left hand side of Equation (16.7) may be constant, but the body deforms as a result of far-field loads. For our purposes it will assumed that this evolution is negligible and therefore S_N will be stationary. The method of determining the spatial friction function $F_s(x,y)$ proceeds as described in the previous section.

Part IV

Modeling of Jointed Structures

Chapter 17

Some Considerations of Dynamics of Jointed Structures

Daniel J. Segalman

17.1 Introduction

An irony of the simulation of jointed structures is that the more fidelity with which the joint models reproduces the actual behavior of joints, the more difficult the solution of the resulting system equations become. These difficulties are manifest as a requirement for extraordinarily small time steps.

Another irony is the compulsion to characterize every type of joint which can be modeled and incorporate it into a structure-level simulation. So, as the number of different kinds of joints that can be modeled grows, the less tractable the analyst driven part of structural simulation becomes.

Both of these issues are addressed in this chapter.

17.2 Discontinuities and Time steps

17.2.1 Nature of the Computational Difficulty

The time step issue is illuminated by consideration first of a linear problem. Consider the structure shown in Figure 17.1.

In this problem, $M_2 >> M1$ and $K_2 >> K_1$ so that the two modes will be approximately as follows. The lowest frequency mode is a near rigid body mode (M_1 and M_2 moving together) at a frequency of approximately $\omega_1 = \sqrt{\frac{K_1}{M_2}}$. The second mode is closely described as mass M_1 moving with respect to mass M_2 at a frequency of about $\omega_2 = \sqrt{\frac{K_2}{M_1}}$. In this particular problem, the parameters are chosen as $K_1 = 1$, $K_2 = 10$, $M_1 = 1$, $M_2 = 80$, $\zeta = 0.02$. (The masses are in kg and

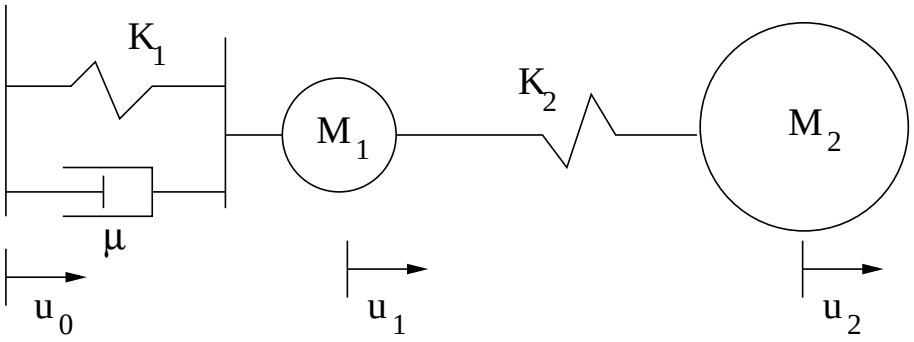

Figure 17.1. Linear, Two Mass, Dynamic Structure with Base Excitation.

the stiffnesses are in Newtons/m.) The base is driven at u_0 from rest harmonically at an angular frequency one quarter of the lower natural frequency: $\omega_0 = \omega_1/4$ with a displacement amplitude $A = 0.2$ so that $u_0(t) = A\sin(\omega_0 t)$.

The kinematics of the masses is calculate using the Newmark β method with parameters chosen for stability ($\beta = 1/4$ and $\gamma = 1/2$). The time step is selected as $\mathrm{d}t = \frac{1}{20}\frac{2\pi}{\omega_2}$ so that there are twenty time steps for each cycle of the highest frequency of the system. The resulting accelerations are presented in Figure 17.2. The accelerations of the base and each mass are presented over a full twenty cycles of base excitation and also over just the first. At the inception of base excitation, the high frequency mode associated with motion of mass M_1 has starts off with a high amplitude and damps down quickly. The second mode also starts out at a finite value, but damps more slowly.

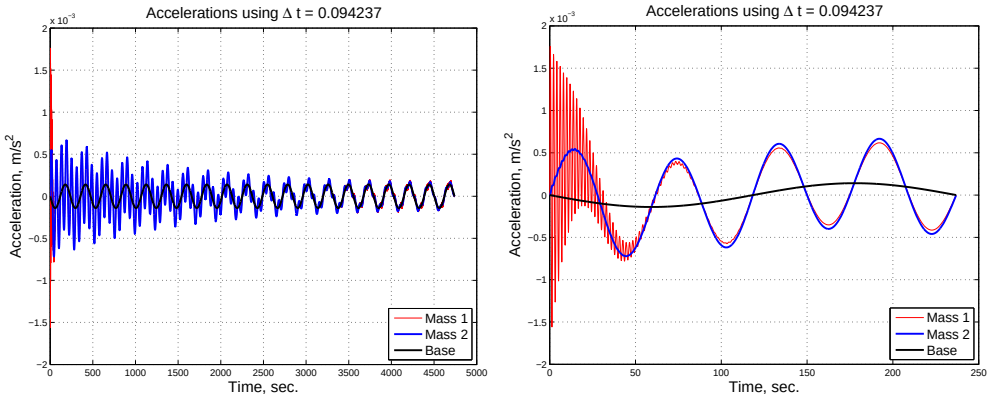

Figure 17.2. Accelerations of Two Mass System Calculated with Small Time Steps.

If there is no interest in the higher frequency response, fewer time steps can be used. Because the integration strategy is implicit, we can set the time step as large as we want. For instance,

consider d$t = 2\frac{2\pi}{\omega_2}$, twice the period of the higher frequency mode. The resulting predictions for acceleration are shown in Figure 17.3. Here, the high frequency mode is essentially suppressed, the motion of the larger mass is essentially unaffected, and the smaller mass is approximately that of the larger mass - consistent with the lower natural frequency.

In structural dynamics of very large systems, having longer but fewer time steps is greatly valued because of the compute time associated with each time step. As illustrated above, employing larger time steps is simple and direct. The situation that follows is more complicated and more difficult in problems that involve joints.

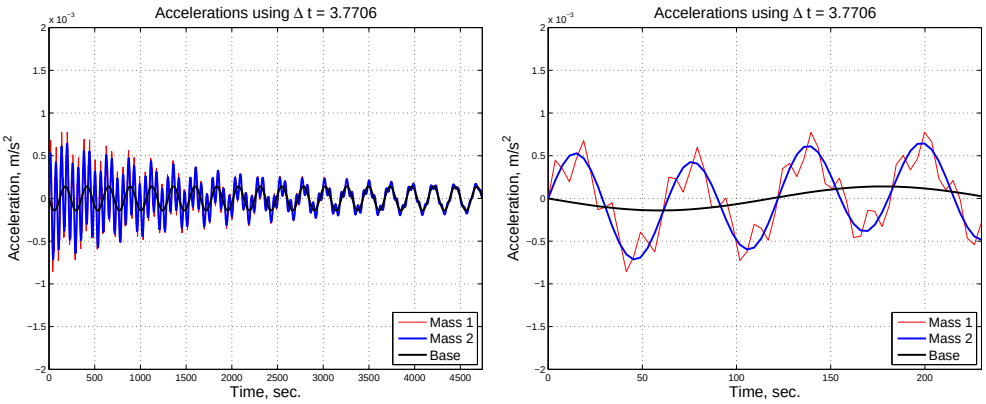

Figure 17.3. Accelerations of Two Mass System Calculated with Large Time Steps.

Next, consider a similar structure but with the second spring replaced by a Jenkins element of the same stiffness. So long as the base accelerations are very small, the response of these two structures is identical.

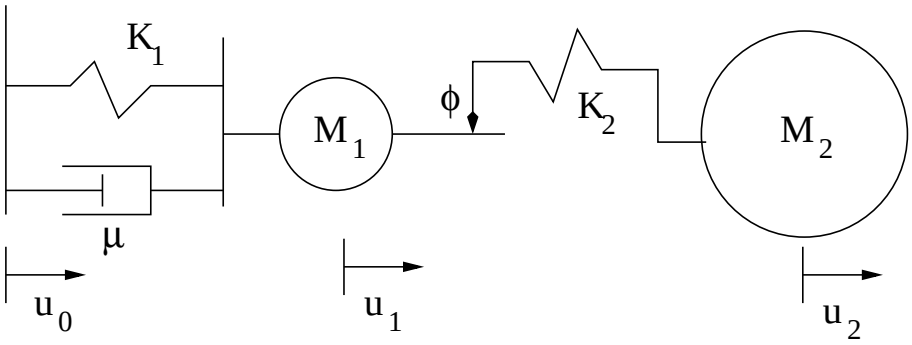

Figure 17.4. Jointed, Two Mass, Dynamic Structure under Base Excitation.

When the base excitations are large, slip is induced in the Jenkins element. Because the load is oscillatory, the slider can switch from stuck to slipping and slipping to stuck twice per period of the driving frequency. The features of the resulting dynamic system are shown in Figure 17.5.

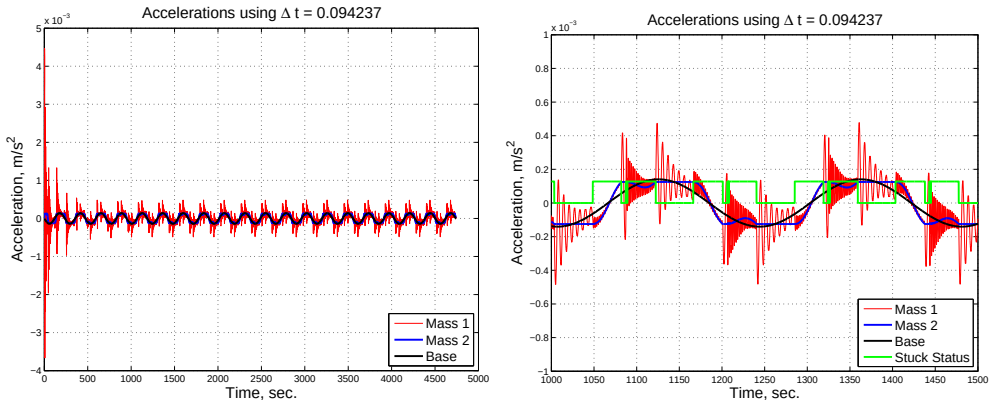

Figure 17.5. Accelerations of Two Mass, Jointed System Calculated with Small Time Steps.

The initiation of high amplitude base excitation ($A = 0.2$), the highest frequency mode is heavily excited but damps down quickly. Very soon a steady state pattern is achieved, in which the slider switches from stick to slipping four times in each load cycle and from slipping to stuck mode four times in each load cycle. The sudden change of stiffness excites all available frequencies of the system at that time. These modal excitations are most visible in the acceleration of the small mass, but the effects of changing system stiffness are also seen in the shape of the acceleration curve of the larger mass. These calculations were performed using a very small time step - $\frac{1}{20}$ of the period of the highest frequency.

The excitation of high frequency resonances from joint nonlinearities is demonstrated experimentally in mechanical systems in Section 17.2.2 of this chapter. Such excitation is also seen in civil structures [95].

If the intent is to perform *nonlinear* dynamics calculations on large structures using time steps that are a fraction of the period of the highest frequency, the analysis would be intractable. The accelerations calculated using a much longer time step - twice the period of the highest natural frequency - are shown in Figure 17.6.

The predicted response is very different from the orderly behavior of the small time step calculations. The acceleration of the smaller mass is almost chaotic, but the motion of the larger mass is distinctly different from that predicted in the earlier calculations.

What is going on here? Why is it that in this problem, implicit integration generates such nonsense when large time steps are employed? A sense of the answer is seen from the following SDOF example. Consider the structure shown in Figure 17.7. Base excitation is sufficient to cause

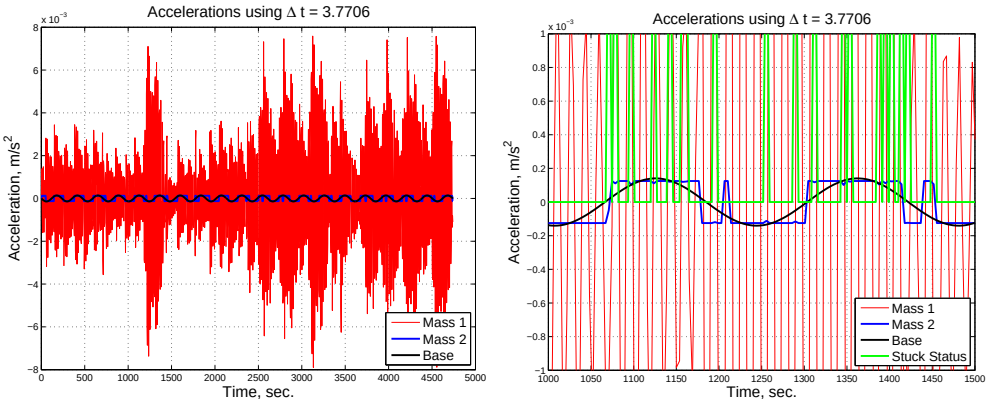

Figure 17.6. Accelerations of Two Mass, Jointed System Calculated with Long Time Steps.

the slider of the Jenkins element to go in and out of slip several times over each period of excitation.

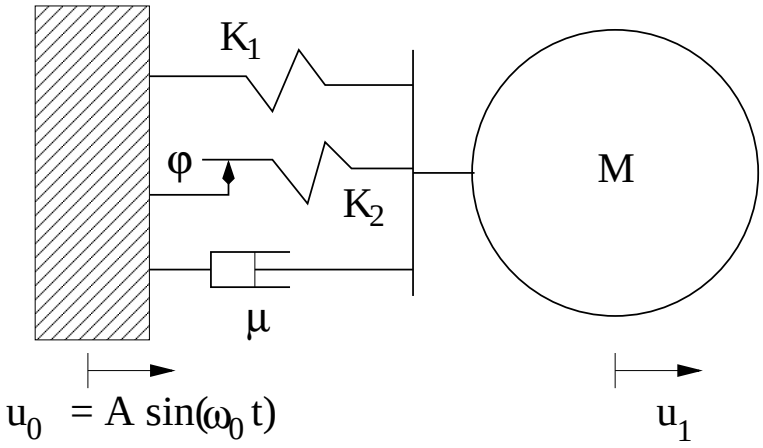

Figure 17.7. Jointed, SDOF System.

In this problem, the parameters are set as $M = 1$, $K_1 = 1$, $K_2 = 1$, $\phi = 1$, $\omega_0 = \omega_2/50$ and $\mu = 2\zeta\omega_2$, where $\omega_2 = \sqrt{\frac{K_1+K_2}{M}}$ and $\zeta = 0.01$. The displacement amplitude of the base is set at $A = 2.5$. All the above are in consistent units (such as SI). The base acceleration and the resulting acceleration of the sprung mass are shown in Figure 17.8. These calculations were performed using the Newmark β method with the conventional $\beta = 1/4$ and $\gamma = 1/2$ using time steps of $\mathrm{d}t = \frac{1}{50}\frac{2\pi}{\omega_2}$, which is a far smaller time step than truly required.

The observed response is the lower frequency acceleration of the base and the higher frequency accelerations of the sprung mass. More insight into the system response can be seen by examina-

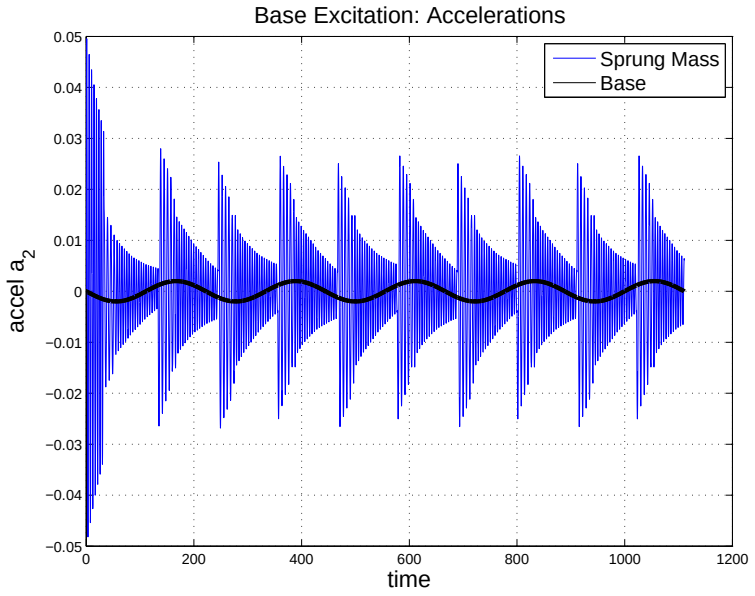

Figure 17.8. Acceleration of Base and Sprung Mass in SDOF System.

tion of Figure 17.9. This figure, showing the normalized acceleration of the sprung mass as well as the normalized instantaneous system stiffness shows that system resonances are excited every time the slider switches status from stuck to slipping. When the slider switches back to the stuck mode, the resonance drops in amplitude and increases in frequency, as would be expected.

When these same calculations are performed using time step $\mathrm{d}t = 5\frac{2\pi}{\omega_2}$, accelerations shown in Figure 17.10 result. Given past experience with the two degree-of-freedom model, the hashy nature of this result is not surprising. However, this simple problem can lend some insight into the source of the difficulty.

Figure 17.10 shows that in most instances, the computed acceleration at each time step is of opposite sign to that of the next. This suggests that there is important information about the state of the system that must be included in the dynamic calculations and that can be known only through short time path dependent integration. In linear structures there is no mechanical energy at frequencies above those at which there are inputs to the system. Implicit integration at time steps corresponding to frequencies above those at which there is energy may maintain a correct energy balance even when there are unexcited modes above that frequency.

In nonlinear systems such as discussed here, the joint transfers energy from low to high frequencies. An implicit integration using time steps that do not permit accurate modeling of those excited high frequency modes will not achieve a correct energy balance and anomalous behavior such as illustrated above results.

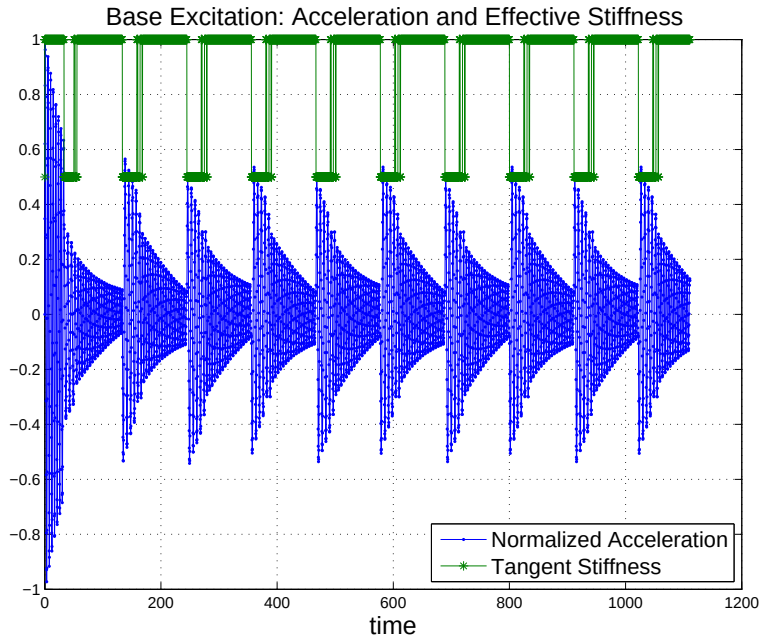

Figure 17.9. Normalized Acceleration of Sprung Mass and Effective System Stiffness.

There are very significant ramifications to the above argument. in particular the requirement to use very small time steps would make direct implementation of joint models into dynamics analysis of large structures intractable.

The next two subsections discuss how such difficulties might be obviated. Both techniques are based on the goal of creating models that are incapable of resonating beyond the frequencies of interest but that are still able to manifest the important structural properties, including energy dissipation and vibration isolation through macroslip.

17.2.2 Model Reduction Exploiting Component Mode Synthesis

One of the classical methods of structural model reduction is that of component mode synthesis (CMS). This method involves treating the structure as a combination of substructures, and capturing the dynamics of each substructure by a reduced-order model. The configuration space of each substructure is approximated by a combination of static modes (static deformation of the substructure in response to displacement of each of the interface degrees of freedom) and dynamic modes (eigen modes of the structure when all interfaces are fixed). This approach is a well developed technology discussed at length and reported often in the literature. A standard citation is [96].

The CMS method is especially popular in the aerospace world where manufacturers of dif-

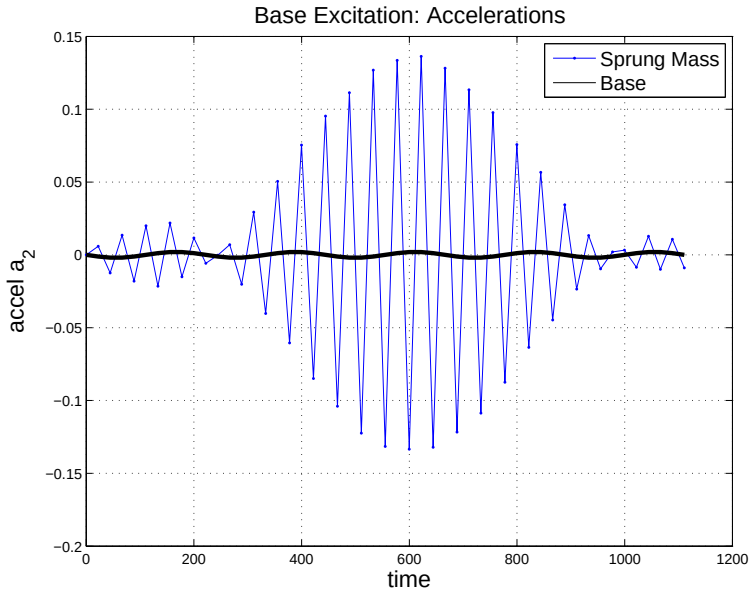

Figure 17.10. Acceleration of Base and Sprung Mass in SDOF System.

ferent components of a system can provide the prime contractor with CMS models of just their subsystems, allowing the prime to integrate these into a full system model.

In the context of jointed structures, CMS would have a slightly different flavor. Here the boundaries between substructures include the mechanical joints. The degrees of freedom available to each substructure are dramatically reduced, so those available to the full system are also reduced. The reduction in degrees of freedom has the effect of reducing the frequencies to which the system is capable of responding. Further, if the configuration space left available to the structure is consistent only with the lower frequency responses, the system cannot resonate at the higher frequencies.

This technique was tested in [97] and, as shown below, this CMS strategy for model reduction has had significant success in suppressing higher frequency resonance and making simulation at larger time steps tractable. On the other hand, it is not as successful as desired. In order to achieve sufficient static flexibility in low order modes, it is necessary to include many resonant modes of each subsystem in the structures structure's configuration space and some high frequency local modes are admitted.

17.2.3 Model Reduction Using the Method of Discontinuous Basis Functions

Another approach, explored in [97], [98], and [99], specifically restricts configurations consistent with high frequency response. This method of discontinuous basis functions employs two sets of structural response from a reference linear system to provide the basis functions that define the configuration space.

Consider a linear system similar to the jointed structure, but with the joints replaced by springs having stiffnesses approximately the tangent stiffness the joints. Bases for the configuration space for dynamic analysis of the nonlinear structure are obtained by:

- retaining the eigen modes of the linear system corresponding to the frequency range of interest.
- static analysis of the linear system where equal and opposite forces are applied at each degree of freedom of each joint - one analysis per degree of freedom. The resulting deformations are discontinuous at that joint. Because these “modes” are have no significant deformation except at the joint, they are also inconsistent with high frequency vibration modes.

These basis functions are used in a Galerkin analysis in the conventional manner [99], exploiting the matrix structure of the linear subsystems. The reference linear model can be either a full finite element model or a CMS reduced order model. The above described method of model reduction is call the Method of Discontinuous Basis Functions (MDBF).

17.2.4 Numerical Experiments with Model Reduction to Enlarge Time Step

Computational experiments reported in [97] included investigation of the dynamic response of the mock AOS shown in Figure 17.11. This structure consists of two monolithic pieces of metal connected by three nominally identical joints.

A series of short duration shock tests were applied to this experimental structure to elicit high amplitude response without causing damage to the structure [100]. The impulse, shown on the left side of Figure 17.12 was designed to excite strongly the first resonance of the structure. Resulting accelerations that were measured at the 270° leg are shown on the right hand side of Figure 17.12. The structural response exhibits the anticipated modal response augmented by the spiky behavior at amplitudes so high as to elicit strong joint nonlinearities.

This structure was then simulated using the structural dynamics code Salinas with whole-joint, Iwan models employed at the interfaces. Parameters for the Iwan models were determined from experimental data taken from single joint specimens. Accelerations calculated using the full FE model using CMS model reduction are shown in Figure 17.13. (The original CMS reduction of this structure was performed by Holzmann [101]).

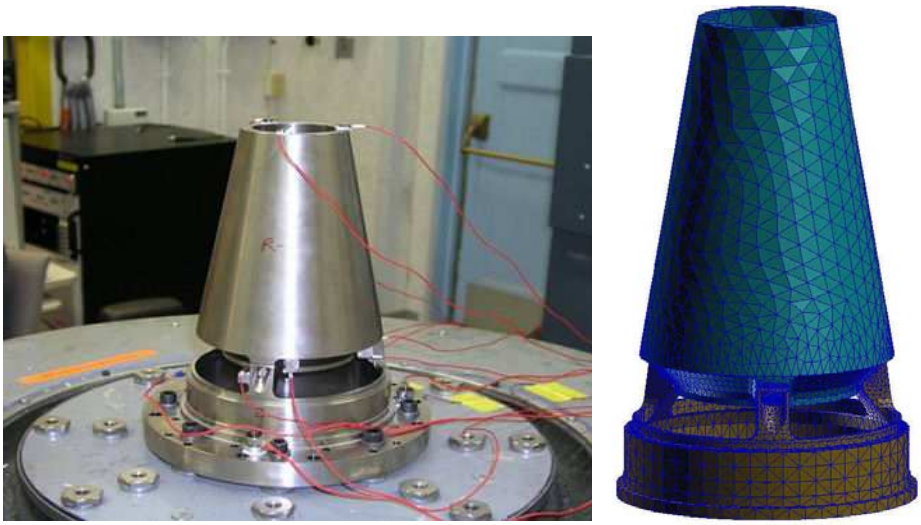

Figure 17.11. Mock AOS Hardware and Solid Model.

The full FE model using a time step of 10^{-6} second predicts the structural response, including the spiky behavior, though there does appear to be some "hash" at that highest amplitude. Simulations using CMS at a time step 10 times as long performs slightly better than that of the full FE model. The full mesh involves over 200,000 degrees of freedom while the CMS model employed 117 degrees of freedom. The CMS predictions are even better when the time is reduced to 10^{-6} seconds, as shown in Figure 17.14.

In a parallel calculation, MDBF was also employed. This method yields very good response, even when employing only 15 degrees of freedom. Figure 17.15 shows when extremely small time steps (10^{-6} seconds) are used the hash disappears almost entirely with both methods. Particularly encouraging is that the hash is gone even with a time step of 10^{-5} seconds when the MDBF is used. More studies using even longer time steps are called for.

17.3 Modeling Spatially Distributed Joint Damping

Another daunting issue in the modeling of jointed structures is the complication that myriad joints introduce to the problem of structural response. Only a small number of those joints can be studied and characterized, either experimentally or numerically. The effect of sometimes hundreds of other joints must be accounted for as well. An approximate method of accommodating joint multiplicity is presented in [102] and is abstracted in this section.

The opportunities to address this issue lie in the following observations:

1. Experimentally, at modest levels of excitation, jointed structures still seem to preserve the

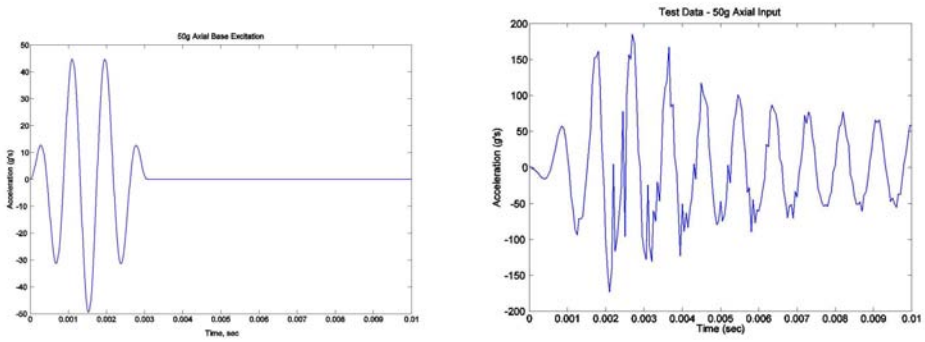

Figure 17.12. Imposed Base Acceleration and the Acceleration Response at the 270° Leg.

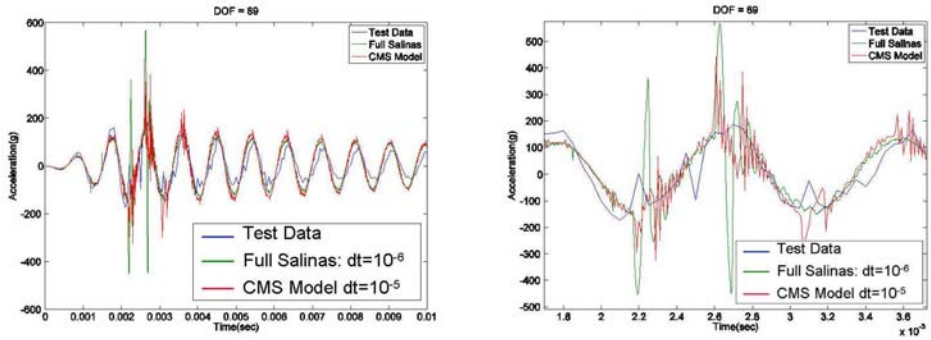

Figure 17.13. Accelerations Calculated from Full FE Model and from CMS.

eigen modes of a reference linear system. (Note that reference linear system is usually tuned to match the near linear behavior measured experimentally at low loads.)

2. at modest excitation levels, the nonlinearities present themselves through ‘joint-like’ energy dissipation (power-law dissipation with slopes greater that 2.2 and generally greater than 2.4) and through some amount of softening as seen through resonance shifts to lower frequency as load increases.

The observation about ‘joint-like’ dissipation was made in a particularly clear manner in experiments on a particular version of the AOS. Base excitation of the full complex structure yielded dissipation that had a power-law slope of 2.6. Further, the dissipation that was measured on that structure was about three times that which could be attributed just to the three discretely-modeled joints. Dissipation in the many other joints in that structure contributed the rest.

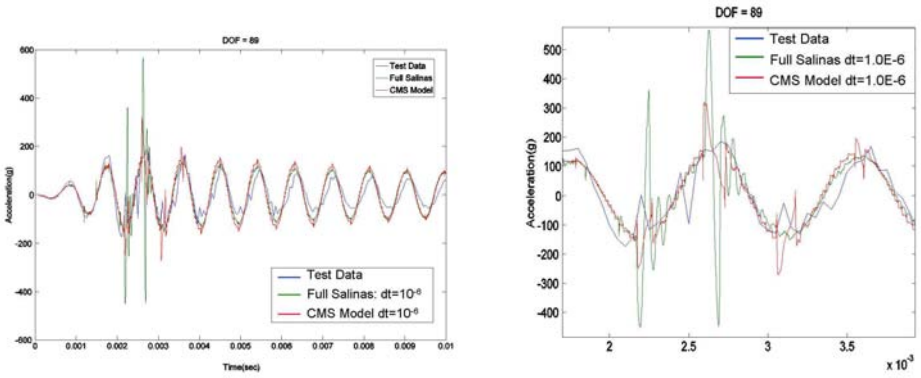

Figure 17.14. Accelerations Calculated from CMS using very Short Time Steps.

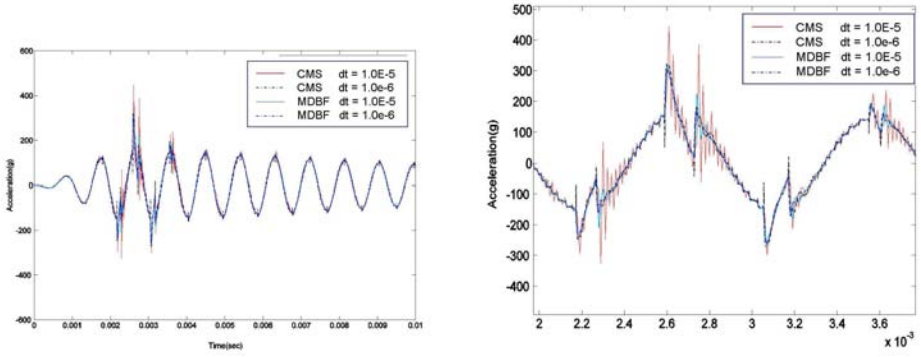

Figure 17.15. Accelerations Calculated using Both the CMS and MDBF Model Reduction Methods.

17.3.1 Development of Formalism

The above suggests employing the notion of a reference linear system. The nonlinear system may be represented by a system of equations

$$M\ddot{u}(t) + C\dot{u}(t) + K_{\infty}u(t) + \Delta\mathcal{N}\left(\{u(\tau), \tau \in (-\infty, t)\}\right) = F(t) \tag{17.1}$$

where M, C, and K_{∞} are all associated with a reference linear system.

The effects of $\Delta\mathcal{N}$ become pronounced as load amplitude increase and are manifest through the dissipation and softening behavior discussed above.

The damping matrix C of the linear system is generally chosen to be consistent with modal damping. Such is the case for proportional damping and Caughey damping, as well as for the

direct imposition of modal damping.

The eigen modes and frequencies of the reference linear system are denoted by $\{\phi_k, \omega_k\}$, and we turn our attention to the first n modes of the linear system. They are used to diagonalize partially the first n modes of Equation (17.1). Letting Y_n be the matrix whose columns are the first n eigenvectors of the linear system and postulating that the kinematics can be represented adequately by

$$u(t) = \Psi_n \lambda(t) \tag{17.2}$$

we may obtain through the usual contractions and changes of variables

$$\mathscr{M}\ddot{\lambda} + \mathscr{C}\dot{\lambda} + \mathscr{K}\lambda + \Psi_n^T \Delta\mathscr{N}\left(\Psi_n\{\lambda(\tau), \tau \in (-\infty, t)\}\right) = \mathscr{F}(t) \tag{17.3}$$

For convenience, assume that the eigenvectors are mass normalized so that $\mathscr{M}$ is the identity matrix. Because of the assumption that the damping matrix was consistent with modal damping, $\mathscr{C}$ is a diagonal matrix with terms $2\zeta_k\omega_k$ and the revised stiffness matrix $\mathscr{K}$ is also diagonal with terms ω_k^2. The right hand side is the projection of force onto the eigen modes $\mathscr{F} = \Psi_n^T F$.

The only coupling among the modal coordinates λ is through the nonlinear term. In the absence of data to the contrary and for the sake of facilitating a tractable process, we complement the assuptions on page 442 with following:

3. The process that diagonalizes the linear elements of the system also diagonalizes the nonlinear elements. Specifically $\Psi_n^T \Delta\mathscr{N}\left(\Psi_n\{\lambda(\tau), \tau \in (-\infty, t)\}\right)$ is diagonal.
4. The nonlinear response of each modal coordinate is independent of all the other modal coordinates.

The equations for modal coordinates are now decoupled:

$$\ddot{\lambda}_k + 2\zeta_k\omega_k\dot{\lambda} + \omega_k^2\lambda_k + Q_k\left(\{\lambda_k(\tau), \tau \in (-\infty, t)\}\right) = \mathscr{F}_k(t) \tag{17.4}$$

This result is significant not only because it decouples the kinematic modes, resulting in great computational economy, but also because it accommodates spatially distributed joint-like interface contributions to the structures nonlinear response.

17.3.2 Partial Nonlinear Modal Expansion

It is sometimes desirable to employ a partial modal expansion

$$u = \sum_1^N \lambda_i(t)\psi_i + z \tag{17.5}$$

where z is the part of u orthogonal to each of the first N eigen mode
and z is solved from the linear system of equations.

There is a method in linear structural dynamics for integrating systems described by combinations of modal and spatial degrees of freedom [103]. The key is to solve the modal equations in the standard manner; balancing generalized inertial, damping, and stiffness forces balance with the projection of the imposed loads on the eigen modes. Forces employed when solving for the spatial degrees of freedom are the imposed loads minus the project of those loads on the eigen modes.

An analogous approach is developed here for integration of our nonlinear system as described by the the first N "model" degrees of freedom employed in Equations (17.4) and by the spatial degrees of freedom z. To avoid performing continuous orthogonalization, it is preferred to achieve the solution for z in a manner involving u itself and conventional mass and stiffness matrices of a reference linear system. This is done by solving the the N decoupled nonlinear equations separately and then applying placing the resulting modal forces on the right hand side of the linear equations:

$$M\ddot{u} + C\dot{u} + Ku = F(t) - \sum_{k=1}^{N} y_k Q_k(t) \tag{17.6}$$

where $y_k = M\psi_k$.

Employing modal damping in the first N modes is not consistent with the modal damping values that would result from C. This is corrected via:

$$M\ddot{u} + C\dot{u} + Ku = F(t) - \sum_{k=1}^{N} y_k \left[Q_k(t) + \left(\zeta_k - \hat{\zeta}_k \right) 2\omega_k \dot{\lambda}_k \right] \tag{17.7}$$

where $2\hat{\zeta}_k \omega_k = \psi_k^T C \psi_k$.

The above expressions are derived using equations presented in the appendix of [104]. The separate treatment of modal damping for the first N modes and system damping for the remainder is along the lines of a method introduced by Alvin [103].

17.3.3 Model Form for Evolution of Modal Coefficients

The next step requires postulating a form for the nonlinear operators Q_k that are capable of manifesting joint-like energy dissipation and softening. The essential rate-independence of the joints argues that Q_k should be as well. Further, the model form must admit parameter sets so as to be tuned to reproduce quantitatively properties that are measured on real structures.

As shown previously, Iwan models can be formed to reproduce power-law dissipation as well as softening; they are a natural first candidate for this application. Therefore postulate

$$Q_k(t) = \int_0^\infty \rho_k(\phi) \left[\lambda_k - x_k(\phi) \right] \mathrm{d}\phi \tag{17.8}$$

where the state variable x_k evolves as

$$\dot{x}_k = \begin{cases} \dot{\lambda}_k & \text{if} \quad \|\lambda_k(t) - x_k(\phi)\| = \phi \quad \text{and} \quad \dot{\lambda}_k\left(\lambda_k(t) - x_k(\phi)\right) > 0 \\ 0 & \text{otherwise} \end{cases} \tag{17.9}$$

The energy dissipation per cycle of mode k is

$$\mathscr{D}_k(\Lambda_k) = 4\int_0^{\Lambda_k} \rho_k(\phi)\,[\Lambda_k - \phi]\,\mathrm{d}\phi \tag{17.10}$$

where Λ_k is the amplitude of the modal oscillation.

Differentiation of Equation (17.10) can be used to uncover the nature of the ρ_k:

$$\rho_k(\phi) = \frac{1}{4\Lambda}\frac{\mathrm{d}^2\mathscr{D}_k}{\mathrm{d}\Lambda^2}\bigg|_{\Lambda=\phi} \tag{17.11}$$

Examination of Equation (17.11) argues that a power-law energy dissipation must be associated with a ρ_k that is singular about $\phi = 0$. This suggests that something like the four parameter joint model discussed earlier in this handbook might be appropriate. Further progress in this approach will require more experimental data and reconciliation of models to that data.

Chapter 18

Example Dynamic Calculations of Jointed Structures

Michael J. Starr

The goal of all the work the previous chapters has been to gain the understandings and the tools to facilitate systematic, physics based modeling and design of jointed structures. The first example has to do with the buttress thread connection of System A threaded housing. The second is a model of the mock System A, AOS where the dynamics is dominated by the three discretely-modeled joints. Each of these is a demonstration of a desired type of *forward* prediction that has not been possible up to now.

18.1 Eigen-Analysis of Threaded Connection

The following is a demonstration of the use of the equivalent anisotropic threaded material formalism within a structural dynamics finite element analysis. Figure 18.1 shows the simplified geometry of a aeroshell-like structure. The blue and light blue elastic structural components are connected through a threaded interface shown in red. The threaded material is given anisotropic properties in a manner consistent with the formalism developed elsewhere in the handbook.

The deduced anisotropic elastic parameters can now be input into a threaded material definition within a SALINAS input deck. In general an anisotropic material will have 21 unique entries in the elasticity matrix. However, the material properties deduced for the buttress threads in this model employed a plane stress idealization. The Salinas input parameters are shown below.

```
// Top hat geometry modal analysis

SOLUTION
  title 'Tophat Aeroshell Equivalent Threads Model'
  eigen
    nmodes=6
```

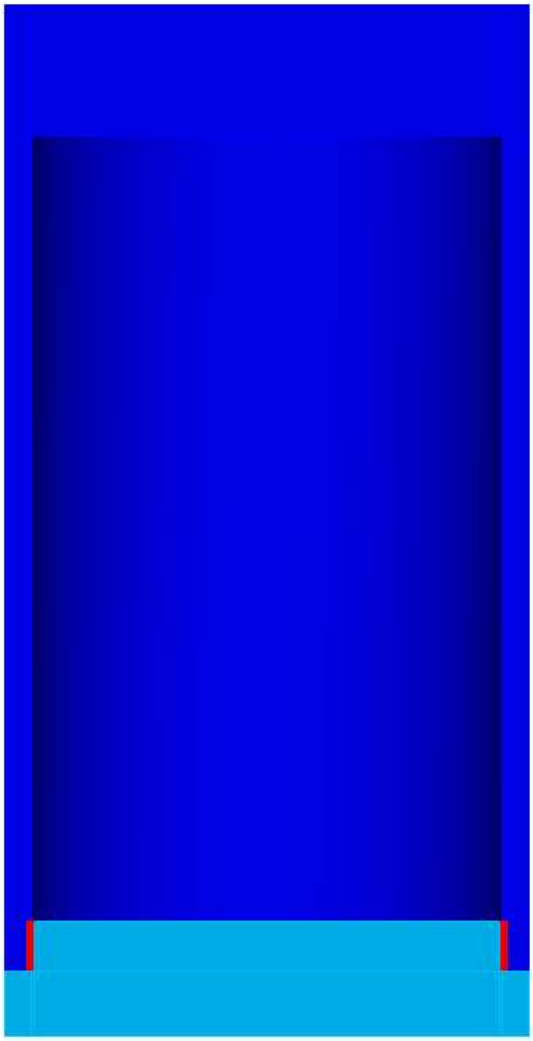

Figure 18.1. Solid Geometry Representation of an Aeroshell-like Structure.

```
END

COORDINATE 1
  cylindrical
     0 0 0
     0 0 1
     1 0 0
END

// Aeroshell Material (Aluminum)
BLOCK 1
  material 1
END

// Forward Mount (Aluminum)
BLOCK 10
  material 1
END

MATERIAL 1
  Isotropic
        E = 69.0e+09
       nu = 0.33
  density = 2.70e+03
END

// Equivalent Threads (Anisotropic Threaded Aluminum)

BLOCK 100 // Threaded Material Region
  material 2
END

MATERIAL 2 //Equivalent Threads (Anisotropic Threaded Aluminum)
  Anisotropic
  Cij
  25.06e+09  10.42e+09  50.35e+09  15.71e+09       0          0
             43.23e+09  50.35e+09  20.82e+09       0          0
                        10.07e+10       0          0          0
                                   44.97e+09       0          0
                                              51.88e+09       0
                                                         51.88e+09
  density = 2.649e+03
END

FILE
```

```
  geometry_file 'topHat_2X.g'
END

BOUNDARY
  nodeset 1
  fixed END

OUTPUTS
  elemqualchecks off
  disp
  stress
  strain
  energy
END

ECHO
  timing
  mass
END
```

Table (18.1) lists the first 6 natural frequencies of the structure shown in Figure 18.1. Two material representations are given: a monolithic aluminum constitutive representation and one in which the threaded zone is replaced by the aforementioned equivalent anisotropic elastic material.

Table 18.1. Top Hat Natural Frequencies, Hz

Mode	Monolithic Aluminum	Equivalent Anisotropic Aluminum
Bending - X	520	505
Bending - Y	520	505
Rotation	1612	1615
Buckling - X	1863	1852
Buckling - Y	1863	1852
Axial	1963	1918

Figures 18.2 and 18.3 show the strain that obtains in the equivalent threaded material (the aeroshell has been removed from the structure).

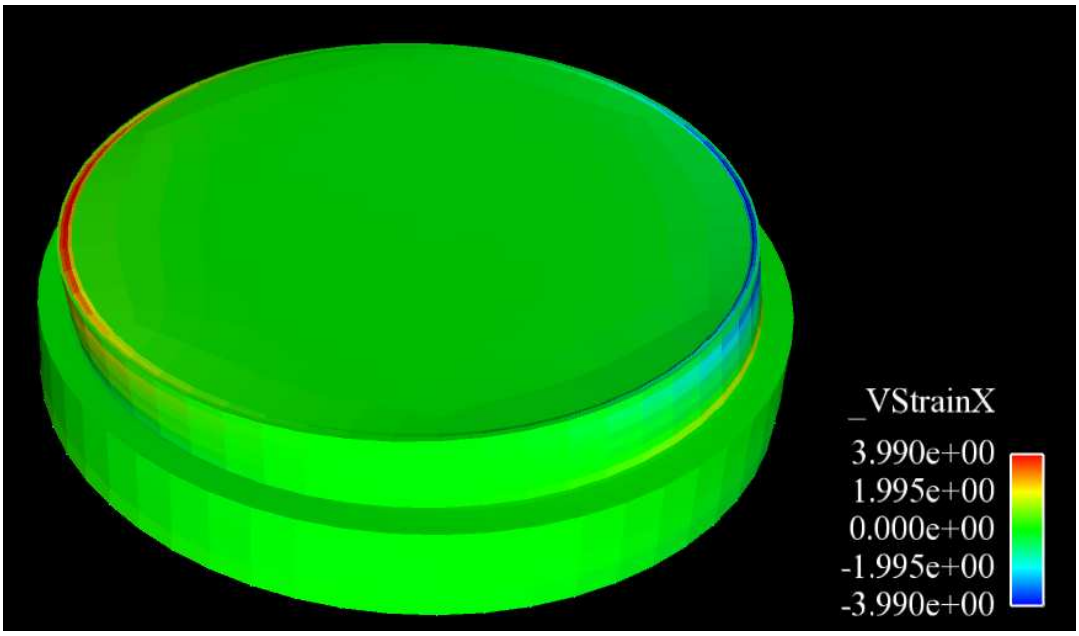

Figure 18.2. Strain in First Bending Mode.

The aeroshell has been removed to show the strain in the equivalent threaded material for the first bending mode.

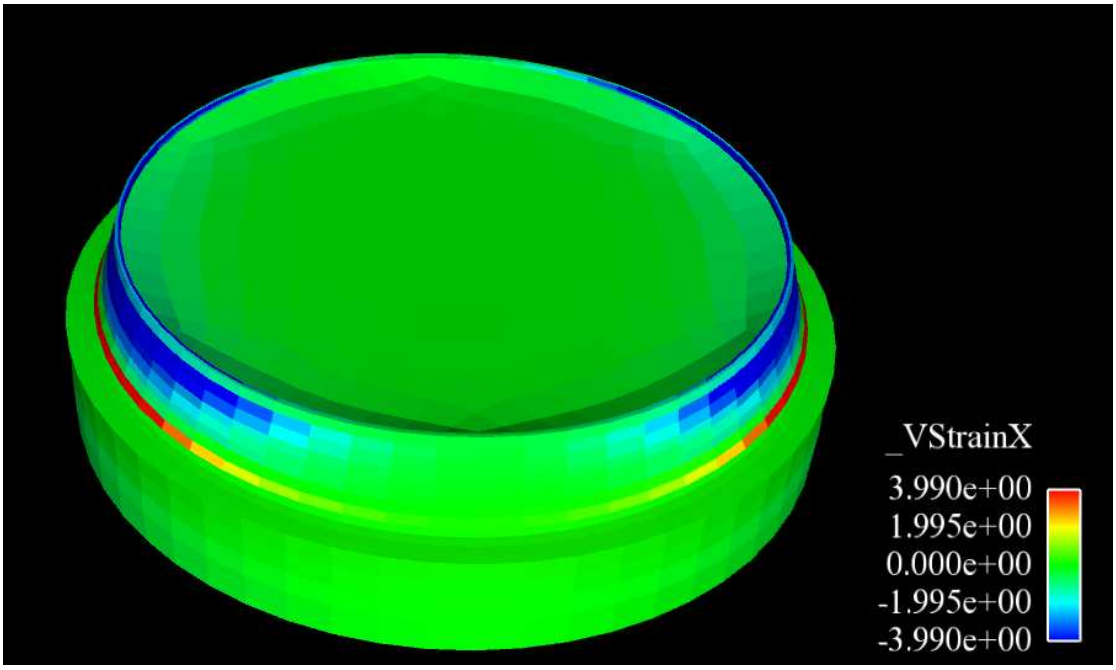

Figure 18.3. Strain in First Axial Mode.

The aeroshell has been removed to show the strain in the equivalent threaded material for the first axial mode.

18.2 Nonlinear Transient Analysis of Structure with Iwan Interfaces

The following is a demonstration of the use of the Iwan interface model formalism within a structural dynamics finite element analysis. Figure 18.4 shows the solid geometry for a full degree of freedom structural model. The structure consists of two elastic components that are connected through the three base attachment location legs. The Iwan interface constitutive parameters were deduced from experimental data.

Figure 18.4. Solid Geometry Representation of a Forward Mount/Mass Mock.

The Salinas input parameters required for a nonlinear transient analysis are given below. The structure is subjected to base excitation shown in Figure 18.5.

```
#include ./base_resor_1145.fun
SOLUTION
  NLtransient
    time_step=1.e-6
    nsteps 10000
    max_newton_iterations=200
```

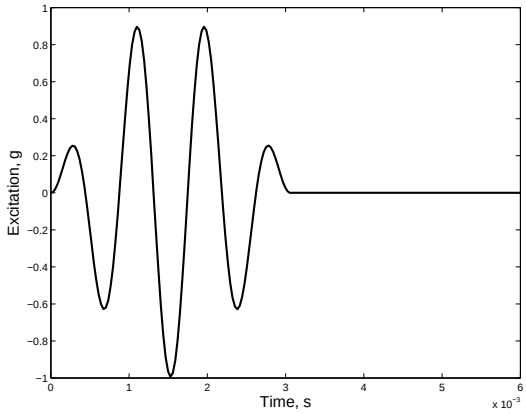

Figure 18.5. Base Excitation.

```
    num_newton_load_steps=50
    tolerance=1e-6
    nskip 1
    update_tangent 200
    rho=0.90
    solver=gdsw
    title 'mock aff and truncated base attachment location with shaped base input'
END

GDSW
        max_iter 2000
        orthog 200
        solver_tol 1e-6
        scale_option 1
        prt_summary 1
        overlap=1
END


FILE
   geometry_file '/3leg_massmock.par.4.%.1d'
   numraid 1
END

PARAMETERS
   wtmass = 0.00259
END
```

```
BOUNDARY
   nodeset 100
   y=0.
   z=0.
   rotx = 0.
   roty = 0.
   rotz = 0.
END


LOADS
   nodeset 100
   force = 1. 0. 0.
   scale = 50.e+06
   function 1
END

OUTPUTS END

HISTORY
   nodeset 1000
   nodeset 100
   nodeset 10
   acceleration
END

ECHO
 echo
END


#include ./Include/armature1.inp

#include ./Include/hex_block1.inp

#include ./Include/iwan1.inp

#include ./Include/ka_shaker1.inp

#include ./Include/matl_block1.inp

#include ./Include/rigid_mpc1.inp

#include ./Include/rigid_boltsurf1.inp
```

```
#include ./Include/mpc_softbeam2.inp

#include ./Include/seismic1.inp
```

The block definition for the armature is

```
#include ./Include/armature1.inp
BLOCK 200
  Beam2
  Area 1.
  I1  1.
  I2  1.
  J   1.
  orientation 1. 1. 0.
  material 200
END

MATERIAL 200
    isotropic
    E 10e12
    nu .3
    density = 1.e-6
END
```

The block definitions for the elastic structural elements are

```
#include ./Include/hex_block1.inp

BLOCK 1
  material 12
END

BLOCK 2
  material 11
END

MATERIAL  11
   Isotropic
    E=2.8572e+07
    NU=0.28
```

```
    density=0.317
END

MATERIAL  12
   Isotropic
    E=1.6e+07
    NU=0.3
    density=0.16
END
```

The block definitions for the Iwan interface models are given below. An identical Iwan parameter is prescribed at each of the three interfaces that connects the base and the sprung mass.

```
#include ./Include/iwan1.inp

BLOCK 50
  nonlinear = yes
  joint2g
    kx = iwan 1
    ky =  elastic 1.0e9
    kz =  elastic 1.0e9
    krx = elastic 1.0e9
    kry = elastic 1.0e9
    krz = elastic 1.0e9
END

BLOCK 60
  nonlinear = yes
  joint2g
    kx = iwan 2
    ky =  elastic 1.0e9
    kz =  elastic 1.0e9
    krx = elastic 1.0e9
    kry = elastic 1.0e9
    krz = elastic 1.0e9
END

BLOCK 70
  nonlinear = yes
  joint2g
    kx = iwan 3
    ky =  elastic 1.0e9
```

```
    kz =  elastic 1.0e9
    krx = elastic 1.0e9
    kry = elastic 1.0e9
    krz = elastic 1.0e9
END

property 1
 chi    =     -0.5565
 R      =   5.61e+06
 S      =   2.39e+06
 phi_max     =   2.29e-4
END

property 2
 chi    =     -0.5565
 R      =   5.61e+06
 S      =   2.39e+06
 phi_max     =   2.29e-4
END

property 3
 chi    =     -0.5565
 R      =   5.61e+06
 S      =   2.39e+06
 phi_max     =   2.29e-4
END
```

The spring stiffnesses that connect the structural model to the shaker are

```
#include ./Include/ka_shaker1.inp

BLOCK 101
  joint2g
    kx = elastic 6.e7
    ky = elastic 1.e9
    kz = elastic 1.e9
    krx = elastic 1e9
    kry = elastic 1e9
    krz = elastic 1e9
END
```

The nodes around the perimeter of the base and the sprung mass bolt holes are connected rigidly to facilitate the whole-joint nature of the Iwan model construction.

```
#include ./Include/rigid_mpc1.inp

RIGIDSET set51
     sideset 51
     nodeset 53
END

RIGIDSET set61
     sideset 61
     nodeset 63
END

RIGIDSET set71
     sideset 71
     nodeset 73
END

RIGIDSET set52
     sideset 52
     nodeset 54
END

RIGIDSET set62
     sideset 62
     nodeset 64
END

RIGIDSET set72
     sideset 72
     nodeset 74
END
```

The surfaces that comprise the aft end of the base attachment location bolt circle are rigidized to accommodate connection to the shaker.

```
#include ./Include/rigid_boltsurf1.inp
```

```
RIGIDSET set101
     sideset 101
END

RIGIDSET set102
     sideset 102
END

RIGIDSET set103
     sideset 103
END

RIGIDSET set104
     sideset 104
END

RIGIDSET set105
     sideset 105
END

RIGIDSET set106
     sideset 106
END

RIGIDSET set107
     sideset 107
END

RIGIDSET set108
     sideset 108
END
```

The following is the definition for the beam that connects the shaker to the structural model

```
#include ./Include/mpc_softbeam2.inp

Beam2
   Area 1e-4
   I1 0.001
   I2 0.001
   J  0.001
   orientation 1 1 1
```

```
   material 99

MATERIAL  99
   Isotropic
    E=2.8572e+3
    NU=0.28
    density=0.289e-9
END
```

The properties for the seismic mass are defined here

```
#include ./Include/seismic1.inp

BLOCK 200
  Beam2
  Area 1.
  I1  1.
  I2  1.
  J   1.
  orientation 1. 1. 0.
  material 500
END

MATERIAL 500
    isotropic
    E 10e12
    nu .3
    density = 1.e-6
END

BLOCK 300
  ConMass
    Mass=1e+06
    Ixx =1e+10
    Ixy =0
    Iyy =1e+10
    Ixz =0
    Iyz =0
    Izz =1e+10
    Offset= 0 0 0
END
```

A comparison of the structural response to the base excitation is shown in Figure 18.6. The upper plot shows the experimental response, while the lower plot is the forward prediction.

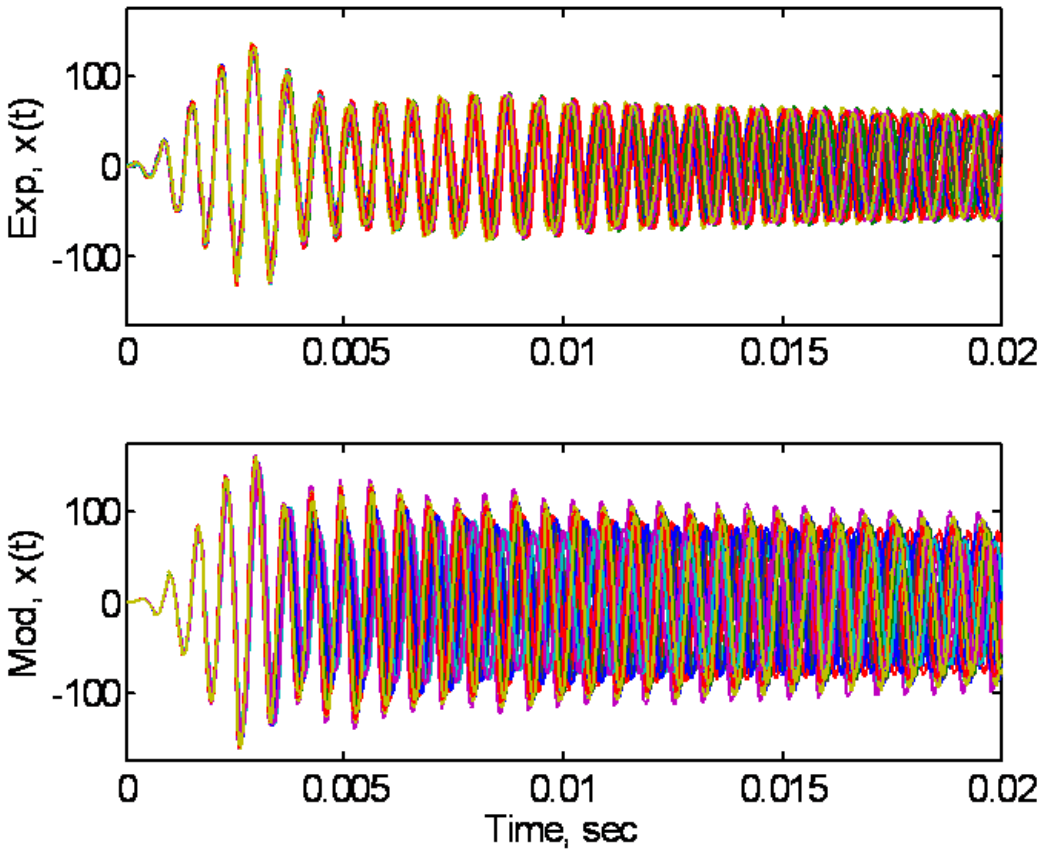

Figure 18.6. Response Comparison.

Part V

Future

Chapter 19

Future Work

Daniel J Segalman and Danny L. Gregory

19.1 Introduction

The careful reader of this handbook will certainly have identified many topics where he might expect to make significant improvements and contributions. It is the goal of this chapter to provide some order to opportunities and challenges for advancing this field.

Much of this issue has been framed in a SNL/NSF workshop in Arlington VA in October 2006 [105] and some of the notions discussed there are repeated here. Additionally, this chapter reflects experiences - some successful and some not - of researchers in SNL trying to achieve the necessary understanding to create useful engineering design and analysis tools for the dynamics of built-up structures.

One of the products of the 2006 workshop was the development of a notional road map for working from the atomistic scale up to that of actual structures. **One of the insights resulting from the process of developing this road map was that better resolution into physics at any level is not necessarily obtained by performing analysis at smaller length scales.** The critical issue is whether the physics that dominate at the smaller length scale are any better understood than those that dominate at the longer length scale. The directionality of that road map is determined largely by the necessity to refine understanding of physics (and some times chemistry) at each length scale before explorations at that length scale can be of quantitative value at a larger length scale.

One of the difficulties of traversing the multi-scale road map of Figure 19.1, is that the problems of relevance are much messier than people would ordinarily choose to address in either laboratory- or simulation-based investigations. For example, looking at the left hand side of the road map a researcher might perform atomistic calculations to examine the properties of individual asperities and employ atomic force microscopy (AFM) to verify those calculations. However, those AFM experiments would have to be preformed on surfaces having an oxide layer such as found in actual joints. Similarly, the atomistic simulations would have to employ postulated inhomogeneities to accommodate oxide layers that are known to occupy metal surfaces. Simulating larger length

scales requires introducing enough mechanics to approximate the processes where oxide layers are sheared off, raw metal bonds locally across the interface, and chemical kinematics and transport phenomena will govern the rates at which exposed metal forms new oxide layers. Fidelity to the actual physics requires layer-upon-layer of additional complexity.

Traversing the road map from left to right requires new experiments, theories, models, and verification strategies at every length scale. Additionally, while looking to smaller length scales to explain the larger, we discover that the small-scale mechanics we study is driven by forces or kinematics defined at a larger length scale. The problem is intrinsically multi-scale. Many of the tools often employed in multi-scale modeling (such as periodicity or homogenization) are not as useful in these interface problems as they have been when studying bulk material properties.

Because the issues at hand are interface problems, it is generally difficult to collect data on the mechanisms of interest directly. The experiments necessary to deduce processes at each length scale are often those that take place at a longer length scale. The procedure involves a progression of postulating processes at small length scales, making predictions to a larger length scale, and employing validation experiments at the longer length scale to assess the small length scale postulates. In this way, progress is obtained through a combination of bottom-up and a top-down procedures.

Since it may be decades before the road map is completely traversed from the one side to the other (small length scale to large), the engineering community cannot wait for a rigorous bottom-up process to provide engineering tools. Some work must be done focusing on longer length scales to generate methods, models, and parameters that can be employed in engineering structures in the nearer term. The work of this handbook focuses on those longer length scales. Further, because the expertise of the SNL joints research team members is primarily in the longer length scales, it is with respect to such work that most of the following recommendations are made. At the same time, we can only encourage people more expert than we are on the physics of smaller length scales to work out a research plan for the left hand side of Figure 19.1.

19.2 Experimental Work

An extensive discussion of future experimental work is in Section 10.2. Topics that receive special attention in that section are

a) Techniques to obtain greater spatial resolution of displacement and deformation of specimens. This could be coupled with finite element analysis to deduce the displacement fields on interfaces.

b) More generalized loadings. These are necessary to reflect that actual field loadings occur in different directions simultaneously and are generally not proportional. This data will be necessary to develop correspondingly sophisticated models.

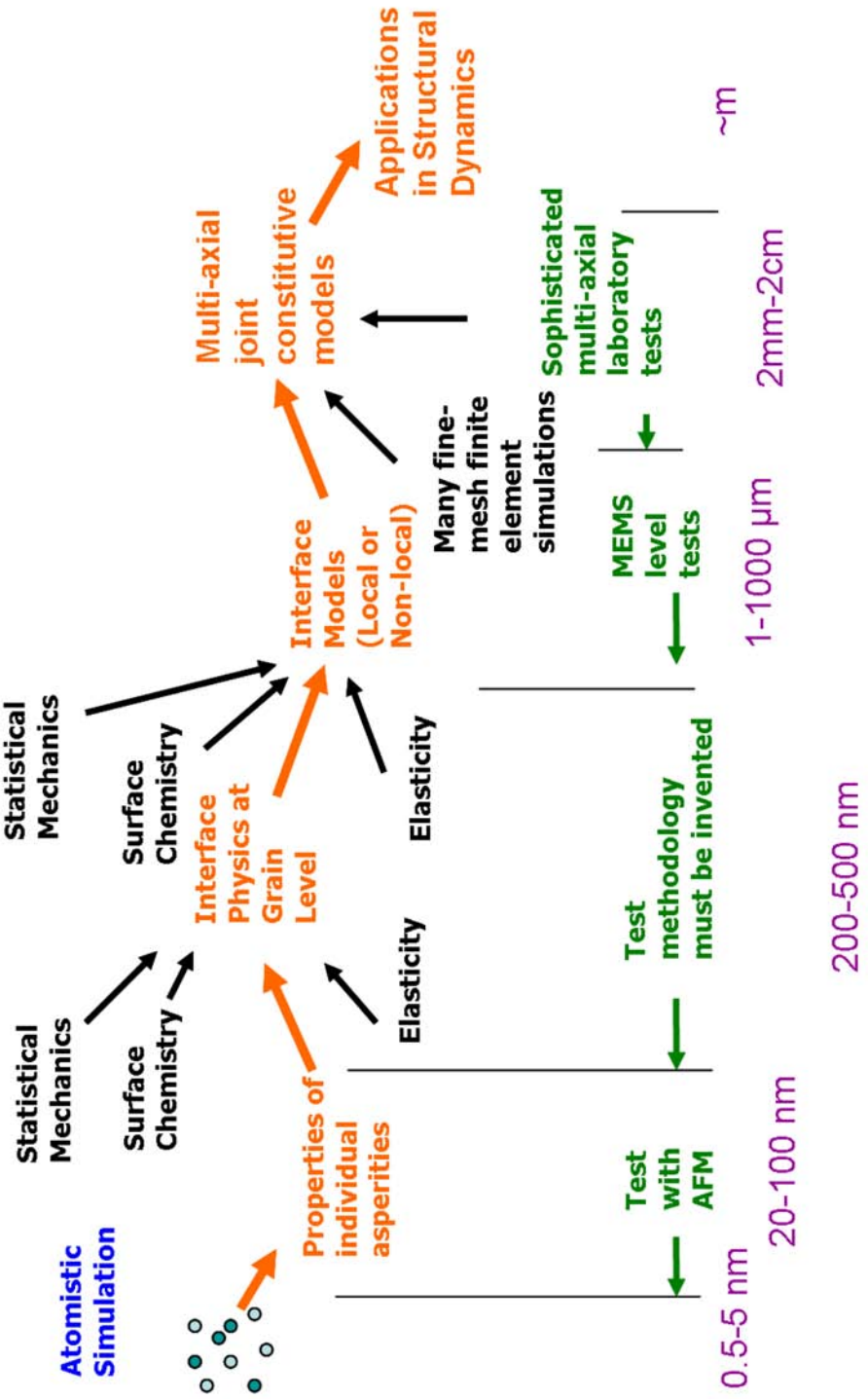

Figure 19.1. Joints road map developed at 2006 International Joints Workshop held in Arlington Va.

Procedings of the 2006 International Joints Workshop can be found in [105].

c) Advanced signal processing techniques. This is necessary to obtain better resolution on the nonlinear response of jointed structures.

d) Experiments on multi-jointed structures. This is required not only to account for coupling of nonlinearities, but also to provide guidance for the model reduction efforts discussed in this handbook.

Elements of this discussion are cited in corresponding examinations of computational or theoretical issues below.

19.3 Joint Models

Joint modeling includes the kinematic simplification necessary to map the continuum (three-dimensional) kinematics and forces of the substructures to the corresponding, lower-dimensional quantities of the joint models. Of course, joint modeling also includes the constitutive model employed for the joint itself. There are opportunities to make improvements to both the kinematic and constitutive elements.

19.3.1 Kinematic Models

The kinematic model employed explicitly and implicitly throughout this handbook is the rigidized "whole-joint" model. (See Chapter 11.) Referring to Figure 11.2, each side of the contact patch is held rigid and constrained to move consistently with a representative node.

As discussed in Chapter 11, the coupling of finite element (or continuum) model components of different dimensionality will always have artifacts. The rigid whole-joint kinematics result in fictitious, but harmless $1/\sqrt{r}$ singularities near the edges of the rigidized regions. These singularities do not have any significance on the predicted system dynamics. However, they do slow down the rate of mesh convergence and they sometimes distract stress analysts who are unfamiliar with these issues.

A more significant problem than the fictitious stress singularity induced by the rigidization of portions of each surface is suggested in Figure 19.2. In this figure, two plates are attached by closely placed bolts. The contact patches between the plates associated with the bolts overlap with those of neighboring bolts. Employing the rigidized whole-joint model, the whole region of overlapping contact patches is connected rigidly. This precludes the natural re-balancing of loads from one bolted region to another that is expected as external loads to the system are changed. Even when the contact patches do not overlap, there is insufficient lateral compliance available from the small elastic regions between the rigidized patches.

Evidence of overlap of contact patches is shown in the bolted ring geometry of the W88 (Figure 19.2). The contact patch overlap is manifest through the non-zero interfacial normal tractions

between the centers of the compressive contact.

An approach to mitigating this over-constrained situation is a weakening of the rigidization constraint. For instance, consider connecting the degrees of freedom associated with each joint node to those of the corresponding nodes of the contact patch by requiring that the joint degrees of freedom evolve as a weighted average of the degrees of freedom of the mesh nodes.

$$u^A_{j,n} = \sum_{k_n} u^A_{j,k_n} w_{k,n} / \sum_{k_n} w_{k,n} \tag{19.1}$$

where $u^A_{j,n}$ = the displacement of the j^{th} degree of freedom of the n^{th} joint on surface A
u^A_{j,k_n} = the displacement of the j^{th} degree of freedom of the k_n^{th} node of contact patch n
and $w_{k,n}$ = a weight assigned to the k^{th} node of contact patch n

Such a weighted relationship is suggested graphically in Figure 19.3. Whether this approach is feasible and what are optimal weightings are topics for further research.

A constraint on any feasible kinematic coupling is that it should be possible to employ a joint of zero compliance in a model for a specimen and recover the stiffness of the interface-free specimen.

19.3.2 Joint Constitutive Models

19.3.2.1 Coupled equations for all 6 DOFs

The proposed experimental program outlined in Section 10.2 emphasized development of experiments to probe the response of jointed structures to combined loads. So far, all experiments have been unidirectional and the constitutive models postulated from the resulting data have also been unidirectional. In general, it is expected that the three axial forces and the three rotational degrees of freedom of joints will not act independently. Development of appropriate constitutive modeling must follow the generation of experimental data, supported by the corresponding fine mesh finite element analysis.

19.3.3 Types of Joints

The content of this handbook focused on bolted and threaded joints, primarily because of the importance and ubiquity of such joints. There are other classes of joints that must be addressed as well, among them being such exotic connections as tape joints. In addressing such joints, the issues of distributed relative slip must be addressed more directly.

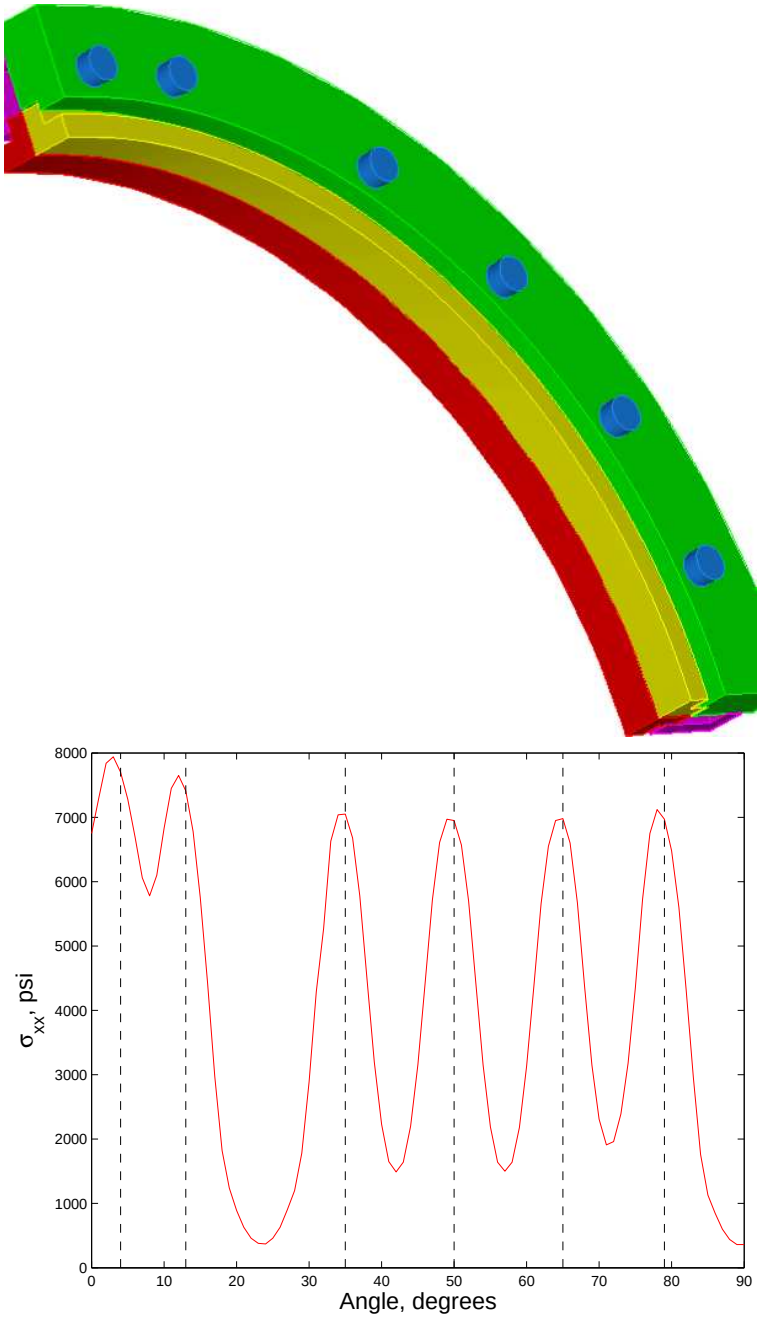

Figure 19.2. Overlapping Contact Patches.

The overlap of the contact patch due to adjacent bolts is indicated by the normal tractions on the interface not going to zero between the bolt centers.

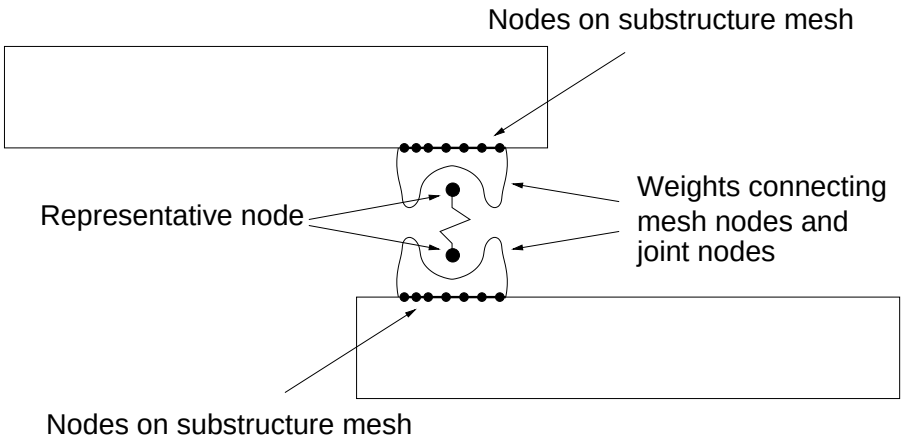

Figure 19.3. Representative Joint Node and Weights of Mesh Nodes.

The kinematics of each representative node is a distributed weight of mesh nodes on the corresponding side of the interface.

19.4 Finite Element Modeling of Joints

The literature of finite element modeling of joint mechanics has been surveyed in the relevant sections of this handbook. There are difficulties and limitations to finite element investigations of joint mechanics, and there are opportunities as well.

Among the limitations are:

- High resolution finite element modeling of interfaces is computationally demanding because of the intrinsically multi-scale nature of the problem. This computational difficulties preclude the direct integration of fine mesh finite element analysis into structural dynamics calculations.
- In general, there is no guarantee that the computational results from these problems of massive contact are close approximations of the corresponding mathematical problem.
- The interface (friction) constitutive models are very crude approximations to true interface mechanics

Despite these limitations, fine mesh finite element (FMFE) analysis has much to contribute to the *understanding* of joint mechanics. For example, as was shown in Chapter 16, though FMFE modeling cannot be expected to give quantitatively correct values for joints properties, it has been helpful in understanding the variability of mechanical properties among nominally identical specimens.

Following are areas of investigation where computational advances will likely extend the utility of FMFE analysis in joint mechanics or where more extensive implementation of FMFE analysis is likely to advance the science of joint mechanics.

a) Investigation of Dependencies: Not only can we look to FMFE analysis to assess the significance and qualitative effect of surface irregularities, but we can hope to investigate the effect of mixed loadings, such as in-phase combinations of tension and moment. Such combinations are actually the norm even in the most careful laboratory investigation of jointed specimens.

b) Which Interface Models to Use? Though the surface physics from which to deduce an appropriate set of interface constitutive models is a distinct area of research, testing of various candidate constitutive models with FMFE of joint can be helpful in assessing those constitutive models.

c) Multi-scale and Model Reduction: The computational difficulties of FMFE analysis derive from two causes: the problem being intrinsically multi-scale in nature and the contact problem involving the solution of contact problems at many locations. Two areas of computational advance may mitigate those problems. The first is the possibility of employing methods of domain decomposition (see [106]) to reduce the number of degrees of freedom of the problem and possibly to increase the admissible time step size. Domain decomposition is complemented by the development of parallel computing resource. Another potential advance is the reduction in dimension of the degrees of freedom associated with contact. This is the nature of the work by Guthrie and Kammer [107].

d) Does Contact Parallelize? Much time and energy has gone into parallelizing quasistatic finite element code with the expectation that it would facilitate solving very large problems in modest periods of time. That expectation has been met in many areas of analysis, but there is still an open question with respect to problems described in the handbook. So far, there is still no demonstration that general contact analysis parallelizes. An answer to this question would be of great value for the investment of future resources.

19.5 Structural Dynamics

Some of the elements of facilitating the use of joint models has been discussed above, there the focus was specifically on structural dynamics models themselves.

19.5.1 Model Reduction

Three model reduction methods were discussed in Chapter 17. Certainly other methods can and should be considered. As importantly, *a posteriori* methods of error estimation must be developed

for each of these tools to guide the analyst in building his models and in employing simulation results in decision making.

19.5.2 Library of Joint Properties

Currently, the only joint models that can be included with any confidence in structural dynamics calculations are those deduced from careful laboratory measurement. Alternatively, models whose parameters are deduced from FMFE modeling can be employed, though with less confidence.

The structural dynamicist needs much more. Ideally, he would have at his disposal a library of joint properties for each class of joint. Parameters and variability in parameters would be provided as functions of geometric, material, and load parameters.

With improvements to FMFE analysis on joints, better material and interface models, and better correlations with key experiments, the desire is to develop a database making the specification of joint properties easier for analysts. All of this involves not only raw computation and testing, but advances in all the underlying sciences.

19.6 Quantification of Model Uncertainty

Predictions of success or robustness of a design requires relying on numerous models; not just the computational model employed. Other aspects of modeling include the basic assumptions about which physics dominate and the nature of the applied loads and boundary conditions.

Quantifying model uncertainty involves assessing the cumulative uncertainty of all of the elements that play a role in prediction. In the following, the contribution to the uncertainty of structural dynamics response from modeling mechanical joints is addressed.

19.6.1 Model Form Error

A model form was postulated in Chapter 12 to capture the most important behaviors of lap joints. Qualitative limitations of the four parameter model introduced in that chapter were discussed. That model is quite successful in that parameters can be found reliably to reproduce to the experimental data.

Much still remains unclear about the fidelity by which this (or any other constitutive) model can predict the response to any input outside the calibration loads (type and magnitude). Addressing this question is one necessary part of the quantification of uncertainty of the predictions.

Another question is how well uniaxial constitutive models can capture the response of actual joints to combined loads. There is need to quantify the coupling of joint response to off axis loads.

Once more sophisticated constitutive models are developed to capture multi-axis coupling, there must be quantification of how well coupling is captured.

19.6.2 Mappings to Reality

As discussed before, computational investigations using FMFE analysis do not capture interface physics with fidelity and do not give quantitatively correct predictions of joint properties. Still, at this stage the FMFE predictions do seem to be *qualitatively* correct.

FMFE will be relied on to provide joint parameters in the most usual cases - when a wealth of experimental data is not available. That being the case, research must be done to assess the quantitative ranges of error in this approach.

Further, research should be directed to identifying systematic differences between predictions of FMFE calculations and laboratory data. If possible, scaling rules should be developed to compensate for systematic differences and to enhance the utility of FMFE analysis in predicting joint parameters.

19.6.3 Nominal Ranges of Joint Parameters

The notion of developing a database of joint constitutive models and parameters for those models as functions of geometry, material, surface condition, load, etc. was presented previously. The huge variability of mechanical properties intrinsic to mechanical joints requires that such a database include processes to compute variability of those parameters as well as the parameters themselves.

19.6.4 Quantification of Variability of Joints

The sparse experimental data available on the very few joint geometries studied showed huge variability. Stiffnesses varied by 30% and dissipation rate varied by factors of three. These data were collected on small numbers of specimens and testing on larger data sets might well have shown even more variability.

Clearly much more investigation - by laboratory experiment supplemented by FMFE analysis - must be done to obtain both nominal properties and statistical statements of variability of the joint types of interest.

Another class of issues that must be addressed is the development of a theoretical framework for predicting the statistical distribution of properties of structures containing many interfaces, each of which has its own distribution of statistical properties. Monte Carlo simulation would appear to be impractical. One would expect that this problem would have to be addressed through a combination of extensive laboratory investigation and theoretical development of statistical me-

chanics of nonlinear networks. Perhaps there is something similar to the law of large numbers whereby the random nature of all of the joints causes the variability net response to be described by a distribution function of modest width.

19.6.5 What Can and Should be Predicted?

Given the huge intrinsic variability and nonlinearity among joints and a corresponding variability and nonlinearity among jointed structures, the questions arise: what quantities can be predicted; which aspects of prediction are sensible to attempt to validate; which aspects of prediction are useful in design or qualification?

Because acceleration histories from slightly dissimilar systems can diverge very quickly, other features need to be considered. Following are some possible features that deserve consideration:

- peak stresses in critical parts over distinct time intervals
- frequency content evaluated over distinct time intervals
- comparison of wavelet content
- traditional Shock Response Spectrum (SRS)

19.7 Conclusion

The future work discussed above is far from inclusive of the full range of research to the science that underlies the dynamics properties of built up structures. It very much reflects the perceived critical path for programmatic need at Sandia National Laboratories. Among the opportunities of the research community is enlargement of this list to connect the engineering approaches discussed here to a rigorous scientific foundation.

References

[1] R. P. Rechard, J. T. Black, Jr, and S. D. Meyer, "Tape joint design guidelines," Sandia Report SAND83-1506, Sandia National Laboratories, Albuquerque NM 87185, September 1983.

[2] R. P. Rechard, "Tape joint stiffness," Sandia Report SAND86-0022, Sandia National Laboratories, Albuquerque, New Mexico 87185, April 1986.

[3] D. J. Mead, "Structural damping and damped vibration," *Applied Mechanics Reviews*, Vol. 55, pp. R45 – R54, November 2002.

[4] E. J. Berger, "Friction modeling for dynamic system simulation," *Applied Mechanics Reviews*, Vol. 55, pp. 535 – 577, November 2002.

[5] L. Gaul and R. Nitsche, "The role of friction in mechanical joints," *Applied Mechanics Reviews*, Vol. 52, pp. 93–106, March 2001.

[6] A. A. Ferri, "Friction damping and isolation systems," *Journal of Mechanical Design*, Vol. 117, pp. 196 – 206, June 1995.

[7] L. Gaul and J. Lenz, "Nonlinear dynamics of structures assembled by bolted joints," *Acta Mechanica*, Vol. 125, No. 1-4, pp. 169 – 181, 1997.

[8] D. L. Gregory, D. O. Smallwood, and R. G. Coleman, "Experimental studies to investigate damping in frictional shear joints," in *Proceedings of the 70th Shock and Vibration Symposium, held Nov 1999 in Albuquerque, NM,*, Shock and Vibration Information Analysis Center, Arvonia, VA 23004, 1999. SAND99-2255A.

[9] L. E. Goodman, "Contributions of continuum mechanics to the analysis of the sliding of unlubricated solids," *AMD (Symposium Series of the ASME Applied Mechanics Division)*, Vol. 39, pp. 1 – 12, 1980.

[10] C. Cattaneo, "Sul contatto di due corpi elastici: Distribuzione locale degli sforzi (on the contact of two elastic bodies: Distribution of local stresses)," *Rendiconti Academia nazionale dei Lincei*, Vol. 27, pp. 342–348, 434–436, 474–478., 1938.

[11] R. Mindlin, "Compliance of elastic bodies in contact," *ASME Journal of Applied Mechanics*, Vol. 16, pp. 259–268, 1949.

[12] E. E. Ungar, "Energy dissipation at structural joints: Mechanisms and magnitudes," Tech. Rep. FDL-TDR-64-98, US Air Force Flight Dynamics Laboratory, 1964.

[13] E. E. Ungar, "The status of engineering knowledge concerning the damping of built-up structures," *Journal of Sound and Vibration*, Vol. 26, No. 1, pp. 141 – 154, 1973.

[14] M. W. Heinstein and D. J. Segalman, "Bending effects in the frictional energy dissipation in lap joints," Tech. Rep. SAND2002-0083, Sandia National Laboratories, PO Box 5800, Albuquerque, NM 87185, January 2002.

[15] L. Jezequel, "Modal synthesis of large structures with nonlinear joints from vibration tests," in *Proceedings of the 2nd International Conference on Recent Advances in Structural Dynamics*, (Southampton, UK), pp. 281–295, 1984.

[16] A. Nobari, D. Robb, and D. Ewins, "A new approach to modal-based structural dynamic model updating and joint identification," *Mechanical Systems and Signal Processing*, Vol. 9, No. 1, pp. 85–100, 1995.

[17] Y. Ren and C. F. Beards, "Identification of joint properties of a structure using FRF data," *Journal Of Sound And Vibration*, Vol. 186, pp. 567–587, 1995.

[18] J. E. Mottershead, M. I. Friswell, G. H. T. Ng, and J. A. Brandon, "Geometric parameters for finite element model updating of joints and constraints," *Mechanical Systems and Signal Processing*, Vol. 10, pp. 171–182, 1996.

[19] D. M. Shamine, S. W. Hong, and Y. C. Shin, "An in situ modal-based method for structural dynamic joint parameter identification," *Proceedings of the Institution of Mechanical Engineers Part C-Journal of Mechanical Engineering Science*, Vol. 214, pp. 641–653, 2000.

[20] S. Sastry, *Nonlinear Systems: Analysis, Stability, and Control*. Berlin: Springer-Verlag, 1999.

[21] M. Bowden and J. Dugundjit, "Effects of joint damping and joint nonlinearity on the dynamics of space structures," in *Proceedings of the Structures Dynamics and Materials Conference, April 1988, Williamsbury, Virginia*, no. 2480 in 88, AIAA, 1988.

[22] M. Bowden and J. Dugundjit, "Joint damping and nonlinearity in dynamics of space structures," *AIAA Journal*, Vol. 28, pp. 740–749, April 1990.

[23] O. Tanrikulu, B. Kuran, H. N. Ozguven, and M. Imregun, "Forced harmonic response analysis of nonlinear structures using describing functions," *AIAA Journal*, Vol. 31, pp. 1313–1320, August 1993.

[24] A. H. Nayfeh and D. T. Mook, *Nonlinear Oscillations*. Pure & Applied Mathematics Series, New York: John Wiley & Sons, 1979.

[25] M. B. Özer and H. N. Özgüven, "A new method for localization and identification of nonlinearities in structures," in *Proceedings of ESDA 2002: 6th Biennial Conference on Engineering Systems Design and Analysis, ASME, Istanbul, Turkey, July 8-11, 2002*, ASME, 2002.

[26] M. B. Özer, H. N. Özgüven, and T. J. Royston, "Identification of structural non-linearities using describing functions and Sherman-Morrison method," in *Proceedings of the 23rd International Modal Analysis Conference, Orlando, Florida, January 30 - February 3, 2005.*, pp. 199–212, Society for Experimental Mechanics, 2005.

[27] H. R. E. Siller, *Non-Linear Modal Analysis Methods for Engineering Structures*. PhD thesis, Imperial College London, August 2004.

[28] D. J. Ewins, "The importance of joints on the dynamics of gas turbine structures," in *Report on the SNL/NSF International Workshop on Joint Mechanics Arlington Virginia, 16-18 October 2006* (D. J. Segalman, L. A. Bergman, and D. J. Ewins, eds.), no. SAND2007-7761, (Albuquerque, New Mexico 87185), Sandia National Laboratories, January 2008.

[29] J. Bauschinger, "Über die Veränderung der Elastizitätsgrenze und der Festigkeit des Eisens und Stahls durch Strecken und Quetschen, durch Erwärmen und Abkühlen und durch oft mal wiederholte Beanspruchung. (on the change in elastic limit and strength of iron and steel in tension and compression through heating and cooling and cyclic stress)," Tech. Rep. vol. 13, n. 1., Mechanisch-technischen Laboratorium der Königlichen Technischen Hochschule, Munich, 1886.

[30] L. Prandtl, "Ein gedankenmodell zur kinetischen theorie der festen körper," *Z. Angew. Math. Mech. (ZAMM)*, Vol. 8, pp. 85–106, 1928.

[31] A. Y. Ishlinskii, "Some applications of statistical methods to describing deformations of bodies," *Izvestiya Akademii Nauk SSSR*, Vol. 9, pp. 580–590, 1944.

[32] W. D. Iwan, "On a class of models for yielding behavior of continuous and composite systems," *ASME Journal of Applied Mechanics*, Vol. 34, No. 3, pp. 612–617, 1967.

[33] W. D. Iwan, "Distributed-element model for hysteresis and its steady-state dynamic response," *ASME Journal of Applied Mechanics*, Vol. 33, pp. 893–900, Dec. 1966.

[34] G. M. Reese, M. K. Bhardwaj, D. J. Segalman, K. F. Alvin, and B. J. Driessen, "Salinas user's notes," Tech. Rep. SAND99-2801, Sandia National Laboratories, PO Box 5800, Albuquerque, NM, November 1999.

[35] S. Doebling, F. Hemez, and W. Rhee, "Statistical model updating and validation applied to nonlinear transient structural dynamics," in *Proceedings of the 4th AIAA Non-Deterministic Approaches Forum, April 22-25, 2002 Denver, Colorado*, no. AIAA-2002-1644, AIAA, 2002.

[36] G. Maidanik, "Energy dissipation associated with gas-pumping in structural joints," *The Journal of the Acoustical Society of America*, Vol. 43, No. 5, pp. 1064–1072, 1966.

[37] A. F. Metherell and S. V. Diller, "Instantaneous energy dissipation rate in a lap joint - uniform clamping pressure," *Journal of Applied Mechanics*, pp. 123–128, 1968.

[38] P. F. Rogers and G. Boothroyd, "Damping at metallic interfaces subjected to oscillating tangential loads," *Journal of Engineering for Industry*, pp. 1087–1093, 1975.

[39] E. F. Crawley and A. C. Aubert, "Identification of nonlinear structural elements by force-state mapping," *AIAA JOURNAL*, Vol. 24, pp. 155–162, 1986.

[40] L. Gaul, "Analytical and experimental study of the dynamics of structures with joints and attached substructures," *Proceedings of the ASME Biennial Conference on Vibratin and Noise, Cincinnati, Ohio, USA*, Sept 1985. Sept 10-13, 1985.

[41] K. K. Padmanabhan and A. S. R. Murty, "Damping in structural joints subjected to tangential loads," *Journal of Mechanical Engineering Science*, Vol. 205, pp. 121–129, 1991.

[42] Y. Ren and C. F. Beards, "An experimental study on the dynamic response of a beam structure containing a pseudo joint," *Journal of Mechanical Engineering Science*, Vol. 128, pp. 321–328, 1994.

[43] Y. Ren and C. F. Beards, "Identification of 'effective' linear joints using coupling and joint identification techniques," *Journal of Vibration and Acoustics*, Vol. 120, No. April, 1998.

[44] C. W. Moloney, D. M. Peairs, and E. R. Roldan, "Characterization of damping in bolted lap joints," *Proceedings of SPIE, the International Society for Optical Engineering*, Vol. 4359, pp. 962–969, 2001.

[45] B. F. Feeny and J. W. Liang, "A decrement method for the simultaneous estimation of coulomb and viscous friction," *Journal of Sound and Vibration*, Vol. 195, pp. 149–154, 1996.

[46] D. L. Gregory, D. O. Smallwood, M. Nusser, and R. G. Coleman, "Experimental device to study the damping in bolted joints," in *Proceedings of the 1999 ASME Design Engineering Technical Conferences, September 12-15, Las Vegas, Nevada*, (Arvonia, VA 23004), Shock and Vibration Information Analysis Center, 1999.

[47] D. O. Smallwood, D. L. Gregory, and R. G. Coleman, "Damping investigations of a simplified frictional shear joint," in *71st Shock and Vibration Symposium*, (Arlington, VA), SAVIAC, 2000.

[48] D. W. Lobitz, D. L. Gregory, and D. O. Smallwood, "Comparison of finite element predictions to measurements from the sandia microslip experiment," in *Proceedings of IMAC XIX Conference on Structural Dynamics, Kissimmee, FL (US), 02/05/2001–02/08/2001*, 2001.

[49] D. L. Gregory, B. R. Resor, R. G. Coleman, and D. O. Smallwood, "Experimental investigations of an inclined lap-type bolted joint," Tech. Rep. SAND2003-1193, Sandia National Laboratories, PO Box 5800, Albuquerque, NM, April 2003.

[50] B. R. Resor and D. L. Gregory, "Bolted joint experiments for structural dynamic model calibration and validation," in *The 24th IMAC Conference and Exposition on Structural Dynamics, held in St Louis, MO, February 2006*, (St. Louis, MO), Society of Experimental Mechanics, 2006.

[51] B. R. Resor and M. J. Starr, "Influence of misfit mechanisms on jointed sturcture response," in *The 26th International Modal Analysis Conference, held Orlando FL*, Socienty of Experimental Mechanics, Feb. 2008.

[52] W. T. Thomson, *Vibration Theory and Applications*. Englewood Cliff, N.J.: Prentice-Hall, Inc., 1965.

[53] J. Gregory, T. Paez, R. Coleman, and D. Gregory, "Identification of a micro-slip friction damping function using directed genetic programming," in *Proceedings of the 2001 ASME International Design Engineering Technical Conferences & Computers And Information In Engineering Conference, Held September 9-12, 2001 Pittsburgh, Pennsylvania*, ASME-Amer Soc Mechanical Eng, 2001.

[54] C. M. Harris and A. G. Piersol, *Harris' Shock and Vibration Handbook*. McGraw-Hill, fifth edition ed., 2002.

[55] L. Gorbatikh, "Mathematical and computational aspects of nonuniform frictional slip modeling.," *Journal of Computational and Applied Mathematics*, Vol. 168, pp. 215 – 24, Jul 2004.

[56] N. Hunter and T. Paez, "Analysis of time series and energy data from the af&f single leg experiment." Unpublished report, September 2003.

[57] J. Juang and R. Pappa, "An eigen-system realization algorithm for modal parameter identification and model reduction," *J. Guidance, Control, and Dynamics*, Vol. 8, pp. 620–627, Sept-Oct 1985.

[58] B. R. Resor Tech. Rep. SAND2003-1505P, Sandia National Laboratories, PO Box 5800, Albuquerque, NM, April 2003.

[59] B. R. Resor, D. L. Gregory, and R. Coleman, "Experimental techniques to isolate the dynamic behavior of bolted connections," *Proceeding of the SEM Annual Conference and Exposition on Experimental and Applied Mechanics, Portland, OR*, june 2005.

[60] D. O. Smallwood, "Shock testing on shakers by using digital control," *Institute of Environmental Sciences Technology*, 1985.

[61] C. M. Vest, *Holographic Interferometry*. New York: John Wiley & Sons, 1979.

[62] W. F. Ranson, M. A. Sutton, and W. Peters, *Handbook on Experimental Mechanics*, ch. Holographic and Laser Speckle Interferometry. Society for Experimental Mechanics, 1993.

[63] L. E. Drain, *The Laser Doppler Technique*. Wiley, New York, 1980.

[64] B. J. Rauch and R. E. Rowlands, *Handbook on Experimental Mechanics*, ch. Thermoelastic Stress Analysis. Society for Experimental Mechanics, 1993.

[65] R. Nitsche and L. Gaul, "Smart friction driven systems," *Smart materials and structures Journal*, Vol. 14, pp. 231–236, 2005.

[66] D. E. Newland, *An Introduction to Random Vibrations and Spectral Analysis*. London: Longman Group Limited, 1995.

[67] D. O. Smallwood, "Using a modified harmonic wavelet (HWT) transform to characterize mechanical shock." Presented at IEST ESTECH Annual Meeting 2007.

[68] M. Palmonella, M. I. Friswell, J. E. Mottershead, and A. W. Lees, "Guidelines for the implementation of the cweld and acm2 spot weld models in structural dynamics," *Finite Elem. Anal. Des.*, Vol. 41, No. 2, pp. 193–210, 2004.

[69] D. J. Segalman, "A four-parameter iwan model for lap-type joints," *ASME Journal of Applied Mechanics*, Vol. 72, pp. 752–760, September 2005.

[70] M. B. Levine and C. White, "Microdynamic analysis for establishing nanometric stability requirements of jointed precision space structures," *Proceedings of the International Modal Analysis Conference, Paper No. 325, Kissimmee Fl.*, Feb 2001.

[71] C.-Y. Peng, *Generalized Model Identification of Linear and Nonlinear Dynamic Systems*. PhD thesis, California Institute of Technology, 1988.

[72] D. J. Segalman, "An initial overview of Iwan modeling for mechanical joints," Tech. Rep. SAND2001-0811, Sandia National Laboratories, 2001.

[73] D. J. Segalman and M. J. Starr, "Relationships among certain joint constitutive models," Tech. Rep. SAND2004-4321, Sandia National Laboratories, PO Box 5800, Albuquerque, NM, September 2004.

[74] L. E. Goodman, "A review of progress in analysis of interfacial slip damping," in *Structural Damping, papers presented at a colloquium on structural damping held at the ASME annual meeting in Atlantic City, NJ, November, 1959* (J. E. Ruzicka, ed.), pp. 35–48, 1959.

[75] R. Mindlin, W. Mason, T. Osmer, and H. Deresiewicz, "Effects of an oscillating tangential force on the contact surfaces of elastic spheres," in *Proc. 1st US National Congress of Applied Mechanics, 1952*, p. 203, ASME-Amer Soc Mechanical Eng, June 1952.

[76] M. Abramowitz and I. A. Stegun, *Handbook of Mathematical Functions with Formulas, Graphs, and Mathematical Tables*. New York: Dover, ninth dover printing, tenth Government Printing Office printing ed., 1964.

[77] P. Jayakumar, "Modeling and identification in structural dynamics," Tech. Rep. EERL 87-01, California Institute of Technology, 1987.

[78] Mathworks, *Matlab Users Guide*. The MathWorks Inc., Natick, Mass., 2002.

[79] D. O. Smallwood, D. Gregory, and R. G. Coleman, "A three-parameter constitutive model for a joint which exhibits a power law relationship between energy loss and relative displacement," *Proceedings of the 72nd Shock and Vibration Symposium, Destin, FL*, Nov 2001. Available form SAVIAC.

[80] D. J. Segalman and M. J. Starr, "Modeling of threaded joints using anisotropic elastic continua," *Journal of Applied Mechanics*, Vol. 74, pp. 575–585, 2007.

[81] D. G. Sopwith, "The distribution of load in screw threads," *Proceedings of the Institute of Mechanical Engineers,* Vol. 159, pp. 373–383, 1948.

[82] J. N. Goodier, "The distribution of load on the threads of screws," *Journal of Applied Mechanics,* Vol. 7, No. 1, pp. 10–16, 1940.

[83] M. Hetenyi, "A photoelastic study of bolt and nut fastenings," *Journal of Applied Mechanics*, Vol. 10, No. 2, pp. 93–100, 1943.

[84] A. Chaaban and M. Jutras, "Static analysis of buttress threads using the finite element method," *Journal of Pressure Vessel Technolgy,* Vol. 114, pp. 209–212, 1992.

[85] N. R. Hansen, V. I. Bateman, R. G. Bell, and F. A. Brown, "Shock transmissibility of threaded joints," in *Proceedings of the 67th Shock and Vibration Symposium, held Monterey, CA, November 18-22, 1996*, Shock and Vibration Information Analysis Center, Arvonia, VA 23004, 1996.

[86] R. I. Zadoks and D. P. R. Kokatam, "Investigation of the axial stiffness of a bolt using a three-dimensionalfinite element model," *Journal of Sound and Vibration*, Vol. 246, No. 2, pp. 349–373, 2001.

[87] J. L. Bretl and R. D. Cook, "Modelling the load transfer in threaded connections by the finite elementmethod," *International Journal for Numerical Methods in Engineering*, Vol. 14, pp. 1359–1377, 1979.

[88] T. Belytschko, W. K. Liu, and B. Moran, *Nonlinear Finite Elements for Continua and Structures*, p. 315. New York: J. Wiley & Sons, 2000.

[89] M. L. Blanford, M. W. Heinstein, and S. W. Key, "JAS3D: A multi-strategy iterative code for solid mechanics analysis," tech. rep., Sandia National Laboratories, 2001. Unpublished Technical Report.

[90] J. R. Stewart and H. C. Edwards, "Sierra framework version 3: h-adaptivity design and use," tech. rep., Sandia National Laboratories, 2002.

[91] S. S. M. Team, "Adagio 2.9 user's guide," tech. rep., Sandia National Laboratories, 2008.

[92] D. F. Kusnezov and N. Frazier, "Advanced simulation & computing roadmap: National nuclear security through leadership in weapons science," tech. rep., NNSA, 2006.

[93] K. Johnson, *Contact mechanics*. Cambridge: Cambridge University Press, 1985.

[94] K. L. Johnson, "Surface interaction between elastically loaded bodies under tangential forces," *Proceedings of the Royal Society of London. Series A, Mathematical and Physical Sciences*, Vol. 230, pp. 531–548, July 1955.

[95] C. Younis and G. Gazetas, "Dynamic response of a tower-pier system on viscoelastic foundation with frictional interface," *Enginering Structures*, Vol. 18, pp. 546–557, Jul 1996.

[96] R. R. Craig, Jr., *Structural Dynamics: An Introduction to Computer Methods*. John Wiley and Sons, 1981.

[97] D. T. Griffith and D. J. Segalman, "Finite element calculations illustrating a method of model reduction for the dynamics of structures with localized nonlinearities," Tech. Rep. SAND2006-5843, Sandia National Laboratories, Albuquerque, New Mexico 87185, October 2006.

[98] D. J. Segalman, "Model reduction of systems with localized nonlinearities," Tech. Rep. SAND2006-1789, Sandia National Laboratories, PO Box 5800, Albuquerque, NM 87185, June 2006.

[99] D. J. Segalman, "Model reduction of systems with localized nonlinearities," *Journal of Computational and Nonlinear Dynamics*, Vol. 2, pp. 249–266, July 2007.

[100] W. Holzmann Sandia Memo, September 2005.

[101] D. J. Segalman and W. Holzmann, "Nonlinear response of a lap-type joint using a whole-interface model," *Proceedings of the 23rd International Modal Analysis Conference (IMAC-XXIII), held in Orlando, Florida, USA*, Feb. 2005.

[102] M. Mesh and D. J. Segalman, "Technical Memo: Proposed strategy of accommodating the vibration damping of many, spatially distributed frictional interfaces," tech. rep., Sandia National Laboratories, May 2009. Technical Memo.

[103] K. Alvin, "Implementation of modal damping in a direct implicit transient algorithm," in *Proceedings of the 42nd AIAA/ASME/ASCE/AHS/ASC Structures, Structural Dynamics, and Materials Conference and Exhibit, Seattle, WA*, Vol. AIAA-2001-1589, April 2001.

[104] D. J. Segalman, "Modelling joint friction in structural dynamics," *Structural Control and Health Monitoring*, Vol. 13, No. 1, pp. 430–453, 2005.

[105] D. J. Segalman, L. A. Bergman, and D. J. Ewins, "Report on the snl/nsf international workshop on joint mechanics arlington virginia, 16-18 october 2006," Tech. Rep. SAND2007-7761, Sandia National Laboratories, Albuquerque, New Mexico 87185, January 2008.

[106] T. I. Zohdi and P. Wriggers, *Introduction to Computational Micromechanics*. Springer, 2005. ISBN 3540228209, 9783540228202.

[107] M. Guthrie and D. Kammer, "A general reduced representation of one-dimensional frictional interfaces," *Journal of Applied Mechanics*, Vol. 75, No. 1, p. 011019, 2008.

[108] C. Truesdell and W. Noll, *The Nonlinear Field Theories of Mechanics: Handbuch der Physik*, Vol. 3. Berlin: Springer-Verlag, 1965.

[109] *ABAQUS Theory Manual, Version 6.4.1*.

[110] *Theoretical Manual LS-DYNA*.

[111] J. L. Lubkin, “The torsion of elastic spheres in contact,” *ASME Journal of Applied Mechanics,* Vol. 18, pp. 183–187, 1951.

[112] J. Jaeger, *Contact Mechanics,* ch. Torsional load-histories of elastic spheres in contact, pp. 405–412. Southampton: Computational Mechanics Publications, 1993.

Appendix A

Test Specimen Drawings

Danny L. Gregory

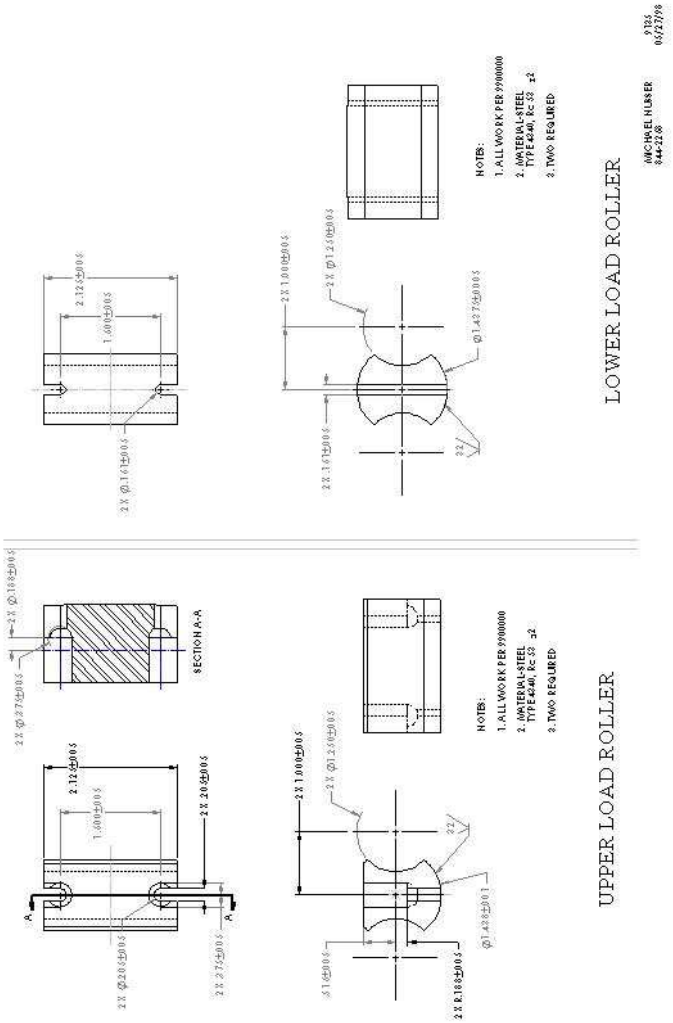

Figure A.1. Drawing of Rollers for Use in the Big Mass Resonance Device.

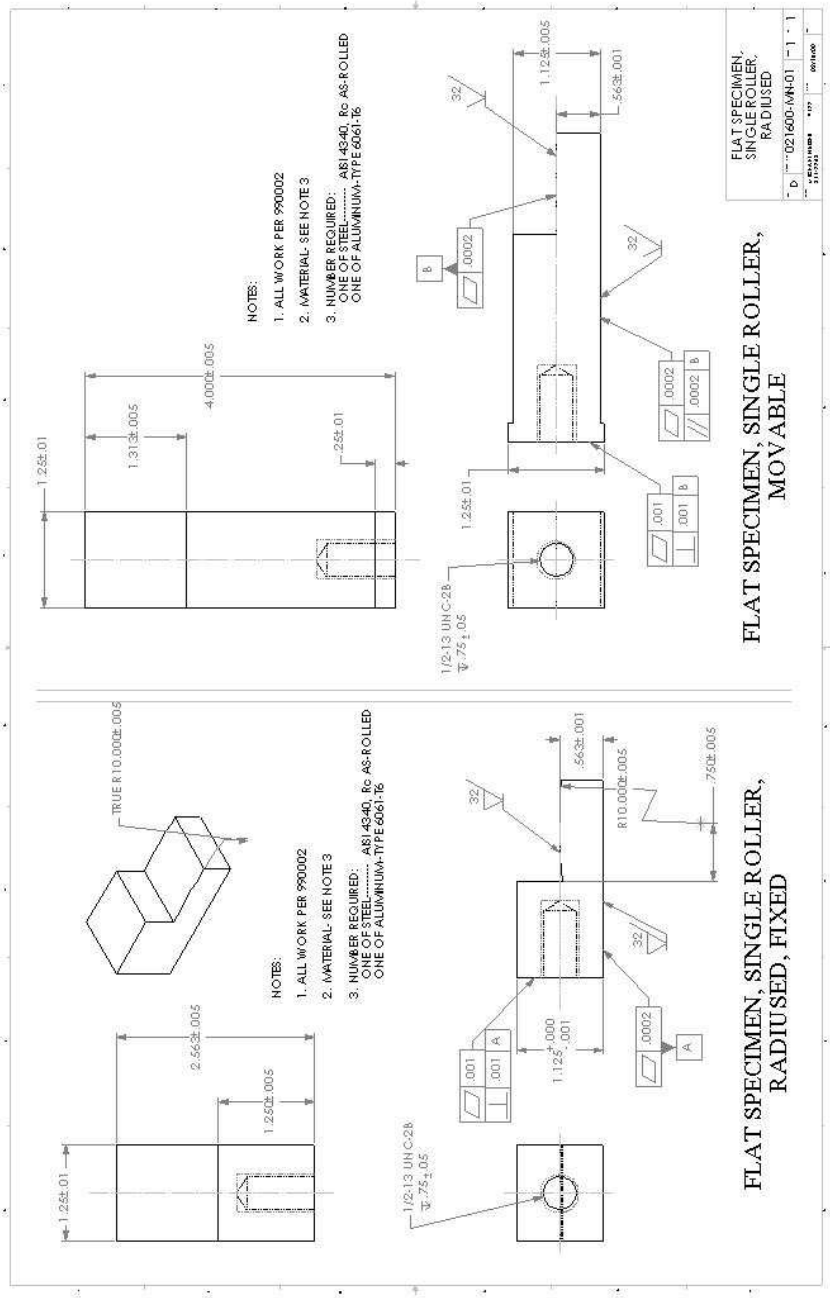

Figure A.2. Drawing of Flat Specimen Connecting to Fixed Roller.

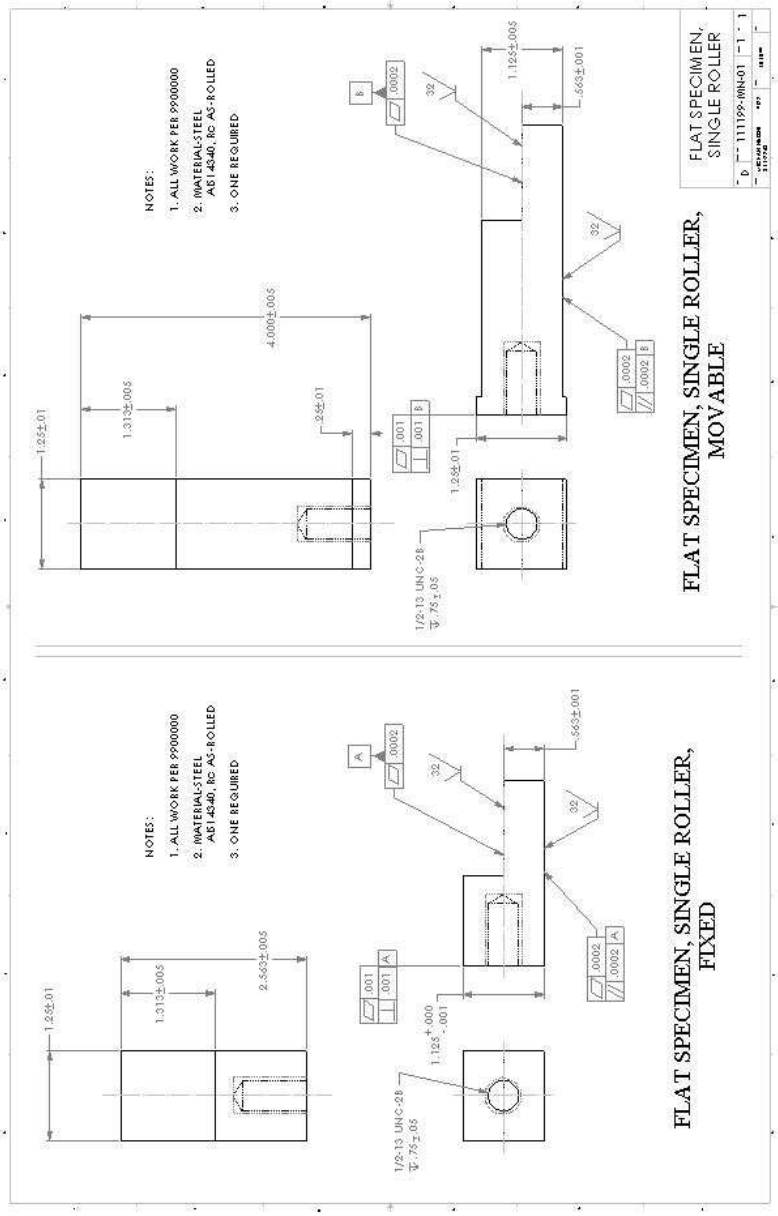

Figure A.3. Drawing of Flat Specimen Connecting to Moveable Roller.

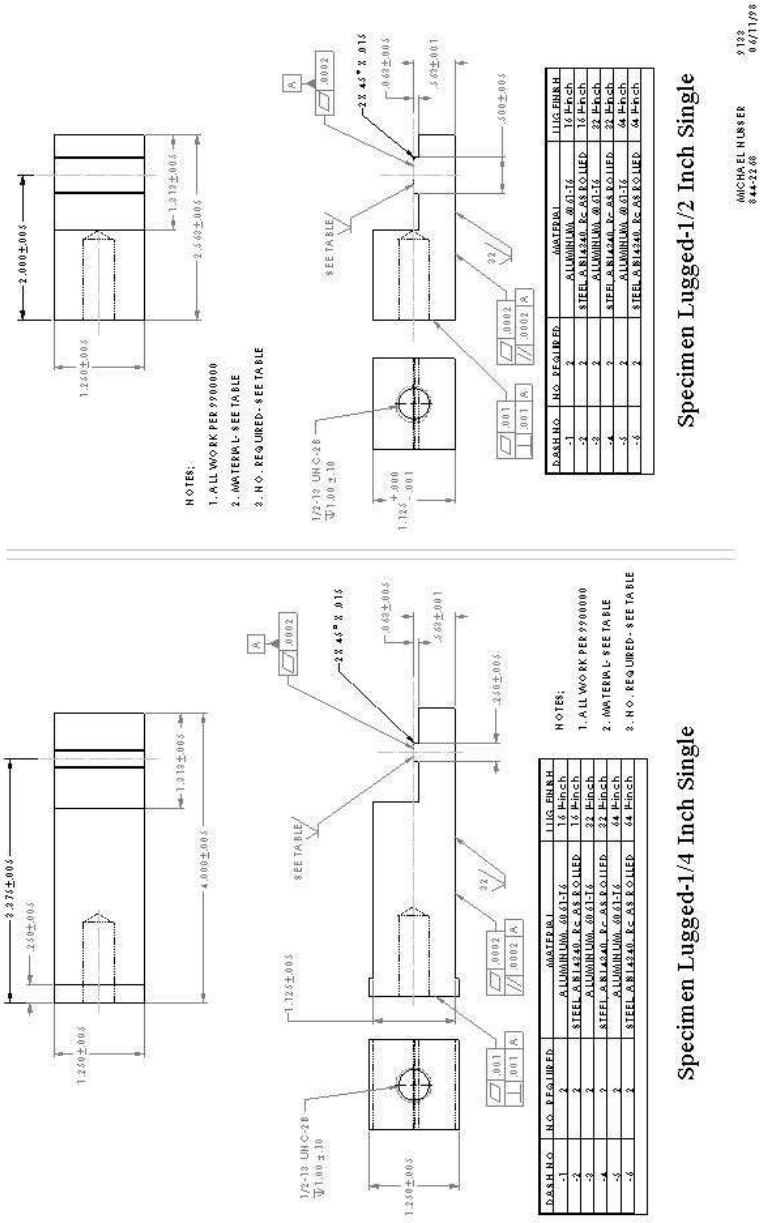

Figure A.4. Drawing of Stepped Specimen.

Appendix B

Finding Iwan Parameters

Daniel J. Segalman

A very robust Matlab code has been written to extract the four parameters or the joint model from the experimental data or micro-mesh FE. An example call to function *get_params_K_T2* follows.

```
% provide the location of the relevant Matlab code
addpath('E:\Joints\matlab\New_find_params');

% The following is collected from specimen B-2
F = [100         200        300        400        500];
D = [7.069e-5    4.106e-4   1.283e-3   2.776e-3   4.951e-3];
K = [ 1.282e7    1.170e7    1.037e7    9.003e6    7.975e6];

% The stiffness value to match
F_Ref = F(4);
K_Ref = K(4);

% the presumed macroslip force
F_S = 700;
%
%
% Find Iwan Parameters
 [chi, beta, K_T, phi_max, R, S] = ...
      get_params_K_T2(F , D,      F_S, ...
              F_Ref ,   K_Ref );
```

The resulting output along with F_S are sufficient to define fully both parameter sets: the primitive set $(R, S, \chi, \phi_{\max})$ and the preferred set (F_S, K_T, χ, β).

The dissipation data from all force levels is employed while only the stiffness data from just one force level is used. The reasons for this can be explained with reference to plots in Figure B.1.

The dissipation curves behave in a manner consistent with a power-law relation with force amplitude. Also, the dissipation easily varies by a factor of three among the specimens and varies by several orders of magnitude over the force ranges investigated.

For six of the specimens, the stiffness decreases continuously with load amplitude and will gradually decline to zero as the load approaches break free force F_S (600 lb in this case). For three of the specimens, the stiffness is nearly constant and experiences a precipitous decline to zero as the load approaches break free force.

Given the qualitative variability from one specimen to another and the fact that the four parameter model predicts stiffnesses very much like those of specimens C-1, C-2, and C-3, but not very much like that of the other six samples, it seems reasonable to be content with matching the model with experiment at just one force level.

The code discussed above is used to deduce the parameters of the four parameter model from all the dissipation data of Specimen B-2, and from the stiffness data of that specimen at a load of 400 lb. The predictions of the resulting four-parameter model are shown in Figure B.2. The model reproduces the energy dissipation very well, but only vaguely captures the decline in stiffness with load.

A listing of *get_params_K_T2.m* is provided in Figure B.3, and listings of two more routines that are called by that function are provided in Figures B.4 and B.5.

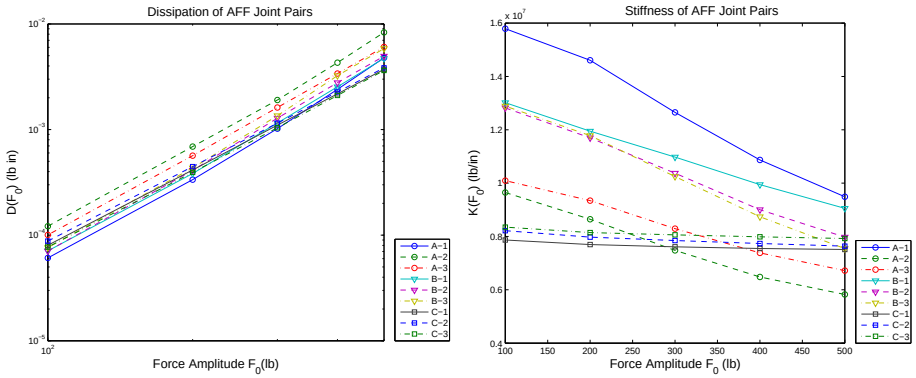

Figure B.1. Joint Energy Dissipation and Stiffness for Nine, Nominally Identical Specimens.

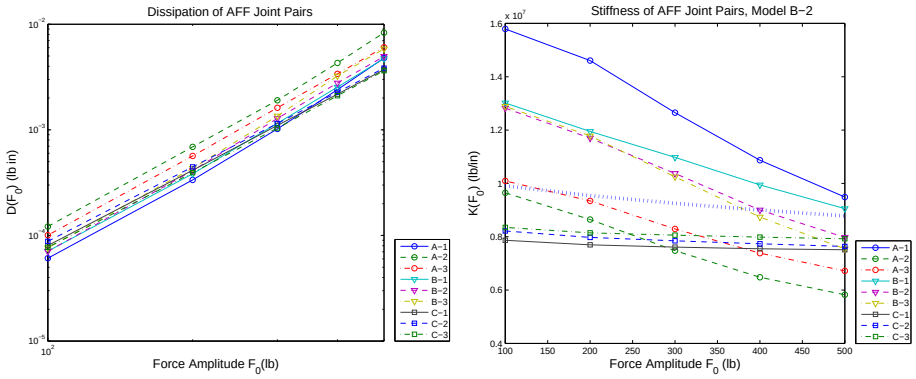

Figure B.2. Plots of Energy Dissipation and Joint Stiffness.

Plots of energy dissipation and joint stiffness for 9 nominally identical specimens plus the predictions of the four parameter Iwan model when fit to data of Specimen B-2.

```
function [chi_out, beta_out, K_T_out, phi_max, R, S] = get_params_K_T2(Force,D, F_S, F_ref, K_ref
)
% routine to generate three of the joint parameters given
%   F_S - the fourth joint parameter = macroslip force
%   a Force-Dissipation curve (Force, D)
%   a measured value of joint stiffness at some reference force
%                   K_ref = K(F_ref)
%
tolerance = K_ref*1.0e-3;
F_ratio = F_ref/F_S;
%
% First and second guesses of K_T
K_Te(1) = K_ref;
K_Te(2)= K_ref*1.02;

% Newton itteration loop to find the set {Ke, chi, beta} that
% reproduce  given dissipations (D) over given force range (F) and
% match experimental stiffness K_ref  at F_ref
for i=1:2
  [chi(i),beta(i)] = find_chi_beta(Force,D, F_S, K_Te(i));
  % find the stiffness at F_ref with these parameters
  r = find_r(F_ratio, chi(i), beta(i));
  Ke(i) = K_Te(i)...
          *( (beta(i)+1)- (r^(chi(i)+1))/(chi(i)+2))/(1+beta(i));
end

error  = Ke(2)-K_ref;
count = 0;  max_count=20;
while (tolerance  < abs(error)) && (count<max_count)
    count = count+1;
  K_Te2_temp = K_Te(2);
  K_Te(2) = K_Te(2)   - error*(K_Te(2)-K_Te(1))/(Ke(2)- Ke(1));
  %
  K_Te(1)= K_Te2_temp;
  chi(1) = chi(2);
  beta(1) = beta(2);
  Ke(1) = Ke(2);
%
  [chi(2),beta(2)] = find_chi_beta(Force,D, F_S, K_Te(2));
  % find the stiffness at F_ref with these parameters
  r = find_r(F_ratio, chi(2), beta(2));
  Ke(2) = K_Te(2)...
          *( (beta(2)+1)- (r^(chi(2)+1))/(chi(2)+2))/(1+beta(2));
  error  = Ke(2)-K_ref;
end
if(count == max_count)
    msg = ['Failure to converge after ', num2str(max_count), 'iterations.']
    Stiffness_error  = Ke(2)-K_ref
    current_K_t = K_Te(2)
end
% having converged,  output values
chi_out = chi(2);
beta_out = beta(2);
K_T_out  = K_Te(2);
phi_max = F_S*(1+beta(2))/(K_Te(2)*(beta(2)+(chi(2)+1)/(chi(2)+2)));
R = F_S*(chi(2)+1)/((phi_max^(chi(2)+2))*(beta(2)+(chi(2)+1)/(chi(2)+2)));
S = (F_S/phi_max)*beta(2)/(beta(2)+(chi(2)+1)/(chi(2)+2));
```

Figure B.3. Listing of Function *get_params_K_T2*.

find_chi_beta.m (unsaved) **1/1**
/cygdrive/e/Joints/matlab/New_find_params/ 07/25/08

```
%This routine finds accepts dissipation data as well as values for
% nominal macro-slip force F_S and initial stiffness K_T to
% calculate values of chi and beta to reproduce the dissipation
% data.
%
function [chi,beta] = find_chi_beta(F,D, F_S, K_T)
%
% Number of dissipation values
N = length(F);
%
% parameters for optimixation
p = zeros(2*N+3,1);
p(1:N)     = F;
p(N+1:2*N) = D;
p(2*N+1) = F_S;
p(2*N+2) = K_T;
p(2*N+3) = N;
%
% initial guess for the unknowns
x = zeros(2,1);
slope  = (log(D(N)) - log(D(1)))/(log(F(N)) - log(F(1)));
x(1) = slope - 3;
x(2) = 1;
%
% call the optimization program
options = optimset('TolX',1e-6,'Display','final','MaxFunEvals', ...
                   8000);
[x,resid,flag]=fminsearch('para_fit3',x,options,p);
chi  = x(1);
beta = x(2);
%
```

Figure B.4. Listing of Function *find_chi_beta*.

```
%
% r = find_r(Ft,chi,beta);
%
% routine to find the r that results in a target value of Ft
%
function r = find_r(Ft, chi, beta)
%
%
% first estimate:
r = Ft;
%
% iteration parameters
i = 1; max_i = 100;
tol = 1.0e-4;
res = Ft;
while (i<max_i & Ft*tol<abs(res))
  F = r*( (beta+1)-(r^(chi+1))/(chi+2) )/ ...
   ( beta+(chi+1)/(chi+2) );
  res = F-Ft;
  slope = ( (beta+1) - r^(chi+1) )/(beta + (chi+1)/(chi+2));
  r = r - res/slope;
  r = max(r, -1);
  r = min(r, 1);
  i = i+1;
end
if ( Ft*tol< abs(res) )
  %disp('did not converge on r');
  %Ft
  %res
  %chi
  %beta
end
```

Figure B.5. Listing of Function *find_r*.

Appendix C

Threaded Joint Derivations

Daniel J Segalman

The sections in this appendix provide tools to deduce parameters of an elastic material equivalent to those of a welded unit thread pair. The key notion is to perform a number of elasticity calculations on a mesh containing an array of unit thread pairs (Figure 13.3) and then to identify the single set of equivalent elastic parameters that best reproduces all those elasticity results. This effort has three elements:

1. For each detailed elasticity result, deduce an equivalent homogeneous strain for the center unit thread pair.
2. For each detailed elasticity result, deduce an equivalent homogeneous stress for the center unit thread pair.
3. From all of those strain and stress pairs, deduce a set of elastic parameters that best maps the strains onto the stresses.

The next three sections address each of these issues separately.

C.0.1 Finding Equivalent Homogeneous Strains

There are subtleties in imposing displacements on the unit cell. These subtleties originate from the fact that in the actual geometry, except at the top and bottom threads, each cell is attached to cells above and below it, as illustrated in Figure 13.3. This constraint is satisfied if periodic boundary conditions are imposed explicitly, however, this is difficult to implement in most FE codes.

Instead, constraints are imposed by embedding the unit cell of interest inside a matrix of similar cells. Displacements are imposed in a manner consistent with homogeneous deformation on the boundaries of that matrix. Labeling locations of nodes, n, on the boundary of the cell matrix as $\mathbf{x}^n$, displacements consistent with the displacement gradient $\mathbf{H}$ [108] are

$$\delta\mathbf{u}^n = \mathbf{H}\cdot\mathbf{x}^n + \mathbf{u}_0 \tag{C.1}$$

where $\mathbf{u}_0$ is a rigid body translation.

The displacement gradient $\mathbf{H}$ is assumed constant over the cell volume and is found by post-multiplying the above equation by the local outwardly pointing normal vector $\mathbf{n}$ and integrating over the surface of the control volume (the central thread-pair):

$$\int_{\partial V} [\delta \mathbf{u}\, \mathbf{n}]\, \mathrm{d}A = \mathbf{H} \int_{\partial V} [\mathbf{x}\, \mathbf{n}]\, \mathrm{d}A + \left[\mathbf{u}_0 \left(\int_{\partial V} \mathbf{n}\, \mathrm{d}A \right) \right] \tag{C.2}$$

where the quantities inside brackets are dyads. If evaluated algebraically, they would be computed as

$$[\mathbf{ab}]_{ij} = a_i b_j \tag{C.3}$$

Noting that

$$\int_{\partial V} \mathbf{n}\, \mathrm{d}A = \mathbf{0} \tag{C.4}$$

Equation (C.2) becomes

$$\mathbf{H} = \mathbf{U}\mathbf{X}^{-1} \tag{C.5}$$

where

$$\mathbf{U} = \int_{\partial V} [\delta \mathbf{u}\, \mathbf{n}]\, \mathrm{d}A \tag{C.6}$$

and

$$\mathbf{X} = \int_{\partial V} [\mathbf{x}\, \mathbf{n}]\, \mathrm{d}A \tag{C.7}$$

The incremental strain corresponding to this deformation is

$$\delta \boldsymbol{\epsilon}_L = \frac{1}{2} \left(\mathbf{H} + \mathbf{H}^T \right) \tag{C.8}$$

C.0.2 Finding Equivalent Homogeneous Stress

The (possibly nonlinear) equilibrium equations are solved to determine the nodal forces and displacements as well as the stresses and strains in the elements. There are two expeditious methods for deducing equivalent, homogeneous approximates for the stress in the thread-pair region:

1. Average the element stresses weighted by the element volumes.

$$\boldsymbol{\sigma} = \sum_k \boldsymbol{\sigma}^k V_k / \sum_k V_k \tag{C.9}$$

2. Appropriately integrate the tractions applied to the boundary of the thread-pair.

Both approaches are mathematically equivalent; the approach used depends on which data are most easily extracted from the FE microanalysis of the thread-pair and its surrounding material. Though the mathematics of the first approach is very simple, that of the second approach requires some explanation, as follows.

From the forces $\delta\mathbf{f}^n$ on the boundary of the unit cell at the center of the array of cells, corresponding tractions are defined as

$$\hat{\boldsymbol{\tau}}^n = \delta\mathbf{f}^n / \mathrm{d}A^n \tag{C.10}$$

where $\mathrm{d}A^n$ is the surface area corresponding to node n.

An expression for $\boldsymbol{\sigma}_L$ is derived in terms of the $\hat{\boldsymbol{\tau}}^n$. If the tractions $\boldsymbol{\tau}$ on the surface are exactly consistent with a uniform stress field $\boldsymbol{\sigma}$, those tractions are expressed in terms of $\boldsymbol{\sigma}$

$$\boldsymbol{\tau}(s) = \boldsymbol{\sigma} \cdot \mathbf{n}(s) \tag{C.11}$$

where $\boldsymbol{\tau}(s)$ is the traction at location s on the surface of the cell
and $\mathbf{n}(s)$ is the unit outwardly pointing normal there.

Taking the outer vector product of Equation (C.11) and integrating over the surface yields

$$\int_{\partial V} [\boldsymbol{\tau}(s)\,\mathbf{n}(s)]\,\mathrm{d}A = \int_{\partial V} \boldsymbol{\sigma} \cdot [\mathbf{n}(s)\,\mathbf{n}(s)]\,\mathrm{d}A \tag{C.12}$$

Factoring $\boldsymbol{\sigma}$ out of the integral on the right and letting $\mathbf{Q} = \int_{\partial V} [\mathbf{n}(s)\,\mathbf{n}(s)]\,\mathrm{d}A$, obtains $\boldsymbol{\sigma}$

$$\boldsymbol{\sigma} = \left\{ \int_{\partial V} [\boldsymbol{\tau}(s)\,\mathbf{n}(s)]\,\mathrm{d}A \right\} \cdot \mathbf{Q}^{-1} \tag{C.13}$$

Equation (C.13) provides a natural manner to define the mean stress $\boldsymbol{\sigma}_L$ associated with the tractions obtained via finite elements

$$\boldsymbol{\sigma}_L = \left\{ \sum_n [\hat{\boldsymbol{\tau}}^n \mathbf{n}^n] \, \mathrm{d}A^n \right\} \cdot \mathbf{Q}^{-1} = \left\{ \sum_n [\delta \mathbf{f}^n \mathbf{n}^n] \right\} \cdot \mathbf{Q}^{-1} \tag{C.14}$$

Since it is assumed that the stress tensor $\boldsymbol{\sigma}$ in Equation (C.11) is symmetric, Equations (C.11) through (C.14) are also derived easily in the following form

$$\boldsymbol{\tau}(s) = \mathbf{n}(s) \cdot \boldsymbol{\sigma} \tag{C.15}$$

$$\int_{\partial V} [\mathbf{n}(s) \, \boldsymbol{\tau}(s)] \, \mathrm{d}A = \int_{\partial V} [\mathbf{n}(s) \, \mathbf{n}(s)] \, \mathrm{d}A \cdot \boldsymbol{\sigma} \tag{C.16}$$

$$\boldsymbol{\sigma} = \mathbf{Q}^{-1} \cdot \left\{ \int_{\partial V} [\mathbf{n}(s) \, \boldsymbol{\tau}(s)] \, \mathrm{d}A \right\} \tag{C.17}$$

and

$$\boldsymbol{\sigma}_R = \mathbf{Q}^{-1} \cdot \left\{ \sum_n [\mathbf{n}^n \, \hat{\boldsymbol{\tau}}^n] \, \mathrm{d}A^n \right\} = \mathbf{Q}^{-1} \cdot \left\{ \sum_n [\mathbf{n}^n \, \delta \mathbf{f}^n] \right\} \tag{C.18}$$

The symmetry of $\boldsymbol{\sigma}$ is guaranteed by averaging the expressions for $\boldsymbol{\sigma}_L$ and $\boldsymbol{\sigma}_R$ in Equations (C.14) and (C.18)

$$\boldsymbol{\sigma} = \frac{1}{2} \left(\left\{ \sum_n [\delta \mathbf{f}^n \mathbf{n}^n] \right\} \cdot \mathbf{Q}^{-1} + \mathbf{Q}^{-1} \cdot \left\{ \sum_n [\mathbf{n}^n \, \delta \mathbf{f}^n] \right\} \right) \tag{C.19}$$

C.0.3 Deducing Elastic Properties

Assuming that a number of elastic FE calculations have been performed as outlined above, a systematic method for processing those results is sought to deduce equivalent elastic parameters for the thread cell.

Each experiment should yield an array S^m, of length M of strain values and another array, T^m, of corresponding stress values where M is the number of components defining the stress or strain state. The superscript m is the index of the numerical experiment. If all the equivalent stress and

strain fields deduced from the FE calculations are consistent with the same elastic response, there is a symmetric M x M matrix, E, relating the equivalent stresses and equivalent strains

$$T^m = ES^m \tag{C.20}$$

Because E is symmetric, it is fully defined by a number, K, of parameters C_k where $K \leq M(M+1)/2$. If further material assumptions, such as isotropy or simple orthotropy, are made on E, the value of K is further reduced. Corresponding to the material parameters C_k are symmetric matrices, B_k, of dimension M x M, which are defined so that

$$E = \sum_{k=1}^{K} C_k B_k \tag{C.21}$$

For full anisotropy in plane strain elasticity ($M = 3$), there are six material properties and E is expressed

$$E = \begin{bmatrix} C_1 & C_3 & C_5 \\ C_3 & C_2 & C_6 \\ C_5 & C_6 & C_4 \end{bmatrix} \tag{C.22}$$

In this case,

$$\begin{aligned} B_1 &= \begin{bmatrix} 1 & 0 & 0 \\ 0 & 0 & 0 \\ 0 & 0 & 0 \end{bmatrix} \quad B_2 = \begin{bmatrix} 0 & 0 & 0 \\ 0 & 1 & 0 \\ 0 & 0 & 0 \end{bmatrix} \\ B_3 &= \begin{bmatrix} 0 & 1 & 0 \\ 1 & 0 & 0 \\ 0 & 0 & 0 \end{bmatrix} \quad B_4 = \begin{bmatrix} 0 & 0 & 0 \\ 0 & 0 & 0 \\ 0 & 0 & 1 \end{bmatrix} \\ B_5 &= \begin{bmatrix} 0 & 0 & 1 \\ 0 & 0 & 0 \\ 1 & 0 & 0 \end{bmatrix} \quad B_6 = \begin{bmatrix} 0 & 0 & 0 \\ 0 & 0 & 1 \\ 0 & 1 & 0 \end{bmatrix} \end{aligned} \tag{C.23}$$

The challenge is to find the material parameters C_k. An objective function $R(C_k)$ associated with Equation (C.20) is defined:

$$R = \max_m \left[\mathrm{tr}((T^m - E\,S^m)^T D (T^m - E\,S^m))\right] \tag{C.24}$$

$$\begin{aligned} = \max_m \big[& C_j C_k \mathrm{tr}\left((S^m)^T B_j^T D B_k S^m\right) - 2C_j \mathrm{tr}\left((S^m)^T B_j^T D T^m\right) \\ & + \mathrm{tr}\left((T^m)^T D T^m\right)\big] \end{aligned} \tag{C.25}$$

where D is a diagonal matrix capturing the mapping between shear strain angle and the corresponding component of the strain tensor.

In plane strain,

$$D = \begin{bmatrix} 1 & 0 & 0 \\ 0 & 1 & 0 \\ 0 & 0 & 2 \end{bmatrix} \tag{C.26}$$

In Equations (C.24) and (C.25), the stress vectors T^m and strain vectors S^m of each case are each normalized by the largest component of S^m.

The objective function $R(C_k)$ represents the maximum error obtained over all of the m numerical experiments used in the constitutive relationship of Equation (C.20) for a particular set of parameters C_k. The simplex (*fminsearch*) tool in the Matlab Optimization Toolbox is used to minimize the objective function (which is the maximum residual error) to find the optimal values of C_k. These optimal values of C_k are then used to construct the elasticity matrix E using Equation (C.21).

Appendix D

Verification Test Suite: ABAQUS and LS DYNA

Nicoli Ames

D.1 Introduction

This section reports an effort to replicate results from the suite of classic contact problems first introduced in the body of the document. In the following sections, the results will be presented from the implicit finite element code Abaqus/Standard [109] and from the finite element code LS-Dyna [110] using implicit integration.

D.2 Indentation by a Rigid, Flat Punch

We have chosen to model the full 3D problem with plane-strain boundary conditions as opposed to using 2D plane-strain elements. The mesh used is shown in Figure D.1. The mesh is sufficiently wide and tall in order to prevent boundary effects near the punch. The inputs used are $2a = 1$, $P = 1$, $E = 1 \times 10^9$, and $\nu = 0.3$.

D.2.1 LS-Dyna

The rigid punch is modeled by a single element with a rigid material definition. Element type 1 with hourglass control type 6 is used for the elastic body (8-node, constant stress solid element with hourglass control). Surface-to-surface contact with a linear penalty method is used between the rigid element and the elastic body.

The results from LS-Dyna are shown along with the analytical solutions in the following figures. The results from LS-Dyna were initially not very promising. There was significant penetration of the slave (elastic) surface into the master (rigid) surface. To reduce the penetration, the

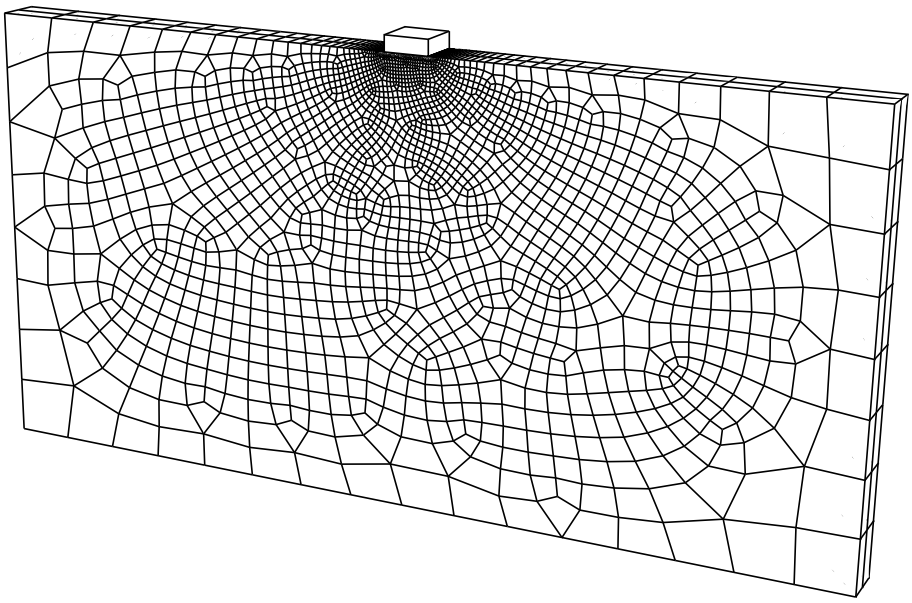

Figure D.1. Three-dimensional Mesh Used in the FE Simulations.

penalty stiffness on the slave surface nodes was increased by a factor of 10^4. This significantly improved the smoothness of all the LS-Dyna solutions. However, there are still issues with the LS-Dyna solution near the punch corner. Figure D.5 shows the pressure contours in the elastic material near the corner of the punch. The maximum pressure is a few elements outside of the contact region in LS-Dyna, whereas the maximum pressure should be located directly under the punch corner.

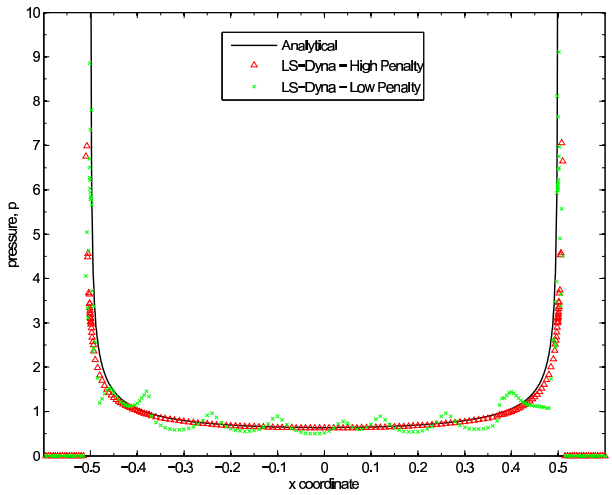

Figure D.2. Pressure Distribution Under Rigid Frictionless Punch.

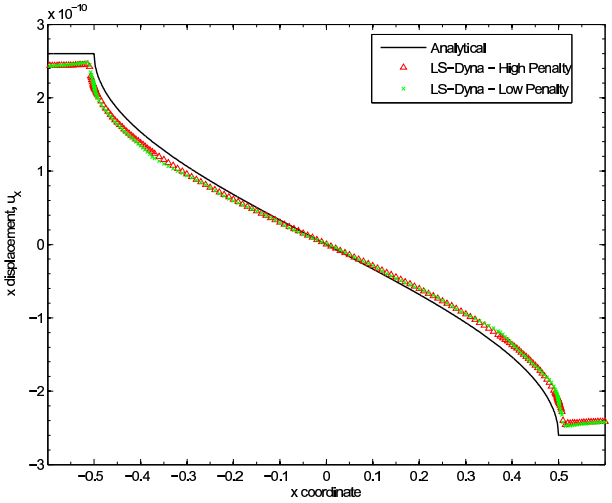

Figure D.3. Displacement of Material in *x*-Direction Under Punch.

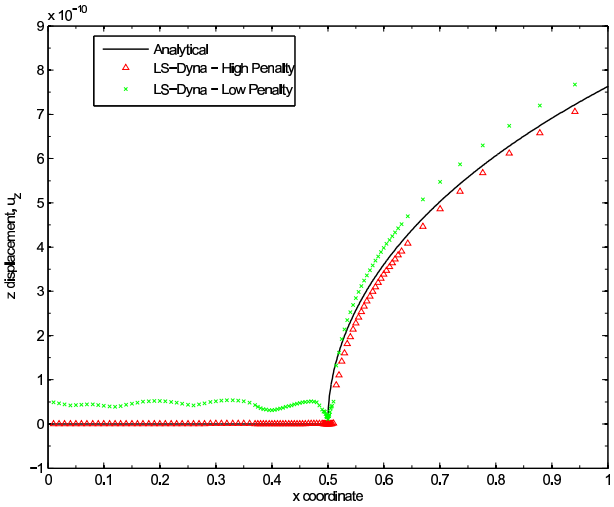

Figure D.4. Displacement of Material in *z*-Direction Outside Punch.

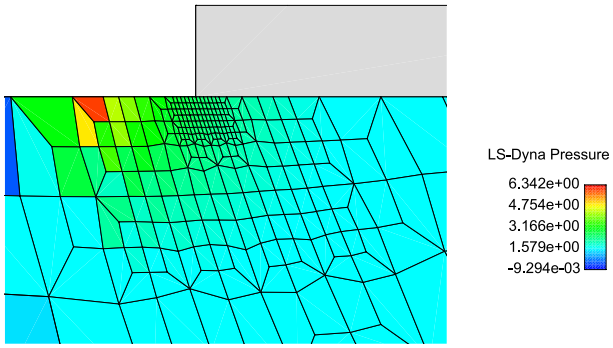

Figure D.5. Pressure Contour Near Punch Corner.

D.2.2 ABAQUS

The rigid punch is modeled with an analytical rigid surface, and C3D8R elements are used for the elastic body (8-node linear brick, reduced integration with hourglass control). Finite-sliding surface-to-surface "hard" contact is used between the rigid surface and the elastic body. With the default settings in Abaqus/Standard, the optimal normal constraint method will be chosen at runtime by Abaqus. This can be a Direct constraint (pure Lagrange multiplier) method, a Penalty constraint method with or without Lagrange multipliers, and an Augmented Lagrange method (a penalty constraint method with augmentation iterations).

The results from Abaqus are shown along with the analytical solutions in the following figures; the agreement between Abaqus and the analytical solutions is excellent for the pressure distribution, x displacement, and z displacement. Figure D.9 shows the pressure contours in the elastic material near the corner of the punch; Abaqus correctly places the maximum pressure under the punch corner.

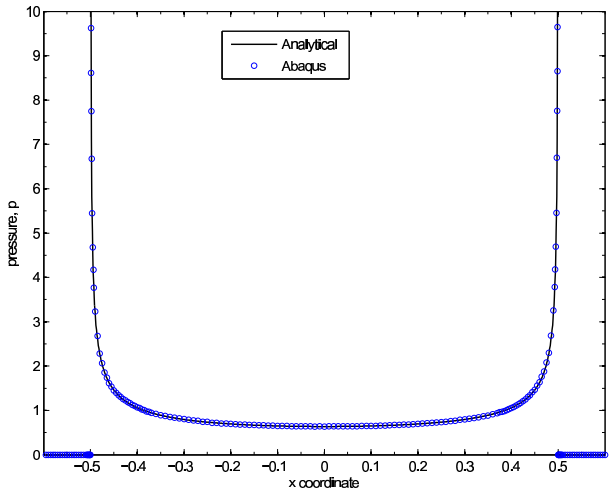

Figure D.6. Pressure Distribution Under Rigid Frictionless Punch.

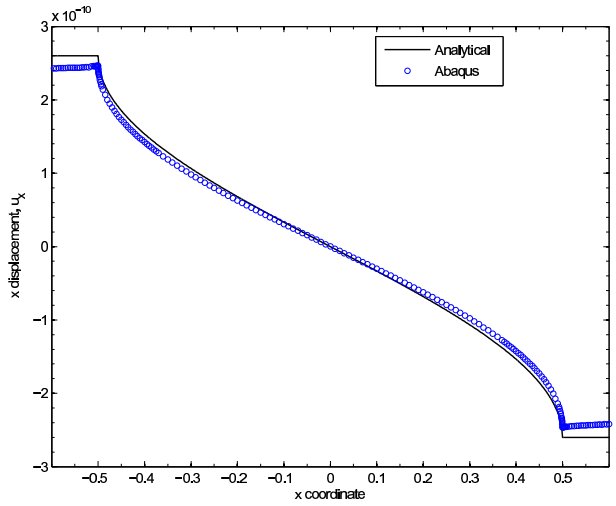

Figure D.7. Displacement of Material in *x*-Direction Under Punch.

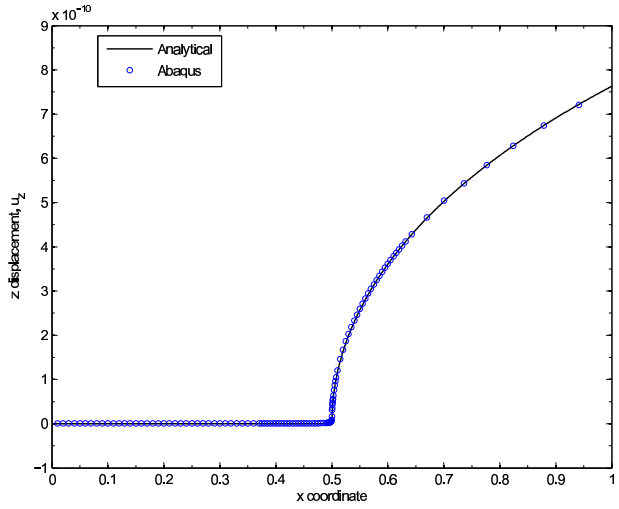

Figure D.8. Displacement of Material in *z*-Direction Outside Punch.

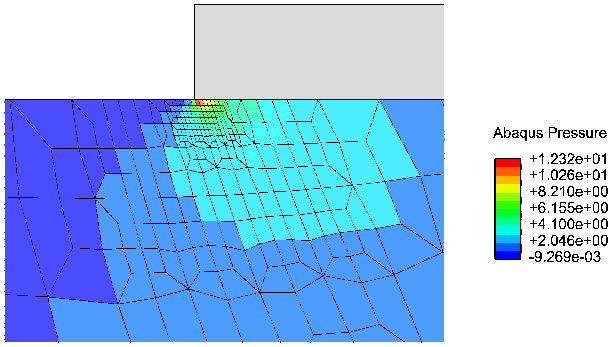

Figure D.9. Pressure Contour Near Punch Corner.

D.3 Static Hertzian Contact

We have chosen to model half of each sphere with 3D elements. The mesh used is shown in Figure D.10. In order to aid in the application of boundary conditions, rigid parts are tied to the exposed mid-plane of each hemisphere. One rigid part is completely fixed and a force is ramped to approximately $P = 45.8 \times 10^6$ on the opposite rigid part. The inputs used are $R_1 = 1$, $E = 68.9 \times 10^9$, and $\nu = 0.33$.

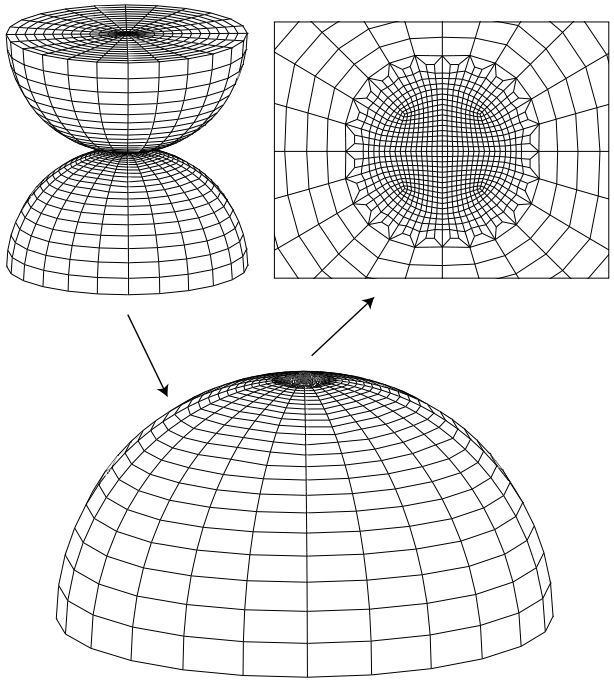

Figure D.10. FE Simulation Meshes.

Three-dimensional mesh used in the FE simulations (upper left). Detail of one hemisphere (lower). Closeup of contact region (upper right). Rigid parts are hidden for clarity.

D.3.1 LS-Dyna

The results are shown along with the analytical solutions in the following figures. With the default penalty stiffness, very poor results are obtained for the vertical displacement (Figure D.11) and the maximum contact pressure (Figure D.12) in comparison with the analytical solution. However, as the penalty stiffness is increased by a factor of 10, the displacement and maximum contact pressure results are significantly improved, however, there is still discrepancy in the contact pressure as a function of contact patch radius as shown in Figure D.14. By further increasing the penalty stiffness

scale factor to 100, the contact pressure as a function of radius in the contact patch is improved further as shown in Figure D.15.

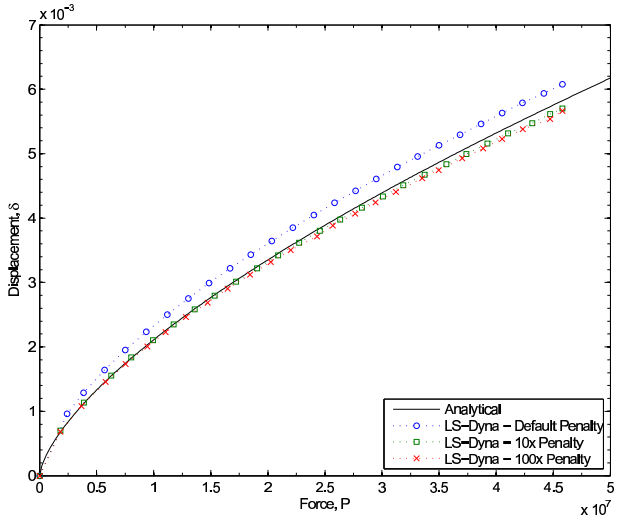

Figure D.11. Vertical Displacement vs Applied Normal Force.

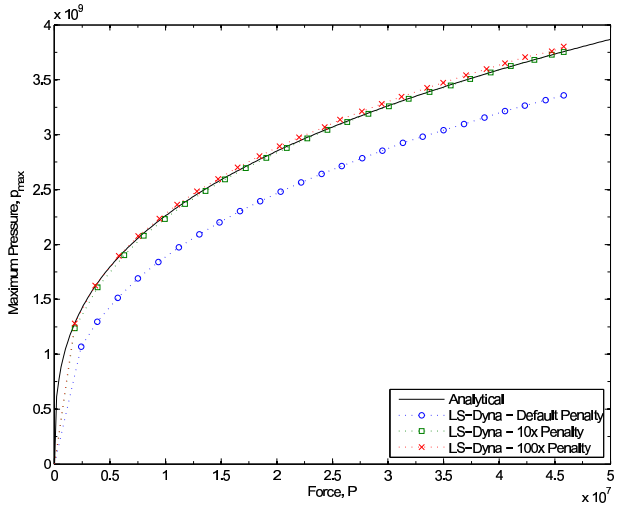

Figure D.12. Maximum Contact Pressure vs Applied Normal Force.

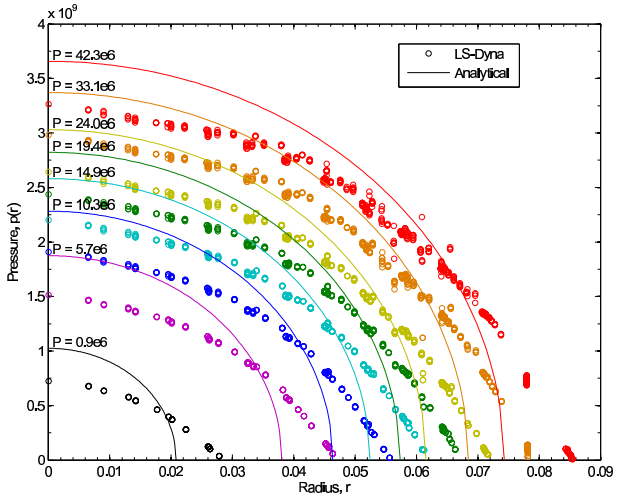

Figure D.13. Pressure in the Contact Patch.

Contact pressure, p, vs position, r, in contact patch at various normal loads P using the default contact penalty stiffness. Analytical results from Equation (14.6) *for* $0 \leq r \leq a$.

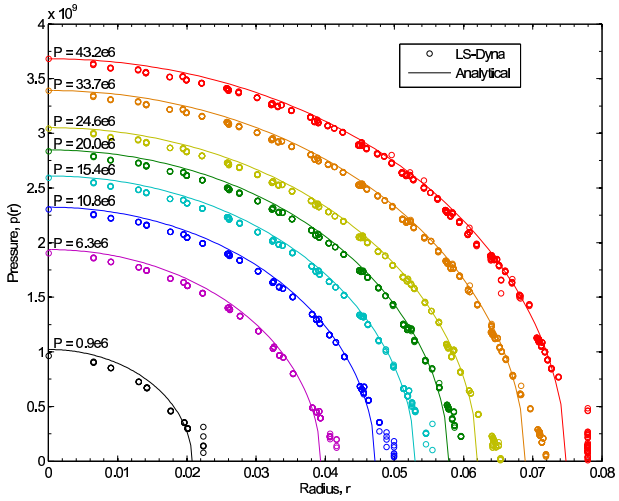

Figure D.14. Pressure in the Contact Patch.

Contact pressure, p, vs position, r, in contact patch at various normal loads P using a 10 scale factor on the contact penalty stiffness. Analytical results from Equation (14.6) *for* $0 \leq r \leq a$.

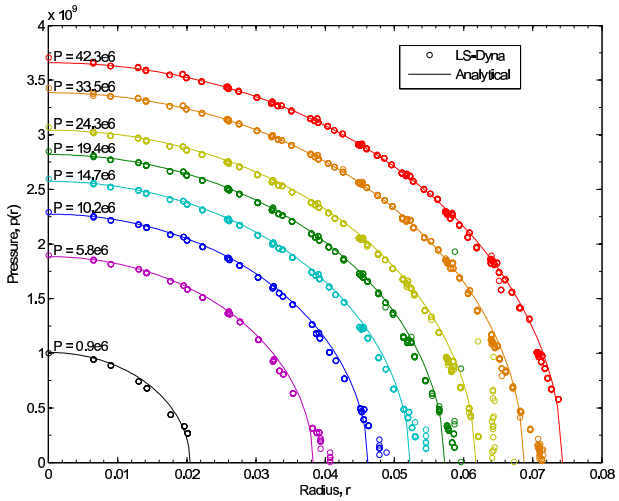

Figure D.15. Pressure in the Contact Patch.

Contact pressure, p, vs position, r, in contact patch at various normal loads P using a 100 scale factor on the contact penalty stiffness. Analytical results from Equation (14.6) *for* $0 \leq r \leq a$.

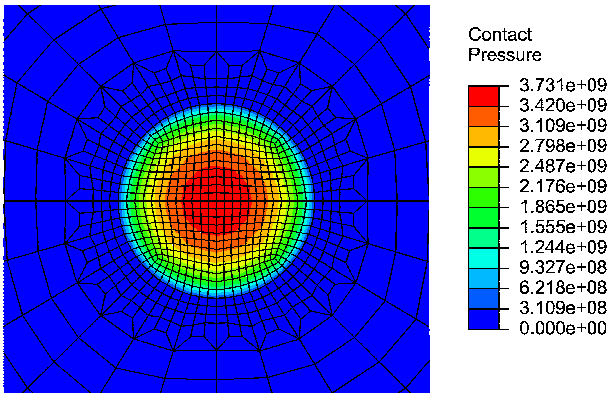

Figure D.16. Contact Pressure Contours.

Contact pressure contours on sphere using a 100 scale factor on the contact penalty stiffness with a force of $P \approx 43 \times 10^6$. *These contours correspond to the outermost (red) curve in the previous figure.*

D.3.2 ABAQUS

One complication arose at the beginning of the analysis when the two spheres are in contact at only one node. When a force is applied as the boundary condition, it is not transmitted properly across the interface and the solution does not converge. In order to avoid this, a small displacement is first applied in order to bring multiple nodes into contact at the interface, then the force boundary condition is introduced.

The results are shown along with the analytical solutions in the following figures. All results agree very well.

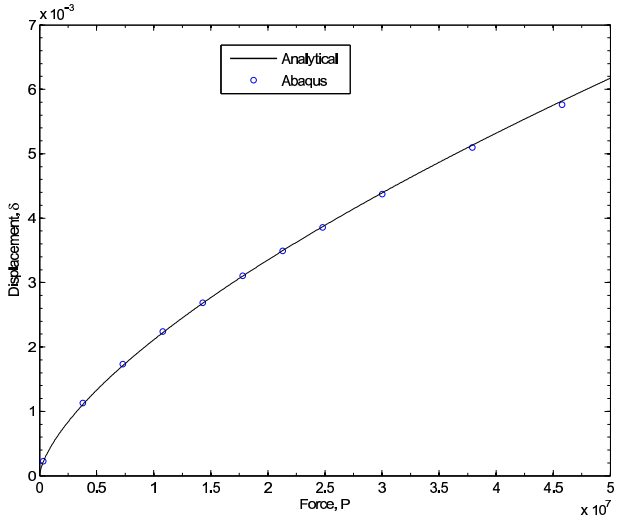

Figure D.17. Vertical Displacement vs Applied Normal Force.

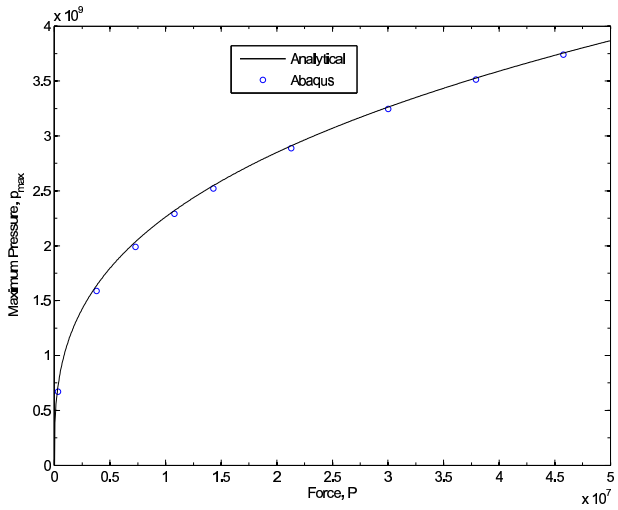

Figure D.18. Maximum Contact Pressure vs Applied Normal Force.

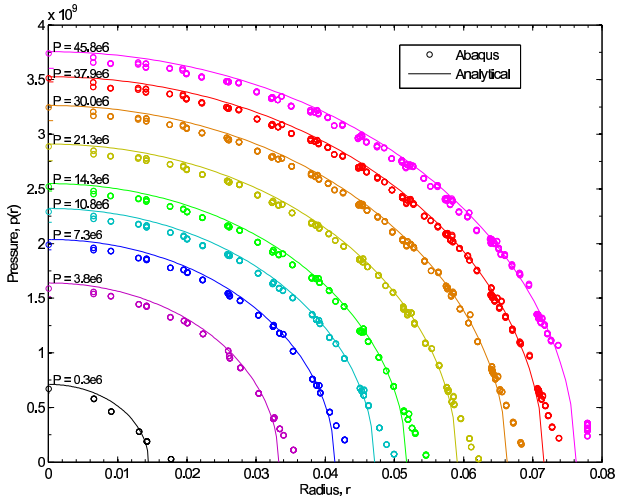

Figure D.19. Pressure in the Contact Patch.

Contact pressure, p, vs position, r, in contact patch at various normal loads P. Analytical results from Equation (14.6) *for* $0 \leq r \leq a$.

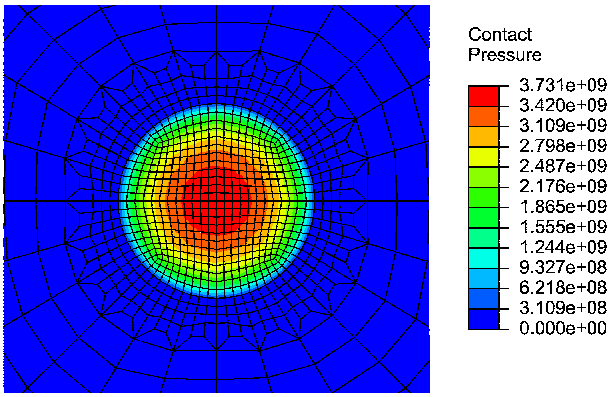

Figure D.20. Contact Pressure Contours.

Contact pressure contours on sphere at a normal force of $P = 45.8 \times 10^6$. *These contours correspond to the outermost (pink) curve in the previous figure.*

D.4 Mindlin Problem

Two identical elastic spheres of radius R_1 are pressed against each other with a force P as in the previous problem. A coefficient of friction μ is assumed at the interface between the spheres. After the application of the normal force, a tangential force $T \leq \mu P$ is applied until the spheres slips completely relative to each other. This is shown schematically in Figure D.21.

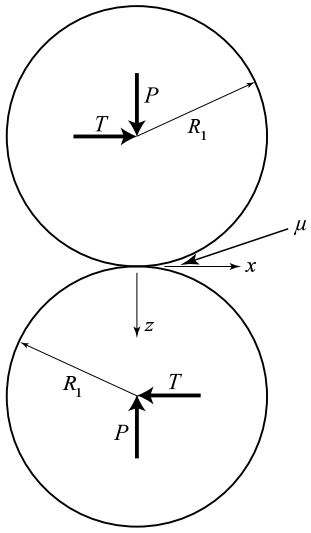

Figure D.21. Schematic of Mindlin Problem.

D.4.1 LS-Dyna

The same model described in the previous section is used for this problem as well. However, it proved difficult to apply the tangential force in LS-Dyna, so a tangential displacement was applied instead. The tangential displacement on the free rigid body was ramped from 0 to 1.2×10^{-3} after the normal load of $P = 2 \times 10^7$ was applied. The coefficient of friction is $\mu = 0.1$, so that a resulting tangential load of 2×10^6 should cause complete slip.

The results for the tangential displacement vs tangential force are shown in Figure D.22. As in the previous problem, the results are strongly dependent on the value of the contact penalty stiffness scale factor. The default value of penalty stiffness grossly underpredicts the tangential stiffness of the interface. The results are improved, but they are not brought into agreement with the analytical solution when the penalty stiffness is scaled by a factor of 10 and further by a factor of 100. The results do not continue to improve with increasing scale factors.

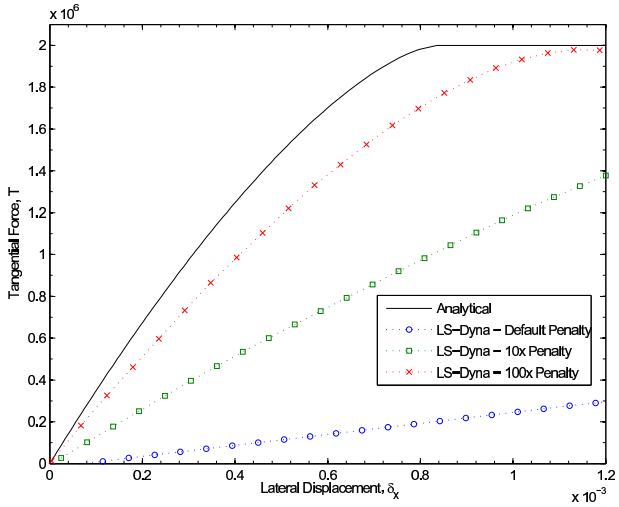

Figure D.22. Mindlin Monotonic Loading Curve.

Lateral displacement vs tangential force for the elastic spheres subjected to compression and a tangential force. Results are shown for various contact penalty stiffness scaling factors.

D.4.2 ABAQUS

The same model described in the previous section is used for this problem as well. In Abaqus, the tangential force was ramped to $T = 2 \times 10^6$ after the normal load of $P = 2 \times 10^7$ was applied. The coefficient of friction is $\mu = 0.1$, so that the maximum tangential load should cause complete slip.

Three different interaction property combinations were used in Abaqus at the contact interface between the spheres:

- Direct (Lagrange multiplier) normal constraint enforcement, with Lagrange multiplier friction formulation
- Default normal constraint enforcement, with Penalty friction formulation
- Default normal constraint enforcement, with Penalty friction formulation using a reduced value of admissible elastic slip (0.01 of the default slip)

All three methods used a "hard" contact relationship for the normal direction behavior. With the default settings in Abaqus/Standard, the optimal constraint method will be chosen at runtime by Abaqus. This can be a Direct constraint (pure Lagrange multiplier) method, a Penalty constraint method with or without Lagrange multipliers, and an Augmented Lagrange method (a penalty constraint method with augmentation iterations).

For the Penalty friction formulations, the allowable elastic slip used by Abaqus is $\gamma = F_f \bar{l}$, where $\bar{l}$ is a characteristic contact surface length of the current facet on the slave surface, and F_f is the user defined slip tolerance. The default value is $F_f = 5 \times 10^{-3}$.

The results from Abaqus for the tangential displacement vs load are shown along with the analytical solution in the following figure. The results from the Direct Lagrange case (Direct normal constraint with Lagrange multiplier friction) matches the results with the Penalty friction with reduced elastic slip. The results from the case with a default value of elastic slip in the Penalty friction formulation are much softer than anticipated. While none of the cases result in a perfect agreement with the analytical expression, this does teach us that we can use both a Penalty and a pure Lagrange Multiplier friction formulation in Abaqus to obtain commensurate results.

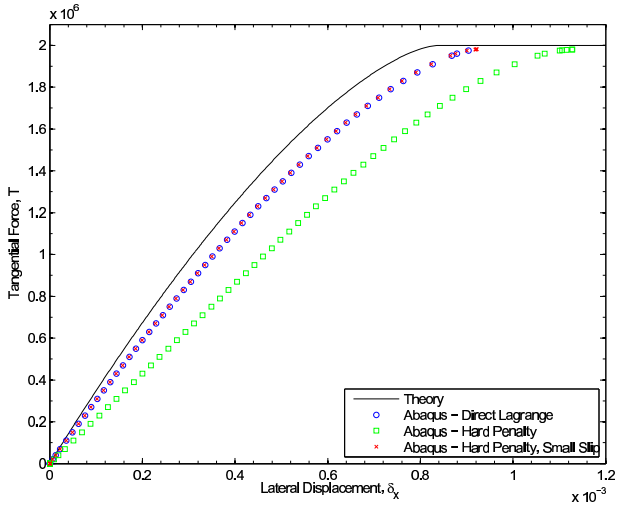

Figure D.23. Mindlin Monotonic Loading Curve.

Lateral displacement vs tangential force for the elastic spheres subjected to compression and a tangential force. Results are shown for various contact penalty stiffness scaling factors.

D.5 Lubkin Problem

Two elastic spheres of radius R_1 are pressed against each other with force P as in the earlier problems. A coefficient of friction μ is assumed at the interface between the spheres. After the application of the normal force, a twisting moment M is applied to the spheres until they slip completely relative to each other. The twist of one sphere relative to the stationary x-y plane is β. This is shown schematically in Figure D.24.

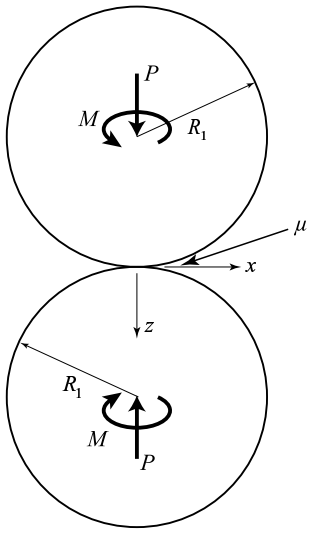

Figure D.24. Schematic of Lubkin Problem.

Lubkin [111] found the following expression for the moment

$$M = \frac{\mu P a}{4\pi}\left\{\frac{3\pi^2}{4} + k'k^2\left[6\mathbf{K}(k) + (4k'^2-3)\mathbf{D}(k)\right] - 3k\mathbf{K}(k)\sin^{-1}k' \right.$$
$$\left. -3k^2\left[\mathbf{K}(k)\int_0^{\pi/2}\frac{\sin^{-1}(k'\sin\alpha)}{(1-k'^2\sin^2\alpha)^{3/2}}d\alpha - \mathbf{D}(k)\int_0^{\pi/2}\frac{\sin^{-1}(k'\sin\alpha)}{\sqrt{1-k'^2\sin^2\alpha}}d\alpha\right]\right\} \tag{D.1}$$

where

$$\mathbf{D}(k) = (\mathbf{K}(k) - \mathbf{E}(k))/k^2 \tag{D.2}$$

and $\mathbf{K}(k)$ and $\mathbf{E}(k)$ are the complete elliptic integrals of the first and second kind, and

$$k' = c/a, \qquad k^2 = 1 - k'^2 \tag{D.3}$$

where a is the contact area and c is the radius of the annulus of the slipping region in the contact area. [111] also found the following expression for the twist of the sphere

$$\beta = \frac{2\mu a}{\pi R_1(1-\nu)}(\mathbf{K}(k) - \mathbf{E}(k)) \tag{D.4}$$

Equations (D.1) and (D.4) may be solved analytically to produce a torque-twist relation, however, [112] shows a simpler approximation to this pair of equations which has less than 3% error

$$M = \frac{3\pi\mu Pa}{16}\left[1 - \exp\left(\frac{-16^2}{3^2\pi}\frac{Ga^2\beta}{\mu P}\right)\right]. \tag{D.5}$$

The moment that causes complete slip can then be approximated as

$$\lim_{\beta\to\infty} M = \frac{3\pi\mu Pa}{16} \tag{D.6}$$

The results are shown along with Lubkin's solution, Equations and (14.18), and Jaeger's approximation, Equation (D.5).

D.5.1 LS-Dyna

The same model described in the previous section is used for this problem, however, the applied tangential displacement is replaced with an applied twist β which is ramped to 0.036 radians ($\beta = 0.018$) after the normal load $P = 2\times10^7$ was applied. The coefficient of friction is $\mu = 0.1$.

As in previous problems, the default penalty stiffness performs very poorly. Larger values of the penalty stiffness scale factor bring the solutions into closer agreement with the analytical solution, but values greater than 100 do not further improve the results.

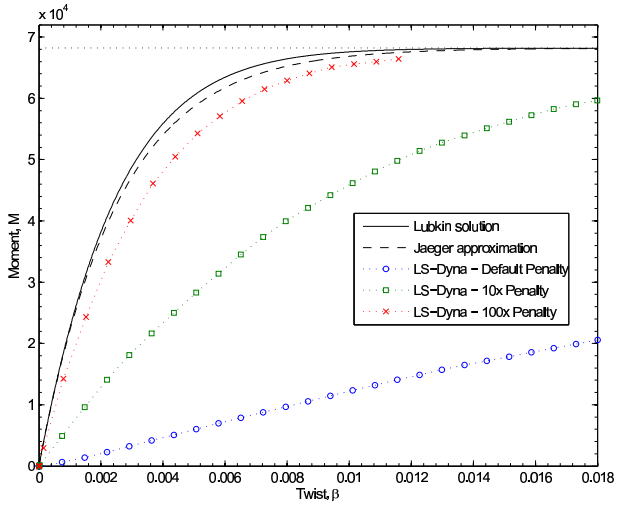

Figure D.25. Lubkin Monotonic Twist Curve.

D.5.2 ABAQUS

The same model described in the previous section is used for this problem, however, the applied tangential force is replaced with an applied moment M which is ramped to 6.8×10^4 after the normal load $P = 2 \times 10^7$ was applied. The coefficient of friction is $\mu = 0.1$.

The Abaqus simulation with small elastic slip matches Lubkin's solution very well. Whereas the simulation with the default elastic slip is about half as stiff. The Abaqus simulation with the Lagrange multiplier friction formulation failed to converge once the twisting stage of the simulation commenced.

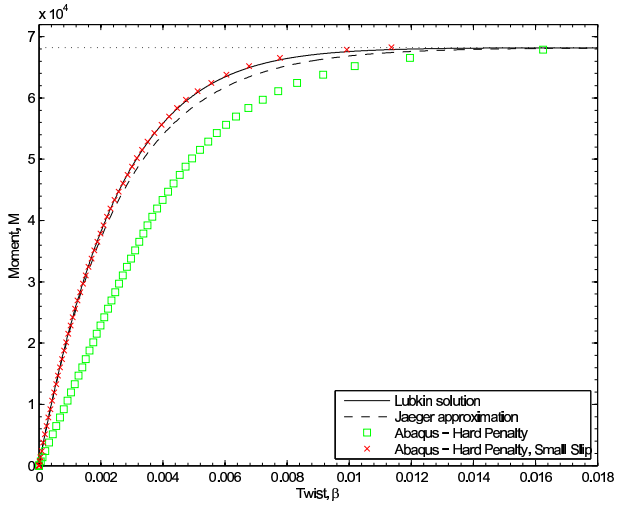

Figure D.26. Lubkin Monotonic Twist Curve.

D.6 Conclusions

For normal contact situations, LS-Dyna Implicit does not perform very well using the default settings in a surface-to-surface penalty type contact. The default penalty stiffness must be scaled by a factor of at least 10 in order to prevent penetrations that incorrectly influence the pressure profile at the contact interface. For tangential frictional behavior, LS-Dyna performs even worse; it requires the default penalty stiffness to be scaled by as much as 100 in order to come close to reproducing analytical results. While it is expected that some scaling would be required in order to simulate the perfect Coulomb friction assumed in the analytical results, the amounts of scaling necessary in LS-Dyna is much larger than one would expect to need to use. Also, the large penalty stiffness values drastically slow down the simulation time. Another drawback of the contact modeling in LS-Dyna is that it does not support a non-penalty (i.e. constraint) type contact formulation in the implicit version of the code.

For normal contact situations, Abaqus/Standard performs very well using the default settings for "hard" contact in a finite-sliding surface-to-surface interaction. When frictional effects are also dominant, it is best to use a penalty formulation for tangential behavior. If the user is very concerned about accurately modeling slip at the interface, then a smaller non-default value of allowable elastic slip should be chosen. For this case, a slip tolerance of $F_f = 5 \times 10^{-5}$ (default $F_f = 5 \times 10^{-3}$) works very well in reproducing results from a pure Lagrange multiplier friction formulation. No noticeable improvements were achieved using smaller values of F_f.

DISTRIBUTION:

,

1 MS 0899 Technical Library, 9536 (electronic)

Sandia National Laboratories